The late Quaternary tephrochronology of the Adriatic region: implications for the synchronisation of marine records

Anna Julie Bourne

Thesis submitted for the degree of Doctor of Philosophy at the University of London

February 2012

Volume I

Institution of study:
Department of Geography
Royal Holloway, University of London

Declaration

This thesis presents the results of original research undertaken by the author and none of the results, illustrations or text are based on the published or unpublished work of others, except where specified and acknowledged.

Signature:  **Date:** 13/02/2012

Abstract

Tephrochronologies for three marine core sequences from the Adriatic Sea have been constructed. Two of the sequences, PRAD 1-2 and RF93-77, are located in the central Adriatic and the third, SA03-03, lies in the southern Adriatic. Isotopic and biostratigraphic records are available for all three sequences, features of which have been used as isochronous markers in the region. This project aimed to establish whether tephra layers provide (a) secure, independent isochronous tie-lines and (b) a robust methodology for testing correlations based on other methods.

A total of 54 tephra layers have been identified within these sequences, of which only 8 are visible layers, the remainder being classified as cryptotephras. Geochemical characterisation of the ash layers has been undertaken using electron microprobe analysis and laser-ablation trace element methods. Geochemical correlation to the detailed tephra record from Lago Grande di Monticchio was performed using chemical element biplots and discriminant function analysis.

Bayesian-based age models were generated for the three Adriatic records using available chronological information that are independent of assumptions of synchroneity between proxy marker events. These models allowed comparisons with tephra and palaeoenvironmental data from Lago Grande di Monticchio and other Mediterranean sites. The results support some assumptions of synchronous regional changes, but not others.

The key outcomes are (a) the recognition of additional (non-visible) distal ash layers that enhance the potential for correlating marine and terrestrial records in the central Mediterranean; (b) volcanic ash records preserved in Lago Grande di Monticchio and in some localities proximal to volcanic sources appear to be incomplete; and (c) isotopic records in Adriatic sediment sequences reflect regional forcing factors more than local conditions.

Acknowledgements

There are a number of people to whom I owe a debt of gratitude and without whom this process would have been considerably more challenging.

Firstly, to my supervisors, **Prof. John Lowe** and **Dr Simon Blockley** for their support, guidance and encouragement, for making me see things in a different light and for challenging my scientific understanding.

To **Dr Ian Matthews** for being interested and enthusiastic and always willing to chat through ideas. You have always gone the extra mile to provide assistance over the last four years, thank you.

To **Dr Fabio Trincardi** for providing access to the core material and for securing funding for this project.

To **Dr Alessandra Asioli, Dr Andrea Piva and Dr Luigi Vigliotti**, from ISMAR Bologna, for allowing me access to proxy data they generated for the marine cores studied in this thesis, for interesting discussions and for willingly answering my numerous questions.

To **Dr Sabine Wulf** for providing her unpublished tephra geochemical database for the Lago Grande di Monticchio sequence, without which this project would not have been possible.

To **Elaine Turton, Dr Adrian Palmer** and **Robyn Christie** for their help and guidance in the laboratories.

To **Norman Chandry, Dr Victoria Smith, Dr Chris Hayward** and **Dr Nick Pearce** for their assistance with the acquisition of geochemical data for this project.

To **Dr Alison MacLeod**, **Mark Hardiman** and **Chris Satow** for useful discussions on tephrochronology and for making lab work considerably more fun.

To the other staff and PhD students at Royal Holloway for their support and guidance. In particular **Dr Ian Candy** for his advice and **Naomi, Tara, Dan, Claire, Dora and Claire** for always being able to provide distraction in the form of tea and cake!

Thank you to my **Mum** and **Dad** for their unwavering support, encouragement and love. Thank you for putting up with me during the writing up process and I am sorry for the pain that proof reading this thesis has caused! You have always been there for me and I am eternally grateful.

Finally, thanks must go to **Pete**, for moving to the "south", for always believing in me and for encouraging me to be the best I can.

Table of Contents

List of Figures

Chapter 4: Methodology

Chapter 5: Results

Chapter 6: Correlation of tephra layers

Chapter 7: Testing regional stratigraphies

List of Tables

Chapter 7: Testing regional stratigraphies

Chapter 8: Constructing independent age models

9. Conclusions

1. Introduction

An important aim of Quaternary Science research is to interpret the geological record over the last 2.6 Myr in order to understand the physical, chemical, biological, atmospheric and human-induced processes that trigger and modulate environmental change at all geographic and temporal scales (Lowe *et al.,* 2007a).

Palaeoenvironmental studies attempt to reconstruct environmental responses to past climatic variations in order to understand the links between different environmental processes and climate and to provide analogues for predictive climate models (Kohfeld and Harrison, 2000). These studies require accurate and precise quantification of past environmental and climatic conditions, as well as their rate of change which in turn is reliant on precise chronology.

This introduction briefly outlines some important paleoenvironmental studies conducted in the Central Mediterranean region which examine events during the last glacial-interglacial cycle and considers how sediment sequences have been linked together to test questions of synchroneity of environmental change throughout the region. It then considers how Mediterranean marine sediment sequences are traditionally dated and the ways in which this aspect of the research can be improved upon. This review of paleoenvironmental research in the region provides the context for the main aims and objectives of this project.

1.1 Mediterranean environmental change over the last glacial-interglacial cycle

Oxygen isotope records from Greenland indicate that numerous rapid climate fluctuations characterise the last glacial-interglacial cycle (Svennson *et al.*, 2008), with some of these rapid climate fluctuations occurring at centennial to millennial scales (e.g. Dansgaard 1985; Alley *et al.,* 1993; Dansgaard *et al.,* 1993; North Atlantic Ice Core Project Members, 2004; Rasmussen *et al.*, 2006).

Alternations between steppe-dominated and forest-dominated ecosystems in the Mediterranean region have been recognised as a reaction to the broad-scale glacial-interglacial climate changes over the Quaternary while there is now evidence from

terrestrial records that Mediterranean vegetation also responded to the more abrupt climatic fluctuations detected in the Greenland ice-core records (Allen, 2003). High frequency oscillation in pollen values during the last glacial-interglacial cycle has been demonstrated in a number of sites across the Mediterranean region (e.g. Tzedakis *et al.,* 1997, Follieri *et al.,* 1998, Magri *et al.,* 1999, Tzedakis *et al.,* 2003). However, investigations at the partially varved sediment sequence Lago Grande di Monticchio, Italy were the first to provide an independently-dated record of millennial-scale variability in the vegetation of Southern Europe throughout this period (Allen *et al.,* 1999) and since then Dansgaard-Oescheger (D-O) cycles have been recognised in a number of Mediterranean terrestrial sites (Figure 1.1a) (Fletcher *et al.,* 2010).

Evidence of millennial-scale climatic oscillations has also been observed in Mediterranean marine sequences (Rohling *et al.,* 1998, Cacho *et al.,* 1999; Paterne *et al.,* 1999, Sanchez-Goni *et al.,* 2002) (Figure 1.1b), suggesting a strong link between oceanographic changes and the atmospheric conditions over the region during the last glacial-interglacial cycle (Sanchez-Goni *et al.,* 2002). In the central Mediterranean, the marine core KET 80-03 from the Tyrrhenian Sea indicates parallels between the frequencies of *Quercus* and *Abies* pollen and the planktic $\delta^{18}O$ record, which has been interpreted as coeval climatic improvements on land and in the sea (Rossignol-Strick and Planchais, 1989). The higher resolution record from the MD90-917 sequence in the Southern Adriatic shows a reduction of arboreal pollen and concomitant expansion of steppic elements, attributed to the Older Dryas and concomitant with Heinrich stadial 1 (Combourieu-Nebout *et al.,* 1998).

These high resolution lake sediment records from southern Europe therefore show rapid environmental fluctuations that appear to correlate well with the Heinrich events recorded in the deep-sea sediments of the North Atlantic and with the D-O cycles of the ice core records from Greenland. This degree of close matching of records suggests that the closely coupled ocean-atmosphere system of the Northern Hemisphere during the last glacial extended its influence at least as far as the central Mediterranean (Woodward and Goldberg, 2001). This connection between the North Atlantic and Mediterranean arises through ocean circulation and currents (Figure 1.2) (Moreno *et al.,* 2005). Atlantic surface waters enter the Western Mediterranean through the Strait of Gibraltar (Figure 1.2). These surface waters are known as Modified Atlantic Water (MAW) throughout the Mediterranean (Moreno *et al.,* 2005) and are then transformed

to Levantine Intermediate Water (LIW) in the Eastern Mediterranean and subsequently become the main contributor to the Mediterranean Outflow Water (MOW) into the Atlantic (Figure 1.2) (Lascaratos *et al.*, 1999).

Despite evidence for millennial-scale climatic oscillations in both Mediterranean terrestrial and marine sequences, it is however, difficult to directly link terrestrial and marine sequences in the region to establish whether the observed millennial-scale oscillations seen in the various proxy records were precisely in phase with one another. One approach would be to undertake pollen analysis on marine cores alongside oxygen isotope analysis (Tzedakis *et al.*, 2001). However the pollen records that currently exist for Mediterranean marine sequences are at too coarse a resolution for studies at sub-millennial scales (e.g. Cheddadi *et al.*, 1991; Cheddadi and Rossignol-Strick, 1995, Combourieu-Nebout *et al.*, 1999).

A second method of linking the terrestrial pollen records of millennial-scale oscillations and fluctuations in marine $\delta^{18}O$ records would be to use tephra layers as a correlation tool. Existing tephrostratigraphical schemes for the Mediterranean are largely or entirely based on analysis of visible tephra layers (e.g. Keller *et al.*, 1978; Paterne *et al.*, 1988, 2008; Calanchi *et al.*, 1998; Calanchi and Dinelli, 2008) and while tephra layers have been regarded by some as a potentially useful tool, their occurrence is too irregular for systematic correlation or dating of sequences (Tzedakis *et al.*, 2001).

That potential has been enhanced, however, with the discovery of discrete, non-visible tephra layers, composed of sub-microscopic glass shards and variously termed cryptotephras or microtephras, preserved in some Mediterranean basins (Siani *et al.*, 2004; Bourne, 2006; Lowe *et al.*, 2007b). These fine-grained tephra deposits can be extracted from host sediments by density separation methods (Turney, 1998; Blockley *et al.*, 2005), the results demonstrating that marine sequences commonly contain considerably more distal tephra layers than previously appreciated. Successful detection of these cryptotephras therefore greatly enhances the potential application of tephrostratigraphy as an independent correlation method to link marine and terrestrial records in the region.

1.2 Traditional approaches to dating Mediterranean sequences

Traditional approaches to the dating and correlation of Mediterranean records of late Pleistocene age include the use of radiocarbon dating, biostratigraphic 'markers' and oxygen isotope stratigraphy, all of which will now be considered in detail.

1.2.1 Radiocarbon dating

Radiocarbon dating is the method most routinely employed to date marine sequences spanning the last ca. 50,000 years (Lowe *et al.*, 2007b). This section will examine the problems that constrain radiocarbon age determinations in paleoenvironmental research, focussing on problems that particularly affect the Mediterranean Sea. A complete review of the principles of radiocarbon research lies outside the scope of this chapter but is provided by Walker (2005, pp: 18-24).

Radiocarbon ages are calculated from the ratio of the radioactive carbon isotope ^{14}C to one of the stable isotopes (^{12}C or ^{13}C) in the sample compared to a standard (Reimer and Reimer, 2007). The precision and accuracy of radiocarbon dates from marine samples are constrained by four groups of uncertainty 1) analytical precision, 2) geological and stratigraphical integrity of the dated material, 3) marine reservoir effects and 4) calibration procedures (Lowe *et al.*, 2007b).

Analytical precision is determined by the ability to measure the amount of ^{14}C present within a sample and is usually presented as a mid-point with associated standard counting error (Scott, 2007). The 1σ analytical error ranges for most radiocarbon dates are in the order of 80 – 150 radiocarbon years (± 40 to ± 75). These errors can be easily quantified but not easily reduced, limiting the potential to date events with a higher temporal resolution (Lowe *et al.*, 2007b). This error term is not an indication of the accuracy of the sample age, only of the precision with which the sample activity has been measured. In order to examine the reliability of an age estimate, it is necessary to evaluate the geological integrity of the sample.

An assumption when using radiocarbon dating is that the constituent carbon in each sampled horizon is contemporaneous with the time of sediment accumulation which is unlikely as sediment horizons are not closed systems (Lowe *et al.*, 2007b), which introduces an unquantifiable source of error into radiocarbon dating. For example,

results can be skewed if even a small amount of organic matter is younger than the true age. Reworking of material, contamination during sampling, growth of modern fungi or bacteria, and rootlet penetration are all factors that can cause a deviation from the true age of a sample. Of these, reworking of material through bioturbation and contamination during sampling are greater sources of error when working in marine environments (Blockley *et al.,* 2007). Whilst these sources of error are difficult to quantify, they can be minimised by undertaking radiocarbon sampling under controlled conditions (Baratt and Reimer, 2007) and by selecting specific types of microfossil to date, such as single species of planktonic foraminifera as even very small fossils can be dated using AMS methods (Bard *et al.*, 2004).

An additional source of error affecting radiocarbon dating of marine fossils is the marine reservoir effect. It is an offset in radiocarbon age between contemporaneous organisms that derive their carbon directly from the atmosphere and those organisms that live wholly or partly in the marine environment (e.g. foraminifera, molluscs) or those that incorporate marine carbon by ingestion (Ascough *et al.,* 2009). This is caused by ocean circulation processes and variations in the rate of carbon exchange between the ocean and atmosphere (Ascough *et al.,* 2005). The oceans have a large store of 'old' carbon and therefore organic matter that draws its carbon partly or completely from a marine environment has an anomalously old radiocarbon age which needs to be corrected for (Reimer and Reimer, 2007). Until comparatively recently, a standard correction of 400 years (R_t) was applied to all marine radiocarbon age estimates but modern ocean surface reservoir effects have subsequently been shown to vary with latitude and circulation effects. Therefore local correction factors now need to be determined and applied to marine radiocarbon dates which are expressed as deviations from R_t known as ΔR (Reimer and Reimer 2001). Whilst a correction can be applied to account for marine reservoir effects, their magnitudes have not remained constant over time, with Siani *et al.* (2001) reporting significant temporal variations in the Mediterranean marine reservoir effect during the recent past. Finally, the marine reservoir effect may also alter with water depth which provides another element of uncertainty and renders radiocarbon-based age modelling of marine sequences extremely problematic (Bronk Ramsey, 2008a).

The Mediterranean Sea and the Adriatic basin in particular can be particularly sensitive to variations in the marine reservoir effect both over time and with water depth, due to

the constrained geometries of both basins. This means that fluvial freshwater influences, in addition to North Atlantic circulation changes and changes in atmospheric ^{14}C, can all contribute to changes in apparent radiocarbon age of surface waters in the basins (Siani *et al.,* 2000). Finally, at times of low sea level the Adriatic basin can become isolated from the wider Mediterranean Sea, due to the presence of sills and structural highs (Piva, 2007) which has an effect on circulation within the sea and subsequently the magnitude of the marine reservoir effect (Siani *et al.,* 2001).

The final source of uncertainty for radiocarbon dates is calibration. The calculation involved in generating a radiocarbon age estimate assumes that the level of ^{14}C in the atmosphere has been constant since the time the sample being analysed grew or formed (Reimer and Reimer, 2007). However, this is not the case and the amount of ^{14}C in the atmosphere has varied over time, meaning that radiocarbon time is not only not calendar time but it is also not linear. Radiocarbon dates therefore require calibration to determine a sample's true age and so that radiocarbon dates can be compared reliably to other calendar ages derived from incremental methods such as those based on ice core layer or varve counting (Reimer *et al.,* 2009). IntCal09 is the current internationally accepted standard model for radiocarbon calibration (Figure 1.3). It is based upon radiocarbon-dated tree ring samples from the present back to 12,550 cal BP, which is unchanged from the IntCal04 model for this particular period (Reimer *et al.,* 2009).

Beyond 12,550 cal BP, the curve is based upon marine coral data sets which are mainly the same as those used for IntCal04 but with a few exceptions. New data has been introduced based on Pacific and Barbados corals (Fairbanks *et al.,* 2005), while some data such as those from the Cutler *et al.* (2004) record were removed as the corals are thought to be affected by a freshwater lens (Reimer *et al.,* 2009). Radiocarbon measurement from the Iberian margin core MD95-2042 (Bard *et al.,* 2004) are also included in IntCal09, while portions of the IntCal09 curve between 14.5 – 50 cal ka BP rely heavily on the non-varved Cariaco Basin data-set of Hughen *et al.* (2004) (Reimer *et al.,* 2009). The timescales of both the Cariaco and MD95-2042 data-sets are produced by correlations to the Hulu Cave speleothem $\delta^{18}O$ record (Wang *et al.,* 2001). Both chronologies must still be considered as work in progress, awaiting refinements by

correlation with more independent data, using more suitable records (Reimer *et al.,* 2009). Whilst IntCal09 is not definitive, it does provide significant improvements for calibrated dates older than ~12 cal ka BP (Reimer *et al.,* 2009), which therefore makes radiocarbon dating more applicable to studies over the last glacial-interglacial cycle as more of the time-period is accessible using the technique.

In conclusion, no matter what the degree to which additional sources of radiocarbon dating error might be reduced, calibration will usually introduce an additional and significant error term, over and above those associated with laboratory precision and geological context. Calibration will therefore normally reduce the precision of a date but improve its accuracy, as the computed calibrated age range is more likely to encompass the true age of the sample (Lowe *et al.,* 2007b).

1.2.2 Biostratigraphic marker events

High-resolution biostratigraphic records of well-dated marine cores provide a valuable contribution to palaeoclimatic studies as they facilitate correlations between different oceanographic basins (Siani *et al.,* 2010).

In the Mediterranean and for the Adriatic Sea in particular, micropalaeontological studies of different taxonomic groups (foraminifera, nannofossils, pteropods and dinocysts) carried out on deep sea sequences have been used to reconstruct the environmental history of the region (e.g. Rohling *et al.,* 1993; Capotondi and Morigi, 1996; Sangiorgi *et al.,* 2002; Giunta *et al.,* 2003), with quantitative analyses of planktic foraminifera used to generate a biochronological framework for the central and southern Adriatic basins (Jorissen *et al.,* 1993; Asioli *et al.,* 1999, 2001; Capotondi *et al.,* 1999; Siani *et al.,* 2010).

The biochronological frameworks that exist for the Mediterranean and Adriatic Seas are based upon foraminiferal events, such as the first occurrence (FO) or entry of a foram species in a sequence as well as a foram species' last occurrence (LO) in the sequence. Significant changes in the distribution of foraminiferal or nannofossil taxonomic units allow the identification of events which comprise ecozones and allow boundaries of different ecozones to be defined (Sprovieri *et al.,* 2003). The boundaries of ecozones and the macrofossil events are then dated using a master sequence chronology, often by

radiocarbon dating of the master sequence and interpolating the age of the events or boundaries, if they cannot be directly dated (Capotondi *et al.,* 1999). The dates for ecozones and bioevents are then imported into other sequences where similar foraminiferal assemblages are noted but where chronological control for the core may be lacking.

The use of biostratigraphic marker events to correlate records assumes synchroneity in both appearance and extinction of different taxa over the whole of the Mediterranean (Asioli *et al.,* 2001). This assumption needs to be tested and may be difficult to demonstrate for events that were extremely abrupt (decadal in manifestation) or very short-lived (centennial or shorter in duration). This is especially important as a recent study of Adriatic biochronological frameworks by Siani *et al.* (2010) has shown that, whilst some of the ecozones and events are in accord between the different frameworks, some key differences can be seen in timing between biozone boundaries and also in the composition of the faunal assemblages that define the zones (Siani *et al.,* 2010). These differences have been attributed to dating uncertainties such as poor marine reservoir corrections and radiocarbon dates performed on mixed Foraminifera and pteropod species (Siani *et al.,* 2010). Previous studies using tephrostratigraphy in New Zealand have also revealed that some macrofossil and nannofossil bioevents are actually diachronous between different basins and whilst many microfossil species do occur in consistent stratigraphic order relative to the position of tephra layers, some key species do not (Shane *et al.,* 1995). This has never been independently tested in the Mediterranean region, something that is important as it is necessary to establish if this approach for dating and correlating regional paleoenvironmental changes is robust, especially as the approach often rests upon radiocarbon dating of the events in the first place.

1.2.3 Oxygen isotope stratigraphy

Beyond the limit of radiocarbon dating, the stratigraphic framework and dating of Quaternary marine sequences has been derived from measuring oxygen isotope ratios in marine carbonates (Anderson, 2007). The marine oxygen isotope record has been divided into a series of isotope stages (MOI stages) and there are two main methods for dating the MOI record (Walker, 2005).

The first uses the palaeomagnetic record in ocean sediments and the major geomagnetic boundaries which reflect reversals in the earth's magnetic field (Walker, 2005). For example the Brunhes-Matuyama boundary, located in MOI stage 20, the onset of the Olduvai event in MOI stage 63 and the Matuyama-Gauss boundary in MOI stage 104 (Shackleton *et al.*, 1990). The reversals are detected in volcanic rock and so their ages can be estimated using Potassium-Argon dating (e.g. Tarling, 1983). The dates of the MOI stage boundaries are then interpolated (using estimated sedimentation rates) from the reversal depths and ages (Walker, 2005). However, as this research will focus on the last glacial-interglacial cycle, the studied sequences will all belong to the Brunhes normal-polarity Magnetozone and therefore this approach to dating the MOI record is not applicable in this case.

The second method relies on the fact that oxygen isotope variations through time are dominated by cycles that are correlated with orbital cycles in solar radiation which can be calculated with a high degree of accuracy independently of the sediment record (Anderson, 2007), a procedure known as orbital tuning. The age of each cycle within the oxygen isotope record (and therefore each MOI stage boundary) can be calculated by extrapolating back from the present day (Walker, 2005). Imbrie *et al.* (1984) created the SPECMAP timescale by tuning an amalgamation of several isotope records (known as stacked records) to the known astronomical variable frequencies over the past 800,000 years (Figure 1.4a). Records were stacked as the global isotopic changes related to ice-sheet waxing/waning would be enhanced in a composite curve, whereas local/regional variations would be cancelled out. Therefore, stacking is useful as it results in a defined set of isotopic events that in principle can be found in all open ocean sediment cores (Bassinot, 2007).

Martinson *et al.* (1987) produced a 300 ka stacked $\delta^{18}O$ record, which has higher temporal resolution than SPECMAP and also contains short events which are of global significance that were not seen in the SPECMAP record (Bassinot, 2007). This allowed for the identification of MOI substages, where events within a stage are given a decimal notation, with negative excursions assigned odd numbers and positive excursions assigned even numbers (Figure 1.4b), making the Martinson *et al.* (1987) record the preferred target record for the upper Pleistocene (Bassinot, 2007).

Since the development of SPECMAP, further stacked records have been produced covering wider timescales (e.g. Shackleton *et al.,* 1990). These also address problems encountered with SPECMAP, such as an erroneous Brunhes–Matuyama magnetic reversal age assignment by Imbrie *et al.* (1984) and the incompleteness of some of the isotope records used by Imbrie *et al.* (1984) (Bassinot, 2007). More recently, Lisiecki and Raymo (2005) have developed a 5.3 Ma stack of 57 globally distributed benthic $\delta^{18}O$ records which were aligned by an automated graphic correlation algorithm and the age model was developed by tuning the $\delta^{18}O$ stack to a simple ice model based on 21st June insolation at 65°N. This is recognised as the most robust reference for benthic oxygen isotopic stratigraphy of the Pliocene–Pleistocene (Bassinot, 2007) and is used to develop chronologies for new core sequences by aligning oxygen isotope records to the stacked $\delta^{18}O$ time series such as the Lisiecki and Raymo (2005) record (Anderson, 2007).

This dating approach has been used widely in central Mediterranean studies (e.g. Capotondi *et al.,* 1999; Kallel *et al.,* 2000; Lourens, 2004; Piva *et al.,* 2008a). Although this oxygen isotope model is widely used, it is not without problems. For example, some marine basins have very low sedimentation rates, meaning a single isotope sample may span a time interval of several thousand years (Walker, 2005). Low stratigraphic resolution may also be exacerbated by sediment mixing on the sea floor and in some cases gaps in the depositional record may lead to the mis-correlation of isotope records. Mis-correlation of isotopic events or the incorrect attribution of a warm stage to a full interglacial can also lead to incorrect tuning to the stacked record (Walker, 2005). Finally, despite its wide application and the assumed synchroneity of the MOI record in different geographic locations, the correlation of records to SPECMAP or other stacked $\delta^{18}O$ records is still based on the assumption that ice volume fluctuations have been globally synchronous, at least when considered with a resolution comparable to the mixing time of the ocean basins which is <100 years for the Mediterranean Sea, according to Lacombe *et al.* (1981), and about 550 years for the Atlantic Ocean according to Broecker (1979). It is important to provide a test of this assumption, especially for long sequences that could also be affected by low stratigraphic resolution and sea-floor mixing, where mis-correlation of MOI stages is more likely.

1.2.4 Summary

Despite the three main methods for dating Quaternary Mediterranean marine sequences being widely applied, at present, errors and untested assumptions beset each method. Some of the problems are compounded when one of these approaches is used to date another, for example the radiocarbon dating of bioevents and ecozones, with the results then being used to validate the assumption of time synchronous bioevents in a region.

In view of these uncertainties, attention has increasingly been turning to the use of other independent dating methods such as volcanic ash chronology (tephrochronology) to provide a more stable framework. Ash layers can firstly provide isochronous marker horizons (tephrostratigraphy) that can be used to corroborate or invalidate correlation schemes based on other approaches. Secondly, if the ash layers can successfully be dated by independent means (e.g. by $^{40}Ar/^{39}Ar$ dating or by varve chronology) then they can provide robust and independent tests of age models based on other methods.

1.3 Thesis structure

Following this brief introduction to (a) the history of environmental change in the Central Mediterranean over the last glacial-interglacial cycle (b) the methods used to date Central Mediterranean sequences and (c) the need for accurate and precise Quaternary chronologies that are independent of biostratigraphic and climatic assumptions (Chapter 1), the remainder of this thesis is divided into eight chapters and three appendices with the following progressive themes.

Chapter 2 – Tephra Studies

This chapter outlines the main Quaternary volcanic provinces in the Mediterranean region and the major eruptions that are known to have generated distal tephra layers. It then considers the main terrestrial and marine sequences in which tephra layers have been preserved and finally the different nomenclatures applied to the definition and classification of various tephra layers.

Chapter 3 – Site and Core descriptions

The geological and oceanographic settings of the Adriatic Sea are considered in this chapter, while previous work in the area that provide the scope for this project is also reviewed. The chapter also introduces the three sediment sequences investigated in this

project and the proxy information that is available for each core, focussing on the oxygen isotope stratigraphy, foraminiferal biostratigraphy, sapropel stratigraphy and magnetostratigraphy of each sequence. Finally, it refers to other palaeoclimate records obtained from other marine and terrestrial sites in the region for which tephra work has been undertaken. Chapter 3 closes with the specification of project aims and objectives in light of the material covered in both chapters 2 and 3.

Chapter 4 – Methodology

This chapter outlines the experimental methods used within this thesis, as well as the data exploration and quality control procedures employed.

Chapter 5 – Results

This chapter presents the body of the tephra results for each core sequence, reporting the quantified number of shards for each layer and the initial chemical classification of each layer.

Chapter 6 – Correlation of tephra layers

Here, the geochemical information obtained for each layer is compared with the geochemical data available from the Lago Grande di Monticchio (LGdM) sequence, a key record of tephra layers from the Central Mediterranean that is first introduced in chapter 2. In order to ease the correlation procedures, the LGdM dataset is initially explored with the eruptions from different volcanic centres being classified into statistical clusters and subsets, which facilitates comparison between the LGdM subsets and clusters and the geochemical data from this study. The most geochemically distinctive layers are correlated first to provide a framework for correlating less geochemically distinctive layers, aided by evidence of stratigraphic superposition.

Chapter 7 – Testing Regional stratigraphies

This chapter uses the tephra layers correlated in chapter 6 as time-parallel stratigraphic marker layers to test whether other events identified in the cores, such as lithostratigraphic boundaries, foraminiferal bioevents, and oxygen isotope variations, occur consistently in the same stratigraphic positions relative to the positions of key tephra layers. This is considered initially for the three cores in the Adriatic Sea studied in this project and then widened to consider other Mediterranean records.

Chapter 8 – Constructing Independent Age Models

This chapter assesses the age estimates of tephra layers considered in chapter 6. Using the best age estimates of the eruptions, age models are generated for each of the 3 sediment sequences examined in this thesis and are compared with existing models for each core based on alternative approaches.

Chapter 9 – Conclusions

The thesis finishes with an assessment of how well the aims and objectives of the investigation have been met. The final chapter also considers some aspects of the research that could have been conducted differently in the light of new findings with suggestions about additional work that could be undertaken in the future to enhance the research.

Three appendices are provided that give full details of (a) tephra shard counts for PRAD 1-2, SA03-03 and RF93-77, (b) the standard data employed including geochemical analysis of standards analysed as part of this research and (c) the raw geochemical data obtained for all samples analysed in this thesis.

2. Tephra Studies

This chapter will explore the principles and background to tephra studies before focussing on tephra research that has been undertaken in the Mediterranean region and the implications this has for the research objectives of this study.

The word tephra is from the Greek word τεφρα meaning 'ashes'. Tephra comprises all the explosively-erupted, unconsolidated pyroclastic products of volcanic eruptions, including both fall deposits and deposits from pyroclastic flows or surges so long as they remain unconsolidated (Alloway *et al.,* 2007). The term tephra applies to all volcanological grain sizes: ash (grains <2 mm in diameter), lapillus or lapilli (2 - 64 mm), and blocks (angular) or bombs (subrounded) (>64 mm). These grain-size units can be subdivided further into classes such as coarse ash and fine ash (Lowe, 2011).

Until relatively recently, tephra studies concentrated on visible ash layers which are prominent in sedimentary sequences either because the individual glass shards are relatively large and/or because the concentration of glass shards is very high (Alloway *et al.,* 2007). However, within the last two decades, developments in detecting tephra layers that are invisible to the naked eye have led to the growth in the application of tephra studies to sites more distal from volcanic centres. These non-visible tephra layers are known as cryptotephras (from the Greek work kryptein meaning 'to hide') and comprise fine to extremely fine ash-sized concentrations of glass shards (typically 10 – 125 microns) (Lowe, 2011). This investigation deals primarily with the identification of the vitreous (glass) component of non-visible ash layers in Adriatic marine sediments. Therefore, any non-visible ash layers (cryptotephras) identified in this research will simply be termed as tephra or ash layers. Where a layer is visible to the naked eye, this distinction will be made.

Tephra deposits have a number of special features: (1) they are erupted over a matter of only hours or days to perhaps weeks or months and therefore can be considered to be deposited instantaneously over geological time; (2) they can be spread widely over land and sea to form a layer that (unless reworked) has the same age wherever it occurs (Alloway *et al.,* 2007); (3) they are preserved within a variety of geological settings (e.g. marine (Calanchi *et al.,* 1998), terrestrial (Machida, 1999), lacustrine (Lowe and Turney, 1997) and glacial contexts (Mortensen *et al.* 2005)). Therefore, once identified

a tephra layer provides a time-parallel marker horizon or isochron for an 'instant' in time, that instant being the date of the eruption that produced the layer (Alloway *et al.*, 2007). These features make tephra layers very useful in paleoenvironmental studies as they allow sequences to be either correlated and/or dated (Lowe, 2011).

Therefore, there are two major applications of tephra in paleoenvironmental research. Firstly, tephrostratigraphy, which refers to the study of sequences of tephra layers and related deposits, relying on the Law of Superposition, which applies in any study that connects deposits in one place with those at another (Lowe, 2011). In order to produce a tephrostratigraphy, tephra layers must be defined, described and characterised using at least one of their physical, mineralogical, or geochemical properties and whether this is achieved through field or laboratory processes depends on the scale of tephra layer being examined (Alloway *et al.*, 2007). Once the key properties (physical and chemical) of tephra layers in different sequences have been established, tephra layers can be correlated between sequences which can test the ordering of other paleoenvironmental events in different sequences.

Secondly, once a tephrostratigraphy has been established for a sequence, it is possible to convert it into a tephrochronology record. Tephrochronology is the use of tephra layers as isochrons or time parallel marker layers, which relies on the determination of absolute or relative ages of the tephra layers. This allows sequences to be synchronised using precise tie-points and the establishment and transfer of relative or numerical ages (Lowe and Hunt, 2001).

Frequently, however, the term tephrochronology has tended to be used in a broader way as a stand-alone term for all aspects of tephra studies (e.g., Shane, 2000; Lowe, 2011).

2.1 Principles of tephra research

Tephrochronology has the potential to provide absolute links between geographically distant sequences with a precision that is currently unmatched by most other chronological tools in palaeoenvironmental research. However, successful tephrochronological research relies on three fundamental principles, 1) Stratigraphy, 2) Characterisation and 3) Chronology. Each of these factors is crucial if tephra layers are

to be successfully matched between different sequences but also linked to known volcanic eruptions. These principles are considered below.

2.1.1 Stratigraphy

The stratigraphic signature of an eruption changes in character depending on the distance from the source volcano. In proximal areas dry-land sites preserve tephra layers ranging from metres to centimetres in thickness that can be mapped and traced from outcrop to outcrop and from proximal to more distal locations using the stratigraphic relationships and physical properties of the layer, including, for example, colour, bedding characteristics, pumice density or the presence of phenocrysts (Lowe, 2011). Tephra layers that are distinctive from other adjacent layers (e.g. in thickness, colour) provide key reference horizons within a sequence and therefore become stratigraphic markers that can be easily traced between sites. With increasing distance from the volcanic source, tephra layers normally become thinner and more fine-grained in comparison to proximal deposits and they may also lose some diagnostic features. Therefore, tracing distal tephra layers and their stratigraphic relationships to link sequences is limited to deposits that are in the order of centimetres in thickness (Lowe, 1988). In proximal areas, air-fall tephra deposits tend to evenly cover the pre-existing topography like snow and this fact, combined with the stratigraphic studies of dry-sites, as well as the study of visible layers in sediment cores from lake or peat bogs, allows tephra distribution patterns to be mapped (Figure 2.1). These maps show isopachs (lines depicting deposits of equal thickness) and allow the volume and magnitude of an eruption to be assessed (Lowe, 2011). However, in distal areas where only cryptotephra layers are preserved, air-fall deposits may not evenly cover the pre-existing topography and, even within a lake basin, other post-deposition processes cause tephra layers to be discontinuous (Pyne-O'Donnell, 2010). Furthermore, at proximal sites, subsequent, more recent eruptions can lead to the evidence of older volcanic events being removed and hence the stratigraphic relationships between tephra layers may differ between proximal and distal sites, an important point to bear in mind when correlating tephra layers based on their stratigraphic succession.

A further important consideration when investigating the stratigraphy of tephra layers is the distinction between primary air fall tephra layers deposited in a single event and secondary deposits arising from reworking or other processes (Lowe, 2011). This is

especially important when studying tephra layers in marine environments, where even though the time taken for tephra particles to sink to the sea bed is rapid, depositional processes in the sea can be complex with thin layers potentially subject to bioturbation leading to reworking, while turbidity currents can rework previously slumped tephra layers (Manville and Wilson, 2004).

The study of cryptotephra layers brings additional challenges. With a cryptotephra layer, there is no visible marker in the sediment and so their identification relies on the application of other techniques, such as magnetic susceptibility and remanent magnetisation measurements (e.g. Hodgson *et al.,* 1998, Rasmussen *et al.,* 2003, Vogel *et al.,* 2010a, Brendryen *et al.,* 2010), X-ray fluorescence (XRF) analysis (Gehrels *et al.,* 2008), X-radiography (Dugmore and Newton, 1992), spectrophotometry (Gehrels *et al.,* 2008), high resolution micro-petrography (de Vleeschouwer *et al.,* 2008) and loss-on-ignition variations (Gehrels *et al.,* 2006). Whilst these techniques have identified low concentrations of glass shards, they require the use of expensive equipment which is not always readily available. Therefore, cryptotephra studies commonly rely on tephra concentration methods such as ashing (burning), stepped acid or alkali digestion to remove organic matter (e.g. Hall and Pilcher, 2002), or density separation by flotation to isolate glass shards from organic material and heavy minerals (e.g. Turney, 1998, Blockley *et al.,* 2005) to study the whole of a sequence and physically extract the glass shards. This is followed by optical microscopy to identify the glass shards, to assess their concentrations and, ultimately, to allow identification of discrete cryptotephra layers.

In the absence of visible markers in the sediment, there may be some debate as to the precise horizon within the sediment column that represents the volcanic eruption. Some assume it to be where the peak glass shard concentrations occur (e.g. Almond, 1996; Matthews *et al.,* 2011), while others suggest the first rise in glass shard concentrations. In some instances, however, there is no clearly defined peak or the glass shards may be spread over a wide stratigraphic interval. Manville and Wilson (2004) find that marine tephra layers that are not bioturbated tend to have sharp bases but gradational upper contacts. In such cases, it may be more appropriate to use the first appearance of glass shards as the volcanic event, with it being the same age or slightly younger than the volcanic eruption. However, as this research will show, few cryptotephra layers show

this ideal arrangement and hence no single criterion is used to denote the eruption event. Each tephra layer is assessed on its own configuration and stratigraphic context.

2.1.2 Characterisation

Tephra studies rely on precise and accurate characterisation of tephra layers which can be undertaken using different techniques depending on distance from the volcanic source. In proximal locations, initial characterisation involves logging lithological and sedimentological features of individual tephra units, as well as measuring grain size variations. For example, for late Pleistocene tephra units on the Campanian Plain, the lithological characteristics of each layer are recorded, including the grain size and sorting of the grains. Then the lithology including morphology and colour of grains is recorded (Di Vito *et al.,* 2008). Similar characterisation can be extended to sites located further from the volcanic source where tephra layers remain visible. For example, tephra layers from the San Gregorio Magno basin were defined initially using grain size characteristics, with colour changes used to distinguish between different layers composed predominantly of sand-sized particles (Munno and Petrosino, 2007). This physical characterisation approach can be aided by petrological analysis of the mineral suite contained within each tephra layer (e.g. Preece *et al.,* 2000, Wulf *et al.,* 2004, Lowe *et al.,* 2008). Whilst the characterisation of the mineral and lithic assemblage can be a useful characterisation tool, preferential settling of tephra with distance from the source volcano can lead to significant variations in mineralogical composition. Hence the mineral composition alone may not provide a consistent basis for tracing tephra layers between sites (Wulf *et al.,* 2004). Atmospheric sorting of volcanic eruptives during transport often results in distal tephra layers (>~100 km from source) being mineral poor which precludes their classification by this means (Alloway *et al.,* 2007).

As a result of the above limitations, chemical classification of tephra layers, in particular using the vitreous tephra phase, has become a more standard procedure for identification purposes. Glass composition approximates the chemical composition of the magma at the time of its eruption and provides a potentially unique signature due to the complexity of the eruptive processes (Lowe, 2011). Tephra chemistry can be obtained from “whole-rock” or bulk (multi particle) tephra deposits. However, the results are of little use for tephra characterisation and, especially, subsequent correlation because the composition may be influenced by mineral inclusions and impurities such

as xenocrysts and xenoliths, as well as the inclusion of detrital grains that are unrelated to volcanic processes (Shane, 2000). Therefore, tephra chemistry of individual glass shards yields the most reliable results in both proximal and distal contexts and is often the only feasible way to characterise cryptotephras. Electron Microprobe Analysis (EPMA) is the technique most widely employed to determine the major element composition of glass shards (Lowe, 2011). Increasingly, single-shard, laser ablation, inductively coupled, plasma mass spectrometry (LA-ICPMS) is being used to provide grain-specific trace element data that can aid in the characterisation of tephra layers (e.g. Pearce *et al.,* 2004, 2007) (Alloway *et al.,* 2007).

A major difficulty that complicates the interpretation of tephra chemistry, however, is that volcanoes can erupt successive tephra layers with the same geochemical signature, as observed in Icelandic, Italian and New Zealand eruptives (Lowe 2011). The Icelandic volcano Katla, for example, has erupted a number of silicic tephra layers, all with the same major element geochemistry. The most widespread of these is the Vedde Ash which occurs in the middle of Greenland Stadial 1 (GS-1, approximately equivalent to the Younger Dryas) (Matthews *et al.,* 2011). This is an important marker layer in sediment sequences but five other distal ash layers with the same Katla-type chemistry as the Vedde Ash have been reported from sites in the North Atlantic region (Matthews *et al.,* 2011); the Dimna ash which predates Greenland Interstadial 1 (GI-1) (Koren *et al.,* 2008); the IA2 ash associated with GI-1 (Bond *et al.,* 2001); a layer only found in the NGRIP ice-core record which pre-dates the Vedde Ash by less than 100 years (Mortensen *et al.,* 2005); a tephra layer found in several sites in Scotland which coincides with the GS-1/Holocene boundary (MacLeod *et al.,* in prep.) and the Suduroy Tephra, dated to ca. 8.0 cal ka BP (Wastegard, 2002; Pilcher *et al.,* 2005; Matthews *et al.,* 2011). This highlights a problem with the use of tephra layers as isochrones because, even though the layers are well characterised, it is not possible to discriminate between them on chemical composition. Consequently, multiple criteria and more than one line of evidence are commonly necessary to correlate a tephra layer with an individual eruption with a high degree of confidence. Stratigraphic position and independent chronological controls should be used, where possible, alongside glass chemistry to discriminate between tephra layers of similar chemical composition (Lowe, 2011). Such an approach was adopted by Wulf *et al.* (2004) for the correlation of tephra layers of Campanian origin preserved in the Lago Grande di Monticchio sediment sequence, in view of the homogeneity of erupted magmas from the Campi Flegrei and

Ischia Island volcanoes. Tephra layers were matched to known eruptions using a combination of geochemical, mineralogical and stratigraphical data (Wulf *et al.,* 2004), an approach similar to the one adopted in the present study.

2.1.3 Chronology

Independent dating of tephra layers is essential for building a regional tephrochronology. Tephra layers can be dated directly or indirectly. In proximal sequences or distal deposits with visible ash layers, tephra layers can be directly dated by radiometric determinations on the primary mineral constituents, e.g. fission-track dating (e.g. Meyer *et al.,* 1991), potassium-argon dating (e.g. Pinti *et al.,* 2001) and $^{40}Ar/^{39}Ar$ dating (e.g. Ton-That *et al.,* 2001) (Walker, 2005). Fission-track (FT) dating of tephra layers uses coexisting zircon and glass phases, though this technique is difficult to apply to distal tephra layers due to the often low abundance of zircons and fine grain sizes (Alloway *et al.,* 2007). $^{40}Ar/^{39}Ar$ dating relies on the presence of potassium-rich minerals such as sanidine or anorthoclase (Lowe, 2011) which limits the application of this technique to calc-alkaline volcanic provinces (Alloway *et al.,* 2007). It has, however, been widely and successfully applied for dating Italian tephra layers and Mediterranean sequences (e.g. De Vivo *et al.,* 2001; Deino *et al.*, 2004, Lanphere *et al.,* 2007). The technique has also been applied to date visible layers in more distal sequences, for example by Kraml (1997) in cores recovered from the Ionian Sea. The technique has yet to be applied to the dating of cryptotephra layers due to the small glass grain size and lack of a mineral phase that characterises distal ash layers. One final method of direct dating of tephra layers is through historical records of eruptions. One of the most widely known historical accounts is that of Pliny the Younger who documented the death of his uncle in a letter whilst observing the AD 79 eruption of Vesuvius. Historical accounts of eruptions have been used to date more than 100 Icelandic eruptions (Alloway *et al.,* 2007).

Where tephra layers are associated with organic material (e.g. leaves, twigs, seeds or shells), then radiocarbon methods (an indirect dating method) can be employed to date the layer (e.g. Birks *et al.,* 1996). The organic material must be contemporaneous with the tephra layer, as for example, where charcoal or carbonised wood is encased within a pyroclastic deposit. Organic material may also over and under lie a tephra layer, for example where tephra is deposited on a peat bog that resumes growth after the eruption.

Radiocarbon dating of the confining organic deposits will bracket the age of the eruption. While radiocarbon dating has been the most widely used technique for dating tephra layers erupted over the past 50 ka (Alloway *et al.,* 2007), the results are frequently imprecise (especially at the older age limit of the technique) and therefore have limited use when using tephra layers to test chronologies (Dugmore *et al.,* 1995).

Incremental (varve) dating of tephra layers is another indirect dating method that has the potential to generate high precision ages of tephra layers. Where tephra layers are preserved in annually-laminated sequences such as ice cores or varved lake sequences, then calendar ages can be assigned to them through annual layer counting (e.g. Grönvold *et al.,* 1995; Zillen *et al.,* 2002 Mortensen *et al.,* 2005), though counting errors must be taken into account (Blockley *et al.,* 2008a). In the Mediterranean region, this dating technique has been used to date the Lago Grande di Monticchio (LGdM) sequence which is varved in parts (Wulf *et al.,* 2004). So far, no tephra material originating from Italian volcanoes have been detected in the Greenland ice cores.

Other indirect methods include luminescence dating of the enclosing sediments (e.g. Toms *et al.,* 2004) and wiggle-match radiocarbon dating, which uses the calibrated probability distributions of multiple radiocarbon dates combined with depth to match the results to variations in the radiocarbon calibration curve (e.g. Pilcher *et al.,* 2005; Alloway *et al.,* 2007).

Results obtained using two or more of these dating methods can be combined in a chronological sequence through the use of depositional age modelling. Using a combination of Bayesian statistical frameworks and the internationally agreed radiocarbon calibration curve IntCal09 to generate age models (Bronk Ramsey, 2008b, Blockley *et al.,* 2008b, Reimer *et al.,* 2009), more precise chronologies for sequences can be achieved (e.g. Wohlfarth *et al.,* 2006, Lowe *et al.,* 2007b, Blockley *et al.,* 2008c). Bayesian modelling procedures are able to combine dating information for a tephra layer in order to achieve a higher precision date. Stratigraphic ordering, succession, and relative spacing by depth or varve age can be included in a model which can be integrated with radiocarbon dates and other age estimates to optimise the resulting age model or tephra layer age (Blockley *et al.,* 2008a). This approach was applied to the dating information of three Italian tephra layers to generate the best

95.4% confidence calendar age estimates for the Agnano Monte Spina tephra (4690 - 4300 cal BP), the Neapolitan Yellow Tuff (14,320 - 13,900 cal BP), and the Pomici Principali (12,380 - 12,140 cal BP) (Blockley *et al.*, 2008a) and is the approach that will be adopted in the present study.

For sequences containing cryptotephra layers, the dating of these layers is usually achieved by importing the date obtained for the equivalent layer in proximal deposits once correlations to that deposit have been established. This makes it essential that the stratigraphical and characterisation procedures are especially rigorous when cryptotephra layers are used as the basis for correlation.

2.2 Tephrochronological framework for the Mediterranean Region

During the Quaternary, two major volcanic centres have generated multiple tephra layers that are preserved around the Mediterranean Region: the Italian volcanic centre, including the Roman, Campanian, Aeolian, Sicilian volcanic provinces, and the Aegean volcanic centre province, which includes the Hellenic Arc (e.g. Santorini) and Central Anatolia, Turkey provinces (Narcissi and Vezzoli, 1999; Wulf *et al.*, 2004). All of these provinces are highly explosive and have quite diverse compositions, giving the Mediterranean region a high potential for tephrochronology. The locations of these volcanic provinces are presented in Figure 2.2. The Italian potassic volcanoes provide the most likely source for tephra found in the Adriatic Sea, as the tephra fallout from Hellenic and Anatolian volcanoes is dispersed only in the very eastern part of the Mediterranean (Keller *et al.*, 1978; Druitt *et al.*, 1995). Therefore, only the Italian volcanic provinces will be considered in greater detail here.

2.2.1 Campanian Province

The Campanian volcanic province comprises the southernmost sector of the Plio-Quaternary volcanic belt along the Italian peninsula and it has been the most active Italian province within the Late Quaternary. This province is formed by the active volcanoes of the Campi Flegrei, Ischia Island and Somma-Vesuvius as well as those of

the islands of Procida and Vivara. A summary of the ages and compositional characteristics of these volcanoes is provided in Table 2.1 (Peccerillo, 2005).

Table 2.1: Age and composition of the Campanian Province volcanoes, adapted from Peccerillo (2005).

Volcano	Age	Volcanology and Petrology
Somma-Vesuvius	25 ka – 1944 AD	Monte Somma = Stratovolcano and Vesuvius = intracaldera cone. Formed of silica undersaturated trachybasalt and leucite-tephrite to trachyte and phonolite composition.
Campi Flegrei	~0.2 Ma – 1538 AD	Multicentre volcanic complex with two nested calderas and several monogenetic cones. Formed of pyroclastic rocks with trachybasaltic to trachyte-phonolite composition.
Ischia Island	150 ka – 1302 AD	Volcano-tectonic horst formed of pyroclastic rocks with trachybasaltic to dominant trachytic composition.
Procida-Vivara islands	55 - 17 ka	Coalescing explosive centres formed of basalt to trachyte pyroclastics.

Somma-Vesuvius

Somma –Vesuvius is located 20 km east of Naples and started its activity approximately 25 ka ago (Santacroce, 1987). Figure 2.3 shows a chronological chart of the major known eruptions from Somma-Vesuvius. The first two eruptions are thought to represent explosions of Mount Somma and are known as the Codola eruption which took place at about 25 ka BP and the Sarno eruption, a second major explosive event occurring about 22 ka BP (Guest *et al.*, 2003). Cioni *et al.* (1999) then recognise four caldera-forming events, each occurring during Plinian eruptions, the first being the Pomici di Base at 18.3 ka BP, which was the eruption that probably truncated Mount Somma (Guest *et al.,* 2003). The other caldera forming eruptions were the 8 ka BP Mercato eruption, the 3.4 ka BP Avellino eruption and the AD 79 Pompeii eruption (Cioni *et al.*, 1999). The timing of each caldera collapse is defined by collapse-marking deposits, characterised by large amounts of lithic clasts from the outer margins of the magma chamber.

There were a number of eruptions between these caldera forming eruptions, most notable being the Greenish Plinian eruption at approximately 16 ka BP. The next large eruption was the Lagno Amendolare at *c.* 11 ka BP, the deposits of which have only been found at a few outcrops. As it does not have the same geochemical signature as other Vesuvius Plinian deposits, it is a useful marker layer in the stratigraphy (Guest *et*

al., 2003). In between the Avellino and AD 79 Pompeii eruptions, volcanic activity was restricted to several sub-Plinian and minor strombolian-vulcanian eruptions (Rolandi *et al.,* 1998), with the last historical eruption recorded in 1944 AD (Wulf *et al.,* 2004). Vesuvius pyroclastics display a wide variability from nearly saturated trachytes–phonolites to highly under saturated, high-potassic rocks (leucititic phonolites to tephrites) (Wulf *et al.,* 2004).

Campi Flegrei

The Campi Flegrei consists of a 12 km diameter depression surrounded by cliffs to the east and north but is less well defined to the west. It is a major caldera complex, the centre of which lies in the Gulf of Pozzuoli. The complex is pock-marked with craters and includes at least five nested caldera depressions within the outer caldera perimeter (Figure 2.4).

Activity in the Campi Flegrei commenced more than 60 ka ago and has been mainly explosive (Orsi *et al.,* 1996). Figure 2.5 summarises the main known eruptions of the Campi Flegrei in chronological order. There have been two massive caldera-forming eruptions, the Campanian Ignimbrite (CI) which has been $^{40}Ar/^{39}Ar$ dated to 39.28 ± 0.11 ka BP (De Vivo *et al.,* 2001) and the Neapolitan Yellow Tuff (NYT) dated by $^{40}Ar/^{39}Ar$ to 14,900 ± 400 yr BP (Deino *et al.,* 2004). Little is known about pre-CI deposits, although exposures at Trefola Quarry, show 12 pre CI units (Orsi *et al.,* 1996) and some lava domes in the Campi Flegrei have ages between 47 ka and 42 ka (Punta Marmolite lava dome and Cuma Lava Dome (De Vivo *et al.,* 2010)). The CI eruption was the largest volume eruption to have taken place in the Campi Flegrei and indeed within the whole Mediterranean region (Guest *et al.,* 2003; Pyle *et al.,* 2006). The Breccia Museo Formation, also dated to ~39 ka (Fedele *et al.,* 2008), is a lithic breccia which has been interpreted as a proximal facies of the CI (Orsi *et al.,* 1996; Pappalardo *et al.,* 1999; Fedele *et al.,* 2008).

In between the CI and NYT eruptions, volcanism was restricted to minor hydro-magmatic eruptions (Wulf *et al.,* 2004) and was characterised by the emplacement of pyroclastic products from monogenetic volcanoes. The most important formation dating to this time period is the Tufi Biancastri Formation (Orsi *et al.,* 1996, De Vivo *et al.,* 2010).

The NYT eruption was phreatoplinian to phreatomagmatic and was the second largest eruption of the Campi Flegrei (Orsi *et al.,* 1996). Since the NYT activity, about 72 eruptions have occurred in three epochs of activity (Di Vito *et al.,* 1999). The first, from about 15 ka to 9.5 ka, saw 34 explosive eruptions including the highly explosive Gauro, Archiaverno and Agnano Pomici Principali eruptions, with a mean eruption frequency one every 70 years (Di Vito *et al.,* 1999; De Vivo *et al.,* 2010). Following a period of quiescence lasting 1000 years, the 2nd Epoch of activity began at 8.6 ka with the Fondi di Baia eruption. Six explosive but lower magnitude eruptions comprise Epoch II, which ended with the San Martino eruption at 8.2 ka (Di Vito *et al.,* 1999). After another 3500 year period of quiescence, the 3rd Epoch began at 4.8 ka BP, during which sixteen explosive and four effusive eruptions took place (Di Vito *et al.,* 1999). The main eruptions during this Epoch were the Agnano Monte Spina eruption at 4.1 ka, the Averno eruption at 3.7 ka and the Astroni eruption the age of which is constrained to between 4.1 and 3.8 ka. (Isaia *et al.,* 2004; De Vivo *et al.,* 2010). The final eruption of the Campi Flegrei was the Monte Nuovo eruption in 1538 AD. This eruption, of one-week duration, built the Monte Nuovo scoria cone along the Pozzuoli coast (Figure 2.4) (De Vivo *et al.,* 2010). The Campi Flegrei is still active today with reoccurring bradyseismic events since the last eruption (Guest *et al.,* 2003), associated particularly with the Solfatara caldera (Figure 2.4).

Ischia Island

The island of Ischia lies 10 km west of the Campi Flegrei and is only 10 km long from east to west and 5 km long from north to south. The oldest dated rocks on the island are 150 ka BP (Guest *et al.,* 2003) and Figure 2.6 summarises the main volcanic activity of Ischia since that time. Ischia volcanics show a uniform peralkaline trachytic composition with K_2O contents $\leq$ Na_2O (Wulf *et al.,* 2004).

Volcanism was mainly characterised by large pyroclastic and numerous smaller monogenetic eruptions which have been grouped into four phases of activity (Poli *et al.,* 1987). The first phase of alkali-trachyte pyroclastic products dates prior to 150 ka BP and the second phase from 150 ka BP to 75 ka BP and resulted in lava dome emplacements. The third phase includes the eruption of the caldera forming Monte Epomeo Green Tuff (MEGT) dated to 55 ka BP and is the most extensive volcanic deposit on the island (Guest *et al.,* 2003). After this eruption, activity continued from

different volcanic centres, the products of which are grouped in the "Citara-Serrata-Fontana Formation" which is a superposition of several minor eruptions dating to between 44 ka and 33 ka BP (Poli *et al.,* 1987). The final, mainly historical phase, was dominated by the emplacement of lava flows, with minor deposition of pyroclastic fallout originating from monogenetic cones.

Procida-Vivara Islands

The island of Procida and the islet of Vivara are located between the Island of Ischia and the Campi Flegrei (Peccerillo, 2005). Activity was mostly characterised by explosive eruptions of limited energy as the products are only dispersed over a few kilometres (Scandone *et al.,* 1991). However, two high-explosive events occurred, firstly the Fiumicello eruption at 31 ka B.P and secondly the more widely dispersed Solchiaro eruption at about 17 ka B.P. Deposits from both of these eruptions are trachybasaltic in composition (Scandone *et al.,* 1991).

2.2.2 Roman Province

The Roman province includes the belt of potassium-rich volcanoes running from Tuscany to Rome, parallel with the Tyrrhenian Sea border. It is formed by the volcanic complexes of Vulsini, Vico, Sabatini and the Colli Albani (Alban Hills), which together have erupted about 900 km^3 of volcanic products spanning from approximately 800 ka to 20 ka (Peccerillo, 2005). The main petrological, geochronological and volcanological features of these volcanoes are summarised in Table 2.2

Table 2.2: Age and composition of the Roman Province volcanoes, adapted from Peccerillo (2005).

Volcano	Age	Volcanology and Petrology
Vulsini	600 – 150 ka	Several multicentre volcanic complexes with calderas. Dominant pyroclastic fall deposits and ignimbrites showing potassic and highly potassic compositions.
Vico	420 – 100 ka	Stratovolcano with central caldera. Dominant pyroclastic fall deposits and ignimbrites showing highly potassic compositions.
Sabatini	800 – 40 ka	Two main multicentre complexes with several calderas formed by pyroclastic fall deposits and ignimbrites showing mostly highly potassic compositions.
Colli Albani	600 – 20 ka	Stratovolcano with central nested calderas consisting of high potassium series pyroclastic fall, flow and hydromagmatic products.

Vulsini

Mount Vulsini is a volcanic district formed by various multi-centre volcanic complexes towards the north of the Roman province (Peccerillo, 2005) and is dominated by the two adjacent calderas of Bolsena and Latera (Parker, 1989). However, there are five main volcanic complexes in total: the Paleo-Vulsini, Bolsena-Orvieto, Southern Vulsini, Latera and Mon tefiascone (Palladino and Agosta, 1997). The evolution of each of these complexes is characterised by Strombolian and effusive activity at first, followed by large, caldera-forming eruptions ending in an eruptive phase marked by magmatic and hydromagmatic events (Nappi *et al.,* 1994). Five major sub-Plinian to Plinian fall deposits of Paleobolsena and Bolsena activity, broadly corresponding to the Paleo-Vulsini and Bolsena-Orvieto complexes (Nappi *et al.,* 1994, Palladino and Agosta, 1997) encompass a period of about 340 ka, between 590 ka and 250 ka (Nappi *et al.,* 1994). The Latera caldera is the main volcanic landform in western Vulsini district (Palladino and Agosta, 1997) and explosive eruptions of this caldera occurred in four main episodes between 232 ka and 155 ka (Turbeville, 1992).

Vico

Vico volcano is located to the north of the Roman Province, where it overlaps with volcanic products of the Tuscan Province to the north and during the Quaternary is has erupted mainly ultrapotassic magmas (Perini *et al.,* 2004). Three main periods of Vico activity are recognised; Period 1 at about 400 ka, Period 2 from 305 ka to 138 ka and Period 3 from 138 ka to 95 ka (Peccerillo, 2005). The first period is composed of mainly pyroclastic fall deposits, the Rio Ferriera formation and San Angelo tephra. After a 100 ka period of quiescence, Period II was dominated by leucite-bearing lava which built up the main cone (305 ka - 258 ka) (Perini *et al.,* 2004). Near the end of Period II, pyroclastic flows were erupted from the main cone including the Sutri formation, which included the Ignimbrite, B, C and D units. These pyroclastic flow eruptions led to the formation of a summit caldera (Perini *et al.,* 2004). The post-caldera activity of Period III saw phreatomagmatic eruptions which generated mainly surge deposits such as the Caprarola formation with the last activity being the Monte Venere lavas at 95 ka BP (Perini *et al.,* 2004).

Sabatini

The Sabatini Volcanic district is located 30 km northwest of Rome and volcanic activity lasted from 600ka to 40ka BP (Peccerillo, 2005; Wulf *et al.,* 2004). Pyroclastics from

Sabatini are generally ultrapotassic in composition and also bear sedimentary rock fragments (De Rita *et al.*, 1993). The Sabatini district consists of two main volcanoes, the Sacrofano volcano in the east and the Bracciano volcano in the west (Peccerillo, 2005). Sabatini volcanic activity has been divided into five main phases based on chronostratigraphic data.

During the first phase, activity was concentrated in the eastern sector of the complex. Notable units include the "*Via Tiberina yellow tuff*" which was emplaced at about 600 ka to 530 ka (Conticelli *et al.*, 1997). The second phase from 510 ka to 430 ka was characterised by explosive activity at Sacrofano which led to the eruption and deposition of the Sacrofano stratified tuffs. Activity also began in the Bracciano volcano centre with the deposition of pyroclastic flow deposits, Peperini Listati and Sabatini Grey tuff at 450 ka and 430 ka respectively (Conticelli *et al.*, 1997). The third phase from about 410 ka to 280 ka saw large-magnitude explosive eruptions and the formation of the Sacrofano caldera (Peccerillo, 2005). The fourth and final phases produced mainly hydromagmatic pyroclastic rocks and some lavas (Peccerillo, 2005).

Colli Albani

The Colli Albani or Alban Hills are located 15 km southwest of Rome (Wulf *et al.*, 2004). The Colli Albani volcano is at present a quiescent volcano characterised by seismic and hydrothermal activity (De Rita *et al.*, 2002). Volcanic activity of the Alban Hills has been characterised by mainly explosive activity since 630 ka, with alternating eruptions of lavas and pyroclastic units which are all ultrapotassic in composition (De Rita *et al.*, 2002, Wulf *et al.*, 2004). Three epochs of activity have been described: 1) The Tuscolano-Artemisio succession from 600 ka to 350 ka which comprises seven large caldera forming ignimbrite units; 2) Le Faete Epoch from 350 ka to 270 ka which was characterised by Strombolian volcanic activity; 3) The Final Hydomagmatic succession which has been characterised by several small volume, monogenetic phreatomagmatic eruptions (De Rita *et al.*, 2002). One of the most recent eruptions was the Peperino Albano phreatomagmatic ignimbrite which erupted at ca. 30 ka BP (Giordano *et al.*, 2002).

2.2.3 The Aeolian Arc

The Aeolian archipelago is an active volcanic arc in the southern Tyrrhenian Sea, consisting of several stratovolcanoes, which form seven main islands and several seamounts (Keller, 1982). However, only the Salina, Lipari, Vulcano and Stromboli volcanoes have exhibited explosive eruptions in the past, and these still only show a fallout dispersal restricted to a local or regional scale (Wulf *et al.,* 2004). Therefore, only these volcanoes will be considered in detail, with their main features summarised in Table 2.3. The volcanic activity that has occurred above sea level took place entirely within the Quaternary (Peccerillo, 2005).

Table 2.3: Age and composition of the Aeolian Arc volcanoes, adapted from Peccerillo (2005).

Volcano	Age	Volcanology and Petrology
Stromboli	200 ka - present	Stratovolcano with summit caldera and flank collapses formed of mafic to intermediate lavas.
Lipari	220 ka – 580AD	Multicentre volcano formed of calc-alkaline and high-K calc-alkaline basaltic andesite and andesite.
Vulcano	120 ka - 1890AD	Composite volcano with two calderas formed of high potassium calc-alkaline and shoshonitic basalt to andesite.
Salina	430 ka to 13 ka	Eroded calc-alkaline basalt to andesite stratovolcanoes overlain by twin andesite cones and by a Rhyolite explosion crater.

Stromboli

Stromboli is the most northerly island of the Aeolian archipelago and has been almost continuously active over thousands of years (Guest *et al.,* 2003). The evolution of Stromboli over the last 100 ka has been divided into seven stages, from oldest to youngest as follows: Palaeostromboli I, II and III, Scari, Vancori, Neostromboli and Recent Stromboli. The Palaeostromboli I stage is dated from 100 ka to 64 ka and is associated with a caldera collapse caused by the Petrazza series dated to between 85 ka and 64 ka occurring during this stage (Gillot and Keller, 1993). The Vancori period was between 25 ka and 13 ka and during this period, explosive activity became more important. The Frontone breccias were erupted during this period and are associated with another caldera collapse (Guest *et al.,* 2003.). The final Stromboli caldera or sector collapse occurred during the Neostromboli stage (Guest *et al.,* 2003).

Lipari

Lipari is the largest of the Aeolian Islands and its volcanic stratigraphy can be divided in two, the older products being basaltic to andesitic in composition and the younger

products being mostly rhyolitic in composition (Guest *et al.,* 2003). Ten cycles of activity are identified, separated by quiescent periods and compositional changes (Crisci *et al.,* 1991). Cycles I – VI from 223 ka to 92 ka erupted basaltic andesite to high K-andesite products (De Rosa *et al.,* 2003), which included products from the Monte Chirica-Costa d'Agosto and Monte St Angelo eruptions. The two products developed broadly contemporaneously and have been dated at 150 ka and 127 ka respectively (Guest *et al.,* 2003). The eruption of Monte St Angelo is the most explosive calc-alkaline eruption from the island (Keller *et al.,* 1978) and lasted until 98 ka BP (Crisci *et al.,* 1991). The island was in a state of volcanic rest between 92 ka and 42 ka and, after this, the second phase observed in the stratigraphy began with the production of rhyolitic domes (Guest *et al.,* 2003). Eruptions in cycles VII to X included the Brown Tuff deposits dated at 23.5 ka (Gioncada *et al.,* 2003) and the Monte Guardia eruption in cycle VIII which occurred at 22.4 ±1.1 ka to 20.3 ± 0.7 ka BP (De Rosa *et al.,* 2003). The latest volcanic activity was in AD 729 (Gioncada *et al.,* 2003).

Vulcano

Vulcano is the southernmost of the Aeolian Islands and the volcanic geology of the island divides into four structural units: 1) Southern or Old Vulcano, 2) Lentia mountains; 3) Fossa Vulcano and 4) Vulcanello peninsula (Guest *et al.,* 2003). The oldest Vulcano subaerial products date back to 120 ka and belong to the shoshonitic "Old Vulcano" (Gioncada *et al.,* 2003). Around 50 ka, the formation of the Foss volcano began with basaltic to shoshonitic eruptions (scoria deposits and lava flows of Sommata, Monte Rosso, Punta Luccia, Piano Luccia). The Mastro Minico sequence dating to 27.9 ka consists of an alternation of latitic to trachytic lava and pyroclastic products (Gioncada *et al.,* 2003). At about 15 ka, the Lentia complex collapsed which completed the formation of the Fossa caldera; this coincided with the large eruption of the Tufi di Grotte dei Rossi. After 15 ka, the activity concentrated in the Vulcanello peninsula and the last eruption occurred in 1888 – 1890, though there is still fumarole activity today (Gioncada *et al.,* 2003).

Salina

Salina is the second largest island of the Aeolian province and includes five main subaerial eruptive centres ranging in age from 430 ka to less than 13 Ka (Calanchi *et al.,* 1993). Two main cycles of activity are identified, the older characterised by the eruption of high aluminium basalts from four volcanoes (Capo, Rivi, Corvo, Fossa delle

Felci) with dacites and andesites as the final products. The younger cycle from 100 ka to 13 ka built up the andesitic cone of Monte dei Porri and ended with the formation of the explosion crater of Pollara on the northwestern edge of the island (Calanchi *et al.*, 1993). Volcanic activity in the Pollara depression has resumed at least three times over the last 30 ka, initially with the effusion of the andesitic to dacitic lava flows of Punta di Perciato at 30ka, which were followed by the explosive eruptions of the Lower and Upper Pollara pyroclasts (Calanchi *et al.*, 1993).

2.2.4 Sicilian Province

This province consists of several young to active volcanoes in eastern Sicily, the Sicily Channel and the southern Tyrrhenian Sea, Etna being by far the most well known volcano in this province (Peccerillo, 2005). The characteristics of the volcanoes which have been active throughout the Quaternary and produced explosive volcanism are summarised in Table 2.4.

Table 2.4: Age and composition of the Sicilian province volcanoes, adapted from Peccerillo (2005).

Volcano	Age	Volcanology and Petrology
Etna	600 ka - present	Several coalescing and superimposed stratovolcanoes mostly formed of lavas. Rocks include tholeiitic basalts followed by sodium-alkaline rocks.
Pantelleria	320 ka - 10 ka	Stratovolcano with central nested calderas formed of peralkaline, rhyolitic and trachytic ignimbrites.

Etna

Etna is located on Sicily and is the largest volcano in Europe (Wulf *et al.*, 2004). It is different from other Italian volcanoes, firstly due to its size and secondly because it has been in a state of almost constant activity (Guest *et al.*, 2003). Over the past 100 ka, five periods of explosive activity have been identified: 1) > 100 ka Strombolian to sub-Plinian activity; 2) 80 ka – 100 ka Plinian benmoreitic activity; 3) 16 ka – 80 ka Strombolian to sub-Plinian basaltic activity; 4) 15 – 16 ka Plinian benmoreitic activity accompanying the caldera forming eruptions of the Ellittico volcano; and 5) the most recent 13 ka basaltic Strombolian to sub-Plinian activity (Coltelli *et al.*, 2000).

In distal areas beyond the Etna edifice, two tephra layers are correlated with Etna explosive activity (Coltelli *et al.*, 2000). The most widespread of these is the Y-1 or Et-1 layer (see section 2.2.5 for more details) which has been attributed to the eruption that

produced the Biancavilla-Montalto ignimbrite and the collapse of the Ellittico caldera (Unit D) at about 17 ka BP (Coltelli *et al.*, 2000). The second distal Etna tephra layer, the X-4, can only be correlated with Unit B by Coltelli *et al.* (2000) which has an age of between 80 ka – 100 ka.

Pantelleria

The Island of Pantelleria lies in the Strait of Sicily, about 70 km from the African coast (Guest *et al.,* 2003). Pyroclastics on Pantelleria Island show high contents of FeO and Na_2O and very low values of Al_2O_3 (Wulf *et al.,* 2004).

From 220 ka to 50 ka there were two episodes of basaltic activity with the main activities dated at about 120 ka B.P and 80 ka B.P (Civetta *et al.,* 1984), the latter of which corresponds to the Ignimbrite Z unit (Mahood and Hildreth, 1986). Also during this period (between 133 ka and 79 ka), huge volumes of welded ignimbrites – the Ante-Green Ignimbrites - were erupted (Wulf *et al.,* 2004). The next major event was the eruption that gave rise to the Green Tuff and the collapse of the central caldera at about 45 ka B.P. This deposit is an important stratigraphic marker and often obscures the stratigraphy of older products and the Y-6 layer from the Mediterranean Sea has been correlated with it (Civetta *et al.,* 1984). Volcanism subsequent to the Green Tuff eruption has been mainly silicic and focussed at the Monastereo Caldera which collapsed subsequent to the Green Tuff eruption (Civetta *et al.*, 1984).

2.2.5 Mediterranean Sea tephra studies

Early work on tephra layers in the Mediterranean Sea began in the 1950's and 1960's but deep-sea drilling projects in the 1970's added significantly to the development of marine stratigraphy in the Mediterranean Region. These led to the first tephrostratigraphy for the region being developed which extended over the last 200 ka (Narcisi and Vezzoli, 1999). The locations of the cores investigated for tephra layers by various authors are shown in Figure 2.7, along with locations of the terrestrial records discussed in section 2.2.6 and of the main volcanic centres discussed in sections 2.2.1 – 2.2.4. Studies that only focus on Holocene tephra layers have not been included in this review, as those sequences are likely to be more expanded than the cores used in this investigation and therefore will not provide useful correlatives.

Keller *et al.* (1978) produced the first tephrostratigraphy for the Mediterranean Sea based on a variety of cores (Figure 2.7). Tephra zones were established based on palaeoclimatic zones V, W, X, Y and Z with V being the oldest zone and Z the youngest. Within each zone, every tephra layer is numbered with 1 being the youngest layer, e.g. W-3 is older than W-1, which is older than X-1 (Narcisi and Vezzoli, 1999). Keller *et al.* (1978) identified twenty tephra layers in piston cores from the Eastern Mediterranean and more than 40 layers from cores in the Tyrrhenian Sea, though the work only considered visible tephra layers. The main layers of Italian origin discussed by Keller *et al.* (1978) are presented in Section 2.2.7, Table 2.8 which presents the main tephra layers identified within marine sequences, their distal terrestrial equivalents and correlation to known eruptions.

Studies of tephra layers in the Central Mediterranean (Tyrrhenian and Adriatic Seas) were undertaken by Paterne *et al.* (1986 and 1988) for sequences spanning the last 90 ka BP and the core locations are shown in Figure 2.7. Tephra layers found were geochemically characterised and assigned to a volcanic system and are labelled by that system, so C = Campanian, E = Aeolian, Et = Etna, V = Vesuvius and P = Pantelleria, with the tephra layers in each system numbered with 1 being the youngest. Twenty two Campanian layers were reported, as well as two Aeolian island layers and one layer from each of Vesuvius, Etna and Pantelleria, although over 100 layers were present in total (Paterne *et al.*, 1988, 2008). The Central Mediterranean tephrostratigraphy is extended back until 200 ka by Paterne *et al.* (2008) who used the same nomenclature as Paterne *et al.* (1988) but extended the numbering. An additional seventy one tephra layers were identified in the time interval 90 ka to 200 ka. Of these, the following are described by Paterne *et al.* (2008); twenty one are Campanian layers (C-22 – C-57), six are from Pantelleria (P-11 – P-16), three are from the Aeolian Islands (E-23 – E-25) and one is from Etna (Et-3). The youngest of these layers were correlated to other tephra records in the region but the older tephra layers (older then E-23 and C-41) are just chemically described and related to a volcanic source. The correlation of the Paterne *et al.* (1986, 1988 and 2008) tephra layers to known eruptions and their equivalent Keller *et al.* (1978) layer is presented in Table 2.8.

A number of tephra studies have also been undertaken in the Adriatic Sea. Firstly, Calanchi *et al.* (1998) identified six visible tephra layers of mainly Campanian and Etnean origins in ten cores from the Western Adriatic shelf and the Mid-Adriatic Deep

(Figure 2.7). These layers were all related to either the Paterne *et al.* (1988) tephra layer nomenclature or the Keller *et al.* (1978) tephra layer nomenclature. The layers found in the Adriatic by Calanchi *et al.* (1998) are the C20, C14, C10, Y-1, C2 and the AMS eruption of the Campi Flegrei. The correlation of these layers to known eruptions and other nomenclature systems are shown in Table 2.8.

Secondly, Siani *et al.* (2004) investigated the tephrostratigraphy of core MD90-917 from the South Adriatic deep basin over the last 18,000 years (Figure 2.7). Tephra layers were identified by the relative abundance of glass shards, with more than 300 detrital particles counted for each 3 cm-thick sample (increased to 2 cm resolution between 140 – 175 cm and 395 – 435 cm). Volcanic glass was present throughout the core at about 3%, so samples were only analysed if the peak in abundance was two times larger than the background (Siani *et al.,* 2004). In total, fourteen tephra layers were recognised in the MD90-917 sequence, seven of which are attributed to eruptions from the Campi Flegrei, two are correlated to Somma-Vesuvius eruptions, one to an eruption of Mount Etna, another to Lipari in the Aeolian Islands, and finally one layer is attributed to the Palinuro seamount. The remaining 2 layers could not be correlated to a volcanic eruption (Siani *et al.,* 2004). The individual eruptions to which each of the MD90-917 tephra layers are correlated are shown in Table 2.8.

Finally, a composite Adriatic tephrostratigraphy for the last 170 ka is produced by Calanchi and Dinelli (2008) based on work from five central Adriatic cores and two southern Adriatic cores (Figure 2.7). The tephra layers are related to the zones of Keller *et al.* (1978). Four layers are assigned to the W-zone which extends from 165 to 125 ka BP, one layer is attributed to the X-zone (125 to 60 ka BP), six layers are correlated to eruptions in the Y-zone (60 to 10 ka BP) and thirteen layers are assigned to the Z-zone which extends from 10 ka to the present (Calanchi and Dinelli, 2008). Within each zone, individual tephra layers are correlated with LGdM layers as classified by Wulf *et al.* (2004) (see section 2.2.6) and also to layers defined by Keller *et al.* (1978), as shown in Table 2.8

2.2.6 Mediterranean terrestrial tephra studies review

Given the proximity of the Italian volcanoes, many tephra studies have been conducted on the Italian mainland and the adjacent Balkan Peninsula but three studies are selected

for special attention here as they cover the whole time period of interest in this study they are Lago Grande di Monticchio (LGdM), San Gregorio Magno Basin, and Lake Ohrid. The location of these sites and the major Italian volcanic centres is shown in Figure 2.7. Studies that only focus on Holocene tephra layers have not been included in this review, as the sequences are likely to be more expanded than the cores used in this investigation and hence do not provide useful correlatives.

2.2.6.1 Lago Grande di Monticchio

Lago Grande di Monticchio (LGdM) is one of the most useful sites for tephra studies due to its proximity to the majority of Italian volcanoes, the presentation of a comprehensive record of volcanic activity with a long sedimentary sequence, a high rate of sedimentation, and the clear stratigraphic order and independent dating of tephra layers afforded by a high resolution varve chronology (Wulf *et al.,* 2008). LGdM is a maar lake in Southern Italy, located 120 km east of Naples (Figure 2.7). It represents the larger of two maar lakes that were formed 132 ± 12 ka ago during the last phreatomagmatic eruption in a caldera of Monte Vulture (Wulf *et al.,* 2004). The lake contains a continuous sediment sequence that spans the last 133,000 years, the majority of which is annually-laminated (Brauer *et al.,* 2007).

A number of cores from LGdM have been analysed for tephra layers. Initially fourteen layers greater than 3 mm in thickness from LGdM-D core were characterised and correlated to known eruptions (Narcissi, 1996). Prior to that, Newton and Dugmore (1993) analysed two layers from the LGdM-C core. The fourteen layers analysed by Narcissi (1996) were numbered L1 to L14 with L1 being the youngest. L1, L2, L3, L4, L8, L9, L10, L11 are attributed to the activity of Vesuvius, L5, L6, L7, L12 to Campi Flegrei activity and L13, L14 to Ischian activity. Wulf *et al.* (2004 and 2008) carried out tephra investigations on 11 cores obtained from LGdM in 1990 and 1994 and identified a total of 349 tephra layers ranging in thickness from 0.1 mm to 33.2 cm (Wulf *et al.,* 2004). The majority of these layers have been geochemically analysed using a Cameca SX-100 electron microprobe with wavelength dispersive spectrometry (WDS) and each chemically analysed tephra layer in the LGdM sequence is labelled TM (Tephra Monticchio) and numbered according to its relevant stratigraphic position in the core, with TM-1 being the youngest. Wulf *et al.* (2004) provide the main results from 24 of the layers dating between 105 ka years and the present day, while Wulf *et al.*

(2008) provide additional results for the last 20 ka and identify, classify and correlate 47 tephra layers. A number of tephra layers dating older than 20 ka BP have been classified and correlated with known volcanic eruptions but the results have not been published. They have, however, been provided to the author by Sabine Wulf for use in this thesis. The results from Wulf *et al.* (2004, 2008 and unpublished) are summarised in Table 2.5, and show the LGdM tephra code, the depth in the LGdM sequence, thickness of tephra layer, its source, the eruption it is correlated with and its LGdM varve age. The LGdM tephra layer nomenclature from Narcisi (1996) is also indicated.

Table 2.5: Thickness, depth, age, origin and correlations of tephra layers occurring in the sediment record of Lago Grande di Monticchio.

Sources: SV Somma-Vesuvius, IS Ischia, CF Campi Flegrei, ET Etna, PR Procida-Vivara, AB Alban Hills, EO Aeolian Islands, PA Pantelleria, RO Roccamonfina, SA Sabatini.
* = Layers described in Wulf *et al.* (2004). Layers 2 – 61 are described in Wulf *et al.* (2008). The remaining layers are unpublished and data is provided by Sabine Wulf for use in the thesis.
L1 - L14 = nomenclature of tephra layers after Narcisi (1996).

No.	Tephra	Tephra layer thickness (mm)	Sediment depth (base of tephra in cm)	LGdM Varve Age (years BP)	Source	Volcanic event
1	TM-0		?	-	SV	1944 AD ?
2	TM-1*	9.00	6.00	88	SV	1631 AD
3	TM-1-1	0.40	50.00	818	SV	AS?
4	TM-1-2	0.25	75.80	1072	SV	AS?
5	TM-2a*	3.00	112.00	1416	SV	MI 1, 512 AD
6	TM-2b*	35.00	116.50	1441	SV	Pollena 472 AD
7	TM-2-1	0.10	252.50	3042	IS	Cannavale
8	TM-2-2	1.00	311.00	3939	SV	AP6
9	TM-3a (L1)*	22.00	315.70	3994	SV	AP4
10	TM-3b (L2)*	24.00	320.20	4018	SV	AP3
11	TM-3c (L3)*	14.00	332.30	4146	SV	AP2
12	TM-3c*	17.00	334.00	4153	SV	AP2
13	TM-4*	6.00	352.60	4313	SV	Avellino
14	TM-5a*	11.00	374.10	4619	CF	Astroni 3
15	TM-5b*	3.00	378.00	4663	CF	Astroni 2
16	TM-5c*	0.75	426.80	5393	CF	AMST
17	TM-5cd1	0.10	433.00	5502	CF ?	reworked
18	TM-5cd2	0.70	445.00	5635	CF	AMST
19	TM-5d*	0.50	448.00	5675	CF	AMST Unit B1
20	TM-5-1a	1.00	507.50	6581	IS?	Maistro
21	TM-5-1b	1.00	508.00	6588	IS	Maistro
22	TM-5-1c	0.50	508.50	6592	IS	Maistro
23	TM-5-2	1.00	544.00	7151	IS	Maistro
24	TM-6a*	1.00	644.50	9620	SV	Mercato
25	TM-6b (L4)*	106.00	658.60	9678	SV	Mercato
26	TM-6-1a	1.00	667.00	9894	CF	Fondi di Baia?
27	TM-6-1b	3.00	668.80	9958	CF	Fondi di Baia?
28	TM-6-2a	0.10	725.60	11187	CF	Casale
29	TM-6-2b	0.10	726.50	11207	CF	Casale
30	TM-6-3a	0.40	737.00	11501	IS	Selva del Napolitano
31	TM-6-3b	0.50	737.50	11516	IS	Selva del Napolitano
32	TM-6-3c	0.40	738.00	11522	IS	Selva del Napolitano
33	TM-6-4a	17.00	745.70	11668	CF	Soccavo 4
34	TM-6-4b	1.00	760.00	11888	CF	Soccavo 3
35	TM-6-4c	3.00	765.30	11983	CF	Soccavo 2
36	TM-6-5a	1.00	768.00	12072	CF	?
37	TM-6-5b	2.00	768.30	12073	CF	?
38	TM-6-5c	2.00	768.70	12074	CF	?
39	TM-7a*	6.00	775.10	12169	CF	Pomici Principali
40	TM-7b (L5)*	47.00	780.70	12181	CF	Pomici Principali
41	TM-7c	2.00	781.20	12184	CF ?	Pomici Principali ?
42	TM-7-1a	0.20	805.30	12591	CF	Gaiola?
43	TM-7-1b	0.10	805.40	12592	CF ?	Gaiola?
44	TM-7-2	0.30	807.90	12643	CF	La Pigna 1
45	TM-7-3	0.10	812.90	12765	CF	?
46	TM-7-4	0.30	817.80	12905	CF ?	?
47	TM-8	4.00	857.40	14106	CF	NYT

No.	Tephra	Tephra layer thickness (mm)	Sediment depth (base of tephra in cm)	LGdM Varve Age (years BP)	Source	Volcanic event
48	TM-8	11.00	858.50	14113	CF	NYT
49	TM-8 (L6)*	7.00	859.50	14115	CF	NYT
50	TM-9 (L7)*	18.00	877.30	14557	CF	Tufi Biancastri, GM1
51	TM-10a	4.00	896.80	15028	CF	Lagno Amendolare
52	TM-10b*	7.00	903.70	15215	CF	Lagno Amendolare
53	TM-10c	1.00	910.30	15296	CF	Lagno Amendolare
54	TM-10d*	4.00	917.70	15551	CF	Lagno Amendolare
55	TM-10-1	12.00	927.00	15822	IS	St. Angelo Tuff
56	TM-11*	0.50	953.00	16444	ET	Biancavilla, Y-1
57	TM-12 (L8)*	55.00	1002.00	17560	SV	Verdoline
58	TM-12-1	1.40	1019.00	17976	ET	Ante Biancavilla
59	TM-12-2a	0.30	1043.30	18496	CF	Pre-Tufi Biancastri
60	TM-12-2b	0.20	1044.10	18538	CF	Pre-Tufi Biancastri
61	TM-13 (L9)*	182.00	1107.00	19282	SV	Pomici di Base
62	TM-14a*	2.00	1166.00	21071	PR?	Solchiaro CD1-b?
63	TM-14b*	1.00	1171.50	21259	PR	Solchiaro, white facies
64	TM-14-1	2.00	1174.70	21353	IS	Faro di Punta Imperatore?
65	TM-14-2	2.00	1202.00	22249	AB	Peperini
66	TM-14-3	2.00	1326.50	25366	CF	?
67	TM-15 (L10)*	286.00	1458.00	27256	CF	Y-3, SMP1-e
68	TM-17a*	9.00	1632.40	29920	AB	Peperini
69	TM-17b*	7.00	1636.70	29998	AB	Peperini
70	TM-16a*	16.00	1648.00	30237	CF?	Codola Top
71	TM-16b (L11)*	68.00	1724.50	31121	CF?	Codola Base
72	TM-17bc	5.00	1792.50	31830	AB	Peperini
73	TM-17c	9.00	1930.00	33768	PR	Fiumicello
74	TM-17d	12.00	1962.40	33920	PR	Fiumicello
75	TM-17e	9.00	1993.30	33962	PR	Fiumicello
76	TM-17f	97.00	2344.50	34528	AB	Peperini
77	TM-17-1a	1.00	2365.80	34862	IS	?
78	TM-17-1b	4.00	2370.50	34956	IS	?
79	TM-17-1c	5.00	2372.80	34980	IS	?
80	TM-17-2	27.00	2417.50	35531	CF ?	Schiava, C-9
81	TM-18 (L12)*	257.00	2637.00	36773	CF	IC
82	TM-18-1a	56.00	2649.20	36843	CF?	SMP1-a
83	TM-18-1b	5.00	2657.00	36943	CF?	SMP1-a
84	TM-18-1c	4.00	2667.80	37059	CF?	SMP1-a
85	TM-18-1d	13.00	2705.60	37363	CF?	SMP1-a
86	TM-18-2	1.00	2722.70	37586	IS	Citara
87	TM-18-3	4.00	2729.00	37809	?	?
88	TM-18-4	15.00	2779.00	38603	CF	TLm
89	TM-18-5a	7.00	2804.00	38833	1	Citara
90	TM-18-5b	4.00	2805.60	38858	IS	Citara
91	TM-18-5c	3.00	2814.50	38878	IS	Citara
92	TM-18-6	?	?	39245	CF	?
93	TM-18-7	1.00	2823.10	40170	PR ?	?
94	TM-18-8a	3.00	2940.00	40557	CF	TGm
95	TM-18-8b	2.00	2940.80	40568	CF	TGm
96	TM-18-9a	1.50	2992.00	41423	IS	Citara
97	TM-18-9b	0.90	2996.20	41472	IS	Citara
98	TM-18-9c	0.50	2997.40	41506	IS	Citara
99	TM-18-9d	1.00	2997.80	41521	IS ?	Citara ?
100	TM-18-9e (L13)	13.00	3005.20	41694	IS	Citara
101	TM-18-9f	0.20	3015.50	41934	IS	Citara
102	TM-18-10a	2.00	3062.10	43281	CF	TGl
103	TM-18-10b	1.30	3159.80	45834	CF	ME039p2, TGl
104	TM-18-10c	1.80	3162.10	45870	CF	TGl
105	TM-18-10d	5.00	3182.90	46459	CF	TGl
106	TM-18-11	2.00	3211.50	47312	PR ?	?
107	TM-18-12a	1.50	3239.60	48113	CF	Santa Lucia
108	TM-18-12b	16.00	3285.00	49409	CF	Santa Lucia, C-15
109	TM-18-13	3.50	3296.00	49631	PR ?	?
110	TM-18-14a	1.00	3345.40	50260	IS	Citara
111	TM-18-14b	0.20	*3337.60*	50315	IS	Citara
112	TM-18-14c	0.30	3338.50	50362	IS	Citara
113	TM-18-15a	1.30	3371.00	51948	CF	TL f
114	TM-18-15b	3.00	3445.20	53529	CF	TL f
115	TM-18-15c	1.00	3447.10	53580	CF	TL f
116	TM-18-16	1.00	?	54729	?	?
117	TM-18-17a	5.00	3508.50	55614	CF	CA1-a, C-16
118	TM-18-17b	4.00	3587.70	57289	CF	CA1-a, C-16
119	TM-19 (L14)*	332.00	3831.00	60055	IS	TVEss
120	TM-19-1	3.50	3846.50	60235	CF	TLc
121	TM-20*	6.00	3923.80	61371	IS	SC2-a, C(i)6
122	TM-20-1a	1.50	4062.60	64047	IS	Y-7
123	TM-20-1b	8.00	4067.60	64136	IS	Y-7
124	TM-20-1c	3.00	4104.70	64470	IS	Y-7
125	TM-20-2a	6.00	4351.30	68619	CF	C-18, SA3-a/SA3-b
126	TM-20-2b	3.00	4393.20	69463	?	666-04
127	TM-20-2c	1.00	4394.50	69517	?	666-04
128	TM-20-3	0.20	4396.00	69585	IS	?

No.	Tephra	Tephra layer thickness (mm)	Sediment depth (base of tephra in cm)	LGdM Varve Age (years BP)	Source	Volcanic event
129	TM-20-4a	8.00	4443.60	70367	?	?
130	TM-20-4b	2.50	4616.40	72107	CF	?
131	TM-20-5	20.00	4657.00	72942	IS	Pignatiello
132	TM-20-6	?	?	74085	?	?
133	TM-20-7	20.00	4780.20	75351	IS	Pignatiello
134	TM-20-8	1.00	4810.00	76467	CF	?
135	TM-20-9	0.30	4916.63	77237	IS	Parata
136	TM-20-10	1.00	4937.50	77552	CF	?
137	TM-21*	1.50	5012.00	78341	EO	Y-9
138	TM-21-1a	20.00	5071.80	79414	CF	?
139	TM-21-1b	0.30	5106.00	79514	CF	?
140	TM-21-2a	7.50	5236.20	80985	IS	Monte Vico
141	TM-21-2b	0.50	5258.00	81427	IS	Monte Vico
142	TM-21-2c	6.00	5339.70	81949	IS	Monte Vico
143	TM-21-3a	0.60	5405.00	82626	?	?
144	TM-21-3b	0.10	5405.50	82656	?	?
145	TM-21-4	0.10	?	83410	?	?
146	TM-21-5	1.00	5474.50	83421	?	?
147	TM-21-6	0.20	5492.80	84089	?	
148	TM-21-6a	0.20	5559.40	85690	CF	?
149	TM-21-6b	4.00	5563.00	85710	CF	?
150	TM-21-6c	1.50	5564.50	85753	CF	?
151	TM-21-6d	0.20	5564.80	85768	CF	?
152	TM-21-6e	0.30	5565.50	85809	CF	?
153	TM-21-7a	5.00	5568.00	85934	CF	?
154	TM-21-7b	8.50	5575.60	86060	CF	?
155	TM-21-7c	7.00	5581.80	86287	CF	?
156	TM-21-8a	1.90	5594.00	86645	CF	?
157	TM-21-8b	9.00	5600.20	86862	CF	?
158	TM-21-8c	8.00	5601.20	86863	CF	?
159	TM-21-9	1.50	5602.00	86910	CF	?
160	TM-21-10a	0.10	5602.80	86987	CF	?
161	TM-21-10b	5.80	5605.30	87081	CF	?
162	TM-21-10c	0.75	5611.00	87492	CF	?
163	TM-22*	1.00	5840.00	89126	PA	Ante Green Tuff (P-10)
164	TM-22-1a	3.00	5902.10	89248	CF	?
165	TM-22-1b	2.00	5916.30	89288	CF	?
166	TM-23*	66.00		89473	SA	Tufo di Baccano
167	TM-23-1a	2.00	5984.00	89479	?	?
168	TM-23-1b	1.00	5985.50	89486	?	?
169	TM-23-2a	30.00	6369.70	91070	CF	?
170	TM-23-2b	0.20	6373.30	91331	CF	?
171	TM-23-3a	2.00	6431.60	92942	CF	?
172	TM-23-3b	6.50	6432.60	92947	CF	?
173	TM-23-3c	22.00	6436.30	92949	CF	?
174	TM-23-4	1.00	6438.00	93034	CF	?
175	TM-23-5	2.30	6450.80	93312	EO	Piano Caldera
176	TM-23-6a	0.60	6458.90	93369	? (ET)	?
177	TM-23-6b	0.10	6459.10	93372	? (ET)	?
178	TM-23-7a	1.50	6459.50	93424	CF ?	?
179	TM-23-7b	0.80	6463.50	93598	CF	?
180	TM-23-7c	4.50	6464.30	93607	CF	?
181	TM-23-7d	2.50	6478.30	93617	CF	?
182	TM-23-7e	2.50	6479.00	93618	CF	?
183	TM-23-7f	3.50	6479.90	93619	CF	?
184	TM-23-8a	4.00	6485.10	93637	CF	?
185	TM-23-8b	6.50	6486.60	93639	CF	?
186	TM-23-8c	2.00	6487.30	93641	CF ?	?
187	TM-23-8d	10.50	6489.00	93644	CF	?
188	TM-23-8e	1.30	6489.30	93654	CF	?
189	TM-23-9	0.80	6489.70	93680	CF	?
190	TM-23-10	2.50	6495.00	93997	CF	?
191	TM-23-11a	5.00	6528.70	95166	CF	?
192	TM-23-11b	3.50	6529.00	95169	CF	?
193	TM-23-11c	2.00	6529.40	95170	CF	?
194	TM-23-11d	7.00	6530.50	95172	CF	?
195	TM-23-11e	4.00	6532.10	95177	CF	?
196	TM-23-11f	4.00	6532.60	95179	CF	?
197	TM-23-11g	5.50	6533.80	95181	CF	?
198	TM-23-12a	0.10	6543.00	95598	CF ?	?
199	TM-23-12b	0.10	6543.40	95623	CF	?
200	TM-23-12c	0.20	6547.30	95798	CF	?
201	TM-23-13	0.20	6548.50	95843	CF	?
202	TM-23-14	0.70	6589.20	96164	IS	?
203	TM-23-15	0.40	6610.00	97010	CF	?
204	TM-23-16	4.60	6625.00	97477	IS	Monte S. Angelo
205	TM-23-17	0.10	6629.70	97794	CF	?
206	TM-23-18a	3.00	6630.60	97866	CF	?
207	TM-23-18b	0.20	6642.00	97944	CF	?
208	TM-23-18c	0.50	6643.40	97982	CF	?
209	TM-23-18d	14.00	6649.90	98079	CF	?

No.	Tephra	Tephra layer thickness (mm)	Sediment depth (base of tephra in cm)	LGdM Varve Age (years BP)	Source	Volcanic event
210	TM-23-18e	48.00	6657.80	98083	CF	?
211	TM-23-19a	1.00	6659.00	98117	CF ?	?
212	TM-23-19b	0.50	6660.70	98159	CF	?
213	TM-23-19c	1.30	6661.00	98180	CF	?
214	TM-23-19d	0.50	6661.50	98251	CF	?
215	TM-23-19e	0.90	6662.00	98293	CF	?
216	TM-23-19f	0.10	6662.80	98348	CF	?
217	TM-23-19g	0.10	6664.80	98593	CF ?	?
218	TM-23-20a	24.00	6685.90	99140	IS	Monte S. Angelo
219	TM-23-20b	1.00	6708.50	99466	IS	Monte S. Angelo
220	TM-23-21a	13.00	6754.00	99653	CF	?
221	TM-23-21b	8.00	6755.10	99654	CF	?
222	TM-23-21c	12.00	6756.90	99656	CF	?
223	TM-23-21d	6.00	6759.70	99658	CF	?
224	TM-23-21e	5.00	6760.30	99660	CF	?
225	TM-23-21f	32.00	6765.10	99661	CF	?
226	TM-23-21g	30.00	6779.90	99670	CF ?	?
227	TM-23-22	0.20	6781.00	99733	CF	?
228	TM-23-23	0.50	6787.00	100105	IS	Monte S. Angelo
229	TM-23-24a	2.50	6787.30	100115	CF	?
230	TM-23-24b	1.50	6792.50	100329	CF	?
231	TM-23-24c	3.50	6800.90	100527	CF	?
232	TM-23-24d	10.00	6815.50	100857	CF ?	?
233	TM-23-24e	4.50	6815.90	100880	CF ?	?
234	TM-23-24f	2.00	6817.50	100881	CF ?	?
235	TM-23-24g	2.50	6820.00	100884	CF ?	?
236	TM-23-24h	12.00	6840.40	100910	CF	?
237	TM-23-24i	13.00	6841.80	100912	CF	?
238	TM-23-25	4.00	6844.90	100917	CF ?	?
239	TM-23-26a	1.40	6873.50	101056	CF ?	?
240	TM-23-26b	11.00	6878.80	101058	CF	?
241	TM-23-26c	3.00	6879.30	101059	CF	?
242	TM-23-26d	2.50	6888.60	101077	CF	?
243	TM-23-26e	3.00	6894.30	101157	CF	?
244	TM-23-26f	0.80	6895.10	101159	CF	?
245	TM-23-26g	1.10	6895.30	101169	CF	?
246	TM-23-27	2.00	6896.50	101211	CF	?
247	TM-24a-1*	70.00	6952.30	101572	CF	X-5
248	TM-24a-2*	3.20	6955.90	101573	CF	X-5
249	TM-24a-3*	6.50	6956.50	101574	CF ?	X-5
250	TM-24a-4*	14.40	6958.00	101575	CF ?	X-5
251	TM-24a-5*	3.60	6958.50	101577	CF	X-5
252	TM-24a-6*	1.25	6959.20	101589	CF ?	X-5
253	TM-24ab-1a	2.00	6960.20	101622	CF	?
254	TM-24ab-1b	4.40	6961.40	101639	CF	?
255	TM-24ab-1c	3.20	6962.00	101653	CF	?
256	TM-24ab-2a	0.80	6967.40	101761	CF	?
257	TM-24ab-2b	0.20	6970.80	101890	CF ?	?
258	TM-24ab-2c	12.00	6972.90	101896	CF	?
259	TM-24ab-3	0.70	7001.90	102322	CF	?
260	TM-24b-1*	2.00	7012.50	102537	CF	X-5
261	TM-24b-2*	0.40	7012.70	102538	CF	X-5
262	TM-24b-3*	3.00	7013.20	102539	CF	X-5
263	TM-24b-4*	5.00	7014.20	102540	CF	X-5
264	TM-24b-5*	1.00	7016.50	102541	CF	X-5
265	TM-24b-6*	5.00	7017.70	102542	CF	X-5
266	TM-24b-7*	12.00	7020.60	102543	CF	X-5
267	TM-24b-8*	1.00	7024.40	102544	CF	X-5
268	TM-24b-9*	1.50	7024.70	102545	CF	X-5
269	TM-24b-10*	2.00	7025.10	102546	CF	X-5
270	TM-24b-11*	13.00	7027.50	102548	CF	X-5
271	TM-24b-12*	12.00	7030.20	102549	CF ?	X-5
272	TM-24b-13*	29.00	7033.00	102552	CF	X-5
273	TM-24b-14*	9.00	7036.00	102553	CF	X-5
274	TM-24b-15*	97.00	7077.50	102556	CF	X-5
275	TM-24b-16	1.00	7158.70	102569	CF	?
276	TM-24-1a	1.60	7178.50	102798	CF	?
277	TM-24-1b	0.50	7182.00	102924	CF	?
278	TM-24-1c	0.10	7184.90	102947	CF	?
279	TM-24-2a	0.20	7217.00	103460	CF ?	?
280	TM-24-2b	8.00	7223.50	103556	CF ?	?
281	TM-24-2c	0.20	7225.00	103602	CF ?	?
282	TM-24-3a	2.60	7238.50	103748	IS	Punta Imperatore
283	TM-24-3b	8.00	7243.60	103803	IS	Punta Imperatore
284	TM-24-3c	2.00	7263.10	104040	IS	Punta Imperatore
285	TM-24-3d	0.20	7264.10	104047	IS	Punta Imperatore
286	TM-24-3e	4.00	7271.50	104120	IS	Punta Imperatore
287	TM-24-4	1.00	7281.80	104326	CF	?
288	TM-24-5a	2.30	7304.90	105007	CF ?	?
289	TM-24-5b	0.70	7305.10	105013	CF ?	?
290	TM-24-5c	4.80	7305.70	105018	CF	?

No.	Tephra	Tephra layer thickness (mm)	Sediment depth (base of tephra in cm)	LGdM Varve Age (years BP)	Source	Volcanic event
291	TM-24-6a	0.20	7312.40	105042	CF ?	?
292	TM-24-6b	0.10	7313.20	105062	CF	?
293	TM-24-6c	0.10	7313.50	105080	CF	?
294	TM-24-7a	0.10	7316.40	105187	CF	?
295	TM-24-7b	1.50	7316.70	105228	CF	?
296	TM-24-7c	0.20	7317.30	105269	CF	?
297	TM-25	113.00	7349	105572	Campania	?
298	TM-26	1.00	7373.9	106397	ET	Acireale
299	TM-27	16.00	7811.1	108429	Campania	X-6, Palinuro
300	TM-28a	21.00	8076.3	110500	IS	?
301	TM-28b	2.00	8080.3	110923	IS	?
302	TM-29-1a	0.60	8096	111576	Vico	Caprarola
303	TM-29-1b	1.00	8113.7	112270	Vico	Caprarola
304	TM-29-1c	1.00	8113.9	112300	Vico	Caprarola
305	TM-29-1d	0.20	8114	112324	Vico	Caprarola
306	TM-29-1e	0.50	8114.3	112324	Vico	Caprarola
307	TM-29-1f	2.30	8114.5	112348	Vico	Caprarola
308	TM-29-1g	0.30	8114.9	112408	Vico	Caprarola
309	TM-29-1h	5.00	8115.6	112428	Vico	Caprarola
310	TM-29-1i	4.00	8118.7	112551	Vico	Caprarola
311	TM-29-2a	6.00	8134	112613	Vico	Caprarola
312	TM-29-2b	2.50	8134.4	112635	Vico	Caprarola
313	TM-29-2c	0.50	8134.6	112651	Vico	Caprarola
314	TM-29-2d	2.50	8135	112672	Vico	Caprarola
315	TM-29-2e	4.00	8136.5	112712	Vico	Caprarola
316	TM-29-2f	7.00	8140.8	112887	Vico	Caprarola
317	TM-29-2g	16.00	8146.9	113086	Vico	Caprarola
318	TM-29-2h	2.50	8147.4	113115	Vico	Caprarola
319	TM-30-1a	2.00	8153	113464	SA	Bracciano
320	TM-30-1b	3.00	8154.4	113584	SA	Bracciano
321	TM-30-1c	18.00	8182.2	113750	SA	Bracciano
322	TM-30-1d	0.50	8182.3	113763	SA	Bracciano
323	TM-30-1e	1.00	8188.4	113974	SA	Bracciano
324	TM-30-1f	12.00	8195.4	114096	SA	Bracciano
325	TM-30-2a	1.50	8200.8	114531	SA	Bracciano
326	TM-30-2b	2.00	8202	114626	SA	Bracciano
327	TM-30-2c	8.00	8203.5	114690	SA	Bracciano
328	TM-30-2d	12.00	8205.4	114810	SA	Bracciano
329	TM-31	0.50	8206	114867	RP	?
330	TM-32	1.00	8211.7	115341	EO	Stromboli?
331	TM-33-1a	10.00	8232.7	115817	IS	?
332	TM-33-1b	1.00	8233	115849	IS	?
333	TM-33-1c	4.00	8237	116205	IS	?
334	TM-33-2a	0.30	8269	118286	IS	?
335	TM-33-2b	4.00	8269.7	118309	IS	?
336	TM-34	0.40	8280.8	118909	EO	Vulcano
337	TM-35a	3.00	8342	120769	IS	?
338	TM-35b	3.50	8410.5	122033	IS	?
339	TM-36	1.50	8456.4	123128	Campania	?
340	TM-37a	11.00	8495	124169	IS	Upper Scarrupata?
341	TM-37b	8.00	8544.8	124425	IS	Upper Scarrupata?
342	TM-37c	1.50	8548.8	124454	IS	Upper Scarrupata?
343	TM-37d	1.00	8581.5	124954	IS	Upper Scarrupata?
344	TM-38a	0.40	8634	125643	Vico	Ignimbrite D
345	TM-39	6.00	9126.2	130627	Campania	?
346	TM-40	5.00	9161.5	130944	IS	?
347	TM-38b1	5.00	9203.3	131097	Vico	Ignimbrite D
348	TM-38b2	1.00	9203.5	131097	Vico	Ignimbrite D
349	TM-41	1.00	9645.8	132085	IS	?

It is clear from Table 2.5 that LGdM provides detailed information about the explosive activity of the Italian volcanoes over the last 130 ka. Most of the tephra layers (n = 313) derive from eruptions of volcanoes in the Campanian province (Campi Flegrei, Vesuvius, Ischia, Procida-Vivara). Seventeen of the eruptions are related to highly explosive events of the Roman, Sicilian or Aeolian provinces and only ten LGdM layers could not be assigned to a volcanic source (Wulf *et al.*, 2004). The eruptions and their source locations are summarised in Figure 2.8. The fact that no eruptions from the Aegean province are recorded in the LGdM sequence supports the assumption in

Section 2.2.1 that these layers are unlikely to be preserved in the Adriatic Sea, probably because the dominant plume direction was towards the north-east, east and south-east.

2.2.6.2 San Gregorio Magno basin

The San Gregorio Magno basin is a tectono-karstic depression located in the Southern Apennines (Figure 2.7). A 61 m core was recovered from the basin and, throughout the recovered core sequences, a total of thirty-nine distinctive sand-sized layers were recognised, twenty-one of them designated as primary tephra layers (Munno and Petrosino, 2007). Only visible layers have been analysed in this sequence, which is likely to contain additional cryptotephra layers. The thickness of the visible tephra layers range between 5 cm and 80 cm. Major element analysis on glass shards was undertaken on an SEM JEOL JSM 5310 with EDS in order for the tephra layers to be correlated to tephra layers in LGdM (Wulf *et al.*, 2004) and tephra layers in deep sea marine cores (Keller *et al.*, 1978, Paterne *et al.*, 1988) (Munno and Petrosino, 2007). Eight of the layers were successfully matched with LGdM tephra layers, a further three were correlated to tephra layers in marine cores and ten tephra layers could not be matched with known eruptions (Table 2.6) (Munno and Petrosino, 2007).

Table 2.6: Depth, correlation to LGdM layer, origin and correlations to volcanic eruptions for tephra layers occurring in the San Gregorio Magno basin (Munno and Petrosino, 2007).
Sources: SV Somma-Vesuvius, CF Campi Flegrei, IS Ischia, ET Etna, PA Pantelleria and CAMP. Campanian

SM tephra layer	Depth (cm)	Correlation to LGdM layer	Source	Volcanic Eruption
S21	4.00 – 4.80	TM-8	CF	NYT
S20	5.80 – 6.00	TM-12	SV	Greenish
S19	6.65 – 6.80	TM-15	CF	Y-3
S18	6.80 – 7.00	TM-16	SV	Codola
S17	7.90 – 8.50	TM-18	CF	Campanian Ignimbrite
S16	11.60 – 11.70	TM-19	IS	MEGT
S15	14.80–14.90	TM-20	IS	Y-7
S14	22.20–22.55	N/A	CAMP.	X-2/C-22
S13	22.60–22.70	N/A	?	?
S12	24.35–24.40	N/A	?	?
S11	24.80–25.10	TM-24	CAMP.	X-5
S10	25.70–26.00	TM-27	CAMP.	X-6
S9	27.80–28.00	N/A	?	?
S8	40.70–40.90	N/A	?	?
S7	41.70–41.75	N/A	CAMP.	W-1
S6	43.70–43.90	N/A	?	?
S5	50.70–51.20	N/A	?	V-2
S4	51.80–51.90	N/A	?	?
S3	52.00 – 52.35	N/A	?	?
S2	52.60 – 52.70	N/A	?	?
S1	55.50 – 56.10	N/A	?	?

2.2.6.3 Lake Ohrid

Lake Ohrid is a transboundary lake shared by the Republics of Albania and Macedonia and is located in a tectonic graben (Figure 2.7). It is considered to be the oldest lake in Europe (Wagner *et al.,* 2009; Vogel *et al.,* 2010a). Due to its geographic position and age, Lake Ohrid represents an important link between paleoenvironmental records from the Mediterranean Sea and nearby terrestrial records (Wagner *et al.,* 2009). Its location downwind of the main Italian volcanic centres makes it an important archive for studying tephra dispersal in the Mediterranean. Therefore, Lake Ohrid has the potential to provide an excellent tephrostratigraphic and paleoenvironmental archive that should provide opportunities to link marine and terrestrial records in the Mediterranean region over a long timescale (Vogel *et al.,* 2010a).

A number of tephra studies have been undertaken at Lake Ohrid from different locations within the lake, as illustrated in Figure 2.9. Wagner *et al.* (2008) undertook the first tephra study on Core Lz1120 from the south-eastern part of the lake, the composite sediment succession obtained from overlapping cores being 1075 cm long. Three tephra layers were identified at 310 - 315 cm, 896 - 897 cm and 1070 – 1075 cm, and, following 1 cm resolution sampling of the core, volcanic particles (glass shards, volcanic lithics) were identified under a microscope. The layers at 896 cm and 1070 cm are visible tephra layers but the layer at 310 cm is a cryptotephra. An EDAX-DX micro-analyser (Energy Dispersive Spectrometry (EDS) analyser) mounted on a Philips SEM 515 was used to geochemically analyse the glass shards and subsequently the layers were correlated to known eruptions. The tephra at 310-315 cm was correlated to the FL eruption of Etna, the layer at 896 – 897 cm to the Y-3 eruption and is directly matched to TM-15 in the LGdM sequence and the layer at 1070-1075 cm is correlated to TM-18 in the LGdM sequence and therefore to the Campanian Ignimbrite (Wagner *et al.,* 2008)

Vogel *et al.* (2010a) undertook a tephra and paleoenvironmental study on core Co1202 from the north-eastern part of the lake (Figure 2.9), the composite core length being 14.94 m long; the core is thought to cover the last glacial-interglacial cycle. Four visible tephra horizons were identified at 1232.5 – 1229 cm (OT0702-9), 1146.5 – 1140 cm (OT0702-8), 752 – 743 cm (OT0702-6), and 620 – 617cm (OT0702-4) depth. In addition, through detection by either XRF element or magnetic susceptibility peaks, fine-grained glass shards were found that led to the identification of cryptotephras at

1447 – 1440 cm (OT0702-10), 825 – 822 cm (OT0702-7), 696 – 689 cm (OT0702-5), 277.5 – 269 cm (OT0702-3), 145.5 – 144 cm (OT0702-2) and 77.5 – 74.5 cm (OT0702-1). Therefore, in total, ten tephra layers have been discovered in this Lake Ohrid core. All were geochemically analysed using energy-dispersive spectrometry (EDS) of glass shards, performed using an EDAX-DX micro-analyser mounted on a Philips SEM 515 (Vogel *et al.,* 2010a). The correlations established with known eruptions are summarised in Table 2.7.

Table 2.7: Depth, origin and correlations of tephra layers occurring in the sediment record of core Co1202 from Lake Ohrid (Vogel *et al.,* 2010a). The correlations of the Lake Ohrid tephra layers to LGdM layers are also shown. Layers marked * Vogel *et al.* (2010a) do not actually refer to a TM layer but the most likely LGdM correlative is indicated
Sources: SV Somma-Vesuvius, CF Campi Flegrei, ET Etna, PA Pantelleria and CAMP. Campanian

Co1202 tephra layer	Depth (cm)	Correlation to LGdM layer	Source	Volcanic Eruption
OT0702-1	77.5–74.5	TM-2a or TM-2b	SV	AD 472 or AD 512
OT0702-2	145.5–144.0	N/A	ET	FL eruption
OT0702-3	277.5 – 269.0	TM-6*	SV	Mercato
OT0702-4	620.0 – 617.0	TM-15	CF	Y-3
OT0702-5	696.0 – 689.0	TM-16	SV	Codola
OT0702-6	752.0 – 743.0	TM-18*	CF	Campanian Ignimbrite
OT0702-7	825.0 – 822.0	N/A	PA	Green Tuff
OT0702-8	1146.5 – 1140.0	TM-24a	CAMP.	X-5
OT0702-9	1232.5 – 1229.0	TM-27*	CAMP.	X-6
OT0702-10	1447.0 – 1440.0	N/A	PA	P-11

The most recent tephra study from Lake Ohrid was undertaken by Caron *et al.* (2010) on core JO2004-1 from the south-western part of the lake (Figure 2.9). The composite core section is 10 m long and was continuously scanned at 1 cm resolution for the presence of volcanic particles. Volcanic material was recognised at 36.5 – 45.5 cm (JO-42) 185.5 – 188.5 cm (JO-187), 235 – 252 cm (JO-244), 571 – 577 cm (JO-575) and 938 – 942 cm (JO-941). The layers at 188 cm and 240 – 246 cm were visible layers whereas the other three are cryptotephras (Caron *et al.*, 2010). The tephra layers were analysed using an EDAX-DX micro-analyser (EDS analyses) mounted on a Philips SEM 515 and were correlated to known eruptions as follows: JO-42, Etna FL eruption, JO-187, Y-3, JO-244, Campanian Ignimbrite, JO-575, X-6 and JO-941, P11 (Caron *et al.*, 2010).

It is clear from this study that there are more tephra layers preserved in the northern parts of the lake, although the difference between the cores may reflect different

methodologies applied in the three studies. The relationship of all the Lake Ohrid tephra layers to LGdM layers and other layers within the Mediterranean is summarised in Table 2.8.

2.2.7 Summary

It is clear from sections 2.2.5 and 2.2.6 that numerous tephra layers have been identified in the Mediterranean region. Whilst this provides useful background knowledge for the current study it can also be confusing for a number of reasons. Firstly, various nomenclature schemes have been used to name tephra layers that are all from the same volcanic eruption. Secondly, some tephra layers are only distally described, meaning they have not been correlated to a proximal deposit or known eruption. However, some of these distally described layers have been traced to other sites and are known by their distal name, e.g. the Y-3. To clarify this situation Table 2.8 highlights the main tephra layers found in the region and also where tephra layers with a different name represent the same eruption.

It is apparent from Table 2.8 that there are numerous tephra layers that are preserved in more than one site over the Mediterranean region. This gives an indication of the tephra layers that are likely to be preserved in the cores studied in this research. As discussed in section 2.1, successful correlation of tephra layers requires the adoption of multiple approaches, including geochemical, stratigraphical and chronological. Therefore it is useful to identify those tephra layers that are likely to be common in the region and also useful for correlation by being either geochemically distinctive or stratigraphically well constrained (Figure 2.10). It is clear that the number of such potential layers reduces further back in time, due to the fact that there are fewer studies that extend to this time period. Of the twenty-one individual tephra layers identified in this review, seven are considered most useful for correlation due to their geochemical distinctiveness or stratigraphical context. These are either Etnan layers (Biancavilla) or layers from Pantelleria (Ante Green Ignimbrite, P-11) which both have generated magmas and therefore tephra layers that are geochemically unique among other Italian volcanic systems. The Mercato and Codola eruptions are both Somma-Vesuvius products that are the only eruptions of this volcano in their respective time period and therefore they can also be geochemically distinguished from other contemporaneous tephra layers. The Mercato tephra layer is also stratigraphically located within Sapropel 1 in the

Mediterranean Sea, making it both stratigraphically and geochemically distinctive. Finally the Y-3 is stratigraphically distinctive as it occurs on the MIS3/MIS2 boundary within the study area (Figure 2.10). Focussing on detecting the equivalents of these layers in the Adriatic marine sequences forms one of the initial objectives of the present study.

3. Site and Core descriptions

Three marine sequences from the Adriatic Sea have been selected for investigation in order to meet the aims and objectives set out in Section 1.3. This chapter will first consider the Adriatic Sea, its geographic and oceanographic setting and the suitability of the area for tephra studies. Secondly, the three marine sequences investigated in this study will be described and the paleoenvironmental data available for each sequence introduced. Palaeoenvironmental data for other key regional tephra sites will then be introduced before more detailed project aims and objectives are defined.

3.1 The Adriatic Sea

3.1.1 Geological setting

The epicontinental Adriatic Sea is an elongated, semi-enclosed basin located in the central Mediterranean between the Italian peninsula and Croatia (Figure 3.1) (Artegiani *et al.,* 1997a). Today, the Adriatic Sea is ca. 200 km by 800 km and is the largest semi-enclosed basin in the Mediterranean (Calanchi *et al.,* 1998), with a low axial topographic gradient in the north and a narrower and steeper shelf further south (Piva, 2007) (Figure 3.1). The Adriatic Sea is elongated in a NW – SE direction and corresponds to the foreland basin of the Apenninic chain (Ori *et al.,* 1986; Royden *et al.,* 1987). At present, sedimentation takes place predominantly along the western flank of the basin, due to basin-wide cyclonic circulation and the location of the Po delta which is the major drainage area feeding the basin and the main sediment entry point (Trincardi *et al.,* 1996; Calanchi *et al.,* 1998).

The basin is divided into three areas, the southern, central and northern Adriatic. The southern Adriatic connects the basin to the rest of the Mediterranean through the Otranto Strait. It is ca. 1200 m deep and continues north-westwards until the Gargano-Lagosta line and Pelagosa Sill (Asioli *et al.,* 1996) (Figure 3.1). The southern Adriatic slope is steep and reflects the impact of tectonic deformation and repeated mass failure (Verdicchio and Trincardi, 2006; Minisini *et al.,* 2006; Verdicchio *et al.,* 2007) making it morphologically complicated. Sediment cores from the south Adriatic slope may exhibit stratigraphic expansion during the Holocene (Verdicchio *et al.,* 2007; Piva *et al.,* 2008b).

The central Adriatic reaches its maximum depth of ca. 260 m in the Mid-Adriatic Deep (MAD), which is surrounded by the Northern and Central Adriatic shelf and is a slope basin partially filled by the glacial Po delta (Figure 3.1) (Piva *et al.,* 2008b). This basin offers an excellent palaeoenvironmental record through the last deglaciation (Asioli *et al.,* 1999, 2001), as a continuous sequence of marine mud was deposited during the Quaternary, including the eustatic minima of the last glacial maximum (LGM) and of previous glacial intervals (Trincardi *et al.,* 1996). Sediment cores from the MAD contain deposits that reflect the influences of atmospheric forcing, river runoff and water mass intrusion from the Mediterranean basin (Piva *et al.,* 2008b).

Finally, the northern Adriatic, extending from the Ancona-Pag Island line, is a low gradient shelf (Ciabatti *et al.* 1987; Trincardi *et al.* 1994) with a maximum depth of *ca* 70 m (Asioli, 1996) (Figure 3.1).

Within the Adriatic, three main factors affect the late-Quaternary sea-level cycle besides eustatic rhythms: 1) short-term changes in supply régime, 2) changes in basin morphology and 3) changes in the degree of connection to the rest of the Mediterranean.

Regional bathymetric contours show that during the LGM the Adriatic basin was connected to the rest of the Mediterranean Sea through a shallow sill (Figure 3.1). This connection was less than 50 m deep and therefore did not allow full exchange of intermediate and deep water masses (Trincardi *et al.,* 1996). This had led to a scarcity or, in some cases, a complete lack of planktonic Foraminifera deposited within the basin during the LGM (Jorissen *et al.,* 1993; Asioli *et al.,* 1996; Asioli, 1996).

Following the LGM at the onset of relative sea level rise, only ca. 14% of the modern Adriatic area was under water, with the majority being subaerially exposed (Trincardi *et al.,* 1996; Correggiari *et al.,* 1996). During the sea level rise following the LGM, sediment deposition was condensed on the outer Adriatic shelf but expanded both in the deeper basin, where a continuous marine record accumulated (Asioli *et al.* 1996) and on the inner shelf, where three seismic units mark distinctive phases of the sea level rise (Trincardi *et al.,* 1996). These units are known as the Late Quaternary Depositional Sequence (LQDS), the characteristics of which are summarised in Table 3.1.

Table 3.1: Late Quaternary Depositional Sequence (LQDS) System Tracts summarised from Calanchi *et al.* (1998); Trincardi *et al.* (1996) and Oldfield *et al.* (2003),

LQDS System Tract	Characteristics of the System Tract
High-stand systems tract (HST)	Corresponds to the late Holocene, base dated to ca. 4-5ka. Consists of a coastal mud prism that accumulated rapidly under the influence of the River Po.
Transgressive systems tract (TST)	Encompasses the early Holocene and late Glacial. Occurs in the interval 4-5 to 16ka.
Low-stand systems tract (LST)	Responds to the last Glacial when sea-level was approximately 120m lower than present.
Falling sea-level systems tract (FST)	Records the sea-level fall that occurred after MIS 5e until MIS 2.

3.1.2 Oceanographic setting

Today, the Adriatic basin has a microtidal régime which is dominated by a cyclonic circulation driven by thermohaline currents (Cattaneo *et al.,* 2003). As discussed in section 3.1.1, the overall Adriatic basin is divided into three areas, which also affect the oceanographic régime of the basin: the Northern basin with shallow sea water mass characteristics; the central Adriatic, which is a transition basin but has some well-defined open sea characteristics and finally the Southern basin with open sea water mass characteristics below a depth of 150 m (Artegiani *et al.,* 1997a). There are also three water masses present in the Adriatic Sea (Cattaneo *et al.,* 2003): 1) a surface temperature-mixed layer from 0 – 30 m, with the upper 10 m of coastal origin (mainly Po River runoff) which is cooler and less saline than deeper waters; 2) Levantine Intermediate Water (LIW) from 30 – 130 m, whose maximum salinity occurs at about 80 m water depth; and 3) a bottom water region below 130 m, with dense waters that form in the Northern Adriatic and then sink southwards (Cattaneo *et al.,* 2003). Finally, circulation in the Adriatic also has three main components: (1) river forcing causing heat loss and low-salinity water gain; (2) wind forcing at the surface producing deep-water masses and seasonal changes in circulation; (3) Otranto channel forcing balancing the exchange between freshwater discharge and northern cooling with the influx of warm and salty waters from the Mediterranean (Artegiani *et al.,* 1997a, b). The ocean currents operating in all three parts of the Adriatic basin are shown in Figure 3.2.

The North Adriatic Sea receives the highest river runoff of the entire Mediterranean Sea. The Po River has an average annual discharge of 1500 m^3s^{-1} and accounts for about

50% of the total northern Adriatic river runoff (Syvitski and Kettner, 2007). The basin is very shallow (less than 35 m deep in the area north of the Po delta) and therefore is highly sensitive to variations in river runoff and atmospheric conditions (Piva, 2007). The Po River plume traps fresh water along the west side of the basin which is the result of a cyclonic circulation gyre. Currents are stronger away from the gyre centre, meaning the prevailing flow of fresh water is towards the South East, along the Italian coast (Figure 3.2) (Cattaneo *et al.,* 2003).

The Northern Adriatic also plays a major palaeoceanographic role, being one of the sites of dense water formation which ventilates the Eastern Mediterranean. Winter outbreaks of the cold and dry north-easterly Bora wind make Northern Adriatic surface waters colder and denser. They then sink and move towards the deeper Ionian Sea and Eastern Mediterranean (Figure 3.2) (Zore-Armanda, 1963; Bignami *et al.,* 1990; Artegiani *et al.,* 1989, 1997a). It is this formation and subsequent southward movement of North Adriatic Dense Water (NAdDW) that causes the northern Adriatic to influence the dynamics of the central and southern parts of the basin, otherwise the northern Adriatic appears to be dynamically independent from the rest of the basin (Artegiani *et al.,* 1997a).

The Northern-Central Adriatic basin is connected to the Southern Adriatic via the Pelagosa sill and the Southern Adriatic is connected to the wider Mediterranean by the Otranto Strait (Figure 3.1). This connection allows shallower Modified Atlantic Waters and Levantine Intermediate Waters to reach the Adriatic basin (Figure 3.2) (Orlic *et al.,* 1992). The bathymetry of the Adriatic basin, including the presence of sills is important in the palaeoceanographic evolution of the Adriatic during the past sea-level oscillations (Piva, 2007). At times of low sea level, the presence of the sills and structural highs meant that deeper water masses were unable to pass and ventilate the Adriatic Sea floor, which had the effect of isolating the Northern-Central basin and making its history slightly different from that of the Eastern Mediterranean (Piva, 2007).

The Southern Adriatic is the site of convergence of two distinct water masses, the North Adriatic Dense Water (NAdDW) and the Levantine Intermediate Water (LIW) (Civitarese *et al.,* 2005). The Southern Adriatic is also a site of dense water formation, which takes place in the Southern Adriatic Pit (SAP) which is 1200 m deep (Figure 3.2). Dense water formation occurs due to outbreaks of cold continental air from the Balkan

Peninsula, which takes heat from the sea surface layer through evaporation and causes movement through the water column (Piva, 2007).

Therefore, there are two categories of deep water in the Adriatic, the first formed in the northern Adriatic region which is cool and relatively fresh and the second of much higher temperature and salinity, formed and found in the Southern Adriatic. Vertical mixing between these water masses is a powerful dynamic process in the basin (Artegiani *et al.,* 1997a).

3.1.3 Seismic and stratigraphical investigations in the Adriatic Sea

The work in this thesis builds upon a great deal of research that has been carried out in the Adriatic Sea. This section summarises some of the key projects that have undertaken work in the Adriatic and which has laid the foundations for this current project.

3.1.3.1 PALICLAS

The PALICLAS (Palaeoenvironmental Analysis of Italian Crate Lake and Adriatic Sediments) project was a two year project between 1994 and 1996, the results of which are published in Guilizzoni and Oldfield. (1996). The main objectives of the project were to:

1. Provide improved fine-resolution proxy palaeoclimate records for the last 25,000 years in central Italy using a range of biological and geochemical indicators.
2. Establish direct comparisons with fine resolution records from neighbouring sources of sediment-based palaeoenvironmental evidence, using the best techniques available for dating, correlating and synchronising the records.
3. Make 'state of the art' reconstructions of past climate conditions on annual to decadal and century levels of temporal resolution, depending on the evidence for rapid change during each period.
4. Provide these reconstructions as a contribution to improving existing climate models in a transitional area between the high latitudes, eccentricity-dominated climate and the more strongly precession-related climate of North Africa (Oldfield, 1996).

The research focussing on the Adriatic Sea saw the following studies undertaken. Firstly, high resolution seismic profiles were obtained for parts of the Adriatic, set within the context of a detailed sequence stratigraphy reflecting the evolution of the marine record in response to changing water depth and volume, shoreline location, major delta migration and internal water circulation (Trincardi *et al.*, 1996). Secondly, a chronological study was undertaken, including radiocarbon dating of planktic forams (Langone *et al.*, 1996), tephrochronology of Adriatic sea cores (Calanchi *et al.*, 1996) and palaeomagnetic stratigraphy (Rolph *et al.*, 1996; Alvisi and Vigliotti, 1996). Thirdly, Foraminifera ecozones were established (Asioli, 1996) and stable isotope stratigraphies were generated for several sites in the Adriatic Sea (Ariztegui *et al.*, 1996).

3.1.3.2 EURODELTA and EUROSTRATAFORM

EURODELTA was a project designed to improve understanding of the depositional processes affecting the Mediterranean prodeltas. The main goals of the project were to

1. Understand the architecture and growth patterns of prodeltas;
2. Improve predictions of prodelta modifications in the future;
3. Define how (and how much) sediment escapes to deeper basins.

Part of the research focussed on The Po-Adriatic system, investigating the river catchments, seismic stratigraphy (e.g. Cattaneo *et al.*, 2003), sedimentary processes, sea floor morphology and geochronology.

The EUROSTRATAFORM project ran from 2002 and 2005 and aimed to understand sedimentary systems from source to sink, in other words, how sediment particles are transported from river mouths, across the shallow shelf and/or through submarine canyons, down to the deep sea. This was achieved by studying the different delta complexes in the NE Atlantic and Mediterranean Seas, by examining how the sedimentary systems vary over time and space, the different pathways that sediment can take across neighbouring shelves, the variability in the amount of sediment supplied to the system, the causes of this variability and how and where sediment accumulates (Weaver *et al.*, 2006).

The work in the Adriatic focussed firstly on the Bari Canyon system which intercepts sediment derived from the Po and southern Apennine rivers and funnels the material to

the deep South Adriatic basin (e.g. Ridente *et al.,* 2007, Trincardi *et al.,* 2007). Other work considered the bedforms of the South Adriatic basin (Verdicchio and Trincardi, 2006) and sedimentation patterns south along the Apennine shelf (Palinkas *et al.,* 2006; Weaver *et al.,* 2006).

One of the key aims of both the projects was the development of more robust age models to underpin precise correlations of marine sediment sequences in various sectors of the Mediterranean, including the Adriatic Sea (e.g. Lowe *et al.,* 2007b).

3.1.3.3 PROMESS

The PROMESS-1 (PROfiles across Mediterranean Sedimentary Systems) European project ran from 2004 – 2006 and had the general objective to obtain detailed high quality geological data in two deltaic margin sites, one in the Gulf of Lions in the north-western Mediterranean Sea, and one in the Adriatic Sea. The purpose of the project was a better understanding of the sedimentological and climatological history of the Adriatic over the last 500,000 years (Fugro Engineers B.V. 2004). The three major objectives were:

1. To reconstruct sea-level and climate changes during the last 500,000 years. Due to the very high sedimentation rates (> 1m/1000 yr on average) of the studied areas, access to very high resolution proxy records of regional change were assured.
2. To analyse the impact of large-scale environmental changes on slope stability, and to quantify slope processes by *in situ* measurements of physical parameters in zones prone to failure, or where slides already occurred.
3. To understand the processes that form strata on continental margins, with respect to sea-level and climatic changes, instabilities and oceanic processes, and recent tectonic activity (Berné *et al.,* 2004).

In the Adriatic, this research focussed on the cores PRAD 1-2 and PRAD 2-4. The coring site for this project was chosen based on the considerable amount of knowledge on the bathymetry and stratigraphy of the basin obtained from the preceding projects (Sections 3.1.3.1 and 3.1.3.2).

3.1.3.4 Adriatic Event Stratigraphy

Foraminifera research from the above projects led to the establishment of regional ecozones for the Adriatic sea. These ecozones are based on the assessment of planktic and benthic foram assemblages obtained from of a number of core sites in the Adriatic Sea (Table 3.2) (Asioli, 1996).

Table 3.2: Ecozones, their age boundary, key species of each ecozone with reported bioevents and duration of last-deglaciation ecozones. The key species defining each ecozone are in bold. Reproduced from Asioli (1996).

Ecozone	Age Boundary (cal kyr BP)	Planktic Foraminifera assemblage	Duration (yr)
1	6 - 0	***G. sacculifer*, *G.* ex gr. *ruber*, *Orbulina*, *G. praecalida***, *G.bulloides*, *G. quinqueloba*	6000
2	8 - 6	last occurrence of *G. inflata* ***G. inflata*, *G.* ex gr. *ruber*, *N.pachyderma*, *Orbulina***, *G. bulloides*, *G. quinqueloba*, *G.sacculifer*, *G. praecalida*	2000
3	9.2 - 8	***G. ex gr. ruber*, *Orbulina*, *G. praecalida***, *G. bulloides*, *G.quinqueloba*	800
4	11.3 - 9.2	last occurrence of *G. truncatulinoides* ***G.* ex gr. *ruber*, *G.inflata*, *G. truncatulinoides*, *N. pachyderma***, *G. bulloides*, *G. quinqueloba*	1700
5	12.55 - 11.3	***G. bulloides*, *G. quinqueloba***, *N. pachyderma*	1300
6e	12.78 - 12.55	***G. quinqueloba*, *G.* ex gr. *ruber***	230
6d	12.98 - 12.78	***G. quinqueloba*, *N. pachyderma***, *G.* ex gr. *ruber*	200
6c	13.32 – 12.98	***G.* ex gr. *ruber*, *G. quinqueloba***	340
6b	13.45 – 13.32	***G. bulloides***, *N. pachyderma*, *G.* ex gr. *ruber*	130
6a	14.3 – 13.45	strong increase of *G.* ex gr. *ruber* abrupt decrease of *G.quinqueloba* ***G.* ex gr. *ruber***, *G. bulloides*, *G. quinqueloba*	850
A	39 ? – 14.3	planktic foraminifera very scarce *G. quinqueloba*, *G.bulloides*	
B	?	***G. inflata*, *G.* ex gr. *ruber*, *Orbulina***, *G. bulloides*, *N.pachyderma*	
C	?	planktic foraminifera very scarce *G. bulloides*, *G.quinqueloba*, *G.* ex gr. *ruber*	
D	I.S.3	***G. bulloides*, *G. inflata*, *G.* ex gr. *ruber***, *Orbulina*, *N. pachyderma*, *N. dutertrei*	
E	I.S.3	***N. pachyderma*, *G. inflata*, *G. truncatulinoides*, *N.dutertrei***, *G.* ex gr. *ruber*, *Orbulina*, *G. bulloides*	
F	I.S. 3-4 ?	***G. bulloides***, *G. inflata*, *G.* ex gr. *ruber*	
G	>67.5	***G.* ex gr. *ruber***, *Orbulina*, *G. inflata*, *G. bulloides*, *G.quinqueloba*	

These ecozones were correlated to the event stratigraphy scheme proposed for the GRIP ice-core record by Björck *et al.* (1998) and Walker *et al.* (1999), based on the GRIP oxygen isotope stratigraphy and chronology (Asioli *et al.*, 1999). Björck *et al.* (1998) discuss the advantages of Event Stratigraphies, namely the emphasis on local evidence and small-scale marker events rather than globally synchronous environmental changes.

The Adriatic Event Stratigraphy is a database of isochronous stratigraphic markers found in the Adriatic region that can be integrated into age-depth models and act as tie-points between sequences (Asioli *et al.,* 1999).

To summarise: due to the collective results generated by these previous research projects, the team at ISMAR, Bologna have a very good understanding of the sedimentological infilling of the Adriatic basin, encompassing the Po influx and counter-clockwise flow in the north, the sequence stratigraphy of the central basin and other sedimentary contexts. The ecozones developed for the Adriatic allow correlations between sequences based on biostratigraphy. This has influenced the research in this thesis, as sites were selected for study on the basis of known sedimentary context, probable continuous sedimentation, and the wealth of palaeoenvironmental data that is available.

3.1.4 Suitability of the basin for tephra studies

As discussed in Chapter 2, there has been an intense and continual recurrence of volcanic activity in the Mediterranean region (Keller *et al.,* 1978). The highly explosive nature of this activity and the fact that different volcanic centres have quite diverse chemical compositions makes the region a favourable area in which to conduct tephra studies (Narcisi and Vezzoli, 1999).

The Adriatic basin, in particular, has favourable conditions for the development of a regional tephrochronology due firstly to its downwind location from and proximity to the Southern Italian volcanoes (Siani *et al.,* 2004) (Figure 2.2). Secondly, there is a continuous sedimentary record from the deep basin to the shelf, with high sediment accumulation rates and expanded records on the Adriatic shelf (Calanchi *et al.,* 1998). Thirdly, in the Central Adriatic, in particular, there are fewer problems associated with strong seismicity and complex bathymetry than those observed in the Aegean and Tyrrhenian Seas (Narcisi and Vezzoli, 1999).

These factors make the area highly suitable for tephra investigations and other studies have documented the presence of tephra layers in marine successions (e.g. Paterne *et al.,* 1988; Calanchi *et al.,* 1996, 1998; Siani *et al.,* 2004 and Calanchi and Dinelli, 2008). However, these studies are mainly based on visible tephra layers, whereas the

current study examines whether far more comprehensive tephrochronologies could be developed if non-visible tephra layers are also exploited. The results may amplify the known spatial extents and dispersal patterns of the products of major eruptions.

3.2 PRAD 1-2

The PRAD 1-2 core was taken as part of the PROMESS 1 (PROfiles across Mediterranean Sedimentary Systems) European Project by the coring device on board R/V Bavenit, a geotechnical vessel owned by FUGRO in June 2004. The core was taken from the western flank of the Central Adriatic basin within the Mid-Adriatic Deep (LAT 42°40′34.7826″N; LONG 14°46′13.5565″E) in 185.5 m water depth (Figure 3.3). The core is a continuous sediment sequence of 71.2 m, with a recovery of 99.96%. It consists of 89 sections, each of which is about 75–80 cm long and 6 cm in diameter. However only the top ca. 35 m are analysed in this research because this section can be compared to other sequences in the area. After splitting, half of the core was archived and the working half was sampled for tephrochronology, micropalaeontology and macropalaeontology, oxygen and carbon isotopes, sedimentology, magnetostratigraphy, geochemistry and sediment properties (Piva, 2007; Piva *et al.*, 2008a).

A CHIRP sonar profile (AMC-236) taken along the core site allows subtle variations in seismic facies to be observed with a less than 0.5 m resolution (Figure 3.4). Figure 3.4 shows that PRAD 1-2 did not pass through any obvious sedimentary breaks or deformities and the sedimentary units cored appear to be stratigraphically continuous in the immediate surrounding area, this is also reflected in the core photographs of the sections analysed in this study (Figure 3.5). PRAD 1-2 is the longest marine record of substantially undisturbed sediment available for the Adriatic Basin (Piva *et al.*, 2008a) and its lithology is composed of predominantly marine muds (Figure 3.6). The position of tephra layers identified by visual scanning of the core or whilst sieving for foraminiferal analysis are indicated on Figure 3.6. These are not the results of the present study. Overall, the available sedimentological data supports the stratigraphical integrity and undisturbed nature of the sampled sequence and indicates its suitability for establishing a continuous tephrochronology.

The proxy information obtained for this core sequence has been reported in Piva (2007) and Piva *et al.* (2008a). Raw isotopic and foraminifera data and information about

sapropel equivalent layers were provided to the author by A.Piva and A. Asioli and raw magnetic data was provided to the author by L. Vigliotti. The main information of use to this study that was not generated by the author will now be summarised.

3.2.1 Oxygen isotope stratigraphy

Two $\delta^{18}O$ records were obtained for the PRAD 1-2 record, the first based on the planktic foraminifera *G. bulloides* and the second on benthic foraminifera *B. marginata*. The two records show very consistent (sub-parallel) trends, albeit with the latter systematically shifted toward higher values (Figure 3.6).

The $\delta^{18}O$ record of *G. bulloides* allows reconstruction of the most significant stratigraphic events, Marine Isotope Stages (MIS). For the studied section, abrupt shifts from highest (~4‰) to the lowest values (less than 0.5‰) at approximately 2 and 32 m below seafloor (mbsf) are observed. These shifts are paralleled by similar ones in the benthic $\delta^{18}O$ record (typically between 5 and 2.5‰) (Figure 3.6) and have been attributed to isotopic terminations at the end of MIS 2 and MIS 6 respectively (Piva *et al.,* 2008a). The combined planktic and benthic isotope records allowed recognition of subordinate climatic oscillations, such as the cold and warm isotopic substages within the MIS 5 (Figure 3.6). These cold stages have been labelled MIS 5.2 and MIS 5.4 by Piva *et al.* (2008a) but are more commonly known as MIS 5b and MIS 5d. For continuity, the nomenclature adopted by Piva *et al.* (2008a) will also be used in this study.

The *G. bulloides* $\delta^{18}O$ record also shows scattered abrupt spikes (with excursions up to 3‰ toward lighter values) in the upper 6 m of the core. This is attributed to diluted surface water salinity over short-lived intervals of increased run off from the Po delta at times when the basin was markedly reduced in extent and fresh water dominated (Cattaneo and Trincardi, 1999; Asioli *et al.,* 2001). This is supported by the fact the warm water component of the planktic assemblage is almost absent in this interval (Figure 3.6) indicating that the abrupt spikes in the $\delta^{18}O$ record are not a temperature effect (Piva *et al.,* 2008a).

Piva *et al.* (2008a) attempted to fine-tune correlations between the PRAD 1-2 and the GISP2 $\delta^{18}O$ records in order to detect Dansgaard – Oeschger (D-O) cycles in the PRAD 1-2 sequence, as D-O cycles had already been identified in sequences from the western Mediterranean (e.g. Rohling *et al.*, 1998; Sànchez Goñi *et al.*, 2002; Sierro *et al.*, 2005) and eastern Mediterranean (Allen *et al.*, 1999). These correlations imply a major atmospheric connection affecting a wider region of the Northern Hemisphere than just the North Atlantic, where the events were first recognised (Piva *et al.*, 2008a).

The *G. bulloides* $\delta^{18}O$ record from PRAD 1-2 was wiggle-matched to the GISP2 $\delta^{18}O$ record, then plotted against time, whereupon most of the D-O stadial (S) and interstadial (IS) events were considered to be represented in the PRAD 1-2 sequence (from S20 to IS3). Other proxies were used to support the correlations such as XRF data (Ca/Ti and K/Ti ratios) and sediment lightness. The results are reproduced in Figure 3.7 with wiggle-matched events highlighted.

3.2.2 Foraminifera biostratigraphy

Piva *et al.* (2008a) use foraminiferal abundance data for stratigraphic purposes through the identification of regional bioevents in the sequence (the species the bioevents refer to are shown in Figure 3.8) and for investigating climate cyclicity.

The first and main planktic foraminiferal bioevent is the Last Occurrence (LO) of *Globorotalia inflata* at 0.60 m (Figure 3.8). This is a well constrained biostratigraphic event for the central Adriatic, of mid-Holocene age, dating to ca. 6 ka B.P. (Jorissen *et al.*, 1993; Asioli, 1996; Ariztegui *et al.*, 2000; Asioli *et al.*, 1999, 2001). The second bioevent recorded is the LO of *Sigmoilina sellii* at 3 m, an event radiocarbon dated to 12.7 ^{14}C ka B.P. and hence occurring near the base of the Bølling interval (Jorissen *et al.*, 1993, Asioli, 1996). The entry of *S. sellii* into the core is also observed at 12.00 m and is radiocarbon dated to 15.3 ^{14}C ka B.P. (Jorissen *et al.*, 1993) (Figure 3.8). The Last Common Occurrence (LCO) of *G. inflata* is observed at 16.9 mbsf within MIS 3. The next bioevents observed in the core relate to the species *Hyalinea balthica*. The entry of this species is observed at 30.60 m and its LCO is observed at 14.00 m. Both

of these are considered new bioevents for the central Adriatic (Piva *et al.,* 2008a). Finally, the entry and subsequent last occurrence of *G. truncatulinoides* in MIS 5.1 are observed at 22.59 m and 22.30 m respectively (Asioli, 2011, *pers comm.*) (Figure 3.8).

Variations in the assemblages of planktic foraminifera were compared and integrated with the isotope stratigraphy (Figure 3.6). There is a good agreement between the oxygen isotope stratigraphy and percentage of warm foraminiferal species, with the planktic foraminifera characteristic, of warm climates, (*Globigerinoides ex gr. ruber, Orbulina, Zeaglobigerina rubescens, Globigerinoides sacculifer, Globigerinella* spp) (Figure 3.6 red curve) being abundant in the interglacial and interstadial periods and scarce or absent in colder periods. Piva *et al.* (2008a) suggest this is because the water column in the Mid Adriatic Deep was substantially reduced when global sea level fell.

The agreement between the planktic and benthic $\delta^{18}O$ records and the percentage of warm planktic foraminiferal species suggests that the oxygen isotope record and both foraminiferal abundances and species assemblages are responding to the same forcing factors.

3.2.3 Sapropel stratigraphy

Sapropels are dark coloured, organic rich sedimentary layers deposited in the Eastern Mediterranean Sea that indicate changes in global and regional climate (Triantaphyllou *et al.,* 2010). Sapropels coincide with precessional minima, which are periods of more humid climate in the Mediterranean (Rohling and Hilgen, 1991), associated with increased river runoff and therefore an increase of soil-derived nutrients entering the sea. The organic rich nature of sapropels implies a combination of deep water anoxic conditions resulting in enhanced organic matter preservation and elevated marine productivity (Triantaphyllou *et al.,* 2010). Hilgen (1991) describes sapropel units as brownish and often laminated, whereas Kidd *et al.* (1978) define the units as having an organic matter content of between 0.5 and 2 %. Neither of these definitions are absolute as post-depositional processes may affect the organic content, while laminations are not always present in sapropels (Piva *et al.,* 2008a).

Piva *et al.* (2008a) recognise sedimentary units within PRAD 1-2 that are dark and in some cases laminated and are accompanied by micropalaeontological, geochemical and

palaeomagnetic properties that indicate less oxygenated seafloor conditions (Figure 3.9). The intervals are characterised by low $\delta^{18}O$ and $\delta^{13}C$ values, minima in magnetic parameters, low colour reflectance and a foraminiferal assemblage that is characteristic of that seen in Eastern Mediterranean sapropel units. Therefore, Piva *et al.* (2008a) term these sedimentary units *sapropel-equivalent layers* and assume them to occur synchronously with Eastern Mediterranean sapropel layers. In diagrams presenting the stratigraphy of PRAD 1-2, the sapropel-equivalent layers are labelled S1, S3, S4, S5 and S6 but it should be borne in mind that they represent sapropel-equivalent events.

3.2.4 Magnetostratigraphy

Palaeomagnetic and rock-magnetic investigations were undertaken on PRAD 1-2 at 1 cm intervals. The Natural Remanent Magnetisation (NRM) data exhibit a constant normal polarity for all the sections, so that the borehole can be completely ascribed to the Brunhes Normal-polarity Magnetozone (Piva *et al.*, 2008a). A short interval with reverse polarity was identified between 37.28 and 37.40 mbsf and is also observed in the Anhysteretic Remanent Magnetisation (ARM) and Saturation of Isothermal Remanent Magnetisation (SIRM) measures (Figure 3.10). This magnetic event occurs close to the boundary between MIS 7 and MIS 6 (Figure 3.10) and was correlated to the Iceland Basin Excursion (IBE) which occurred at around 188 ka B.P. (Laj *et al.*, 2006; Piva *et al.*, 2008a).

Also visible in Figure 3.10 are the minima in the magnetic measures that occur during the sapropel-equivalent units (section 3.2.3), which is another indicator of fresh surface waters, accompanied by less-oxygenated seafloor conditions (Piva *et al.*, 2008a). There are also sharp peaks in the ARM and SIRM measures observed throughout the core (e.g. ~16, ~25, ~32 and ~34 mbsf) which L. Vigliotti (*pers. comm)* attributes to the presence of tephra layers.

3.2.5 Summary

The proxy information available for PRAD 1-2 and the interpretations made from them allow some questions to be tested through the establishment of a tephrostratigraphy and tephrochronology for the core.

1. Are the oxygen isotope records recording a local (Adriatic Sea) scale influence or a more regional (Mediterranean Sea) scale forcing?
2. Are the correlations made between shifts in the PRAD 1-2 $\delta^{18}O$ records and the GISP2 Dansgaard-Oeschger stadials and interstadials robust?
3. Are the regional bioevents (especially the new ones identified for the first time in this sequence) time-parallel markers for different sequences?
4. Is the assumed synchroneity between the Central Adriatic sapropel-equivalent events and the Eastern Mediterranean Sapropels valid?

An attempt will be made to answer these questions by using tephra isochrons identified in PRAD 1-2 and their equivalents in other marine and terrestrial records in the region.

3.3 SA03-03

The SA03-03 core was collected during the SAGA-2003 cruise by the coring device on board the R/V Urania. The core was taken on the down-current limb of a sediment wave (Verdicchio *et al.*, 2006), from the Southern Adriatic basin (LAT 41°56.8860′N; LONG 16°57.4564′E) in 470.7 m water depth (Figure 3.3) (Piva, 2007). The core is a continuous sediment sequence of 10.44 m consisting of predominantly marine muds. A CHIRP sonar profile (AMC-161), taken across the sediment wave from which core SA03-03 was obtained from, shows subtle erosion at the sea floor and in the sub-surface (Figure 3.11) (Verdicchio *et al.*, 2006). However, Figure 3.11 also shows that the SA03-03 core sequence does not pass through any obvious sedimentary breaks or structures, which makes it appropriate for a comprehensive tephra study. The lithostratigraphic description of the core, shown in Figure 3.12 was generated by Piva (2007). The positions of tephra layers shown in Figure 3.12 were assigned following visual scanning of the core during lithological descriptions and whilst sieving for foraminiferal assemblages, and are not the results of the present study.

The core was subsequently sub-sampled for tephrochronology (this study), micropalaeontological study, oxygen isotope variations based on planktic foraminifera, and magnetostratigraphy. Raw isotopic and foraminifera data and information about sapropel equivalent layers were provided to the author by A.Asioli and A.Piva and raw magnetic data was provided to the author by L. Vigliotti. Some of this proxy information is reported in Piva (2007).

3.3.1 Oxygen isotope stratigraphy

One oxygen isotope record based on the planktic foraminiferal species *G. bulloides* was obtained for SA03-03 (Figure 3.12). This record allows the reconstruction of MIS events, which suggest that the lowermost 8 m of the core represent deposits of the last glacial interval (Verdicchio *et al.,* 2006). The core does not reach the present day, as values for the first 2 m show enriched $\delta^{18}O$ values of 3 – 4 ‰, which is considered too enriched for Holocene values, suggesting the top of the sequence dates to the last glacial period.

There is little variation in the $\delta^{18}O$ record, possibly as the sequence is fairly expanded throughout MIS 2 and 3 and therefore isotopic measurements at 10 cm resolution are not detailed enough to identify some of the changes observed in the PRAD 1-2 record (Section 3.2.1). The $\delta^{18}O$ values rise to 4 ‰ at about 7.60 m, interpreted as representing the transition to MIS 4 within the core.

The base of the core sequence records a very light peak in $\delta^{18}O$ values of approximately 0 ‰, which seems to correspond to the MIS 5.5 sub-stage (Piva, 2007). However, it is believed that the $\delta^{18}O$ record at the base of the sequence shows evidence of discontinuous sedimentation during MIS 5, as there is not a clear expression of MIS 5.2 and MIS 5.3 (A. Asioli, 2009 *pers. comm.)* which is interpreted as evidence of strong seafloor erosion during the later part of Stage 5 (Verdicchio *et al.,* 2006). For this reason the other MIS 5 sub-stages are not identified in the core stratigraphy (Figure 3.12).

Piva *et al.* (2008c) also attempt to correlate the *G. bulloides* $\delta^{18}O$ record for SA03-03 with the GISP2 $\delta^{18}O$ records by matching oscillations in the SA03-03 $\delta^{18}O$ record with D-O interstadials and cross-checking the results against oscillations in percentages of foraminiferal species (Figure 3.13)

3.3.2 Foraminifera biostratigraphy

The foraminiferal results obtained from core SA03-03 have been used for stratigraphical subdivision and evidence for climate cyclicity (Piva, 2007) (Figure 3.14).

The first bioevent is the Entry of *Sigmoilina sellii* at 1.40 m (A. Asioli, 2011, *pers. comm.*), this event is radiocarbon dated in another sequence to 15.3 ^{14}C ka B.P. (Jorissen *et al.*, 1993). The core does not extend far enough into MIS 2 for the LO of *S. sellii* to be detected. The LCO of *G. inflata* is observed at 5.00 m within MIS 3, where warm planktic species become more common (Piva, 2007). Finally, the Entry and subsequent LO of *G. truncatulinoides* are observed at 10.00 m and 7.80 m respectively. The former characterises MIS 5 sediments, whilst the latter approximates the boundary between MIS 5 and MIS 4 (Piva, 2007). All of the bioevents noted in SA03-03 are also detected in PRAD 1-2 (Section 3.1.2) which will allow a comparison of the timing of events in each sequence using tephra isochrons.

Variations in the assemblages of planktic foraminifera were compared and integrated with the isotope stratigraphy (Figure 3.12). There is a good agreement with the oxygen isotope stratigraphy and the percentage of warm foraminiferal species, those planktic foraminifera characteristic of warm climates (Figure 3.12 red curve) being abundant in warmer (interstadial) periods and scarce or absent in colder periods. There also seem to be spikes in the warm species curve that are concurrent with the spikes in the δ^{18}O records, such as at around 10.00m. This agreement between the planktic δ^{18}O records and the percentage of warm planktic foraminiferal species suggests that the oxygen isotope record and foram assemblages are responding to the same forcing factors. As shown in Figure 3.12, the variations in abundance of selected foraminiferal species have also been used alongside the δ^{18}O record to match oscillations in the SA03-03 records with GISP2 D-O events.

3.3.3 Sapropel stratigraphy

Sapropel-equivalent events (see section 3.2.3) are also identified in SA03-03. In diagrams presenting the stratigraphy of SA03-03, the sapropel-equivalent layers are labelled Sapropel 3 (S3) and Sapropel 5 (S5) but it should be borne in mind that they represent sapropel-equivalent events. The base of the core encounters Sapropel 5 (Verdicchio *et al.*, 2006) between 10.20 and 10.40 m. This sapropel is identified due to depleted δ^{18}O values at this point (Figure 3.12). Sapropel 3 is the only other sapropel layer identified in the sequence from 8.30 – 9.50 m where the δ^{18}O values are also depleted (Figure 3.12). As discussed in section 3.3.1, the lower part of the core does not seem to represent fully the MIS 5 interval. Sapropel 4 would be expected at the base of

MIS 5.3 but this sapropel is not clearly visible in core SA03-03 (A. Asioli, 2009 *pers comm*.).

3.3.4 Magnetostratigraphy

Magnetic susceptibility measures have been undertaken on SA03-03 and are presented in Figure 3.12. This is a different magnetic measure to those undertaken on PRAD 1-2 (Section 3.2.4). However, the minima in magnetic susceptibility characterising sapropel units (section 3.3.3) are still visible. As in PRAD 1-2, there are also sharp peaks in the magnetic measures observed throughout the core at approximately 1, 4 and 9 m depth which L. Vigliotti (*pers. comm)* attributes to the presence of tephra layers.

3.3.5 Summary

The proxy information available for SA03-03 and the interpretations made from them allow for some additional questions to those posed in Section 3.3.5, that can be tested using tephrostratigraphy and tephrochronology. They are:

1. Do the oxygen isotope records of PRAD 1-2 and SA03-03 record similar variations or is there a difference in isotopic response between the central and southern sectors of the Adriatic?
2. Does tephrostratigraphical information support the matching of $\delta^{18}O$ variations to D-O cycles between PRAD 1-2 and SA03-03?
3. Do the bioevents common to SA03-03 and PRAD 1-2 occur within the same time period?

These questions will be addressed using tephra layers identified in SA03-03 and comparing them with the PRAD 1-2 tephra record.

3.4 RF93-77

The RF93-77 core sequence was collected as part of the PALICLAS (Palaeoenvironmental Analysis of Italian Crater Lake and Adriatic Sediments) project (Section 3.1.3.1) during the RF93 cruise using the 12 m piston coring device on board

the R/V Urania (Trincardi *et al.*, 1996). The core was taken on the southern flank of the MAD in the Central Adriatic basin where it is possible to reach deposits older than the Last Glacial Maximum (LAT 42°26′36.6″N; LONG 15°05′59.7″E) in 152 m water depth (Figure 3.3) (Asioli, 1996) and at a location very close to that of PRAD 1-2. The core sequence is 8.15 m long and composed of predominantly marine muds (Figure 3.15). Tephra layers shown on the core lithological log were identified purely by visual scanning of the core, and do not represent results derived from the present study. Due to the sampling techniques employed, the sediment record is greatly compressed (Langone *et al.*, 1996) and crosses two erosional hiatuses (Trincardi *et al.*, 1996). This may have led to sediment reworking and will need to be considered when interpreting the results of the new tephra investigations (this study).

The core has been sampled for tephra content (Calanchi *et al.*, 1998 and this study), micropalaeontological studies (Asioli, 1996), oxygen isotope ratios based on planktic and benthic forams, (Ariztegui *et al.*, 1996) and magnetostratigraphy (Alvisi and Vigliotti, 1996). The information has been published as part of the PALICLAS project report in Guilizzoni and Oldfield (1996) and only key information of relevance to the present study is summarised below. Raw isotopic and foraminifera data and information about sapropel equivalent layers were provided to the author by A.Asioli and raw magnetic data was provided to the author by L. Vigliotti.

3.4.1 Oxygen isotope stratigraphy

Two $\delta^{18}O$ records were obtained for the RF93-77 record, the first from the planktic foraminifer *G. ruber* and the second from the benthic foraminifer *B. marginata* (Figure 3.15).

The planktic record is not continuous. From the bottom of the core to 7.20 m, the isotopic values fluctuate between 2.5 and 0.5‰ and then from 7.20 m to 6.50 m an increasing trend can be observed, reaching values of 2.5‰. There is a short appearance of *G. ruber* between 4.10 and 4.40 m and a $\delta^{18}O$ value of about 1.5‰ is recorded. An increasing $\delta^{18}O$ trend is observed between 220 and 180 cm, with the record being interrupted during the Younger Dryas. During the Holocene, fluctuations of 0.5 ‰ are observed, although there is a sustained trend from values of 0 to 1.5 ‰ (Ariztegui *et al.*, 1996).

The benthic $\delta^{18}O$ record of *B. marginata* is more continuous and shows a very consistent (sub-parallel) trend to the planktic record (where it is available), albeit that the benthic record is systematically shifted towards heavier isotopic values (Figure 3.15). There is a shift to heavier $\delta^{18}O$ values at about 7.50 m, which has been taken to mark the MIS 5.2 oscillation. From this depth there is a trend to more depleted $\delta^{18}O$ values, until 7.30 m when values are at their lowest of 2.0‰. From this depth to 5.50 m a trend towards heavier values can be observed, reaching maximum values of 5.0‰ (Ariztegui *et al.*, 1996). From this depth to 4.00m, there is a shift to more depleted $\delta^{18}O$ values (around 3.0‰), which is used to signify MIS3. This trend reverses to reach another maximum $\delta^{18}O$ ratio at 3.20 m. From then, the values trend to more depleted $\delta^{18}O$ ratios reaching their most depleted of ~2.0 ‰ at 0.5 m, with an oscillation occurring at ~1.8 – 1.5 m which marks the Younger Dryas episode. Like the planktic record for the Holocene, there are fluctuations of 0.5‰ can be observed, although the variation is minimal around the mean of c. 2.0 ‰ (Ariztegui *et al.*, 1996).

It is important to note that the planktic record for RF93-77 has been measured on a different foram species to the records for PRAD 1-2 and SA03-03, which could lead to systematic differences between the $\delta^{18}O$ records when they are compared. However, Ariztegui *et al.* (1996) undertook oxygen isotope analysis on both *G. bulloides* (PRAD 1-2, SA03-03) and *G. ruber* (RF93-77) for the Adriatic core CM92-43. They found that the isotope ratios from both taxa showed similar trends, though the values for *G. ruber* where shifted towards slightly more depleted values (Ariztegui *et al.*, 1996). This suggests that the records for PRAD 1-2, SA03-03 and RF93-77 can be compared on the basis of trends in isotopic values but there may be systematic differences in absolute values.

3.4.2 Foraminifera biostratigraphy

The foraminifera results for RF93-77 were reported in Asioli (1996) and have been used for stratigraphic purposes by the identification of regional bioevents in the sequence (Figure 3.16). The first and main planktic foraminifera bioevent is the Last Occurrence (LO) of *Globorotalia inflata* at 0.84 m. This is a well constrained biostratigraphic event for the central Adriatic, of mid-Holocene age, dated to 6 ka B.P. (Jorissen *et al.*, 1993). The LCO of *Hyalinea balthica* is observed at 3.30 m, however the core is not old enough to record the entry of this species. The LCO of *G. inflata* is observed at 4.00 m

within MIS 3. Finally, the entry and subsequent last occurrence of *G. truncatulinoides* in MIS 5.1 are observed at 7.30 mbsf and 6.97 mbsf respectively (Asioli, 1996.). These bioevents are recorded in each of the three studied cores and Piva (2007) suggests the LO of *G. truncatulinoides* corresponds to the MIS4/MIS5 boundary.

The sum of warm planktic species is not available for this core, so it is not possible to establish how species abundances correspond to the oxygen isotope record for the RF93-77 core.

3.4.3 Sapropel stratigraphy

Sapropel-equivalent events (Section 3.2.3) are also identified in RF93-77. In diagrams presenting the stratigraphy of RF93-77, the sapropel-equivalent layers are labelled Sapropel 1 (S1) and Sapropel 3 (S3) but it should be borne in mind that they are assumed sapropel-equivalent events. 'Sapropel 1' is identified between 1.00 m and 1.20 m and 'Sapropel 3' between 7.10 m and 7.30 m depth (A. Asioli, 2010 *pers. comm.*). However, Figure 3.15 shows that at these points neither the planktic nor benthic oxygen isotope records show depleted $\delta^{18}O$ values; neither do these sapropel-equivalent units correspond to minima in magnetic measures. Hence the criteria for marking these units as 'sapropels' is different to that used for PRAD 1-2 and SA03-03 and has been based on foraminiferal assemblages for these intervals.

3.4.4 Magnetostratigraphy

Magnetic susceptibility measures have been undertaken on RF93-77 and are presented in Figure 3.15. This is a measure of magnetic susceptibility and is equivalent to that measured for SA03-03. As alluded to above, there are no apparent minima in magnetic susceptibility values during deposition of the sapropel-equivalent events (Figure 3.15). There are sharp fluctuations in the magnetic measure observed throughout the core at approximately 0.5 m, 3.5 m, and 6.0 m depths, though only one of them corresponds to the position of tephra layers marked on the lithological log (Figure 3.15). This could mean that there are non-visible tephra layers present at these depths or that the peaks in magnetic susceptibility are not always indicative of tephra layer deposition.

3.4.5 Summary

A variety of proxy information is available for RF93-77 that enables further testing of the questions already posed following the reviews of the data available for PRAD 1-2 and SA03-03. Additional questions that can now be posed in light of the RF93-77 data are:

1. Do PRAD 1-2 and RF93-77 preserve the same tephra layers given their proximity to one another?
2. Does the benthic RF93-77 oxygen isotope record show similar changes during the same time intervals as PRAD 1-2, given that they are both located in the Central Adriatic?
3. Do the bioevents common to all three cores occur within the same time period?

These questions will be addressed by integrating the results of tephrostratigraphical investigations conducted on all three Adriatic core sequences.

3.5 Mediterranean region palaeoenvironmental records

In section 1.1, Mediterranean environmental change over the last glacial-interglacial cycle and some key marine and terrestrial sequences that record millennial-scale climatic fluctuations were introduced. In sections 2.2.5 and 2.2.6 a review of the marine and terrestrial sites that preserve tephra layers and are therefore important contributors to the regional tephrostratigraphy and tephrochronology were also introduced. In this section, the palaeoenvironmental records for some of these key marine and terrestrial sites are explored in more detail to provide wider-scale regional comparisons for the core sequences studied in this investigation. Only important sites that have published tephra records will be considered in this section.

3.5.1 Marine sequences

In section 2.2.5 the main sites within the Central Mediterranean Sea which contain tephra layers were introduced (Figure 2.10). Of these records, only five of the core sequences have robust palaeoenvironmental records that span the time period of interest to this study.

Cores KET 80-04, KET 80-22, KET 80-03, KET 82-18 and KC01B all have planktic oxygen isotope records. In addition, positions of sapropel layers have been detected in the KET 80-04 and KC01B records, and pollen data are available for KET 80-03. The location of the cores is shown in Figure 3.17.

3.5.1.1 Core KET 80-22

Core KET 80-22 is located furthest north in the Tyrrhenian Sea and one oxygen isotope record based on the planktic foraminiferal species *G. bulloides* was obtained for the sequence (Figure 3.17). An abrupt shift in $\delta^{18}O$ values from ~3.5‰ near the base of the core to a value of ~ 1‰ at 7.5m is interpreted as the termination of MIS 6 (Paterne *et al.,* 1986). From here substages MIS 5.4 and MIS 5.2 are identified by fluctuations to higher $\delta^{18}O$ values at ~7 m and 6 m respectively. All other marine isotope stages are also identified in the sequence (Paterne *et al.,* 1986).

3.5.1.2 Core KET 80-04

Core KET 80-04 is located in the central Tyrrhenian Sea, and one oxygen isotope record based on the planktic foraminiferal species *G. bulloides* was obtained for the sequence (Figure 3.17). The $\delta^{18}O$ record of *G. bulloides* allows reconstruction of the MIS 6 event to the present. Abrupt shifts from the highest (~4‰) to the lowest (~1‰) $\delta^{18}O$ values occur at approximately 2 and 11.5 m (Figure 3.17) and have been attributed to terminations at the end of MIS 2 and MIS 6 respectively (Paterne *et al.,* 1986). As well as the main isotope stage, sub-stages of MIS 5.4, MIS 5.2 and the Younger Dryas are also identified in the core (Paterne *et al.,* 1986).

Sapropel layers are also identified in KET 80-04 (Paterne *et al.,* 2008). Sapropel 1 is identified between 7.60 and 7.70 m, Sapropel 4 between 9.30 and 9.35 and Sapropel 5 between 10.67 and 10.75 m (Figure 3.17) (Kallel *et al.*, 2000; Paterne *et al.*, 2008). The sapropels are identified by the presence of black sediment layers in the core, which coincide with negative $\delta^{18}O$ peaks (Kallel *et al.,* 2000).

3.5.1.3 Core KET 80-03

This core is located in the southern Tyrrhenian Sea and also has a planktic oxygen isotope record based on the planktic foraminiferal species *G. bulloides* (Figure 3.17).

Low $\delta^{18}O$ values of ~1‰ at the base of the core indicate that the core preserves a full record of marine oxygen isotope stages from MIS 5 to the present (Paterne *et al.,* 1986). MIS sub-stages 5.4 and 5.2 are present in the core at approximately 9 m and 8 m depth, identified by more positive $\delta^{18}O$ peaks. At 2 m, there is a shift from the heaviest $\delta^{18}O$ value of 4 ‰ to more negative values which is interpreted as the termination at the end of the last glacial period (Figure 3.17) (Paterne *et al.,* 1986).

A pollen record for the core covering the period from 55 ka to 9 ka BP was developed by Rossignol-Strick and Planchais (1989). Variations in the pollen percentages of *Quercus, Abies, Populus,* Poaceae, *Artemisia,* Chenopodiaceae and *Ephedra* are shown in Figure 3.18. The *Artemisia* and Poaceae fluctuations record the shift between continental semi-desert and oceanic steppe climates during MIS 3 (Rossignol-Strick and Planchais, 1989). The $\delta^{18}O$ record from KET 80-03 and the *Quercus* pollen abundance co-vary in phase with one another, with peaks in *Quercus* abundance accompanying $\delta^{18}O$ depletions. This is interpreted as a climate improvement with the reverse indicating climate deterioration (Rossignol-Strick and Planchais, 1989). The co-variation of *Quercus* abundance variations with the $\delta^{18}O$ record is regarded as an indication of the coherence of the fluctuations of the climate system at the millennial timescale in its regional and global expressions (Rossignol-Strick and Planchais, 1989).

3.5.1.4 Core KC01B

Core KC01B is a 37 m long record from the Ionian Sea, and the age of the base of the core is estimated to be ~1,200 ka BP (Rossignol-Strick *et al.,* 1998). As this is much older than the timescale of interest in this project only the top 12 m, which covers the period from MIS 6 to the present, are considered here (Lourens, 2004). The lithology of the core is characterised by hemipelagic marls, with sapropel units, tephra layers and thin turbiditic sandy levels also present (Cita *et al.,* 2005). The core has an oxygen isotope record based on the planktic foraminiferal species *G. ruber* (Figure 3.17). This high resolution record shows the familiar pattern of shifts from heavy (~3 ‰) to lighter (~-1 ‰) $\delta^{18}O$ values at 9.50 and 2.50 m respectively indicating terminations at the end of MIS 6 and MIS 2 respectively (Lourens, 2004). Light oxygen isotope values mark the MIS 5 sub-stages, 5.5 (-1.46‰), 5.3 (-1.76‰) and 5.1 (0.3‰) (Figure 3.17) (Cita *et al.,* 2005), as well as all the marine isotope stages between MIS 6 and the present. The

location of the core in the Ionian Sea makes it more oceanic than the others referred to above (Piva, 2007) and therefore the oxygen isotope record is more likely to be responding to the global ice-volume effect on the $\delta^{18}O$ values of sea water, rather than local forcing factors such as changes in sea surface temperature and salinity (Rossignol-Strick *et al.*, 1998).

In the time period of interest to this study, five sapropel layers (S1, S3, S4, S5 and S6) are identified in the core based on their low colour reflectance values (Lourens, 2004). These are marked on the stratigraphic scheme for KC01B shown in Figure 3.17. Sapropel units also correspond to (or are immediately followed by) a peak of light $\delta^{18}O$ values (Cita *et al.*, 2005). The sapropel units have been dated through orbital tuning and in each case the date relates to the midpoint of the depth interval of each unit depth (Lourens, 2004). S1 is located between 1.10 m and 1.30 m and is dated to 8.5 ka, S3 is located between 6.55 m and 6.70 m and is dated to 81 ka. The depth of S4 is 7.77 m – 7.84 m and the age at the midpoint of this unit is 101 ka. S5 is located between 8.76 m and 8.80 m and its age is 124 ka and finally S6 is between 11.92 m and 12.18 m and is dated to 172 ka (Rossignol-Strick and Paterne, 1999; Lourens, 2004).

3.5.1.5 Core KET 82-18

This sequence, located in the southern Adriatic Sea, also has an oxygen isotope record based on the planktic foraminiferal species *G. bulloides* (Figure 3.17). Paterne *et al.* (1988) attribute the base of the core to MIS 5 but as the $\delta^{18}O$ values are light near the base it is assumed that only the end of MIS 5 is recorded in the sequence. MIS 4 is characterised by heavier $\delta^{18}O$ values (3.5 ‰), with shifts to isotopically lighter $\delta^{18}O$ values thought to indicate MIS3 and MIS2. The Last Termination is observed at 1.5 m depth by a shift in $\delta^{18}O$ values from 3.5 ‰ to 2 ‰ (Figure 3.17) (Paterne *et al.*, 1988).

3.5.1.6 Summary

The palaeoenvironmental records of five marine sequences in the central Mediterranean have been summarised. Each of the sequences also contain tephra records, which were introduced in section 2.2.5. The cores are located in different basins of the central Mediterranean (Figure 3.17) and comparison between their isotopic records will establish whether there is temporal consistency between them, which might imply that

they are responding to the same forcing factors. For example, as the western Mediterranean Sea experiences stronger temperature/salinity gradients, much larger than the open ocean, the Tyrrhenian Sea sediments should provide a highly amplified and more sensitive oxygen isotopic signal with respect to more open ocean sediments, than those from the Ionian Sea (Paterne *et al.,* 1986). Equally, at times of low sea level, the Northern-Central Adriatic basin can become isolated from the rest of the Mediterranean (Piva, 2007) and therefore marked differences between the records from this region and those from other Mediterranean basins might be expected. This poses additional questions relevant to the present research project, such as:

1. Are the timings of the isotopic changes seen in the Adriatic cores synchronous with those observed in other Mediterranean basins?
2. Are the series of sapropel equivalent events identified in Adriatic marine sediments synchronous with those in the KET 80-04 and KC01B records?

3.5.2 Terrestrial sites

Three Mediterranean terrestrial records with tephrostratigraphical data covering the time period of interest to this study were introduced in section 2.2.6. However, detailed palaeoenvironmental information has not been published for one of these, the San Gregorio Magno basin, and hence only the LGdM and Lake Ohrid sites are considered here.

3.5.2.1 The Lago Grande di Monticchio record

As discussed in section 2.2.2.1, LGdM is one of the most useful sites for tephra studies in the region, as it contains a comprehensive record of volcanic ash deposition over >130 ka. It is also a very important record of past environmental change in the region for a number of reasons: 1) the site lies far enough south to have suffered no direct effects of the last (Weichselian) glaciation (Figure 2.7) yet is sufficiently close to and downwind of the North Atlantic to be influenced by Atlantic weather conditions (Allen *et al.,* 2000); 2) the lake has a restricted hydrological catchment and has never had any substantial throughput of water, meaning the sediments have accumulated without hiatuses (Allen *et al.,* 2000); and 3) the sediment record is annually laminated in parts (Brauer *et al.,* 2007).

The lake has been cored a number of times; and the locations of the cores from which detailed palaeoenvironmental records were obtained and the corresponding core lithologies are shown in Figure 3.19. Various sedimentological proxy records have been obtained from LGdM, which include, dry density, loss on ignition (LOI), and total organic carbon (TOC) (Figure 3.20). LOI and TOC reflect the amount of organic components and, in general, high values reflect stable environmental conditions, with vegetation cover reducing erosion and high biological productivity in the lake (warm climate). Dry density reflects the amount of minerogenic detritus in the sediment, which increases with increasing erosion due to reduced vegetation cover (Brauer *et al.*, 2000). Three main periods are identified, the Holocene and Lateglacial with high LOI and TOC (1, Figure 3.20), the middle Weichselian from ca. 14,700 to 73,500 years BP, where LOI and TOC values are low and dry density values are high but fluctuating (2, Figure 3.20) and finally the early Weichselian period with higher LOI and TOC during interstadials and marked dry density peaks during cold periods (3, Figure 3.20) (Brauer *et al.*, 2000).

High resolution pollen analysis has also been conducted on the sequence. The pollen record from LGdM core D and J was divided into 19 Pollen Assemblage Zones (PAZ) and subzones (Figure 3.21a), numbered from the top down, PAZ 1 being the most recent (Allen *et al.*, 1999). PAZ 19 – 17c comprise the early Weichselian period, with PAZz 19, 17e and 17c indicating the landscape was predominantly forested, whereas during PAZs 18 and 17d open steppe vegetation dominated (Allen *et al.*, 2000). The Weichselian glacial period is comprised of PAZs 17b to 4. The inferred palaeo-vegetation alternating between open steppe during stadials (PAZs 16, 14, 13b, 12, 10, 8, 6, 4) and wooded steppe, mainly comprised of broadleaf leaf deciduous taxa during interstadials (PAZs 15, 13c, 13a, 11, 9, 7, 5b) (Figure 3.21a) (Allen *et al.*, 2000). Finally, PAZs 3, 2, and 1 comprise the Lateglacial and Holocene, where the abundance of woody taxa increases to levels not seen since the early Weichselian. There was a return to wooded steppe vegetation during the Younger Dryas but no return to open steppe. *Quercus* was the dominant tree taxon and the climate is inferred to have been relatively warm and moist, with a fluctuation thought to indicate cooler and seasonally dry conditions during the Younger Dryas (PAZ 2, Figure 3.21a) (Allen *et al.*, 2000).

As well as the broad scale record of environmental change shown by these three periods, the record has also been interpreted as recording millennial and sub-millennial environmental fluctuations (Allen *et al.*, 1999). Records of *N. pachyderma (s.)* from DSDP-609 in the North Atlantic and of $\delta^{18}O$ variations from the GISP2 ice core record were correlated with the LGdM record (Figure 3.21a) with different PAZs being correlated to the GISP2 interstadial events. For example interstadial 19 is correlated with PAZ 15 and interstadial 20 is correlated with PAZ 17a (Allen *et al.*, 1999).

The pollen record of Brauer *et al.* (2007) obtained from LGdM cores M/O extends the record at the site back to 132ka BP. The upper 72.5m of this composite core sequence correlates perfectly with the cores analysed by Allen *et al.* (1999, 2000). This extends the pollen record at LGdM back to MIS6, meaning it covers the same intervals as the Adriatic cores under investigation in this study. The pollen record indicates that during MIS 2, 4, 6 and most of the MIS 3 and 5 stadials the regional vegetation was dominated by herbaceous taxa, with a steppic element. Mesic woody taxa dominated during the Holocene, St. Germain I and II and the Last Interglacial (Figure 3.21b) (Brauer *et al.*, 2007). Changes in pollen assemblages are related to changes in the $\delta^{18}O$ record from the Iberian margin core MD95-2042, such as the increase in mesic woody taxa at the transition from Melisey I to St. Germain I (Figure 3.21b) coinciding with a rapid decrease in the planktic $\delta^{18}O$ record, suggesting a common trigger for these changes (Brauer *et al.*, 2007).

LGdM therefore has a detailed palaeoenvironmental record that covers the same time period under investigation in the present study. Millennial and sub-millennial environmental changes have been observed in the sequence and those changes have also been linked to the Greenland ice core records, as is the case for PRAD 1-2 and SA03-03. As the LGdM sequence also preserves numerous tephra layers and is the regional tephra-stratotype (Section 2.2.2.1), there is the potential to tie the palaeoenvironmental records from this site with the Adriatic records under investigation in this study using tephra isochrons common to each sequence.

3.5.2.2 Lake Ohrid

Lake Ohrid, located on the Albanian and Macedonia border (Figure 2.7), has undergone numerous palaeoenvironmental investigations. The different core locations were

presented in Figure 2.9c; however, the review of the tephra studies on these cores showed more tephra layers were preserved in the northern parts of the lake, suggesting that Co1202 from Vogel *et al.* (2010a) may be the most useful record to compare with the Adriatic sequences in this study (Figure 2.9c).

Vogel *et al.* (2010b) undertook high resolution X-ray fluorescence (XRF) magnetic susceptibility measurements and also sub-sampled for analysis of Total Carbon (TC), Total Nitrogen (TN), Total Sulphur (TS) and Total Organic Carbon (TOC). Concentrations of Total Inorganic Carbon (TIC) were determined through the difference between TC and TOC, whilst $CaCO_3$ content was calculated from the TIC values, while variations in biogenic silica (BSi) concentrations were also assessed.

TOC concentrations are influenced by the primary productivity in the lake and the calcite concentration is affected by the concentration of Ca^{2+} and HCO_3^- ions which are modified by the rate of evaporation, which in turn is controlled by temperature and wind intensity. The Zr/Ti ratio serves as a proxy for the intensity of wind-induced surface currents and erosion in the catchment, as does the Cr/Ti ratio. The Ti concentration is thought to represent fluvial clastic input to the lake (Figure 3.22).

Two distinct lithofacies were recognised which were further subdivided into sub-lithofacies (1a, b, c and 2a, b) (Figure 3.22). Lithofacies 1 is almost devoid of carbonates and also has low concentrations of organic matter, as indicated by the TOC content. Terrestrial and subaquatic macrofossils are absent and poorly preserved diatoms only occur in low abundances, indicated by low BSi concentrations (Figure 3.22) (Vogel *et al.,* 2010b). In Lithofacies 2, coarse sand and gravel is absent, carbonate content is high and detrital clastic material content is low, indicated by low Ti and MS values. Carbonate microfossils are abundant but terrestrial and subaquatic macrofossils are absent. The organic matter content is higher than in Lithofacies 1, as is the abundance and presentation of diatoms (BSi concentrations; Figure 3.22) (Vogel *et al.,* 2010b)

Core Co1202 provides substantial information on climatic variability and its imprint on the local hydrology and catchment dynamics from MIS6 to the present. Proxy records show the environment during the penultimate and last glacial to be similar and characterised by a cold climate and a relatively stable, low lake productivity (Figure

3.22). Quasi-cyclic fluctuations in the Cr/Ti and Zr/Ti ratios are a result of the cold dry climate which led to increased erosion of sparsely vegetated soils. Parts of MIS 5 and the Holocene are characterised by elevated calcite and organic matter concentrations, indicating improved climatic conditions and enhanced productivity. Several abrupt events during the interglacials, indicated by rapid fluctuations in all proxies, are thought to reflect short-term cooling events (Figure 3.22).

The other palaeoenvironmental record from Lake Ohrid that covers the last glacial-interglacial cycle is from core JO2004-1 from the south-western part of the lake (Lézine *et al.,* 2010). Pollen analysis was undertaken on the sequence (Figure 3.23) and, at the base of the sequence, steppe taxa (mainly *Artemisia* and Chenopodiaceae) dominated the surroundings of the lake, suggesting a climate characterised by strong seasonal moisture deficiency (Lézine *et al.,* 2010). From 136,000 to 127,000 yr BP steppic taxa decrease, whilst mesic trees increase, suggesting the climate became progressively warmer and wetter. From 127,000 yr BP, the Last Interglacial period began, characterised by the increase in Mediterranean tree species and the disappearance of cold steppic taxa (Figure 3.23). The end of the interglacial climatic optimum was marked by a dramatic shift in forest composition, with a decline in Mediterranean forest and an increase *Abies*- and *Picea*- dominated conifer forests (Lézine *et al.,* 2010). Significant expansion of herbaceous steppic taxa at the expense of forest taxa suggests a climate deterioration coeval with the Melisey 1 and 2 stadials (Figure 3.23). A major hiatus of roughly 12,000 years corresponds to a large part of the St. Germain I period. The position of the hiatus being confirmed by the absence of the X5 tephra layer in core JO2004-1 (Lézine *et al.,* 2010). Cold-tolerant trees such as *Juniperus* and *Betula* expanded, together with steppic herbaceous plant types, during the last glacial period (Figure 3.23) (Lézine *et al.,* 2010). The pollen records from Lake Ohrid, core JO2004-1 and LGdM were compared and found to reflect similar changes, although the chronologies of the two records suggest some changes in pollen percentages occur earlier in LGdM than in Lake Ohrid (Lézine *et al.,* 2010).

The two glacial-interglacial cycle records from Lake Ohrid indicate that the lake contains an excellent archive of climate and environmental variability over the time period of interest in the present study. It has already been correlated with other records

in the region but, due to the presence of tephra layers, these correlations can be independently tested and widened to include the Adriatic marine sequences.

3.5.2.3 Summary

The study of the palaeoenvironmental records available from LGdM and Lake Ohrid, combined with the tephra layers present in each sequence (section 2.2.6), poses questions that might be addressed by directly comparing those records with the marine sequences investigated in the present project which are:

1. Are the correlations between LGdM pollen fluctuations and Greenland interstadials supported by the correlations of the PRAD 1-2 and SA03-03 $\delta^{18}O$ fluctuations with the same Greenland interstadials as tested by the positions of tephra layers common to each sequence?
2. Are the environmental changes reflected in records which form a transect across the Adriatic Sea synchronous or not?

These questions will be addressed by integrating the results of tephrostratigraphical investigations conducted on all three Adriatic core sequences.

3.6 Project aims and objectives

The overarching aim of this investigation is to use tephrochronology as a tool for improving the chronology of palaeoenvironmental records in the Central Mediterranean. The key goals are:

1. To examine the potential of distal tephra layers as a stratigraphic tool to improve the synchronisation of Central Mediterranean marine records and to compare marine sequences with terrestrial records.
2. To develop age models for Central Mediterranean marine records that are not only independent of climatic and biostratigraphic assumption but that also avoid the problems of marine-based radiocarbon dating.
3. To use tephra-based age models to determine the timing of regional palaeoenvironmental changes and to assess the reliability of synchronous isotopic and biostratigraphic events and boundaries.

Following the review of proxy information available for the three sequences to be investigated and other key paleoenvironmental records and published interpretations relating to several keys sites previously investigated in the region, the following specific objectives are defined for the thesis, which will be tested by tephrostratigraphical correlation:

1. To examine whether oxygen isotope records show consistent temporal variations between the Central and Southern Adriatic.
2. To establish whether Adriatic records are dominated by local (Adriatic Sea) influences or reflect wider regional (Mediterranean) forcing factors.
3. To examine whether regional bioevents identified in the Adriatic records provide time-parallel marker layers.
4. To test the assumed synchroneity between Central Adriatic sapropel-equivalent events and Eastern Mediterranean Sapropels.
5. To examine whether the correlation of the PRAD 1-2 and SA03-03 $\delta^{18}O$ variations to D-O cycles is robust and are those correlations supported by the correlation of LGdM pollen fluctuations with Greenland interstadials.
6. To test for synchroneity of environmental changes in a transect of sites (those listed above) across the Adriatic Sea.

These objectives will be achieved by initially using tephra layers common to the different sequences as stratigraphic marker layers to tie records together and examine the synchroneity of other proxy records between the bounding tephra layers. The ages of the tephra layers will then also be considered in order to aid the achievement of the objectives.

4. Methodology

This section will expand on the analytical and classificatory methods used in this study, review specific methods used for certain samples, justify processes employed and examine some of the limitations associated with certain steps of the methodology.

4.1 Initial laboratory methods

4.1.1 Laboratory protocols

A tephra slide in this study is assessed based on the presence or absence of glass shards. As the Adriatic basin is a near-proximal site, it is likely that the sediment cores will preserve some tephra layers consisting of a great number of shards. However, the study also includes the aim to detect cryptotephras, which frequently contain very few shards. Strict laboratory protocols are therefore required to reduce the risk of cross contamination of tephra between samples from the same sequence and from other laboratory users. To prevent contamination, this research was always carried out in the same laboratory area, which was always cleaned before and after use. No other laboratory user working on tephra worked in this laboratory area. This should have reduced the risk of air-borne contamination. Deionised water was used and sieve meshes were changed every 5 samples for initial scan samples. When analysing sediments at a refined 1 cm resolution scale and also for all samples prepared for geochemical analysis the sieve mesh was changed after every sample. All samples were stored in sealed centrifuge tubes. In addition, a sample to check the background level of tephra was analysed with each batch of samples. This background sample underwent the same processes as the regular tephra samples resulting in a slide that enabled any cross contamination from the laboratory to be analysed. In all cases, these background samples were negative, indicating that the protocols for reducing laboratory contamination were effective.

4.1.2 Sediment description

The sediment sequences have all been described to record significant visual changes from the marine mud which dominates the sequence. These changes included marking areas of bioturbation and the presence of shells, tephra layers, and sapropel equivalent layers.

4.1.3 Core sub-sampling

4.1.3.1 PRAD 1-2 and SA03-03

U-channels were removed from the original cores stored at ISMAR, Bologna, in order to carry out the tephra work (labelled A in Figure 4.1 part 1). The first phase of tephra sampling was a scanning phase to check for the presence or absence of tephra in the sequence. Contiguous samples 5 cm long by 0.5 cm wide and 0.5 cm deep were initially removed from the u-channels (B in Figure 4.1 part 2). Prior to sub-sampling, the core surface was cleaned using a scalpel fitted with a new blade. The sample was then carefully removed from the U-channel using a scalpel and spatula. All equipment was cleaned with deionised water between successive samples.

The second phase of sub-sampling depended on the type of any tephra peak detected in the first phase. The rationale behind subsequent sub-sampling is described in the flow diagram presented in Figure 4.2.

Where geochemical analysis was to be undertaken on the 5 cm sample, a second 5 cm by 0.5 cm by 0.5 cm strip of sediment was removed from the u-channel (C in Figure 4.1 part 2).

Where refinement of the 5 cm tephra counts was required, 1 cm blocks of sediment were removed from those parts of the core in which tephra had been detected in the scan samples and from at least 5 cm either side of the tephra bearing intervals (D in Figure 4.1 part 2). Samples for geochemical analysis were then removed from the remaining 1 cm thick slice of sediment containing the greatest concentration of glass shards (E in Figure 4.1 part 2).

4.1.3.2 RF93-77

Due to the length of time over which this core had been stored, it was only possible to remove u-channels from the top 3 m of the core sequence. The sediment in the remaining 5 m was too compacted to remove entire u-channels of long length. Instead, small blocks of 2 cm^3volume had to be cut from the sequence (Figure 4.1 part 3). For

the u-channelled sections of the core, sub-sampling proceeded as outlined in Section 4.1.3.1 and Figure 4.2 but the initial scanning phase was undertaken using 6 cm, not 5 cm long blocks, to maintain consistency with the remainder (lower part) of the sequence.

The 2 cm^3 blocks had to be homogenised as it was not always possible to preserve the orientation of each block. Once samples were homogenised, half a gram of sediment was removed from each sample and combined to create a 6 cm resolution sample (Figure 4.1 part 4). These samples could be refined to a 2cm resolution, where needed, using the original, homogenised 2 cm^3 blocks.

4.1.4 Sediment storage

The u-channels from all 3 sequences were stored in a refrigerated room to prevent bacterial growth. All u-channels were stored in their plastic containers with clingfilm wrapped over the top of the sediment to prevent contamination when opening the u-channel boxes. The RF93-77 homogenised samples were stored in sealed labelled bags to prevent contamination between samples. Once samples were processed, they were stored in sealed centrifuge tubes, again to prevent cross-contamination.

4.2 Tephra preparation for optical identification

The process for the preparation of tephra samples for optical identification is summarised by the flow diagram in Figure 4.3.

In order to extract any non-visible ash from the samples, a refined version of the tephra extraction procedure proposed by Blockley *et al.* (2005) was used. This involves the stepped flotation of material from samples using sodium polytungstate (SPT) prepared to pre-determined specific gravities. The specific gravities used in the two floats for this study differ from those outlined in Blockley *et al.* (2005) and have been calculated based on previous work carried out on other cores from the Adriatic Sea (e.g. Abbott, 2005, Lowe *et al.*, 2007b). A cleaning float of 1.95 gcm^{-3} is used, which is lower than the one described by Blockley *et al.* (2005) as very little organic matter is present in the Adriatic Sea cores. An extraction float of 2.5 gcm^{-3} is utilised, which is again lower than the recommendations of Blockley *et al.* (2005) due to the high vesicularity of

Italian tephras. The residues from the extraction process (material <1.95 gcm^{-3} or > 2.5 gcm^{-3}) were routinely examined to ensure that the selected densities were correct and that no tephra shards were present in the residues.

4.3 Optical identification of tephra shards

The presence of glass shards within samples was assessed using light microscopy and key optical properties. Tephra slides were analysed using an Olympus CX-41 transmitted light microscope fitter with a Vernier stage. The microscope was equipped with 10x, 40x and 100x magnification objectives and 10x magnification eyepieces. The microscope used was fitted with polarising filters, so that samples could be examined under plane-polarised light and under cross-polarised light. Initially, a slide reference collection was studied to build up a familiarity with shard morphology and surface characteristics and internal features such as vesicles and mineral inclusions.

Ideally, the slide preparation procedure (Figure 4.3) would remove all non-tephra objects from slides. Unfortunately, this is never the case with mineral material and biologically produced silica frequently being encountered. Some shards can look very similar to this minerogenic and biogenic material and hence careful analysis of the morphology and optical properties of shards is necessary to make a secure distinction. These are now considered in greater detail.

4.3.1 Shard morphology

Shard morphology is an important factor in tephra identification. Figure 4.4 displays the critical morphological features that are used in identifying tephra from Italian volcanic provinces. These features have been checked against the slide reference collection.

4.3.2 Optical properties

The first optical property used was the behaviour of shards under cross-polarised light. Due to the rapid cooling of magma during the formation of the glass phase of tephra, little or no crystallisation of the mineral phases takes place, whereas mineralogical material may have a crystalline structure (Fisher and Schminke, 1984). When viewed

under cross-polarised light, glass shards extinguish because plane polarised light is unaffected by their non-crystalline structure. Most minerals that mimic tephra are anisotropic, meaning they have a crystalline structure that bends the plane-polarised light passing through them and appear as bright objects, due to their high birefringence colours (Enache and Cumming, 2006). However, some minerals are isotropic meaning they also extinguish under cross-polarised light; this is also true of biogenic silica. This is why an assessment of the grain's morphology is also crucial in tephra identification and why other optical properties of tephra shards can also be useful.

The second optical property that can help to distinguish tephra shards from mimics is the refractive index (RI) of the tephra. Biogenic silica (diatoms, phytoliths and sponge spicules) cannot be excluded as shard candidates using cross-polarised light, however, when whole these objects are morphologically distinct from glass shards, but, broken fragments of biogenic silica objects can mimic tephra shards. The RI of tephra shards and biogenic silica differs; tephra silica contents range from 75 % – 45% with the remaining composition made up from metallic elements, whereas biogenic silica has a SiO_2 content of 95 – 98%, with water making the remaining composition. Tephra therefore, has a higher atomic mass and therefore a higher RI. The maximum RI of biogenic silica is 1.47, whereas the minimum RI of unaltered tephra is 1.485 (Enache and Cumming, 2006). Therefore by using a mounting media with an RI of between 1.47 and 1.485 tephra and biogenic silica can be distinguished using the RI and the Becke line test (Blockley *et al.*, 2005).

In this study, Euparal, a permanent mount, was employed because it has an RI of 1.482 (Blockley *et al.*, 2005). This affects the behaviour of the Becke line, a bright halo of light that appears around a particle due to the concentration of refracted light induced by differences between the refractive indices of particles and the surrounding mounting medium. When the microscope stage is lowered, the Becke line moves towards the centre of a glass shard but outwards from biogenic silica (Nesse, 2000). Mounting slides in Euparal also affects the colour of some particles with biogenic silica appearing pink, while tephra shards appear green.

4.3.3 Assessing glass shard concentration

Where tephra was present on the slide, the absolute numbers of glass shards were counted. These were converted to glass shards per gram of dry sediment (per g dry wt.) using the mass of dry sediment calculated at step 2 in the preparation procedures (Figure 4.3). Shards were classified into two groups based on their colour, namely colourless shards and brown shards, which included shards with any noticeable degree of colour (Figure 4.4). For any scan sample (5 cm or 6 cm resolution samples) with absolute numbers of glass shards greater than 10,000, the value could not be determined absolutely. These cases are recorded as >10,000 shards per g dry wt. Whilst this reduces the accuracy of vertical tephra distribution, it nevertheless highlights the horizons at which excessive numbers of shards were encountered. It also avoided unnecessary counting and hence the assessment of core sequences could be conducted efficiently. Where refinement to 1 cm was required (Figure 4.2), it was necessary to attempt to quantify the shard counts for each centimetre, as 1 cm resolution counts were often undertaken to evaluate a mixed geochemical signature in some 5 cm samples. In these cases, a methodology widely used in pollen stratigraphy and adapted from Gehrels *et al.* (2006) using *Lycopodium* spores was applied:

1. After step 18 in Figure 4.3, add one *Lycopodium* tablet to the sample
2. Add 3 drops of 10% HCl and place the centrifuge tube in a beaker of deionised water on a hot plate at a temperature of 50^{o}C. Leave for 2 hours or until *Lycopodium* tablet has fully dissolved.
3. Fill centrifuge tube with deionised water and centrifuge for 5 mins, at 2500 rpm. Then discard water. Repeat 4 times or until acid is completely removed.
4. Dry 3 drops of sample onto a slide on hotplate at 80^{o}C.
5. Make slide by covering sample with Euparal and coverslip.
6. If the concentration of tephra on the slide is low, count all of the glass shards and *Lycopodium* spores present on the slide. If the concentration of tephra on the slide is high, then count the glass shards and *Lycopodium* spores on 3 vertical transects of the slide (Figure 4.5.). The difference between low and high tephra concentrations was assessed based upon information from the 5 cm resolution samples and upon the amount of material present before the slide mounting stage.

7. Calculate the glass shard concentration, *c* (reported as glass shards per gram of dry sediment) using the following formula:

$$c = l \times a/bd$$

where *a* = glass shard count, *b* = *Lycopodium* spore count, *d* = sample dry weight in grams and *l* = number of *Lycopodium* spores in the tablet. In all cases in this study *l* was 18538 spores per tablet (Gehrels *et al.*, 2006).

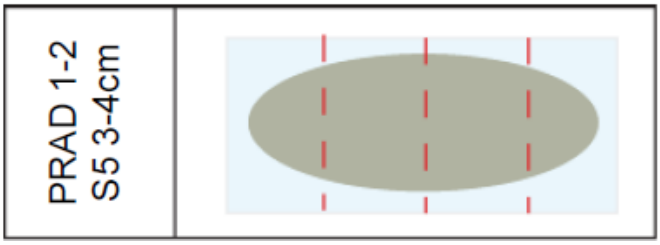

Figure 4.5: Tephra slide with sample spiked with *Lycopodium* (brown area) underneath a coverslip (blue area). The red dashed lines indicate the positions of the 3 transects counted when analysing a slide with a high concentration of glass shards.

Whilst this technique will still not provide fully accurate absolute counts, it does provide a means of assessing which samples contain the greatest relative concentration of glass shards, an important criterion as this is the sample selected for extraction of shards for geochemical analysis in this study.

For cryptotephra layers, the tephra layer depth was taken as the peak in glass shards and this sample was geochemically analysed. For any visible tephra layers, the depth at the base of the visible layer was used as the tephra layer depth. Geochemical analysis was undertaken on peaks in glass shards throughout the visible layer depth.

4.4 Tephra preparation for geochemical analysis

4.4.1 Sample preparation

Once peaks in glass shards had been identified, glass shards were extracted and prepared for geochemical analysis using the same procedure as outlined in Figure 4.3, except the process was stopped at step 19. The shards then needed mounting onto a resin stub before geochemical analysis was undertaken. The methods for achieving this are described below.

4.4.2 Micromanipulation of shards

In samples with low concentrations of tephra shards, it was necessary to manipulate individual shards to concentrate them in the centre of the resin stubs. This differs from tephra samples with high concentrations of shards, where the stub can be prepared by directly pippetting the sample material onto the centre of a resin stub. If the ratio of glass shards to other material is very low, however, the processing and analysis procedures are problematic. The problems are twofold. Firstly, glass shards have a different hardness to other materials (e.g. biogenic silica, minerals and resin), causing problems when polishing the stub. Secondly it requires much more time to search through all the material on the stub to isolate the glass shards, which has time and cost implications.

In this research, a micromanipulation procedure was adopted for application to samples with low shard concentrations, in order to circumvent these problems. The procedure was developed at Royal Holloway and involves use of a 5 μl gas chromatography syringe, fitted with a 100 μm diameter needle and mounted on a mechanical manipulation device. Samples were mounted in water and assessed using light microscopy. When glass shards were detected, use of the micromanipulator while viewing down the microscope allowed the needle to be manoeuvred to the position of each shard. The shards could then be drawn into the needle. This was repeated for a number of shards and when the needle was full the shards were transferred to the centre of a resin stub, which was then covered, sectioned and polished as described below.

4.4.3 Stub preparation and covering

The flowchart in Figure 4.6 outlines the procedure for preparing resin stubs for geochemical analysis. During this study, a Buehler Alpha polisher and grinder, with a vector powerhead was employed in order to control the polishing process (Figure 4.6 step 10). This was pre-tested to establish the optimal performance for smooth finish and shard protection. The preferred protocol is outlined in Figure 4.7.

Department of Geography, Royal Holloway: Geochemical Stub Grinding and Polishing Programme

This is a guide – all stubs are different depending on the amount and type of sample, if in doubt check the stub regularly. The machine can only be used with samples on Buehler Phenolic Rings.

1. Grinding Settings using a 1200 paper
    - Time – **20s** do at 10s or 20s intervals checking in between.
    - Force – **10N**
    - Water – **on**
    - Contra Rotation

   The total time taken to section shards will depend on the depth of resin on the stub – check regularly at 20s intervals

   The paper removes on average 0.135mm or 135microns over a 20s run. (However sharp papers grind faster than blunt ones!)

↓

2. Cleaning Programme
    - Time – **60s**
    - Force – **0N**
    - Water – **on**

   This should be done to clean the 9µm paper before use and repeat once the 9µm programme is over. It must be repeated for each diamond plate before and after use.

↓

3. 9µm Diamond Paste Polishing Setting
    - Time - **20s** then check followed by **60s** if wanting to section more shards run for a further **60s**
    - Force – **15N**
    - Water – **off**
    - Contra Rotation

   For BASALTIC shards pressure needs to be increased to 20N
   If doming is present after the first 20s run then increase pressure to 20N for rest of programme

↓

4. 3µm Diamond Paste Polishing Setting
    - Time - **20s** then check followed by **20s**
    - Force – **25N**
    - Water – **off**
    - Contra Rotation

   For BASALTIC shards pressure needs to be increased to 35N for 40s
   If doming is present after the first 20s run then increase pressure to 35N for rest of programme

↓

5. 0.3µm Aluminium Powder Polishing Setting
    - Time - **5s** (have to manually stop the machine after 5s)
    - Force – **0N**
    - Water – **off**
    - Contra Rotation

   The powder domes the sample if used with any pressure so it may be necessary to finish this stage by hand

Figure 4.7: Royal Holloway Geography Department Geochemical Stub polishing programme for the Buehler Alpha polish and grinder with vector powerhead. This was developed using Italian tephra samples, by varying the time and pressures applied to the sample, to find an optimal programme that resulted in a well polished sample but did not risk the loss of the sample.

4.5 Geochemical analysis of tephra shards

Geochemical analysis is an essential first step when attempting to correlate tephra layers with one another. The composition of glass shards represents the composition of the magma at the time of the volcanic eruption (Lowe, 2011). This can produce a unique "fingerprint" for different eruptions, reflecting the chemical complexity of the eruptive processes (Tryon *et al.*, 2008). However, in reality there is often significant overlap in chemical data from different eruptions from the same volcano.

With all geochemical analytical procedures the regular analysis of both primary and secondary standards is essential to maintain a check over the reliability of results. Primary standards are used to calibrate the machinery before analysis begins and regular analyses of secondary standards are used to check this calibration throughout the duration of analysis (Lowe, 2011).

The analytical methods used to acquire geochemical data from tephra layers in this study are now discussed in greater detail.

4.5.1 Major and minor element analysis: WDS-EPMA

Electron probe microanalysis, using wavelength dispersive spectroscopy (WDS-EPMA), was used to carry out analysis of the major and minor element concentrations of glass shards. Electron probe microanalysis (EPMA) is widely adopted in tephra studies as a technique to measure the major element composition of individual glass shards (Lowe, 2011). This technique involves the bombardment of shards with an electron beam and then the analysis of the spectrum of generated X-rays. In this study wavelength dispersive spectrometry (WDS) was used to count the X-rays, determined by X-rays diffraction by crystals according to wavelength and counting one element at a time. This differs from Energy Dispersive Spectrometry (EDS) where the x-rays are counted according to their energy level (Reed, 2005). The elemental composition of a sample can be ascertained as the energy of X-rays produced by each element is unique and their intensity is proportional to the amount of that element present in the sample. This is converted from counts per minute to weight % of each oxide by comparison with the primary standards and the correction procedure used by the microprobe laboratory (Hunt and Hill, 1993).

WDS requires a longer counting time and higher beam current than EDS. However, it provides a higher level of analytical precision because the behaviour of each element can be determined individually and sequentially (Davies *et al.*, 2002). Sequential monitoring means that the mobility of alkalis can be more closely monitored during analysis (Hunt and Hill, 1993). This is important as the mobilisation of alkalis can cause elements measured after them to be over represented due to sequential element analysis. This can be particularly noticeable with silica as it has the greatest abundance. Therefore, it is important to try and minimise alkali mobilisation through the probe set-up to avoid causing problems with the abundance of all elements (Hunt and Hill, 1993). Finally, within WDS there is less dead time (time interval after the arrival of an X-ray pulse during which the system does not respond to further pulses) which is important as dead time means the measured X-ray count rate is less than the true count rate (Hunt and Hill, 1993; Reed, 2005).

All tephra layers found within PRAD 1-2, SA03-03 and RF93-77 were analysed using WDS-EPMA. Analysis was carried out at three locations: Department of Earth Sciences, University of Oxford; the Research Laboratory for Archaeology and the History of Art, University of Oxford; and the School of Geosciences, University of Edinburgh. The following nine major and minor elements were analysed as weight percent oxides at all 3 locations: SiO_2, TiO_2, Al_2O_3, FeO, MnO, MgO, CaO, Na_2O, K_2O. However, 4 additional minor elements could also be analysed at Edinburgh: P_2O_5, SO_2, Cl and F. The operating conditions of each of the microprobes used and details of the primary and secondary standards employed are provided in Table 4.1.

The operating conditions in Table 4.1 are close to those set out by Hunt and Hill (1996, 2001) based on their laboratory comparison of the electron probe microanalysis of glass geochemistry. However, the operating conditions for each probe do vary slightly, therefore repeat analysis of selected samples were undertaken on each microprobe as a test for inter-laboratory comparison. The results of this test are shown in Figure 4.8 and show that the results from the 3 laboratories are comparable. Therefore, data generated at the three locations can be compared. The assays for the secondary standards used are detailed in Table 4.2.

Table 4.1: Operating conditions and standards employed for the 3 microprobes used in this study. * denotes synthetic material

	Department of Earth Sciences, University of Oxford	**Research Laboratory for Archaeology and the History of Art, University of Oxford**	**School of Geosciences, University of Edinburgh (Hayward, 2010)**
Probe	Jeol JXA8800R superprobe: 4 WD spectrometers	Jeol 8600: 4 WD spectrometers	CAMECA SX100: 5 WD spectrometers
Accelerating voltage	20 kV	15 kV	15kV
Current	15nA	6 nA	2 nA (Na,K,Si,Al,Mg,Fe,Ca) 80 nA (F,Cl,S,Mn,Ti,P)
Element analysis time	Si, Al, Mn, Mg, 30 s Ca, Na, K 30s Fe 40 s Ti 20 s	Si, Ti, Al, Fe, Mn, 30 s Mg, Ca, K 30s Na 10s	Si, Ti, Al, Mg, Ca, 30 s Na, K, P, S, Cl 30s F, Mn 90 s Fe 80 s
Beam diameter	10 µm	10 µm	5 µm
Correction procedure	ZAF	PAP	X-PHI - using Cameca PeakSight (V.3.2)
Primary standards	Si Wollastonite	Si Wollastonite	Si Wollastonite
	Ti Titanium oxide	Ti Rutile	Ti Rutile*
	Al Aluminium oxide	Al Jadeite	Al BIIRG1 glass*
	Fe Haematite	Fe Haematite	Fe Fatalite*
	Mn Manganese oxide	Mn Fowlerite	Mn 99.9% pure metal*
	Mg Magnesium oxide	Mg Periclase	Mg AlMg spinel*
	Ca Wollastonite	Ca Wollastonite	Ca Wollastonite
	Na Jadeite	Na Jadeite	Na Jadeite
	K Orthoclase	K Orthoclase	K Orthoclase
			P Apatite
			S Pyrite
			Cl Halite
			F Fluorite
Secondary standards	NIST 612, KL2 Basalt, Lipari Obsidian	StHs6/80-G, ATHO-G	StHs6/80, Lipari Obsidian, BHV02g

Table 4.2: Assay for the glass standards used within this study, with maximum and minimum values for each standard shown. Data for StHs6/80-G and ATHO-G from Jochum *et al.* (2005, 2006), data from Lipari Obsidian and BHV02 from C. Hayward *pers comm.*

	SiO_2	TiO_2	Al_2O_3	FeO	MnO	MgO	CaO	Na_2O	K_2O	P_2O_5
NIST 612	69.9	0.00	1.79	0.00	0.00	0.00	11.5	12.8	0.00	
	73.9	0.05	2.43	0.05	0.05	0.05	12.3	15.2	0.05	
Lipari Obsidian	73.43	0.07	12.52	1.70	0.07	0.00	0.70	3.96	5.08	
	74.63	0.09	12.92	1.80	0.09	0.00	0.74	4.16	5.28	
StHs6/80-G	63.2	0.682	17.6	4.3	0.072	1.93	5.19	4.3	1.27	0.14
	64.2	0.724	18.0	4.44	0.08	2.01	5.37	4.58	1.31	0.18
ATHO-G	74.90	0.24	12.00	3.17	0.10	0.09	1,67	3.44	2.55	0.02
	76.30	0.27	12.40	3.37	0.11	0.11	1.73	4.06	2.73	0.03
BHV02g	49.3	2.69	13.3	10.87	0	7.11	11.2	2.14	0.51	0.25
	50.5	2.77	13.7	11.27	0	7.35	11.6	2.30	0.53	0.29
KL2 Basalt	50.0	2.47	13.1	10.6	0.156	7.25	10.7	2.27	0.47	
	50.6	2.65	13.5	10.8	0.174	7.43	11.1	2.43	0.49	

The full standard results for the geochemical analyses undertaken during this project can be found in Appendix B, whilst the full geochemical dataset for the tephra layers analysed during this study can be found in Appendix C.

4.5.2 Trace element analysis: LA-ICP-MS

Laser-ablation inductively-coupled plasma mass spectrometry (LA-ICP-MS) is a relatively new technique which provides an efficient and precise method for determining the abundances of a variety of trace elements (including Rare Earth Elements (REEs) at low concentrations in individual glass shards (Lowe, 2011).

A laser system was first coupled to an ICP-MS in the mid 1980's (Pearce *et al.,* 2007). The addition of a laser ablation sample introduction system allows the direct sampling of solids by ICP-MS, which in turn removes the need for analysis of bulk tephra layers which have been dissolved into a solution (Pearce *et al.,* 2007). This is advantageous because the analysis of bulk tephra samples can cause inaccuracies due to the presence of lithic grains within the tephra layer, or even the occurrence of micro-inclusions within the glass shards themselves (Pearce *et al.*, 2007).

A laser beam interacts with the sample which is housed within an ablation chamber, filled with a helium-argon gas mix. This interaction ablates the sample surface, releasing fine aerosol particles which are transported in the ICP-MS by the argon carrier gas (Thomas, 2001a). The sample is injected into the plasma torch and ionised, forming a beam of positively charged ions. This ion beam passes via two platinum cones which isolate the beam and transfer it into the high vacuum mass spectrometer (Thomas 2001b). The ions are then focussed by a number of lenses into the quadrupole mass analyser, which separates the ions according to their mass to charge ratio (m/z) before they are analysed by the detector.

A further advantage with LA-ICP-MS analysis is the ease of sample preparation. Samples selected for analysis by LA-ICP-MS were first analysed by WDS-EPMA. The coordinates of each shard analysed by WDS-EPMA were recorded, as were the coordinates of 3 reference crosses on the surface of the stub. These crosses were then located on the LA-ICP-MS system and the new coordinates entered into a coordinate transfer spreadsheet to calculate the new coordinates of the shards, allowing the same shards to be analysed by the LA-ICP-MS, and the data obtained using the two procedures to be directly comparable. This is similar to the method described by Kuehn and Froese (2010).

LA-ICP-MS analyses were conducted on the Coherent GeoLas ArF 193 nm Excimer laser ablation system coupled to the Thermo Finnegan Element 2 sector field (SF) ICP-MS at the Department of Geography and Earth Sciences, University of Aberystwyth. Trace element data were collected for individual shards using 20 μm and 10 μm diameter ablation craters at a laser energy of 10 J cm^{-2} and a repetition rate of 5 Hz over a 24 second acquisition. The crater size chosen depended on the area of material available for analysis. ^{29}Si values for individual shards (which were normalised to the anhydrous state) collected via EMPA were used as the internal standard during data processing. Calibration was assessed using NIST SRM 612 and the concentrations supplied in Pearce *et al.* (1997), with different calibration used for the 20 μm or 10 μm diameter craters to overcome any analytical variation resulting from different crater sizes (Pearce *et al.*, in press).

4.6 Analysis of geochemical data

It is normal practice in the geochemical analysis of non-visible tephra layers to "filter" the data before interpretation. There are two main reasons for this which are addressed here before discussing the statistical interpretation of the data.

4.6.1 Removal of outliers

The floatation process for isolating vitreous tephra (Section 4.3, Figure 4.3) does not guarantee complete removal of mineral matter and biogenic silica. Some non-vitreous material mimics glass shards in appearance and therefore individual geochemical determinations may represent non-vitreous material (Pollard *et al.,* 2006). These outliers are usually distinctive (e.g. biogenic silica with ~100% SiO_2) and were removed following inspection of the raw data. Another potential cause of geochemical "outliers" is determinations being carried out on shards with heterogeneous inclusions, such as mineral microliths. Again, these are easily identifiable (e.g. potassium feldspar inclusions, with high K_2O and Al_2O_3 concentrations) and were removed when assessing the raw data. This approach is essential because it is futile carrying out comparisons of data-sets that contain variable amounts of non-vitreous material (Pollard *et al.,* 2006).

4.6.2 Treatment of samples with low total oxides

The major oxide values reported by EPMA are percentages of sample weight and the sum of the oxide percentages for individual measurements should equal 100%. However, this is rare and the reasons why analytical totals may fall below 100% include:

1. The influence of water in volcanic glass, either from phreatomagmatic eruptions (water introduced into the magma chamber) or from the uptake of water by shards after deposition. This can only account for a few percent however, especially as the dry core of the glass is normally analysed (Froggatt, 1983; Pollard *et al.,* 2006).
2. Low analytical totals may be derived from poorly polished and mounted samples, or because the electron beam intersects a vesicle in the glass or the edge of the sample (Pollard *et al.,* 2006).
3. The presence of unmeasured minor elements such as fluorine or phosphorus (Turney *et al.,* 2004). Certain measured elements may be adversely affected, such

as beam-induced migration of sodium but this should be accounted for by adjusting the probe operating conditions, as outlined in Table 4.1 (Pollard *et al.,* 2006).

4. The characteristics of individual shards may have an impact on the totals, particularly, for example, when the shard has a very small surface area on which to fit the electron beam (Turney *et al.,* 2004).

Originally, it was proposed that all geochemical data should be normalised to 100% to overcome the low oxide totals problem (Froggatt, 1992), partly because Froggatt (1983) had demonstrated that differences from 100% were similar to gravimetric weight loss when heating to 1000^{o}C. Froggatt (1992) argued that as the degree of hydration (water content) of a particular tephra is not related to its formation but to its environment of deposition, all analyses should be normalised to facilitate comparisons and shards with analytical totals as low as 90-91% could be considered acceptable. Hunt and Hill (1993) advised against the normalisation approach, arguing that no adjustment of the original measurements should be undertaken but that samples returning analytical totals below 95% should be rejected because low totals occur due to poor point selection, or to inappropriate probe conditions, or to analysis of shards altered chemically by processes other than hydration.

Despite the normalisation approach being widely undertaken (e.g. Westgate *et al.,* 2001), Stokes and Lowe (1988) demonstrated that the use of normalised data made little difference in correctly assigning glass shards to their source volcano. Pollard *et al.* (2006) also concluded that normalisation of data should be avoided because it is unnecessary if the logratio approach is used (see section 4.7.3.2) and also unhelpful because it masks the quality of the data. Therefore the recommendation of Hunt and Hill (1993) to remove data with analytical totals below 95% has been adopted in this study.

4.7 Graphical and statistical treatment of data

This section outlines the procedures used in this study for the chemical classification and correlation of glass shards.

4.7.1 Displaying tephra data

Tephra compositional data is often displayed using a mean value, with the standard deviation shown to express variance (e.g. Wulf *et al.*, 2004). However, this assumes that the sample population is either normally or log-normally distributed, an assumption that can rarely be made for geochemical data (Rollinson, 1993).

Presenting data as means with standard deviations can seriously oversimplify the picture. For example, bimodal distributions (e.g. 2 mixed geochemical signatures) will give false signals leading to erroneous correlations. Hence the data generated for tephra horizons in this thesis were not reduced to means and standard deviations. At all times the full geochemical data-set is presented and graphical and statistical interpretations of the data are based on consideration of the full variance displayed by the data.

4.7.2 Classifying tephra layers

Once a geochemical data-set has been screened and shards with low totals or any non vitreous grains removed, it should be possible to classify tephra layers based on internationally recognised chemical classification systems. Tephra layers can be classified using a Total Alkali vs. Silica (TAS) plot of Le Bas *et al.* (1986) (Figure 4.9). The TAS plot divides volcanic products into 4 categories - acidic, intermediate, basic and ultrabasic - based on SiO_2 content. It then uses the sum of Na_2O and K_2O to assign the volcanic product a name such as trachyte, phonolite, basalt etc. (Rollinson, 1993).

Tephra layers can also be classified according to their volcanic source. For example, Paterne *et al.* (1988) and Wulf *et al.* (2004) use an alkali ratio diagram (Na_2O+K_2O vs. K_2O/Na_2O) to match tephra layers to source volcanoes in the Mediterranean region (Figure 4.10). Calanchi and Dinelli (2008) also used a CaO vs. MgO/TiO_2 diagram to classify tephra layers older than 60 ka BP to various Mediterranean volcanic sources (Figure 4.11).

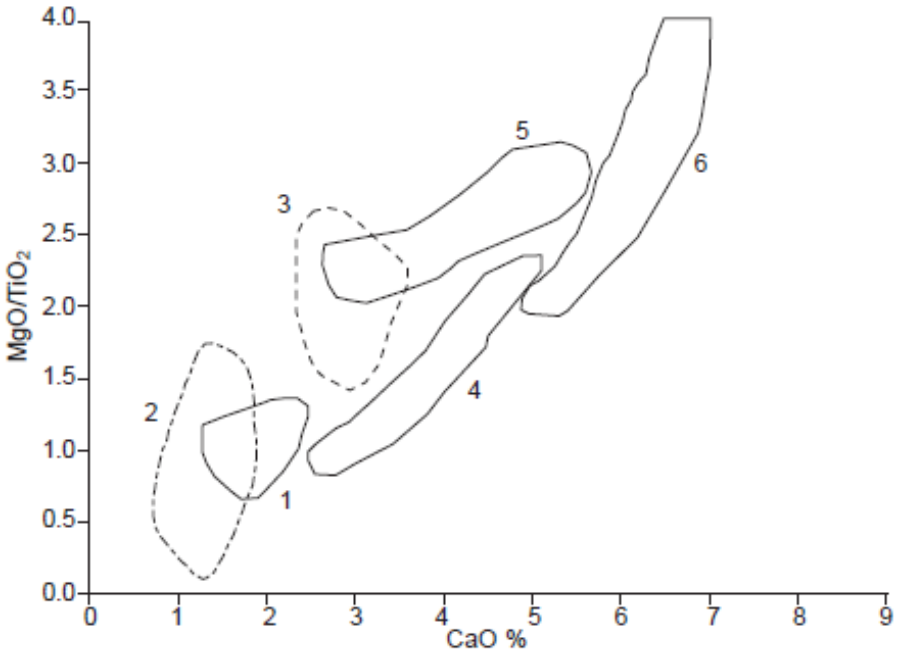

Figure 4.11: CaO vs. MgO/TiO_2 used to discriminate the sources of tephra layers in this study. Fields 1-6 are defined by on-land volcanic products older than 60 ka BP based on data from (1) the Campi Flegrei pre-Campanian Ignimbrite deposits, (2) Ischia pre-Monte Epomeo Green Tuff (Rosi and Sbrana (1987); Pappalardo *et al.* (1999); Webster *et al.* (2003); Vezzoli (1988)); (3) the average composition of tephra layer X5 (Vezzoli (1991); Calanchi and Dinelli (2008)): (4) Vico (Perini et al. 2004); (5) Vulsini (Tubeville (1992); Palladino *et al.* (1994)); and (6) Alban Hills (Trigila (1995); Peccerillo (2005)) for the Roman area (adapted from Calanchi and Dinelli, 2008).

As a first step in evaluating the nature and volcanic source of tephra layers in this study, a TAS plot and alkali ratio diagram will be produced for each layer with an age of less than 60 ka B.P. For each layer older than 60 ka BP, a TAS diagram and a CaO vs. MgO/TiO_2 diagram will be used to classify the nature and origin of each layer respectively. Some of the fields in the classification diagrams in Figures 4.9, 4.10 and 4.11 are constructed based on whole rock geochemical data which is not always comparable with geochemical data obtained from single glass shards (Section 2.1.2). However, they are still used for classification in this study as the diagrams are widely used in other Mediterranean tephra studies and therefore the fields and terms are widely used in the literature. However, due to the differences in the type of geochemical data used to construct these diagrams, Figures 4.9, 4.10 and 4.11 are only used as a classificatory tool and not for direct matching of tephra layers.

4.7.3 Data correlation

Ash layers are best assigned to source volcanoes and eruptive events and/or correlated with other ash layers, by element-specific geochemical comparison, which at present

relies on comparison of the ratio variations of nine major elements (Pollard *et al.,* 2006). For this, a data-set of type geochemical data is required against which the new data can be compared statistically. Commonly this involves comparisons using biplots or triplots of selected major oxides, although multivariate statistical methods are becoming increasingly employed (Pollard *et al.,* 2006).

Limitations with these procedures include the following. First, the full sequence of eruptions over the last glacial-interglacial cycle may not be represented at proximal sites or sedimentary basins, or their products may be inaccessible because of subsequent erosion or burial. Second, eruptions are rarely single, short-lived events; instead, major eruptions may be episodic over decades or longer, generating complex sequences of pyroclastic deposits of varying chemical composition (van den Bogaard and Schmincke 1985). Thirdly, not all geochemical data reported in the literature, whether for proximal or distal layers, have been obtained using the same analytical procedures or comparative standards, increasing the statistical variability. Statistical analysis can only produce meaningful data-matches if the training sets employed are sufficiently comprehensive and display well ordered (clustered) data; for the reasons given above, this is not always the case. Furthermore, selection of data for inclusion in biplots and triplots can be subjective and possibly misleading, while multivariate approaches, although using all the available data, merely establish the nearest matches between data-sets, which do not necessarily indicate common origin. Hence, the procedures employed for correlation of tephra layers often generate equivocal results.

The most robust way to provenance distal tephra layers is by comparing their chemical signatures directly with those of equivalent proximal deposits at source volcanoes, using standardised analytical procedures. However, for this to be achievable in practice, a comprehensive data-base would be needed of chemical data obtained from all proximal layers representing the complete sequence of volcanic eruptions during the period of interest. Such comprehensive and analytically coherent data-bases do not yet exist for volcanic centres in the Mediterranean region. In the light of these limitations and to test to what degree unequivocal correlations are possible between tephra layers detected in the Adriatic sequences analysed in this study, as well as with published Italian tephra geochemical data for other sites, the following strategy was adopted in this study.

The data were initially compared with a database of geochemical data generated by Wulf *et al.* (2004, 2007, 2008 and unpublished[1]) for the volcanic ash record preserved in the Lago Grande di Monticchio (LGdM) sequence, located in southern Italy (see sections 2.2.5.1 and 3.5.1.1 for full information about the site). Each chemically analysed tephra layer in the LGdM sequence is labelled TM (Tephra Monticchio) and numbered according to its relevant stratigraphic position in the core. The LGdM geochemical data-set is hereafter referred to as the *TM data-set*. The key reasons for initially focussing on this data-set, therefore, are (a) it is the most comprehensive single-site record of tephra layers in the Mediterranean region; (b) the record extends over the time period of relevance to this study; (c) a number of the tephra layers can be dated by both radiocarbon and varve chronology (Brauer *et al.,* 2000) which through correlation of tephra layers allows a terrestrial chronology to be applied to marine sequences and; (d) Wulf *et al.,* consistently employed WDS-EPMA to generate the data-set, unlike the majority of tephra studies for this region, making it compatible therefore with the analyses undertaken in the present study

Correlating tephra layers with data from known eruptions has often been undertaken through graphical means (biplots or triplots of major element oxides). However, whilst biplots such as a TAS plot have geological value, they can be potentially misleading as they are only partial segments through the data (Pollard *et al.,* 2006). Other authors have attempted to use statistical techniques to correlate tephra layers (e.g. Toms *et al.,* 2004; Payne *et al.,* 2008), however these tests assume normally distributed data-sets and fail to address the issues of compositional data and the unit sum problem. Aitchison (1986) argued that the problems associated with the unit sum in geochemical analyses can be overcome by using a logratio method (Pollard *et al.,* 2006).

The remainder of this section will explore compositional data and the unit sum problem (section 4.7.3.1) followed by the two methods used to compare the geochemical data generated in this study with the TM; log-ratio discriminant function analysis (DFA) (statistical, section 4.7.3.2) and biplots of selected major elements (graphical, section 4.7.3.3).

[1] An unpublished geochemical data-base generated by Sabine Wulf that is more comprehensive than those published in Wulf et al. 2004, 2007 and 2008, has been made available for use in this thesis.

4.7.3.1 Compositional data and the unit sum problem

Major element compositions of glass shards are presented as percentages of a whole (weight %), therefore it, along with data expressed as parts per million (ppm) can be described as compositional data (Rollinson, 1993). Analysis of compositional data presents problems for statistical comparisons due to the fact that percentages are highly complex ratios containing variables in their denominators that represent all the constituents being examined, meaning the components of percentage data are not free to vary independently (Rollinson, 1993). This is known as the unit sum problem and, when considering its effect on tephra data, it means that by defining an oxide concentration as a percentage, it involves not only the concentration of that particular oxide but also the sum of the concentrations of the remaining oxides (Pollard *et al.,* 2006) e.g.

$$\text{wt\% } SiO_2 = \frac{[SiO_2]}{[SiO_2]+[Al_2O_3]+[TiO_2]+[FeO]+[MnO]+[CaO]+[MgO]+[K_2O]+[Na_2O]} \text{ x100}$$

Therefore each element is constrained by the sum of the elements that have gone before it. This introduces negative bias when using biplots as any increase in a dominant element (e.g. SiO_2 which is the major constituent of tephra shards) along the x-axis leads to a decrease of any element plotted on the y-axis (Rollinson, 1993). A second problem of using compositional data is that it forces a correlation between components of the data-set, apparent matches can be forced in unrelated elements due to the co-dependency of compositional data (Rollinson, 1993). As tephra data are often correlated using biplots or triplots this issue of false correlation is particularly important (Pollard *et al.,* 2006).

One of the best known attempts to overcome the problem of compositional data is that of Aitchison (1986). The premise is that the study of compositions is concerned with the relative magnitudes of the ingredients rather than their absolute values which leads to the conclusion that ratios of the ingredients should be considered (Rollinson, 1993). A number of possible ratios can be used to overcome the unit sum problem: (1) the natural log of all possible oxide ratios, (2) the natural log of the ratio of all other oxides to a common oxide, effectively sacrificing one element to form the ratio or (3) the natural log of the ratio of all oxide values to the geometric mean of the data (Pollard *et al.,* 2006). Pollard *et al.,* 2006 state that any divisor should make no difference to the analysis and often using the geometric mean is preferred as this preserves all of the

elemental data which can then be used for correlation (Rollinson, 1993). Based on these facts and other studies where different divisors have been compared (Pollard *et al.,* 2006; Matthews, 2009), the geometric mean will be used as the divisor for multivariate analyses in this research project.

4.7.3.2 Statistical

Multivariate statistical techniques can aid in the correlation of tephra layers between sequences, as differences and similarities between tephra layers can be quantified (Turney *et al.,* 2008). Multivariate techniques are also beneficial in correlating tephra horizons as they combine information on all oxides (Pollard *et al.,* 2006).

Discriminant function analysis (DFA) is the multivariate technique applied to the data in this study. DFA is a multivariate statistical method that provides a non-subjective means of comparing geochemical data obtained from tephra layers based on compositional or other variable characteristics (Stokes *et al.,* 1992). It produces a number of linear combinations of the quantitative variables which best discriminate pre-defined groups (Lowe, 2011). In this case a group is the geochemical data derived for each tephra layer. A reference data-set of geochemical measurements with pre-defined groupings is required as a reference or target for comparison and DFA is used to establish the degree of discrimination between the unknown group (new tephra layer) and the groups in the reference data-set (Cronin *et al.,* 1997). In this study, the TM dataset was used as the DFA reference training-set. DFA has been previously applied to tephrostratigraphical data by (*inter alia*) Stokes *et al.* (1992), Kuehn and Foit (2006) and Lowe *et al.* (2007b).

DFA was carried out using SPSS v.16. Before carrying out the DFA procedures, all geochemical data were log-transformed using the geometric mean as the root to correct for the unit sum problem (see section 4.7.3.1) and to ensure that the full spectrum of statistical variance was taken into account.

A major assumption with this approach, however, concerns the robustness and completeness of the LGdM tephra record and of the associated TM chemical data-base. Wulf *et al.* (2004) correlated a number of the LGdM tephra layers with known eruptive events represented in proximal deposits, based on closest chemical matches and age

information. If either or both of the proximal or LGdM tephra records are incomplete, however, then false correlations may ensue, because DFA will readily find nearest matches that appear plausible but which may not be valid. Hence, interpretation of the tephrochronology of the Adriatic sequences is reliant partly on the completeness of the original LGdM data. Also the TM chemical data available for some of the reported layers are insufficiently robust to distinguish them from others with broadly similar chemical spectra when using analysis of major elements alone. A further problem that is magnified by the use of techniques such as DFA relates to sample size, as the nearest matches between an unknown sample and the largest clusters of geochemical data in the training set are more likely than with training set data that have a small number of values. While this problem is also encountered in *ad hoc* allocations used in bi-plots, the constraints of sample size have a direct impact on the likelihood of a correlation based on formal statistical procedures.

DFA was used initially to explore the LGdM by volcanic system (based on the allocations of Wulf *et al.*, 2004, 2008 and unpublished) and then to match unknown layers to the predefined groups, based on visual assessment of the canonical plots produced. The process undertaken is explained fully in Section 6.1.1.

4.7.3.3 Graphical

Due to some of the problems associated with DFA, all data generated within this study were also evaluated using tools such as major element bi-plots and, where applicable, trace element spider diagrams, the latter normalised to chondrite values (Thompson, 1982).

In all cases numerous biplots were consulted before attempting to correlate tephra layers. However, plots of all major and minor elements against Silica (Harker diagrams) are presented for each tephra layer as well as plots of FeO vs. CaO and MgO vs TiO_2. These have been shown to be particularly useful when correlating tephra layers of Italian origin (e.g. Abbott, 2005; Pyle *et al.*, 2006).

Graphical representation of trace element data presents further challenges, mainly because 27 elements have been measured by LA-ICP-MS for the tephra layers examined within this thesis. For this reason trace element data are initially presented

using spider diagrams, with all elements normalised to chondrite values (Thompson, 1982). This allows for comparison of data to different volcanic systems and for broad-scale correlation purposes. However, these plots often require the data to be averaged and are also presented on a logarithmic scale, meaning that minor variations between samples can be missed. Therefore, spider diagrams are always presented alongside biplots of the trace element data, to guard against subtle variations in the data being overlooked.

4.7.3.4 Summary

In view of the points above, both bi-plots and DFA were used in partnership to correlate Adriatic tephra layers to known volcanic eruptions. DFA was initially used to assign tephra layers to the most likely proximal volcanic system. The results were tested further by comparing the geochemical data generated in this study with published geochemical data reported for tephra layers registered in other Mediterranean marine sequences and/or for relevant proximal volcanic material (e.g. Davies *et al.,* 2002; Turney *et al.,* 2008). Wherever possible, independent stratigraphical information was also used to provide supporting evidence for the order of superposition of key tephra layers.

4.8 Tephrochronology

Producing a reliable tephrochronological scheme for Adriatic sequences relies on firstly being able to directly date the ash layers found in each sequence, for example by argon-argon dating, and secondly on the identification of tephra layers that already have known ages associated with them, for example where they have been dated at proximal sites. As discussed in section 2.1.3, tephra layers can be directly dated using a number of methods. Whilst radiocarbon dating of organic material associated with tephra layers is still the most popular method for dating them (Lowe, 2011), the potential age of the study sites means that not all of the sequence can be radiocarbon dated. In addition, the fact the sites are all marine sequences brings additional sources of error from the marine reservoir effect (see section 1.2.1). Therefore, argon-argon dating is attempted to directly date some of the tephra layers in the study sites. This direct dating of ash layers can be combined with tephra layers correlated to volcanic eruptions of known age to produce age models for the sequences that are independent of climatic and biostratigraphic assumptions and also avoid marine radiocarbon dating. The methods

used to prepare samples for argon-argon dating and then the subsequent age modelling of sequences are now discussed in greater detail.

This study uses both of these approaches to derive chronologies for the PRAD 1-2 sequence. However the SA03-03 and RF93-77 sequences are too young for argon-argon dating of tephra layers, and hence rely entirely on imported dates by correlation of the tephra layers to known dated eruptions. Both of these methods are now discussed in greater detail.

4.8.1 Argon-Argon dating

Argon-Argon (Ar-Ar) dating is a radiometric dating technique that involves the measurement of ratios between two isotopes of argon, ^{40}Ar and ^{39}Ar and is a derivative of Potassium-Argon (K-Ar) dating (Twyman, 2007). Both K-Ar and Ar-Ar dating techniques are based upon the decay of a naturally occurring isotope of potassium, ^{40}K to an isotope of argon, ^{40}Ar (Kelley, 2002). The essential difference between K-Ar and Ar-Ar dating is the measurement of potassium. In K-Ar dating, measurements of potassium are made on a separate aliquot of sample to the measurement of ^{40}Ar, whereas in Ar-Ar dating the ^{40}K concentration is measured indirectly by using the known proportions between the potassium and argon isotopes (Kelley, 2002; Walker, 2005). Samples are placed in a nuclear reactor and irradiated. This converts a portion of the stable ^{39}K isotope to ^{39}Ar. The abundance of ^{39}Ar is proportional to that of ^{39}K, which in turn is proportional to the abundance of ^{40}K meaning the $^{40}Ar/^{40}K$ ratio in a sample can be inferred from a single measurement (Walker, 2005).

There is a greater degree of analytical precision associated with Ar-Ar compared with K-Ar dating so that younger samples can be dated using this approach, making it more applicable to Quaternary studies (Walker, 2005). Other advantages of the $^{40}Ar/^{39}Ar$ method compared with K-Ar dating is that as potassium and argon can be measured from the same material, there is no need to determine the absolute abundance of potassium and the need for orders of magnitude less material than the K/Ar method (Nomade *et al.,* 2005).

One problem with traditional Ar-Ar dating is the presence of xenocrysts (older feldspar grains) within a sample, which can give an erroneous age estimate (Walker, 2005). The

problem can be circumvented through a technique called single-crystal laser fusion (SCLF) $^{40}Ar/^{39}Ar$ dating, where a single crystal is targeted and a high-powered laser is used to drive off the argon, which is measured in a highly sensitive mass-spectrometer (Wintle, 1996).

4.8.1.1 Sample selection for Argon-Argon dating

Ar-Ar dating relies on the presence of potassium rich minerals within tephra layers. Dating of the glass shards themselves is problematic, due to the potential for potassium and argon mobility as well as problems of ^{37}Ar and ^{39}Ar recoil artefacts (Smith *et al.*, in press). Sanidine crystals are favoured for analysis because they are potassium-rich and are thought to efficiently exclude initial argon at magmatic temperatures (Renne *et al.*, 1997). SCLF $^{40}Ar/^{39}Ar$ dating is preferable as it reduces the risk of xenocrystic contamination, however, as the age of a sample decreases, the size of a single crystal needed to obtain a date increases. For example a 2mm diameter sanidine crystal with 10 weight % K only produces about 2×10^{-18} moles of ^{40}Ar in 5000 years, which is one or two orders of magnitude below the best attainable background levels of ^{40}Ar (Renne *et al.*, 1997).

Therefore, sample selection for dating relies upon having coarse grained tephra layers so that large sanidine crystals could be extracted. As Ar-Ar dating of distal tephra layers is relatively untested and problematic (Smith *et al.*, in press), only samples from PRAD 1-2 were selected for dating, as older samples could be analysed, meaning slightly smaller crystals were needed. A mixture of visible and non-visible tephra layers were chosen as a test to establish if Ar-Ar dating could be applied to non-visible distal ash layers.

4.8.1.2 Sample Preparation for Argon-Argon dating

The procedure used to prepare samples for argon-argon dating is outlined in Figure 4.12. Once this protocol had been applied to sediment samples both size fractions from each sample were studied for the presence of sanidine crystals.

A similar technique to that described in section 4.4.2 was used to separate the sanidine crystals from the remainder of the sample. For this purpose a 2.5 ml gas chromatography syringe fitted with a 394 μm diameter needle was mounted on a micromanipulator. When a sanidine crystal was located the micromanipulator and microscope allowed the needle to be manoeuvred to the position of the crystal. The sanidine was then drawn into the needle and deposited in a labelled glass vial.

4.8.1.3 Summary

Samples were sent to the QUADLAB argon-argon dating laboratory based at the University of Roskilde, Denmark. However due to the small crystal size and comparatively young age of the samples, results were not forthcoming in time for inclusion in this thesis.

4.8.2 Age modelling

Age modelling has two applications in this thesis; 1) to provide the best age estimates for tephra layers with a number of associated age estimates from different sources and 2) to provide a chronology for each studied core sequence based solely on independent age estimates obtained from tephra layers found in each sequence.

In all cases, age models were constructed using OxCal version 4.1.7 (Bronk Ramsey, 2001, 2009), a Bayesian-based tool for age model construction and evaluation. Bayesian analysis utilises prior knowledge and assumptions when generating an age model from a chronological dataset, this is termed the **prior**. The prior includes the raw data and any prior knowledge or assumptions, so for a series of dates through time the assumption is that age should increase with stratigraphic depth and in a *P-Sequence* the actual depth of the dated horizon is included in the prior (Blockley *et al.,* 2008a). The results of applying a prior model to some data is known as the **posterior**, with the most likely age range known as the **highest probability density function** (HPD) (Blockley *et al.,* 2008b).

When modelling the best age estimates for tephra layers with a number of associated age estimates both a ***Phase*** model and a ***Sequence*** model were used. A *Phase* model assumes that all of the dating information within the phase form a coherent group but

there is no information about the internal ordering of the dating information (Blockley *et al.,* 2008a). A *Sequence* model, however, again assumes all the dating information form a coherent group but it assumes that the each date within the sequence is in a relative order. For the cases in this study that order is that age (with youngest samples at the top of the sequence) should increase with depth (Bronk Ramsey, 2008b). Where a tephra layer was dated using radiocarbon dating these were calibrated using the INTCAL 09 calibration curve for terrestrial samples and the MARINE 09 calibration curve for marine samples (Reimer *et al.,* 2009) (see section 1.2.1).

In this study age models for the three marine sequences have been constructed using a ***P_Sequence.*** This uses a prior based on the Poisson distribution and uses the relative position of a dated layer to help produce a more constrained model than if only the assumption of age increasing with depth is used (Bronk Ramsey, 2008b). The model allows varying sedimentation rates between dated horizons and calculates realistic age estimates for undated levels. This allows age estimates for tephra layers that cannot be correlated to a dated volcanic eruption to be generated and for the refinement of existing tephra layer age estimates. The estimation of a **factor (k)** which is the relationship between the events and the overall stratigraphical process is required for a *P_Sequence* to set the rigidity of the model. The k factor gives the number of accumulation events per unit depth (Bronk Ramsey, 2008b). A high value for k would constrain the data quite rigidly, whereas a low k value would be the opposite (Blockley *et al.,* 2008b). An optimal k factor can be found by initially running the model with a low k factor of 1 and then re-running the model and increasing the k factor each time until the agreement index for the model falls below 60 % (Blockley *et al.,* 2007; 2008b).

Construction of both the *Sequence and P_Sequence* models requires the use of **boundaries**. Boundaries are mathematical features of the model that are placed at the start and end of the sequence to constrain the modelling of the data to a fixed time period (Blockley *et al.,* 2008b). However in the case of a *P_Sequence* model, boundaries can also be used to separate different sedimentological sections within a sequence. Boundaries can be inserted at the depths that the lithostratigraphy suggests there was a change in sedimentation rate, for example at the start and end of a sapropel layer (Blockley *et al.,* 2008b).

Finally in all age models, it is important to have a measure of how well the data and model fit together, in OxCal this is performed by the **Agreement Index (AI)** (Blockley *et al.*, 2008b). An AI is derived for the model as a whole and for each modelled data. The AI value is expressed as a percentage and is calculated from the area of overlap from the prior unmodelled data and the HPD function. The lower the AI percentage, the lower the overlap between the prior and posterior (Blockley *et al.*, 2008b). The cut off for acceptance of overlap is 60% (Bronk Ramsey, 2008b). A glossary of the main age modelling terms used in this thesis and in chapter 8 in particular, is provided in Table 4.3.

Table 4.3: Glossary of main age modelling terms. References for definitions: 1. Blockley *et al.* (2008a), 2. Blockley *et al.* (2008b), 3. Bronk Ramsey (2008b).

Age modelling term	Definition	Ref.
Prior	The prior is used to define the model and includes the raw data and any prior knowledge or assumptions	1
Posterior	Is the result of applying a prior model to some data	2
Highest Probability Density Function	The most likely modelled age range.	2
Phase	Phases are groups of events which all form one coherent group in some context but for which there is no information on the internal ordering, e.g. a series of radiocarbon dates on a palaeosol beneath a tephra layer.	1
Sequence	A sequence is a group of events which all form one coherent group in some context but it is assumed that all of the events within each group have a predefined order	3
P_Sequence	Is a depositional model that uses a prior based on the Poisson distribution and uses the relative position of a dated layer to help produced a more constrained model than a *Sequence* model alone.	3
Boundary	Boundaries are used with *Sequence* and *P_Sequence*, models and when paired with another Boundary defines a uniformly distributed group	2
K-factor	The k factor gives the number of accumulation events per unit depth and is used in a *P_Sequence*. A high value for k would constrain the data quite rigidly, whereas a low k value would be the opposite.	2, 3
Agreement Index (AI)	A measure of the overlap between the prior or posterior, expressed as a percentage and is generated for the overall model and individually modelled dates. The cut off for acceptance of a date or model is an AI of 60. Where agreement between the prior and posterior is very good the AI value can be over 100%.	2

4.9 Summary

This chapter has outlined the experimental methods used within this thesis. The main laboratory methods for processing tephra samples have been explained. This has led to the identification of tephra layers which is explained in the next chapter. The methods

employed to analyse the geochemical data for tephra layers have been explained and is expanded upon in Section 6.1.1. Finally, the procedures undertaken to provide chronologies for the studied sequences have been outlined and the exact methods used are outlined later in sections 8.1 and 8.2.

5. Results

This section presents the main results for the three studied marine sequences. In all cases, tephra layers found have been given a unique label. For non-visible tephra layers, this is derived from the position of the peak glass shard concentration within the sequence. For example, PRAD 055 has peak shard concentration at 55 cm depth in the profile. For visible tephra layers, the unique label is derived from the position of the base of the visible layer, for example PRAD 2525 with its base at 2525 cm. This approach is important as it will reduce confusion and potential ambiguity if additional tephra layers are detected during subsequent research (Lowe, 2011).

For all tephra layers identified in the three sequences, the shard counts per g dry wt., the colour and dominant morphology are presented. In addition, for samples for which geochemical information was obtained, the tephra layers are also classified using the TAS plot of Le Bas *et al.* (1986). Finally, these tephra layers have also been classified by their volcanic source based on the system of Paterne *et al.* (1988) and Wulf *et al.* (2004) (See section 4.7.2 for further information). Therefore, when a layer is assigned to a volcanic source, it is based on the definitions used by Paterne *et al.* (1988) and Wulf *et al.* (2004).

5.1 PRAD 1-2 tephra descriptions and classifications

The tephra results for PRAD 1-2 will be considered based upon the resolution at which the work was carried out (see Figure 4.2 for methodology details). Work undertaken at 5 cm resolution will be considered first (Section 5.1.1), with subsequent work undertaken at 1 cm resolution compared with the original results in Section 5.1.2.

5.1.1 Analysis at 5 cm vertical resolution

The stratigraphical positions of the PRAD 1-2 tephra layers, the numbers of shards counted per sample, their chemical classification (classified by total alkalis against silica (Le Bas *et al.*, 1986)) and shard morphological descriptions are summarised in Table 5.1 and shown in Figure 5.1. Figure 5.2 shows photomicrographs of the various shard morphologies described in the text.

PRAD-055 has a peak of 1095 shards per g dry wt., with a vertical distribution of glass shards over 20 cm. The layer is comprised of predominantly clear shards which are mainly fluted with some large open vesicles (Figure 5.2). The shard distribution (Figure 5.1) was unimodal, therefore geochemical analysis was undertaken on the 5 cm sample. There was no mixed geochemical signal (see Figure 4.2) in the 5 cm sample therefore this tephra layer was not refined to 1 cm resolution (see Figure 4.2 for details of decision-making process). The geochemical data show PRAD-055 is phonolitic/trachytic in composition (Figure 5.3a) and is grouped in the Campanian Volcanic Zone by its alkali composition (Figure 5.4a).

PRAD-120 has a peak of 200 shards per g dry wt., with a vertical distribution of glass shards over 15 cm. The layer has a sparse glass shard population, consisting of small (<50μm), clear shards with a predominantly fluted morphology. The shard distribution was unimodal (Figure 5.1), therefore geochemical analysis was undertaken on the 5 cm sample. As there was no mixed geochemical signal in the 5 cm sample, this tephra layer was not refined to 1 cm resolution. The geochemistry shows it is a trachyphonolite tephra layer which lies in the Campanian Volcanic Zone of the alkali diagram (Figures 5.3a and 5.4a).

PRAD-203, PRAD-218 these layers constitute a multi-modal distribution in glass shards (Figure 5.1) One peak at 203 cm has 746 shards per g dry wt., with a vertical distribution of glass shards over 30 cm, while a second peak at 218 cm has greater than 10,000 shards per g dry wt., with a vertical distribution of 15 cm. Both layers comprise mainly clear and fluted shards. Some shards are browner in colour and some have mineral inclusions (Figure 5.2). Due to this multi-modal distribution, this section was refined to 1 cm resolution before geochemical analysis was undertaken, the results of which are presented in section 5.1.2.

PRAD-268 is a tephra layer with a unimodal peak in glass shards of 1238 shards per g dry wt. The vertical distribution of the glass shards is 15 cm. The morphology of the shards is very similar to the two layers above it, with predominantly clear, fluted shards, with some browner shards present. Geochemical analysis was undertaken on the 5 cm resolution sample and indicates the layer to be a trachyte/phonolite/tephriphonolite (Figure 5.3a). There are two populations of geochemical data present, so this layer was

also resolved to 1 cm resolution. Both geochemical populations, however, plot within the Campanian Volcanic Zone (Figure 5.4a).

PRAD-324 has a peak of greater than 10,000 shards per g dry wt., with a vertical distribution of glass shards over 20 cm. The layer is comprised of predominantly clear fluted shards, though some were brown and contained mineral inclusions (Figure 5.2B). As the shard distribution was unimodal, geochemistry was undertaken on the 5 cm resolution samples. The layer is classified as a trachyte/phonolite/tephriphonolite (Figure 5.3a). There are two populations present, both of which plot in the Campanian Volcanic Zone (Figures 5.4a). Due to the presence of two geochemical populations, this layer was resolved to 1 cm resolution.

PRAD-404 is a unimodal tephra layer with a peak of 3187 shards per g dry wt., with a vertical distribution of glass shards over 15 cm. Both clear and intermediate shards are present, although clear ones dominate. The morphology of the shards is predominantly fluted. Geochemical analysis of the 5 cm resolution samples shows a trachyte/phonolite/tephriphonolite chemistry indicating a Campanian origin (Figures 5.3a and 5.4a). The geochemical data for PRAD 268, 324 and 404 are indistinguishable based on WDS-EPMA.

PRAD-480 has a peak of 308 shards per g dry wt., with a vertical distribution of glass shards over 10 cm. The layer is comprised of brown and clear shards, which are predominantly platy, although some shards with closed vesicles are present. The shard distribution was unimodal (Figure 5.1), therefore geochemical analysis was undertaken on the 5 cm sample. There was no mixed geochemical signal in the 5 cm sample therefore, this tephra layer was not refined to 1 cm resolution. The geochemical data shows the layer has a phonolitic/trachytic chemistry, which lies in the Campanian Volcanic Zone of the alkali diagram (Figures 5.3a and 5.4a).

PRAD-566 has a very sparse shard concentration of only 26 shards per g dry wt., with a vertical distribution of glass shards over 5 cm. The shards are small and clear with evidence of alteration. The sample was prepared for geochemical analysis but failed to generate successful results.

PRAD-608 also has a very sparse shard concentration of only 17 shards per g dry wt., with a vertical distribution of glass shards over 5 cm. The shards are small and clear with evidence of alteration. The sample was prepared for geochemical analysis but failed to generate successful results.

PRAD-650 has a peak of 36 shards per g dry wt., with a vertical distribution of glass shards over 5 cm. The shards are small and clear and, despite their sparse concentrations (Table 5.1), sufficient geochemical data were obtained on the 5 cm sample to indicate a phonolitic/trachytic chemical composition (Figure 5.3a) with the majority of data points plotting within the Campanian Volcanic Zone. However, a second smaller cluster plots closest to data obtained from the Ischia field (Figure 5.4a), hence analysis of this layer was refined to 1 cm resolution (Section 5.1.2).

PRAD-784 has a peak of 359 shards per g dry wt., with a vertical distribution of glass shards over 15 cm. The shards are predominantly clear but are also very vesicular (Figure 5.2C). Geochemical analysis, undertaken at 5 cm resolution, indicates the layer is trachyphonolitic in composition (Figure 5.3a). The chemical data places the layer within the Campanian Volcanic Zone. However, there is also a population of data from the layer that plots in the Ischia field (Figure 5.4a). Due to this mixed geochemical signal, this section of the core was refined to 1 cm resolution, the results of which are discussed in Section 5.1.2.

PRAD-845 has a peak of 156 shards per g dry wt., with a vertical distribution of glass shards over 10 cm. This layer also consists of clear vesicular shards. Geochemical analysis at 5 cm resolution characterised the layer as trachyphonolitic (Figure 5.3a). This layer also has a mixed geochemical signature at 5 cm resolution with one population plotting within the Campanian Volcanic Zone and the other in the Ischia field (Figure 5.4b). Analysis of this layer has also been refined to 1 cm resolution due to this mixed geochemical population (Section 5.1.2).

PRAD-875 has a peak of 178 shards per g dry wt., with a vertical distribution of glass shards over 10 cm. The shards are clear, with a large number of closed vesicles. Geochemical analysis at 5 cm resolution characterised the layer as trachytic in composition (Figure 5.3a). There are two geochemical populations, one which plots in

the Campanian Volcanic Zone and one in the Ischia zone (Figure 5.4b). Consequently, this layer was also resolved to 1 cm resolution.

PRAD-1100 has a peak of greater than 10,000 shards per g dry wt., with a vertical distribution of glass shards over 15 cm. The shards are all clear, with no intermediate or brown shards at all, and have a platy morphology (Figure 5.2). The distribution of glass shards is unimodal therefore geochemical analysis was conducted at 5 cm resolution. This shows the layer is of trachytic composition and of an Ischian origin (Figure 5.3b, 5.4b). Analysis of this layer was refined to 1 cm resolution to provide a test of the methodology described in Figure 4.2; the results are discussed in section 5.1.2.

PRAD-1125 has a peak of 145 shards per g dry wt., with a vertical distribution of glass shards over 15 cm. The layer is composed entirely of clear shards which are predominantly platy in morphology. Geochemical analysis at 5 cm resolution indicates it is a trachyphonolitic layer with alkali ratios that suggest an origin from the Campanian Volcanic Zone (Figures 5.3b and 5.4b). However, there is a second smaller population that is classified as being from Ischia (Figure 5.4b) and hence analysis of this layer was refined to 1 cm resolution.

PRAD-1332 has a peak of 53 shards per g dry wt., with a vertical distribution of glass shards over 10 cm. Despite this layer having a sparse shard concentration, geochemical analysis on the 5 cm resolution samples was possible and indicated the layer to be trachytic with an origin in the Campanian Volcanic Zone (Figures 5.3b and 5.4b).

PRAD-1474 has a unimodal peak of 204 shards per g dry wt., with a vertical distribution of glass shards over 5 cm (Figure 5.1). The layer comprises highly pumiceous glass (Figure 5.2E). The shards are clear, small (<50μm) and vesicular. This meant geochemical analysis was difficult and had to be conducted using the 5 μm diameter beam at the University of Edinburgh Microprobe. The results indicated this layer to be trachyphonolitic, with an origin in the Campanian Volcanic Zone (Figures 5.3b and 5.4b).

PRAD-1494 has a peak of 1878 shards per g dry wt., with a vertical distribution of glass shards over 5 cm, meaning it is a unimodal distribution. The layer is composed of only small clear shards (<50μm) which are predominantly vesicular, with no mineral

inclusions. Geochemical analysis at 5 cm resolution indicates it is a trachyphonolitic layer with alkali ratios which suggest an origin from the Campanian Volcanic Zone (Figures 5.3b and 5.4b).

PRAD-1653 has a unimodal peak of greater than 10,000 shards per g dry wt., with a vertical distribution of glass shards over 10 cm. The layer is composed of predominantly clear shards (with some more brown in colour) which are highly fluted with some closed vesicles (Figure 5.2A). Geochemical analysis at 5 cm resolution indicates it is a trachyphonolitic layer with alkali ratios which suggest an origin from the Campanian Volcanic Zone (Figures 5.3b and 5.4b).

PRAD-1752 has a peak of 5448 shards per g dry wt., with a vertical distribution of glass shards over 10 cm. The shards are clear and highly fluted. Geochemical analysis at 5 cm resolution characterised the layer as trachytic in composition (Figure 5.3b) with a probable source in the Campanian Volcanic Zone, although some data lie within the Ischia field (Figure 5.4c).

PRAD-1870 has a peak of greater than 10,000 shards per g dry wt., with a vertical distribution of glass shards over 10 cm. The shards are clear (no intermediate shards are present) with a platy morphology. The peak is unimodal, therefore geochemical analysis was undertaken on the 5 cm resolution samples. Analysis of geochemical data indicates the layer to be trachytic in composition (Figure 5.3b) and of Ischian origin (Figure 5.4c).

PRAD-2040 has a unimodal peak of 1931 shards per g dry wt. with a vertical distribution of glass shards over 10 cm. The shards are all clear and have a platy morphology. Geochemical analysis at 5 cm resolution characterised the layer as trachyphonolitic in composition (Figure 5.3b) with an origin in the Campanian Volcanic Zone, although the data are tightly clustered near the Ischia field with an alkali ratio in the region of 1.25 (Figure 5.4c).

PRAD-2375 has a peak of 217 shards per g dry wt., with a vertical distribution of glass shards over 5 cm, meaning the peak is unimodal. The shards are clear and intermediate but show evidence of alteration, such as hydration rims on intermediate shards (Figure 5.2F and Figure 4.4). Geochemical analysis was undertaken at 5 cm resolution.

Initially, only 8 electron probe measurements were obtained. These are scattered and fall in the following classification groups; Phonolite, Trachyte, Rhyolite, Trachyandesite (Figure 5.3b). With regard to volcanic system, Figure 5.4c shows that, although four of these points plot in the Campanian Volcanic Zone field, they do not cluster closely. Of the other four results, two plot in the Alban Hills, one in the Pantelleria and one in the Ischia fields. Further geochemical analysis was undertaken at the University of Edinburgh which yielded additional electron probe measurements and increase the number of points classified in the Pantelleria, Ischia and Campanian Volcanic Zone fields. Nevertheless the data fail to form close clusters but show a large spread, indicating alteration of shards. Due to this evidence of alteration, this layer has not been refined to 1 cm resolution.

PRAD-2525 is visible in the core, with its base at 2525.5 cm and a visible thickness of 10 cm. The layer was analysed at 1 cm resolution and the samples were spiked with *Lycopodium* spores (see section 4.3). The vertical distribution of glass shards is 46 cm, which is longer than the visible layer and stretches the entire length of core section 32. The core sections are normally 70 – 80 cm long and the fact that this one is significantly shorter may be because the tephra layer was not fully recovered. The maximum peak in glass is 7,390,076 shards per g dry wt. The layer is multimodal, so geochemistry was carried out on each of the peaks within the 46 cm spread. The geochemical data for each peak is homogeneous, indicating the multiple peaks may be an artefact of the *Lycopodium* counting method. Therefore, this is considered as one tephra layer which is trachyphonolitic in composition and has an origin in the Campanian Volcanic Zone (Figures 5.3c and 5.4c). It also plots in the average composition field of the X5 tephra layer field in Figure 5.5a.

PRAD-2605 has a peak of greater than 10,000 shards per g dry wt., with a vertical distribution of glass shards over 15 cm. The layer is comprised only of clear shards which are predominantly fluted. The shard distribution is unimodal (Figure 5.1); therefore geochemical analysis was undertaken on the 5 cm sample. The geochemical data are tightly clustered and therefore analysis was not refined to 1 cm resolution. The geochemical data show the layer has a phonolitic chemistry, best matching the Campanian Volcanic Zone of the alkali diagram (Figures 5.3c and 5.4c). It also plots in the average composition field of the X5 tephra layer field in Figure 5.5a.

PRAD-2812 is a visible layer in the core and therefore the samples were spiked with *Lycopodium* spores (see section 4.3). The visible layer is 5 cm thick, but the overall vertical distribution of glass shards is 25 cm. The maximum peak in glass is estimated to 24.76 million shards per g dry wt. which occurs at 2805 cm, a little above the visible layer. The layer is unimodal, so geochemistry was carried out on the 5 cm sample containing the peak of glass. The geochemistry classifies the layer as trachyphonolitic in composition with an origin in the Campanian Volcanic Zone, although some of the data clusters in the Ischia field (Figures 5.3c and 5.4c). This is supported by data plotting in the Ischia pre Monte Epomeo Green Tuff (MEGT) field in Figure 5.5.

PRAD-3065 has a peak of 843 shards per g dry wt., of which 803 are clear and 40 are brown in colour. The shards have a vertical distribution of 5 cm and are predominantly platy, although some shards with closed vesicles are present. The shard distribution was unimodal (Figure 5.1) therefore geochemical analysis was attempted on the 5 cm sample. However, when sampling for geochemical analysis, it was not possible to extract any shards from the sample. Resampling was attempted on three occasions and no glass shards were found. This could be due to sediment focussing within a core section (Davies *et al.,* 2007; Pyne-O'Donnell, 2010). Therefore, it was not possible to obtain geochemical analysis on this layer.

The remaining 5 cm resolution work on core sections below 3065 cm was focussed on parts of the core that were targets for argon-argon dating. Therefore, it is mainly visible tephra layers that have been sampled and geochemically analysed in these lower sections. Non visible tephra layers with fewer glass shards (under 1000 shards per g dry wt.) within the analysed sections have not been geochemically analysed as part of this project. The stratigraphical positions of the PRAD 1-2 tephra layers, the numbers of shards counted per sample, their chemical classification (classified by total alkalis against silica (Le Bas *et al.,* 1986)) and shard morphological descriptions are still summarised in Table 5.1 and Figure 5.1. As these layers are older, it is not appropriate to classify them by volcanic system using the diagram in Figure 5.4, as the products of volcanic sources change over time, therefore the fields defined in Figure 5.4 will not be accurate for layers older than 40 ka. Therefore, they will be classified to a volcanic system using the CaO vs. MgO/TiO2 diagram in Figure 5.5

PRAD-3225 is a visible layer which is 3.6 cm thick with its base at 3225.6 cm (Core Section 41 – 25.6 cm). The core section was sampled at 5 cm resolution which shows the vertical distribution of glass shards is 30 cm, with a maximum shard concentration of greater than 10,000 shards per g dry wt. sediment between 3215 cm and 3225 cm. The morphology of the shards is a mix of both platy and fluted shards which are predominantly clear, albeit with very few brown shards present. Geochemical analysis classifies this layer as principally phonolitic in composition, although there are some data points that range from phono-tephritic to tephri-phonolitic and then to the main cluster of phonolites. There are only three data points not in the main cluster. This could indicate an altered layer but, as this is visible in the core, it is more likely that a shard of different chemical composition has been analysed (Figure 5.3c). The majority of the data plots in or along the same trend as the Vico field (Figure 5.5b).

PRAD-3336 is a non-visible layer with a peak of greater than 10,000 shards. The vertical shard distribution is 15 cm and the shards are predominantly platy with large open vesicles. The layer is comprised of mainly clear shards. The shard distribution is unimodal and geochemical analysis classifies the layer as a phonolitic, with a potential source from Vico (Figures 5.3c and Figure 5.5b).

PRAD-3383 is a visible tephra layer which is 5.5 cm thick with its base at 3383.5 cm (Core Section 43-23.5 cm). The maximum shard count is greater than 10,000 with a vertical distribution of 30cm, with shards 5 cm below the start of the visible layer. The shard distribution is unimodal and the shards are highly fluted and vesicular. In particular, there are a number of large closed vesicles present. Geochemical analysis classifies this layer as trachyphonolitic (Figure 5.3c). The data do not fall within one of the source fields in Figure 5.5 but appears to follow the trend of the Vico field.

PRAD-3472 is a visible layer which is 3.1 cm thick and located in Core Section 44. The maximum shard concentration is greater than 10,000 shards per g dry wt. and there is a vertical distribution of glass shards over 15 cm. The shard distribution is unimodal and the dominant shard morphology is platy (Figure 5.2G). However, the small numbers of brown shards present have a high concentration of small closed vesicles. Geochemical analysis was carried out at 5 cm resolution and classifies the layer as trachytic with a possible source from the Campi Flegrei (Figure 5.3c and 5.5).

PRAD-3586 is a 6.7 cm thick visible layer in Core Section 45 of the core. The peak in glass is greater than 10,000 shards per g dry wt. with a 30 cm vertical distribution which begins with the sample containing the base of the visible layer. The shard distribution is unimodal and the dominant shard morphology is platy and there are very few brown shards present. Geochemical analysis on the 5 cm resolution sample classifies the layer as a phonolite (Figure 5.3c) with a potential source from Vico (Figure 5.5b).

PRAD-3666 is a visible layer which is 14 cm thick. However glass shards are vertically distributed over 47 cm and for 40 cm, the shard concentration is greater than 10,000 shards per g dry wt. The shard distribution is unimodal and the shards are highly vesicular. There are also more brown shards present in this layer than in the others of a similar age (Figure 5.2H). Geochemical analysis classifies this layer as phonolitic with a source from Vico (Figure 5.3c and Figure 5.5b).

5.1.2 Analysis at 1 cm vertical resolution

The areas of the core that have been refined to 1 cm resolution will now be considered. The results are compared with the original 5 cm resolution work conducted on the same core sections and the degree to which multi-modal peaks or mixed geochemical signals are resolved is assessed. The 1 cm shard counts can be seen in Figure 5.6.

PRAD 178 cm – PRAD 277 cm

This area of core encompasses the 5 cm resolution peaks of PRAD-203, PRAD-218 and PRAD-268. These were resolved to 1 cm resolution as the first two peaks were multi-modal. This is still the case at 1 cm resolution with three separate peaks at 205, 223 and 231 cm (Figure 5.6) together covering a vertical distribution of glass shards over 59 cm. All the samples have been counted using *Lycopodium* and the peaks in glass are 38,068 clear, 799 brown; 131,349 clear, 5,029 brown and 229,238 clear, 12,993 brown shards per g dry wt. for the three peaks respectively. The peaks are consistent with the 5 cm resolution shard counts. These main peaks and some other samples within this core section have been geochemically analysed and they have a trachyte/phonolite/tephriphonolite chemistry (Figure 5.7a) with a source in the Campanian Volcanic Zone (Figure 5.8a). There are two geochemical populations present in all 1 cm samples.

PRAD-268 was resolved to 1 cm resolution as there were two geochemical populations in the 5 cm geochemical data. Although this layer was unimodal at 5 cm resolution (Figure 5.1), it is multimodal at 1 cm resolution with peaks in glass at 267 cm (27,588 clear and 170 brown shards per gram) and 273 cm (23,165 clear and 110 brown shards per gram) (Figure 5.6A). This is likely to be an artefact of the Lycopodium counting method. The first of these peaks are consistent with the 5 cm peak at 268 cm. Both of these samples were geochemically analysed and both have a trachyte/phonolite/tephriphonolite chemistry with a source in the Campanian Volcanic zone (Figure 5.7a and Figure 5.8a). The chemistry of all samples analysed in this section appears to be identical based on this classification.

PRAD 306 cm – PRAD 338 cm

The 1 cm resolution sampling shows glass peaks at 323 cm, 329 cm and 336 cm (Figure 5.6A). The first two of these are consistent with the 5 cm resolution peak at 324 cm which had two geochemical populations. All peaks have shards which are predominantly clear and fluted. The peaks are 323 cm, 51,343 clear and 439 brown shards per gram, 329 cm, 43,116 clear and 221 brown shards per gram and 336 cm, 18,570 clear and 48 brown shards per gram. All samples were counted with reference to *Lycopodium* spore counts. The multi-modal peaks may be artefacts of the slide counting method. Each of these peaks were geochemically analysed and they are all classified as having a trachyte/phonolite/tephriphonolite chemistry (Figure 5.7a). The alkali data suggests a source from the Campanian Volcanic zone in all three cases (Figure 5.8a). The chemistry of all samples analysed in this section appears to be identical based on this classification.

PRAD 648 cm – PRAD 657 cm

This section encompasses the 5 cm resolution peak of 36 shards per gram at 650 cm, which had a mixed geochemical signal. However, at 1 cm resolution, a peak in glass is not resolved with shards present in very low concentrations throughout the core section (Figure 5.6bi). As there was no discrete layer detected, geochemical analysis was not undertaken as the shards are likely to represent a background signal that was artificially concentrated into 1 sample at 5 cm resolution.

PRAD 774 cm – PRAD 789 cm

Analysis at 1 cm resolution identified a peak in glass of 58 clear shards per gram at 784 cm. This is consistent with the 5 cm peak also at 784 cm, although the shard concentration is significantly lower. There is also a second peak of 26 clear shards per gram at 789 cm (Figure 5.6Bii). Both peaks have been geochemically analysed and both are trachyphonolitic in composition (Figure 5.7b). The chemical data places both peaks within the Campanian Volcanic Zone. However, there are no data that sit in the Ischia field, unlike the 5 cm resolution sample (Figure 5.8b).

PRAD 834 cm – PRAD 884 cm

There are two main tephra layers within this section. The first is a multi-modal peak with a vertical distribution of glass shards over 16 cm. There are peaks at 837 cm (856 clear shards per gram), 839 cm (962 clear shards per gram), 841 cm (545 clear shards per gram) and 844 cm (260 clear shards per gram). In each case, the shard concentration drops between these peaks. The 5 cm resolution peak was at 845 cm and was unimodal but with two geochemical populations. All these peaks have been geochemically analysed at 1 cm resolution and all are classified as trachyphonolitic (Figure 5.7b). In all four of the samples, the majority of the data plot in the Campanian Volcanic Zone but there is at least one data point in each layer which plots in the Ischia field (Figure 5.8b). This was seen in the 5 cm sample and suggests that there are not two layers present in this section but actually some reworking of shards from an older Ischia layer. These four peaks in glass will be considered as one layer for future correlations, with 839 cm taken as the depth for the tephra layer, as this is the level of the greatest peak in glass shards.

The second tephra layer in this section consists of a peak in glass of only 57 clear shards per gram at 873 cm (Figure 5.6) which is consistent with the 5 cm peak at 875 cm. Geochemical analysis classifies this layer, as well as a smaller peak in glass at 868 cm, as trachyphonolitic in composition (Figure 5.7b). Like the layers in the first tephra event in the section, the majority of the data plots in the Campanian Volcanic Zone but there is at least one data point in each layer which plots in the Ischia field (Figure 5.8b). This was seen in the 5 cm sample and suggests that there are not two layers present in this section but actually some reworking of shards from an older Ischia layer.

PRAD 1087 – PRAD 1140

The first part of this section which encompasses PRAD 1100 was analysed at 1 cm resolution to provide a test of the methodology used to resolve layers to 1 cm resolution (Section 4.1.3 for details). PRAD 1100 had a unimodal shard distribution and no mixed geochemical signal. When resolved to 1 cm, the peak in glass is at 1104 cm with 143,240 clear shards per gram and 203 brown shards per gram. The peak remains unimodal (Figure 5.6C) and is consistent with the 5 cm resolution sample, suggesting the methodology to be sound.

Analysis of the second part of the section was undertaken to resolve PRAD 1125, which had two geochemical populations in the 5 cm sample. The layer is resolved into 2 peaks at 1 cm resolution with 24 clear shards per gram at 1127 cm and 100 clear shards per gram at 1130cm (Figure 5.6Ci). This is consistent with the 5 cm resolution peak. Both these layers were geochemically analysed and are both classified as trachyphonolitic (Figure 5.7B). PRAD 1127 has a spread of data plotting in the Campanian Volcanic Zone and again some points in the Ischia field (Figure 5.8B). The PRAD 1130 data plots in the Campanian Volcanic Zone (Figure 5.8B). Due to the spread of the PRAD 1127 data, this layer probably represents a background signal but PRAD 1130 is considered a discrete tephra layer.

5.1.3 PRAD 1-2 results summary

Of the 34 tephra layers originally identified in PRAD 1-2, 26 were geochemically analysed at 5 cm resolution. They were all successfully classified based upon the TAS scheme of Le Bas *et al.* (1986) and also to a volcanic zone based upon the schemes of Paterne *et al.* (1988) and Wulf *et al.* (2004). 2 layers could not be geochemically analysed due to small shard concentrations. 9 layers were refined to 1 cm resolution due to either multi modal shard distributions or mixed geochemical signals in the 5 cm resolution sample. 1 cm resolution sampling has resolved 8 discrete layers between 205 cm and 336 cm which have identical major element geochemistry. 1 small layer present at 5 cm resolution could not be replicated at 1 cm resolution. In 2 of the 1 cm resolution layers the mixed geochemical signal is still observed suggesting some shard re-working.

5.2 SA03-03 tephra descriptions and classifications

The tephra results for SA03-03 will be presented based upon the resolution at which the work was carried out (see Figure 4.2 for methodology details). Work undertaken at 5 cm resolution is considered first (Section 5.2.1), then analysis undertaken at 1 cm resolution is compared with the 5 cm results in Section 5.2.2.

5.2.1 Analysis at 5 cm vertical resolution

The stratigraphical positions of the SA03-03 tephra layers, the numbers of shards counted per sample, their chemical classification (classified by total alkalis against silica (Le Bas *et al.*, 1986)) and shard morphological descriptions are summarised in Table 5.2 and shown in Figure 5.9. Figure 5.10 shows photomicrographs of the various shard morphologies described in the text.

Table 5.2: Summary of SA03-03 tephra layers identified in this study including shard content, number of geochemical determinations obtained, classification of glass shards where applicable, and descriptions of shard characteristics. All samples were coded by depth to allow for possible addition of new horizons to the sequence. Classifications (based on Le Bas *et al.,* 1986): Tr = trachyte, P = phonolite.

Layer code	Shards/g dry wt.	Total analyses	Classification	Shard morphological characteristics
SA03-03-25	> 10000	10	P	Predominantly clear, highly vesicular shards.
SA03-03-85	> 10000	10	Tr	Predominantly clear, highly vesicular shards.
SA03-03-383	458234	8	Tr/P	Predominantly clear, highly vesicular shards.
SA03-03-413*	215396	116	Tr/P	Mainly clear shards which have a fluted morphology
SA03-03-427	99047	24	Tr/P	Mainly clear shards which have a fluted morphology
SA03-03-645	618	8	Tr	Only clear shards, fluted and platy morphology
SA03-03-685	> 10000	10	Tr	Predominantly clear platy shards.
SA03-03-925	> 10000	12	P/Tr	Only clear shards, highly fluted.
SA03-03-995	> 10000	13	Tr	Clear platy shards only.

SA03-03-25 has a peak of greater than 10,000 shards per g dry wt., with a vertical distribution of glass shards over 20 cm. The layer is comprised of predominantly clear shards which are highly vesicular (Figure 5.10a). The shard distribution (Figure 5.9) is unimodal, so geochemical analysis was undertaken on the 5cm sample. There was no

* Denotes visible layer

mixed geochemical signal in the 5cm sample therefore this tephra layer was not refined to 1cm resolution (see Figure 4.2 for details of decision making process). The geochemical data show this layer is a phonolite in composition (Figure 5.11) and is grouped in the Campanian Volcanic Zone by alkali ratios (Figure 5.12).

SA03-03-85 has a unimodal peak of greater than 10,000 shards per g dry wt., with a vertical distribution of glass shards over 20 cm. The layer is comprised of clear, highly vesicular shards (Figure 5.10b). Geochemical analysis was undertaken on the 5cm sample and, as there was no mixed geochemical signal, this tephra layer was not refined to 1 cm resolution. The layer is classified as a trachyte with an origin in the Campanian Volcanic Zone (Figure 5.11 and 5.12).

SA03-03-385, SA03-03-405 and SA03-03 430 are layers that form a multi-modal tephra layer with a vertical distribution of 55 cm (Figure 5.9). There is a visible layer with its base at 419.5 cm that is 7 cm thick, so this layer encompasses the peak in glass at 405 cm. The peak in glass at 385 cm is greater than 10,000 shards per g dry wt. and the shards are all clear and highly vesicular (Figure 5.10c). The glass then tails off slightly but there is a mix in morphologies with clear fluted shards being present as well as vesicular shards. There is a second peak in glass at 405 cm of greater than 10,000 shards per g dry wt. These are all clear fluted shards (Figure 5.10d). This again tails off but above this is a third peak at 430 cm of 6138 shards per g dry wt. These shards are all fluted in morphology and are predominantly clear (5957 clear shards per g dry wt. and 181 brown shards per g dry wt.). Due to this multi-modal peak, this core section was refined to 1 cm resolution before geochemical analysis was undertaken. These results are discussed in section 5.2.2

SA03-03-645 has a peak of 618 shards per g dry wt., with a vertical distribution of glass shards over 5 cm. The layer is comprised of only clear shards, which are fluted and platy. The shard distribution (Figure 5.9) is unimodal therefore geochemical analysis was undertaken on the 5 cm sample. There was no mixed geochemical signal in the 5 cm sample therefore this tephra layer was not refined to 1 cm resolution. The geochemical data shows SA03-03-645 is trachytic in composition (Figure 5.11) and is grouped in the Ischia field by its alkalis (Figure 5.12).

SA03-03-685 has a unimodal peak of greater than 10,000 shards per g dry wt., with a vertical distribution of glass shards over 15 cm. The layer is comprised of predominantly clear platy shards (Figure 5.10f). Geochemical analysis was undertaken on the 5 cm sample and the layer was not refined to 1 cm resolution. The geochemical data show the layer is trachytic in composition (Figure 5.11) with an origin in the Ischia field (Figure 5.12).

SA03-03-925 has a peak of greater than 10,000 shards per g dry wt. The vertical distribution of this layer is large with glass shards spread over 90 cm. Despite this, the peak is still unimodal, therefore geochemical analysis was undertaken only on the 5 cm resolution sample and was not refined further to 1 cm resolution. The shards are all fluted and clear (Figure 5.10g). The geochemical data show SA03-03-925 is phonolitic/trachytic in composition (Figure 5.11) and is grouped in the Campanian Volcanic Zone by its alkalis (Figure 5.12).

SA03-03-995 has a peak of greater than 10,000 shards per g dry wt., with a vertical distribution of glass shards over 15 cm. The layer is comprised of clear platy shards (Figure 5.10h). The shard distribution (Figure 5.9) was unimodal so geochemical analysis was undertaken on the 5cm sample. As there was no mixed geochemical signal in the 5 cm sample, this tephra layer was not refined to 1 cm resolution. The layer is classified as a trachyte in composition (Figure 5.11) and is grouped in the Campanian Volcanic Zone by its alkalis (Figure 5.12).

5.2.2 Analysis at 1 cm vertical resolution

The areas of the core that have been refined to 1 cm resolution will now be considered. A comparison with the original 5 cm resolution work and an assessment of the degree to which the 1 cm resolution results resolve multi-modal peaks or mixed geochemical signals will be made.

SA03-03 375 cm – 435 cm

The 1 cm sampling resolved the multi-modal peaks seen in section 5.2.1 into two main tephra layers. The first of these layers is a unimodal with a peak in glass shards at 383 cm (Figure 5.13a) and a vertical distribution of glass shards over 8 cm. The section has been counted using *Lycopodium* spores and the peak in glass is 458,234 shards per g dry

wt., of which 457,160 shards are clear, meaning the layer is composed of mainly clear shards which are highly vesicular. Geochemical analysis was undertaken on the 1 cm sample which contained the peak in glass. This classifies the layer as trachyphonolite (Figure 5.14) which plots in the Campanian Volcanic Zone of the alkali diagram (Figure 5.15). The peak in glass at 383 cm is in line with the multimodal peak in the 5 cm resolution samples, which was located at 385 cm.

The second tephra layer has a vertical distribution of 41 cm. Figure 5.13a indicates that, despite being resolved to 1 cm resolution, the shard distribution is still multimodal. There are peaks in glass at 392 cm, 399 cm, 407 cm, 413 cm, 418 cm, 424 cm, and 427 cm. These samples were all counted using *Lycopodium* spores and have peaks in glass shards of 96,433, 102,733, 97,344, 215,396, 112,962, 83,402 and 99,047 shards per g dry wt. respectively. All the layers are comprised of predominantly clear shards with only 421, 0, 2669, 2952, 1671, 495, and 1421 brown shards per g dry wt. respectively. However, in most cases, the peaks in brown shards correspond to the peaks in clear shards (Figure 5.13b). In all cases, the dominant shard morphology is fluted (Figure 5.10e). All these samples are trachyphonolitic in composition (Figure 5.14) and all plot in the Campanian Volcanic Zone of the alkali diagram (Figure 5.15).

However, the geochemical data for all of these peaks in glass appears very similar (Figures 5.14 and 5.15). The peaks in glass at 392 cm, 399 cm, 407 cm, 413 cm, 418 cm, 424 cm all form one tephra event and will therefore be considered as one feature with a maximum concentration of glass shards at 413 cm. The peak in glass at 427 cm is separated from the other glass peaks by a few cm where no glass is present (Figure 5.13), therefore this will be considered as a separate event.

5.2.3 SA03-03 results summary

Of the 9 tephra layers originally identified in SA03-03, 6 were geochemically analysed at 5 cm resolution. They were all successfully classified based upon the TAS scheme of Le Bas *et al.* (1986) and also to a volcanic zone based upon the schemes of Paterne *et al.* (1988) and Wulf *et al.* (2004). A tephra layer with 3 multimodal peaks was refined to 1 cm resolution due to the multi modal shard distributions. 1 cm resolution sampling has resolved 3 discrete layers at 383 cm, 413 cm and 427 cm, these were all successfully

classified based upon the TAS scheme of Le Bas *et al.* (1986) and also to a volcanic zone based upon the schemes of Paterne *et al.* (1988) and Wulf *et al.* (2004).

5.3 RF93-77 tephra descriptions and classifications

This core was originally analysed for tephra layers by Calanchi *et al.* (1998), who worked solely on the visible tephra layers observed in the core. Tephra layers were identified at depths of 83 cm, 208 cm, 364 cm, 384 cm, 449 cm and 797 cm (Calanchi *et al.*, 1998). Due to the length of time the core had been stored, it was not possible to detect the visible layers when sub-sampling for the present investigation. The work was therefore conducted at a contiguous 6 cm resolution and the results compared with those of Calanchi *et al.* (1998).

The tephra results for RF93-77 will be considered based upon the resolution at which the work was carried out (see Figure 4.2 for methodology details). Work undertaken at 6 cm is considered first (Section 5.3.1), followed by results obtained at 2 cm resolution (Section 5.3.2).

5.3.1 Analysis at 6 cm vertical resolution

The stratigraphical positions of the RF93-77 tephra layers, the numbers of shards counted per sample, their chemical classification (classified by total alkalis against silica (Le Bas *et al.*, 1986)) and shard morphological descriptions are summarised in Table 5.3 and shown in Figure 5.16. Figure 5.17 shows photomicrographs of the various shard morphologies described in the text.

Table 5.3: Summary of RF93-77 tephra layers identified in this study including shard content, number of geochemical determinations obtained, classification of glass shards and descriptions of shard characteristics. All samples were coded by depth to allow for possible addition of new horizons to the sequence. Classifications (based on Le Bas *et al.,* 1986): Tr = trachyte, P = phonolite, TP = tephriphonolite, TrA = trachyandesite.

Layer code	Shards/g dry wt.	Total analyses	Classification	Shard morphological characteristics
RF93-77-68	226022	22	P	1 brown shard for every 2 clear shards, highly vesicular.
RF93-77-73	10204	22	Tr/P	Predominantly clear, fluted shards.
RF93-77-88	70103	21	Tr/P	Predominantly clear, fluted shards.
RF93-77-144	1694	21	TP/TrA/Tr/P	Mainly clear shards which have a fluted morphology.
RF93-77-198	> 10000	20	Tr/P	Predominantly clear shards, mainly fluted with some large open vesicles.
RF93-77-267	1012	19	Tr/P	Predominantly clear platy shards.
RF93-77-372	7696	24	Tr/P	Mainly clear shards which have a fluted morphology.
RF93-77-414	1453	33	Tr/P	Predominantly clear platy shards.
RF93-77-450	6511	29	Tr/P	Predominantly clear platy shards.
RF93-77-540	441	29	Tr/P	Predominantly clear platy shards.
RF93-77-604	287	18	Tr/P	Only clear shards with a predominantly platy morphology.
RF93-77-790	23832	28	P	Large mainly clear, fluted shards.

RF93-77-72 and RF93-77-84 form a bi-modal tephra layer with a vertical distribution of 42 cm (Figure 5.16). This area of tephra deposition equates with the visible layer identified by Calanchi *et al.* (1998) at 83 cm. The peak of glass shards at 72 cm is greater than 10,000 shards per g dry wt. and the shards are highly vesicular. There is a high concentration of brown shards in this peak, with approximately a ratio of 1 brown shard to every 2 clear shards (Figure 5.17a). The tephra concentration then drops, although there are still some brown shards present. The second peak in glass is at 84 cm and, again, there are greater than 10,000 shards per g dry wt. These are mainly clear fluted shards, with noticeably fewer brown shards present than the first peak (Figure 5.17b). Due to this bi-modal peak, this core section was refined to 2 cm resolution before geochemical analysis was undertaken. These results are discussed in section 5.3.2.

RF93-77-144 this is a unimodal tephra layer with a peak of 1,694 glass shards per g dry wt. and, of this total, only 5 shards per gram were brown. The layer has a vertical distribution of glass shards over 24 cm and the dominant shard morphology is fluted (Figure 5.17c). Geochemical analysis was undertaken on the 6 cm resolution samples. The geochemical data shows there is a range in the data and it is not very well clustered. Data points sit in all of the following groups: tephriphonolite, trachyandesite, trachyte

and phonolite (Figure 5.18). Despite this spread of data on the TAS plot, the data is well clustered in the alkali ratio diagram which suggests an origin in the Campanian Volcanic Zone (Figure 5.19).

RF93-77-198 has a peak of greater than 10,000 shards per g dry wt., with a vertical distribution of glass shards over 60 cm. This distribution corresponds to the visible layer at 208 cm identified by Calanchi *et al.* (1998). The layer is comprised of predominantly clear shards which are mainly fluted with some large open vesicles (Figure 5.17d). The shard distribution (Figure 5.16) was unimodal, therefore geochemical analysis was undertaken on the 6 cm sample. There was no mixed geochemical signal in the 6 cm sample therefore this tephra layer was not refined to 2 cm resolution (see Figure 4.2 for details of decision making process). The geochemical data show RF93-77-198 is phonolitic/trachytic in composition (Figure 5.18) and is grouped in the Campanian Volcanic Zone by its alkalis (Figure 5.19).

RF93-77-267 has a peak of 1,012 shards per g dry wt., with a vertical distribution of glass shards over 6 cm. The layer is composed of mainly clear shards which are predominantly platy in morphology (Figure 5.17e). 6 cm geochemistry indicates it is a trachyphonolitic layer with alkali ratios which suggest an origin from the Ischia field (Figures 5.18 and 5.19).

RF93-77-372 has a peak of 7,696 shards per g dry wt. of which 7511 are clear and 185 are brown. The vertical distribution of glass shards is 48 cm and the dominant shard morphology is fluted (Figure 5.17f). The distribution of glass shards encompasses both the visible layers at 364 cm and 384 cm that Calanchi *et al.* (1998) identified. The peak is unimodal, therefore geochemistry was carried out on the 6 cm resolution sample. There was no mixed geochemical signal present, therefore this section was not refined to a higher resolution. Geochemical analysis indicates it is a trachyphonolitic layer with alkali ratios which suggest an origin from the Campanian Volcanic Zone (Figures 5.18 and 5.19).

RF93-77-414 has a peak of 1,453 shards per g dry wt., with a vertical distribution of glass shards over 12 cm. The layer is composed of mainly clear shards which are predominantly platy in morphology. 6 cm geochemistry indicates it is a

trachyphonolitic layer with alkali ratios which suggest an origin in the Campanian Volcanic Zone (Figures 5.18 and 5.19).

RF93-77-450 has a peak of 6,511 shards per g dry wt., with a vertical distribution of glass shards over 30 cm. This corresponds to the visible layer at 449 cm that Calanchi *et al.* (1998) identified. The layer is composed of mainly clear shards (only 61 shards per gram are brown) which are predominantly platy in morphology (Figure 5.17g). The peak is unimodal therefore geochemistry was undertaken on the 6 cm resolution sample. The geochemical signal was not mixed therefore this layer was not refined to 2 cm resolution. Geochemistry indicates it is a trachyphonolitic layer with alkali ratios which suggest an origin from Ischia (Figures 5.18 and 5.19).

RF93-77-540 has a peak of 441 shards per g dry wt., with a vertical distribution of glass shards over 12 cm. The shards are mainly clear with a platy morphology. 6 cm geochemistry indicates it is a trachyphonolitic layer with alkali ratios which suggest an origin from the Campanian Volcanic Zone, although some of the data clusters in the Ischia field (Figures 5.18 and 5.19).

RF93-77-604 has a peak of 287 shards per g dry wt. with a vertical distribution of glass shards over 24 cm. The layer is comprised solely of clear shards which have a platy morphology. As the peak is unimodal, 6 cm geochemistry was undertaken which classifies the layer as trachyphonolitic. The alkali ratio diagram suggests the origin of the layer is Ischia (Figures 5.18 and 5.19).

RF93-77-790 has a peak of 23,832 shards per g dry wt. (greater than 10,000 shards in the sample). The vertical distribution of glass shards is 24 cm but this is to the base of the sequence. Calanchi *et al.* (1998) identified a visible layer at 797 cm which corresponds to the vertical shard distribution seen here. The peak is unimodal and the shards are predominantly clear and fluted (Figure 5.17h). 6 cm geochemistry indicates it is a phonolitic layer with alkali ratios which suggest an origin from the Campanian Volcanic Zone (Figures 5.18 and 5.19).

5.3.2 Analysis at 2 cm vertical resolution

The areas of the core that have been refined to 2 cm resolution will now be considered. Their correlation to the original 6 cm resolution work will be examined and also an assessment made as to whether the 2 cm resolution clarifies any of the multi-modal peaks.

RF93-77 60 cm – 96 cm

The 2 cm sampling resolved the bi-modal peaks seen in section 5.3.1 into three main tephra layers. The first of these events is a unimodal tephra layer with a peak in glass shards at 68 cm (Figure 5.20) and a vertical distribution of glass shards over 8 cm. The section has been counted using *Lycopodium* spores and the peak in glass is 226,022 shards per g dry wt., of which 149,711 shards are clear and 76,310 are brown. This means the ratio of 1 brown shard to 2 clear shards seen in the 6 cm resolution samples is evident at 2 cm resolution as well. Both the clear and brown shards are highly vesicular (Figure 5.17a). This peak in glass is slightly closer to the top of the sequence than the original 6 cm peak at 72 cm. Geochemical analysis was undertaken on the 2 cm sample which contained the peak in glass and this classifies the layer as a phonolite (Figure 5.21) which plots in the Campanian Volcanic Zone of the alkali diagram (Figure 5.22).

The second tephra layer has a peak in glass of 10,204 shards per gram at 73 cm with a vertical distribution of 4 cm. The shards are mainly clear (9,763 clear and 441 brown shards per gram) and have a predominantly fluted morphology. This peak could correspond to the 6 cm resolution peak at 72 cm. However, the ratio of clear to brown shards is not consistent, neither is the shard morphology. Both these indicators are more consistent with the peak at 63 cm. 2 cm resolution geochemical analysis classifies the layer as a trachyphonolite which the alkali diagram plots in the Campanian Volcanic Zone (Figures 5.21 and 5.22).

The final tephra layer has a vertical distribution of 10 cm, however, despite being resolved to 2 cm resolution, this is still a multi-modal. The first peak of 62,084 shards per gram is at 86 cm and the second peak of 70,103 shards per gram is at 88 cm. In both cases, the shards are predominantly clear with only 4,335 and 5,512 brown shards in each respective layer (Figure 5.17b). These peaks are consistent with the 6 cm resolution peak at 84 cm (Figures 5.20a and b). The dominant shard morphology in

both layers in fluted. Geochemical analysis was undertaken on each of these 2 cm peaks and this classifies both layers as trachyphonolitic and plots both layers within the Campanian Volcanic Zone (Figures 5.21 and 5.22).

5.3.3 RF93-77 results summary

Of the 11 tephra layers originally identified in RF93-77, 9 were geochemically analysed at 6 cm resolution. They were all successfully classified based upon the TAS scheme of Le Bas *et al.* (1986) and also to a volcanic zone based upon the schemes of Paterne *et al.* (1988) and Wulf *et al.* (2004). A tephra layer with 2 multimodal peaks was refined to 2 cm resolution due to the multi modal shard distributions. 2 cm resolution sampling has resolved 2 discrete layers at 68 cm 73 cm and a tephra event with 2 multimodal peaks at 86 cm and 88 cm respectively. Each of these layers were successfully classified based upon the TAS scheme of Le Bas *et al.* (1986) and also to a volcanic zone based upon the schemes of Paterne *et al.* (1988) and Wulf *et al.* (2004).

6. Correlation of tephra layers

This chapter is divided into two sections. The first explores the geochemical data available for tephra layers in Southern Europe in order to compile a robust data-set for comparison. The second concerns the correlation of the tephra layers detected, analysed and classified in this study with other tephra layers represented in the Southern European Geochemical data-set, with the aim of resolving corresponding volcanic eruptive events.

6.1 Southern European geochemical data

As discussed in Chapter 4, there is a dearth of appropriate volcanic geochemical data available in the literature with which to compare the data generated in this study. The single most comprehensive data-set is that reported for Lago Grande di Monticchio (LGdM) which is therefore the key data-set used to compare to the Adriatic data. Other available data have been consulted to provide additional comparative materials where needed, these are highlighted in the text at the appropriate points. However, the majority of the data comparisons focus on the LGdM data-set.

6.1.1 Lago Grande di Monticchio

In order to ensure the most robust correlations possible with the geochemical data generated in this study an attempt has been made to geochemically classify all the tephra layers recorded by Wulf *et al.* (2004, 2008 and unpublished) in the LGdM data-set. The classification system follows that devised by Matthews (2009) and aims to generate clusters of tephra layers considered to show similar geochemical signatures, in an attempt to streamline the number of possible correlatives to unknown layers. This also accords with the approach adopted by Lowe *et al.* (2007b). The tephra layers in the LGdM data-set were consequently assessed and statistically grouped using SPSS v.16. The raw geochemical data are available on the RHOXTOR database.

Wulf *et al.* (2004, 2007, 2008 and unpublished) assigned all of the LGdM tephra to specific volcanic systems. Due to the large number of tephra layers involved (349), initial data exploration was based on the volcanic system assigned by Wulf *et al.* (2004, 2007, 2008 and unpublished) and therefore this is used to group the data. This therefore means that correlations made in this study are reliant on the original

correlations made by Wulf *et al.* (2004, 2007, 2008 and unpublished). Whilst the ideal approach would be to compare the results of this study directly to proximal data, this was not possible during this study. Therefore, when a volcanic centre is referred to in the chapter it is based solely on the correlations of Wulf *et al.* (2004, 2007, 2008 and unpublished) and not to proximal data.

Data from all the tephra layers in the LGdM data-set were firstly explored using biplots of major element data, including a TAS plot based on the divisions of Le Bas *et al.* (1986) (Figure 6.1). The data were then transformed into log-ratios of the geometric mean. Discriminant Function Analysis (DFA) was then employed to identify discrete groups of data based on the first two discriminant functions (see section 4.7.3 for the explanation of the approach). A hierarchical structure for classifying tephra geochemical data was then generated, based upon the approach outlined in Matthews (2009) and summarised in Table 6.1.

Table 6.1: Hierarchical structure for classifying tephra geochemical data from Lago Grande di Monticchio (adapted from Matthews 2009).

Order	Name	Description
1	Subset	Subsets can be differentiated using both biplots and multivariate approaches. They represent volcanism from different volcanic provinces but not necessarily specific volcanoes, e.g. Campanian and Roman volcanoes as opposed to Aeolian islands.
2	Major Cluster	Differentiation of major clusters is difficult with biplots but can be achieved using DFA. In most cases, they represent multiple eruptions from the same volcanic centre, therefore differentiating between volcanic centres. They also represent eruptions from different volcanic centres but with similar geochemical signatures.
3	Minor Cluster	Minor clusters can only be easily identified using multivariate approaches. They represent different types of volcanism within a single volcanic centre.
2 or 3	Unique Layer	These are identified either from a major or minor cluster and represent individual layers that are geochemically unique within a specific grouping.

The first two canonical axes of the whole data-set initially explained 74.3% of the total variability in the data (Figure 6.2A). The multivariate analysis of the full data-set generated two subsets, which are separated into (A) Volcanic sources from Etna, the Aeolian Islands and Pantelleria and (B) all other volcanic sources in the data-set (Figure 6.2A). The level of discrimination can also be seen in the biplots (Figure 6.1), although the use of only two elemental axes could be subjective (see Section 4.7.3).

Subset A contains two major clusters and three unique layers (Figure 6.2B), the first two canonical axes explaining 80.0% of the total variability in the data. TM 12-1, TM-11 and TM-22 do not group with any other layers in the LGdM data-set and can be considered geochemically exclusive within the LGdM data-set. Two major clusters are formed, each containing three layers; both clusters contain layers assigned to Etna and the Aeolian Islands. When DFA is undertaken on the major clusters, the first and second canonical axes show all layers to be distinctive from one another (Figure 6.3).

Subset B contains the majority of the tephra layers in the data-set, therefore more major clusters are identified (Figure 6.2C). The first two canonical axes explain 86.0% of the data variability in this subset. Due to the large volume of data involved, a stepped procedure for identifying major clusters was employed. This is necessary because when DFA is used the most distinctive layers cause other less distinctive layers to appear to cluster together. The problem can be resolved by identifying distinctive groups of data and removing them from the data-set. The analysis is then re-run to identify the next most distinctive cluster, which is subsequently also removed. This procedure is continued until no more major clusters can be identified (Lowe *et al.,* 2007b). Three major clusters emerged from Subset B of the LGdM data-set (Figure 6.2C). The first consists of tephra layers with an Ischian source, the second of tephra layers emanating from Vesuvius and the third comprises the remainder, with volcanic sources in the Campi Flegrei, Procida, Alban Hills, Sabatini Hills and Vico. Unlike subset A, all of the major clusters in Subset B contain considerable internal variability and consist of a number of minor clusters (Figure 6.4).

The Ischia data (major cluster B1) consists of 2 minor clusters and one unique layer (TM-31). The majority of data (51 layers) are contained in minor cluster B1i (Figure 6.4) with only 5 layers in minor cluster B1ii which makes these five layers easier to discriminate from others in the sequence. Major cluster B2 comprises material from Vesuvius and these can be split into 3 minor clusters, which separates layers by age and cycles of volcanic activity as defined by De Vivo *et al.* (2010) (Figure 6.4). The oldest layers (I cycle) cluster in minor cluster B2iii, with II cycle represented by minor cluster B2ii and III cycle grouped in minor cluster B2i (De Vivo *et al.,* 2010).

Major Cluster B3 represents the majority of the data (216 layers) and forms two minor clusters. Due to the large number of tephra layers in this cluster it is not possible to distinguish between individual layers and hence the data were plotted according to volcanic source in Figure 6.4C. The Campi Flegrei data form Minor Cluster B3i, with the Alban Hills and Vico data forming minor cluster B3ii. The Procida and Sabatini Hills data do not group in either cluster and are therefore included in both.

The large quantity of data constituting these minor clusters requires the application of DFA in order to further resolve the data into individual layers. Minor Cluster B3ii can be resolved into individual layers (Figure 6.5B) with the Alban Hills layers forming a distinctive group. However, it is not possible to discriminate other layers within the cluster. Minor cluster B3i, does not, however, resolve individual layers. This is because there are still 194 layers represented in this cluster, 177 of which have a Campi Flegrei source. Therefore, the Procida and Sabatini Hills data are presented as individual layers but the Campi Flegrei data are presented as groups of layers distinguished by time period (according to the Epochs defined by Di Vito *et al.* (1999) for the last 12,000 years and then by layers between major Campi Flegrei eruptions for the earlier period) (Figure 6.5). This illustrates how the Campi Flegrei layers overlap considerably for all time periods rendering them of limited value for correlation purposes when geochemical composition data alone are considered. This is illuminated further in Figure 6.6 which shows 3 of the most widespread Campi Flegrei layers in the LGdM sequence (TM-8, TM-18 and TM-24a) compared with the rest of the Campi Flegrei data. It is clear that without other information (e.g. stratigraphical position or reliable age control), these layers cannot be discriminated from other Campi Flegrei layers in the sequence.

In order to establish which tephra layers in the LdGM sequence are most useful for correlation purposes, a ranking system based purely on geochemical composition has been created (Table 6.2). The tephra layers are ranked from 1 – 6, with 1 being the most useful for correlation purposes and 6 being the least useful. A rank 1 tephra layer is one that can be discriminated from others at a subset level (e.g. unique layers in Figure 6.2B). A rank 2 tephra layer is one that is a unique layer at the major cluster level (e.g. Figure 6.2B and 6.3A) and a rank 3 tephra layer is one that can be discriminated from others at a minor cluster level. A rank 4 tephra layer is one that is

grouped in a minor cluster but cannot be discriminated from other layers in that cluster, though it can be distinguished from other layers originating from different volcanic systems (e.g. Figure 6.4A and B). A rank 5 tephra layer is a layer in a minor cluster than cannot be distinguished from other layers within the cluster or from layers originating from other volcanic systems. Finally, a rank 6 tephra layer is one that cannot be discriminated at the minor cluster scale (e.g. Figure 6.6, Campi Flegrei layers).

This ranking system is adopted for classifying the tephra layers detected within the PRAD 1-2, SA03-03 and RF93-77 sediment sequences according to geochemical composition. It also underpins comparisons made between the new geochemical data reported in this thesis and the LGdM data-set. The tephra layers from this study are queried against the LGdM data-set and then ranked depending on which subset and cluster the Adriatic tephra layers best accord with. Initial comparisons focus on the tephra layers ranked 1, 2, 3 or 4 since these provide the most secure correlations. Attention is then turned to those ranked lower in the classification system, which can be assessed on the basis of both their geochemical signatures and their stratigraphic positions, relative to the positions of the higher-ranked tephra layers in each sequence. In this way, a comprehensive tephra 'lattice' can be constructed and levels of confidence in tephra correlations assessed, as set out in the remainder of this chapter. For each tephra layer, biplots of major element data are also considered after the data has been queried to the LGdM data-set using DFA, in order to provide a check on the groupings made by DFA (see section 4.7.3 for the rationale).

Table 6.2: LGdM tephra layers that form the reference data-set used for correlation purposes in this research. Layers were allocated to a subset, major and minor cluster using DFA of the data (see text). Finally, tephra layers were ranked based upon their geochemical distinctiveness, with 1 being the most distinctive and 6 being the least distinctive (CF layers – Campi Flegrei layers).

Layer	Subset and Cluster	Rank
TM-11	A	1
TM-12-1	A	1
TM-22	A	1
TM-23-5	A1	2
TM-23-6a	A1	2
TM-32	A1	2
TM-21	A2	2
TM-26	A2	2
TM-34	A2	2
TM-20-5	B1	2
TM-10-1	B1i	3
TM-14-1	B1i	3
TM-18-16	B1i	3
TM-20-7	B1ii	3
TM-28	B1ii	3
TM-33-1a	B1ii	3
TM-33-2b	B1ii	3
TM-35a	B1ii	3
TM-4	B2ii	3
TM-6a	B2ii	3
TM-6b	B2ii	3
TM-12	B2iii	3
TM-13	B2iii	3
TM-16b	B2iii	3
TM-17a	B3ii	3
TM-17b	B3ii	3
TM-17bc	B3ii	3
TM-17-1a	B1i	4
TM-17-1b	B1i	4
TM-17-1c	B1i	4
TM-18-14	B1i	4
TM-18-2	B1i	4
TM-18-5a	B1i	4
TM-18-5b	B1i	4
TM-18-5c	B1i	4
TM-18-9a	B1i	4
TM-18-9b	B1i	4
TM-18-9c	B1i	4

Layer	Subset and Cluster	Rank
TM-18-9d	B1i	4
TM-18-9e	B1i	4
TM-18-9f	B1i	4
TM-19	B1i	4
TM-20	B1i	4
TM-20-1a	B1i	4
TM-20-1b	B1i	4
TM-20-1c	B1i	4
TM-20-3	B1i	4
TM-2-1	B1i	4
TM-21-2	B1i	4
TM-21-3	B1i	4
TM-23-14	B1i	4
TM-23-16	B1i	4
TM-23-20	B1i	4
TM-23-23	B1i	4
TM-24-3	B1i	4
TM-33-1c	B1i	4
TM-33-2a	B1i	4
TM-37a	B1i	4
TM-37b	B1i	4
TM-37c	B1i	4
TM-37d	B1i	4
TM-40	B1i	4
TM-41	B1i	4
TM-5-1b	B1i	4
TM-5-1c	B1i	4
TM-5-2	B1i	4
TM-6-3a	B1i	4
TM-6-3b	B1i	4
TM-6-3c	B1i	4
TM-1	B2i	4
TM-1-1	B2i	4
TM-1-2	B2i	4
TM-16a	B2i	4
TM-2-2	B2i	4
TM-2a	B2i	4
TM-2b	B2i	4
TM-3a	B2i	4
TM-3b	B2i	4
TM-3c	B2i	4

Layer	Subset and Cluster	Rank
TM-14a	B3	5
TM-14b	B3	5
TM-17c	B3	5
TM-17d	B3	5
TM-17e	B3	5
TM-18-11	B3	5
TM-18-13	B3	5
TM-18-7	B3	5
TM-30-1a	B3	5
TM-30-1b	B3	5
TM-30-1c	B3	5
TM-30-1d	B3	5
TM-30-1e	B3	5
TM-30-1f	B3	5
TM-30-2b	B3	5
TM-30-2c	B3	5
TM-30-2d	B3	5
TM-29-1a	B3ii	5
TM-29-1b	B3ii	5
TM-29-1c	B3ii	5
TM-29-1d	B3ii	5
TM-29-1e	B3ii	5
TM-29-1f	B3ii	5
TM-29-1g	B3ii	5
TM-29-1h	B3ii	5
TM-29-1i	B3ii	5
TM-29-2a	B3ii	5
TM-29-2b	B3ii	5
TM-29-2c	B3ii	5
TM-29-2d	B3ii	5
TM-29-2e	B3ii	5
TM-29-2f	B3ii	5
TM-29-2g	B3ii	5
TM-29-2h	B3ii	5
TM-38a	B3ii	5
TM-38b-1	B3ii	5
CF layers	B3i	6

6.2 PRAD 1-2

As discussed in the previous section the PRAD 1-2 tephra layers have been queried against the LGdM data-set using DFA. The subsets and clusters that each PRAD 1-2 tephra layer has been assigned to are summarised in Table 6.3. Those layers that could be allocated to a subset or cluster ranked 1-4 were matched to an individual LGdM tephra layer first, to establish a primary tephrostratigraphy which reduces the possible correlatives for other, more equivocal, layers. The tephra layers best constrained stratigraphically by the higher ranked tephra layers could then be correlated using superposition principles. Therefore based on the ranking in Table 6.3, PRAD-2375 will be considered first, followed by the rank 3 layers considered in stratigraphic order, then the rank 4 layers also considered in stratigraphic order. PRAD-1653 is considered next, as it is the rank 6 layer most constrained stratigraphically by higher ranked layers.

Table 6.3: PRAD 1-2 tephra layers, their chemical classification (after Le Bas *et al.,* 1986) and the subset and cluster from the LGdM data-set that each tephra layer is allocated to through DFA (see section 6.1 for full information). Layers highlighted in grey are allocated to subsets and clusters ranked 1 – 4 in Table 6.2.

Layer code	Chemical Classification	Allocated Subset and Cluster	Rank
PRAD-055	P/Tr	B3i	6
PRAD-120	Tr/P	B3i	6
PRAD-205	Tr/P	B3i	6
PRAD-223	Tr/P	B3i	6
PRAD-231	Tr/P/TP	B3i	6
PRAD-267	Tr/P/TP	B3i	6
PRAD-323	Tr/P/TP	B3i	6
PRAD-329	Tr/P/TP	B3i	6
PRAD-404	Tr/P/TP	B3i	6
PRAD-480	P/Tr	B3i	6
PRAD 784	P/Tr	B2iii	3
PRAD 845	P/Tr	B2?	4
PRAD 873	Tr	B2iii	3
PRAD 1104	Tr	B1i	4
PRAD 1130	Tr/P	B3i	6
PRAD 1332	Tr	B3i	6
PRAD 1474	Tr/P	B3i	6
PRAD 1494	Tr/P	B2iii	3
PRAD 1653	P/Tr	B3i	6
PRAD 1752	Tr	B3i	6
PRAD 1870	Tr	B1i	4
PRAD 2040	P/Tr	B1ii	3
PRAD 2375	Unknown	A*	1
PRAD 2525	P/Tr	B3i	6
PRAD 2605	P	B3i	6
PRAD 2812	P/Tr	B1ii	3
PRAD 3225	P	B3ii	5
PRAD 3336	P	B	6
PRAD 3383	P/Tr	B3i	6
PRAD 3472	Tr	B3i	6
PRAD 3586	P	B3	6
PRAD 3666	P	B3i	6
*Mixed geochemical signal but major population allocated to Subset A			

Biplots for each PRAD 1-2 layer and its allocated subset or cluster are also consulted to provide a test for the DFA methodology. The PRAD 1-2 WDS-EPMA analytical results and standard measurements are provided in Appendices B and C respectively.

6.2.1 PRAD-2375

The geochemical data for this layer are widely scattered, suggesting possible shard alteration. The data group in a number of volcanic zones (Figure 5.3c) and, due to this, it was not refined to 1 cm resolution (Section 5.1.1). However, when queried against the LGdM data-set using DFA, the majority of data points plot in subset A (Figure 6.7A) although the spread in the data is still observed. Within subset A these data points are grouped with unique layer A3, which is correlated to TM-22, the only layer from Pantelleria in the LGdM data-set, an observation also supported by biplots (Figure 6.8). TM-22 has been correlated to the Ignimbrite Z unit of Pantelleria which erupted at 79.3 ± 4.2 ka (Wulf *et al.,* 2004). Despite the mixed geochemical signal, this layer can be used to constrain correlations of other layers using its supposition because the majority of the chemical data points are distinctive. This layer was one identified as useful for correlation in Figure 2.10.

6.2.2 PRAD-784

This layer is grouped in minor cluster B2iii, which contains 3 layers: TM-12, TM-13 and TM-16b (Figure 6.7B). As there are 3 PRAD layers assigned to this minor cluster (Table 6.3), it would indicate a correlation to TM-12, the first layer stratigraphically in the cluster from LGdM. This is supported by biplots of the major element data (Figure 6.9) which show the layer has closest similarities to the data for TM-12. TM-12 has been correlated with the Greenish/Verdoline eruption of Vesuvius and radiocarbon dated at a terrestrial site to 16,130 ± 110 ^{14}C yr BP (19,480 - 19,050 cal yr BP; Andronico *et al.,* 1995). This tephra layer has also been recognised in other Adriatic sites, including MD90-917 (Siani *et al.,* 2004).

6.2.3 PRAD-873

PRAD-873 is also grouped in minor cluster B2iii and must be older than TM-12, based on its position with respect to PRAD-784 (Figure 6.7C). As discussed in section 5.1.1, there is a mixed geochemical signal found in this layer at 1 cm resolution, with a second

population plotted in the Ischia field in Figure 5.3a. Biplots of the data show the larger geochemical population has close affinity to TM-13, the Pomici di Base, which supports the DFA results (Figure 6.10). TM-13 has been correlated to the caldera-forming Pomici di Base eruption (18,300 ± 180 ^{14}C yr BP) (22,240 - 21,150 cal yr BP; Andronico *et al.,* 1995) (Wulf *et al.,* 2004). This correlation represents the second finding of the Pomici di Base in the Adriatic Sea, the first being in MD90-917 (Siani *et al.,* 2004). The Ischia population is thought to result from reworking from an older Ischian layer within the PRAD 1-2 sequence.

6.2.4 PRAD-1494

This layer is grouped in minor cluster B2ii by DFA (Table 6.3). There are only 3 LGdM layers in this cluster and only one is older than TM-13 which has been correlated to PRAD-873. Therefore, this would indicate that TM-16b is the likely correlative for PRAD-1494, which is supported when plotting the data with minor cluster B2iii (Figure 6.7d) and by biplot distributions (Figure 6.11). Wulf *et al.* (2004) correlated TM-16b with the base of the Plinian Codola eruption, considered to have originated from Vesuvius and dated by the LGdM varve chronology to 31,160 cal yr BP (Brauer *et al.,* 2007). This does not, however, agree with the radiocarbon age estimate of 25,100 ± 400 ^{14}C yr BP for this horizon (Alessio *et al.,* 1974; Santacroce, 1987). Giaccio *et al.* (2008) suggest that the marine equivalent of this layer is the C-10, a widespread layer in the Tyrrhenian and Adriatic seas previously attributed to the Campanian Ignimbrite (Paterne *et al.,* 1988). They also suggest that the age of 25,100 ± 400 ^{14}C yr BP (Alessio *et al.,* 1974) is unreliable due to the significant inconsistencies with the tephro- and climatostratigraphic position of the Codola tephra layer. They propose an age of about 33 cal ka BP based on its stratigraphic position in the LGdM pollen record and assumed relationship with Greenland Interstadial 5. Therefore, care needs to be taken when using the age of this layer to construct age models for the sequence (see Chapter 8). This tephra layer has also been recognised in Lake Ohrid (Vogel *et al.,* 2010a), and was identified as useful for correlation in Figure 2.10.

6.2.5 PRAD-2040

PRAD-2040 is grouped by DFA to minor cluster Bii (Table 6.3). This layer is younger than PRAD-2375 (Section 6.2.1) and therefore the LGdM layer should also be younger

than TM-22. The only LGdM layer in the cluster that fits the criteria is TM-20-7 (Figure 6.3a). This correlation is supported by biplots and DFA of the minor cluster itself (Figure 6.12 and 6.13a). The LGdM data-set suggests that TM-20-7 correlates with the Pignatiello Formation of Ischia, dated at 79,120 – 71,580 cal yr BP in the LGdM sequence. Brown *et al.* (2008) equated this formation with the upper part of the pre-Monte Epomeo Green Tuff stratigraphy of southern Ischia, which comprises a succession of bedded phonolite-trachyte pumice fall deposits dated to between 74 and 55 ka (De Astis *et al.*, 2004). Excluding the LGdM sequence, this layer has not been observed in any other marine or terrestrial sequences, therefore its occurrence in PRAD 1-2 has widen the distribution of the layer to the east.

6.2.6 PRAD-2812

PRAD-2812 is grouped by DFA to minor cluster B1ii and due to superposition is likely to be older than PRAD-2040 which is also grouped in this cluster. This layer shows closest similarities to TM-27 based on DFA of the constrained minor cluster B1ii and biplots of major elements (Figure 6.13b and 6.14). TM-27 has been correlated to the X-6 eruption of generic Campanian origin (Wulf *et al.*, 2007). The X-6 is also recognised in cores from the Ionian and Tyrrhenian Seas (Keller *et al.*, 1978; Paterne *et al.*, 2008), in the San Gregorio Magno basin (Munno and Petrosino, 2007) and in Lake Ohrid on the Albania/Macedonia border (Vogel *et al.*, 2010a). It has been dated in Mediterranean marine sequences using $^{40}Ar/^{39}Ar$ dating to 107 ± 2 ka (Kraml, 1997; Brauer *et al.*, 2007), which is in agreement with the age of 108,430 years obtained from the LGdM varve supported chronology (Brauer *et al.*, 2007).

6.2.7 PRAD- 839

This layer is grouped in minor cluster B2iii by DFA (Figure 6.13c). However, there are only 3 layers in this cluster and they have all been correlated to other PRAD 1-2 layers. As this layer is comprised of a multi-modal peak in glass with relatively few glass shards, it is considered to consist of reworked glass shards from PRAD-873, which was correlated to TM-13, the Pomici di Base eruption of Vesuvius (Wulf *et al.*, 2004).

6.2.8 PRAD-1104

DFA assigns this layer to minor cluster B1ii and within that cluster it is assigned to group 9, layer TM-14-1 (Figure 6.13d) and biplots of major elements support this correlation (Figure 6.15). TM-14-1 is dated to between 22,420 and 20,280 cal yr BP by the Monticchio varve and sedimentation rate chronology (Wulf *et al.*, 2004). TM-14-1 in turn can be correlated with the Faro di Punta Imperatore eruptives from Ischia at around 20 ka BP (Guest *et al.*, 2003). This tephra layer has not been recognised in other Mediterranean sites.

6.2.9 PRAD-1870

DFA groups this layer in minor cluster B1i (Table 6.3) which contains 45 tephra layers (Figure 6.3). However, the number of potential correlatives is constrained by stratigraphic superposition as PRAD-1870 sits between PRAD-1494 and PRAD-2040, suggesting a correlative between TM-16b and TM-20-7. When DFA analysis is repeated with this constraint, the data aligns with TM-19, TM-20 and TM-21a,b,c, all of which are geochemically very similar (Figure 6.16a). Biplots show PRAD-1870 to match with either TM-19 or TM-20 in the training set (Figure 6.17). The biplots reveal that the general spread and trends exhibited by the PRAD-1870 data have stronger similarities to TM-19 and TM-20. Wulf *et al.* (2004) correlate TM-19 with the Monte Epomeo Green Tuff (MEGT) *s.s.f* eruption of Ischia. This layer has been directly dated in the LGdM sequence by $^{40}Ar/^{39}Ar$ dating to 55 ± 2 ka (Watts *et al.*, 1996). TM-20 has been correlated with the marine 'Y-7' tephra, dated by laser $^{40}Ar/^{39}Ar$ measurement on sanidine to 56 ± 4 ka (Kraml, 1997; Allen *et al.*, 1999). Its terrestrial counterpart is still under discussion, though Wulf *et al.* (2004) suggested that it correlates with the Unita di Monte San Angelo (UMSA) tephra of Ischia, erupted during an initial phase of the Monte Epomeo Green Tuff eruption. The LGdM data-set indicates that TM-20-1 may also correlate with the marine Y-7 tephra layer, which is widespread over the Ionian and Tyrrhenian Seas (Keller *et al.*, 1978). The fact that the PRAD-1870 chemical signature resembles TM-19, TM-20 and TM-20-1 strongly suggests that it represents an eruptive from a phase of the MEGT eruption and thus may correlate with the Y-7 tephra found in other marine sequences. However, as TM-19 is the thickest layer of these three (332mm, Wulf *et al.*, 2004), it is assumed to be a larger eruption and hence to have delivered farther travelled tephra. On this assumption, PRAD-1870 is considered to

correlate with TM-19 which represents an eruptive from a phase of the MEGT eruption, dated to 55 ± 2 ka BP.

6.2.10 PRAD-1653

This is grouped in minor cluster B3i, although within this cluster it sits with the Campi Flegrei layers comprising the CI to the X5 (Figure 6.4a). The potential correlatives for this layer are constrained to between TM-16b and TM-19 based on the correlations of PRAD-1494 and PRAD-1870 respectively. When DFA is rerun with only the Campi Flegrei layers for this time period included, PRAD-1653 is grouped with TM-18 but does not clearly overlap with it (Figure 6.16b), though it is more clearly matched with TM-18 by biplot distributions (Figure 6.18). TM-18 has been correlated with the Campanian Ignimbrite (CI), an eruptive from the Campi Flegrei dated by $^{40}Ar/^{39}Ar$ dating to 39.28 ± 0.11 ka (De Vivo *et al.*, 2001). The CI was one of the largest volume eruptions of the Late Quaternary in the Mediterranean region (Pyle *et al.*, 2006) and the attribution of PRAD-1653 to the CI is supported by the high concentration of glass shards found in this layer (greater than 10,000, see Table 5.1). To test this correlation, the geochemical data for PRAD-1653 were compared with those of the glass fraction of the Breccia Museo, assigned to the Campanian Ignimbrite eruption by Fedele *et al.* (2008) (Figure 6.19). This supports the attribution of PRAD-1653 to TM-18 and therefore to the Campanian Ignimbrite.

6.2.11 PRAD-1752

This layer, grouped in minor cluster B3i is stratigraphically constrained between TM-18 and TM-19 based on the correlations on PRAD-1653 and PRAD-1870. The layer is correlated on the basis of biplot distributions with TM-18-1 (Figure 6.20), which in turn has been equated with the SMP1-a eruption. TM-18-1, dated by the LGdM varve and sedimentation chronology to 38,680 – 35,000 cal yr BP, directly underlies the CI layer in the LGdM sequence. Di Vito *et al.* (2008) report that this layer has a trachytic composition and alkali ratio of around 1, consistent with an origin in Ischia Island. However, Wulf *et al.* (unpublished) assign this layer to an eruption of the Campi Flegrei, therefore it was grouped in minor cluster B3i. This correlation did not seem incorrect, though this discordance in attribution highlights that the volcanic source of this eruption is ambiguous. Di Vito *et al.* (2008) comment that little is known about this

eruption due to the paucity of available data from proximal deposits and it has also not been recognised in any Mediterranean sites. The identification of this layer in PRAD 1-2 is the first time this layer has been recorded outside of the LGdM sequence.

6.2.12 PRAD-2525

This layer is grouped in minor cluster B3i and is stratigraphically constrained by TM-22 and TM-27 based on the correlations of PRAD-2375 and PRAD-2812. It has been assigned using both biplots (Figure 6.16c) and DFA distributions (Figure 6.21) to TM-24a and TM-24b, both of which were correlated with eruptives of the X5 eruption of the Campi Flegrei by Wulf *et al.* (2004). An $^{40}Ar/^{39}Ar$ date of 105 ± 2 ka has been obtained for the X5 tephra (Kraml, 1997; Allen *et al.*, 1999). This correlation is supported by Figure 5.4 which indicates the PRAD-2525 data to plot within the average composition of the tephra layer X5 field. The X-5 tephra layer is also recognised in cores from the Ionian and Tyrrhenian Seas (Keller *et al.*, 1978; Paterne *et al.*, 2008), Lake Ohrid, Albania (Vogel *et al.*, 2010a) and the San Gregorio Magno Basin (Munno and Petrosino, 2007).

6.2.13 PRAD-2605

DFA results group this layer in minor cluster B3i and it is stratigraphically constrained by TM-24a/TM-24b and TM-27 based on the correlations of PRAD-2525 and PRAD 2812 respectively. Yet when DFA is re-run using these constraints, PRAD-2605 does not match with any LGdM layer (Figure 6.16d). While biplots clearly show this layer is similar to others in the LGdM sequence (Figure 6.22), there is no match with any specific LGdM layer which also suggests that PRAD-2605 has no correlative within the LGdM sequence.

6.2.14 PRAD-1130

PRAD-1130 is grouped in minor cluster B3i and is therefore a rank 6 layer. However, it is stratigraphically constrained by the correlations of PRAD-1104 to TM-14-1 above it and PRAD-1494 to TM-16b below it. This means the DFA for minor cluster B3i can be rerun with these stratigraphic controls placed upon it. However, it is clear from Figures

6.23a and 6.24 that both DFA and biplots show no correlative for this layer in the LGdM sequence.

6.2.15 PRAD-1332

Like PRAD-1130, this layer is grouped in minor cluster B3i and is stratigraphically constrained by the correlations of PRAD-1104 to TM-14-1 above it and PRAD-1494 to TM-16b below it, as PRAD-1130 could not be correlated to a LGdM layer. DFA and biplots suggest PRAD-1332 corresponds to the TM-15 tephra layer in the LGdM sequence (Figures 6.23b and 6.25), which in turn has been correlated with the Y-3 eruption of Keller *et al.* (1978), of Campi Flegrei origin. The SMPe-1 eruption of the Campi Flegrei is currently considered to be the best terrestrial candidate for the marine Y-3 tephra layer (Zanchetta *et al.*, 2008). The Y-3 has a wide distribution over the central Mediterranean (Keller *et al.*, 1978, Paterne *et al.*, 1988, Munno and Petrosino, 2004, Vogel *et al.*, 2010a). Radiocarbon dates on foraminifera from below the tephra layer suggest a maximum age for the layer of 30,690 – 30,370 cal yr BP (Munno and Petrosino, 2004). This corresponds to an $^{40}Ar/^{39}Ar$ age from the VRa deposit, which is correlated to the SMP1-e layer, dated to 30,500 – 30,100 yr BP (Di Vito *et al.*, 2008). This layer was one identified as useful for correlation in Figure 2.10.

6.2.16 PRAD-1474

This layer is also grouped in minor cluster B3i but because the layers above and beneath it have been correlated to TM-15 and TM-16b respectively, there are no additional layers within minor cluster B3i that provide an obvious correlative for PRAD-1474. It is also clear from DFA and biplots of layers in the correct stratigraphic position (but in the wrong cluster) that there is no other clear correlative for PRAD-1474 in the LGdM sequence (Figure 6.23c and 6.26) and that this layer may represent an unknown eruption from the Campi Flegrei.

6.2.17 PRAD-055

This is the youngest tephra layer in the PRAD 1-2 sequence and therefore can only be constrained by the correlation of PRAD-783 to TM-12 (Section 6.2.2). PRAD-055 has been grouped in minor cluster B3i and when DFA on this cluster is run using data only from layers younger than TM-12, it aligns with the TM-5 group in the training set

(Figure 6.23d), a match also supported by biplots of major elements (Figure 6.27). TM-5 comprises of five separate eruption phases (TM-5a, b, c, cd and d) but it is not possible to assign PRAD-055 to a particular TM-5 phase using the chemical data alone. Wulf *et al.* (2008) equate TM-5a and TM-5b with the Astroni, TM-5c with the Agnano Monte Spina (AMS) and TM-5d and TM-5cd with the Averno 1 eruptions, respectively. It is clear from Figure 6.28 that the PRAD-055 data match closely with those of the published field for the AMS eruption of the Campi Flegrei, which has been dated to 4,130 ± 50 ^{14}C yr BP by de Vita *et al.* (1999), calibrated by Bayesian modelling to 4,690 – 4,300 cal yr BP by Blockley *et al.* (2008a). This layer is fairly widespread over the Adriatic Sea being found in both central and southern Adriatic sites (Calanchi *et al.*, 1998; Siani *et al.*, 2004; Lowe *et al.*, 2007b).

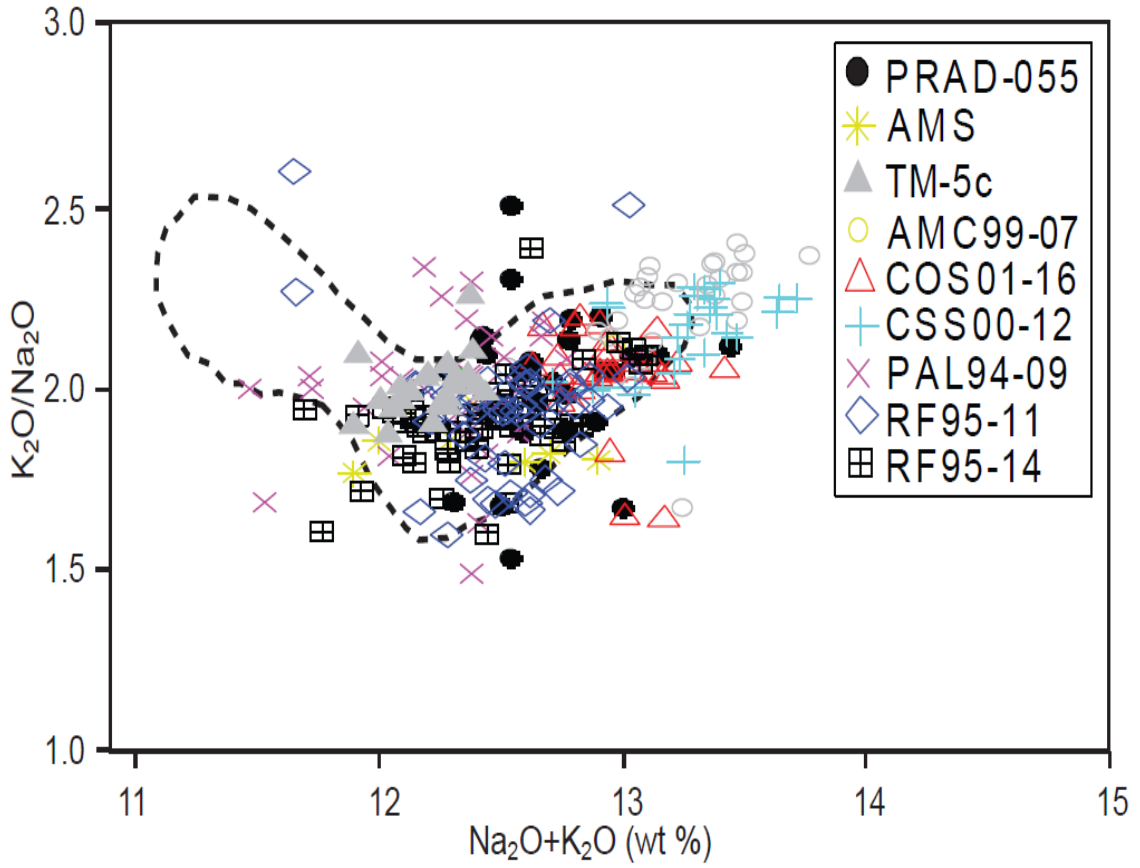

Figure 6.28: Na_2O+K_2O (wt %) vs. K_2O/Na_2O biplots showing comparison of PRAD-055 data with available data for the Agnano Monte Spina volcanic eruption. The field (dashed line area) shows AMS data for near-vent and distal tephra equivalents as follows: EMP data of Calanchi *et al.* (1998); XRF data of de Vita *et al.* (1999); EMP data of near-vent deposits of Wulf *et al.* (2004). Plotted on the diagram are individual WDS analyses obtained from glass shards in tephra layers correlated to the AMS eruption. (TM-5c in the LGdM sequence Wulf *et al.* (2004, 2008); proximal AMS deposits, Turney *et al.* (2008); and Adriatic Sea cores, AMC99-07, COS01-16, CSS00-12, PAL94-09, RF95-11and RF95-14, Lowe *et al.* (2007b)).

6.2.18 PRAD-120

This layer is grouped in minor cluster B3i, although potential correlations are constrained by the correlation of PRAD-055 to TM-5 and by PRAD-783 to TM-12. However, both biplots and DFA fail to assign PRAD-120 to an LGdM layer in this time period (Figures 6.23e and Figure 6.29), suggesting that this layer represents a volcanic eruption from the Campi Flegrei that is not preserved in the LGdM sequence.

6.2.19 PRAD-205, PRAD-223, PRAD-231, PRAD-267, PRAD-323 and PRAD-329

As discussed in section 5.1.1, these tephra layers all have indistinguishable major element geochemistry, despite being refined to 1 cm resolution (Figure 5.5). All the layers are grouped in minor cluster B3i, suggesting they are of Campi Flegrei origin, as was suggested by Figure 5.7. They are constrained by the correlation of PRAD-055 to TM-5 and by the correlation of PRAD-784 to TM-12. There are many Campi Flegrei eruptions during this time period (Di Vito *et al.,* 1999) but the DFA of minor cluster B3i with layers between TM-5 and TM-12 group all 6 PRAD layers with either TM-8 or the 4 layers that comprise the TM-10 group (Figure 6.23f). However, biplots suggest the data equate closest with the TM-8 layer in the TM data-set and that allocation to the TM-10 group is based upon only one cluster within the full geochemical range exhibited by these layers (Figure 6.30).

TM-8 has been correlated to the Neapolitan Yellow Tuff (NYT) eruption of the Campi Flegrei. It is crucial to resolve which eruptions these layers correlate with because the NYT is such a critical marker for the onset of the Lateglacial Interstadial in this region (Lowe, 2001; Turney *et al.,* 2008). It is dated by $^{40}Ar/^{39}Ar$ to 14,900 ± 400 yr BP (Deino *et al.,* 2004) and by radiocarbon to 12,300 ± 300 ^{14}C yr BP (15,326 – 13,842 cal yr BP), the latter recently revised by Blockley *et al.* (2008a) to 14,320 – 13,900 cal yr BP. Biostratigraphic records (Piva *et al.,* 2008a) suggest that the Lateglacial Interstadial (Greenland Interstadial One: GI-1) is represented in the PRAD 1-2 sequence between 1.60 m and 2.30 m depth which encompasses the PRAD-205 and PRAD-223 tephra layers.

The PRAD data has been compared with other distal tephra layers correlated to the NYT (Figure 6.31). This shows the strong chemical similarity between the PRAD layers and also with other distal tephra layers correlated to the NYT eruption (TM-8 and

Prato Spilla). The observed chemical trends (Figure 6.31a) evident in the PRAD 1-2 layers are seen only in the data from the other layers that have been correlated with the NYT and not in the records of other broadly contemporaneous Campi Flegrei tephra layers, such as TM-9 (Tufi Biancastri) or TM-10a,b,c,d (Lagno Amendolare). Hence, Figure 6.30 supports the view that all six layers match closest with the major element chemical spectra of tephra layers assigned to the NYT eruption.

As a suite of stratigraphically discrete tephra layers with identical major element geochemistry has not been previously observed in the distal record, trace-element analysis (see section 4.5.2) was undertaken on these layers in an attempt to discriminate between them. Figure 6.32a shows a spider diagram of the trace element profiles which shows that there are no discernable differences between the trace elements of these layers, an observation also supported by biplots of the trace element data in Figure 6.32 b and c. Figure 6.32 also compares the PRAD 1-2 trace element data to trace element data from TM-8 and the layer correlated to the NYT in Adriatic core SA03-11 (Lane 2009). This supports the theory that these are 6 separate tephra layers with indistinguishable major and trace element compositions which correlate best to the distal equivalents of the NYT at a number of sites.

The proximal NYT stratigraphy can be subdivided into a lower and upper member. The lower member eruptive phase was characterised by alternating phreatoplinian and magmatic explosions and the upper by a random series of phreatomagmatic and magmatic explosions (Orsi *et al.,* 1992). Furthermore, recent investigations also suggest that the TM-8 layer in the LGdM sequence may comprise three sub-layers (Wulf *et al.,* 2008). Hence, the NYT stratigraphy appears to be complex and this complexity may be reflected in the PRAD 1-2 sequence, although some could reflect deposition of ash layers derived from other Campi Flegrei eruptions that are not recorded in the LGdM sequence but which are strikingly similar in major element chemistry to layers that have previously been assigned to the NYT. The possibility of shard reworking has been considered but is thought unlikely given the discrete nature of the PRAD 1-2 tephra layers (Figure 5.5) and the fact that biological proxies, such as foraminifera assemblages, do not show evidence of reworking throughout this core section (A. Piva, 2009 *pers comm.*). It is not possible to resolve this matter on the basis of current evidence but as PRAD-223 sits in the correct stratigraphic position for the

NYT eruption and also comprises the greatest number of tephra shards (Table 5.1), it is assigned to that event dated to 14,320 – 13,900 cal yr BP. PRAD-205, PRAD-231, PRAD-267, PRAD-323 and PRAD 329 are classified as representative of un-named eruptions of the Campi Flegrei, with major element chemical compositions closely similar to those of the NYT, as reflected in the LGdM record.

6.2.20 PRAD-404

DFA groups this layer in minor cluster B3i and potential correlatives are constrained by the correlation of PRAD-223 to TM-8 and by the correlation of PRAD-784 to TM-12. However, DFA of the constrained minor cluster B3i and biplots show that there is no correlative for PRAD-404 in the LGdM sequence (Figure 6.33a and 6.34). Therefore this is considered to represent another unknown eruption of the Campi Flegrei.

6.2.21 PRAD-480

This layer is grouped in minor cluster B3i and potential correlatives are constrained to those layers between TM-8 and TM-12. This layer could not be assigned to any layer in the TM data-set using biplots, though DFA suggested an affinity with TM-9 and TM-10c. PRAD-480 is a chemically ambiguous layer and biplots do not support the DFA correlation (Figure 6.33b and 6.35), suggesting that this layer also is not represented in the LGdM sequence.

6.2.22 PRAD-3225

This layer is stratigraphically below PRAD-2812, therefore any correlatives for this layer must be older than TM-27. DFA group the layer in minor cluster B3ii but when DFA is run with the stratigraphical constraints, PRAD-3225 groups with TM-38a and TM-38b1 (Figure 6.33c), both of which are correlated to the Ignimbrite D eruption of Vico, an attribution also supported by major element biplots of the data (Figure 6.36). The Ignimbrite D eruption of Mt Vico has been dated using $^{40}Ar/^{39}Ar$ dating to 120 ± 6 ka BP (Turbeville, 1992) and has not been distally described before.

6.2.23 PRAD-3336

This layer is initially grouped in Subset B, though it does not group in any of the major clusters (Figure 6.33d). As PRAD-3225 is correlated to TM-38a, then PRAD-3225 can only correlate to a Monticchio layer older than TM-38a. Biplots of PRAD-3336 and all layers older than TM-38a support the DFA and show that this layer does not correlate to any layer within the LGdM sequence (Figure 6.37). However, the fact that this layer does not group in any of the major clusters indicates that this is an eruption from a volcanic system that has not delivered tephra layers to LGdM.

6.2.24 PRAD-3383

DFA groups this layer in minor cluster B3i and, due to the correlation of PRAD-3225 to TM-38a, there is only one layer that PRAD-3336 could correlate to, namely TM-39 (Figure 6.38a). Biplots support this correlation (Figure 6.37) and also show that the remaining layers in the PRAD 1-2 sequence do not correlate to any other layers in LGdM. TM-39 is a layer of Campanian origin but S. Wulf (*pers. comm.*, 2009) does not correlate it to a specific eruption. It is dated to 130,627 Monticchio varve years by the LGdM sediment chronology and has not been distally described before.

6.2.25 PRAD-3472

DFA groups this layer in minor cluster B3i (Figure 6.38b) but since PRAD-3383 has been correlated to TM-39, there are no more layers in this cluster that could correlate to PRAD-3472. This is supported by Figure 6.37 which shows that PRAD-3472 does not match to any layer in the LGdM sequence. However, the fact it groups in minor cluster B3i suggests that this layer represents an eruption from the Campi Flegrei, Sabatini or Procida.

6.2.26 PRAD-3586

This layer groups in major cluster B3 but cannot be resolved to a minor cluster (Figure 6.38c). Biplots show that this layer is too old to be represented in the LGdM sequence (Figure 6.37). As the layer groups in major cluster B3, this suggests it could be a product of one of the volcanic systems that comprise this major cluster.

6.2.27 PRAD-3666

DFA groups this layer in minor cluster B3i (Figure 6.38d), however based on the correlation of PRAD-3383 to TM-39, it is also too old to be correlated to an LGdM layer (Figure 6.37). However the fact it groups in minor cluster B3i suggests that this layer represents an eruption from the Campi Flegrei, Sabatini or Procida.

6.2.28 Summary of PRAD 1-2 tephrochronology

Of the 32 PRAD 1-2 tephra layers that geochemical analyses were obtained from, 30 have been matched to an Italian volcanic source. Of these, 16 have been correlated to eruptions preserved in LGdM. The correlations made are summarised in Table 6.4 and all the information about the PRAD 1-2 sequence is synthesised in Figure 6.39. The remaining layers are either older than the LGdM sequence or represent tephra layers that are not identified within LGdM. Three of the layers identified (the Y-3 (PRAD-1332, Codola (PRAD-1494) and the Ante Green Tuff (PRAD-2375) were those marked as useful for correlation in Figure 2.10. However, the other layers useful for correlation have not been identified.

6.3 SA03-03

The SA03-03 tephra layers have been queried against the LGdM data-set using DFA. The subsets and clusters each SA03-03 tephra layer is assigned to are summarised in Table 6.5. Those layers that allocate to a subset or cluster ranked 1-4 will be matched to an individual LGdM tephra layer first to enable stratigraphic superposition to constrain the possible correlatives for the other layers. The layers best constrained by the more chemically distinctive layers will then be correlated. Therefore based on the ranking in Table 6.5, SA03-03-25 will be considered first, followed by the other rank 3 layers considered in stratigraphic order and then the rank 4 layers. SA03-03-413 is considered next, as it is the rank 6 layer most constrained stratigraphically by higher ranked layers. The SA03-03 WDS-EPMA analytical results and standard measurements are provided in appendices B and C respectively.

Table 6.5: SA03-03 tephra layers, their chemical classification (after Le Bas *et al.,* 1986) and the subset and cluster from the LGdM data-set that each tephra layer is allocated to through DFA (see section 6.1 for full information). Layers highlighted in grey are allocated to subsets and clusters ranked 1 – 4 in Table 6.2.

Layer code	Chemical Classification	Allocated Subset and Cluster	Rank
SA03-03-25	P	B2iii	3
SA03-03-85	Tr	B2iii	3
SA03-03-383	Tr/P	B2iii	3
SA03-03-413	Tr/P	B3i	6
SA03-03-427	Tr/P	B3i	6
SA03-03-645	Tr	B1i	4
SA03-03-685	Tr	B1i	4
SA03-03-925	P/Tr	B3i	6
SA03-03-995	Tr	B3i	6

6.3.1 SA03-03-25

DFA groups this layer in minor cluster B2iii, along with 2 other SA03-03 layers (Table 6.5). There are only 3 layers in this cluster which suggests SA03-03-25 should correlate with the youngest of these. This assumption is supported by the DFA of minor cluster B2iii as well as biplots of major elements (Figures 6.40a and Figure 6.41). Therefore, this layer can be confidently correlated to the data for TM-12, which in turn has been correlated with the Greenish/Verdoline eruption of Vesuvius and radiocarbon dated at a terrestrial site to 16,130 ± 110 ^{14}C yr BP (19,480 - 19,050 cal yr BP; Andronico *et al.*, 1995). This layer was also found in PRAD 1-2 as well as other Adriatic sequences (Siani *et al.,* 2004).

6.3.2 SA03-03-85

This layer is also grouped in minor cluster B2iii of the LGdM data-set (Table 6.5). Both the biplots and DFA show closest affinity between this layer and the data for TM-13 (Figure 6.40b and 6.42). Wulf *et al.* (2004) correlated TM-13 with eruptives from the caldera-forming Pomici di Base eruption (18,300 ± 180 ^{14}C yr BP) (22,240 - 21,150 cal yr BP; Andronico *et al.,* 1995). This is the third reported discovery of the Pomici di Base in the Adriatic Sea, after PRAD 1-2 (Bourne *et al.,* 2010) and MD90-917 (Siani *et al.,* 2004).

6.3.3 SA03-03-383

This is the third SA03-03 layer to be grouped in minor cluster B2iii and, as the first two have been correlated to TM-12 and TM-13, it suggests a correlation to the final layer in this cluster TM-16b. This is supported by biplot distributions and DFA when only compared with minor cluster B2iii, results suggesting a correlation with TM-16b (Figure 6.43 and 6.40c). This is dated by the LGdM varve chronology to 31 160 cal. yr BP (Brauer *et al.,* 2007), which does not accord with a radiocarbon date of 25,100 ± 400 ^{14}C yr BP from the same horizon (Alessio *et al.,* 1974; Santacroce, 1987). TM-16b has been correlated with the base of the Plinian Codola eruption, considered to have originated from Vesuvius with the marine equivalent of this layer being the C-10, a widespread layer in the Tyrrhenian and Adriatic seas (Wulf *et al.,* 2004; Paterne *et al.,* 1988). This layer was also found in PRAD 1-2, suggesting a distribution in both the central and southern Adriatic Sea.

6.3.4 SA03-03-685

DFA groups this layer in minor cluster B1i (Table 6.3) which contains 45 tephra layers (Figure 6.3). The numbers of potential correlatives are only constrained by the correlation of SA03-03-383 to TM-16b, meaning this layer has to be older than TM-16b. Biplots show SA03-03-685 to correlate with TM-19 in the training set (Figure 6.44). Wulf *et al.* (2004) correlate TM-19 with the Monte Epomeo Green Tuff (MEGT) *s.s.f* eruption of Ischia. This layer has been directly dated in the LGdM sequence by ^{40}Ar/^{39}Ar to 55 ± 2 ka (Watts *et al.,* 1996). DFA on the constrained minor cluster B1i shows this layer to group with TM-19, TM-20 and TM-20-1 (Figure 6.40d). However as TM-19 is the thickest layer of these three (332mm, Wulf *et al.,* 2004), it is assumed

to be a larger eruption and hence to have delivered farther travelled tephra. On this assumption SA03-03-685 is considered to correlate with TM-19 which represents an eruptive from a phase of the MEGT eruption, dated to 55 ± 2 ka. This layer was also observed in the PRAD 1-2 sequence.

6.3.5 SA03-03-645

This layer is grouped in minor cluster B1i by DFA. However, it is constrained by the fact that SA03-03-383 is correlated to TM-16b and SA03-03-685 to TM-19, which reduces the number of layers in this cluster to 16. DFA on the constrained minor cluster B1i, indicates that whilst SA03-03-645 groups with the layers in the cluster, it does not completely match any of them (Figure 6.45a). This is supported by the biplots shown in Figure 6.46. However, according to Wulf *et al.* (unpublished) all of layers represent phases of the Citara eruption of Ischia, and hence SA03-03-645 is considered to be a phase of the Citara series of eruptions from Ischia. The marine equivalent of the Citara series is the C-13 which has been found in a number of marine cores (Paterne *et al.*, 1988). Paterne *et al.* (1988) give the only approximate age estimate for this layer, as between 42 and 25 ka BP. The LGdM sediment chronology dates these units to between 50,362 years (TM-18-14c) and 38,833 years (TM-18-5a) which is in agreement with the Paterne *et al.* (1988) age range.

6.3.6 SA03-03-413

SA03-03-413 was one of six multi-modal peaks in glass resolved at 1 cm sampling interval throughout this tephra event, that were considered to represent one tephra layer due to their identical major element geochemistry (see section 5.2.2).

This layer is grouped in minor cluster B3i and is therefore a rank 6 tephra layer. However, based on the correlation of SA03-03-383 to TM-16b and that of SA03-03-685 to TM-19, the number of potential correlatives is limited. The layer is matched with TM-18 on the basis of both biplot and DFA analysis (Figures 6.45b and 6.47). TM-18 has in turn been correlated with the Campanian Ignimbrite (CI), an eruptive from the Campi Flegrei dated by $^{40}Ar/^{39}Ar$ measurement to 39.28 ± 0.11 ka (De Vivo *et al.*, 2001). The CI was one of the largest volume eruptions of the Late Quaternary in the

Mediterranean region and has been found in numerous sites across the region (Pyle *et al.,* 2006), including in the PRAD 1-2 sequence (Bourne *et al.,* 2010).

6.3.7 SA03-03-427

DFA groups this layer in minor cluster B3i. However, the potential correlatives are limited by the correlations of SA03-03-413 to TM-18 and SA03-03-645 to the Citara series of eruptions (TM-18-5, TM-18-9, TM-18-14) (Figure 6.45c). Biplots match this layer to TM-18-1d, which in turn has been correlated with the SMP1-a eruption (Figure 6.48). TM-18-1, dated by the LGdM varve and sedimentation chronology to 38,680 – 35,000 cal yr BP, directly underlies the CI layer in the LGdM sequence. Di Vito *et al.* (2008) report that this layer has a trachytic composition and alkali ratio of around 1 but little is known about this eruption because of the paucity of available data from proximal deposits (Di Vito *et al.,* 2008). This layer was also identified in the PRAD 1-2 sequence but otherwise has not been recognised in any other Mediterranean sequences.

6.3.8 SA03-03-925

This layer is grouped in minor cluster B3i by DFA. Although this is a rank 6 tephra layer, it is constrained by the correlation of SA03-03-685 to TM-19. It has been assigned using biplots to TM-24a and TM-24b (Figure 6.49), both of which were correlated with eruptives of the X5 eruption of the Campi Flegrei by Wulf *et al.* (2004). An $^{40}Ar/^{39}Ar$ date of 105 ± 2 ka has been obtained for the X5 tephra (Kraml, 1997; Allen *et al.,* 1999). This layer was also recognised in PRAD 1-2, as well as being fairly widespread in a number of Mediterranean marine and terrestrial sites (Keller *et al.,* 1978; Paterne *et al.,* 2008; Munno and Petrosino, 2007; Vogel *et al.,* 2010a).

6.3.9 SA03-03-995

This layer is grouped in minor cluster B3i but the number of potential correlatives are constrained by the fact SA03-03-925 is correlated to TM-24a and b. DFA shows this layer groups with TM-24-2 (Figure 6.45, shaded in blue) and this is supported by the biplots in Figure 6.50. TM-24-2 is an unknown eruption of the Campi Flegrei which is dated by the LGdM sediment chronology to 103,556 yrs BP (Wulf, *pers. comm.*). This is the first identification of this layer at a site other than LGdM.

6.3.10 Summary of SA03-03 tephrochronology

All nine tephra layers identified in SA03-03 have been assigned to an Italian volcanic source and then to an LGdM tephra layer. Eight of the LGdM tephra layers that match the SA03-03 layers have been correlated to a known volcanic eruption, which will allow the SA03-03 tephra layers to be used to date the sequence. The correlations are summarised in Table 6.6 and all the information about the SA03-03 sequence is synthesised in Figure 6.51. Of the layers identified in SA03-03, seven of them are also recognised in the PRAD 1-2 sequence which will allow the two records to be tied to one another in a number of locations.

Of the layers correlated to known eruptions only one of them (the Codola, SA03-03-383) was marked as useful for correlation in Figure 2.10. The other layers useful for correlation have not been identified.

6.4 RF93-77

As discussed in Section 5.1.3, this core was originally analysed for tephra layers by Calanchi *et al.* (1998), who worked solely on visible layers in the core and identified tephra layers at depths of 83 cm, 208 cm, 364 cm, 384 cm, 449 cm and 797 cm (Calanchi *et al.*, 1998). These tephra layers were all found during the sub-sampling for this project and will be correlated to tephra layers from the LGdM dataset independently of the results from Calanchi *et al.* (1998) and using the same methods for correlation employed in sections 6.2 and 6.3.

The RF93-77 tephra layers have been queried against the LGdM data-set using DFA. The subsets and clusters to which each RF93-77 tephra layer can be assigned are summarised in Table 6.7. Those layers that allocate to a subset or cluster ranked 1-4 will be correlated to an individual LGdM tephra layer first, to enable stratigraphic superposition to reduce the possible correlatives for the other layers. The layers best constrained by the more chemically distinctive layers will be correlated next. Therefore based on the ranking in Table 6.7, RF93-77-68 will be considered first, followed by RF93-77-267 and then the rank 4 layers will be considered in stratigraphic order. RF93-77-790 is considered next, as it is the rank 6 layer most constrained stratigraphically by higher ranked layers.

Table 6.7: RF93-77 tephra layers, their chemical classification (after Le Bas *et al.,* 1986) and the subset and cluster from the LGdM data-set that each tephra layer is allocated to through DFA (see section 6.1 for full information). Layers highlighted in grey are allocated to subsets and clusters ranked 1 – 4 in Table 6.2.

Layer code	Chemical Classification	Allocated Subset and Cluster	Rank
RF93-77-68	P	B2i	3
RF93-77-73	Tr/P	B3i	6
RF93-77-78	Tr/P	B3i	6
RF93-77-86	Tr/P	B3i	6
RF93-77-88	Tr/P	B3i	6
RF93-77-144	TP/TrA/Tr/P	B3i	6
RF93-77-198	Tr/P	B3i	6
RF93-77-267	Tr/P	B1i	3
RF93-77-372	Tr/P	B3i	6
RF93-77-414	Tr/P	B3i	6
RF93-77-450	Tr/P	B1i	4
RF93-77-540	Tr/P	B3i	6
RF93-77-604	Tr/P	B1i	4
RF93-77-790	P	B3i	6

The RF93-77 WDS-EPMA analytical results and standard measurements are provided in Appendices B and C respectively.

6.4.1 RF93-77-68

DFA groups this layer in minor cluster B2i (Table 6.7) which represents Vesuvius eruptions from the III cycle of activity as described by De Vivo *et al.* (2010). This layer can be correlated to TM-3b on the basis of biplots and the DFA of minor cluster B2i (Figure 6.52 and 6.53a). TM-3b has been correlated to AP3, one of the inter-Plinian Avellino-Pompeii activities of Somma-Vesuvius. The AP3 eruption has been radiocarbon dated to 2710 ± 60 ^{14}C yr BP (Andronico and Cioni, 2002). This layer has been found in other Adriatic marine cores including RF93-30 (Calanchi *et al.,* 1998, Wulf *et al.,* 2008) but was not identified in either PRAD 1-2 or SA03-03.

6.4.2 RF93-77-267

DFA assigns this layer to minor cluster B1i (Table 6.7) and, within that cluster, it matches best with group 9, layer TM-14-1 (Figure 6.53b). This match is supported by biplots of major elements (Figure 6.54). TM-14-1 is dated to between 22,420 and 20,280 cal yr BP by the Monticchio varve and sedimentation rate chronology (Wulf *et al.,* 2004). TM-14-1 in turn can be correlated with the Faro di Punta Imperatore eruptives from Ischia at around 20 ka BP (Guest *et al.,* 2003). This tephra layer has not been recognised in other Mediterranean sites, other than PRAD 1-2.

6.4.3 RF93-77-450

This layer is assigned to minor cluster B1i by DFA. It is stratigraphically constrained by the correlation of RF93-77-267 to TM-14-1. When DFA is undertaken on minor cluster B1i with this stratigraphical constraint, RF93-77-450 shows similarity to a number of layers but clusters best with TM-19, TM-20 and the TM-20-1 group, an observation supported by biplots (Figure 6.53c and 6.55). Wulf *et al.* (2004) correlate TM-19 with the Monte Epomeo Green Tuff (MEGT) *s.s.f* eruption of Ischia. This layer has been directly dated in the LGdM sequence by ^{40}Ar/^{39}Ar measurement to 55 ± 2 ka (Watts *et al.,* 1996). TM-20 has been correlated with the marine 'Y-7' tephra, dated by laser ^{40}Ar/^{39}Ar measurement on sanidine to 56 ± 4 ka (Kraml, 1997; Allen *et al.,* 1999). Its terrestrial counterpart is still under discussion, though Wulf *et al.* (2004) suggest that it correlates with the Unita di Monte San Angelo tephra of Ischia, erupted during an initial phase of the MEGT eruption. The TM data-set indicates that TM-20-1 may also correlate with the marine Y-7 tephra layer which is widespread over the Ionian and

Tyrrhenian Seas (Keller *et al.*, 1978). The fact that the RF93-77-450 chemical signature resembles TM-19, TM-20 and TM-20-1 strongly suggests that this layer represents an eruptive from a phase of the MEGT eruption and thus may correlate with the Y-7 tephra found in other marine sequences. However, as TM-19 is the thickest layer of these three (332mm, Wulf *et al.*, 2004), it is assumed to be a larger eruption and hence to have delivered farther travelled tephra. On this assumption, RF93-77-450 is considered to correlate with TM-19, which represents an eruptive from a phase of the MEGT eruption, dated to 55 ± 2 ka. This layer has been recognised in both PRAD 1-2 and SA03-03 and therefore will be a useful tie-point for comparing the three sequences.

This correlation supports that of Calanchi and Dinelli (2008) who reassigned the layer they described at 449cm in RF93-77 to TM-19 in the LGdM sequence.

6.4.4 RF93-77-604

This layer is constrained by the correlation of RF93-77-450 to a phase of MEGT eruption, meaning this layer has to be older. DFA also group this layer in minor cluster B1i, however RF93-77-604 does not seem to group with any of these layers (Figure 6.53d). This conclusion is supported by biplots (Figure 6.56) which indicate that RF93-77-604 does not group with a specific layer within the cluster. Therefore, RF93-77-604 appears to represent an eruption of Ischia that is not represented in the LGdM sequence.

6.4.5 RF93-77-790

This layer is grouped in minor cluster B3i and potential correlatives are constrained by the fact that RF93-77-450 is correlated to TM-19, so RF93-77-790 must be older. It has been assigned using both biplots and DFA distributions to TM-24 (Figure 6.57a and 6.58). TM-24 has in turn been correlated with the X-5 eruption of the Campi Flegrei by Wulf *et al.* (2004). An $^{40}Ar/^{39}Ar$ date of 105 ± 2 ka has been obtained for the X5 tephra (Kraml, 1997; Allen *et al.*, 1999). Calanchi *et al.* (1998) originally attribute the layer at 797 cm to the C20 layer dated at 67.5 ka BP, but then reattributed this layer to TM-24 from the LGdM sequence (Calanchi and Dinelli, 2008), which supports the correlation made in this study. TM-24 (X-5) has been observed in both the PRAD 1-2 and SA03-03 sequences making it a useful tie-point for further investigation and correlation of the three Adriatic records.

6.4.6 RF93-77-540

This layer is a rank 6 tephra layer, grouped by DFA in minor cluster B3i. As RF93-77-450 has been correlated to TM19/TM-20 and RF93-77-790 has been correlated to TM-24, this reduces the number of layers remaining in minor cluster B3i to 33. However, the layer still does not closely match with an LGdM layer (Figure 6.57b and 6.59). Therefore, this suggests that RF93-77-540 represents an eruption from the Campi Flegrei that is not represented in the LGdM sequence.

6.4.7 RF93-77-372

DFA group this layer in minor cluster B3i making it a rank 6 tephra layer (Table 6.2). The potential correlatives for this layer are constrained by the correlation of RF93-77-267 to TM-14-1 and the correlation of RF93-77-450 to TM-19. This layer is correlated with TM-18 on the basis of both biplot and DFA analysis (Figure 6.60 and 6.57c). TM-18 has in turn has been correlated with the Campanian Ignimbrite (CI), an eruptive from the Campi Flegrei dated by $^{40}Ar/^{39}Ar$ to 39.28 ± 0.11 ka (De Vivo *et al.,* 2001). The CI was one of the largest volume eruptions of the Late Quaternary in the Mediterranean region (Pyle *et al.,* 2006) and was also identified in the PRAD 1-2 and SA03-03 sequences. This makes it the third layer that is identified in each of the studied cores.

Calanchi *et al.* (1998) identify two tephra layers at 364 cm and 384 cm in RF93-77 which have very similar compositions and have scattered distributions. They fail to correlate these layers to a volcanic eruption and suggest they may represent reworking (Calanchi *et al.,* 1998). The C14 thought to be the Campanian Ignimbrite is correlated to the layer identified at 449 cm by Calanchi *et al.* (1998). However this has been revised by Calanchi and Dinelli (2008). The fact that the CI had already been erroneously identified in RF93-77 may explain why it was not correlated to either of the layers at 364 cm and 384 cm.

6.4.8 RF93-77-414

This layer is grouped minor cluster B3i by DFA. When DFA is rerun on a constrained number of layers in B3i (constrained by the correlations on RF93-77-372 to TM-18 and RF93-77-450 to TM-19), there are no correlatives for this layer. This is the case when RF93-77-414 is queried against other clusters (Figure 6.57d). The biplots in Figure 6.61

supports the DFA and this suggests that RF93-77-414 does not have a correlative in LGdM. The possibility that this layer could represent reworked shards from RF93-77-450, an older Ischia layer in the core has been considered but the geochemical signature of the two layers does not match. Therefore, it is unlikely that this layer have been reworked from an older layer within RF93-77.

6.4.9 RF93-77-73, RF93-77-78, RF93-77-86, RF93-77-88

These four layers form a multimodal peak in glass shards at 1 cm resolution with very similar geochemical data for all 4 layers (see Section 5.3.2). All the layers have been grouped in minor cluster B3i by DFA. The correlative for this layer must lie between TM-3b and TM-14-1 based on the correlations of other RF93-77 layers. The data matches closest, using both biplot and DFA methods, with the TM-5 group in the training set, which consists of five separate eruption phases (TM-5a, b, c, cd and d) (Figure 6.62a and 6.63).

Wulf *et al.* (2008) equate TM-5a and TM-5b with the Astroni, TM-5c with the Agnano Monte Spina (AMS) and TM-5d and TM-5cd with the Averno 1 eruptions, respectively. It is possible that each of the four eruptions in RF93-77 represent a different phase of the TM-5 eruption, although this cannot be determined with the available geochemistry alone, as the geochemistry for RF93-77-73, RF93-77-78, RF93-77-86, RF93-77-88 is indistinguishable. Therefore, this layer will be considered as one eruptive event with a peak in glass shards at 86 cm. Of the layers discussed above, the AMS eruption of the Campi Flegrei is more widespread having been found in both central and southern Adriatic sites (Calanchi *et al.*, 1998; Siani *et al.*, 2004; Lowe *et al.*, 2007b) and also found by this investigation in PRAD 1-2, therefore it is also matched to RF93-77-68. The AMS has been dated to 4130 ± 50 ^{14}C yr BP by de Vita *et al.* (1999), calibrated by Bayesian modelling to 4690 - 4300 cal yr BP by Blockley *et al.* (2008a). Calanchi *et al.* (1998) correlate the layer they identified at 83 cm to the AMS eruption, which supports the correlation made in this investigation.

6.4.10 RF93-77-144

DFA groups this layer in minor cluster B3i, making it a rank 6 tephra layer. However the number of potential correlatives for RF93-77-144 are constrained by the correlation

of RF93-77-88 to TM-5 and the correlation of RF93-77-267 to TM-14-1. DFA groups this layer with TM-6-5b and TM-6-5c (Figure 6.62b), which is supported by biplots (Figure 6.64). TM-6-5 is attributed to an eruption of the Campi Flegrei but it is not correlated to a specific eruption. It has been dated through the Monticchio varve time-scale to 12,073 yr BP (Wulf *et al.,* unpublished). This is the first identification of TM-6-5 in a sequence other than LGdM.

6.4.11 RF93-77-198

This layer is also grouped in minor cluster B3i. However, due to the correlations of RF93-77-144 and RF93-77-267 there are only 10 layers in the LGdM sequence with which this layer could correlate. When DFA is re run on the constrained minor cluster B3i, RF93-77 groups with TM-10a (Figure 6.62c) and biplots also suggest a correlation to TM-10a (Figure 6.65). TM-10 has been correlated with the Lago Amendolare eruption of the Campi Flegrei which has been dated at a terrestrial site to 13,070 ± 90 ^{14}C years (Wulf *et al.,* 2004, 2008).

However, Calanchi *et al.* (1998) correlate a visible layer at 208 cm (which overlaps the shard distribution of this layer) to the NYT. Lane (2009) also analyse a unit of RF93-77 from 199 cm – 213 cm, with a peak in glass at 209 cm – 210 cm. This layer is also correlated to TM-8, the NYT and corresponds to the vertical distribution of glass shards seen in the RF93-77-198 layer.

It is crucial to resolve this matter because the NYT is such a critical marker for the onset of the Lateglacial Interstadial (Lowe, 2001; Turney *et al.,* 2008). It is dated by ^{40}Ar/^{39}Ar measurement to 14, 900 ± 400 yr BP (Deino *et al.,* 2004) and by radiocarbon to 12,300 ± 300 ^{14}C yr BP (15,326 – 13,842 cal yr BP), the latter recently revised by Blockley *et al.* (2008a) to 14,320 – 13,900 cal yr BP. Therefore, this would be an important marker layer within RF93-77.

Figure 6.66 shows the RF93-77 data from this study, from Lane (2009) and the TM-8 and TM-10a data from Wulf *et al.* (2004) as well as additional data for TM-8 from Lane (2009). In Figure 6.66a, an inflection point related to changes in fractionating minerals can be seen for all of the Lane (2009) RF93-77 layers and for TM-8 but is not visible in the TM-10 layers. There is one point in the RF93-77-198 data from this study that

causes this inflection point. However, the shape of the data is more akin to the TM-10 layers. In Figure 6.66b, there is clear bimodal distribution in the Lane (2009) layer and TM-8 (blue shaded sections). The TM-10 data sits in between these clusters. The RF93-77-198 data groups mainly in one cluster with the same one data point in the other.

The fact that RF93-77-198 has data sitting in both the observed populations of the NYT data suggests that the correlation of Calanchi *et al.* (1998) is correct. Sampling bias is probably responsible for more data being collected from one geochemical population, maybe due to shard size or vesicularity of one population verses the other. More data from RF93-77-198 would be required to test this and be certain that this layer does represent the NYT eruption of the Campi Flegrei. This shows the importance of considering all factors, not just geochemical data when correlating tephra layers, as otherwise incorrect correlations could be made.

However, due to the similarity of the majority of the data with previous data for this level in RF93-77, this layer will be correlated to TM-8 which represents the NYT eruption of the Campi Flegrei that is dated to 14,320 – 13,900 cal yr BP (Wulf *et al.*, 2004, Blockley *et al.*, 2008a). The NYT eruption is also present in the PRAD 1-2 sequence making it another tie-point between the sequences that will be useful for further investigations in this study.

6.4.12 Summary of RF93-77 tephrochronology

All of the eleven geochemically analysed tephra layers in this sequence have been correlated to an Italian volcanic origin. However, only eight of the eleven layers have been correlated with tephra layers present in LGdM, the other three are all thought to represent eruptions of Ischia and Campi Flegrei not preserved in LGdM. Of the eight layers matched to LGdM layers seven are correlated to known dated eruptions, whilst the eighth has no known correlative and therefore only has an LGdM varve age. The correlations of each of the RF93-77 layers are summarised in Table 6.8 and all the information about the RF93-77 sequence is synthesised in Figure 6.67. Six of the layers in RF93-77 are also present in the PRAD 1-2 sequence and three of these (those correlated to TM-18, TM-19 and TM-24) are also present in the SA03-03 sequence. None of the layers identified were marked as useful for correlation in Figure 2.10.

7. Testing regional stratigraphies

As discussed in Section 1.2 and Chapter 3, marine sequences in the Adriatic Sea and Mediterranean region have often been tuned to one another using regional bio- and isotope stratigraphies. This chapter will use the tephra layers identified and correlated to LGdM layers and known eruptions in chapters 5 and 6 to test whether this tuning approach is robust or not. The chapter will focus on the application of tephra layers as time-parallel isochrons and therefore correlations between sequences will be based purely on tephrostratigraphy. The chronology of the sequences and timing of changes observed will be addressed in Chapter 8.

Initially, the three sequences studied in this research project will be examined using the presence of tephra layers to establish the robustness of correlations and tuning proposed for the Adriatic Sea. Comparisons based on the stratigraphic schemes of the cores are considered first, then comparisons using bioevents and finally correlations based on oxygen isotope stratigraphies.

The second half of the chapter will consider correlations over the wider Mediterranean region, concentrating initially on other marine records obtained from the Ionian, Tyrrhenian and Adriatic seas, which were introduced in sections 2.2.5 and 3.5.1. Finally, the Adriatic sequences investigated in this study will be compared and correlated to terrestrial environmental records that were introduced in section 2.2.6 and section 3.5.2 from Lago Grande di Monticchio, Italy and Lake Ohrid, Albania.

7.1 Adriatic stratigraphies

The positions of tephra layers common to PRAD 1-2, SA03-03 and RF93-77 will be related to the stratigraphic scheme, bioevents and oxygen isotope curve to provide an independent test of whether events across the Adriatic sea are synchronous or not.

7.1.1 Stratigraphic scheme

The tephra layers that are common to more than one of the sequences will be used to see if the stratigraphic divisions assigned to each sequence are robust. Particular attention will be paid to the position of sapropel equivalent events.

Figure 7.1 shows the positions of tephra layers found in each of the three sequences, in relation to major stratigraphic boundaries of each core. Three tephra layers are found in all three sequences (TM-18, TM-19 and TM-24) while a further seven layers are common to two of the sequences.

From the positions of these key tephra layers in relation to sapropel layers and MIS boundaries (Figure 7.2), it is clear that the tephra layers support the stratigraphic correlations of the three records. TM-19 occurs near the beginning of MIS3 and TM-24 is consistently found just below Sapropel 3 (and also MIS 5.2, where it can be identified in the core) (Figure 7.2a). Similarly, TM-14-1 lies within the lower part of MIS2, TM-8 at the end of MIS2 and TM-5 above Sapropel 1 in the PRAD 1-2 and RF93-77 records (Figure 7.2b). This suggests that the criteria used to generate the stratigraphic scheme are robust.

7.1.2 Regional bioevents

The bioevents that are common to two or three of the studied sequences are listed in Table 7.1. The tephrostratigraphy for the 3 sequences will be used to test whether these events are indeed synchronous across the Adriatic.

Table 7.1: Common bioevents found across the Adriatic Sea region, their presence/absence in each of the three sequences and if present their depth (in m) within the sequence (X = not recorded).

Regional Bioevent	PRAD 1-2	SA03-03	RF93-77
Last Occurrence (L.O.) *G. inflata*	0.60	X	0.84
Last Occurrence (L.O.) *S. sellii*	3.00	X	X
Entry *S. sellii*	12.00	1.40	X
Last Common Occurrence (L.C.O.) *H. balthica*	14.00	X	3.30
Last Common Occurrence (L.C.O.) *G. inflata* in MIS 3	16.90	5.00	4.00
Last Occurrence (L.O) *G. truncatulinoides* in MIS 5.1	22.30	7.80	6.97
Entry *G. truncatulinoides* in MIS 5.1	22.59	10.00	7.30

It is clear from Table 7.1 that not all regional bioevents are present across the 3 cores. In the case of SA03-03 this is because the sequence does not extend to the present day, therefore the youngest bioevents are not preserved within the sediments. On the other hand, the Entry and Last Occurrence of *S. sellii* is not recorded in RF93-77 as this foraminifera species is near absent throughout the sequence (Asioli, 1996).

If the bioevents are synchronous in the region then their relationship with a tephra layer should be the same in different sequences (e.g. whether the bioevent occurs before or after a tephra layer). The position of the bioevents and their relationships to the stratigraphic positions of tephra layers are presented in Figure 7.3. It is clear from Figure 7.3a that the position of the L.O of *G. inflata* is not synchronous as it occurs before the deposition of the tephra layer correlated to TM-5 in PRAD 1-2 and after the deposition of the same tephra layer in RF93-77. However, the glass shards from RF93-77-86 do extend to 84 cm, which is the same depth as the bioevent. This might indicate that deposition of the ash layer and the L.O. of *G.inflata* are synchronous but the key point is that the bioevent precedes the TM-5 ash deposition in PRAD 1-2. The position of this bioevent and its relationship to the TM-5 tephra layer will be considered further in Section 7.2.2 when the data from this study are compared with other data from the region.

The L.C.O of *G. inflata* in MIS 3 (Figure 7.3c) also does not appear to be synchronous between the three sequences. In all cases, it occurs after the tephra layer which is correlated to TM-19 and before the deposition of the tephra layer correlated to TM-18. However, in PRAD 1-2 and SA03-03 where TM-18-1 is also present the bioevent occurs before the deposition of TM-18-1 in SA03-03 but after it in PRAD 1-2. However, the SA03-03 *G. inflata* curve (Figure 7.3C) shows that the species does continue beyond the point marked as its last common occurrence and beyond the deposition of TM-18-1. Therefore, the fact that the events appear to not be synchronous is due to the definition of the Last Common Occurrence of a foram species, rather than its actual last occurrence in a sequence. A. Asioli (2011, *pers. comm.*) defined the L.C.O. of a foram species as the last time that species appears in any abundance in that core section. As this definition could be open to different interpretations, this supports the idea that the difference seen in the position of the L.C.O of *G. inflata* and the TM-18-1 tephra layer could be due to the definition of the L.C.O itself.

The entry of *G. truncatulinoides* is also not synchronous in all three sequences (Figure 7.3d). In PRAD 1-2 and RF93-77, it occurs after the deposition of TM-24 (Figure 7.3d) but the reverse is true in SA03-03. The L.O of *G. truncatulinoides* however occurs prior to TM-19 in all three cores which indicates that, based on the data available, this event seems synchronous, although in SA03-03 it is assigned to MIS 4, while in PRAD 1-2 and RF93-77 it is assigned to MIS 5.1. The difference between the Central and

Southern Adriatic basins suggests that this bioevent can only be used as a regional marker in the Central Adriatic.

The L.C.O of *H. balthica* occurs between TM-14-1 and TM-18 in both PRAD 1-2 and RF93-77 but, as there are a number of other layers that occur between TM-14-1 and TM-18, the timescale covered is too wide and there are not enough tephra layers preserved in RF93-77 to ascertain if the L.C.O of *H. balthica* occurs precisely synchronously in both cores. This is the same for the Entry of *S. sellii* in PRAD 1-2 and SA03-03, which in both cores occurs between the layers correlated to TM-13 and TM-16b. However, there are a number of other layers between these layers in PRAD 1-2 but not in SA03-03 therefore it is not possible to ascertain if the L.O. of *S. sellii* occurs precisely synchronously in both cores based on stratigraphy alone. The age of the tephra layers will be used to test the synchroneity of both these bioevents in Chapter 8.

7.1.3 Oxygen isotope records

The PRAD 1-2 planktic and benthic and SA03-03 planktic isotope analyses were undertaken at 10 cm resolution throughout the entire sequences, though SA03-03 has a far more expanded temporal resolution than PRAD 1-2. The RF93-77 benthic record has been analysed at 5 cm vertical resolution but in the case of the RF93-77 planktic record only the top 1.5 m and the lowermost 1.5 m have been analysed at 5 cm vertical resolution. The remainder of the core (an interval of c. 4.5 m) has only 4 measurements. This means it is not possible to compare the planktic records of all three cores for every time period.

Using the positions of the tephra layers with respect to the oxygen isotope curves (Figure 7.4), the curves are adjusted in Figure 7.5 to the same time and isotope scales. As RF93-77 does not have continuous isotopic measurements, the benthic record has been included to extend the length of its correlation to the other sequences. It is important to note that the cores are only tied to one another at the position of the tephra layers. In between layers, it is not possible to tell if events are truly synchronous as sedimentation rates could vary significantly in each sequence.

The broad trends in isotope values of the 3 cores delimited between TM-24 and TM-19 are generally similar. A shift to ^{18}O depleted values is observed before shifting back to more ^{18}O enriched values (number 1, Figure 7.5). This shift again changes to lighter $\delta^{18}O$ values and then there is a sustained shift to heavier $\delta^{18}O$ values towards the top of this interval (number 2, Figure 7.5). Finally, just prior to the deposition of TM-19, there is a rapid shift to more depleted $\delta^{18}O$ values (number 3, Figure 7.5), a pattern seen in all three sequences, although whilst the trends are the same, the absolute values are not. For example, in number 3 of Figure 7.5, the rapid shift of 1.5 ‰ to more depleted $\delta^{18}O$ values at 19.86 m in PRAD 1-2 is also seen in SA03-03 at 7.40 m, although the shift is only 0.5 ‰ and in RF93-77 the shift is closer to 2.0 ‰ .

Between TM-19 and TM-18-1 in PRAD 1-2, there is a shift to heavier $\delta^{18}O$ values from 2.99 ‰ at 18.60 m to 3.55 ‰ at 18.40 m and returning to 2.67 ‰ at 18.10 m (number 4, Figure 7.5). During the same time period, the SA03-03 isotope values shift to lighter $\delta^{18}O$ values from 3.34 ‰ at 6.50 m to 2.37 ‰ at 6.20 m and returning to 3.19 ‰ at 5.80 m. This is a similar magnitude change but the 2 curves appear to be in anti-phase. The benthic record of RF93-77 does not show any change of this magnitude but TM-18-1 is not present in RF93-77 therefore it is not possible to establish whereabouts this change would occur. As PRAD 1-2 is located in the Central Adriatic and SA03-03 is located in the Southern Adriatic, this could suggest that at certain times the isotopic controls on the central and southern Adriatic basins are different and the implications of this will be discussed in Chapter 8.

This general trend in the shape of the PRAD 1-2 and SA03-03 isotope curves continues. Between the deposition of TM-18 and TM-16b, the $\delta^{18}O$ values remain similar, although in PRAD 1-2 there are stronger fluctuations, that the isotope measurements in SA03-03 are not able to resolve. Similar trends also characterise the PRAD 1-2 and SA03-03 records between TM-16b and TM-13 (number 6, Figure 7.5).

It is clear, therefore, that although the tephra layers can be used to show that the general trends in the $\delta^{18}O$ curves are replicated, the SA03-03 has not been examined with sufficient resolution to determine whether the isotopic shifts are exactly synchronous between the sequences.

Fluctuations in the $\delta^{18}O$ records of both PRAD 1-2 and SA03-03 have been related to D-O events (Sections 3.21 and 3.31). Figure 7.6 shows the numbered interstadial part of the D-O cycle to which the isotope fluctuation in each sequence has been assigned. The tephra layers common to both sequences are marked on the diagram and, as these are time-parallel marker horizons, the tephra layers should bracket the same interstadials in both sequences. However, it is clear that this is not the case. All the interstadials in both PRAD 1-2 and SA03-03 occur between the deposition of TM-24 and TM-13 but the tephra layers in between do not show synchroneity between the D-O events in both sequences. TM-19 in PRAD 1-2 occurs between Interstadial 16 (I16) and Interstadial (I17), whereas in SA03-3 its deposition precedes I15 (Figure 7.6). In PRAD 1-2, interstadials 16 – 14 occur between the deposition of TM-19 and TM-18-1, whereas in SA03-03 interstadials 14 – 10 occur between the same tephra layers. The deposition of TM-18-1 occurs between I13 and I14 in PRAD 1-2 but is concurrent with I10 in SA03-03. Equally, I11 is concurrent with TM-18 in PRAD 1-2 but I9 is concurrent with the same tephra layer in SA03-03 (Figure 7.6). In this case, it would appear that the SA03-03 record is correct as others suggest that the Campanian Ignimbrite (TM-18) occurred during Greenland Interstadial 9 (Pyle *et al.,* 2006, Giaccio *et al.,* 2008, Blockley *et al.,* 2008c). Finally, the deposition of TM-16b precedes I6 in PRAD 1-2 but precedes I8 in SA03-03.

Therefore, it is clear that the numbering of the assumed D-O events is not consistent between PRAD 1-2 and SA03-03. This assumes that the correlations with tephra layers are correct but, as the stratigraphic position of the tephra layers has shown the general trends in the $\delta^{18}O$ records of both cores to be consistent, this is thought to be unlikely. Therefore, as at no time during the sequence do the tephra layers bracket or occur concurrently with the same interstadial in either sequence, this suggests that the numbering of one or both of the records is incorrect and therefore these D-O cycles cannot be used as a method of correlation or synchronisation.

7.1.4 Summary

The comparison of the proxy records available for each of the cores studied in this investigation show that the tephra layers confirm that the major stratigraphic units identified in each core appear compatible in all 3 locations. Some of the bioevents recognised in these records appear broadly contemporaneous between sequences based

on the position of tephra layers common to each core. However, three exceptions were noted which will be considered in the wider regional context provided in Section 7.2.2. Finally, the general trend in $\delta^{18}O$ values between the three sequences is broadly similar, although absolute values are not the same. In at least one interval (between the deposition of TM-19 and TM-18-1), the $\delta^{18}O$ records for PRAD 1-2 and SA03-03 seem to be in anti-phase, suggesting different factors could be forcing $\delta^{18}O$ variations in the Central and Southern Adriatic. However, the isotope curve for SA03-03 is at too low a resolution and that for RF93-77 is incomplete, which constrains attempts to establish whether oxygen isotope variations are exactly synchronous within these Adriatic cores.

7.2 Mediterranean stratigraphies

Having established that the stratigraphic scheme, bioevents and oxygen isotope stratigraphy for the three studied cores appear to be broadly synchronous, the same approach will be applied to other sequences from the Adriatic and Mediterranean seas, introduced in Section 3.5.1 (Figure 3.17), to test for synchroneity at a larger scale.

7.2.1 Stratigraphic scheme

To aid in establishing whether the wider Mediterranean stratigraphic scheme is robust, the tephra layers that lie close to important stratigraphic boundaries are listed in Table 7.2.

Table 7.2: Tephra layers present in PRAD 1-2, SA03-03 and RF93-77 that are positioned close to or within stratigraphic markers (S = Sapropel, X = not present).

TM-layer	PRAD 1-2	SA03-03	RF93-77	Correlation	Stratigraphic Position
Unknown	PRAD-3666	X	X	Unknown	Prior to S6
Unknown	PRAD-3586	X	X	Unknown	Within S6
Unknown	PRAD-3472	X	X	Unknown	Post S6
TM-39	PRAD-3383	X	X	Unknown	Post S6/MIS6
TM-27	PRAD-2812	X	X	X-6	Within MIS5.4
TM-24	PRAD-2525	SA03-03-925	RF93-77-790	X-5	Post S4 and Prior to MIS 5.2
TM-22	PRAD-2375	X	X	Anti Green Tuff	Within MIS 5.2
TM-19/20	PRAD-1870	SA03-03-685	RF93-77-450	MEGT/Y-7	Onset MIS 3
TM-15	PRAD-1332	X	X	Y-3	MIS3/2 transition
TM-8	PRAD-218	X	RF93-77-198	NYT	GI-1/Onset YD
TM-5	PRAD-055	X	RF93-77-86	AMS	Post S1

The stratigraphic positions of the tephra layers listed in Table 7.2 will be compared with the stratigraphic positions of the same tephra layers in sites reported in the literature to establish if tephra layers correlated with the same volcanic eruption are in the same stratigraphic order. Comparisons with the tephra layers identified in this study are limited to those layers reported in the literature that can be related to MIS boundaries or sapropel layers, as listed in Table 7.3.

Table 7.3: Tephra layers from marine sequences in the Mediterranean region that correlate to layers in PRAD 1-2, SA03-03 or RF93-77. The stratigraphic positions assigned by authors to each layer are also listed.

Tephra Layer	Correlation	Stratigraphic Position	Reference
C-31	X-6	MIS 5.4	Paterne *et al.* (2008)
I9	X-6	Between S4 and S5	Lourens (2004)
C-27	TM-24b, X-5	Prior to S4	Paterne *et al.* (2008)
C-26	Unknown	Post S4	Paterne *et al.* (2008)
I8	X-3 or X-4	Between S3 and S4	Lourens (2004)
C-17	MEGT	Post S3	Paterne *et al.* (2008)
I4	Y-7/MEGT	Post S3	Lourens (2004)
I2	Y-3	Post S3	Lourens (2004)
C-10/C-7?	Y-3	MIS3/2 transition	Keller *et al.* (1978) Zanchetta *et al.* (2008)
MD90-917-395	NYT	GI-1	Siani et al. (2004)
MD90-917-167	AMS	Post S1	Siani et al. (2004)

Figure 7.7 shows the relationship between tephra layers in PRAD 1-2, SA03-03 and RF93-77 and the equivalent tephra layers in other marine sequences listed in Table 7.3. In most, cases it is clear that the stratigraphic positions of these tephra layers is wholly consistent in marine sequences across the Mediterranean. For example, layers correlated to the Y-3 (green line in Figure 7.7) occur at the MIS3/2 boundary in all cases. Equally, the layers correlated to the X-6 tephra (blue line on Figure 7.7) always occur within MIS 5.4. These tephra layers therefore also indicate that the oxygen isotope stratigraphic scheme is consistent across the region.

However, the stratigraphic position of the X-5 tephra layer is not consistent across the region. Its stratigraphic position is consistent between the three cores in this investigation (Section 7.1.1), and Figure 7.7 shows this to be prior to MIS 5.2 (where this event is recognised) and prior to Sapropel 3. However, in cores KET 80-04 and DED 87-08 (Paterne *et al.*, 2008), the C-27 layer (which correlates to the X-5 - orange

line in Figure 7.7) is positioned prior to Sapropel 4. The C-27 layer is described as being a High Alkali Ratio (HAR - greater than 1.5) layer which is also true for the layers correlated to the X-5 in PRAD 1-2, SA03-03, RF93-77 and LGdM, suggesting that the geochemical data match for KET 80-04 and DED 87-08. However, the raw data for the cores studied by Paterne *et al.* (2008) is not available so a direct comparison cannot be made. There is a tephra layer in both KET 80-04 and DED 87-08 in the same stratigraphic position (post S4, prior to MIS 5.2) as the X-5 layers in this study (black lines in e) and f) on Figure 7.7). This layer is the C-26, which is not correlated to a known eruption by Paterne *et al.* (2008). Although it is in the same stratigraphic position as the X-5 layer in this study, Paterne *et al.* (2008) describe it as having a Low Alkali Ratio (LAR) of an average 0.8, with Na_2O_2 values of 7.00% on average. Neither of these factors are consistent with the geochemical data from PRAD-2525, SA03-03-925 or RF93-77-790. This therefore suggests that the geochemical data for the C-26 does not correlate with the X-5 layer in PRAD 1-2, SA03-03 and RF93-77, which suggests that the stratigraphy of the cores in the wider region is not consistent. In particular, Sapropel 4 in the Eastern Mediterranean does not appear to be synchronous with the Sapropel-equivalent event identified in the Adriatic Sea.

The X-5 tephra layer is not recognised in KC01B by Lourens (2004) (Figure 7.7d). There is a tephra layer in the same stratigraphic position as the X-5 tephra layer in PRAD 1-2, SA03-03 and RF93-77 (black line in Figure 7.7d). This has been correlated to the X-3 or X-4 layer (Lourens 2004). However, this correlation is based solely on the layer's estimated age and its stratigraphic position in the core, in relation to other published work. No geochemical data were obtained and given the fact the X-5 does not appear to have a consistent stratigraphic position across the region, this layer could potentially represent the X-5 tephra layer, although geochemical analysis of this layer are required to test this.

The data summarised above suggest that, whilst the broad stratigraphic scheme derived from oxygen isotope records appears to be consistent across the region, the sapropel layers in the Mediterranean do not appear to equate with the sapropel-equivalent layers recognised in the Adriatic Sea. However, this has only been tested on the basis of one tephra layer and one sapropel layer thus far and should be further tested using the older layers in the PRAD 1-2 sequence which occur between sapropel-equivalents 5 and 6,

something which cannot be achieved at present due to the lack of available, relevant geochemical data.

7.2.2 Regional bioevents

As discussed in section 7.1.2, three of the bioevents recognised in the three Adriatic sequences (L.O *G. inflata* and L.C.O *G. inflata* in MIS3 and the Entry of *G. truncatulinoides*) do not appear synchronous or consistent between cores. Figure 7.8 compares the position of the L.O. *G. inflata* and the AMS tephra layer in a number of cores from the Adriatic Sea (Lowe *et al.*, 2007b) and these show that the L.O. *G. inflata* precedes the deposition of the tephra layer. This supports the order of events seen in PRAD 1-2 (section 7.1.3) and suggests that RF93-77 is anomalous, as it is the only sequence in which the AMS layer precedes the L.O. *G. inflata*.

The events are very closely spaced in RF93-77, with the L.O. of *G. inflata* occurring at 0.84 m, the peak in glass shards at 0.86 m and the spread in glass from 0.88 – 0.84 m. However, even when taking the vertical distribution of glass shards into account, they do not occur after the L.O. of *G. inflata*. As discussed in Section 4.1.3.2, the core had been stored for a long period before it was sub-sampled for this investigation which could have distorted the relationship between the two events since the foraminiferal work that led to the identification of the L.O. of *G. inflata* was undertaken by Asioli (1996). Calanchi *et al.* (1998) undertook analysis on the visible tephra layers in RF93-77 and identified the AMS eruption at 0.83 cm which is posterior to the L.O. of *G. inflata* identified by Asioli (1996). There is a difference of 3 cm between the Calanchi *et al.* (1998) position of the AMS eruption at 0.83 cm and the position of the same tephra layer identified in this investigation (0.86 cm). It is possible that if the foram analysis was undertaken again, the depth of the L.O. of *G. inflata* may have changed due to core shrinkage and it could still precede the deposition of the AMS eruption. Therefore, it appears that the reason for the discrepancy in the sequence of events in RF93-77 is due to the length of time the core had been stored before sub-sampling and subsequent core shrinkage.

Whilst other marine cores contain the AMS tephra layer (e.g. Siani *et al.*, 2004), no other studies found in the literature record both the L.O. of *G. inflata* and the deposition of the AMS tephra layer in the same sequences. Equally, whilst many authors discuss

the L.C.O of *G. inflata* in MIS3 (e.g. Triantaphyllou *et al.*, 2010; Budillon *et al.*, 2009; Ducassou *et al.*, 2007), they do not present parallel tephra results to aid correlation with the cores in this study. The Entry of *G. truncatulinoides* is not considered as a bioevent by other authors, therefore it cannot be discussed further.

7.2.3 Oxygen isotope records

The cores selected for comparison were introduced in section 3.5.1 and provide records for the Southern Adriatic (KET 82-18), Tyrrhenian Sea (KET 80-22, KET 80-04 and KET 80-03) and Ionian Sea (KC01B) (Figure 3.17). As only planktic records are available for these cores, only isotopic data derived from planktic species are considered here. Due to the low resolution of the planktic $\delta^{18}O$ record of SA03-03 and the lack of planktic $\delta^{18}O$ data for RF93-77, only the oxygen isotope record of PRAD 1-2 will be compared with the other marine cores. The positions of the tephra layers on the $\delta^{18}O$ records are presented in Figure 7.9. The $\delta^{18}O$ isotope record of *G. bulloides* is presented for all of the cores except KC01B for which isotopic analysis has been undertaken on *G. ruber*.

It is clear from Figure 7.9 that the absolute values for KC01B are systematically shifted to more depleted $\delta^{18}O$ values. However, the trends in the isotope record should be comparable with those based on *G. bulloides* (Ariztegui *et al.*, 1996). It is clear that whilst there are a number of tephra layers preserved within the sequences not all of them have been correlated to tephra layers in LGdM and are therefore not all directly comparable with the PRAD 1-2 record.

Using the positions of tephra layers common to the six sequences with respect to the $\delta^{18}O$ records (Figure 7.9), the curves are adjusted in Figure 7.10 to correspond to the same time and isotopic scales. There is generally a very good agreement between all the records. After the deposition of TM-27 (yellow line), the isotope curves in A, D and F shift to more depleted $\delta^{18}O$ values (number 1, Figure 7.10). One difference does occur, as in PRAD 1-2 the curve shifts back to more enriched $\delta^{18}O$ values before the deposition of the TM-24 layer (orange line) and, in KET 80-04 this shift to more enriched $\delta^{18}O$ values occurs after the deposition of TM-24. TM-24 is not present in KC01B and therefore cannot be used to determine if the difference between PRAD 1-2 and KET 80-04 is due to the difference in core location. However, there are

inconsistencies in the stratigraphic position of the X-5 (TM-24) tephra layers between PRAD 1-2 and KET 80-04, as discussed in section 7.2.1 and this could explain the difference observed here. The agreement in the curves between the layers correlated to TM-24 (orange line) and TM-22 (dark blue) (number 2, Figure 7.10) is also not perfect although the general trend is the same. In both cores, the deposition of TM-22 occurs when $\delta^{18}O$ values are heavier, before a shift to lighter values, after the deposition of TM-22. Number 3 on Figure 7.10 shows that both sequences shift gradually to heavier $\delta^{18}O$ values prior to the deposition of TM-19 (excluding the anomalous point in the PRAD 1-2 record discussed in Chapter 3). Similar trends are observed in both KET 80-22 and KC01B. However, as TM-22 is not recorded in these sequences, it is not possible to establish whether the changes in these cores occur at the same times as those in PRAD 1-2 and KET 80-04.

Between the deposition of TM-19 (purple line) and TM-18 (green line), it is possible to compare cores from each basin. In all the sequences, there are repeated shifts between lighter $\delta^{18}O$ values (of ~2.5 ‰ for the Adriatic/Tyrrhenian Sea cores and of ~1.0 ‰ for the Ionian Sea core) to heavier $\delta^{18}O$ values (~3.5 ‰ for the Adriatic/Tyrrhenian Sea cores and of ~2.0 ‰ for the Ionian Sea core). However, in the cores from the Adriatic and Tyrrhenian Seas the overall trend is for $\delta^{18}O$ values when TM-18 was deposited to be the same as when TM-19 was deposited (number 4, Figure 7.10). However, in KC01B (E, Ionian Sea), the $\delta^{18}O$ values trend to more enriched values. This difference between the isotopic response in the Adriatic/Tyrrhenian Seas and the Ionian Sea could be because the Ionian Sea is a less enclosed basin and therefore represents the wider Mediterranean isotopic response during this time. This difference between the Ionian Sea Core (F) and the Adriatic/Tyrrhenian Sea cores (A-E) continues between the deposition of TM-18 and TM-15 (red line). PRAD 1-2, KET 82-18 and KET 80-04 continue the earlier trend to more enriched $\delta^{18}O$ values (number 5, Figure 7.10), whereas KC01B initially trends to ^{18}O depleted values after the deposition of TM-18, before shifting to more enriched values prior to the deposition of TM-15. The $\delta^{18}O$ value in KC01B when TM-15 is deposited is ~2.0 ‰, which is the same as when TM-19 was deposited. This suggests that the overall trend in the Ionian Sea between the deposition of TM-19 and TM-15 is the same as the Adriatic and Tyrrhenian Sea cores, indicating that the records may all be reflecting a regional signal.

The agreement between the Adriatic and Tyrrhenian Sea records continues between the deposition of TM-15 and TM-8 (pale blue line), with each sequence showing a shift to more depleted $\delta^{18}O$ values immediately prior to the deposition of TM-8. The resolution of the isotope samples is higher in PRAD 1-2 at this point and therefore some of the detail in the PRAD 1-2 curve is not observed in the other cores.

Figure 7.10 shows that both isotope records from the Adriatic Sea (A and B) are in agreement for all time periods, despite KET 82-18 being located in the South Adriatic. This was not the case for PRAD 1-2 and SA03-03 which appeared to be in anti-phase during some time periods (section 7.1.3). As the PRAD 1-2 record also agrees with all the Tyrrhenian Sea cores, it suggests that the discrepancy between the PRAD 1-2 and SA03-03 records could be due to SA03-03 responding to a different signal, and not PRAD 1-2 as was previously assumed (Piva *et al.*, 2008a).

This agreement between the records suggests the controls on oxygen isotope values in the Adriatic and Tyrrhenian seas during this time period are similar, as the curves follow the same pattern between the deposition of isochrons. Therefore this suggests that the PRAD 1-2 isotopes and potentially other Central Adriatic sequences are responding coherently with wider Mediterranean signals even during periods of low sea level.

7.2.4 Marine-Terrestrial correlations

The presence of tephra layers in PRAD 1-2 allow it to be correlated with terrestrial records in the region as well as other marine sequences. The PRAD 1-2 oxygen isotope record has been correlated to the Lago Grande di Monticchio pollen record (Figure 7.11) and the Lake Ohrid $CaCO_3$ and TOC records, using the depths of the tephra layers that are preserved in each record (Figure 7.12). The significance of the environmental records was discussed in section 3.5.2. These three sequences form a west to east transect across the Adriatic Sea and will allow comparisons between environmental responses across the transect (Figure 7.13).

7.2.4.1 Lago Grande di Monticchio

TM-39 in LGdM is positioned near the base of the LGdM sequence, which corresponds to the end of MIS 6, just prior to an increase in Mesic woody taxa pollen abundance, which is indicative of transitions from glacial conditions (Brauer *et al.,* 2007). TM-39 in PRAD 1-2 is positioned in a heavier isotope peak, just before the isotopes shift to lighter values again suggesting the tephra layer is deposited prior to the transition from glacial conditions and therefore supporting the view that the records are synchronous at this time (Figure 7.11).

TM-38a in LGdM is deposited just prior to when the percentages of Mediterranean and Mesic woody taxa decline suddenly. This decline suggests the environment deteriorates rapidly just after the deposition of TM-38a, when woody taxa could not be supported, which has been interpreted as indicating an interval of hot summers and seasonal moisture deficiency (Brauer *et al.,* 2007). In PRAD 1-2, this layer occurs at a light oxygen isotope peak, just prior to a rapid excursion to heaver isotope values. This again suggests conformity between marine and terrestrial records. This pattern is seen again with the deposition of the TM-27 layer, which in LGdM occurs within the Melisey 1 terrestrial stage (Figure 7.11) when pollen percentages are low and just prior to the transition to the St Germain 1 stage (Brauer *et al.,* 2007). In PRAD 1-2 TM-27 is deposited as the isotope values shift to heavier values and before the rapid decrease in $\delta^{18}O$, which suggests the events are synchronous. The transition from Melisey 1 to St Germain 1 in LGdM also corresponds to a rapid decrease in planktonic $\delta^{18}O$ in MD95-2042 from the Portuguese coast. This suggests there is a common trigger for both events (Brauer *et al.,* 2007) and the position of the TM-27 tephra layer in PRAD 1-2 and LGdM supports this suggestion.

TM-24 in LGdM is deposited at the onset of a period of stable climate where percentages of Mesic woody taxa are high (about 90%) and stay at this percentage for approximately 10,000 years, according to the LGdM varve chronology (Figure 7.11). However, in PRAD 1-2 TM-24 is deposited when the $\delta^{18}O$ values are increasing to heavier values. The isotope curve does not suggest a period of stable values at this time, indicating that the factors causing the isotopic variations at this time are different to those affecting the vegetation.

In LGdM, the percentage of Mesic woody taxa decline rapidly at about 90,000 varve years BP and the pollen record is dominated by steppe taxa (Pollen Assemblage Zone (PAZ 18, Allen *et al.,* 1999). This represents the Melisey 2 terrestrial stage on land and has been correlated to MIS5.2 by Brauer *et al.* (2007) (Figure 7.11). The TM-22 tephra layer is deposited during this period prior to the transition to the St Germain 2 terrestrial stage (Figure 7.11). In PRAD 1-2, the TM-22 tephra layer is deposited when $\delta^{18}O$ values are high, within MIS 5.2, suggesting that it occurs within the period correlated to the Melisey 2 terrestrial stage in LGdM (Figure 7.11) and therefore TM-22 is deposited in what appears to be compatible terrestrial and marine conditions, supporting the view that they are synchronous between PRAD 1-2 and LGdM.

TM-20-7 in PRAD 1-2 is deposited as $\delta^{18}O$ values shift to heavier values at the transition to MIS 4. The tephra layer in LGdM occurs in PAZ 16 (Allen *et al.,* 1999), as Mesic woody taxa percentages are declining and the pollen record is becoming dominated by steppic taxa, at a time period correlated to the onset of MIS 4 (Brauer *et al.,* 2007). This synchrony of events suggests there may be a common trigger for the changes seen in the marine and terrestrial records. The records also appear to be synchronous at the time TM-19 was deposited. In LGdM, the layer is deposited when percentages of tree species are low but at a transition to higher percentages of mesic woody taxa, (*Pinus* plus *Juniperus* and *Betula)* and in PRAD 1-2 the layer is deposited on a transition to lighter isotope values (Figure 7.11). TM-18 in LGdM is deposited when *Pinus* and *Juniperus* percentages are low in PAZ 6 and just prior to the increase in *Pinus* and *Juniperus* percentages and the transition to PAZ 5b, which suggests that it accords with the beginning of the transition to MIS 2 and the last glacial maximum (Allen *et al.,* 1999). In PRAD 1-2, this layer is deposited on the transition to heaver $\delta^{18}O$ values, which also suggests the beginning of the transition to MIS 2.

TM-16b is deposited prior to a rapid rise in *Pinus* plus *Juniperus* pollen, Mesic woody taxa and steppic taxa in LGdM and, in PRAD 1-2, prior to a shift to lighter $\delta^{18}O$ values, although this isotope shift occurs when the overall trend is towards heaver $\delta^{18}O$ values. TM-15 is correlated to the Y-3 layer by Wulf *et al.* (2004) and its stratigraphic position in the Mediterranean is on the MIS3/MIS2 boundary (Zanchetta *et al.,* 2008; Table 7.3). This relationship is also observed in the PRAD 1-2 record, with TM-15 occurring on the transition as $\delta^{18}O$ values approach their heaviest. In LGdM, TM-15 occurs on a vegetation transition, as steppic taxa, mesic woody taxa, *Pinus* and *Juniperus* all

decrease rapidly. Therefore both TM-16b and TM-15 seem to occur during similar environmental transitions in both the marine and terrestrial environments.

TM-14-1, TM-13, and TM-12 are deposited within 2 m of each other in LGdM and are therefore very closely spaced (Figure 7.11) and occur within PAZ 4, which represents the last full glacial (Allen *et al.*, 2000). TM-14-1 is deposited when *Pinus* plus *Juniperus,* Mesic woody taxa, steppic taxa and grasses are all at their highest percentages. The percentages of each of those taxa then decrease and are at minimal values when TM-13 is deposited. Finally, between the deposition of TM-13 and TM-12, the percentages of each of those taxa rise again but then fall and are low when TM-12 is deposited (Figure 7.11). This suggests that during this period there are a number of climatic oscillations within the overall cold conditions. In PRAD 1-2, these layers all occur within MIS 2 but the sequence is more expanded than the LGdM record for this time. The $\delta^{18}O$ curve fluctuates between heaver and lighter $\delta^{18}O$ values between the deposition of these tephra layers. However, the resolution of the isotope values is low, with only one measurement between the deposition of TM-13 and TM-12, therefore it is not possible to examine the PRAD 1-2 record in the same detail as that for LGdM. Nevertheless, it does appear that changes are occurring synchronously between the marine and terrestrial records when TM-14-1, TM-13 and TM-12 were deposited.

TM-8 in PRAD 1-2 is deposited at the start of the Younger Dryas, as $\delta^{18}O$ values shift to heavier values (Figure 7.11). Brauer *et al.* (2007) state that the LGdM pollen record does not record a Younger Dryas-like oscillation. However, PAZ 2 shows a decrease in *Quercus* and other woody taxa and an increase in *Betula* (Allen *et al.*, 1999). This would be indicative of a shift to cooler climates and consequently may represent the Younger Dryas, this oscillation being reflected in Figure 7.11 where steppic and mesic woody taxa decrease. TM-8 in LGdM is deposited when the percentages of mesic woody taxa are still high but marks the beginning of the transition to lower pollen percentages, suggesting that TM-8 is deposited just before a climatic deterioration which appears synchronous with its position in PRAD 1-2. Finally, TM-5 in both records is deposited during a stable climate period, when the percentage of mesic and Mediterranean woody taxa in LGdM are the highest recorded since the last interglacial interval (Brauer *et al.,* 2007) and the isotopes are depleted in ^{18}O, meaning both the terrestrial and marine records indicate Holocene conditions and that the position of the tephra layer shows a synchronous response between the two sequences.

The correlation of PRAD 1-2 and LGdM using the tephra layers shows that, for the majority of tephra layers, the proxy data do record similar climatic changes at similar times suggesting that both records are generally responding to a regional driver, which presumably is climate.

7.2.4.2 Lake Ohrid

Lake Ohrid and PRAD 1-2 only have five tephra layers in common (Figure 7.12) and hence it is not possible to compare proxy responses throughout the whole sequence.

The X-6 (TM-27) tephra layer in Lake Ohrid coincides with when $CaCO_3$ values are at a minimum on the transition to higher values, which Vogel *et al.* (2010b) suggest indicates that temperature decreased during this time. The TOC percentages are also at a minimum at this time which supports the suggestion of prevailing colder temperatures. In PRAD 1-2, TM-27 is deposited as the isotope values shift to heavier values, and before the rapid decrease in $\delta^{18}O$, which suggests that TM-27 is deposited as conditions are deteriorating. Therefore, this suggests that whilst the proxy records show broadly contemporaneous changes at the time TM-27 was deposited, the Lake Ohrid record seems to be responding earlier to a forcing factor than the PRAD 1-2 record.

The X-5 (TM-24) tephra layer is also deposited during a $CaCO_3$ and TOC minimum, which again represents colder temperatures (Vogel *et al.,* 2010b). In PRAD 1-2, TM-24 is deposited when the $\delta^{18}O$ values are increasing but are not at their heaviest value, which suggests a difference between the timing of events in PRAD 1-2 and Lake Ohrid and hence again the proxy records in Lake Ohrid appear to have responded to a forcing factor before those in the PRAD 1-2 record.

The Campanian Ignimbrite (TM-18), Codola (TM-16b) and Y-3 (TM-15) tephra layers were all deposited during low amounts of TOC and CaCO3 which indicates low productivity, thought to reflect low spring-summer surface temperatures and reduced supply of nutrients and dissolution of calcite by a well oxygenated water column (Vogel *et al.,* 2010b). TM-18 is deposited as TOC percentages were increasing (Figure 7.12), suggesting productivity in the lake and lake surface temperatures were also increasing (Vogel *et al.,* 2010b). TM-18 in PRAD 1-2 was deposited when the $\delta^{18}O$ value is ~3.5

‰ just before a transition to heavier $\delta^{18}O$ values. This again suggests that proxy records in Lake Ohrid respond to a forcing factor before the proxies in PRAD 1-2. In Lake Ohrid, TM-16b occurs when TOC percentages are low, immediately prior to them increasing and in PRAD 1-2 the same tephra is deposited immediately prior to a shift to lighter $\delta^{18}O$ values, although this isotope shift occurs when the overall trend is towards heaver $\delta^{18}O$ values. This suggests that at the deposition of TM-16b, the proxy records in Lake Ohrid and PRAD 1-2 are responding synchronously. Finally, TM-15 (the Y-3) in PRAD 1-2 is deposited on the transition from MIS 3 to MIS 2 as $\delta^{18}O$ values approach their heaviest. The Y-3 in Lake Ohrid is deposited when $CaCO_3$ values peak, but TOC percentages are low. Vogel *et al.* (2010a) state that around the deposition of the Y-3 maxima in the fine sand, Cr/Ti and Zr/Ti ratios point to stronger wind activity and enhanced erosion of sparsely vegetated soils. This cold and dry climate with relatively sparse vegetation coverage is confirmed by a multiproxy study on core Lz1120 from the SE part of the lake (Wagner *et al.,* 2009). Therefore the stratigraphic position of the tephra layers suggests the Lake Ohrid proxy records have responded to a forcing factor before PRAD 1-2, as TM-15/Y-3 in Lake Ohrid was deposited during a cold environment period whereas in PRAD 1-2 it falls on the transition to colder environments.

The correlation of PRAD 1-2 and Lake Ohrid using the tephra layers shows that for the majority of tephra layers the proxy data do record different changes during similar time periods. This suggests that these changes are not synchronous between the records and that the marine isotope record seems to be responding to a different signal compared with the terrestrial record, or that the records are responding at different times to the same forcing factors.

7.2.4.3 Adriatic Sea transect

The proxy records from LGdM, PRAD 1-2, and Lake Ohrid have been correlated using the stratigraphic positions of the five tephra layers that are common to each sequence (Figure 7.13). Vogel *et al.* (2010b) relate the minima in the $CaCO_3$ record when TM-27 is deposited to the decrease in pollen percentages during the Melisey 1 stage at LGdM. However, the stratigraphic position of the TM-27 layer suggests that the decrease in $CaCO_3$ values in Lake Ohrid preceded the decrease in pollen percentages at LGdM (Figure 7.13).

The records also show differing proxy record responses when TM-24 was deposited. Lake Ohrid $CaCO_3$ and TOC records suggest cold temperatures, PRAD 1-2 $\delta^{18}O$ values are in transition to heavier values and LGdM pollen percentages are high and have just risen. This is also the case for TM-18 as in Lake Ohrid TOC percentages are rising, in PRAD 1-2 $\delta^{18}O$ values are at their heaviest before shift to lighter values and in LGdM pollen percentages are low also. The same pattern is observed for TM-15 with the layer in PRAD 1-2 and LGdM recording similar environmental transitions and Lake Ohrid showing different a different response.

This suggests that terrestrial records to the west of the Adriatic Sea respond in phase with the marine records and events can be considered broadly synchronous. However for terrestrial records to the east of the Adriatic Sea, environmental changes cannot be considered synchronous with marine or western terrestrial records. This supports the observation of Lézine *et al.* (2010) that some changes in pollen percentages occurred earlier in LGdM than in Lake Ohrid.

7.2.4.4 Wider scale comparisons

Fluctuations in the PRAD 1-2 $\delta^{18}O$ record and the LGdM pollen percentages have been assumed to represent D-O cycles (Piva *et al.,* 2008a, Fletcher *et al.,* 2010, Allen *et al.,* 1999). Figure 7.14 shows the numbered interstadial part of the D-O cycle that each pollen or isotope fluctuation has been assigned to. The tephra layers common to both sequences are marked on the diagram and, as these are time-parallel marker horizons, the tephra layers should bracket the same interstadials in both sequences. However, it is clear that this is not the case (Figure 7.14). All of the interstadials in both PRAD 1-2 and LGdM occur between the deposition of TM-22 and TM-15 but the tephra layers in between do not show synchroneity between the D-O events in both sequences. The deposition of TM-20-7 in PRAD 1-2 post-dates interstadial 19 (I19) but in LGdM TM-20-7 precedes both I19 and I20. TM-19 in PRAD 1-2 occurs between I16 and I17, whereas in LGdM its deposition precedes I17. In PRAD 1-2, interstadials 16 – 14 occur between the deposition of TM-19 and TM-18-1, whereas in LGdM interstadials 17 – 10 occur between the same tephra layers. The deposition of TM-18-1 is concurrent with I13 in PRAD 1-2 but concurrent with I9 in LGdM. Equally I11 is concurrent with TM-18 in PRAD 1-2 but I9 is concurrent with the same tephra layer in LGdM. In this case, it would appear that the LGdM record is correct as other authors suggest that the

Campanian Ignimbrite (TM-18) occurred during Greenland Interstadial 9 (Pyle *et al.*, 2006, Giaccio *et al.*, 2008, Blockley *et al.*, 2008c). Finally, the deposition of TM-16b precedes I6 in PRAD 1-2 but occurs between I5 and I6 in LGdM.

Therefore, at no time during the sequence do the tephra layers bracket or occur concurrently with the same interstadial in either sequence. This suggests that the numbering of one or both of the records is incorrect and therefore these D-O cycles cannot be used as a method of correlation or synchronisation. It is not possible to determine if either record is correct or not using stratigraphy alone, as none of the tephra layers present in PRAD 1-2 or LGdM have been recorded in any Greenland Ice Cores. The fact that in LGdM TM-18 (the CI) is concurrent with interstadial 9 suggests maybe the numbering of interstadials in this record is more robust. The ages of the tephra layers can be compared to the ages of the Interstadials from the Greenland ice cores to see if the assumed correlation to D-O cycles in either record is correct, this will be considered in Chapter 8.

7.2.5 Summary

Comparison of the records investigated in this study with other records in the region has shown a number of things. The lack of comparable data has limited some of the comparisons, mainly because, whilst proxy information may be available for a number of sequences in the wider Mediterranean region, it is not available with tephra depth information which means records cannot be linked using isochrons.

Firstly, the stratigraphic positions of tephra layers between sequences in the Adriatic and the wider Mediterranean Sea appear to be robust where the correlation is based on marine isotope stages. This is also supported by the comparison of the oxygen isotope curves of PRAD 1-2 in the Adriatic, Tyrrhenian and Ionian Sea cores, where changes between the isochrons appear to be the same, with the same directional shifts and similar absolute values. However, where the stratigraphic position of a tephra layer is defined by a sapropel position, greater differences between the Adriatic and Mediterranean records are apparent, which suggests the Eastern Mediterranean sapropels and Adriatic sapropel-equivalent layers are not synchronous events.

Secondly, the oxygen isotope stratigraphic records suggest that changes in the Adriatic are responding to the same signal as sequences from the wider Mediterranean basin. This suggests that the planktic oxygen isotope record from the Central Adriatic basin is not affected by the potential isolation of the basin during times of low sea level.

This synchroneity between the PRAD 1-2 oxygen isotope record and other Mediterranean oxygen isotope records is supported by the comparison of the PRAD 1-2 isotope record and LGdM pollen record. The stratigraphic position of tephra layers common to both PRAD 1-2 and LGdM show that the environmental response of both cores appear synchronous, supporting the fact that PRAD 1-2 is showing a wider Mediterranean regional signal and not just a central Adriatic signal. However comparison of the PRAD 1-2 isotope record and Lake Ohrid proxy records suggests that the two sequences are not responding synchronously to a common forcing factor or that the factors forcing the proxy changes are different.

Finally, the tephrostratigraphy of PRAD 1-2 and its relationship to tephra layers present in LGdM have shown that the assumed D-O cycles in both records have been numbered incorrectly and that they cannot be used as synchronous marker layers at this point in time. Therefore, PRAD 1-2 cannot be linked directly to the Greenland Ice core record as it is not possible to tell if either the LGdM D-O cycle numbering or the PRAD 1-2 D-O cycle numbering is correct or if there are errors in both approaches. The correlation of the PRAD 1-2 isotope record to the Greenland ice cores will be considered further in the next chapter.

8. Constructing independent age models

So far, the stratigraphic boundaries, bioevents and isotopic changes observed in the three studied marine cores have been compared based on their stratigraphic relationships to the tephra layers alone. This has identified where events appear to occur synchronously or not but, in some cases, the information is limited as few tephra layers occur close to other key changes. Therefore, age models are needed to enable a fuller examination of the time differences between events.

The age models for the studied marine cores will be based solely on independent age estimates obtained from tephra layers found in each sequence and will not include any radiocarbon dates from the sequences in order to circumvent the problem of marine reservoir effects distorting the models. The aim was to develop independent age models that are free of climatic and biostratigraphical assumptions which are frequently employed to align marine records.

8.1 Assigning ages to tephra layers

Where a radiometric age is available for a tephra layer, this will be used in preference to the varve age from the LGdM sediment chronology for the same tephra layer. This is because annual laminations are restricted to 10% of the total LGdM sequence (Wulf *et al.*, 2004), while the chronology for the sequence was established by counting the varved sections but using estimated sedimentation rates for the remaining intervals. It is thought that varve ages underestimate the true ages of events (Brauer *et al.*, 2000). Where no other age exists, however, the LGdM varve age will be used as a first-order age approximation.

Before an age model can be generated, it is necessary to ensure that the best age estimates for the tephra layers identified in each sequence are used. In some cases, the best available age estimates are those already reported in the literature, such as those for the AMST (TM-5) and NYT (TM-8) eruptions published by Blockley *et al.* (2008a). In other instances, however, multiple age estimates for the same eruption are available and these data can be integrated using Bayesian statistical techniques in order to produce models from which 95.4% confidence limits can be computed. The ages of the tephra layers that have been refined using these procedures are summarised in the following

sections. Definitions of the main age modelling terms used in the chapter can be found in Section 4.8.2, Table 4.3, page 166.

8.1.1 Greenish (TM-12)

A number of radiocarbon dates have been obtained from palaeosols that underlie the Greenish tephra layer in a variety of sites and from associated charcoal. There are two direct dates obtained on the Greenish tephra layer, one based on the LGdM lake sediment chronology and the other based on $^{39}Ar/^{40}Ar$ dating of sanidine crystals extracted from the tephra layer (Table 8.1).

Table 8.1: Dates from the literature for the Greenish eruption used in this study, with 1σ uncertainty values. Radiocarbon dates presented are uncalibrated.

Type of Date	Material	Date	Error	Source Ref.
Radiocarbon a	Palaeosol	14,420	160	Delibrias *et al.* (1979)
Radiocarbon b	Palaeosol	15,500	170	Delibrias *et al.* (1979)
Radiocarbon c	Palaeosol	16,780	170	Andronico *et al.* (1995)
Radiocarbon d	Charcoal	16,120	110	Andronico *et al.* (1995)
Radiocarbon e	Charcoal	15,970	70	Siani *et al.* (2001)
Radiocarbon f	Charcoal	16,020	130	Siani *et al.* (2001)
Varve age	N/A	17,560	880	Wulf *et al.* (2004)
Ar/Ar	Sanidine	18,456	302	Lanphere *et al.* (2008)

Using the ages reported in Table 8.1 and the stratigraphic position of the dated samples, a Bayesian *Sequence* model has been constructed for the Greenish tephra layer. The model comprises three depositional *Phases*: 1) a *Phase* for radiocarbon dates that immediately precedes the deposition of the Greenish tephra layer; 2) a *Phase* using only those dates obtained from the Greenish tephra layer directly and 3) a *Phase* using dates for the Biancavilla eruption of Etna, which is known to stratigraphically fall after the Greenish tephra, based on the relative positions of the tephra layers in LGdM (Wulf *et al.*, 2004) (See Table 4.3, page 166 for definition of age modelling terms).

The dates within each *Phase* are stratigraphically unordered with respect to each other but the three *Phases* have relative stratigraphic order. The *Phase* model assumes the dated material to have been deposited at slightly different times around the time of the eruption. This is more appropriate than combining all the radiocarbon dates together as this would assume all the dated material to come from the same depositional event, as for example when multiple dates were obtained from a single fossil tree that was buried

by the eruption (Blockley *et al.*, 2008a). This information is not known for the samples and age estimates listed in Table 8.1.

The output of the model is presented in Figure 8.1 which shows that there is conformity between the radiocarbon ages and the chronological scheme. Radiocarbon date "a" in phase 1 is clearly too young in be in agreement with the model. The percentages (in brackets) next to the label for each date are the agreement indices (AI) for each date (see section 4.9.2 for details). Those dates marked with a question mark have agreement indices lower than the recommended limit (60%). They were rejected from the model because their inclusion lowered the AI for the whole model beneath the recommended 60% level (Bronk Ramsey, 2008b).

It is possible to calculate a 95.4 % confidence Highest Probability Density (HPD) for the onset and end of a phase and hence to derive a 95.4% confidence HPD estimate for the age of the Greenish. This gives the calculated onset age for the Greenish eruption as 18.96 – 17.95 cal ka BP and the calculated end of the eruption as 18.63 – 17.37 cal ka BP, resulting in a modelled calibrated age range for the eruption of 18.98 – 17.37 cal ka BP. This result is in good agreement (within 2σ errors) with the $^{40}Ar/^{39}Ar$ age and varve age but takes into account all the available dating information rather than assuming the validity of a single selected estimate.

8.1.2 Pomici di Base (TM-13)

There are a number of dates for this eruption, including direct measurements on the ash itself as well as radiocarbon measurements based on samples obtained from palaeosols beneath the ash. These dates are summarised in Table 8.2.

Table 8.2: Published dates for the Pomici di Base eruption used in this study with 1σ uncertainty values. Radiocarbon dates presented are uncalibrated.

Type of Date	Material	Date	Error	Source Ref.
Ar/Ar	Sanidine	21759	306	Delibrias *et al.* (1979)
Ar/Ar	Sanidine	21568	328	Delibrias *et al.* (1979)
K/Ar	Sanidine	22,520	1000	Capaldi *et al.* (1985)
Varve	N/A	19,280	970	Wulf *et al.* (2004)
Ar/Ar	Sanidine	21,313	408	Lanphere *et al.* (2008)
Radiocarbon a	Palaeosol	17,050	140	Delibrias *et al.* (1979)
Radiocarbon b	Charcoal	18,300	180	Andronico *et al.* (1995)
Radiocarbon c	Palaeosol	18,759	420	Bertagnini *et al.* (1998)
Radiocarbon d	Palaeosol	19,170	420	Bertagnini *et al.* (1998)
Radiocarbon e	Charcoal	18,220	714	Siani *et al.* (2004)
Radiocarbon f	Palaeosol	17,229	398	Aleisso et al. (1974)

All the radiocarbon dates are from palaeosols lying directly beneath the tephra layer and hence provide maximal age estimates for the ash. The K/Ar, Ar/Ar and varve measurement date the ash directly.

The dates in Table 8.2 were modelled using the same approach as those for the Greenish tephra layer (section 8.1.1). A Bayesian *Sequence* model has been constructed for the Pomici di Base tephra layer, again comprising three depositional *Phases*: 1) a *Phase* for the radiocarbon dates obtained from palaeosols that immediately precede the deposition of the Pomici di Base tephra layer; 2) a *Phase* of dates from the Pomici di base tephra layer and 3) the date modelled for the Greenish eruption in Section 8.1.1, as the Greenish tephra is known to lie stratigraphically above the Pomici di Base tephra (Wulf *et al.,* 2004) and hence provides a limiting age for the latter (See Table 4.3, page 166 for definition of age modelling terms).

The output from this model is shown in Figure 8.2 and, although there is good agreement between the majority of the dates, it is clear that both radiocarbon dates "a" and "f" in phase 1 and the "PB varves" age estimate in phase 2 form younger outliers in the model, giving AI values too low for model acceptance. They are rejected because their inclusion would lower the AI for the whole model to below the recommended 60% level.

The calculated age for the onset of the Pomici di Base eruption is 22.12 – 21.31 cal ka BP and for the end of the eruption as 21.87 – 20.54 cal ka BP resulting in a modelled, calibrated age range for the eruption of 22.12 – 20.54 cal ka BP, at a 95.4% confidence level. This is in good agreement (within 2σ errors) with the $^{40}Ar/^{39}Ar$ ages but with a 2σ age uncertainty range reduced from an average of 1000 to 790 calendar years.

8.1.3 Codola (TM-16b)

The Codola eruption was dated by the LGdM varve chronology to 31.16 ka BP (Brauer *et al.,* 2007) but this is not in agreement with the radiocarbon age estimate of 25,100 ± 400 ^{14}C yr BP for this horizon (Alessio *et al.,* 1974; Santacroce, 1987). Giaccio *et al.* (2008) suggest that the age of 25,100 ± 400 ^{14}C yr BP is unreliable due to the significant inconsistencies with the tephro- and climatostratigraphic position of the Codola tephra layer and this age. The Codola tephra is correlated with the C-10 layer

(Paterne *et al.,* 1988) (Table 2.8, pages 78 and 79), which has been radiocarbon dated in Tyrrhenian Sea core, KET 80-03, providing an alternative age estimate for the layer. Giaccio *et al.* (2008) correlate a tephra layer preserved in the Paglicci Cave, southern Italy to the Codola eruption. The units above and below the tephra layer have been radiocarbon dated, providing additional dates for constraining the age of the Codola eruption and all these dates are summarised in Table 8.3.

Table 8.3: Published dates for the Codola eruption used in this study with 1σ uncertainty values. Radiocarbon dates presented are uncalibrated. A ΔR value of 61±30 was applied to the marine radiocarbon date (Siani *et al.,* 2000).

Type of Date	Material	Date	Error	Source Ref.
Radiocarbon (marine)	Foraminifera	29,300	700	Paterne *et al.* (1999)
Radiocarbon	Palaeosols	25,100	400	Alessio *et al.* (1974)
Radiocarbon a	Palaeosols	26,800	300	Giaccio *et al.* (2008)
Radiocarbon b	Palaeosols	28,300	400	Giaccio *et al.* (2008)
Radiocarbon c	Palaeosols	28,100	400	Giaccio *et al.* (2008)
Radiocarbon d	Palaeosols	26,300	400	Giaccio *et al.* (2008)
Radiocarbon e	Palaeosols	29,300	600	Giaccio *et al.* (2008)
Radiocarbon f	Palaeosols	34,300	800	Giaccio *et al.* (2008)
Varve	N/A	31,121	1560	Wulf *et al.* (2004)

The marine radiocarbon date is taken from a foram associated with the tephra layer and therefore can be considered to represent the age of the eruption, as is the case with the varve age. Whilst this is a marine date, there are very few dates of this eruption, therefore, it is included in the age modelling process as it appears consistent with the other available information and it is not being used in isolation. The Giaccio *et al.* (2008) form a sequence of dates in stratigraphic order, some pre-dating the Codola deposition and others post-dating Codola it (Figure 8.3a). These dates have been modelled as a *Sequence* in OxCal, as the stratigraphic relationship between the Giaccio *et al.* (2008) dates is known. A depositional *Phase* was inserted into the model to represent the tephra layer deposition and the dates directly associated with the ash were inserted as unordered dates within this phase. Due to the concerns of Giaccio *et al.* (2008) about the Alessio *et al.* (1974) date and lack of precise information about its stratigraphic position with respect to the tephra layer, it was not included in the age model, the output from which is shown in Figure 8.3b.

There is generally a good agreement between the dates and the model, although radiocarbon date D plots as an outlier and has therefore been rejected because its inclusion lowers the AI for the whole model beneath the recommended 60% level.

The age estimate for the Codola eruption can be calculated from the modelled ages of the Codola *Phase* in Figure 8.3. Therefore the calculated onset age for the Codola eruption is 34.62 – 32.46 cal ka BP and the calculated end of the eruption as 33.91 – 31.99 cal ka BP, resulting in a modelled calibrated age range of 34.62 – 31.99 cal ka BP. This is in good agreement (within 2σ errors) of the marine radiocarbon date but significantly better constrained than the 2σ errors of the varve date.

In summary, Bayesian modelling of all available dates for the three tephra layers considered in this section has produced the best calendar age estimates for these eruptions, based on the currently available dating evidence. The 95.4% confidence model ages for these eruptions are Greenish tephra (18.96 – 17.37 cal ka BP), Pomici di Base tephra (22.12 – 20.54 cal ka BP) and Codola tephra (34.62 – 31.99 cal ka BP). These dates will now be incorporated into age models generated for the marine core sequences studied in this thesis.

8.2 Independent age models for marine sequences

Using the dating information available for the tephra layers preserved in the PRAD 1-2, SA03-03 and RF93-77 sequences, age models can be constructed for each sequence. These enable age estimates to be determined for other events identified in the cores, such as the LO and entry of foram species or the isotope variations (see Chapter 7). Age modelling will introduce uncertainty, causing an additional level of complexity. However, correlations drawn in this section are only considered valid if supported by the stratigraphic correlations made in Chapter 7.

In each case, a version of the *Sequence* models used in section 8.1 is applied to the dating evidence available for the three core sequences. The *P_Sequence* incorporates relative depth information into the age model (Blockley *et al.*, 2008b). The prior assumption used in the model is a Poisson process model of deposition being made up of multiple events over time, in this case the punctuated deposition of various tephra layers over time. The *k factor* included in the calculation is a measure of the level of rigidity with which the model is imposed on the data: a high k factor (10 depositional events per cm) implies very uniform deposition, while a low k factor implies rapidly varying deposition (Bronk Ramsey, 2008b).

8.2.1 PRAD 1-2

A *P-Sequence* model was applied to the dating information available for PRAD 1-2 (Table 8.4). A low k-factor of 1.3 was applied to the model, as the age model is running over *c.* 130,000 years and therefore, changes in sedimentation rate are more likely. 50 cm interpolation was also added to the model, meaning that age was calculated by the model for stratigraphic levels 50 cm apart.

Table 8.4: Depths, ages and errors for the tephra layers used to construct the PRAD 1-2 age model. The errors for the modelled dates are at 2σ, the errors for the $^{40}Ar/^{39}Ar$ dates are 1σ and the errors on the varve dates are expressed as 5% of the date itself, as recommended by Brauer *et al.* (2000).

	Depth (m)	LGdM tephra layer	Volcanic event	Age (yrs B.P)	Error	Dating method
1	0.55	TM-5	AMS	4,495	195	Modelled
2	2.23	TM-8	NYT	14,110	210	Modelled
3	7.84	TM-12	Greenish	18,171	804	Modelled
4	8.75	TM-13	Pomici di Base	21,332	790	Modelled
5	11.03	TM-14-1	Faro di Punta Imperatore	21,353	1000	Varves
6	13.32	TM-15	Y-3	30,300	400	$^{40}Ar/^{39}Ar$
7	14.94	TM-16b	Codola (base)	33,307	1314	Modelled
8	16.53	TM-18	CI	39,280	110	$^{40}Ar/^{39}Ar$
9	17.52	TM-18-1	SMP1-a	39,313	2000	Varves
10	18.70	TM 19	MEGT	55,000	2000	$^{40}Ar/^{39}Ar$
11	20.40	TM-20-7	Pignatiello Formation	75,351	4000	Varves
12	23.75	TM-22	Ignimbrite z unit	79,300	4200	Unknown
13	25.25	TM-24	X-5	105,000	2000	$^{40}Ar/^{39}Ar$
14	28.12	TM-27	X-6	107,000	2000	$^{40}Ar/^{39}Ar$
15	32.25	TM-38a	Ignimbrite D	120,000	6000	$^{40}Ar/^{39}Ar$
16	33.83	TM-39	Unknown	130,627	6000	Varves

The graphical output for the age model is shown in Figure 8.4 with the modelled dates for the tephra layers and boundaries presented in Table 8.5.

Table 8.5: OxCal model output for the PRAD 1-2 sequence. The Modelled (BP) column is the output for each date. The layers labelled with a PRAD tephra code are layers that were not correlated to an LGdM layer and therefore could not be dated; therefore their age has been interpolated from the model. The A column shows the agreement index for each date.

Name	Unmodelled (BP)		%	Modelled (BP)		%	Aoverall 72.3	Depth (m)
	from	to		from	to		A	
	4926	-24	95.4	4646	386	95.4	100	0
AMST	4691	4301	95.4	4697	4307	95.4	99.8	0.55
S1top	11421	5481	95.4	11198	4475	95.4	100	0.9
PRAD120				11309	5941	95.4		1.2
S1base	11426	6476	95.4	14270	8277	95.4	100	1.5
PRAD-205				14361	10161	95.4		2.05

Name	Unmodelled (BP)		%	Modelled (BP)		%	Aoverall 72.3	Depth (m)
	from	to		from	to		A	
NYT	14321	13901	95.4	14304	13825	95.4	99.4	2.23
PRAD231				14544	13832	95.4		2.31
PRAD267				15361	13880	95.4		2.67
PRAD323				15822	13942	95.4		3.23
PRAD329				16149	13999	95.4		3.29
PRAD404				16909	14231	95.4		4.04
PRAD480				17574	14602	95.4		4.8
Greenish	18975	17370	95.4	19176	17622	95.4	93.6	7.84
Pomici di Base	22125	20537	95.4	21639	20238	95.4	81.2	8.75
TM-14-1	22352	20355	95.4	22749	21137	95.4	74.4	11.03
PRAD1130				26164	21077	95.4		11.3
Y3	30701	29901	95.4	30692	29897	95.4	100.1	13.32
PRAD1474				34583	31260	95.4		14.74
Codola	34620	31996	95.4	34660	32126	95.4	101.3	14.94
CI	39501	39061	95.4	39497	39058	95.4	100	16.53
TM-18-1	43304	35324	95.4	43570	39227	95.4	93.2	17.52
TM-19	58991	51011	95.4	58809	50959	95.4	100.5	18.7
TM-20-7	79342	71362	95.4	76577	69338	95.4	71.1	20.4
S3top				81490	72430	95.4		22.75
S3base				84118	75511	95.4		23.35
TM-22	83491	75111	95.4	84763	77166	95.4	89.4	23.75
X5	108991	101011	95.4	106247	99334	95.4	76.4	25.15
PRAD2605				108253	100478	95.4		26.05
S4top				109887	101908	95.4		26.75
S4base				111376	104073	95.4		27.45
X6	110991	103011	95.4	111813	104940	95.4	94	27.97
S5top				121397	105825	95.4		29.8
S5base				128715	109051	95.4		30.6
TM38a	131974	108028	95.4	132530	115927	95.4	96.9	32.064
PRAD3336				136858	122912	95.4		33.36
TM39	137213	124043	95.4	137703	126471	95.4	99.4	33.589
S6	189686	137216	95.4	154759	137216	95.4	100	34.6

The model agreement index is 72.3% with all the dates being accepted by the model. The model employs 95.4% probability error ranges for each date. Some of the age uncertainty ranges are large, especially towards the base of the sequence. This is to be expected, as there are only four dated points covering 40 ka, therefore the large errors are realistic. In other parts of the sequence, errors of only a few hundred years are achieved, which is relatively low for a marine sequence like PRAD 1-2.

It is clear that there are large changes in sedimentation rate within the sequence, particularly around the deposition of the tephra layer correlated with the X-5 event but also that sedimentation rates are not linear throughout the core, but reflect repeated small changes.

The model provides age estimates for the tephra layers in PRAD 1-2 that could not be correlated with dated tephra layers in the LGdM sequence (Table 8.5). The layers with identical major, minor and trace element geochemistry to the NYT (see section 6.2.19) date to between 16.9 ka and 13.8 ka BP, with PRAD-231 assigned to between 14.5 ka and 13.8 ka BP, PRAD-267 to between 15.3 ka and 13.8 ka BP, PRAD-323 to between 15.8 ka and 13.9 ka BP, PRAD-329 to between 16.1 ka and 13.9 ka BP and PRAD-404 to between 16.9 ka and 14.2 ka BP (Table 8.5). The modelled dates for PRAD 231, PRAD-267 and PRAD-323 encompass the age range of the NYT eruption (14,304 – 13,825 years BP) supporting the hypothesis that some of these layers represent multiple phases of the NYT eruption (section 6.2.19). The fact that the dates for PRAD-329 and PRAD-404 are older than the NYT age range suggests that these layers represent eruptions of the Campi Flegrei not represented in the LGdM sequence and which are older than the NYT, but showing an identical geochemical signature to it.

The other unidentified tephra layers that can be assigned ages are PRAD-480, dated to 17.5 ka – 14.6 ka BP, PRAD-1130 dated to 30.7 ka – 29.9 ka BP, PRAD-1474 dated to 34.5 ka – 31.2 ka BP, PRAD-2605 dated to 108.2 ka - 100.4 ka BP and PRAD-3336 dated to 136.8 ka – 122.9 ka BP. This enables these layers to be used a time-synchronous marker layers if they are identified in other sequences, as they now have geochemical information and an age associated with them.

As well as providing dates for previously unrecognised tephra layers the model has significantly refined the age ranges for some tephra layers. The age of the Pomici di Base (TM-13) in PRAD 1-2 is further refined from the age modelled in Section 8.1.2 to 21.64 – 20.24 ka BP and the age of TM-14-1 in PRAD 1-2 is refined to 22.75 – 21.14 ka BP, an improvement of 200 years on the 2σ error range, compared with the LGdM varve age. Equally the age range of the TM-18-1 tephra layer has reduced from 43.3 – 35.3 ka BP (the LGdM varve age for this layer, Wulf *et al.,* unpublished) to 43.5 – 39.2 ka BP, a reduction of c. 1700 years. The modelled age range for TM-20-7 is now 76.58 – 69.34 ka BP, which has reduced the 2σ error range by 500 years compared to the

LGdM varve age. Finally the 2σ error range for TM-22 (84.76 – 77.17 ka BP) eruption has reduced by 400 years from the original date. This provides more constrained age estimates for these layers that will be of benefit when they are identified in other sequences.

Therefore, in total, ten newly identified and characterised tephra layers have been dated, providing ten additional isochrons for future tephra studies in the region. The model also provides an independent test of the isotopic stratigraphic scheme for the core, as the dates have been independently derived solely from tephra-based ages and avoiding biostratigraphical or climatic assumptions.

8.2.2 SA03-03

A *P_Sequence* model was applied to the dating information available for SA03-03 (Table 8.6). A k-factor of 15 was applied to the model, as was 25 cm interpolation, meaning the age every 25 cm is calculated by the model. Boundaries were placed at the top and base of the sequence and at the start and end of sapropel three, to reflect changes in sedimentation rate. They were also placed at the end of TM-24 deposition and prior to the deposition of TM-19 as this interval spans 40 ka with no additional dating information to refine the sequence of events during this period (Bronk Ramsey, 2001, Blockley *et al.*, 2004).

Table 8.6: Depths, ages and errors for the tephra layers used to construct the SA03-03 age model. The errors for the modelled dates are given at 2σ, the errors for the $^{40}Ar/^{39}Ar$ dates are at 1σ and the errors on the varve dates are expressed as 5% of the date itself, as recommended by Brauer *et al.* (2000).

	Depth (m)	LGdM tephra layer	Volcanic event	Age (yrs B.P)	Error	Dating method
1	0.25	TM-12	Greenish	18,171	804	Modelled
2	0.80	TM-13	Pomici di Base	21,332	790	Modelled
3	3.83	TM-16b	Codola (base)	33,307	1314	Modelled
4	4.13	TM-18	CI	39,280	110	$^{40}Ar/^{39}Ar$
5	4.27	TM-18-1	SMP1-a	39,313	2000	Varves
6	6.85	TM 19	MEGT	55,000	2000	$^{40}Ar/^{39}Ar$
7	9.25	TM-24	X-5	105,000	2000	$^{40}Ar/^{39}Ar$
8	9.95	TM-24-2	Unknown	103,556	5180	Varves

The graphical output for the model is shown in Figure 8.5 with the modelled dates for the tephra layers and boundaries presented in Table 8.7.

Table 8.7: OxCal model output for the SA03-03 sequence. The Modelled (BP) column is the output for each date. The layer labelled SA03-03-645 could not be correlated to a specific LGdM tephra layer and so could not be dated; its age has therefore been interpolated from the model. The A column shows the agreement index for each date.

Name	Unmodelled (BP)		%	Modelled (BP)		%	Aoverall 87.2	Depth (m)
	from	to		from	to		A	
	17931	13971	95.4	17931	15267	95.4	100	0
Greenish	18975	17370	95.4	18901	17451	95.4	105	0.25
Pomici di Base	22123	20538	95.4	21928	20458	95.4	100.1	0.8
Codola	34620	31996	95.4	35642	33226	95.4	46.5	3.83
CI	39501	39061	95.4	39476	39036	95.4	98.8	4.13
TM-18-1	43304	35324	95.4	41002	39211	95.4	130.9	4.27
SA03-03-645				55611	49036	95.4		6.45
TM-19	58991	51011	95.4	58038	51337	95.4	106.3	6.85
S3A				58011	51252	95.4		6.86
S3top				94476	53209	95.4		8.7
S3base				105871	64317	95.4		9.1
S3B				108132	100422	95.4		9.2
TM-24	108991	101011	95.4	108171	100519	95.4	97.5	9.24
TM-24-2	113745	93460	95.4	113353	101895	95.4	99	9.9
S5	121851	102051	95.4	116731	102051	95.4	100	10.1

The models overall agreement index is 86.7% and all dates are accepted by the model with all except one yielding individual AI's over 60%. The exception is the date for the Codola layer with an agreement index of 46.6%. However, as the AI of the model overall exceeds 60%, this date has been retained and does not need to be rejected. The model employs 95.4% probability error ranges for all dates.

An age has been modelled for SA03-03-645 which was correlated to one of the Citara eruptions of Ischia (see section 6.3.5) but it was not possible to say which specific layer it correlates with. The modelled age of the eruption is 55.6 – 49.0 ka BP, which would place it at the older end of the Citara age range, suggesting it could accord with the TM-18-14 group in the LGdM sequence.

The age ranges between the layers correlated to TM-19 and TM-24 are very large (up to 40,000 years in some instances) due to the limited dating information between the two layers which are separated by some 50,000 years.

In an attempt to refine the age estimates, this model was tied to the PRAD 1-2 age model using matching tephra layers. The PRAD 1-2 sequence has more dated horizons and the age ranges throughout the sequence are lower than in SA03-03. Therefore PRAD 1-2 can be viewed as the master sequence. As PRAD 1-2 has more dated tephra layers than SA03-03, this should reduce the errors for the ages in SA03-03. The resulting output of the combined age models is shown in Figure 8.6.

Figure 8.6 shows that the models have been successfully combined and that tephra layers common to both cores are assigned the same age. However, it has not reduced the uncertainty on other tephra layers within each core. Therefore the original model shown in Figure 8.5 will be used to model the ages of the isotopic changes and other bioevents discussed in Chapter 7.

8.2.3 RF93-77

A *P_Sequence* model was applied to the dating information available for RF93-77 (Table 8.8). A k-factor of 30 was applied to the model, as was 25 cm interpolation, meaning the age every 25 cm is calculated by the model. Boundaries were placed at the top and base of the sequence and at the start and end of sapropels one and three, to reflect changes in sedimentation rate. They were also placed at the end of TM-24 deposition and prior to the deposition of TM-19 as this interval spans 40 ka with no additional dating information to refine the sequence of events during this period (Bronk Ramsey, 2001, Blockley *et al.*, 2004).

Table 8.8: Depths, ages and errors for the tephra layers used to construct the RF93-77 age model. The errors for the modelled dates are 2σ, for the $^{40}Ar/^{39}Ar$ dates are 1σ and the errors on the varve dates are expressed as 5% of the date itself, as recommended by Brauer *et al.* (2000).

	Depth (m)	LGdM tephra layer	Volcanic event	Age (yrs B.P)	Error	Dating method
1	0.68	TM-3b	AP3	2,845	101	^{14}C
2	0.78	TM-5	AMS	4,495	195	Modelled
3	1.44	TM-6-5	N/A	12,073	600	Varves
4	1.98	TM-8	NYT	14,110	210	Modelled
5	2.67	TM-14-1	Faro di Punta Imperatore	21,353	1000	Varves
6	3.72	TM-18	CI	39,280	110	$^{40}Ar/^{39}Ar$
7	4.50	TM 19	MEGT	55,000	2000	$^{40}Ar/^{39}Ar$
8	7.90	TM-24	X-5	105,000	2000	$^{40}Ar/^{39}Ar$

The graphical output for the model is shown in Figure 8.7 with the modelled dates for the tephra layers and boundaries being presented in Table 8.9.

Table 8.9: OxCal model output for the RF93-77 sequence. The Modelled (BP) column provides the output for each date. The layers labelled with a RF93-77 tephra code are layers that were not correlated to an LGdM layer and therefore could not be dated; therefore their ages have been interpolated from the model. The A column shows the agreement index for each date.

Name	Unmodelled (BP)		%	Modelled (BP)		%	Aoverall 86.9	Depth (m)
	from	to		from	to		A	
	3468	-25	95.4	936	-56	95.4	100	0
TM-3b	3064	2789	95.4	3140	2794	95.4	90.9	0.68
AMST	4691	4301	95.4	4664	4280	95.4	99.2	0.78
S1top	11421	5481	95.4	6285	4653	95.4	100	0.99
S1base	11426	6476	95.4	7859	4903	95.4	100	1.14
NYT	14321	13901	95.4	14330	13911	95.4	100	1.98
TM-14-1	22352	20355	95.4	22533	20640	95.4	97	2.67
CI	39501	39061	95.4	39501	39061	95.4	100	3.72
RF93-77 414				49911	43359	95.4		4.14
TM-19	58991	51011	95.4	56043	49298	95.4	75.2	4.5
Boundary				57139	49895	95.4		4.55
RF93-77 540				67904	51506	95.4		5.4
RF93-77 604				77228	51770	95.4		6.04
S3top				92707	51930	95.4		7.08
S3base				105199	63318	95.4		7.27
Boundary				108869	95241	95.4		7.85
X5	108991	101011	95.4	108993	101394	95.4	100	7.9
	121851	102051	95.4	114791	102051	95.4	100	8.1

The model's overall agreement index is 86.9% and all dates are accepted by the model, with all individual AI's over 60%. The model employs 95.4% probability error ranges for each date. The age ranges between the layers correlated to TM-19 and TM-24 are very large (up to 40,000 years in some places) due to the limited dating information between the two layers, which spans some 50,000 years, and hence the errors are realistic. In an attempt to improve these age estimates, the RF93-77 model was tied to the PRAD 1-2 model using the tephra layers that are common to both sequences (Figure 8.8). Figure 8.8 shows the output of the combined models, where each of the tephra layers common to both cores are assigned the same age. This has reduced the age ranges of some of the older layers and boundaries within the core. These new modelled ages for RF93-77 are shown in Table 8.10.

Table 8.10: OxCal model output for the RF93-77 dates and boundaries from the combined PRAD 1-2 and RF93-77 model.

Name	Modelled (BP) from Table 8.9		New Modelled (BP)		%	Depth (m)	Significant improvement to date made?
	from	to	from	to			
	936	-56	933	-56	95.4	0	NO
TM-3b	3140	2794	3140	2794	95.4	0.68	NO
AMST	4664	4280	4671	4286	95.4	0.78	NO
S1top	6723	5481	6285	4653	95.4	0.99	NO
S1base	8366	6476	7859	4903	95.4	1.14	NO
NYT	14330	13911	14315	13896	95.4	1.98	NO
TM-14-1	22533	20640	22850	21262	95.4	2.67	NO
CI	39501	39061	39497	39059	95.4	3.72	NO
RF93-77 414	49911	43359	49879	43339	95.4	4.14	NO
TM-19	56043	49298	56223	49367	95.4	4.5	NO
Boundary	57139	49895	57093	49858	95.4	4.55	NO
RF93-77 540	67904	51506	67236	51415	95.4	5.4	YES
RF93-77 604	77228	51770	76319	51717	95.4	6.04	YES
S3top	92707	51930	91095	51995	95.4	7.08	YES
S3base	105199	63318	102877	62497	95.4	7.27	YES
Boundary	108869	95241	106098	92591	95.4	7.85	YES
X5	108993	101394	106180	99434	95.4	7.9	NO
	114791	102051	121851	102951	95.4	8.1	NO

The dates in Table 8.10 will now be used in further models when calculating the ages of the other bio- and isotopic events in the core.

The model allows dates to be estimated for the layers that could not be correlated with LGdM tephra layers (Table 8.10). RF93-77-414 is dated to between 49.8 and 43.3 ka BP, RF93-77-540 to between 67.2 and 51.4 ka BP and RF93-77-604 to between 76.3 – 51.7 ka BP. Using the geochemical information available for these tephra layers (see Sections 5.1.3, 6.4.4, 6.4.6 and 6.4.8), alongside the dates generated here, these tephra layers can now be used as isochrons if they are preserved in other sequences in the region.

8.3 Testing the published age models

Age models already exist for all three sequences, although in all cases these are not independent models. They are constructed using a combination of marine sample radiocarbon dates, bioevent correlations that assume synchronous fossil index points and the ages of the midpoints of Eastern Mediterranean Sapropel layers, which again

assume synchroneity with sapropel-equivalent events in the Adriatic Sea. These existing age models will be compared with the independent results generated in this project. In all cases, the published models are presented exactly as they are shown in the original publications, dates have not been re-calibrated or re-modelled using Bayesian statistical procedures.

8.3.1 PRAD 1-2

The dates that comprise the original PRAD 1-2 age model published for the section of the core studied in this investigation are shown in Table 8.11.

Table 8.11: Control points for the PRAD 1-2 age model of Piva *et al.* (2008a). Ages were calibrated using two calibration programmes: Calib 5.0.2 (Stuiver and Reimer, 1993) for radiocarbon ages B.P. younger than 20,000 years (marine sample = 100%, Calibration data set: Marine04 14C according to Hughen *et al.* (2004)) and the Fairbanks *et al.* (2005) programme for ages older than 20,000 years. Marine reservoir corrections were applied to all dates: ΔR value of 135.8 ± 40.8 years for the Calib 5.0.2 programme and a mean age of 258 years for the Fairbanks *et al.* (2005) programme. Those dates calibrated using Calib 5.0.2 represent 95.4% (2σ) probability error ranges and those calibrated using Fairbanks *et al.* (2005) represent 1σ probability error ranges. Dates given for sapropels represent the midpoint of each sapropel unit.

Depth (m)	Age Range (years BP)	Source
0.000	0	Modern Time
0.600	6000	L.O. *G. inflata* from Ariztegui *et al.* (2000)
1.288	8500	S1 from Lourens (2004)
1.800	12000	Top of YD from Asioli *et al.* (1999)
5.976	17726 - 16760	^{14}C date, Piva *et al.* (2008a)
7.8	19411 - 18968	^{14}C date, Piva *et al.* (2008a)
13.4	27835 - 27473	^{14}C date, Piva *et al.* (2008a)
13.8	27723	D-O IS3 Meese *et al.* (1997)
14	28287	D-O S4 Meese *et al.* (1997)
14.1	28941	D-O IS4 Meese *et al.* (1997)
14.5	30102	D-O S5 Meese *et al.* (1997)
14.6	30123	D-O IS5 Meese *et al.* (1997)
14.8	32913	D-O S6 Meese *et al.* (1997)
14.9	33455	D-O IS6 Meese *et al.* (1997)
15.22	34120	D-O S7 Meese *et al.* (1997)
15.3	35147	D-O IS7 Meese *et al.* (1997)
15.5	35706	D-O S8 Meese *et al.* (1997)
15.8	38201	D-O IS8 Meese *et al.* (1997)
16.096	39678	D-O S9 Meese *et al.* (1997)
16.386	41497	D-O S11 Meese *et al.* (1997)
16.578	42486	D-O IS11 Meese *et al.* (1997)
16.781	47130	D-O S12 Meese *et al.* (1997)
16.9	43100	14C L.C.O *G. inflata* in MIS3 Asioli (1996)
17.3	46194	D-O S13 Meese *et al.* (1997)
17.4	46911	D-O IS13 Meese *et al.* (1997)
17.5	47245	D-O S14 Meese *et al.* (1997)
18.4	54331	D-O S16 Meese *et al.* (1997)
18.7	56238	D-O IS16 Meese *et al.* (1997)
18.8	56884	D-O S17 Meese *et al.* (1997)

Depth (m)	Age Range (years BP)	Source
18.9	57539	D-O IS17 Meese *et al.* (1997)
19.486	60524	D-O S18 Meese *et al.* (1997)
19.676	61870	D-O IS18 Meese *et al.* (1997)
19.981	64441	D-O S19a Meese *et al.* (1997)
20.5	65736	D-O IS19a Meese *et al.* (1997)
20.6	66022	D-O S19 Meese *et al.* (1997)
20.9	68437	D-O IS19 Meese *et al.* (1997)
21.2	69368	D-O S20 Meese *et al.* (1997)
21.6	72751	D-O IS20 Meese *et al.* (1997)
21.8	73623	D-O S21 Meese *et al.* (1997)
23.059	81000	S3 from Lourens (2004)
24.094	91000	MIS 5.2 Martinson *et al.* (1987)
27.3	101000	S4 from Lourens (2004)
28.0	111000	MIS 5.4 Martinson *et al.* (1987)
30.6	124000	S5 from Lourens (2004)
30.95	130000	Termination II from Lisiecki and Raymo (2005)
32.5	135000	MIS 6.2 Martinson *et al.* (1987)
33.581	152500	MIS 6.4 Martinson *et al.* (1987)
35.3	172000	S6 from Lourens (2004)

A comparison between the age model for the studied section of PRAD 1-2 derived in Section 8.2.1 and the original age model of Piva *et al.* (2008a) outlined in Table 8.11 is provided in Figure 8.9. It is important to note that the Fairbanks *et al.* (2005) calibration model used by Piva *et al.* (2008a) does not use a marine based calibration curve and is not the consensus curve for this time period. The model also reports ages with only 1σ uncertainties. Therefore this may be responsible for any differences observed between the two models.

For the most part, the new results support the published model of Piva *et al.* (2008a), especially for the portion of the core covering the last 40 ka BP and certainly the general trend between the two models is the same over the entire timescale. The Piva *et al.* (2008a) model is more linear than the tephra-derived model which is more variable by comparison. Even though the trends of the models are similar both models disagree at seven key junctures. Many of these points represent important periods of climatic change (Figure 8.9) therefore resolving these differences is important. These significant offsets are not only evident in the intervals where the age errors are best constrained (Figure 8.9) but also in the older sections of the core.

At point number one, the difference between age models is only small, between 1.3 and 1.7 ka. This increases at point number two to between 1.0 and 3.0 ka. At number three, the difference between models is between 2.8 and 4.1 ka, showing another increase with depth. The differences between the models are between 3.6 and 8.0 ka at point 4,

between 3.6 and 10.8 ka at point 5, 11.9 and 5.0 ka at point 6 and finally between 14.8 and 26.0 ka at point 7. Therefore, the differences between the models increase with age and represent significant offsets between the models. This is important as the models disagree close to the timings of important climatic changes, such as the last termination, Heinrich event 3 or the last glacial maximum (Figure 8.9), which all require accurate dating if questions of synchroneity are to be addressed.

However, it is difficult to compare the models precisely for the majority of the core sequence, as the Piva *et al.* (2008a) model shows only age midpoints with no calculated error estimates. The fact that the models disagree at points where the tephra-derived model is most constrained begs the question as to whether better constrained tephra ages would lead to even further discrepancy between the two models. It also highlights the importance of taking into account error ranges when constructing age-depth plots, rather than relying on mid-point values.

8.3.2 SA03-03

Piva (2007) produced an age model for SA03-03 based on radiocarbon dates obtained from marine samples and a sequence of bioevents represented in the core that were dated in other sequences. The dates that comprise the original age model for SA03-03 are shown in Table 8.12.

Table 8.12: Control points for the SA03-03 age model from Piva (2007). Radiocarbon dates were calibrated using the Fairbanks *et al.* (2005) online calibration programme (http://radiocarbon.LDEO.columbia.edu) for ages between 0 and 55000 years. A mean age of 258 years was used as a marine reservoir correction. The calibrated dates are shown as an age range with errors reported to 2σ.

Depth (m)	Age Range (years BP)	Source
0.2	19221 - 18937	^{14}C date, Piva (2007)
1.0	23883 - 23211	^{14}C date, Piva (2007)
2.3	31128 - 30812	^{14}C date, Piva (2007)
3.6	37324 - 36532	^{14}C date, Piva (2007)
4.7	43118	L.C.O. *G. inflata* in MIS3 from PRAD 1-2, Piva (2007)
6.6	44668 - 43328	^{14}C date Piva (2007)
7.9	62000	MIS 4.2 (Bassinot *et al.,* 1994)

A comparison of the age model for SA03-03 derived in Section 8.2.2 and the original age model of Piva (2007) outlined in Table 8.12 is shown in Figure 8.10. The models can only be compared for the last 60 ka BP but even over this relatively short time scale there is very limited agreement. The models only agree at around 4 m depth and just below this, coincident with the deposition of the Campanian Ignimbrite tephra layer.

The models show most discordance between 6 and 7 metres, where the difference is between 7.0 and 13.0 ka BP. At this point, the Piva (2007) age model is controlled by a single radiocarbon date, which although calibrated, lies at the older limit of the technique when calibration is equivocal (van der Plicht *et al.*, 2004), which could be the cause of the model disagreement over this period. Even for the younger parts of the core where radiocarbon dates should be more reliable, the Piva (2007) age model is consistently older than the tephra-derived age model (Figure 8.10). The offsets between the two models could be caused by the fact the radiocarbon dates in the Piva (2007) model are derived from fossil marine organisms, with the marine reservoir correction applied to the dates unreliable.

The Piva (2007) model provides 99.9% probability error ranges for the radiocarbon dates that comprise the majority of the data-points. These are not comparable with the 95.4% ranges of the tephra-based model. With comparable error ranges, the models might show a higher level of agreement. Whilst the error ranges for the new model are high, they are considered realistic for the age of the sediments. The bottom control point of the Piva (2007) model is in good agreement with the tephra-based age model at that point (Figure 8.10) but no error range is provided for this date and so its reliability is difficult to judge.

8.3.3 RF93-77

An age model for RF93-77 was originally produced by Langone *et al.* (1996) based on radiocarbon dates obtained from foraminiferal samples. The control points used in this model are outlined in Table 8.13.

Table 8.13: Control points for the RF93-77 age model of Langone *et al.* (1996). Ages were calibrated using the calibration programme CALIB 3.0 (Stuiver & Reimer 1993) and reservoir ages of 570±35 and 660±50 years for planktic and benthic foraminifera, respectively. The errors were expressed to 1 σ. *This oldest date was calibrated using OxCal v.4.1.7 with 95.4% probability error ranges (2 σ) (Bronk Ramsey, 2009) as part of this study as it was considered too old for calibration in the original study.

Depth (m)	Age Range (years BP)	Source
0.83	5360 - 5220	^{14}C date planktic Foraminifera, Langone *et al.* (1996)
1.34	11010 - 10870	^{14}C date planktic Foraminifera, Langone *et al.* (1996)
1.84	13480 - 13280	^{14}C date planktic Foraminifera, Langone *et al.* (1996)
3.94	43970 – 41508*	^{14}C date benthic Foraminifera, Langone *et al.* (1996)

A comparison of the age model for RF93-77 derived in Section 8.2.3 and the original age model of Langone *et al.* (1996) outlined in Table 8.13 is provided in Figure 8.11.

The results can only be compared for the last ca. 45 ka BP, as the Langone *et al.* (1996) age model is based on radiocarbon dating which is limited to 50 ka (Lowe *et al.*, 2007b).

Over this time period, however, the models are generally in agreement, although the Langone *et al.* (1996) model tends to have slightly older ages. The oldest date in the Langone *et al.* (1996) data-set when calibrated using OxCal provides an age-estimate that is in close agreement with the tephra-derived model. The agreement level between the models might be much higher if 95.4% error ranges were provided for the Langone *et al.* (1996) data.

8.3.4 Summary

Comparison between the new tephra-derived age models for PRAD 1-2, SA03-03 and RF93-77 and published age models for those sequences shows general agreement. It also highlights the importance of providing 2σ error ranges rather than 1σ ranges; whilst the former reduces precision, it provides more realistic representations of accuracy. In general, the models disagree more for older parts of each sequence, which is probably due to the fact that radiocarbon dating, the most precise dating method used, applies only to the last 50 ka or so and is subject to a number of limitations, especially concerning calibrations, which generally increase in severity with age (see section 1.2.1) (Lowe *et al.*, 2007b).

8.4 Modelling the timing of isotopic and stratigraphic changes

Using the age models created for PRAD 1-2, SA03-03 and RF93-77 in section 8.2, ages of the isotope variations and stratigraphic boundaries in each of the three sequences can be interpolated, using linear regression (in Excel) between the age estimates generated by OxCal. As the OxCal models interpolate the age every 25 or 50 cm, linear interpolation is only calculating the age over short intervals where sedimentation rates will not have varied a great deal. Ages generated in this way can be validated using the *Date* function in OxCal, which provides estimates of the age for a particular depth included in the model. Both methods give comparable results and therefore the Excel method was selected for general use, as it generated more data more efficiently.

8.4.1 Timing of selected stratigraphic changes

As sapropel-equivalent events represent changes in deposition rate within the core, boundaries were placed at positions marking the start and end of each sapropel-equivalent event. This provided an age range for each sapropel-equivalent layer in each core sequence, as summarised in Table 8.14.

Table 8.14: Modelled ages for Sapropel-Equivalent events present in PRAD 1-2, SA03-03 and RF93-77, these are reflected as age ranges rather than midpoints as this reflects the true age uncertainty. Ages are in ka B.P. and X means the corresponding sapropel-equivalent event is not present in the core. The Lourens (2004) ages are calculated for the midpoints of the sapropel layers thickness in core sequence KC01B in the Mediterranean Sea.

	PRAD 1-2	SA03-03	RF93-77	Lourens (2004)
S1 end	11.6 – 4.2	X	6.2 – 4.7	
S1 start	14.3 – 8.3	X	7.8 – 4.9	
S1 age range	14.3 – 4.2	X	7.8 – 4.7	8.5
S3 end	81.5 – 72.4	94.4 – 53.2	92.9 – 51.9	
S3 start	84.1 – 75.5	105.8 – 64.3	105.1 – 63.1	
S3 age range	84.1 – 72.4	105.8 – 53.2	105.1 –63.1	81
S4 end	109.8 – 101.9	X	X	
S4 start	111.3 – 104.0	X	X	
S4 age range	111.3 – 101.9	X	X	101
S5 end	121.3 – 105.8	116.7 – 102.0	X	
S5 start	128.7 – 109.0	X	X	
S5 age range	128.7 – 105.8	X	X	124

The age ranges for sapropel-equivalent layer 3 in SA03-03 and RF93-77 are very broad, due to the fact that that it lies between tephra layers correlated to TM-19 and TM-24. As discussed in sections 8.2.3 and 8.2.4, these layers cover a span of some 50 ka BP with no other dating information, so unsurprisingly, errors for events between these layers are very large. The error ranges for all the sapropel-equivalent layers in PRAD 1-2 are better constrained, as this is a better dated sequence. Despite the large errors, however, the age ranges for sapropel-equivalent layers in each core sequence are similar and overlap, suggesting the events to be synchronous within the Adriatic. This supports the stratigraphic scheme which shows each of the sapropel-equivalent layers to be in the same stratigraphic position relative to tephra layers, when the sapropels occur in more than one sequence (see Section 7.1.1).

Piva *et al.* (2008a) apply the age of the sapropel layers in the eastern Mediterranean, using the scheme of Lourens (2004) to the sapropel-equivalent events in PRAD 1-2, making the assumption that the events in the Adriatic are synchronous with those in the wider Mediterranean Sea. When comparing these ages to the modelled ages in Table

8.14, there is broad agreement between the Lourens (2004) ages and the modelled ages. It is difficult to make more precise observations as no age errors are provided for the Lourens (2004) dates.

The age of S4 and its assumed equivalent in the Adriatic is the one noticeable discrepancy between the modelled ages and those of Lourens (2004), with the age range for the S4 equivalent event in PRAD 1-2 being older than the midpoint age of the event from Lourens (2004), suggesting the sapropel-equivalent event in the Adriatic to be significantly older than Sapropel 4 in the Mediterranean. This is supported by the tephrostratigraphic information: the tephra layer correlated to TM-24 (X-5) in all three Adriatic core sequences was deposited post-S4 and pre-S3 but in Mediterranean cores the stratigraphic position of the X-5 tephra layer is pre-S4 (Chapter 7.2.1). It therefore appears that these events are not synchronous. This could be due to mis-identification of the sapropel-equivalent event in the Adriatic sequences or to the causal mechanism for sapropel-equivalent deposition in the Adriatic differing from that influencing sapropel deposition in the wider Mediterranean.

8.4.2 Timing of regional bioevents

As discussed in Chapter 7, not all the bioevents recorded in the three sequences occur in the same stratigraphic position, whereas those that do are not well constrained by the bounding tephra layers. Given the large uncertainties, therefore, it was not possible to determine whether the bioevents are synchronous between core sequences. In order to test the evidence further, therefore, the ages of the bioevents were calculated using the *Date* function in OxCal, as explained above.

Table 8.15: Ages of bioevents common to marine cores recovered from the Adriatic Sea. Ages are presented in ka BP. X indicates absence of the relevant bioevent. Stratigraphic consistency refers to the relationship between a particular bioevent and bounding tephra layers: YES indicates consistency between the core sequences.

Regional Bioevent	Stratigraphic Consistency	PRAD 1-2	SA03-03	RF93-77
L.O. *G. Inflata*	NO	7.3 – 4.2	X	5.4 – 4.4
L.O. *S. Sellii*	N/A	15.8 – 13.9	X	X
Entry *S. Sellii*	YES	29.4 – 21.9	25.5 – 22.2	X
L.C.O. *H. balthica*	YES	32.4 – 29.6	X	35.2 – 29.1
L.C.O. *G. inflata* in MIS 3	NO	41.8 – 39.0	46.6 – 41.8	46.9 – 41.3
L.O *G. truncatulinoides* in MIS 5.1	YES	80.2 – 71.3	65.0 – 55.2	95.5 – 75.0
Entry *G. truncatulinoides* in MIS 5.1	NO	81.7 – 73.2	114.2 – 101.9	106.8 – 84.6

The L.O. of *G. Inflata* bioevent did not occur in the same stratigraphic position with respect to the position of the tephra layer correlated to TM-5 in both PRAD 1-2 and RF93-77. Nevertheless, the age ranges for this event in both cores overlap suggesting the events to be broadly synchronous. This supports the suggestion made in section 7.2.2 that the reason for the apparent discrepancy in the sequence of events in the RF93-77 sequence is due to the length of time the core had been stored before sub-sampling. Core shrinkage has distorted the RF93-77 sequence, rather than the events being ordered in a different way from PRAD 1-2. The date of this bioevent in PRAD 1-2 of 7.3 – 4.2 ka BP is in agreement with a published age for the same event of c. 6 ka BP (Jorissen *et al.,* 1993) but the former has more realistic errors.

The L.O. of *S. sellii* is observed only in the PRAD 1-2 sequence. Its age is modelled as 15.8 – 13.9 ka BP, which is in agreement with the published radiocarbon age of 12.7 ^{14}C ka B.P. When calibrated this gives an age range of approximately 15.5 – 14.7 ka B.P (Jorissen *et al.,* 1993, Asioli, 1996).

The Entry of *S. sellii* and the L.C.O of *H. balthica* both sit between the same boundary tephra layers (see section 7.1.2) but are not constrained tightly enough in each sequence to ascertain whether they occurred synchronously. However, when one considers the ages derived for these events, it is possible they were contemporaneous. The Entry of *S. sellii* is dated to 29.4 – 21.9 ka BP in PRAD 1-2 and to 25.5 – 22.2 ka BP in SA03-03 (Table 8.15). The SA03-03 age range is better constrained but falls within the age range of the PRAD 1-2 event. The L.C.O of *H. balthica* is dated to between 32.4 and 29.6 ka BP in PRAD 1-2 and between 35.3 and 29.1 ka BP in RF93-77, again with the more constrained age from PRAD 1-2 fitting within the RF93-77 age range. These data support the view that this bioevent is synchronous within the Adriatic.

However, it should be noted that the modelled ages for the Entry of *S. sellii* are both markedly older than the published radiocarbon date obtained for this event of 15.3 ^{14}C ka B.P. (Jorissen *et al.,* 1993). No uncertainty values are provided but when the midpoint of the age is calibrated, an age range of 18.7 – 18.2 ka B.P is generated.

The L.C.O of *G. inflata* was not found to be in the same stratigraphic position in all three cores, suggesting it was not synchronous across the Adriatic Sea. It was found to lie between the TM-18 and TM-19 tephra layers in all three sequences but preceded the

deposition of the TM-18-1 layer in SA03-03 while it post-dated the TM-18-1 layer in PRAD 1-2. This relationship is supported by the age estimates obtained for the event in each sequence. In SA03-03, the event is dated to between 46.4 and 41.8 ka BP, which is very similar to the event age obtained in RF93-77 of 46.9 - 41.3 ka BP. The age for this event in PRAD 1-2 however, is 41.8 to 39.0 ka BP, which does not overlap with the ages in the other two sequences, possibly indicating the event to be diachronous within the Adriatic.

On the other hand, the dates obtained for the L.O of *G. truncatulinoides* in MIS 5.1 indicate that this bioevent could be synchronous in the central Adriatic basin. Age ranges of 80.2 – 71.3 ka BP and 95.5 – 75.0 ka BP were obtained from the PRAD 1-2 and RF93-77 sequences respectively. However, the age of the L.O of *G. truncatulinoides* in MIS 5.1 in the SA03-03 sequence is considerably younger (Table 8.15) with no overlap with the age ranges from the other cores. This event does not, therefore, appear to be synchronous across the whole Adriatic Sea.

Finally, the dates for the entry of *G. truncatulinoides* in MIS 5.1 support the stratigraphy which indicated that the events were not synchronous in the central and southern Adriatic basins (Table 8.15). However, the dates of the event in PRAD 1-2 (81.7 – 73.2 ka BP) and RF93-77 (106.8 – 84.6 ka BP) also show the events are unlikely to be synchronous within the central Adriatic basin as well, even though the event occurs between the same bounding tephra layers (Figure 7.3).

The independent dating of foram bioevents in each of the Adriatic sequences has shown that not all the events thought to represent regional bioevents are synchronous across the Adriatic. There is no overall consistency, with some events, such as the L.O. of *S. sellii*, appearing to be synchronous between the central and southern Adriatic. However, the L.O. of *H. balthica* appears to be synchronous in the central Adriatic basin only and the L.O. of *G. inflata* and the Entry of *G. truncatulinoides* to be diachronous across the whole basin or within the central Adriatic basin alone. Hence, caution should be exercised when assigning a single age to some bioevents and assuming it to apply to other records, even within the confined body of the Adriatic Sea.

8.4.3 Timing of $\delta^{18}O$ isotopic changes

The timing of $\delta^{18}O$ isotopic changes in the studied sections of each of the core sequences are shown in Figure 8.12. In some cases, the age uncertainties for individual isotope data-points are only centennial in scale, whereas for others the uncertainties rise as high as ± 20,000 years, which may limit the ability to robustly correlate the records at these points. The PRAD 1-2 sequence (Figure 8.12a) has smaller uncertainties than the other 2 sequences which is to be expected as there are more dating control points contributing to the age model. Both the SA03-03 and RF93-77 records have poor chronological control before c. 55 ka BP (Figure 8.12 b+c). As PRAD 1-2 has more dating information and lower age uncertainties, it is considered the master record against which SA03-03 and RF93-77 can be compared.

The records have been aligned by age in Figure 8.13 to assess whether the main isotopic changes evident in each sequence are coeval. It is important to note that the stratigraphic boundaries marked on Figure 8.13 are plotted at the mid-point of the computed age-range for each boundary and therefore do not reflect the statistical errors on each boundary.

It is clear that PRAD 1-2 and SA03-03 show the same isotopic trends at similar times, such as lighter $\delta^{18}O$ values at the end of S3 at about 75 ka BP (number 1 on Figure 8.13) shifting to heavier $\delta^{18}O$ values in MIS 4 at about 60 ka BP (number 2 on Figure 8.13). The first trend is also observed in RF93-77 but it is not possible to make further comparisons as the $\delta^{18}O$ *G. ruber* record is not complete.

In general, the marine isotope stage boundaries appear to occur at similar times and last for similar durations in each of the three sequences. For example, the start of MIS 3 is dated to 58.8 – 50.9 ka BP in PRAD 1-2, to 67.6 – 51.7 ka BP in SA03-03 and to 59.1 – 50.5 ka BP in RF93-77. These dates all show significant overlap, which supports the overall stratigraphic scheme and suggests the events to be synchronous across the Adriatic. The end of MIS 3 is dated to 30.2 – 23.3 ka BP in PRAD 1-2, to 29.0 – 25.0 ka BP in SA03-03 and to 34.2 – 28.2 ka BP in RF93-77. The RF93-77 date is older but its range still overlaps with the other ages for this boundary, again indicating the event to be synchronous between the sequences. The duration of MIS 3 in PRAD 1-2 is between 35 and 20 ka, in SA03-03 is between 42 and 22 ka and in RF93-77 is between

30 and 16 ka, again showing a degree of accordance in the estimated durations for all three sequences in the central and southern Adriatic Sea.

There is also a good agreement between PRAD 1-2 and RF93-77 in the younger parts of each record. The onset of the Younger Dryas (YD) is dated to 14.3 – 11.5 ka BP in PRAD 1-2 and to 13.9 – 12.3 ka BP in RF93-77, while the end of the YD is dated to 14.1 – 8.2 ka BP in PRAD 1-2 and to 10.2 – 7.3 ka BP in RF93-77 (Figure 8.13). The timing of MIS 5.2, on the other hand, appears to be different between RF93-77 and PRAD 1-2 (Figure 8.13). However, the relationship demonstrated between MIS 5.2 and the tephra layers in each sequence correlated to TM-24 suggests MIS 5.2 was in the same stratigraphic position in each core. Therefore, when the errors on the isotope ages are considered, the start of MIS 5.2 is estimated to between 90.2 – 77.7 ka BP in PRAD 1-2 and to 105.5 – 78.9 in RF93-77, while the end of MIS 5.2 is dated to 84.5 – 76.5 in PRAD 1-2 and to 104.5 – 78.3 ka BP. Since there is considerable overlap in the age ranges of this event, the possibility that the records are synchronous cannot be discounted. Greater chronological control for the RF93-77 record is needed to reduce the dating errors and to test this hypothesis more robustly.

In general, it is concluded that there is a satisfactory degree of agreement between the timing of the main isotopic changes in each record. The independent age models therefore support the stratigraphic schemes proposed by Piva *et al.* (2008a), Piva (2007) and Asioli (1996) for PRAD 1-2, SA03-03 and RF93-77 respectively, which showed that tephra layers common to each core are positioned in the same isotopic subdivisions (Section 7.1.3). There is a need, however, to reduce the uncertainties in the age models for both SA03-03 and RF93-77, in order to increase the confidence of this conclusion. The PRAD 1-2 sequence is better dated with realistic age ranges throughout and therefore will be used as the master sequence for comparison with other records.

8.4.4 Marine-Terrestrial correlations

8.4.4.1 The LGdM record

In section 7.2.4.1, the stratigraphic positions of tephra layers common to PRAD 1-2 and the LGdM record were compared and the majority occurred in comparable positions on the pollen record for LGdM and the isotope stratigraphy for PRAD 1-2, suggesting that

the proxy data from both sequences record similar changes at similar time periods. This suggestion of synchroneity between the two records can now be tested using the independent PRAD 1-2 age model and the age model generated for the LGdM sequence by Brauer *et al.* (2007).

The TM-27 tephra in LGdM occurs during the Melisey 1 stage (Figure 7.10) and the tephra layer correlated to TM-27 in PRAD 1-2 occurs during MIS 5.4, both of these events represent cold stages. The stratigraphic correlations are supported by the ages of both events generated by the independent models. The onset of MIS 5.4 in PRAD is dated to 109.2 ± 4.2 ka BP and the onset of the Melisey 1 stage in LGdM is dated by the LGdM varve chronology to 109.5 ± 1.4 ka BP (Brauer *et al.*, 2007). The end of MIS 5.4 in PRAD 1-2 is dated to 108.0 ± 3.5 ka BP and the end of the Melisey 1 stage is dated by Brauer *et al.* (2007) to 107.6 ka BP. No errors are quoted for this age but if a 5% error is adopted, as recommended by Brauer *et al.* (2000) then the full age estimate for the end of the Melisey 1 stage in LGdM is 107.6 ± 5.3 ka BP. This indicates that the ages for the MIS 5.4 event in PRAD 1-2 generated by the tephra-derived age model, are comparable to the independent varve ages of the event in LGdM.

The Melisey 2 stage on land was correlated with MIS 5.2 by Brauer *et al.* (2007). In the LGdM sequence, the TM-22 tephra layer is deposited during this period prior to the transition to the St Germain 2 stage (Figure 7.10). The layer correlated to TM-22 in PRAD 1-2 is also deposited during MIS 5.2 and therefore the correlation of these events is supported by the new tephrostratigraphic correlations. MIS 5.2 in PRAD 1-2 is dated to between 86.0 ± 7.9 ka BP and 80.7 ± 3.9 ka BP, which agrees within errors with the age of the Melisey 2 stage in LGdM (between 90.65 ± 4.5 ka and 87.98 ± 4.3 ka BP). Even though the uncertainty on the PRAD 1-2 ages is large, the presence of the same tephra layer in both of these events supports the idea of synchroneity between the marine and terrestrial systems at this point and highlights the importance of tephra layers as a stratigraphic tool.

Overall, the correlation of Melisey 1 with MIS 5.4 and of Melisey 2 with MIS 5.2 is supported by the new chronology as well as the tephrostraigraphy, suggesting these events occur synchronously on land and in the sea in this region. In turn this would imply a common forcing factor affecting the pollen percentages on land and the oxygen isotope ratio values in the Adriatic.

8.4.4.2 Comparisons with Greenland ice-core records

Fluctuations in both the PRAD 1-2 $\delta^{18}O$ record and the LGdM pollen percentages have been assumed to represent D-O cycles (Piva *et al.,* 2008a; Fletcher *et al.,* 2010; Allen *et al.,* 1999). In section 7.2.4.4, it was shown that at no time during the sequences are the numbered interstadials bracketed by the same pairs of tephra layers which suggests that the numbering of the interstadials in one or possibly both of the records is incorrect and therefore cannot be used as a basis for correlation or synchronisation between records.

Using the tephra-derived age model for PRAD 1-2, it is possible to independently date the interstadials that have been correlated with the GISP2 ice core record and to compare the derived ages of the sequence of interstadials with corresponding ice core ages (Figure 8.14 A).

The general trends of the PRAD 1-2 $\delta^{18}O$ record on the independent timescale (Figure 8.14A (iii)) and the GISP2 $\delta^{18}O$ record (Figure 8.14A (i)) are similar, with the PRAD 1-2 record shifting to heavier values just after a light isotope peak at 90 ka BP and the GISP2 record shifting to lighter values after a heavy isotope peak also at 90 ka BP. The PRAD 1-2 record shifts to heavier values ending at about 72 ka BP, which corresponds to a shift to lighter values also ending around 72 ka BP in the GISP2 record. From about 25 ka BP, the isotope values shift to lighter values in PRAD 1-2 and to heavier values in GISP2. Therefore, the general trend in the records appears to occur at similar times in both sequences.

However, when the detail of the PRAD $\delta^{18}O$ record plotted on the new tephra derived time-scale are compared with their equivalent isotope fluctuation on the GISP2 ice core, it is clear that the fluctuations do not occur at the same time (Figure 8.14A). This is supported by Figure 8.14B which directly compares the PRAD 1-2 isotope fluctuations plotted on the different PRAD timescales and include the age error for both models. Whilst some of the isotope changes occur at similar times within errors (e.g. IS18 at 61.8 ± 6 ka on the GISP2 timescale and at 62.4 ± 9 ka on the tephra timescale), and some of the fluctuations do not overlap even within errors (e.g. IS11 at 42.4 ± 0.85 ka on the GISP2 timescale and at 39.4 ± 0.37 ka on the tephra timescale), the majority of the fluctuations only partially overlap when the errors are considered, this is summarised in Table 8.16.

Table 8.16: Age estimates for the assumed D-O stadials and interstadials using the GISP2 age-depth model and the independent PRAD 1-2 tephra-based age-depth model. Those ages highlighted in grey do not accord. Errors for the GISP 2 Timescale are calculated from Meese *et al.* (1997).

	GISP 2 Timescale		PRAD 1-2 Tephra Timescale	
	Age (years BP)	**Error**	**Age (years BP)**	**Error**
GI-3	27723	554	30268	1396
GS-4	28287	566	31043	1450
GI-4	28941	579	31430	1477
GS-5	30102	602	31938	1707
GI-5	30123	602	32066	1765
GS-6	32913	658	32421	1711
GI-6	33455	669	32598	1684
GS-7	34120	682	34107	1913
GI-7	35147	703	34346	2128
GS-8	35706	714	34822	2559
GI-8	38201	764	35585	2829
GS-9	39678	794	36374	2913
GS-11	41497	830	38116	1297
GI-11	42486	850	39418	369
GS-12	42713	854	39698	669
GS-13	46194	2310	40569	1504
GI-13	46911	2346	40794	1697
GS-14	47245	2362	41020	1890
GS-16	54331	2717	47542	7237
GI-16	56238	2812	54884	3925
GS-17	56884	2844	55177	4336
GI-17	57539	5754	55470	4747
GS-18	60524	6052	60596	8397
GI-18	61870	6187	62444	9140
GS-19a	64441	6444	64580	9246
GI-19a	65736	6574	73044	3662
GS-19	66022	6602	73130	3705
GI-19	68437	6844	73406	3814
GS-20	69368	6937	73773	3948
GI-20	72751	7275	74502	4192
GS-21	73623	7362	74858	4271

This shows that when the PRAD 1-2 $\delta^{18}O$ fluctuations are plotted on an independent timescale, many of the events do not correspond to the numbered stadials or interstadials assumed by Piva *et al.* (2008a). This supports the findings in Chapter 7 and goes further to show that the assumed millennial-scale isotopic variations between Greenland and PRAD 1-2 are invalid on the basis of available evidence. The $\delta^{18}O$ fluctuations may be incorrectly numbered, as the independent ages from PRAD 1-2 do not correspond to the ice core ages. It is not possible to say whether the $\delta^{18}O$ fluctuations are D-O cycles but this shows that caution should be exercised in assuming events are synchronous and therefore, importing ages into new sequences as the use of an independent age model in this case has shown that many of the events cannot be synchronous.

However, the more recent NGRIP ice core is now seen as the standard reference core. Firstly, because it is complete and continuous through the last glacial-interglacial cycle (Wolff *et al.,* 2010) and it also has the most complete multi-parameter layer counting dating over the last 60 ka (Svensson *et al.,* 2008). Secondly, the Meese-Sowers GISP2 time scale (Meese *et al.,* 1997) disagreed with the modelled "ss09sea" time scale that was applied to the GRIP ice cores by several thousand years after 40 ka (Svensson *et al.,* 2008). The current timescale based mainly on annual layer counting of the NGRIP core is known as GICC05 (Wolff *et al.,* 2010).

In order to establish if the disagreement in time scales over some of the period covering D-O cycles is responsible for the lack of agreement between the PRAD 1-2 $\delta^{18}O$ fluctuations plotted on the GISP2 timescale and the tephra-derived timescale, the PRAD 1-2 $\delta^{18}O$ fluctuations will now be compared with the GICC05 timescale back to 60.2 ka b2k and beyond 60.2 ka b2k with the "ss09sea" model timescale shifted to younger ages by 705 years (Wolff *et al.,* 2010). Due to assumptions with the method of extending the timescale beyond 60.2 ka b2k, the ages of events older than this must be treated with some caution.

The comparison of the PRAD $\delta^{18}O$ record and NGRIP $\delta^{18}O$ record is shown in Figure 8.15 and it is clear, once again, that the midpoints of the isotope ages do not match as closely as they should if the PRAD $\delta^{18}O$ fluctuations do indeed represent D-O cycles and are correctly numbered. When comparing the two records, it appears that only GI-5 and GI-6 correlate satisfactorily in both records. However, Figure 8.15 does not take into account the errors on each isotope measurement, which may affect the potential correlations. Therefore, the errors on each of the interstadials from both records are compared in Table 8.17.

Table 8.17: Ages of the assumed Greenland interstadials (GI) using the GICC05modelext timescale and independent PRAD 1-2 tephra age-depth model. The GICC05modelext uses the GICC05 timescale for dates until 60.2 ka b2k. Dates older than this are based on the "ss09sea" modelled time scale, shifted by 705 years to younger ages. For both the GICC05modelext and PRAD tephra timescales 2σ errors are shown. Those ages highlighted in grey do not agree with each other at all.

	GICC05modelext Timescale			**PRAD 1-2 Tephra Timescale**	
	Age (years BP)	**Error**	**Reference**	**Age (years BP)**	**Error**
GI-3	27730	832	Andersen *et al.* (2006)	30268	1396
GI-4	28850	898	Andersen *et al.* (2006)	31430	1477
GI-5	32450	1132	Andersen *et al.* (2006)	32066	1765
GI-6	33690	1212	Andersen *et al.* (2006)	32598	1684
GI-7	35430	1322	Andersen *et al.* (2006)	34346	2128
GI-8	38170	1450	Andersen *et al.* (2006)	35585	2829
GI-11	43290	1736	Svensson *et al.* (2008)	39418	369
GI-12	46810	1912	Svensson *et al.* (2008)	39978	968
GI-13	49230	2030	Svensson *et al.* (2008)	40794	1697
GI-14	54170	2300	Svensson *et al.* (2008)	43860	4599
GI-15	55750	2392	Svensson *et al.* (2008)	45502	6217
GI-16	58230	2512	Svensson *et al.* (2008)	54884	3925
GI-17	59390	2574	Svensson *et al.* (2008)	55470	4747
GI-18	64045	?	Wolff *et al.* (2010)	62444	9140
GI-19	72280	?	Wolff *et al.* (2010)	73406	3814
GI-20	76400	?	Wolff *et al.* (2010)	74502	4192

When considering the age ranges of the interstadials, 5 of the 16 do not overlap at all and a further 3 only partially overlap. Interstadials 18 – 20 do not have error estimates but, if their error ranges were similar to GI-17 and, given the large error ranges on the PRAD 1-2 tephra timescale events, these ages are likely to agree within errors. Interestingly, when comparing the events, with the GICC05 timescale, the ages of interstadials 5, 6, 7 and 17 agree, whereas when comparing with the GISP2 timescale the ages of interstadials 6, 7, 8, 16, 17, 18 agreed. Therefore, when comparing with the newer GICC05 timescale, fewer of the events agree, supporting the fact that if the PRAD 1-2 $\delta^{18}O$ fluctuations do represent D-O cycles, they are incorrectly numbered.

Despite the supposed D-O cycles in PRAD 1-2 not correlating with the correct Greenland Interstadial on either the GISP2 or the GICC05 timescale, Figure 8.14A showed that the general trends in $\delta^{18}O$ values between PRAD 1-2 and GISP2 occurred at similar times. The trend in the NGRIP and PRAD 1-2 $\delta^{18}O$ records can be observed in Figure 8.16 and again, for a large part of the time period, the trends are very similar. Between 120 ka and 80 ka the records are slightly offset, with similar trends being observed in both sequences but with the main changes occurring slightly later in the

PRAD 1-2 profile. However, from 80 ka to the present, the main trends in both records appear to occur at similar times (Figure 8.16).

Therefore, this suggests that whilst the rapid and short lived $\delta^{18}O$ fluctuations such as D-O cycles may not be replicated in the PRAD 1-2 sequence, the general trend seen in the Greenland ice core $\delta^{18}O$ record is replicated by the PRAD 1-2 sequence. This suggests that the age model for PRAD 1-2 requires further refinement before more precise correlations with Greenland ice-core records will be possible. It does, however, suggest that the PRAD 1-2 oxygen isotopic variations reflect regional climatic forcing. This is also supported by the synchroneity between the PRAD 1-2 and LGdM records (section 4.4.1).

8.5 Key age modelling outcomes

This chapter has examined the chronologies of the three studied Adriatic sequences and through this process has produced best-estimate age models for each. The age models are independent of any climatic or biostratigraphic assumptions and do not include any radiocarbon dates based on marine samples, in order to avoid distortions caused by the marine reservoir effect. Through the production of these age models and their applications, a number of key outcomes of the information presented in this chapter are as follows:

- The PRAD 1-2 $\delta^{18}O$ fluctuations which were correlated with GISP2 D-O cycles by Piva *et al.* (2008a) appear to be incorrectly numbered and cannot be supported with the tephra based evidence presented here. When the same PRAD 1-2 $\delta^{18}O$ fluctuations are compared with the GICC05 timescale, the proposed interstadial events are also not in accord, which casts doubt over the correlation of PRAD 1-2 $\delta^{18}O$ fluctuations to D-O events (Figure 8.14 and 8.15).
- The general trend of the PRAD 1-2 $\delta^{18}O$ and NGRIP records is very similar between 80 ka and the present day (Figure 8.16), suggesting the PRAD 1-2 isotope variations reflect regional climatic forcing.
- Bioevents that are assumed to represent synchronous markers across the Adriatic are in some cases not synchronous, while in other cases, are, but only in part of the basin. Care should therefore be taken when importing ages for these events

into other sequences where no independent tests of the validity of the correlations are available.

- The timings of sapropel-equivalent events within the Adriatic do appear to be synchronous across the basin but the age ranges for some of the events is too large to be certain of this.
- There is good agreement with the timing of the sapropel-equivalent events in the Adriatic and the sapropel events in the wider Mediterranean, with the exception of S4, where age estimates are offset between the Adriatic and wider Mediterranean.
- Improved age estimates for three Italian tephra layers (the Greenish, the Pomici di Base and the Codola) that incorporate all the available dating information for each layer have been generated.
- The importance of presenting age-depth models with realistic error estimates (2σ) has been highlighted by comparing the new age models for the sequences with previously published chronological information.

9. Conclusions

In this concluding chapter, following a brief re-cap of the thesis objectives, the main findings of the research project will be summarised, with emphasis on those that are considered to (a) advance the regional tephrostratigraphy of the Adriatic Sea and adjacent areas and (b) those that have an important bearing on published correlation and chronological schemes for the region. Following this, attention is drawn to particular problems encountered in this research, which fall into three categories: (i) practical, in terms of detecting, extracting and 'fingerprinting' individual tephra layers; (ii) taphonomic, in terms of establishing the processes that led to tephra deposition and preservation in a marine sedimentary context and (iii) interpretational, in terms of testing the validity and precision of the age models presented on the basis of the new tephra-based evidence. The chapter closes with some suggestions for improvement in future tephrostratigraphical research in the region.

9.1 Thesis aims and objectives

The overarching aim of this investigation was to use tephrochronology as a tool for improving the chronology of palaeoenvironmental records in the Central Mediterranean. The key objectives were:

1. To examine the potential of distal tephra layers as a stratigraphic tool to improve the synchronisation of Central Mediterranean marine records and to compare marine sequences with terrestrial records. This aim encompassed the following specific objectives:
    a. To establish whether Adriatic records are dominated by local (Adriatic Sea) influences or reflect wider regional (Mediterranean) forcing factors.
    b. To test the assumed synchroneity between Central Adriatic sapropel-equivalent events and Eastern Mediterranean Sapropels.
    c. To examine whether the correlation of the PRAD 1-2 and SA03-03 $\delta^{18}O$ variations to D-O cycles are robust and whether those correlations are supported by the correlation of LGdM pollen fluctuations with Greenland interstadials.
    d. To test for synchroneity of environmental changes in a transect of sites across the Adriatic Sea.

2. To develop age models for Central Mediterranean marine records that are not only independent of climatic and biostratigraphic assumptions but that also avoid the problems of marine-based radiocarbon dating.
3. To use tephra-based age models to determine the timing of regional palaeoenvironmental changes and to assess the reliability of synchronous isotopic and biostratigraphic events and boundaries. In particular:
    a. To examine whether oxygen isotope records show consistent temporal variations between the Central and Southern Adriatic.
    b. To examine whether regional bioevents identified in the Adriatic records provide time-parallel marker layers.

9.2 Summary of main findings

The main findings of this research can be divided into two main areas, tephra findings and Central Mediterranean stratigraphy findings.

9.2.1 Tephra findings

- A total of 54 tephra layers have been identified across all three of the Adriatic marine cores studied, of which only 8 are visible layers, the remainder being classified as cryptotephras. 52 of the layers have been geochemically characterised, 50 have been matched to an Italian source volcano and 32 have been correlated to individual tephra layers preserved in the Lago Grande di Monticchio record.
- Of the 20 layers that could not be correlated to an LGdM tephra layer, 3 that occur in PRAD 1-2 are older than the LGdM sequence and 1 layer in PRAD 1-2 is thought to represent reworking of an older layer. However, the remaining 16 layers represent tephra layers that are not preserved in LGdM and therefore it has not been possible to assign them to a known eruption. It is likely that most of these represent previously unknown eruptions of Italian volcanoes.
- Six of the tephra layers (TM-14-1, TM-18-1d, TM-20-7, TM-24-2, TM-38a and TM-39) identified in this study have been recognised for the first time outside the LGdM sequence, extending the known distributions of these layers eastwards.
- The shard counts presented in sections 5.1, 5.2 and 5.3 show that discrete non-visible tephra layers can be preserved in discrete bands and in order of superposition in a marine setting.

- A hierarchical structure for grouping tephra layers has been adapted from Matthews (2009) and applied to Italian volcanoes for the first time. This has led to a tephra ranking system for the LGdM dataset which ranked tephra layers according to their geochemical distinctiveness. 1^{st} – 4^{th} ranked tephra layers provide structure for the less geochemically distinctive 5^{th} and 6^{th} ranked tephra layers, which can then be assessed on the basis of both their geochemical signatures and their stratigraphic positions, relative to the positions of the higher-ranked tephra layers in each sequence. This has allowed a comprehensive tephra 'lattice' to be constructed for the LGdM tephra layers and enables unknown eruptions to be queried against a reference dataset in an objective manner.
- Three tephra layers (TM-18, TM-19 and TM-24) are common to all three of the studied Adriatic sequences. A further three layers (TM-5, TM-8 and TM-14-1) are common to PRAD 1-2 and RF93-77 and four layers (TM-12, TM-13, TM-16b, TM-18-1d) are common to PRAD 1-2 and SA03-03.
- The age estimates of three LGdM tephra layers that are widespread in the region have been revised using Bayesian age modelling procedures that incorporate all of the available dating information. The results suggest that at present, the best 95.4% confidence calendar age estimate for the Greenish tephra (TM-12) is 18,975 – 17,367 cal yr BP, the Pomici di Base tephra (TM-13) is 22,123 – 20,542 cal yr BP and the Codola tephra (TM-16b) is 34,622 – 31,993 cal yr BP. The 2σ error ranges for both the Pomici di Base and Codola layers were significantly improved compared with previously published age estimates.
- The refined tephra-based age-estimates have been integrated with other tephra dating information and used to provide Bayesian-based age models for each of the three studied sequences. The age models do not assume linear sedimentation rates and do not make any climatic or biostratigraphical assumptions.
- The age modelling process has improved the error ranges of five of the tephra layers present in the three studied sequences. The age of the Pomici di Base (TM-13) in PRAD 1-2 is further refined to 21,639 – 20,238 cal yr BP. The age of TM-14-1 in PRAD 1-2 is refined to 22,749 – 21,137 cal yr BP, an improvement of 200 years on the 2σ error range, compared with the LGdM varve age. The age of TM-18-1 in SA03-03 is refined to 41,002 – 39,211 cal yr BP, which reduces the 2σ error range by 1200 years from the LGdM varve age. The modelled age range for TM-20-7 is now 76,577 – 69,338 cal yr BP, which has reduced the 2σ error range by 500 years compared to the LGdM varve age. Finally, the 2σ error range for the

TM-22 (84,763 – 77,166 cal yr BP) eruption has been reduced by 400 years from the original date (Section 8.2).

- Age ranges for the 16 layers that represent tephra layers not identified in LGdM and therefore not assigned to known eruptions have been modelled. These, along with the geochemical data for these layers, will allow them to be used as isochronous markers if found in future tephra studies. These results are summarised in Table 9.1.

Table 9.1: Tephra layers in PRAD 1-2, SA03-03 and RF93-77 that were not correlated to an LGdM tephra layer, their chemical classification (after Le Bas *et al.* (1986) and their 95.4% confidence calendar age estimate. Tr = trachyte, P = phonolite, TP = tephriphonolite

Tephra Layer	Chemical Classification	Modelled 95.4% calendar age estimate (BP)	
		from	to
PRAD-120	Tr/P	11,309	5,941
PRAD-205	Tr/P	14,361	10,161
PRAD-231	Tr/P/TP	14,544	13,832
PRAD-267	Tr/P/TP	15,361	13,880
PRAD-323	Tr/P/TP	15,822	13,942
PRAD-329	Tr/P/TP	16,149	13,999
PRAD-404	Tr/P/TP	16,909	14,231
PRAD-480	P/Tr	17,574	14,602
PRAD-1130	Tr/P	26,164	21,077
PRAD-1474	Tr/P	34,583	31,260
PRAD-2605	P	108,253	100,478
PRAD-3336	P	136,858	122,912
SA03-03-645	Tr	55,611	49,036
RF93-77-414	Tr/P	49,911	43,359
RF93-77-540	Tr/P	67,904	51,506
RF93-77-604	Tr/P	77,228	51,770

9.1.2 Central Mediterranean stratigraphic findings

The identification of tephra layers in three Adriatic marine sequences has led to the following conclusions being drawn about the existing Central Mediterranean stratigraphic schemes.

- The general trends in the $\delta^{18}O$ records from the three studied Adriatic sequences indicate the response to have been broadly similar in each of the locations. However, in one interval (between the deposition of TM-19 and TM-18-1) the $\delta^{18}O$ records for PRAD 1-2 and SA03-03 seem to be in anti-phase, suggesting different

factors could have been forcing $\delta^{18}O$ variations in the Central and Southern Adriatic at that time. However, the isotope curve for SA03-03 is at too low a resolution while that for RF93-77 is incomplete, which constrains attempts to establish whether oxygen isotope variations are exactly synchronous within these three Adriatic core sequences.

- Planktic $\delta^{18}O$ records from the Adriatic, Tyrrhenian and Ionian Seas appear to be responding to the same forcing factor in those intervals bounded by key tephra isochrons. The tephra evidence suggests that the Central Adriatic record, in particular, reflects regional forcing factors more than local conditions, such as the potential isolation of the basin during episodes of low sea level. This also suggests that the difference observed between the PRAD 1-2 and SA03-03 $\delta^{18}O$ records could indicate that at times, the Southern Adriatic Sea is responding to local forcing factors and is not representing the regional signal.
- Caution is advised when assuming foraminiferal bioevents occur synchronously across the Adriatic Sea. Tephrostratigraphy and tephra-based age modelling suggests instead that key bio-event markers such as the L.C.O of *G.inflata* in MIS 3 and the Entry of *G. truncatulinoides* in MIS 5.1 are not synchronous.
- Sapropel-equivalent events in the Adriatic appear to occur synchronously between the Central and Southern Adriatic basins.
- However, the sapropel-equivalent events in the Adriatic cannot be assumed to be synchronous with Eastern Mediterranean sapropels. The stratigraphic relationship between the X-5 tephra layer and sapropel 5/sapropel-equivalent 5 are not consistent. While such disparity has been demonstrated for only one example so far, nevertheless, this raises questions about such assumptions which need to be tested more robustly.
- The correlation of PRAD 1-2 and SA03-03 $\delta^{18}O$ fluctuations to GISP2 interstadials does not appear to be robust, as the numbered interstadials in each sequence are not bounded by the same tephra layers. This suggests the numbering of one or both of the sequences to be incorrect.
- The same is true when the LGdM pollen variations assigned to Greenland interstadials are compared with the PRAD 1-2 $\delta^{18}O$ fluctuations, assigned independently to Greenland interstadials. At no time during the studied interval do the tephra layers bracket or occur concurrently within the same interstadial in either sequence. This suggests that the numbering of one or both of the records is

incorrect and casts doubt on the matching of assumed D-O cycles as a method of correlation or synchronisation.

- However, the stratigraphic position of tephra layers in PRAD 1-2 and LGdM suggests that the marine oxygen isotope and terrestrial pollen record responds synchronously to external forcing factors.
- The PRAD 1-2 $\delta^{18}O$ fluctuations which were correlated with GISP2 D-O cycles by Piva *et al.* (2008a) appear to be incorrectly numbered. When the same PRAD 1-2 $\delta^{18}O$ fluctuations are compared with the GICC05 timescale, the proposed interstadial events also are not in accord, which therefore also casts doubt over the correlation of PRAD 1-2 $\delta^{18}O$ fluctuations to D-O events (Figures 8.14 and 8.15).
- The general trends of the PRAD 1-2 $\delta^{18}O$ and NGRIP records appear very similar between 80 ka and the present day (Figure 8.16), suggesting that the PRAD 1-2 isotope variations reflect regional climatic forcing.

9.2.3 Summary

The main findings of the thesis discussed in the preceding sections have highlighted how the thesis aims and objectives have been met. Tephra layers have been used as stratigraphic tools to improve the synchronisation of Central Mediterranean marine records and to compare marine sequences with terrestrial records. Age models for Adriatic marine sequences have been produced which are free from climatic and biostratigraphic assumptions. These age models have been used to determine the timing of regional palaeoenvironmental changes and also to assess the reliability of synchronous isotopic and biostratigraphic events and boundaries in the region.

9.3 Procedural difficulties encountered in the research

Some of the challenges associated with conducting cryptotephra studies in marine deposits were discussed in section 2.1. As anticipated, and despite attempts to minimise their influence, several procedural difficulties have proved particularly challenging during this research project, as summarised below.

9.3.1 Assessing the stratigraphic integrity of tephra horizons

As introduced in section 2.1.1, pinpointing the precise stratigraphic horizon in a cryptotephra layer that equates with the time of instantaneous deposition of volcanic ash following a volcanic eruption can be difficult (Davies *et al.*, in press). In this study, the onset of ash deposition was assumed to be represented by the peak value in glass concentration for cryptotephra layers and, in the case of visible tephra layers, the base of the visible part of each layer. Whilst this approach provides a consistent basis for interpretation, it is nevertheless based on assumptions about the mode of deposition of both visible and crypto- tephra layers. Some layers could be affected by bioturbation, re-sedimentation and other depositional artefacts. If the assumptions are incorrect, then an additional level of complexity needs to be considered when deriving age models using tephra layers, especially in the case of those with a large vertical distribution of glass shards, which span unknown intervals of time. The complications they introduce are highlighted in Figure 9.1.

9.3.2 Small glass shard surface area

Despite the location of the Adriatic Sea downwind of the major Italian volcanoes, some of the tephra layers reported here are composed of glass shards of very small size (<50μm). A number of tephra layers also contain high numbers of very vesicular shards (Chapter 5), which limits the available surface area on which to attempt to focus an electron beam (Figure 9.2). This meant that for some tephra layers, the original WDS-EPMA geochemical analyses carried out at the University of Oxford were not successful. This problem was circumvented by carrying out WDS-EPMA analysis at the University of Edinburgh using a 5 μm beam diameter. Whilst the same samples were analysed on the different microprobes to check for machine drift, the need to analyse samples at different locations will have introduced an additional level of uncertainty when comparing geochemical data derived using different machines.

The problems of such small shard sizes may have implications for constraining further work, for example in the procurement of trace element data. The smallest laser beam diameter that can be routinely used for this purpose is 10 μm, for Pearce *et al.* (in press) have shown that 6 μm and 4 μm laser beam diameters are affected by fractionation effects which cannot be corrected for.

9.3.3 Repeated geochemical signatures

A number of tephra layers in this study are indistinguishable on the basis of major element geochemistry. In some cases, this is thought to be where multiple peaks in glass characterise one tephra layer. For example, the 1 cm glass peaks between 392 cm and 424 cm in SA03-03 (Sections 5.2.2 and 6.3.6) and the peaks in glass at 86 cm and 88 cm in RF93-77 (Sections 5.3.2 and 6.4.9) (Figure 9.3). It is clear that the peaks in these core sections are part of one tephra event and as they were not evident in the original 5 cm resolution sampling, they are thought to be artefacts of the *Lycopodium* counting method.

However, in PRAD 1-2, six tephra layers between 205 cm and 324 cm were identified each showing very similar major and trace element geochemical signatures (Sections 5.1.2 and 6.2.19), with an additional tephra layer at 404 cm also indistinguishable on major element geochemistry (Section 6.2.20). These tephra layers are each thought to represent individual tephra layers and not the same event, because not only was the same shard distribution observed at both 5 cm and 1 cm resolution, but also there are core sections between the main peaks with no glass shards present (Figure 9.3).

As trace element data were unable to differentiate between these layers, they can only be considered as unknown eruptions, which have been geochemically classified and have been dated using the PRAD 1-2 age model (see Table 9.1). However, this has reduced the number of isochrons available in this study but also highlighted the problem of repeating geochemical signatures in different eruptions that was discussed in section 2.1.2. This may be resolved with additional research at proximal sites (see section 9.4).

It may be possible to discriminate between these two potential causes of multiple peaks with similar geochemical signatures through the use of thin section analysis of the tephra layers. This is discussed further in Section 9.4.

9.3.4 Establishing high-precision age estimates

Whilst this project appears to have successfully refined the age estimates for some of the widespread Italian tephra layers (Section 8.1.1) and tephra-based age models have been constructed for each of the Adriatic marine sequences, no reliable age estimates are available for a number of the tephra layers. Whilst age estimates can be assigned

using the derived age models (Table 9.1), there is a need to date these layers directly, where possible, using argon-argon dating.

This was attempted as part of this project (section 4.8.1). However, the results could not be generated in time for inclusion in the thesis. Although sanidine crystals were detected in, and extracted from, some samples, these were too fine-grained to yield sufficient argon for satisfactory analysis; some hundreds of additional crystals were required (see section 4.8.1). Laboratory processing of the initial sanidine crystals extracted have shown that there is the potential to date non-visible ash layers from Adriatic marine sequences (M. Storey, 2011, *pers comm*.) but only if much larger samples are supplied, which is necessary to reduce the age uncertainties to acceptable levels. Initially, 10 grams of sample material from each tephra layer were processed for sanidine extraction (Figure 4.12) and additional material is not available from the core u-channels stored at Royal Holloway. The possibility of supplying additional material from the archived halves of the original cores stored in Bologna is being investigated.

9.3.5 Procedures for classifying shards by their geochemical signature.

In this study, a combination of graphical and statistical methods has been used to match the tephra layers identified in Adriatic marine sequences with the LGdM dataset. This follows the recommendations of Davies *et al.*, (in press) who advise that statistical methods should not be used in isolation but in combination with graphical approaches. The use of DFA to create a hierarchical structure for grouping tephra layers in this thesis has been supported by the graphical data interpretation in all instances. However, in the case of both these approaches, the degree of overlap between geochemical data-clusters commonly relies on visual and subjective examination of the data. The development of appropriate, more objective statistical measures of the degree of overlap between data sub-sets is urgently required. This has been attempted here by using DFA to generate the training set clusters (see sections 4.7.3 and 6.1.1), but the results are constrained by aforementioned sample size limitations and with the original training set. The possibility of developing more objective data comparisons using more sophisticated data transformations, such as kernel densities, is currently being explored within the RESET project[2] but is proving complex.

[2] RESET: a UK research initiative funded by the Natural Environment Research Council: see http://c14.arch.ox.ac.uk/reset/

9.4 Recommendations for further work

There are a number of ways that this research can be built upon and subsequently enhanced. This will enable the application of distal tephrochronology to be further extended and made more robust throughout the region.

- The hierarchical classification system and correlations proposed in this research rely on geochemical matches made with the Wulf *et al.* (2004, 2008 and unpublished) classification of LGdM layers and their attribution to known eruptions. This approach was considered the most pragmatic to adopt at the time, in light of the lack of comparable proximal geochemical information available; a comprehensive and analytically-secure data-base of proximal tephra layers does not currently exist for most volcanic centres in the Mediterranean region. However, work is under way to develop them. For example, the RESET project [3] is collaborating with many Italian partners to generate a comprehensive data-base of proximal-to-distal chemical signatures for Italian volcanic centres active during the last c. 100 ka, the results to be made available on the RHOXTOR web site. When this database is complete, a comparison of the geochemical data generated in this study and the geochemical data in the database should be undertaken to provide a check on the correlations suggested here and indeed those proposed by Wulf *et al.*, (2004, 2008 and unpublished).
- There are a number of tephra layers in each of the sequences that could not be correlated with an LGdM layer. If correlations can be found for these layers, it will increase the number of isochrons available for building age models, which will in turn improve the error ranges of those age models. This may be achieved through the construction of a robust proximal dataset for the region or by re-visiting the LGdM sequence to analyse additional layers, as only visible layers in the sequence were originally analysed by Wulf *et al.* (2004, 2008 and unpublished).
- So far, trace element data has only been obtained for six of the PRAD 1-2 tephra layers with the same geochemical signature as the NYT. However, trace element data from individual glass shards of these unknown layers may help to establish firm correlations with known eruptions. In the near future, however, this may be limited to tephra layers containing shards with a surface area large enough to use a 10 μm diameter laser beam.

[3] RESET: a UK research initiative funded by the Natural Environment Research Council: see http://c14.arch.ox.ac.uk/reset/

- The work could be improved upon if independent age estimates were obtained for layers that either have no correlative at this time or where their only age estimate is a Monticchio varve age. This could be achieved in part by the application of argon-argon dating to the older unknown tephra layers in the sequences. This research is still ongoing.
- The detection of cryptotephras in Adriatic marine cores has extended the known distribution of a number of eruptions, as well as increasing the number of layers found in each core sequence, compared with just visible tephra layers alone. Their ability to link both marine and terrestrial sequences has also been demonstrated suggesting that cryptotephra studies and sampling should be incorporated as a routine and systematic procedure in marine and terrestrial palaeoenvironmental studies in the region.
- Whilst the tephra layers in the studied marine sequences appear to be discrete layers that have not been reworked, this could be tested by taking thin sections through the tephra layers. This approach may also help to determine where the input of tephra shards is and therefore which specific depth represents the initial horizon of tephra deposition. Folkes (2010) demonstrated that it is possible to make thin sections from Adriatic marine sequences and therefore this approach can be used more frequently. The application of thin section micromorphology to tephra layers may also help to identify situations where patchy deposition occurs within a core sequence. This may help to resolve problem layers like PRAD-3605 (Section 5.1.1), where geochemical analysis could not be undertaken because glass shards could not be detected at the re-sampling stage.

10. Bibliography

Abbott, P.M., 2005. Towards a tephrochronology for a southern Adriatic deep marine sequence. MSc Thesis, University of London, unpublished.

Aitchison, J., 1986. The Statistical Analysis of Compositional Data, Blackburn Press, Cadwell, NJ (reprinted 2003).

Alessio, M., Bella, F., Improta, S., Belluomini, G., Calderoni, G., Cortesi, C,. Turi, B., 1974. University of Rome Carbon-14 dates XII. Radiocarbon, 16, 358-367.

Allen, H.D., 2003. Response of past and present Mediterranean ecosystems to environmental change. Progress in Physical Geography, 27(3), 359 – 377.

Allen, J.R.M., Brandt, U., Brauer, A., Hubberten, H.-W., Huntley, B., Keller, J., Kraml, M., Mackensen, A., Mingram, J., Negendank, J.F.W., Nowaczyk, N.R., Oberhänsli, H., Watts, W.A., Wulf, S., Zolitschka, B., 1999. Rapid environmental changes in southern Europe during the last glacial period. Nature, 400, 740-743.

Allen, J.R.M., Watts, W.A., Huntley, B., 2000. Weichselian palynostratigraphy, palaeovegetation and palaeoenvironment; the record from Lago Grande di Monticchio, southern Italy. Quaternary International, 73/74, 91 – 110.

Allen, J.R.M., Huntley, B., 2009. Last Interglacial palaeovegetation, palaeoenvironments and chronology: a new record from Lago Grande di Monticchio, southern Italy. Quaternary Science Reviews, 28, 1521-1538.

Alley, R.B., Meese, D.A., Shuman, C.A., Gow, A.J., Taylor, K. C., Grootes, P. M., White, J. W. C., Ram , M., Waddington, E. D., Mayewski, P. A., Zielinski, G. A., 1993. Abrupt increase in Greenland snow accumulation at the end of the Younger Dryas event. Nature, 362, 527 – 529.

Alloway, B.V., Larsen, G., Lowe, D.J., Shane, P.A.R., Westgate, J.A., 2007. Tephrochronology. In Elias, S.A., 2007. Encyclopedia of Quaternary Science, Elsevier, 2869 – 2898.

Almond, P.C., 1996. Loess, Soil Stratigraphy and Aokautere ash on surfaces in South Westland, New Zealand: Interpretation and correlation with the Glacial Stratigraphy. Quaternary International, 34-36, 163 – 176.

Alvisi, F., Vigliotti, L., 1996. Magnetic signature of marine and lacustrine sediments from central Italy (PALICLAS Project). In Oldfield, F., Guilizzoni, P. (eds) Italian crater lake and Adriatic sediments, Memorie dell'Instituto Italiano di Idrobiologia, 55, 285 – 302.

Andersen, K.K., Svensson, A., Johnsen, S.J., Rasmessen, S.O., Bigler, M., Röthlisberger, R., Ruth, U., Siggaard-Andersen, M-L., Steffensen, J.P., Dahl-Jensen, D., Vinther, B.M., Clausen, H.B., 2006. The Greenland Ice Core Chronology 2005, 15-42 ka. Part 1: constructing the time scale. Quaternary Science Reviews, 25, 3246 – 3257.

Anderson, D.M., 2007. Paleoceanography. In Elias, S.A., 2007. Encyclopedia of Quaternary Science, Elsevier, 1599 – 1609.

Andronico, D., Calderoni, G., Cioni, R., Sbrana, A., Sulpizio, R., Santacroce, R., 1995. Geological map of Somma-Vesuvius Volcano. Periodico di Mineralogia, 64, 77-78.

Andronico, D., Cioni, R., 2002. Contrasting styles of Mount Vesuvius activity in the period between the Avellino and Pompeii Plinian eruptions, and some implications for assessment of future hazards. Bulletin of Volcanology, 64, 372-391.

Ariztegui, D., Chondrogianni, C., Wolff, G., Asioli, A., Teranes, J., Bernasconi, S.M., McKenzie, J.A., 1996. Paleotemperature and paleosalinity history of the Meso Adriatic Depression (MAD) during the Late Quaternary: a stable isotopes and alkenones study. In Oldfield, F. and Guilizzoni, P. (eds) Italian crater lake and Adriatic sediments, Memorie dell'Instituto Italiano di Idrobiologia, 55, 219 – 230.

Ariztegui, D., Asioli, A., Lowe, J.J., Trincardi, F., Vigliotti, L., Tamburini, F., Chondrogianni, C., Accorsi, C.A., Bandini Mazzanti, M., Mercuri, A.M., Van der Kaars, S., McKenzie, J.A., Oldfield, F., 2000. Paleoclimate and the formation of sapropel S1: inferences from Late Quaternary lacustrine and marine sequences in the central Mediterranean region. Palaeogeography, Paleoclimatology, Palaeoecology, 158, 215-240.

Artegiani, A., Azzolini, R., Salusti, E., 1989. On the dense water in the Adriatic Sea. Oceanologica Acta 12, 151-160.

Artegiani, A., Bregant, D., Paschini, E., Pinardi, N., Raicich, F., Russo, A., 1997a. The Adriatic Sea General Circulation. Part 1: Air-Sea Interactions and Water Mass Structure. Journal of Physical Oceanography, 37, 1492 – 1514.

Artegiani, A., Bregant, D., Paschini, E., Pinardi, N., Raicich, F., Russo, A., 1997b. The Adriatic Sea general circulation. 2. Baroclinic circulation structure. Journal of Physical Oceanography, 27, 1515-1532.

Ascough, P., Cook, G., Dugmore, A., 2005. Methodological approaches to determining the marine radiocarbon reservoir effect. Progress in Physical Geography, 29, 532-547.

Ascough, P.L., Cook, G.T., Dugmore, A.J., 2009. North Atlantic marine (14)C reservoir effects: Implications for late-Holocene chronological studies. Quaternary Geochronology, 4, 171-180.

Asioli, A., 1996. High resolution foraminifera biostratigraphy in the central Adriatic basin during the last deglaciation: a contribution to the PALICLAS project. In Oldfield, F. and Guilizzoni, P. (eds) Italian crater lake and Adriatic sediments, Memorie dell'Instituto Italiano di Idrobiologia, 55, 197-217.

Asioli, A., Trincardi, F., Correggiari, A., Langone, L., Vigliotti, L., Van Der Kaars, S., Lowe, J.J., 1996. The late-Quaternary deglaciation in the Central Adriatic basin. In: Late-Glacial and Early Holocene climatic and environmental changes in Italy. Il Quaternario, Italian Journal of Quaternary Sciences, 9, (2), 627-642.

Asioli, A., Trincardi, F., Lowe, J.J., Oldfield, F., 1999. Short-term climate changes during the Last Glacial-Holocene transition: comparison between Mediterranean records and the GRIP event stratigraphy. Journal of Quaternary Science, 14, 373-381.

Asioli, A., Trincardi, F., Lowe, J.J., Ariztegui, D., Langone, L., Oldfield, F., 2001. Sub-millennial climatic oscillations in the Central Adriatic during the last deglaciation: paleoceanographic implications. Quaternary Science Review, 20, 1201-1221.

Baratt, P., Reimer, P.J., Eds. 2007. Radiocarbon Dating: A Practical Overview. Environmental Archaeology in Ireland. Oxford, Oxbow Books.

Bard, E., Rostek, F., Menot-Combes, G., 2004. Radiocarbon calibration beyond 20,000 C-14 yr BP by means of planktonic foraminifera of the Iberian Margin. Quaternary Research 61, 204-214.

Bard, E., Rostek, F., Menot-Combes, G., 2004. Radiocarbon calibration beyond 20,000 C-14 yr BP by means of planktonic foraminifera of the Iberian Margin. Quaternary Research 61, 204-214.

Bassinot, F. C., Labeyrie, L.D., Vincent, E., Quidelleur, X., Shackleton, N.J., Lancelot, Y., 1994. The astronomical theory of climate and the age of the Brunhes Matuyama magnetic reversal. Earth Planetary Science Letters, 126, 91—108.

Bassinot, F.C., 2007. Oxygen Isotope Stratigraphy of the Oceans. In Elias, S.A., 2007. Encyclopedia of Quaternary Science, Elsevier, 1740 – 1748.

Berné, S, Shipboard Scientific Party, 2004. PROMESS1 Summary cruise Report: past global changes investigated by drilling Mediterranean continental margins. Unpublished cruise report, Research Institute for Exploitation of the Sea (IFREMER), Brest, France, Unpublished: 1-7

Bertagnini, A., Landi, P., Rosi, M., Vigliargio, A., 1998. The Pomici di Base Plinian eruption of Somma-Vesuvius. Journal of Volcanology and Geothermal Research, 83, 219-239.

Bignami, F., Salusti, E., Schiarini, S., 1990. Observations on a bottom vein of dense water in the Southern Adriatic and Ionian Seas. Journal of Geophysical Research-Oceans, 95, 7249-7259.

Birks, H.H., Gulliksen, S., Haflidason, H., Mangerud, J., Possnert, G., 1996. New radiocarbon dates for the Vedde Ash from western Norway. Quaternary Research, 45, 119 – 127.

Björck, S., Walker, M.J.C., Cwynar, L.C., Johnson, S., Knudsan, K-L., Lowe, J.J., Wohlfarth, B., INTIMATE Members., 1998. An event stratigraphy for the Last Termination in the North Atlantic region based on the Greenland ice-core record: a proposal by the INTIMATE group. Journal of Quaternary Science, 13, 283-292.

Blockley, S.P.E., Lowe, J.J., Walker, M.J.C., Asioli, A., Trincardi, F., Coope, G.R., Donahue, R.E., Pollard, A.M., 2004. Bayesian analysis of radiocarbon chronologies: examples from the European Late-glacial. Journal of Quaternary Science, 19, 159-175.

Blockley, S.P.E., Pyne-O'Donnell, S.D.F., Lowe, J.J., Matthews, I.P., Stone, A., Pollard, A.M., Turney, C.S.M., Molyneux, E.G., 2005. A new and less destructive

laboratory procedure for the physical separation of distal glass tephra shards from sediments. Quaternary Science Reviews, 16-17, 1952-1960.

Blockley, S.P.E., Blaauw, M., Ramsey, C.B., van der Plicht, J., 2007. Building and testing age models for radiocarbon dates in Lateglacial and Early Holocene sediments. Quaternary Science Reviews, 26, 1915-1926.

Blockley, S.P.E., Bronk Ramsey, C., Pyle, D.M., 2008a. Improved age modelling and high-precision age estimates of late Quaternary tephras, for accurate palaeoclimate reconstruction. Journal of Volcanology and Geothermal Research, 177(1), 251 – 262.

Blockley, S.P.E., Ramsey, C.B., Lane, C.S., Lotter, A.F., 2008b. Improved age modelling approaches as exemplified by the revised chronology for the Central European varved lake Soppensee. Quaternary Science Reviews, 27, 61-71.

Blockley, S.P.E., Ramsey, C.B., Higham, T.F.G., 2008c. The Middle to Upper Paleolithic transition: dating, stratigraphy, and isochronous markers. Journal of Human Evolution, 55, 764-771.

Bond, G., Kromer, B., Beer, J., Muscheler, R., Evans, M.N., Showers, W., Hoffmann, S., Lotti-Bond, R., Hajdas, I., Bonani, G., 2001. Persistent solar influence on north Atlantic climate during the Holocene. Science, 294, 2130-2136.

Bourne, A., 2006. An Initial Tephrochronology of the Adriatic Core, PRAD 1-2 for 40ka BP. MSc Thesis, University of London, unpublished.

Bourne, A.J., Lowe, J.J., Trincardi, F., Asioli, A., Blockley, S.P.E., Wulf, S., Matthews, I.P., Piva, A., Vigliotti, L., 2010. Distal tephra record for the last ca 105,000 years from core PRAD 1-2 in the central Adriatic Sea implications for marine tephrostratigraphy. Quaternary Science Reviews, 29, 3079-3094.

Brauer, A., Mingram, J., Frank, U., Günter, C., Schettler, G., Wulf, S., Zolitschka, B., Negendank, J.F.W., 2000. Abrupt environmental oscillations during the Early Weichselian recorded at Lago Grande di Monticchio, southern Italy. Quaternary International, 73/74, 79-90.

Brauer, A., Allen, J.R.M., Mingram, J., Dulski, P., Wulf, S., Huntley, B., 2007. Evidence for last interglacial chronology and environmental change from Southern Europe. PNAS, 104, 450-455.

Brendryen, J., Haflidason, H., Sejrup, H.P., 2010. Norwegian Sea tephrostratigraphy of marine isotope stages 4 and 5: Prospects and problems for tephrochronology in the North Atlantic region. Quaternary Science Reviews, 29, 847-864.

Broecker, W.S., 1979. Revised estimate for the radiocarboon age of North Atlantic deep-water. Journal of Geophysical Research-Oceans and Atmospheres, 84, 3218-3226.

Bronk Ramsey, C., 2001. Development of the Radiocarbon Program OxCal. Radiocarbon, 43(2a), 355-363.

Bronk Ramsey, C., 2008a. Radiocarbon Dating: Revolutions in Understanding. Archaeometry, 50(2), 249 – 275.

Bronk Ramsey, C., 2008b. Deposition models for chronological records. Quaternary Science Reviews, 27(1-2), 42-60.

Bronk Ramsey, C., 2009. Bayesian analysis of radiocarbon dates. Radiocarbon, 51(1), 337-360.

Brown, R.J., Orsi, G., de Vita, S., 2008. New insights into Late Pleistocene explosive volcanic activity and caldera formation on Ischia (southern Italy). Bulletin of Volcanology, 70, 583–603.

Budillon, F., Lirer, F., Iorio, M., Macri, P., Sagnotti, L., Vallefuoco, M., Ferraro, L., Garziglia, S., Innangi, S., Sahabi, M., Tonielli, R., 2009. Integrated stratigraphic reconstruction for the last 80 kyr in a deep sector of the Sardinia Channel (Western Mediterranean). Deep-Sea Research Part Ii-Topical Studies in Oceanography, 56, 725-737.

Cacho, I., Grimalt, J.O., Pelejero, C., Canals, M., Sierro, F.J., Flores, J.A., Shackleton, N., 1999. Dansgaard-Oeschger and heinrich event imprints in Alboran Sea paleotemperatures. Paleoceanography, 14, 698-705.

Calanchi, N., De Rosa, R., Mazzuoli, R., Rossi, P., Santacroce, R., Ventura, G., 1993. Silicic magma entering a basaltic magma chamber: eruptive dynamics and magma mixing – an example from Salina (Aeolian islands, Southern Tyrrhenian Sea). Bulletin of Volcanology, 55, 504-522.

Calanchi, N., Dinelli, E., Lucchini, F., Mordenti, A., 1996. Chemostratigraphy of late Quaternary sediments from Lake Albano and central Adriatic Sea core (PALICLAS Project). In Oldfield, F. and Guilizzoni, P. (eds) Italian crater lake and Adriatic sediments, Memorie dell'Instituto Italiano di Idrobiologia, 55, 247 – 263.

Calanchi, N., Cattaneo, A., Dinelli, E., Gasparotto, G., Lucchini, F., 1998. Tephra layers in Late Quaternary sediments of the central Adriatic Sea. Marine Geology, 149, 191-209.

Calanchi, N., Dinelli. E., 2008. Tephrostratigraphy of the last 170 ka in sedimentary successions from the Adriatic Sea. Journal of Volcanology and Geothermal Research, 177, 81- 95.

Capaldi, G., Gillot, P.Y., Munno, R., Orsi, G., Rolandi, G., 1985. Sarno Formation: the major plinian eruption of the Somma-Vesuvius. IAVCEI 1985 Scientific Assembly Giardini Naxos (Abstr).

Capotondi, L., Morigi, C., 1996. The last deglaciation in the south Adriatic Sea: biostratigraphy and paleoceanography. Italian Journal of Quaternary Science, 9, 679 – 686.

Capotondi, L., Borsetti, A.M., Morigi, C., 1999. Foraminiferal ecozones, a high resolution proxy for the late Quaternary biochronology in the central Mediterranean Sea. Marine Geology, 153, 253-274.

Caron, B., Sulpizio, R., Zanchetta, G., Siani, G., Santacroce, R., 2010. The Late Holocene to Pleistocene tephrostratigraphic record of Lake Ohrid (Albania). Comptes Rendus Geoscience, 342, 453-466.

Cattaneo, A., Trincardi, F., 1999. The late-Quaternary transgressive record in the Adriatic epicontinental Sea: basin widening and facies partitioning. In: Bergman, K., Snedden, J., (Eds.), Isolated Shallow Marine Sand Bodies: Sequence Stratigraphic Analysis and Sedimentologic Interpretation. SEPM Special Publication, 64, 127-146.

Cattaneo, A., Correggiari, A., Langone, L., Trincardi, F., 2003. The late-Holocene Gargano subaqueous delta, Adriatic shelf: Sediment pathways and supply fluctuations. Marine Geology, 193, 61-91.

Cheddadi, R., Rossignol-Strick, M., Fontugne, M., 1991. Eastern Mediterranean palaeoclimates from 25 to 5 ka B.P. documented by pollen and isotopic analysis ofa core in the anoxic Bannock Basin. Marine Geology 100, 53–566.

Cheddadi, R., Rossignol-Strick, M., 1995. Improved preservation of organic-matter and pollen in eastern Mediterranean sapropels. Paleoceanography, 10, 301-309.

Ciabatti, M., Curzi, P.V., Ricci Lucchi, F., 1987. Quaternary sedimentation in the Central Adriatic Sea. Giornale di Geologia, 49, 113-125.

Cioni, R., Santacroce, R., Sbrana, A., 1999. Pyroclastic deposits as a guide for reconstructing the multi-stage evolution of the Somma-Vesuvius Caldera. Bulletin of Volcanology, 60, 207-222.

Cita Sironi, M.B., Capotondi, L., Asioli, A., 2005. The Tyrrhenian stage in the Mediterranean: definition, usage and recognition in the deep-sea record. A proposal. Rend. Fis. Acc. Lincei, 9(16), 297 – 310.

Civetta, L., Cornette, Y., Crisci, G., Gillot, P.Y., Orsi, G., Requejo, C.S., 1984. Geology, Geochronology and chemical evolution of the Island of Pantelleria. Geological Magazine, 121, 541-562.

Civitarese, G., Gacic, M., Cardin, V., Ibello, V., 2005. Winter Convection Continues in the Warming Southern Adriatic. Eos, 86, 45(8), 445-451.

Coltelli, M., Del Carlo, P., Vezzoli, L., 2000. Stratigraphic constraints for explosive activity in the past 100ka at Etna Volcano, Italy. International Journal of Earth Sciences, 89, 665 – 677.

Combourieu-Nebout, N., Paterne, M., Turon, J.L., Siani, G., 1998. A high-resolution record of the last deglaciation in the Central Mediterranean Sea: Palaeovegetation and palaeohydrological evolution. Quaternary Science Reviews, 17, 303-317.

Combourieu-Nebout, N., Londeix, L., Baudin, F., Turon, J-L., von Grafenstein, R., Zahn, R., 1999. Quaternary marine and continental palaeoenvironments in the western Mediterranean (SITE 976, Alboran Sea): palynological evidence. In: Zahn, R., Comas, M.C., Klaus, A. (Eds), Proceedings ofthe Ocean Drilling Program, Scientific Results 161, 457–468.

Conticelli, S., Francalanci, L., Manetti, P., Cioni, R., Sbrana, A., 1997. Petrology and geochemistry of the ultrapotassic rocks from the Sabatini Volcanic District, central Italy: The role of evolutionary processes in the genesis of variably enriched alkaline magmas. Journal of Volcanology and Geothermal Research, 75, 107-136.

Correggiari A., Field, M.E., Trincardi, F., 1996. Late-Quaternary transgressive large dunes on the sediment-starved Adriatic shelf. In: DeBatist & Jacobs (Eds), Siliciclastic Shelf Seas. Geol. Soc. Spec. Pubbl., 117, 155-169.

Crisci, G.M., Derosa, R., Esperanca, S., Mazzuoli, R., Sonnino, M., 1991. Temporal evolution of a 3 component system – the island of Lipari (Aeolian Arc), Southern Italy. Bulletin of Volcanology, 53, 207-221.

Cronin, S.J., Neall, V.E., Palmer, A.S., Stewart, R.B., 1997. Methods of identifying late Quaternary tephras on the ring plains of Ruapehu and Tongariro volcanoes, New Zealand. New Zealand Journal of Geology and Geophysics, 40, 175-184.

Cutler K.B., Gray S.C., Burr G.S., Edwards R.L., Taylor F.W., Cabioch G., Beck J.W., Cheng H., Moore J., 2004. Radiocarbon calibration to 50 kyr BP with paired ^{14}C and ^{230}Th dating of corals from Vanuatu and Papua New Guinea. Radiocarbon, 46(3), 1127–60.

Dansgaard, W., 1985. Greenland Ice Core Studies. Palaeogeography Palaeoclimatology Palaeoecology, 50, 185-187.

Dansgaard, W., Johnsen, S.J., Clausen, H.B., Dahljensen, D., Gundestrup, N.S., Hammer, C.U., Hvidberg, C.S., Steffensen, J.P., Sveinbjornsdottir, A.E., Jouzel, J,. Bond, G., 1993. Evidence for General Instability of Past Climate from a 250-KYR Ice-Core record. Nature, 364, 218 – 220.

Davies, S.M., Branch, N.P., Lowe, J.J., Turney, C.S.M., 2002. Towards a European tephrochronological framework for Termination 1 and the Early Holocene. Philosophical Transactions of the Royal Society of London, A360, 767-802.

Davies S.M., Elmquist, M., Bergman, J., Wohlfarth, B., Hammarlund, D., 2007. Crypotephra sedimentation processes within two lacustrine sequences from west central Sweden. Holocene, 17(3), 319 – 330.

Davies, S.M., Abbott, P.M, Pearce, N.J.G., Wastegard, S., Blockley, S.P.E., in press. Integrating the INTIMATE records using tephrochronology: rising to the challenge. Quaternary Science Reviews, doi:10.1016/j.quascirev.2011.04.005.

De Astis, G., Pappalardo, L., Piochio, M., 2004. Procida volcanic history: New insights into the evolution of the Phlegrean Volcanic District (Campanian region, Italy). Bulletin of Volcanology, 66, 622 – 641.

De Rita, D., Funiciello, R., Corda, L., Sposato, A., Rossi, U., 1993. Volcanic Units. In: Di Filippo, M. (Ed.), Sabatini Volcanic Complex. Consiglio Nazionale delle Ricerche Quaderni de 'La ricerca scientifica'. 114(11), 33–79.

De Rita, D., Giordano, G., Esposito, A., Fabbri, M., Rodani, S., 2002. Large volume phreatomagmatic ignimbrites from the Colli Albani Volcano (Middle Pleistocene, Italy). Journal of Volcanology and Geothermal Research, 118, 77-98.

De Rosa, R., Donato, P., Gioncada, A., Masetti, M., Santacroce, R., 2003. The Monte Guardia eruption (Lipari, Aeolian Islands): an example of a reversely zoned magma mixing sequence. Bulletin of Volcanology, 65, 530-543.

de Vita, S., Orsi, G., Civetta, L., Carandente, A., D' Antonio, M., Deino, A., di Cesare, T., Di Vito, M.A., Fisher, R.V., Isaia, R., Marotta, E., Necco, A., Ort, M., Pappalardo, L., Piochi, M., Southon, J., 1999. The Agnano-Monte Spina eruption (4100 years BP) in the restless Phlegrean Fields caldera (Italy). Journal of Volcanology and Geothermal Research, 91, 269–301.

De Vivo, B., Rolandi, G., Gans, P.B., Calvert, A., Bohrson, W.A., Spera, F.J., Belkin, H.E., 2001. New constraints on the pyroclastic eruptive history of the Campanian volcanic plain (Italy). Mineralogy and Petrology, 73, 47–65.

De Vivo, B., Petrosino, P., Lima, A., Rolandi, G., Belkin, H.E., 2010. Research progress in volcanology in the Neapolitan area, southern Italy: a review and some alternative views. Mineralogy and Petrology, 99, 1-28.

De Vleeschouwer, F., van Vliët-Lanoe, B., Fagel, N., Richter, T., Boës, X., 2008. Development and application of high-resolution petrography on resin-impregnated Holocene peat columns to detect and analyse tephras, cryptotephras, and other materials. Quaternary International, 178(1), 54-67.

Deino, A.L., Orsi, G., de Vita, S., Piochi, M., 2004. The age of the Neapolitan Yellow Tuff caldera-forming eruption (Campi Flegrei caldera - Italy) assessed by $^{40}Ar/^{39}Ar$ dating method. Journal of Volcanology and Geothermal Research, 133, 157 – 170.

Delibrias, G., Di Paola, G.M., Rosi, M., Santacroce, R., 1979. La storia eruttiva del complesso vulcanico Somma Vesuvio ricostruita dalle successioni piroclastiche del Monte Somma. Reniconti Societa Italiana di Mineralogia e Petrologia, 35, 411–438.

Delibrias, G., Guillier, M.-T., Labeyrie, J., 1986. Gif natural radiocarbon measurements X. Radiocarbon, 28, 9–68.

Di Vito, M.A., Isaia, R., Orsi, G., Southon, J., de Vita, S., D'Antonio, M., Pappalardo, L., Piochi, M., 1999. Volcanism and deformation since 12000 years at the Campi Flegrei caldera (Italy). Journal of Volcanology and Geothermal Research, 91, 221-246.

Di Vito, M., Sulpizio, R., Zanchetta, R., D'Orazio, M., 2008. The late Pleistocene pyroclastic deposits of the Campanian Plain: new insights on the explosive activity of Neapolitan volcanoes. Journal of Volcanology and Geothermal Research, 177, 19–48.

Druitt, T.H., Brenchley, P.J., Gökten, Y.E., Francaviglia, V., 1995. Late Quaternary rhyolitic eruptions from the Acigöl Complex, central Turkey. Journal of the Geological Society, London, 152, 655–667.

Ducassou, E., Capotondi, L., Murat, A., Bernasconi, S.M., Mulder, T., Gonthier, E., Migeon, S., Duprat, J., Giraudeau, J., Mascle, J., 2007. Multiproxy late quaternary

stratigraphy of the Nile deep-sea turbidite system - Towards a chronology of deep-sea terrigeneous systems. Sedimentary Geology, 200, 1-13.

Dugmore, A.J., Newton, A.J., 1992. Thin tephra layers in peat revealed by X-radiography. Journal of Archaeological Science, 19, 163-170.

Dugmore, A.J., Cook, G.T., Shore, J.S., Newton, A.J., Edwards, K.J., Larsen, G., 1995. Radiocarbon dating tephra layers in Britain and Iceland. Radiocarbon, 37, 379-388.

Enache, M.D., Cumming B.F., 2006. The morphological and optical properties of volcanic glass: a tool to assess density-induced vertical migration of tephra in sediment cores. Journal of Paleolimnology, 35, 661 – 667.

Fairbanks, R.G., Mortlock, R.A., Chiu, T.C., Cao, L., Kaplan, A., Guilderson, T.P., Fairbanks, T.W., Bloom, A.L., Grootes, P.M., Nadeau, M.J., 2005. Radiocarbon calibration curve spanning 0 to 50,000 years BP based on paired Th-230/U-234/U-238 and C-14 dates on pristine corals. Quaternary Science Reviews, 24, 1781-1796.

Fedele, L., Scarpati, C., Lanphere, M., Melluso, L., Morra, V., Perrotta, A., Ricci, G., 2008. The Breccia Museo formation, Campi Flegrei, southern Italy: geochronology, chemostratigraphy and relationship with the Campanian Ignimbrite eruption. Bulletin of Volcanology, 70, 1189 – 1219.

Fisher, R.V., Schmincke, H.-U., 1984. Pyroclastic rocks. Springer-Verlag, Berlin.

Fletcher, W.J., Goni, M.F.S., Allen, J.R.M., Cheddadi, R., Combourieu-Nebout, N., Huntley, B., Lawson, I., Londeix, L., Magri, D., Margari, V., Mueller, U.C., Naughton, F., Novenko, E., Roucoux, K., Tzedakis, P.C., 2010. Millennial-scale variability during the last glacial in vegetation records from Europe. Quaternary Science Reviews, 29, 2839-2864.

Folkes, H., 2010. The micromorphology of volcanic ash layers in marine sequences: an example from core SA03-11 in the Southern Adriatic. MSc Thesis, University of London, unpublished.

Follieri, M., Giardini, M., Magri, D., Sadori, L., 1998. Palynostratigraphy of the last glacial period in the volcanic region of Central Italy. Quaternary International, 47-8, 3-20.

Froggatt, P.C., 1983. Toward a comprehensive Upper Quaternary tephra and ignimbrite stratigraphy in New Zealand using electron microprobe analysis of glass shards. Quaternary Research, 19, 188-200.

Froggatt, P.C., 1992. Standardization of the chemical analysis of tephra deposits. Report of the ICCT Working Group, Quaternary International, 13/14, 93-96.

Fugro Engineers B.V., 2004. Geotechnical Report: geotechnical and operational data, scientific research on deltaic margins, Mediterranean and Adriatic Sea. Fugro Report No. N4373/01 - Issue 2, Promess-1.

Gehrels, M.J., Lowe, D.J., Hazell, Z.J., Newnham, R.M., 2006. A continuous 5300-yr Holocene cryptotephrostratigraphic record from northern New Zealand and implications for tephrochronology and volcanic hazard assessment. Holocene, 16, 173-187.

Gehrels, M.J., Newnham, R.M., Lowe, D.J., Wynne, S., Hazell, Z.J., Caseldine, C., 2008. Towards rapid assay of cryptotephra in peat cores: Review and evaluation of various methods. Quaternary International, 178, 68-84.

Giaccio, B., Isaia, R., Fedele, F.G., Di Canzio, E., Hoffecker, J., Ronchitelli, A., Sinitsyn, A.A., Anikovich, M., Lisitsyn, S.N., Popov, V.V., 2008. The Campanian Ignimbrite and Codola tephra layers: two temporal/stratigraphic markers for the Early Upper Palaeolithic in southern Italy and eastern Europe. Journal of Volcanology and Geothermal Research, 177, 208 – 226.

Gillot, P.-Y., Keller, J., 1993. Radiochronological dating of Stromboli. Acta Vulcanologica, 3, 69–77.

Gioncada, A., Mazzuoli, R., Bisson, M., Pareschi, M.T., 2003. Petrology of volcanic products younger than 42 ka on the Lipari-Vulcano complex (Aeolian Islands, Italy): an example of volcanism controlled by tectonics. Journal of Volcanology and Geothermal Research, 122, 191-220.

Giordano, G. De Rita, D., Cas, R., Rolandi, S., 2002. Valley pond and ignimbrite veneer deposits in the small-volume phreatomagmatic 'Peprino Albano' basic ignimbrite, Lago Albano maar, Colli Albani volcano, Italy: influence of topography. Journal of Volcanology and Geothermal Research, 118, 131-144.

Giunta, S., Negri, A., Morigi, C., Capotondi, L., Combourieu-Nebout, N., Emeis, K.-C., Sangiorgi, F., Vigliotti, L., 2003. Coccolithophorid ecostratigraphy and multi-proxy paleoceanographic reconstruction in the Southern Adriatic Sea during the last deglacial time (Core AD91-17). Palaeogeography Palaeoclimatology Palaeoecology, 190, 39-59.

Grovöld, K., Óskarsson, N., Johnsen, S.J., Clausen, H.B., Hammer, C.U., Bond, G., Bard, E., 1995. Ash layers from Iceland in the Greenland GRIP ice core correlated with oceanic and land sediments. Earth and Planetary Science Letters, 135, 149-155.

Guest, J., Cole, P., Duncan, A., Chester, D., 2003. Volcanoes of Southern Italy. The Geological Society, 284 p.p..

Guilizzoni, P, Oldfield, F., (Eds), 1996. Palaeoenvironmental Analysis of Italian Crater Lake and Adriatic Sediments (PALICLAS). Mem. Ist. ital. Idrobiol., 55, 328 p.p.

Hall, V. A., Pilcher, J.R., 2002. Late-Quaternary Icelandic tephras in Ireland and Great Britain: detection, characterization and usefulness. Holocene, 12(2), 223 – 230.

Hayward, C., in press. High spatial resolution electron probe microanalysis of tephras and melt inclusions without beam-induced chemical modification. The Holocene, DOI: 10.1177/0959683611409777

Hilgen, F.J., 1991. Astronomical calibration of Gauss to Matuyama sapropels in the Mediterranean and implication for the geomagnetic polarity time scale. Earth and Planetary Science Letters, 104, 226-244.

Hodgson, D.A., Dyson, C.L., Jones, V.J., Smellie, J.L., 1998. Tephra analysis of sediments from Midge Lake (South Shetland Islands) and Sombre Lake (South Orkney Islands), Antarctica. Antarctic Science, 10(1), 13 – 20.

Hughen, K.A., Southon, J.R., Bertrand, C.J.H., Frantz, B., Zermeno, P., 2004. Cariaco basin calibration update: Revisions to calendar and C-14 chronologies for core PL07-58PC. Radiocarbon, 46, 1161-1187.

Hunt, J.B., Hill, P.G., 1993. Tephra geochemistry: a discussion of some persistent analytical problems. The Holocene, 3, 271-278.

Hunt, J.B., Hill, P.G., 1996. An inter-laboratory comparison of the electron probe microanalysis of glass geochemistry. Quaternary International, 34-36, 229-241.

Hunt, J.B., Hill, P.G., 2001. Tephrological implications of beam size - Sample-size effects in electron microprobe analysis of glass shards. Journal of Quaternary Science, 16(2), 105-117.

Imbrie, J., Hays, J.D., Martinson, D.G., McIntyre, A., Mix, A.C., Morley, J.J., Pisias, N.G., Prell, W.L., Shackleton, N.J., 1984. The orbital theory of Pleistocene climate: support from a revised chronology of the marine δ18Orecord. In: Berger, A., Imbrie, J., Hays, J., Kukla, G., Saltzman, B. (Eds). Milankovitch and Climate, Reidel, Dordrecht, 269-306.

Isaia, R., D'Antonio, M., Dell'Erba, F., Di Vito, M., Orsi, G., 2004. The Astroni volcano: the only example of closely spaced eruptions in the same vent area during the recent history of the Campi Flegrei caldera (Italy). Journal of Volcanology and Geothermal Research, 133, 171–192.

Jochum, K.P., Nohl, U., Herwig, K., Lammel, E., Stoll, B., Hofmann, A.W., 2005. GeoReM: A new geochemical database for reference materials and isotopic standards. Geostandards and Geoanalytical Research, 29, 333-338.

Jochum, K.P., Stoll, B., Herwig, K., Willbold, M., Hofmann, A., Amini, M., Aarburg, S., Abouchami, W., Hellebrand, E., Mocek, B., Raczek, I., Stracke, A., Alard, O., Bouman, C., Becker, S., Dücking, M., Brätz, H., Klemd, R., de Bruin, D., Canil, D., Cornell, D., de Hoog, C.-J., Dalpé, C., Danyushevsky, L., Eisenhauer, A., Gao, Y., Snow, J.E., Groschopf, N., Günther, D., Latkoczy, C., Guillong, M., Hauri, E.H., Höfer, H.E., Lahaye, Y., Horz, K., Jacob, D.E., Kasemann, S.A., Kent, A.J.R., Ludwig, T., Zack, T., Mason, P.R.D., Meixner, A., Rosner, M., Misawa, K., Nash, B.P., Pfänder, J., Premo, W.R., Sun, W.D., Tiepolo, M., Vannucci, R., Vennemann, T., Wayne, D., Woodhead, J.D., 2006. MPI-DING reference glasses for in situ microanalysis: New reference values for element concentrations and isotope ratios. Geochemistry Geophysics and Geosystems, 7, Q02008.

Jorissen, F.J., Asioli, A., Borsetti, A.M., Capotondi, L., Devisser, J.P., Hilgen, F.J., Rohling, E.J., Vanderborg, K., Grazzini, C.V., Zachariasse, W.J., 1993. Late Quaternary Central Mediterranean Biochronology. Marine Micropaleontology, 21, 169-189.

Kallel, N., Duplessy, J.C., Labeyrie, L., Fontugne, M., Paterne, M., Montacer, M., 2000. Mediterranean pluvial periods and sapropel formation over the last 200,000 years. Palaeogeography Palaeoclimatology Palaeoecology, 157, 45-58.

Keller, J., Ryan, W.B.F., Ninkovich, D., Altherr, R., 1978. Explosive volcanic activity in the Mediterranean over the past 200,000 years as recorded in deep-sea sediments. Geological Society of America Bulletin, 89, 591–604.

Keller, J., 1982. Mediterranean island arcs. In Thorpe, R.S. (ed) Andesites, Wiley, Chichester, 307-325.

Kelley, S. P.**,** 2002. K-Ar and Ar-Ar Dating. In Porcelli D, Ballentine C and Wieler (eds). Noble Gases in geochemistry and Cosmochemistry, Reviews in Mineralogy and Geochemistry, vol 47, Mineralogy Society of America, Washington, 785-810

Kidd, R. B., Cita, M.B., Ryan, W.B.F., 1978, Stratigraphy of eastern Mediterranean sapropel sequences recovered during Leg 42A and their paleoenvironmental significance. Initial Report Deep Sea Drill. Project, 42A, 421–443.

Kohfeld, K.E., Harrison, S.P., 2000. How well can we simulate past climates? Evaluating the models using global palaeoenvironmental datasets. Quaternary Science Reviews, 19, 321-346.

Koren, J.H., Svendsen, J.I., Mangerud, J., Furnes, H., 2008. The Dimna Ash - a 12.8 14C ka-old volcanic ash in Western Norway. Quaternary Science Reviews, 27(1-2), 85-94.

Kraml, M., 1997. Laser-40Ar/39Ar-Datierungen an distalen marinen Tephren des jung-quart.aren mediterranen Vulkanismus (Ionisches Meer, METEOR-Fahrt 25/4). Ph.D. Thesis, Albert-Ludwigs-Universit.at Freiburg i.Br., 216pp.

Kuehn, S.C., Foit, F.F., 2006. Correlation of widespread Holocene and Pleistocene tephra layers from Newberry Volcano, Oregon, USA, using glass compositions and numerical analysis. Quaternary International ,148, 113-137.

Kuehn, S.C., Froese, D.G., 2010. Tephra from ice a simple method to routinely mount, polish, and quantitatively analyze sparse fine particles. Microscopy and Microanalysis, 16, 218 - 225.

Lacombe, H., Gascard, J.C., Gonella, J., Béthoux, J.P., 1981. Response of the Mediterranean to the water and energy fluxes across its surface, on seasonal and interannual scales, Oceanologica Acta, 4, 247–255.

Laj, C., Kissel, C., Roberts, A.P., 2006, Geomagnetic field behavior during the Iceland Basin and Laschamp geomagnetic excursions: A simple transitional field geometry? Geochemistry, Geophysics, Geosystems, 7, Q03004, doi:10.1029/ 2005GC001122.

Lane, C.S., 2009. Exploring the variability of microtephra deposits: chemical characterisation and discrimination methods. D.Phil thesis, University of Oxford, unpublished.

Langone, L., Asioli, A., Correggiari, A., Trincardi, F., 1996. Age-depth modelling through the Late-Quatenary deposits of the central Adriatic Basin. In: P. Guilizzoni and F. Oldfield, eds, Palaeoenvironmental Analysis of Italian Crater Lake and Adriatic Sediments (PALICLAS project), Special Issue, Memorie dell'Istituto Italiano di Idrobiologia, International Journal of Limnology, Istituto di Idrobiologia: Verbania Pallanza, 177-196.

Lanphere, M., Champion, D., Melluso, L., Morra, V., Perrotta, A., Scarpati, C., Tedesco, D., Calvert, A., 2007. $^{40}Ar/^{39}Ar$ ages of the AD 79 eruption of Vesuvius, Italy. Bulletin of Volcanology, 69, 259-263.

Lanphere, M. A., Calvert, A. T., Scarpati, C., Melluso, L., Morra, V., Perrotta, A., Thornber, C.; Cioni, R., Champion, D. E., 2008. $^{40}Ar/^{39}Ar$ ages of the older eruptive units of Somma-Vesuvius volcano, Italy. Eos Transactions. AGU 89(53), Fall Meeting Supplement, Abstract

Lascaratos, A., Roether, W., Nittis, K., Klein, B., 1999. Recent changes in deep water formation and spreading in the eastern Mediterranean Sea: a review. Progress in Oceanography, 44, 5-36.

Le Bas, M.J., Le Maitre, R.W., Streckeisen, A., Zanettin, B., 1986. A chemical classification of volcanic rocks based on the Total Alkali-Silica diagram. Journal of Petrology, 27, 745–750.

Lézine A.-M., von Grafenstein, U., Anderson, N., Belmecheri, S., Bordon, A., Caron, B., Cazet, J.-P., Erienkeuser, H., Fouache, E., Grenier, C., Huntsman-Mapila, P., Hureau-Mazaudier, D., Manelli, D., Mazaud, A., Robert, C., Sulpizio, R., Tiercelin, J.-J., Zanchetta, G., Zeqollari, Z., 2010. Lake Ohrid, Albania, provides an exceptional multi-proxy record of environmental changes during the last glacial-interglacial cycle. Palaeogeography, Palaeoclimatology, Palaeoecology, 287, 116-127.

Lisiecki, L.E., Raymo, M.E., 2005. A Pliocene-Pleistocene stack of 57 globally distributed benthic delta O-18 records. Paleoceanography, 20, PA1003, doi: 10.1029/2004PA001071.

Lourens, L.J., 2004. Revised tuning of Ocean Drilling Program Site 964 and KC01B (Mediterranean) and implications for the delta O-18, tephra, calcareous nannofossil, and geomagnetic reversal chronologies of the past 1.1 Myr. Paleoceanography, 19. PA3010, doi:10.1029/2003PA000997

Lowe, D.J., 1988. Stratigraphy, Age, Composition and Correlation of Late Quaternary tephras interbedded with organic sediments in Waikato lakes, North Islands, New Zealand. New Zealand Journal of Geology and Geophysics, 31, 125-165.

Lowe, D.J., Hunt, J., 2001. A summary of terminology used in tephra-related studies. Tephra: Les Dossiers de l'Archeo-Logis, 1, 17-22.

Lowe, D.J., Shane, P.A.R., Alloway, B.V., Newnham, R.M., 2008. Fingerprints and age models for widespread New Zealand tephra marker beds erupted since 30,000 years ago: a framework for NZ-INTIMATE. Quaternary Science Reviews, 27(1-2), 95-126.

Lowe, D.J., 2011. Tephrochronology and its application: A review. Quaternary Geochronology, 6, 107 – 153.

Lowe, J.J., Turney, C.S.M., 1997. Vedde Ash layer discovered in small lake basin on Scottish mainland, Journal of the Geological Society, 154, 605-612.

Lowe, J.J., 2001. Abrupt climate changes in Europe during the last glacial-interglacial transition: the potential for testing hypotheses on the synchroneity of climate events using tephrochronology. Global and Planetary Change, 30, 73-84.

Lowe, J.J., Walker, M.J.C., Porter, S.C., 2007a. Understanding Quaternary Climatic Change. In Elias, S.A., 2007. Encyclopedia of Quaternary Science, Elsevier, 28 – 39.

Lowe, J.J., Blockley, S., Trincardi, F., Asioli, A., Cattaneo, A., Matthews, I.P., 2007b. Age modelling of late Quaternary marine sequences from the Adriatic: towards improved precision and accuracy. Continental Shelf Research, 27, 560-582.

Machida, H., 1999. The stratigraphy, chronology and distribution of distal marker-tephras in and around Japan. Global and Planetary Change, 21, 71 – 94.

MacLeod, A., Matthews, I.P., Lowe, J.J., Pyne-O'Donnell, S.D.F., Palmer, A. Albert, P. (in prep). The tephrostratigraphy of Northern Europe during the Younger Dryas

Magri, D., Sadori, L., 1999. Late Pleistocene and Holocene pollen stratigraphy at Lago di Vico, central Italy. Vegetation History and Archaeobotany, 8, 247-260.

Mahood, G.A., Hildreth, W., 1986. Geology of the peralkaline volcano at Pantelleria, Straight of Sicily. Bulletin of Volcanology, 48, 143 – 172.

Manville, V., Wilson, C.J.N., 2004. Vertical density currents: a review of their potential role in the deposition and interpretation of deep-sea ash layers. Journal of the Geological Society, 161, 947-958.

Martinson, D.G., Pisias, N.G., Hays, J.D., Imbrie, J., Moore, T.C., Shackleton, N. J., 1987. Age dating and the orbital theory of the Ice Ages: Development of a high-resolution 0–300,000 year chronostratigraphy. Quaternary Research, 27, 1–29.

Matthews, I.P., 2009. The potential of tephrostratigraphy in the investigation of wetland archaeological records. PhD thesis, University of London, unpublished.

Matthews, I.P., Birks, H.H., Bourne, A.J., Brooks, S.J., Lowe, J.J., MacLeod, A., Pyne-O'Donnell, S.D.F., 2011. New age estimates and climatostratigraphic correlations for the Borrobol and Penifiler Tephras: evidence from Abernethy Forest, Scotland. Journal of Quaternary Science, 26(3), 247 – 252.

Meese, D.A., Gow, A.J., Alley, R.B., Zielinski, G.A., Grootes, P.M., Ram, M., Taylor, K.C., Mayewski, P.A., Bolzan, J.F., 1997. The Greenland Ice Sheet Project 2 depth-age scale: Methods and results. Journal of Geophysical Research-Oceans, 102, 26411-26423.

Meyer, E., Sarna-Wojcicki, A.M., Hillhouse, J.W., Woodward, M.J., Slate, J.L., Sorg, D.H., 1991. Fisson-track age (400,000 yr) of the Rockland Tephra, based on inclusions of zircon grains lacking fossil fission tracks. Quaternary Research, 35, 367 – 382.

Minisini, D., Trincardi, F., Asioli, A., 2006. Evidence of slope instability in the Southwestern Adriatic Margin. Natural Hazards and Earth System Sciences, 6, 1-20.

Moreno, A., Cacho, I., Canals, M., Grimalt, J.O., Sanchez-Goni, F., Shackleton, N., Sierro, F.J., 2005. Links between marine and atmospheric processes oscillating on a millennial time-scale. A multi-proxy study of the last 50,000 yr from the Alboran Sea (Western Mediterranean Sea). Quaternary Science Reviews, 24, 1623-1636.

Mortensen, A.K., Bigler, M., Grönvold, K., Steffensen, J.P., Johnsen, S.J., 2005. Volcanic ash layers from the Last Glacial Termination in the NGRIP ice core. Journal of Quaternary Science, 20, 209-219.

Munno, R., Petrosino, P., 2004. New constraints on the occurrence of Y-3 Upper Pleistocene tephra marker layer in the Tyrrhenian sea. Il Quaternario, 17, 11–20.

Munno, R., Petrosino, P., 2007. The late Quaternary tephrostratigraphical record of the San Gregorio Magno basin (southern Italy). Journal of Quaternary Science, 22, 247-266.

Nappi, G., Capaccioni, B., Mattioli, M., Mancini, E., Valentini, L., 1994. Plinian fall deposits from Vulsini volcanic district (Central Italy). Bulletin of Volcanology, 56, 502-515.

Narcisi, B., 1996. Tephrochronology of a Late Quaternary lacustrine record from the Monticchio maar (Vulture volcano, Southern Italy). Quaternary Science Reviews, 15, 155-165.

Narcisi, B., Vezzoli, L., 1999. Quaternary stratigraphy of distal tephra layers in the Mediterranean- an overview. Global and Planetary Change, 21, 31-50.

Nesse, W., 2000. Introduction to Optical Mineralogy. Oxford University Press, New York, USA, 442 pp.

Newton, A.J., Dugmore, A.J., 1993. Tephrochronology of Core C from Lago Grande di Monticchio. In: Negendank, J.F.W., Zolitschka, B. (Eds.), Paleolimnology of European Maar Lakes. Lecture Notes in Earth Sciences 49. Springer, Berlin, Heidelberg, 333 - 348.

Nomade, S., Renne, P.R., Vogel, N., Deino, A., Sharp, W.D., Becker, T.A., Jaouni, A.R., Mundil, R., 2005. Alder Creek sanidine (ACs-2): A Quaternary Ar/Ar dating standard tied to the Cobb Mountain geomagnetic event. Chemical Geology 218, 315 - 338.

North Greenland Ice-Core Project Members, 2004. High resolution climate record of the Northern Hemisphere reaching into the last Glacial Interglacial Period. Nature, 431, 147–151.

Oldfield, F., 1996. The PALICLAS project: synthesis and overview. Special issue: Palaeoenvironmental Analysis of Italian Crater Lake and Adriatic Sediments. Istituto Italiano di Idrobiologia. 329-357.

Oldfield, F., Asioli, A., Accorsi, C.A., Mercuri, A.M., Juggins, S., Langone, L., Rolph, T., Trincardi, F., Wolff, G., Gibbs, Z., Vigliotti, L., Fringnani, M., van der Post, K., Branch, N., 2003. A high resolution late Holocene palaeo environmental record from the central Adriatic Sea. Quaternary Science Reviews, 22, 319 – 342.

Ori, G.G., Roveri M., Vannoni, F. 1986. Plio-Pleistocene sedimentation in the Apenninic-Adriatic foredeep (Central Adriatic sea, Italy). In: Allen, P.A., Homewood, P. (Eds.) Foreland Basins. IAS Spec. Publ. 8, 183-198.

Orlic, M., Gacic, M., Laviolette, P.E., 1992. The Currents and Circulation of the Adriatic Sea. Oceanologica Acta, 15, 109-124.

Orsi, G., D'Antonio, M., de Vita, S., Gallo G., 1992. The Neapolitan Yellow Tuff, a large magnitude trachytic phreatoplinian eruption: Eruptive dynamics, magma withdrawal and caldera collapse. Journal of Volcanology and Geothermal Research, 53, 275 – 287.

Orsi, G., Piochi, M., Campajola, L., D'Onofrio, A., Gialanella, L., Terrasi, F., 1996. ^{14}C geochronological constraints for the volcanic history of the island of Ischia (Italy) over the last 5000 years. Journal of Volcanology and Geothermal Research, 71, 249-257.

Palinkas, C.M., Nittrouer, C.A., 2006. Clinoform sedimentation along the Apennine shelf, Adriatic Sea. Marine Geology, 234, 245-260.

Palladino, D.M., Agosta, E., Freda, C., Spaziani S., Trigila, R., 1994. Geo-petrographic and volcanological study of Southern Vulsini: the Valentano-Marta-La Rocca sector. Mem. Descr. Carta Geol. Ital. XLIX 255–276.

Palladino, D.M., Agosta, E., 1997. Pumice fall deposits of the western Vulsini Volcanoes (Central Italy). Journal of Volcanology and Geothermal Research, 78, 77-102.

Pappalardo, L., Civetta, L., D' Antonio, M., Deino, A., Di Vito, M., Orsi, G., Carandente, A., de Vita, S., Isaia, R., Piochi, M., 1999. Chemical and Sr-isotopical evolution of the Phlegrean magmatic system before the Campanian Ignimbrite and the Neapolitan Yellow Tuff eruptions. Journal of Volcanology and Geothermal Research, 91, 141–166.

Parker, R.J., 1989, Geochemical and petrographic characteristics of potassium-rich pyroclastic and lava samples from Vulsini volcano, Roman magmatic region, Italy, Journal of Volcanology and Geothermal Research, 39, 297-314.

Paterne, M., Guichard, F., Labeyrie, J., Gillot, P.Y., Duplessy, J.C., 1986. Tyrrhenian Sea tephrochronology of the oxygen isotope record for the past 60,000 years. Marine Geology, 72, 259–285.

Paterne, M., Guichard, F., Labeyrie, J., 1988. Explosive activity of the South Italian volcanoes during the past 80,000 years as determined by marine tephrochronology. Journal of Volcanology and Geothermal Research, 34, 153-172.

Paterne, M., Kallel, N., Labeyrie, L., Vautravers, M., Duplessy, J.-C., Rossignol-Strick, M., Cortijo, E., Arnold, M., Fontugne, M., 1999. Hydrological relationship between the North Atlantic Ocean and the Mediterranean Sea during the past 15 – 75 kyr. Paleoceanography, 14(5), 626 – 638.

Paterne, M., Guichard, F., Duplessy, J.C., Siani, G., Sulpizio, R., Labeyrie, J., 2008. A 90,000–200,000 yrs marine tephra record of Italian volcanic activity in the Central Mediterranean Sea. Journal of Volcanology and Geothermal Research, 177, 187 – 196.

Payne, R., Blackford, J., van der Plicht, J., 2008. Using cryptotephras to exten regional tephrochronologies: An example from southeast Alaksa and implications for hazard assessment. Quaternary International, 69, 42-55.

Pearce, N.J.G., Perkins, W.T., Westgate, J.A., Gorton, M.P., Jackson, S.E., Neal, C.R., Chenery, S.P., 1997. A compilation of new and published major and trace element data for NIST SRM 610 and NIST SRM 612 glass reference materials. Geostandards Newsletter, 21, 115 - 144.

Pearce, N.J.G., Westgate, J.A., Perkins, W.T., Preece, S.J., 2004. The application of ICP-MS methods to tephrochronological problems. Applied Geochemistry, 19, 289 – 322.

Pearce, N.J.G., Denton, J.S., Perkins, W.T., Westgate, J.A., Alloway, B.V., 2007. Correlation and characterisation of individual glass shards from tephra deposits using trace element laser ablation ICP-MS analyses: current status and future potential. Journal of Quaternary Science, 22, 721-736.

Pearce, N.H.G., Perkins, W.T., Westgate, J.A., Wade, S.C. in press. Trace-element microanalysis by LA-ICP-MS: The quest for comprehensive chemical characterisation of single, sub-10 μm volcanic glass shards. Quaternary International, doi:10.1016/j.quaint.2011.07.012

Peccerillo, A., 2005. Plio-Quaternary Volcanism in Italy. Springer, 360 p.p.

Perini, G., Francalanci, L., Davidson, J.P., Conticelli, S., 2004. Evolution and Genesis of Magmas from Vico Volcano, Central Italy: Multiple Differentiation Pathways and Variable Parental Magmas. Journal of Petrology, 45(1), 139 – 182.

Pilcher, J., Bradley, R.S., Francus, P., Anderson, L., 2005. A Holocene tephra record from the Lofoten Islands, Arctic Norway. Boreas, 34, 136–156.

Pinti, D.L., Quidelleur, X., Chiesa, S., Ravazzi, C., Gillot, P.Y., 2001. K-Ar dating of an early Middle Pleistocene distal tephra in the interglacial varved succession of Pianico-Sellere (Southern Alps, Italy). Earth and Planetary Science Letters, 188, 1-7.

Pisias, N. G., Martinson, D. G., Moore, T. C., et al. 1984. High resolution stratigraphic correlation of benthic oxygen isotopic records spanning the last 300,000 years. Marine Geology, 56, 119–136.

Piva, A., 2007. High-resolution stratigraphy of Central and Southern Adriatic Quaternary deposits: impact of sub-Milankovian climate change on Mediterranean circulation. PhD. thesis, University of Bologna, unpublished.

Piva, A., Asioli, A., Schneider, R.R., Trincardi, F., Andersen, N., Colmenero-Hidalgo, E., Dennielou, B., Flores, J-A., Vigliotti, L., 2008a. Climatic cycles as expressed in sediments of the PROMESS1 borehole PRAD1-2, central Adriatic, for the last 370 ka: 1. Integrated stratigraphy. Geochemistry, Geophysics, Geosystems, 9(3), 1 – 21.

Piva, A., Asioli, A., Trincardi, F., Schneider, R.R., Vigliotti, L., 2008b. Late-Holocene climate variability in the Adriatic sea (Central Mediterranean). Holocene, 18, 153-167.

Piva, A., Andersen, N., Asioli, A., Schneider, R.R., Dennielou, B., Massamba, I., Mercuri, A.M., Tateo, F., Trincardi, F., and RHUL TEAM., 2008c. High-resolution record of Dansgaard-Oeschger variability in the Adriatic Sea (Central Mediterranean). Geophysical Research Abstracts, 10.

Poli, S., Chiesa, S., Gillot, P.-Y., Gregnanin, A., Guichard, F., 1987. Chemistry versus time in the volcanic complex of Ischia (Gulf of Naples, Italy): evidence of successive magmatic cycles. Contributions to Mineralogy and Petrology, 95, 322 – 335.

Pollard, A.M., Blockley, S.P.E., Lane, C.S., 2006. Some Numerical Considerations in the Geochemical Analysis of Distal Microtephra. Applied Geochemistry, 21, 1692–1714.

Preece, R.C., Westgate, J.A., Alloway, B.V., Milner, N.W., 2000. Characterisation, identity, distribution, and source of the late Cenozoic Tephra beds in the Klondike district of the Yukon, Canada. Canadian Journal of Earth Sciences, 37, 983 - 996

Pyle, D.M., Ricketts, G.D., Margari, V., van Andel, T.H., Sinitsyn, A.A., Praslov, N.D., Lisitsyn, S., 2006. Wide dispersal and deposition of distal tephra during the Pleistocene 'Campanian Ignimbrite/Y5' eruption, Italy. Quaternary Science Reviews, 25, 2713 – 2728.

Pyne-O'Donnell, S., 2011. The taphonomy of Last Glacial–Interglacial Transition (LGIT) distal volcanic ash in small Scottish lakes. Boreas, 40, 131 – 145.

Rasmussen, S.O., Andersen, K.K., Svensson, A.M., Steffensen J.P., Vinther, B., Clausen, H.B., Siggaard-Andersen, M.L., Johnsen, S.J., Larsen, L.B., Dahl-Jensen, D.,Bigler, M., Röthlisberger, R., Fischer, H., Goto-Azuma, K., Hansson, M., Ruth, U., 2006. A new Greenland ice core chronology for the last glacial termination. Journal of Geophysical Research, 111, p. D06102.

Rasmussen, T.L., Wastegård, S., Kuijpers, A., van Weering, T.C.E., Heinemeier, J., Thomsen, E., 2003. Stratigraphy and distribution of tephra layers in marine sediment cores from the Faeroe Islands, North Atlantic. Marine Geology, 199, 263-277.

Reed, S.J.B., 2005. Electron microprobe analysis. Cambridge Monographs on Physics, second edition, Cambridge University Press, Cambridge.

Reimer, P.J., Reimer, R.W., 2001. A marine reservoir correction database and on-line interface. Radiocarbon, 43, 461-463.

Reimer, P.J., Reimer, R.W., 2007. Radiocarbon Dating: Calibration, In Elias, S.A., 2007. Encyclopedia of Quaternary Science, Elsevier, 2941 – 2950.

Reimer, P.J., Baillie, M.G.L., Bard, E., Bayliss, A., Beck, J.W., Blackwell, P.G., Bronk Ramsey, C., Buck, C.E., Burr, G.S., Edwards, R.L., Friedrich, M., Grootes, P.M., Guilderson, T.P., Hajdas, I., Heaton, T.J., Hogg, A.G., Hughen, K.A., Kaiser, K.F., Kromer, B., McCormac, F.G., Manning, S.W., Reimer, R.W., Richards, D.A., Southon, J.R., Talamo, S., Turney, C.S.M., van der Plicht, J., Weyhenmeyer, C.E,. 2009. IntCal09 and Marine09 radiocarbon age calibration curves, 0 - 50,000 years cal BP. Radiocarbon, 51, 1111–1150.

Renne, P.R., Sharp, W.D., Deino, A.L., Orsi, G., Civetta, L., 1997. $^{40}Ar/^{39}Ar$ Dating into the Historical Realm: Calibration Against Pliny the Younger. Science, 277, 1279 – 1280.

Ridente, D., Foglini, F., Minisini, D., Trincardi, F., Verdicchio, G., 2007. Shelf-edge erosion, sediment failure and inception of Bari Canyon on the Southwestern Adriatic Margin (Central Mediterranean). Marine Geology, 246, 193 – 207.

Rohling, E.J., Hilgen, F.J., 1991. The Eastern Mediterranean climate at times of sapropel formation – a review. Geologie En Mijnbouw, 70, 253-264.

Rohling, E. J., De Stigter, H.C., Vergnaud Grazzini, C., Zaalberg R., 1993. Temporary repopulation by low-oxygen tolerant benthic foraminifera within an Upper Pliocene sapropel: Evidence for the role of oxygen depletion in the formation of sapropel. Marine Micropaleontogy, 22, 207-219.

Rohling, E. J., Hayes, A., De Rijk, S., Kroon, D., Zachariasse, W.J., Eisma D., 1998. Abrupt cold spells in the northwestern Mediterranean, Paleoceanography, 13(4), 316–322.

Rolandi, G., Petrosino, P., McGeehin, J., 1998. The interplinian activity at Somma-Vesuvius in the last 3500 years. Journal of Volcanology and Geothermal Research, 82, 19-52.

Rollinson, H.R., 1993. Using Geochemical Data: Evaluation, Presentation, Interpretation. Longman, Harlow.

Rolph, T.C., Oldfield, F., van der Post, K.D., 1996. Palaeomagnetism and rock-magnetism results from Lake Albano and Adriatic Sea (Italy). In Oldfield, F., Guilizzoni, P., (eds) Italian crater lake and Adriatic sediments, Memorie dell'Instituto Italiano di Idrobiologia, 55, 39-70.

Rosi, M., and Sbrana, A., 1987. Phlegrean Fields. Consiglio Nazionale delle Ricerche, Roma, 176pp.

Rossignol-Strick, M., Planchais, N., 1989. Climate patterns revealed by pollen and oxygen isotope records of a Tyrrhenian Sea core. Nature 342, 413-416.

Rossignol-Strick, M., Paterne, M., Bassinot, F.C., Emeis, K.C., De Lange, G.J., 1998. An unusual mid-pleistocene monsoon period over Africa and Asia. Nature 392, 269-272.

Rossignol-Strick M., Paterne, M., 1999. A synthetic pollen record of eastern Mediterranean sapropels of the last 1 Ma: implications for the time-scale and formation of sapropels. Marine Geology, 153, 221-238.

Royden, L., Patacca, E., Scandone, P., 1987. Segmentation and configuration or subducted lithosphere in Italy – an important control on thrust-belt and foredeep-basin evolution. Geology, 15, 714-717.

Sànchez Goñi, M. F., Cacho, I., Turon, J.-L., Guiot, J., Sierro, F., Peypouquet, J.-P., Grimalt, J.O., Shackleton, N.J., 2002. Synchroneity between marine and terrestrial responses to millennial scale climate variability during the last glacial period in the Mediterranean region. Climate Dynamics, 19, 95-105.

Sangiorgi, F., Capotondi, L., Brinkhuis, H., 2002. A centennial scale organic-walled dinoflagellate cyst record of the last deglaciation in the South Adriatic Sea (Central Mediterranean). Palaeogeography, Palaeoclimatology, Palaeoecology, 186, 3-4, 199-216.

Santacroce, R., 1987. Somma-Vesuvius, Consiglio Nazionale della Ricerche, Roma.

Scandone, R., Bellucci, F., Lirer, L., Rolandi, G., 1991. The structure of the Campanian Plain and the activity of the Neapolitan volcanoes (Italy). Journal of Volcanology and Geothermal Research, 48, 1-31.

Scott, E.M., 2007. Radiocarbon Dating, Sources of Error. In Elias, S.A., 2007. Encyclopedia of Quaternary Science, Elsevier, 2918-2923.

Shackleton, N.J., Berger, A., Peltier, W.A., 1990. An alternative astronomical calibration of the lower Pleistocene timescale based on ODP Site 677. Transactions of the Royal Society of Edinburgh: Earth Sciences, 81, 251–261.

Shane, P., Froggatt, P., Black, T., Westgate, J., 1995. Chronology of Pliocene and Quaternary bioevents and climatic events from Fisson-Track ages on tephra beds, Wairarapa, New Zealand. Earth and Planetary Science Letters, 130, 141-154.

Shane, P., 2000. Tephrochronology: a New Zealand case study. Earth-Science Reviews, 49, 223-259.

Siani, G., Paterne, M., Arnold, M., Bard, E., Métivier, B., Tisnert, N., Bassinot, F., 2000. Radiocarbon reservoir ages in the Mediterranean Sea and Black Sea, Radiocarbon, 42, 271-280

Siani, G., Paterne, M., Michel, E., Sulpizio, R., Sbrana, A., Arnold, M., Haddad, G., 2001. Mediterranean sea surface radiocarbon age changes since the Last Glacial Maximum, Science, 294, 1917-1920.

Siani, G., Sulpizio, R., Paterne, M., Sbrana, A., 2004. Tephrostratigraphy study for the last 18,000 ^{14}C years in a deep-sea sediment sequence for the South Adriatic. Quaternary Science Reviews, 23, 2485-2500.

Siani, G., Paterne, M., Colin, C., 2010. Late glacial to Holocene planktic foraminifera bioevents and climatic record in the South Adriatic Sea. Journal of Quaternary Science, 25, 808-821.

Sierro, F.J., Hodell, D.A., Curtis, J.H., Flores, J.A., Reguera, I., Colmenero-Hidalgo, E., Barcena, M.A., Grimalt, J.O., Cacho, I., Frigola, J., Canals, M., 2005. Impact of iceberg melting on Mediterranean thermohaline circulation during Heinrich events. Paleoceanography, 20.

Smith, V.C., Mark, D.F., Staff, R.A., Blockley, S.P.E., Bronk Ramsey, C., Bryant, C.L., Nakagawa, T., Kyu Han, K., Weh, A., Takemura, K., Danhara, T., Suigetsu 2006 Project Members. 2011, in press. Toward establishing precise $^{40}Ar/^{39}Ar$ chronologies for Late Pleistocene palaeoclimate archives: an example from Suigetsu SG06, Japan. Quaternary Science Reviews, doi:10.1016/j.quascirev.2011.06.020.

Sprovieri, R., Di Stefano, E., Incarbona, A., Gargano, M.E., 2003. A high-resolution record of the last deglaciation in the Sicily Channel based on foraminifera and calcareous nannofossil quantitative distribution. Palaeogeography Palaeoclimatology Palaeoecology, 202, 119-142.

Stokes, S. and Lowe D.J., 1988. Discriminant Function Analysis of Late Quaternary Tephra from Five Volcanoes in New Zealand Using Glass Shard Major Element Chemistry. Quaternary Research, 30, 270 – 283.

Stokes, S., Lowe, D.J., Froggatt, P.C., 1992. Discriminant Function Analysis and Correlation of Late Quaternary Rhyolitic Tephra Deposits from Taupo and Pkataina Volcanoes, New Zealand, using Glass Shard major element composition. Quaternary International, 13/14, 103 – 117.

Stuiver, M., Reimer, P.J., 1993. Extended C-14 data-base and revised CALIB 3.0 C-14 age calibration program. Radiocarbon, 35, 215-230.

Svensson, A., Andersen, K.K., Bigler, M., Clausen, H.B., Dahl-Jensen, D., Davies, S.M., Johnsen, S.J., Muscheler, R., Parrenin, F., Rasmussen, S.O., Roethlisberger, R., Seierstad, I., Steffensen, J.P., Vinther, B.M., 2008. A 60,000 year Greenland stratigraphic ice core chronology. Climate of the Past, 4, 47-57.

Syvitski, J.P.M., Albert J Kettner, A.J., 2007. On the flux of water and sediment into the Northern Adriatic Sea. Continental Shelf Reserach, 27, 296 – 308.

Tarling, D.H., 1983. Palaeomagnestism: Principles and Applications in Geology, Geophysics and Archaeology, Chapman and Hall, London.

Thomas, R., 2001a. A beginner's guide to ICP-MS, part II: the sample-introduction system. Spectroscopy, 16(5), 56-60.

Thomas, R., 2001b. A beginner's guide to ICP-MS, Part IV: The interface region. Spectroscopy, 16(7), 26-28.

Thompson, R.N., 1982. British Tertiary province. Scottish Journal of Geology, 18, 49-107.

Toms, P.S., King, M., Zárate, M.A., Kemp, R.A., Foit Jr., F.F., 2004. Geochemical characterization, correlation, and optical dating of tephra in alluvial sequences of central western Argentina. Quaternary Research, 62, 60-75.

Ton-That, T., Singer, B., Paterne, M., 2001. $^{40}Ar/^{39}Ar$ dating of latest Pleistocene (41ka) marine tephra in the Mediterranean Sea: implications for global climate records. Earth and Planetary Science Letters, 184, 645-658.

Triantaphyllou, M.V., Antonarakou, A., Dimiza, M., Anagnostou, C., 2010. Calcareous nannofossil and planktonic foraminiferal distributional patterns during deposition of sapropels S6, S5 and S1 in the Libyan Sea (Eastern Mediterranean). Geo-Marine Letters, 30, 1-13.

Trigila, R., 1995. The volcano of the Alban Hills. Tipografia della Scuola Grafica Salesiana, Roma, 283 pp.

Trincardi, F., Correggiati, A., Roveri, M., 1994. Late-Quaternary transgressive erosion and deposition in a morden epicontinental shelf the Adriatic semienclosed basin. Geo-Marine Letters, 14, 41-51.

Trincardi, F., Asioli, A., Cattaneo, A., Correggiari, A., Langone, L., 1996. Stratigraphy of the late-Quaternary deposits in the Central Adriatic basin and the record of short-term climatic events. In Oldfield, F., Guilizzoni, P., (eds) Italian crater lake and Adriatic sediments, Memorie dell'Instituto Italiano di Idrobiologia, 55, 39-70.

Trincardi F., Foglini F., Verdicchio G., Asioli A., Correggiari A., Minisini D., Piva A., Remia A., Ridente D., Taviani M., 2007. The impact of cascading currents on the Bari Canyon System, SW-Adriatic Margin (Central Mediterranean). Marine Geology, 246(2-4), 208 – 230.

Tryon, C.A., Roach, N.T., Logan, M.A.V., 2008. The Middle Stone Age of the northern Kenyan Rift: age and context of new archaeological sites from the Kapedo Tuffs. Journal of Human Evolution, 55, 652-664.

Turbeville, B.N., 1992. Tephra fountaining, rheomorphism and spatter flow during the emplacement of the Pitigliano Tuffs, Latera caldera, Italy. Journal of Volcanology and Geothermal Research, 53, 309 – 327.

Turney, C.S.M., 1998. Extraction of rhyolitic ash from minerogenic lake sediments. Journal of Paleolimnology, 19, 199 - 206.

Turney, C.S.M., Lowe, J.J., Davies, S.M., Hall, V., Lowe, D.J., Wastegård, S., Hoek, W.Z., Alloway, B., SCOTAV and INTIMATE Members, 2004. Tephrochronology of Last Termination Sequences in Europe: a protocol for improved analytical precision and robust correlation procedures (a joint SCOTAV-INTIMATE proposal). Journal of Quaternary Science, 19, 111-120.

Turney, C.S.M., Blockley, S.P.E., Lowe, J.J., Wulf, S., Branch, N.P., Swindle, G., Nathan, R., Pollard, M., 2008. Geochemical Characterisation of Quaternary Tephras from the Campanian Province, Italy. Quaternary International, 178(1), 288 – 305.

Twyman, R.M., 2007. K/Ar and Ar/Ar dating. In Elias, S.A., 2007. Encyclopedia of Quaternary Science, Elsevier, 1313 – 1317.

Tzedakis, P.C., Andrieu, V., de Beaulieu, J.-L., Crowhurst, S., Follieri, M., Hooghiemstra, H., Magri, D., Reille, M., Sadori, L., Shackleton, N.J., Wijmstra, T.A., 1997. Comparison of terrestrial and marine records of changing climate of the last 500,000 years. Earth and Planetary Science Letters, 150, 171–176.

Tzedakis, P.C., Andrieu, V., de Beaulieu, J.-L., Birks, H.J.B., Crowhurst, S., Follieri, M., Hooghiemstra, H., Magri, D., Reille, M., Sadori, L., Shackleton, N.J., Wijmstra, T.A., 2001. Quaternary Science Reviews, 20, 1583 - 1592

Tzedakis, P.C., McManus, J.F., Hooghiemstra, H., Oppo, D.W., Wijmstra, T.A., 2003. Comparison of changeds in vegetation in northeast Greece with records of climate variability on orbital and suborbital frequencies over the last 450 000 years. Earth and Planetary Science Letters, 212, 197 – 212.

van den Bogaard, P., and Schmincke, H., 1985. "Laacher See Tephra: A widespread isochronous late Quaternary tephra layer in central and northern Europe". Geological Society of America Bulletin, 96 (12), 1554–1571.

van der Plicht, J., Beck, J.W., Bard, E., Baille, M.G.L., Blackwell, P.G., Buck, C.E., Friedrich, M., Guilderson, T.P., Hughen, K.A., Kromer, B., McCormac, F.G., Bronk Ramsey, C., Reimer, P.J., Reimer, R.W., Remmele, S., Richards, D.A., Stuiver, M., Weyhenmeyer, C.E., 2004. NOTCAL04 – Comparison/Calibration ^{14}C records 26 – 50 cal kyr BP. Radiocarbon, 46, 1225 - 1238

Verdicchio, G., Trincardi, F., 2006. Short-distance variability in slope bed-forms along the southwestern Adriatic Margin (Central Mediterranean). Marine Geology, 234, 271-292.

Verdicchio, G., Trincardi, F., Asioli, A., 2007. Mediterranean bottom-current deposits: an example from the Southwestern Adriatic Margin. In Viana, A.R., Rebesco, M. (Eds.) Economic and palaeoceanographic importance of Contourite. Geol. Soc. Spec. Pub. 199 – 224.

Vezzoli, L., 1988. Island if Ischia. Consiglio Nazionale delle Ricerche, Roma, 132 pp.

Vezzoli, L., 1991. Tephra layers in Bannock Basin (Eastern Mediterranean). Marine Geology, 100, 21–34.

Vogel, H., Zanchetta, G., Sulpizio, R., Wagner, B., Nowaczyk, N., 2010a. A tephrostratigraphic record for the last glacial-interglacial cycle from Lake Ohrid, Albania and Macedonia. Journal of Quaternary Science, 25, 320-338.

Vogel, H., Wagner, B., Zanchetta, G., Sulpizio, R., Rosen, P., 2010b. A paleoclimate record with tephrochronological age control for the last glacial-interglacial cycle from Lake Ohrid, Albania and Macedonia. Journal of Paleolimnology, 44, 295-310.

Wagner, B., Sulpizio, R., Zanchetta, G., Wulf, S., Wessels, M., Daut, G., Nowaczyk, N., 2008. The last 40 ka tephrostratigraphic record of Lake Ohrid, Albania and Macedonia: a very distal archive for ash dispersal from Italian volcanoes. Journal of Volcanology and Geothermal Research, 177, 71-80.

Wagner, B., Lotter, A.F., Nowaczyk, N., Reed, J.M., Schwalb, A., Sulpizio, R., Valsecchi, V., Wessels, M., Zanchetta, G., 2009. A 40,000-year record of environmental change from ancient Lake Ohrid (Albania and Macedonia). Journal of Paleolimnology, 41, 407-430.

Walker, M.J.C., Björck, S., Lowe, J.J., Cwynar, L.C., Johnsen, S., Knudsen, K.-L., Wohlfarth, B., and INTIMATE group, 1999. Isotopic 'events' in the GRIP ice core: a stratotype for the Late Pleistocene. Quaternary Science Reviews, 18, 1143 – 1150.

Walker, M.J.C., 2005. Quaternary Dating Methods. John Wiley and Sons, Chichester.

Wang, Y.J., Cheng, H., Edwards, R.L., An, Z.S., Wu, J.Y., Shen, C.C., Dorale, J.A., 2001. A high-resolution absolute-dated Late Pleistocene monsoon record from Hulu Cave, China. Science, 294, 2345-2348.

Wastegard, S., 2002. Early to middle Holocene silicic tephra horizons from the Katla volcanic system, Iceland: new results from the Faroe Islands. Journal of Quaternary Science, 17, 723-730.

Watts, W.A., Allen, J.R.M., Huntley, B., 1996. Vegetation history and palaeoclimate of the last glacial period at Lago Grande di Monticchio, southern Italy. Quaternary Science Reviews, 15, 133–153.

Weaver, P.P.E., 2006. EUROSTRATAFORM Special Issue of Marine Geology. Marine Geology, 234, 1-2.

Webster, J.D., Raia, E., Tappen, C., De Vivo, B., 2003. Pre-eruptive geochemistry of the ignimbrite-forming magmas of the Campanian Volcanic Zone, Southern Italy, determined from silicate melt inclusions. Mineralogy and Petrology, 79, 99 – 125.

Westgate, J.A., Preece, S.J., Froese, D.G., Walter, R.C., Sandhu, A.S., Schweger, C.E., 2001. Dating Early and Middle (Reid) Pleistocene glaciations in central Yukon by tephrochronology. Quaternary Research, 56, 335–348.

Wintle, A.G., 1996. Archaeologically-relevant dating techniques for the next century - Small, hot and identified by acronyms. Journal of Archaeological Science, 23, 123-138.

Wohlfarth, B., Blaauw, M., Davies, S.M., Andersson, M., Wastegard, S., Hormes, A., Possnert, G., 2006. Constraining the age of Lateglacial and early Holocene pollen zones and tephra horizons in southern Sweden with Bayesian probability methods. Journal of Quaternary Science, 21, 321-334.

Wolff, E.W., Chappellaz, J., Blunier, T., Rasmussen, S.O., Svensson, A., 2010. Millennial-scale variability during the last glacial: The ice core record. Quaternary Science Reviews, 29, 2828-2838.

Woodward, J.C., Goldberg, P., 2001. Special issue: Rockshelter sediment records and environmental change in the mediterranean region: Part I - Introduction. Geoarchaeology-an International Journal, 16, 323-325.

Wulf, S., Kraml, M., Brauer, A., Keller, J., Negendank, J.F.W., 2004. Tephrochronology of the 100ka lacustrine sediment record of Lago Grande di Monticchio. Quaternary International, 122, 7-30.

Wulf, S., Brauer, A., Mingram, J., Zolitschka, B., Negendank, J.F.W., 2007. Distal tephras in the sediments of Monticchio maar lakes. In: Principe, C. (ed.), Geologia del Monte Vulture. Bollettino della Società Geologica Italiana, 105-122.

Wulf, S., Kraml, M., Keller, J., 2008. Towards a detailed distal tephrostratigraphy in the Central Mediterranean: The last 20,000 yrs record of Lago Grande di Monticchio. Journal of Volcanology and Geothermal Research, 177, 118 – 132.

Zanchetta, G., Sulpizio, R., Giaccio, R., Siani, G., Paterne, M., Wulf, S., D'Orazio, M., 2008. The Y-3 tephra: a stratigraphic marker for the Last Glacial successions of the Central Mediterranean Basin. Journal of Volcanology and Geothermal Research, 177, 145–154.

Zillen, L.M., Wastegård, S., Snowball, I.F., 2002. Calendar ages of three mid-Holocene Tephra layers identified in varved lake sediments in west central Sweden. Quaternary Science Reviews, 21, 1583-1591.

Zore-Armanda, M., 1963. Water exchange between the Adriatic and the Eastern Mediterranean. Deep Sea Research and Oceanographic Abstracts, 16(2), 171 – 178.

Appendix A

PRAD 1-2 5 cm resolution Tephra Shards Counts

Core Section	Section Depth (cm)	Absolute Depth (cm)	Clear Shards per g dry wt	Brown Shards per g dry wt
1	0	0.00	9	N/A
1	5	0.05	8	N/A
1	10	0.10	5	N/A
1	15	0.15	2	N/A
1	20	0.20	3	N/A
1	25	0.25	18	N/A
1	30	0.30	57	N/A
1	35	0.35	84	N/A
1	40	0.40	198	N/A
1	45	0.45	62	N/A
1	50	0.50	1,089	N/A
1	55	0.55	1,095	N/A
1	60	0.60	338	N/A
1	65	0.65	251	N/A
1	70	0.70	48	N/A
1	75	0.75	27	N/A
2	0.5	0.80	13	N/A
2	5.5	0.85	19	N/A
2	10.5	0.90	9	N/A
2	15.5	0.95	7	N/A
2	20.5	1.00	5	N/A
2	25.5	1.05	17	N/A
2	30.5	1.10	15	N/A
2	35.5	1.15	149	N/A
2	40.5	1.20	200	N/A
2	45.5	1.25	189	N/A
2	50.5	1.30	36	N/A
2	55.5	1.35	28	N/A
2	60.5	1.40	0	N/A
2	65.5	1.45	1	N/A
2	70.5	1.50	2	N/A
2	75.5	1.54	0	N/A
3	0	1.58	0	N/A
3	3	1.63	0	N/A
3	8	1.68	1	N/A
3	13	1.73	5	N/A
3	18	1.78	5	N/A
3	23	1.83	21	N/A
3	28	1.88	136	N/A
3	33	1.93	146	N/A
3	38	1.98	191	N/A
3	43	2.03	746	N/A
3	48	2.08	572	N/A
3	53	2.13	500	N/A
3	58	2.18	10,000	N/A
3	63	2.23	3,858	N/A
3	68	2.28	5,847	N/A
3	73	2.33	61	N/A
4	2	2.38	17	N/A
4	7	2.43	24	N/A
4	12	2.48	14	N/A
4	17	2.53	8	N/A
4	22	2.58	7	N/A
4	27	2.63	26	N/A
4	32	2.68	1,238	N/A
4	37	2.73	767	N/A
4	42	2.78	1	N/A
4	47	2.83	0	N/A
4	52	2.88	0	N/A
4	57	2.93	1	N/A
4	62	2.98	2	N/A
4	67	3.03	0	N/A
4	72	3.08	0	N/A
5	0.5	3.13	117	N/A
5	4.5	3.24	10,000	N/A
5	9.5	3.28	1,492	N/A
5	14.5	3.32	1,448	N/A
5	19.5	3.36	0	N/A
5	24.5	3.40	0	N/A
5	29.5	3.44	0	N/A
5	34.5	3.48	0	N/A
5	39.5	3.52	1	N/A
5	44.5	3.56	0	N/A
5	49.5	3.60	0	N/A

Core Section	Section Depth (cm)	Absolute Depth (cm)	Clear Shards per g dry wt	Brown Shards per g dry wt
5	54.5	3.64	0	N/A
5	59.5	3.68	0	N/A
5	64.5	3.72	0	N/A
5	69.5	3.76	0	N/A
5	74.5	3.80	0	N/A
5	79.5	3.84	0	N/A
6	0	4.00	102	N/A
6	4	4.04	3,187	N/A
6	9	4.09	767	N/A
6	14	4.14	5	N/A
6	19	4.19	61	N/A
6	24	4.24	2	N/A
6	29	4.29	0	N/A
6	34	4.34	15	N/A
6	39	4.39	0	N/A
6	44	4.44	4	N/A
6	49	4.49	3	N/A
6	54	4.54	130	N/A
6	59	4.59	151	N/A
6	64	4.64	0	N/A
6	69	4.69	1	N/A
7	74	4.80	308	N/A
7	4	4.84	82	N/A
7	9	4.89	5	N/A
7	14	4.94	0	N/A
7	19	4.99	0	N/A
7	24	5.04	0	N/A
7	29	5.09	0	N/A
7	34	5.14	0	N/A
7	39	5.19	0	N/A
7	44	5.24	0	N/A
7	49	5.29	0	N/A
7	54	5.34	0	N/A
7	59	5.39	0	N/A
7	64	5.44	0	N/A
7	69	5.49	0	N/A
7	74	5.54	0	N/A
8	1.5	5.59	8	N/A
8	6.5	5.66	26	N/A
8	11.5	5.71	0	N/A
8	16.5	5.75	2	N/A
8	21.5	5.79	0	N/A
8	26.5	5.83	0	N/A
8	31.5	5.87	0	N/A
8	36.5	5.91	0	N/A
8	41.5	5.95	0	N/A
8	46.5	6.04	0	N/A
8	51.5	6.08	17	N/A
8	56.5	6.14	0	N/A
8	61.5	6.18	0	N/A
8	66.5	6.23	0	N/A
8	71.5	6.28	0	N/A
8	76.5	6.33	0	N/A
9	0.5	6.40	0	N/A
9	5.5	6.45	0	N/A
9	10.5	6.50	36	N/A
9	15.5	6.55	1	N/A
9	20.5	6.60	0	N/A
9	25.5	6.65	0	N/A
9	30.5	6.70	0	N/A
9	35.5	6.75	0	N/A
9	40.5	6.80	0	N/A
9	45.5	6.85	0	N/A
9	50.5	6.90	0	N/A
9	55.5	6.95	0	N/A
9	60.5	7.00	0	N/A
9	65.5	7.05	0	N/A
9	70.5	7.10	0	N/A
9	75.5	7.15	0	N/A
10	0	7.20	0	N/A
10	4	7.24	0	N/A
10	9	7.29	0	N/A
10	14	7.34	0	N/A
10	19	7.39	0	N/A
10	24	7.44	0	N/A
10	29	7.49	0	N/A
10	34	7.54	0	N/A
10	39	7.59	0	N/A
10	44	7.64	0	N/A
10	49	7.69	1	N/A
10	54	7.74	1	N/A
10	59	7.79	353	N/A
10	64	7.84	359	N/A
10	69	7.89	30	N/A

Core Section	Section Depth (cm)	Absolute Depth (cm)	Clear Shards per g dry wt	Brown Shards per g dry wt
11	0.5	8.00	27	N/A
11	4.5	8.05	15	N/A
11	9.5	8.10	3	N/A
11	14.5	8.15	0	N/A
11	19.5	8.20	0	N/A
11	24.5	8.25	0	N/A
11	29.5	8.30	0	N/A
11	34.5	8.35	0	N/A
11	39.5	8.40	0	N/A
11	44.5	8.45	156	N/A
11	49.5	8.50	24	N/A
11	54.5	8.55	5	N/A
11	59.5	8.60	2	N/A
11	64.5	8.65	0	N/A
11	69.5	8.70	101	N/A
11	74.5	8.75	178	N/A
12	2	8.80	6	N/A
12	7	8.85	0	N/A
12	12	8.90	0	N/A
12	17	8.95	0	N/A
12	22	9.00	0	N/A
12	27	9.05	0	N/A
12	32	9.10	0	N/A
12	37	9.15	0	N/A
12	42	9.20	0	N/A
12	47	9.25	0	N/A
12	52	9.30	0	N/A
12	57	9.35	0	N/A
12	62	9.40	0	N/A
12	67	9.45	0	N/A
12	72	9.50	0	N/A
12	77	9.55	0	N/A
13	0	9.60	0	N/A
13	5	9.65	0	N/A
13	10	9.70	0	N/A
13	15	9.75	0	N/A
13	20	9.80	0	N/A
13	25	9.85	0	N/A
13	30	9.90	0	N/A
13	35	9.95	0	N/A
13	40	10.00	0	N/A
13	45	10.05	0	N/A
13	50	10.10	7	N/A
13	55	10.15	0	N/A
13	60	10.20	0	N/A
13	65	10.25	0	N/A
13	70	10.30	0	N/A
13	75	10.35	0	N/A
13	80	10.40	0	N/A
14	0	10.45	0	N/A
14	5	10.50	0	N/A
14	10	10.55	0	N/A
14	15	10.60	0	N/A
14	20	10.65	0	N/A
14	25	10.70	0	N/A
14	30	10.75	0	N/A
14	35	10.80	0	N/A
14	40	10.85	0	N/A
14	45	10.90	0	N/A
14	50	10.95	0	N/A
14	55	11.00	6	N/A
14	60	11.05	8,000	N/A
14	65	11.10	8,000	N/A
14	70	11.15	418	N/A
15	0	11.20	32	N/A
15	5	11.25	145	N/A
15	10	11.30	113	N/A
15	15	11.35	82	N/A
15	20	11.40	1	N/A
15	25	11.45	12	N/A
15	30	11.50	0	N/A
15	35	11.55	0	N/A
15	40	11.60	0	N/A
15	45	11.65	0	N/A
15	50	11.70	0	N/A
15	55	11.75	0	N/A
15	60	11.80	0	N/A
15	65	11.85	0	N/A
15	70	11.90	0	N/A
15	75	11.95	0	N/A
16	2	12.00	0	N/A
16	7	12.05	0	N/A
16	12	12.10	0	N/A
16	17	12.15	0	N/A

Core Section	Section Depth (cm)	Absolute Depth (cm)	Clear Shards per g dry wt	Brown Shards per g dry wt
16	22	12.20	0	N/A
16	27	12.25	0	N/A
16	32	12.30	0	N/A
16	37	12.35	0	N/A
16	42	12.40	0	N/A
16	47	12.45	0	N/A
16	52	12.50	0	N/A
16	57	12.55	0	N/A
16	62	12.60	0	N/A
16	67	12.65	0	N/A
16	72	12.77	0	N/A
17	2	12.82	0	N/A
17	7	12.87	0	N/A
17	12	12.92	0	N/A
17	17	12.97	1	N/A
17	22	13.02	1	N/A
17	27	13.07	2	N/A
17	32	13.12	0	N/A
17	37	13.17	0	N/A
17	42	13.22	2	N/A
17	47	13.27	8	N/A
17	52	13.32	53	N/A
17	57	13.37	28	N/A
17	62	13.42	0	N/A
17	67	13.47	0	N/A
17	72	13.52	0	N/A
18	0	13.60	0	N/A
18	5	13.65	3	N/A
18	10	13.70	0	N/A
18	15	13.75	2	N/A
18	20	13.80	0	N/A
18	25	13.85	0	N/A
18	30	13.90	0	N/A
18	35	13.95	0	N/A
18	40	14.00	0	N/A
18	45	14.05	1	N/A
18	50	14.10	0	N/A
18	55	14.15	0	N/A
18	60	14.20	0	N/A
18	65	14.25	3	N/A
18	70	14.30	0	N/A
18	75	14.35	1	N/A
19	0	14.40	0	N/A
19	4	14.44	0	N/A
19	9	14.49	2	N/A
19	14	14.54	0	N/A
19	19	14.59	4	N/A
19	24	14.64	0	N/A
19	29	14.69	0	N/A
19	34	14.74	204	N/A
19	39	14.79	0	N/A
19	44	14.84	3	N/A
19	49	14.89	2	N/A
19	54	14.94	1,878	N/A
19	59	14.99	2	N/A
19	64	15.04	2	N/A
19	69	15.09	5	N/A
19	74	15.14	2	N/A
20	2	15.22	1	N/A
20	7	15.27	0	N/A
20	12	15.32	1	N/A
20	17	15.37	0	N/A
20	22	15.42	0	N/A
20	27	15.47	0	N/A
20	32	15.52	1	N/A
20	37	15.57	0	N/A
20	42	15.62	0	N/A
20	47	15.67	0	N/A
20	52	15.72	0	N/A
20	57	15.77	1	N/A
20	62	15.82	0	N/A
20	67	15.87	1	N/A
20	72	15.92	1	N/A
21	0	15.98	1	N/A
21	5	16.03	4	N/A
21	10	16.08	1	N/A
21	15	16.13	0	N/A
21	20	16.18	0	N/A
21	25	16.23	0	N/A
21	30	16.28	2	N/A
21	35	16.33	0	N/A
21	40	16.38	1	N/A
21	45	16.43	7	N/A
21	50	16.48	5,376	N/A

Core Section	Section Depth (cm)	Absolute Depth (cm)	Clear Shards per g dry wt	Brown Shards per g dry wt
21	55	16.53	10,000	N/A
21	60	16.58	29	N/A
21	65	16.63	1	N/A
21	70	16.68	2	N/A
21	75	16.73	1	N/A
22	2.5	16.82	1	N/A
22	7.5	16.87	0	N/A
22	12.5	16.92	0	N/A
22	17.5	16.97	2	N/A
22	22.5	17.02	0	N/A
22	27.5	17.07	0	N/A
22	32.5	17.12	0	N/A
22	37.5	17.17	1	N/A
22	42.5	17.22	0	N/A
22	47.5	17.27	1	N/A
22	52.5	17.32	0	N/A
22	57.5	17.37	7	N/A
22	62.5	17.42	0	N/A
22	67	17.47	0	0
22	72	17.52	5,448	0
23	0	17.60	18	0
23	5	17.65	0	0
23	10	17.70	0	0
23	15	17.75	0	0
23	20	17.80	0	0
23	25	17.85	0	0
23	30	17.90	1	0
23	35	17.95	0	0
23	40	18.00	0	0
23	45	18.05	0	0
23	50	18.10	0	0
23	55	18.15	0	0
23	60	18.20	2	0
23	65	18.25	25	0
23	70	18.30	0	0
23	75	18.35	0	0
24	0	18.40	6	0
24	5	18.45	0	0
24	10	18.50	3	0
24	15	18.55	0	0
24	20	18.60	0	0
24	25	18.65	0	0
24	30	18.70	9,809	0
24	35	18.75	7,398	0
24	40	18.80	3	0
24	45	18.85	2	0
24	50	18.90	1	0
24	55	18.95	0	0
24	60	19.00	0	0
24	65	19.05	0	0
24	70	19.10	0	0
24	75	19.15	0	0
25	0	19.20	0	0
25	5	19.25	0	0
25	10	19.30	0	0
25	15	19.35	0	0
25	20	19.40	0	0
25	25	19.45	0	0
25	30	19.50	0	0
25	35	19.55	0	0
25	40	19.60	0	0
25	45	19.65	0	0
25	50	19.70	0	0
25	55	19.75	0	0
25	60	19.80	0	0
25	65	19.85	0	0
25	70	19.90	0	0
25	75	19.95	0	0
26	0	20.00	0	0
26	5	20.05	0	0
26	10	20.10	0	0
26	15	20.15	0	0
26	20	20.20	0	0
26	25	20.25	0	0
26	30	20.30	0	0
26	35	20.35	0	0
26	40	20.40	1,908	23
26	45	20.45	25	0
26	50	20.50	0	0
26	55	20.55	0	0
26	60	20.60	0	0
26	65	20.65	0	0
26	70	20.70	0	0
26	75	20.75	0	0

Core Section	Section Depth (cm)	Absolute Depth (cm)	Clear Shards per g dry wt	Brown Shards per g dry wt
27	0	20.80	0	0
27	5	20.85	0	0
27	10	20.90	0	0
27	15	20.95	0	0
27	20	21.00	0	0
27	25	21.05	0	0
27	30	21.10	0	0
27	35	21.15	0	0
27	40	21.20	0	0
27	45	21.25	0	0
27	50	21.30	0	0
27	55	21.35	0	0
27	60	21.40	0	0
27	65	21.45	0	0
27	70	21.50	0	0
27	75	21.55	0	0
28	0	21.60	0	0
28	5	21.65	0	0
28	10	21.70	0	0
28	15	21.75	0	0
28	20	21.80	0	0
28	25	21.85	0	0
28	30	21.90	0	0
28	35	21.95	0	0
28	40	22.00	0	0
28	45	22.05	0	0
28	50	22.10	0	0
28	55	22.15	0	0
28	60	22.20	0	0
28	65	22.25	0	0
28	70	22.30	0	0
28	75	22.35	0	0
29	0	22.40	0	0
29	5	22.45	0	0
29	10	22.50	0	0
29	15	22.55	0	0
29	20	22.60	0	0
29	25	22.65	0	0
29	30	22.70	0	0
29	35	22.75	0	0
29	40	22.80	0	0
29	45	22.85	0	0
29	50	22.90	0	0
29	55	22.95	0	0
29	60	23.00	0	0
29	65	23.05	0	0
29	70	23.10	0	0
29	75	23.15	0	0
30	0	23.20	0	0
30	5	23.25	0	0
30	10	23.30	2	0
30	15	23.35	0	0
30	20	23.40	0	0
30	25	23.45	1	0
30	30	23.50	0	0
30	35	23.55	0	0
30	40	23.60	0	0
30	45	23.65	0	0
30	50	23.70	0	0
30	55	23.75	207	11
30	60	23.80	0	0
30	65	23.85	0	0
30	70	23.90	0	0
30	75	23.95	0	0
31	0	24.00	0	0
31	5	24.05	0	0
31	10	24.10	0	0
31	15	24.15	0	0
31	20	24.20	0	0
31	25	24.25	0	0
31	30	24.30	0	0
31	35	24.35	0	0
31	40	24.40	0	0
31	45	24.45	0	0
31	50	24.50	0	0
31	55	24.55	0	0
31	60	24.60	0	0
31	65	24.65	0	0
31	70	24.70	0	0
31	75	24.75	0	0
32	0	24.80	46	N/A
32	5	24.85	47	N/A
32	10	24.90	253	N/A
32	15	24.95	360,438	N/A

Core Section	Section Depth (cm)	Absolute Depth (cm)	Clear Shards per g dry wt	Brown Shards per g dry wt
32	20	25.00	639,275	N/A
32	25	25.05	1,134,207	N/A
32	30	25.10	2,477,894	N/A
32	35	25.15	2,539,869	N/A
32	36	25.16	2,228,068	N/A
32	37	25.17	7,390,076	N/A
32	38	25.18	6,250,536	N/A
32	39	25.19	4,867,808	N/A
32	40	25.20	5,650,389	N/A
32	41	25.21	5,231,100	N/A
32	42	25.22	4,306,442	N/A
32	43	25.23	7,201,465	N/A
32	44	25.24	7,278,171	N/A
32	45	25.25	6,842,037	N/A
33	0	25.60	0	0
33	5	25.65	0	0
33	10	25.70	0	0
33	15	25.75	0	0
33	20	25.80	0	0
33	25	25.85	0	0
33	30	25.90	4	0
33	35	25.95	36	0
33	40	26.00	8,751	0
33	45	26.05	167	0
33	50	26.10	0	0
33	55	26.15	0	0
33	60	26.20	0	0
33	65	26.25	0	0
33	70	26.30	0	0
33	75	26.35	0	0
34	0	26.40	0	0
34	5	26.45	0	0
34	10	26.50	0	0
34	15	26.55	1	0
34	20	26.60	0	0
34	25	26.65	0	0
34	30	26.70	0	0
34	35	26.75	0	0
34	40	26.80	0	0
34	45	26.85	0	0
34	50	26.90	0	0
34	55	26.95	0	0
34	60	27.00	0	0
34	65	27.05	0	0
34	70	27.10	0	0
34	75	27.15	0	0
35	0	27.20	0	0
35	5	27.25	0	0
35	10	27.30	0	0
35	15	27.35	0	0
35	20	27.40	0	0
35	25	27.45	0	0
35	30	27.50	0	0
35	35	27.55	1	0
35	40	27.60	0	0
35	45	27.65	0	0
35	50	27.70	0	0
35	55	27.75	0	0
35	60	27.80	0	0
35	65	27.85	89	0
35	70	27.90	1,790	5
35	75	27.95	6,753	N/A
36	0	28.00	8,017,845	N/A
36	5	28.05	24,755,166	N/A
36	10	28.10	14,298,682	N/A
36	15	28.15	8,060,100	N/A
36	20	28.20	2,234	N/A
36	25	28.25	3	0
36	30	28.30	2	0
36	35	28.35	4	0
36	40	28.40	2	0
36	45	28.45	2	0
36	50	28.50	3	0
36	55	28.55	1	0
36	60	28.60	3	0
36	65	28.65	7	0
36	70	28.70	2	0
36	75	28.75	9	0
37	0	28.80	3	0
37	5	28.85	1	0
37	10	28.90	1	0
37	15	28.95	0	0
37	20	29.00	0	0
37	25	29.05	0	0

Core Section	Section Depth (cm)	Absolute Depth (cm)	Clear Shards per g dry wt	Brown Shards per g dry wt
37	30	29.10	0	0
37	35	29.15	0	0
37	40	29.20	0	0
37	45	29.25	1	0
37	50	29.30	0	0
37	55	29.35	0	0
37	60	29.40	0	0
37	65	29.45	0	0
37	70	29.50	0	0
37	75	29.55	0	0
38	0	29.60	0	0
38	5	29.65	0	0
38	10	29.70	0	0
38	15	29.75	0	0
38	20	29.80	0	0
38	25	29.85	0	0
38	30	29.90	0	0
38	35	29.95	0	0
38	40	30.00	0	0
38	45	30.05	0	0
38	50	30.10	0	0
38	55	30.15	0	0
38	60	30.20	0	0
38	65	30.25	0	0
38	70	30.30	0	0
38	75	30.35	0	0
39	0	30.40	0	0
39	5	30.45	0	0
39	10	30.50	1	0
39	15	30.55	0	0
39	20	30.60	0	0
39	25	30.65	803	40
39	30	30.70	0	0
39	35	30.75	0	0
39	40	30.80	0	0
39	45	30.85	0	0
39	50	30.90	0	0
39	55	30.95	0	0
39	60	31.00	0	0
39	65	31.05	0	0
39	70	31.10	0	0
40	0	31.20	16	0
40	5	31.25	9	0
40	10	31.30	3	0
40	15	31.35	8	0
40	20	31.40	0	0
40	25	31.45	0	0
40	30	31.50	9	0
40	35	31.55	12	0
40	40	31.60	0	0
40	45	31.65	0	0
40	50	31.70	2	0
40	55	31.75	7	0
40	60	31.80	5	0
40	65	31.85	5	0
40	70	31.90	0	0
40	75	31.95	0	0
41	0	32.00	1,388	2
41	5	32.05	98	1
41	10	32.10	1,651	6
41	15	32.15	10,000	0
41	20	32.20	10,000	0
41	25	32.25	1,094	5
41	30	32.30	6,802	0
41	35	32.35	61	0
41	40	32.40	6	0
41	45	32.45	10	0
41	50	32.50	5	0
41	55	32.55	10	0
41	60	32.60	9	0
41	65	32.65	4	0
41	70	32.70	3	0
41	75	32.75	64	0
42	0	32.80	3	0
42	5	32.85	0	0
42	10	32.89	0	0
42	15	32.94	1	0
42	20	32.99	0	0
42	25	33.04	1	0
42	30	33.08	0	0
42	35	33.13	0	0
42	40	33.18	0	0
42	45	33.22	78	4
42	50	33.27	0	0

Core Section	Section Depth (cm)	Absolute Depth (cm)	Clear Shards per g dry wt	Brown Shards per g dry wt
42	55	33.32	1,094	20
42	60	33.36	10,000	0
42	65	33.41	1,344	14
42	70	33.46	10	0
42	75	33.51	1	0
43	0	33.60	2,465	185
43	5	33.65	41	2
43	10	33.70	10,000	0
43	15	33.75	10,000	0
43	20	33.80	10,000	0
43	25	33.85	10,000	0
43	30	33.90	77	1
43	35	33.95	2	0
43	40	34.00	10	0
43	45	34.05	1	0
43	50	34.10	1	0
43	55	34.15	0	0
43	60	34.20	1	0
43	65	34.25	1	0
43	70	34.30	0	0
43	75	34.35	0	0
44	0	34.40	186	14
44	5	34.45	13	1
44	10	34.50	13	2
44	15	34.55	13	0
44	20	34.60	37	0
44	25	34.65	10,000	0
44	30	34.70	10,000	0
44	35	34.75	1,084	3
44	40	34.80	2	0
44	45	34.85	6	0
44	50	34.90	48	0
44	55	34.95	122	0
44	60	35.00	8	0
44	65	35.05	159	0
44	70	35.10	7	0
44	75	35.15	4	0
45	0	35.20	2	0
45	5	35.25	14	0
45	10	35.30	3	0
45	15	35.35	0	0
45	20	35.40	23	0
45	25	35.45	131	0
45	30	35.50	454	0
45	35	35.55	0	0
45	40	35.60	10,000	0
45	45	35.65	10,000	0
45	50	35.70	10,000	0
45	55	35.75	10,000	0
45	60	35.80	10,000	0
45	65	35.85	10,000	0
45	70	35.90	2	0
45	75	35.95	33	0
46	0	36.00	7	0
46	5	36.05	1	0
46	10	36.10	5	0
46	15	36.15	3	0
46	20	36.20	2	0
46	25	36.25	0	0
46	30	36.30	1,292	28
46	35	36.35	10,000	0
46	40	36.40	10,000	0
46	45	36.45	10,000	0
46	50	36.50	10,000	0
46	55	36.55	10,000	0
46	60	36.60	10,000	0
46	65	36.65	10,000	0
46	70	36.70	10,000	0
46	75	36.75	4,577	87

PRAD 1-2 1cm Resolution Shard Counts

PRAD 178 cm – PRAD 277 cm

Core Section	Section Depth (cm)	Absolute Depth (m)	Clear Shards per g dry wt	Brown Shards per g dry wt
3	18	1.78	6	1
3	19	1.79	34	2
3	20	1.80	68	7
3	21	1.81	129	36
3	22	1.82	450	24
3	23	1.83	618	16
3	24	1.84	17	0
3	25	1.85	1528	76
3	26	1.86	790	24
3	27	1.87	357	13
3	28	1.88	840	43
3	29	1.89	484	16
3	30	1.90	221	8
3	31	1.91	1077	45
3	32	1.92	3113	65
3	33	1.93	4029	227
3	34	1.94	4042	230
3	35	1.95	4066	216
3	36	1.96	4290	197
3	37	1.97	5491	203
3	38	1.98	13421	321
3	39	1.99	15060	349
3	40	2.00	24934	480
3	41	2.01	26585	521
3	42	2.02	26665	694
3	43	2.03	26321	575
3	44	2.04	25332	499
3	45	2.05	38068	799
3	46	2.06	19020	549
3	47	2.07	16106	2145
3	48	2.08	6921	438
3	49	2.09	7297	154
3	50	2.10	7854	199
3	51	2.11	18089	206
3	52	2.12	30295	777
3	53	2.13	53504	2392
3	54	2.14	69981	2822
3	55	2.15	29716	1648
3	56	2.16	56912	2119
3	57	2.17	43612	2399
3	58	2.18	52810	2753
3	61	2.21	114352	2909
3	62	2.22	117974	4990
3	63	2.23	131349	5029
3	64	2.24	115427	7339
3	65	2.25	115610	8399
3	66	2.26	84888	8018
3	67	2.27	82616	2585
3	68	2.28	78702	4038
3	69	2.29	78026	4224
3	70	2.30	43300	1814
3	71	2.31	229238	14993
3	72	2.32	122474	6697
3	73	2.33	80069	4785
3	74	2.34	5423	128
3	75	2.35	1042	13
3	76	2.36	353	4
4	0	2.40	2	0
4	1	2.41	135	3
4	2	2.42	127	8
4	3	2.43	31	2
4	4	2.44	19	2
4	5	2.44	17	1
4	6	2.45	18	2
4	7	2.46	19	2
4	8	2.47	65	0
4	9	2.48	77	1
4	10	2.49	86	1
4	11	2.50	1835	44
4	12	2.51	265	8
4	13	2.52	20	3
4	14	2.53	18	6
4	15	2.53	21	1
4	16	2.54	20	1
4	17	2.55	112	5
4	18	2.56	4	0
4	19	2.57	29	0
4	20	2.58	1087	15
4	21	2.59	1115	20
4	22	2.60	309	7
4	23	2.61	4514	74
4	24	2.62	2253	33

Core Section	Section Depth (cm)	Absolute Depth (m)	Clear Shards per g dry wt	Brown Shards per g dry wt
3	59	2.19	60791	5008
3	60	2.20	111263	2768
4	27	2.64	38	1
4	28	2.65	15113	89
4	29	2.66	15530	158
4	30	2.67	27588	170
4	31	2.68	15113	0
4	32	2.69	8721	0
4	33	2.70	3942	0
4	34	2.71	49	2

Core Section	Section Depth (cm)	Absolute Depth (m)	Clear Shards per g dry wt	Brown Shards per g dry wt
4	25	2.62	54	2
4	26	2.63	1	0
4	35	2.71	16086	191
4	36	2.72	17805	150
4	37	2.73	23165	110
4	38	2.74	23	2
4	39	2.75	5	1
4	40	2.76	0	0
4	41	2.77	0	0

PRAD 306 cm – PRAD 338 cm

Core Section	Section Depth (cm)	Absolute Depth (m)	Clear Shards per g dry wt	Brown Shards per g dry wt
4	73	3.06	0	0
4	74	3.07	0	0
4	75	3.07	0	0
4	76	3.08	0	0
4	77	3.09	0	0
5	0	3.20	2957	23
5	1	3.21	27348	148
5	2	3.22	46337	398
5	3	3.23	51343	439
5	4	3.24	40912	321
5	5	3.25	17509	74
5	6	3.26	23247	98
5	7	3.27	27202	629

Core Section	Section Depth (cm)	Absolute Depth (m)	Clear Shards per g dry wt	Brown Shards per g dry wt
5	8	3.28	7019	126
5	9	3.28	16898	67
5	10	3.29	43116	221
5	11	3.30	24702	73
5	12	3.31	17454	60
5	13	3.32	17104	57
5	14	3.33	3060	21
5	15	3.34	6181	36
5	16	3.35	8932	46
5	17	3.36	18570	48
5	18	3.37	175	0
5	19	3.38	3	0

PRAD 648 cm – PRAD 657 cm

Core Section	Section Depth (cm)	Absolute Depth (m)	Clear Shards per g dry wt	Brown Shards per g dry wt
9	8	6.48	4	0
9	9	6.49	4	0
9	10	6.50	1	0
9	11	6.51	0	0
9	12	6.52	3	0

Core Section	Section Depth (cm)	Absolute Depth (m)	Clear Shards per g dry wt	Brown Shards per g dry wt
9	13	6.53	4	0
9	14	6.54	0	0
9	15	6.55	0	0
9	16	6.56	0	0
9	17	6.57	2	0

PRAD 774 cm – PRAD 789 cm

Core Section	Section Depth (cm)	Absolute Depth (m)	Clear Shards per g dry wt	Brown Shards per g dry wt
10	54	7.74	0	0
10	55	7.75	3	0
10	56	7.76	1	0
10	57	7.77	0	0
10	58	7.78	3	0
10	59	7.79	4	0
10	60	7.80	2	0
10	61	7.81	3	0
10	62	7.82	8	0
10	63	7.83	12	0
10	64	7.84	58	0
10	65	7.85	1	0
10	66	7.86	1	0
10	67	7.87	0	0
10	68	7.88	0	0
10	69	7.89	26	0

PRAD 834 cm – PRAD 884 cm

Core Section	Section Depth (cm)	Absolute Depth (m)	Clear Shards per g dry wt	Brown Shards per g dry wt
11	34	8.34	81	0
11	35	8.35	102	0
11	36	8.36	225	3
11	37	8.37	856	12
11	38	8.38	175	2
11	39	8.39	962	21
11	40	8.40	218	5
11	41	8.41	545	16
11	42	8.42	188	0
11	43	8.43	154	0
11	44	8.44	260	9
11	45	8.45	26	0
11	46	8.46	18	3
11	47	8.47	2	0
11	48	8.48	2	0
11	49	8.49	1	0
11	50	8.50	0	0
11	51	8.51	0	0
11	52	8.52	0	0
11	53	8.53	0	0
11	54	8.54	0	0
11	55	8.55	0	0
11	56	8.56	0	0
11	57	8.57	0	0
11	58	8.58	0	0
11	59	8.59	0	0
11	60	8.60	0	0
11	61	8.61	0	0
11	62	8.62	0	0
11	63	8.63	0	0
11	64	8.64	0	0
11	65	8.65	0	0
11	66	8.66	0	0
11	67	8.67	1	0
11	68	8.68	9	1
11	69	8.69	8	0
11	70	8.70	0	0
11	71	8.71	0	0
11	72	8.72	0	0
11	73	8.73	57	0
11	74	8.74	14	1
11	75	8.75	2	0
11	76	8.76	0	0
12	0	8.80	0	0
12	1	8.81	13	0
12	2	8.82	10	0
12	3	8.83	0	0
12	4	8.84	0	0

PRAD 1087 cm – PRAD 1140 cm

Core Section	Section Depth (cm)	Absolute Depth (m)	Clear Shards per g dry wt	Brown Shards per g dry wt
14	47	10.87	0	0
14	48	10.88	0	0
14	49	10.89	0	0
14	50	10.90	0	0
14	51	10.91	0	0
14	52	10.92	0	0
14	53	10.93	0	0
14	54	10.94	0	0
14	55	10.95	5	0
14	56	10.96	9	0
14	57	10.97	8	0
14	58	10.98	6	0
14	59	10.99	51	0
14	60	11.00	48	0
14	61	11.01	45	0
14	62	11.02	83	0
14	63	11.03	49720	0
14	64	11.04	143240	204
14	65	11.05	46691	0
14	66	11.06	16969	0
14	67	11.07	16094	0
14	68	11.08	8765	0
14	69	11.09	27	0
14	70	11.10	1	0
14	71	11.11	0	0
14	72	11.12	0	0
14	73	11.13	0	0
14	74	11.14	0	0
14	75	11.15	1	0
14	76	11.16	5	0
15	0	11.20	14	0
15	1	11.21	0	0
15	2	11.22	1	0
15	3	11.23	0	0
15	4	11.24	13	0
15	5	11.25	10	0
15	6	11.26	4	0
15	7	11.27	24	3
15	8	11.28	11	0
15	9	11.29	10	0
15	10	11.30	100	0
15	11	11.31	10	0
15	12	11.32	2	0
15	13	11.33	0	0
15	14	11.34	0	0
15	15	11.35	0	0
15	16	11.36	0	0
15	17	11.37	0	0
15	18	11.38	0	0
15	19	11.39	0	0
15	20	11.40	0	0

SA03-03 5 cm Resolution Tephra Shard Counts

Depth (cm)		Clear Shards per g dry wt	Brown Shards per g dry wt
0	5	12	0
5	10	10	0
10	15	7	0
15	20	15	0
20	25	2605	54
25	30	10120	0
30	35	141	0
35	40	0	0
40	45	0	0
45	50	6	0
50	55	8	0
55	60	14	0
60	65	0	0
65	70	1	0
70	75	3	0
75	80	6060	0
80	85	7594	0
85	90	8293	0
90	95	48	0
95	100	0	0
100	105	0	0
105	110	2	0
110	115	0	0
115	120	2	0
120	125	1	0
125	130	0	0
130	135	0	0
135	140	0	0
140	145	1	0
145	150	0	0
150	155	0	0
155	160	0	0
160	165	0	0
165	170	0	0
170	175	1	0
175	180	0	0
180	185	0	0
185	190	0	0
190	195	0	0
195	200	0	0
400	405	11705	0
405	410	14386	0
410	415	9815	0

Depth (cm)		Clear Shards per g dry wt	Brown Shards per g dry wt
200	205	0	0
205	210	0	0
210	215	0	0
215	220	0	0
220	225	0	0
225	230	0	0
230	235	0	0
235	240	0	0
240	245	0	0
245	250	0	0
250	255	0	0
255	260	0	0
260	265	0	0
265	270	0	0
270	275	6	5
275	280	26	5
280	285	13	2
285	290	15	0
290	295	13	0
295	300	23	0
300	305	0	0
305	310	0	0
310	315	0	0
315	320	0	0
320	325	0	0
325	330	0	0
330	335	0	0
335	340	0	0
340	345	0	0
345	350	0	0
350	355	3	0
355	360	0	0
360	365	0	0
365	370	1	0
370	375	0	0
375	380	19	0
380	385	8454	0
385	390	8810	0
390	395	1163	0
395	400	3907	0
620	625	0	0
625	630	1	0
630	635	1	0

Depth (cm)		Clear Shards per g dry wt	Brown Shards per g dry wt
415	420	12130	0
420	425	1404	27
425	430	2743	53
430	435	5957	181
435	440	12	0
440	445	3	0
445	450	0	0
450	455	4	1
455	460	0	0
460	465	0	0
465	470	0	0
470	475	0	0
475	480	0	0
480	485	0	0
485	490	0	0
490	495	0	1
495	500	0	0
500	505	0	0
505	510	0	0
510	515	0	0
515	520	0	0
520	525	0	0
525	530	0	0
530	535	0	0
535	540	0	0
540	545	0	0
545	550	0	0
550	555	0	0
555	560	0	0
560	565	0	0
565	570	0	0
570	575	0	0
575	580	0	0
580	585	0	0
585	590	0	0
590	595	0	0
595	600	0	0
600	605	0	0
605	610	0	0
610	615	0	0
615	620	0	0
840	845	0	0
845	850	0	0
850	855	1	0
855	860	0	0

Depth (cm)		Clear Shards per g dry wt	Brown Shards per g dry wt
635	640	0	0
640	645	0	0
645	650	618	0
650	655	1	0
655	660	2	0
660	665	0	0
665	670	0	0
670	675	0	0
675	680	0	0
680	685	0	0
685	690	12115	0
690	695	8135	0
695	700	948	4
700	705	2	0
705	710	2	0
710	715	8	0
715	720	6	0
720	725	6	0
725	730	68	0
730	735	0	0
735	740	0	0
740	745	0	0
745	750	2	0
750	755	0	0
755	760	1	0
760	765	0	0
765	770	0	0
770	775	0	0
775	780	0	0
780	785	0	0
785	790	0	0
790	795	0	0
795	800	0	0
800	805	0	0
805	810	0	0
810	815	0	0
815	820	0	0
820	825	0	0
825	830	0	0
830	835	0	0
835	840	0	0
945	950	13106	0
950	955	2305	59
955	960	3974	155
960	965	26	0

Depth (cm)		Clear Shards per g dry wt	Brown Shards per g dry wt
860	865	0	0
865	870	2	0
870	875	0	0
875	880	0	0
880	885	5	0
885	890	29	0
890	895	14	0
895	900	13	0
900	905	4074	287
905	910	5418	0
910	915	13799	0
915	920	10108	0
920	925	13175	0
925	930	19467	0
930	935	9667	0
935	940	15591	0
940	945	10862	0

Depth (cm)		Clear Shards per g dry wt	Brown Shards per g dry wt
965	970	1116	33
970	975	248	9
975	980	3	0
980	985	0	0
985	990	3	0
990	995	7047	0
995	1000	9727	0
1000	1005	2083	25
1005	1010	1	0
1010	1015	3	0
1015	1020	0	0
1020	1025	1	0
1025	1030	0	0
1030	1035	1	0
1035	1040	11	1
1040	1045	1	0

SA03-03 1 cm Resolution Tephra Shard Counts

Depth (cm)		Clear Shards per g dry wt	Brown Shards per g dry wt
375	376	0	0
376	377	0	0
377	378	0	0
378	379	0	0
379	380	2	5
380	381	204	7
381	382	8218	52
382	383	43869	0
383	384	457160	1074
384	385	214026	1499
385	386	163093	668
386	387	54962	103
387	388	106	3
388	389	75	0
389	390	12	0
390	391	4	0
391	392	9	0
409	410	102604	1229
410	411	77755	950
411	412	92469	744
412	413	133945	933
413	414	215396	2952

Depth (cm)		Clear Shards per g dry wt	Brown Shards per g dry wt
392	393	96433	421
393	394	6547	41
394	395	16709	264
395	396	4276	25
396	397	29157	444
397	398	57069	781
398	399	81118	868
399	400	102733	0
400	401	58279	311
401	402	45935	310
402	403	43314	1117
403	404	7108	90
404	405	70318	995
405	406	78413	883
406	407	36189	585
407	408	97344	2669
408	409	63513	648
422	423	42745	552
423	424	68362	985
424	425	83402	495
425	426	636	0
426	427	6476	357

Depth (cm)		Clear Shards per g dry wt	Brown Shards per g dry wt
414	415	104571	1333
415	416	24147	66
416	417	65975	1169
417	418	90725	772
418	419	112962	1671
419	420	90126	669
420	421	59588	545
421	422	59241	1103

Depth (cm)		Clear Shards per g dry wt	Brown Shards per g dry wt
427	428	99047	1421
428	429	40024	722
429	430	38897	745
430	431	440	8
431	432	17037	310
432	433	10580	77
433	434	27	0
434	435	2	0

RF93-77 6 cm Resolution Tephra Shard Counts

Depth (cm)		Clear Shards per g dry wt	Brown Shards per g dry wt
0	6	13	0
6	12	2	1
12	18	6	0
18	24	20	0
24	30	2	0
30	36	17	0
36	42	5	0
42	48	0	0
48	54	0	0
54	60	1	0
60	66	1	57
66	72	98	0
72	78	11686	0
78	84	1580	320
84	90	8175	0
90	96	699	39
96	102	27	4
102	108	4	0
108	114	132	12
114	120	128	16
120	126	6	0
126	132	2	0
132	138	18	1
138	144	4	0
144	150	1689	5
302	308	1	0
308	314	1	0
314	320	4	0
320	326	4	0
326	332	5	0
332	338	194	17
338	342	50	7

Depth (cm)		Clear Shards per g dry wt	Brown Shards per g dry wt
150	156	20	0
156	162	13	0
162	168	11	0
168	174	3	0
174	180	2	0
180	186	84	0
186	192	8565	55
192	198	8309	50
198	204	8169	0
204	210	8176	0
210	216	8559	0
216	218	8357	37
218	224	2810	48
224	231	50	1
231	236	145	0
242	248	39	0
248	254	12	1
254	260	6	0
260	267	5	0
267	272	1010	2
272	278	50	1
278	284	21	0
284	290	18	0
290	296	15	1
296	302	10	0
552	558	20	2
558	564	128	0
564	570	37	0
570	574	6	0
574	580	1	0
580	586	21	1
586	592	29	1

Depth (cm)		Clear Shards per g dry wt	Brown Shards per g dry wt
342	348	15	4
348	354	10	2
354	360	1001	59
360	366	841	43
366	372	6958	339
372	378	7512	185
378	384	1211	21
384	390	908	36
390	396	786	16
396	402	163	3
402	408	41	0
408	414	4	0
414	420	1429	24
420	426	1072	14
426	432	3	0
432	438	970	16
438	444	1278	13
444	450	1448	17
450	456	6451	61
456	462	5589	6
462	468	111	7
468	474	205	2
474	480	361	12
480	486	491	12
486	492	792	11
492	498	507	9
498	504	20	1
504	510	21	4
510	516	25	3
516	522	9	0
522	528	0	0
528	534	11	0
534	540	22	0
540	546	436	5
546	552	170	7

Depth (cm)		Clear Shards per g dry wt	Brown Shards per g dry wt
592	598	15	0
598	604	121	1
604	610	287	0
610	616	156	0
616	622	219	6
622	628	3	0
628	634	2	0
634	640	0	0
640	646	0	0
646	652	0	0
652	658	6	0
658	664	2	0
664	670	0	0
670	676	0	0
676	682	0	0
682	688	0	0
694	700	0	0
700	706	0	0
706	712	0	0
712	718	0	0
718	724	0	0
724	730	0	0
730	736	0	0
736	742	0	0
742	748	0	0
748	754	0	0
754	760	0	0
760	766	0	0
766	772	0	0
772	778	0	0
778	784	6192	63
784	790	14245	0
790	796	23832	0
796	800	9973	100

RF93-77 2 cm resolution shard counts

Depth (cm)		Clear Shards per g dry wt	Brown Shards per g dry wt
60	61	0	0
61	62	0	0
62	63	3	8
63	64	5	2
64	65	64	33
65	66	581	204
66	67	1743	756
67	68	65059	21040
68	69	149711	76310
69	70	32648	10081
70	71	1280	401
71	72	279	186
72	73	599	41
73	74	9763	441
74	75	1343	58
75	76	185	36
76	77	95	88
77	78	1402	544
78	79	1765	165

Depth (cm)		Clear Shards per g dry wt	Brown Shards per g dry wt
79	80	1120	139
80	81	97	29
81	82	31	33
82	83	108	53
83	84	2403	209
84	85	26479	3507
85	86	24795	2136
86	87	57749	4336
87	88	24491	3141
88	89	64591	5512
89	90	25000	4000
90	91	100	50
91	92	42	0
92	93	4	0
93	94	3	0
94	95	0	0
95	96	0	0
96	97	0	0

Appendix B

Standard Data for PRAD 1-2, SA03-03 and RF93-77 geochemical samples. Data is grouped by the standard name. Means and Standard Deviations of the standards analysed throughout the run are shown. Samples that were analysed alongside these standards are listed. The microprobe analyses were undertaken on is also indicated. The assay for these glass standards is shown in Table 4.2, page 153.

NIST 612

Samples:	**PRAD-055, PRAD-203, PRAD-218, PRAD-268, PRAD-1494, PRAD-1653**												
Microprobe:	Oxford Earth Sciences												
	SiO_2	**TiO_2**	**Al_2O_3**	**FeO**	**MnO**	**MgO**	**CaO**	**Na_2O**	**K_2O**	**P_2O_5**	**SO_2**	**Cl**	**F**
Mean	71.44	0.01	2.11	0.01	0.01	0.01	11.92	14.47	0.02	N/A	N/A	N/A	N/A
S.D.	0.65	0.01	0.03	0.02	0.02	0.01	0.22	0.21	0.01	N/A	N/A	N/A	N/A

LIPARI

Samples:	**PRAD-404**												
Microprobe:	Oxford Earth Sciences												
	SiO_2	**TiO_2**	**Al_2O_3**	**FeO**	**MnO**	**MgO**	**CaO**	**Na_2O**	**K_2O**	**P_2O_5**	**SO_2**	**Cl**	**F**
Mean	73.87	0.07	13.17	1.52	0.06	0.04	0.75	3.74	5.32	N/A	N/A	N/A	N/A
S.D.	0.34	0.01	0.06	0.06	0.04	0.01	0.03	0.48	0.06	N/A	N/A	N/A	N/A
Samples:	**PRAD-205, PRAD-250, PRAD-273, PRAD-329, PRAD-336, PRAD1104, RF93-77-414, RF93-77-73**												
Microprobe:	Edinburgh												
	SiO_2	**TiO_2**	**Al_2O_3**	**FeO**	**MnO**	**MgO**	**CaO**	**Na_2O**	**K_2O**	**P_2O_5**	**SO_2**	**Cl**	**F**
Mean	74.27	0.08	13.21	1.44	0.07	0.04	0.73	4.11	5.13	0.01	0.00	0.38	0.15
S.D.	0.38	0.01	0.10	0.17	0.01	0.01	0.03	0.09	0.08	0.01	0.00	0.00	0.02
Samples:	**PRAD-214, PRAD-223, PRAD-231, PRAD-250, PRAD-261**												
Microprobe:	Edinburgh												
	SiO_2	**TiO_2**	**Al_2O_3**	**FeO**	**MnO**	**MgO**	**CaO**	**Na_2O**	**K_2O**	**P_2O_5**	**SO_2**	**Cl**	**F**
Mean	73.36	0.08	12.93	1.50	0.07	0.06	0.75	4.13	5.15	0.01	0.00	0.37	0.18
S.D.	0.37	0.00	0.24	0.10	0.01	0.00	0.06	0.08	0.05	0.00	0.00	0.01	0.02
Samples:	**PRAD-267, PRAD-273, PRAD-323, PRAD-329, PRAD-336, PRAD-1104**												
Microprobe:	Edinburgh												
	SiO_2	**TiO_2**	**Al_2O_3**	**FeO**	**MnO**	**MgO**	**CaO**	**Na_2O**	**K_2O**	**P_2O_5**	**SO_2**	**Cl**	**F**
Mean	73.38	0.08	12.90	1.47	0.07	0.04	0.74	4.03	5.14	0.01	0.00	0.37	0.19
S.D.	0.38	0.00	0.26	0.14	0.01	0.02	0.03	0.13	0.07	0.00	0.00	0.01	0.01
Samples:	**PRAD-784, PRAD-837, PRAD841, PRAD-1474, PRAD-2375, RF93-77-73**												
Microprobe:	Edinburgh												
	SiO_2	**TiO_2**	**Al_2O_3**	**FeO**	**MnO**	**MgO**	**CaO**	**Na_2O**	**K_2O**	**P_2O_5**	**SO_2**	**Cl**	**F**
Mean	73.74	0.08	13.07	1.47	0.07	0.04	0.75	4.04	5.14	0.01	0.01	0.38	0.18
S.D.	0.61	0.00	0.23	0.13	0.01	0.01	0.03	0.09	0.06	0.00	0.01	0.01	0.01

LIPARI

Samples	PRAD-789, PRAD-839, PRAD-844, PRAD-868, PRAD-873, PRAD-1130												
Microprobe:	Edinburgh												
	SiO_2	TiO_2	Al_2O_3	FeO	MnO	MgO	CaO	Na_2O	K_2O	P_2O_5	SO_2	Cl	F
Mean	74.03	0.08	13.18	1.44	0.07	0.03	0.74	4.02	5.17	0.01	0.00	0.39	0.17
S.D.	0.30	0.01	0.28	0.13	0.00	0.01	0.04	0.06	0.05	0.00	0.01	0.01	0.01
Samples:	PRAD-3225, PRAD-3383												
Microprobe:	Edinburgh												
	SiO_2	TiO_2	Al_2O_3	FeO	MnO	MgO	CaO	Na_2O	K_2O	P_2O_5	SO_2	Cl	F
Mean	74.04	0.09	12.94	1.84	0.08	0.06	0.81	4.04	5.11	0.01	0.00	0.37	0.15
S.D.	1.16	0.03	0.27	1.07	0.03	0.06	0.34	0.13	0.17	0.00	0.00	0.02	0.02
Samples:	PRAD-3336, PRAD-3472, PRAD-3586, PRAD-3666												
Microprobe:	Edinburgh												
	SiO_2	TiO_2	Al_2O_3	FeO	MnO	MgO	CaO	Na_2O	K_2O	P_2O_5	SO_2	Cl	F
Mean	74.62	0.08	13.08	1.52	0.07	0.04	0.74	3.87	4.93	0.01	0.00	0.38	0.14
S.D.	1.20	0.00	0.29	0.08	0.01	0.02	0.04	0.94	0.94	0.01	0.00	0.01	0.01
Samples:	SA03-03-25												
Microprobe:	Edinburgh												
	SiO_2	TiO_2	Al_2O_3	FeO	MnO	MgO	CaO	Na_2O	K_2O	P_2O_5	SO_2	Cl	F
Mean	74.57	0.083	13.15	1.52	0.071	0.046	0.753	3.912	4.955	0.006	0.002	0.379	0.173
S.D.	1.182	0.008	0.252	0.1	0.008	0.017	0.035	0.897	0.913	0.005	0.003	0.007	0.02
Samples:	SA03-03-25, SA03-03-85, SA03-03-383, SA03-03-685												
Microprobe:	Edinburgh												
	SiO_2	TiO_2	Al_2O_3	FeO	MnO	MgO	CaO	Na_2O	K_2O	P_2O_5	SO_2	Cl	F
Mean	74.17	0.081	13.02	1.67	0.071	0.034	0.736	4.063	5.121	0.005	0.002	0.378	0.165
S.D.	0.881	0.005	0.243	0.607	0.005	0.013	0.032	0.12	0.172	0.005	0.004	0.009	0.012
Samples:	SA03-03-925, SA03-03-995												
Microprobe:	Edinburgh												
	SiO_2	TiO_2	Al_2O_3	FeO	MnO	MgO	CaO	Na_2O	K_2O	P_2O_5	SO_2	Cl	F
Mean	74.06	0.101	12.97	2.032	0.074	0.041	0.73	4.062	5.083	0.006	0.002	0.373	0.148
S.D.	1.214	0.05	0.142	1.341	0.015	0.018	0.045	0.115	0.121	0.005	0.003	0.021	0.017
Samples:	RF93-77-78, RF93-77-88, 372, PRAD-205												
Microprobe:	Edinburgh												
	SiO_2	TiO_2	Al_2O_3	FeO	MnO	MgO	CaO	Na_2O	K_2O	P_2O_5	SO_2	Cl	F
Mean	73.52	0.08	12.97	1.51	0.07	0.04	0.75	4.05	5.11	0.01	0.00	0.38	0.18
S.D.	0.70	0.00	0.18	0.07	0.00	0.02	0.03	0.10	0.12	0.01	0.00	0.01	0.02

LIPARI

Samples:	RF93-77-267, RF93-77-414, RF93-77-540, RF93-77-604												
Microprobe:	Edinburgh												
	SiO_2	TiO_2	Al_2O_3	FeO	MnO	MgO	CaO	Na_2O	K_2O	P_2O_5	SO_2	Cl	F
Mean	73.58	0.08	13.20	1.48	0.07	0.05	0.75	4.06	5.18	0.00	0.01	0.38	0.17
S.D.	0.37	0.01	0.15	0.12	0.01	0.01	0.05	0.14	0.11	0.00	0.00	0.01	0.02

KL2 BASALT

Samples:	PRAD-324, PRAD-480												
Microprobe:	Oxford Earth Sciences												
	SiO_2	TiO_2	Al_2O_3	FeO	MnO	MgO	CaO	Na_2O	K_2O	P_2O_5	SO_2	Cl	F
Mean	50.73	2.53	13.50	10.27	0.16	7.27	10.97	2.39	0.52	N/A	N/A	N/A	N/A
S.D.	0.16	0.05	0.03	0.09	0.03	0.07	0.05	0.05	0.02	N/A	N/A	N/A	N/A

StHs6/80-G

Samples:	PRAD-120, PRAD-203, PRAD-324, PRAD-404, PRAD-480, PRAD-1332												
Microprobe:	Oxford Earth Sciences												
	SiO_2	TiO_2	Al_2O_3	FeO	MnO	MgO	CaO	Na_2O	K_2O	P_2O_5	SO_2	Cl	F
Mean	63.89	0.70	18.14	4.19	0.08	1.94	5.21	4.57	1.32	N/A	N/A	N/A	N/A
S.D.	0.20	0.02	0.18	0.08	0.02	0.03	0.04	0.08	0.02	N/A	N/A	N/A	N/A
Samples:	PRAD-205, PRAD-214, PRAD-223, PRAD-261, PRAD-231												
Microprobe:	Edinburgh												
	SiO_2	TiO_2	Al_2O_3	FeO	MnO	MgO	CaO	Na_2O	K_2O	P_2O_5	SO_2	Cl	F
Mean	31.97	0.37	9.04	2.23	0.04	1.00	2.71	2.43	0.68	0.08	0.00	0.01	0.02
S.D.	32.23	0.36	9.00	2.15	0.03	0.98	2.70	2.18	0.65	0.08	0.00	0.01	0.01
Samples:	PRAD-205, PRAD-250, PRAD-273, PRAD-329, PRAD-336, PRAD-1104, RF93-77-73, RF93-77-414												
Microprobe:	Edinburgh												
	SiO_2	TiO_2	Al_2O_3	FeO	MnO	MgO	CaO	Na_2O	K_2O	P_2O_5	SO_2	Cl	F
Mean	63.45	0.73	17.82	4.36	0.08	1.97	5.35	4.64	1.30	0.15	0.00	0.02	0.02
S.D.	0.35	0.01	0.19	0.22	0.00	0.04	0.09	0.07	0.06	0.01	0.00	0.00	0.01
Samples:	PRAD-267, PRAD-273, PRAD-323, PRAD-329, PRAD-336, PRAD-1104												
Microprobe:	Edinburgh												
	SiO_2	TiO_2	Al_2O_3	FeO	MnO	MgO	CaO	Na_2O	K_2O	P_2O_5	SO_2	Cl	F
Mean	63.00	0.72	17.54	4.35	0.08	1.98	5.28	4.58	1.31	0.14	0.00	0.02	0.02
S.D.	0.51	0.01	0.15	0.11	0.01	0.04	0.12	0.09	0.05	0.01	0.00	0.00	0.01
Samples:	PRAD-650, PRAD-875, PRAD-1100, PRAD-1125, PRAD-1332												
Microprobe:	Oxford Earth Sciences												
	SiO_2	TiO_2	Al_2O_3	FeO	MnO	MgO	CaO	Na_2O	K_2O	P_2O_5	SO_2	Cl	F
Mean	63.06	0.71	17.83	4.25	0.08	1.92	5.26	4.65	1.32	N/A	N/A	N/A	N/A
S.D.	0.33	0.03	0.13	0.06	0.02	0.03	0.03	0.21	0.02	N/A	N/A	N/A	N/A

StHs6/80-G

Samples:	**PRAD-784, PRAD-845**												
Microprobe:	Oxford Earth Sciences												
	SiO_2	**TiO_2**	**Al_2O_3**	**FeO**	**MnO**	**MgO**	**CaO**	**Na_2O**	**K_2O**	**P_2O_5**	**SO_2**	**Cl**	**F**
Mean	63.24	0.70	18.23	4.18	0.08	1.97	5.37	4.59	1.33	N/A	N/A	N/A	N/A
S.D.	0.34	0.03	0.14	0.07	0.02	0.02	0.04	0.35	0.02	N/A	N/A	N/A	N/A
Samples:	**PRAD-784, PRAD-837, PRAD-841, PRAD-1474, PRAD-2375, RF93-77-73**												
Microprobe:	Edinburgh												
	SiO_2	**TiO_2**	**Al_2O_3**	**FeO**	**MnO**	**MgO**	**CaO**	**Na_2O**	**K_2O**	**P_2O_5**	**SO_2**	**Cl**	**F**
Mean	63.03	0.73	17.85	4.32	0.08	1.95	5.33	4.65	1.31	0.14	0.00	0.02	0.03
S.D.	0.57	0.01	0.25	0.21	0.01	0.05	0.10	0.11	0.05	0.01	0.00	0.00	0.01
Samples:	**PRAD-789, PRAD-844, PRAD-1130, PRAD-868, PRAD-839, PRAD-873**												
Microprobe:	Edinburgh												
	SiO_2	**TiO_2**	**Al_2O_3**	**FeO**	**MnO**	**MgO**	**CaO**	**Na_2O**	**K_2O**	**P_2O_5**	**SO_2**	**Cl**	**F**
Mean	63.22	0.74	17.93	4.34	0.08	1.94	5.35	4.66	1.31	0.14	0.00	0.02	0.03
S.D.	0.39	0.01	0.24	0.18	0.01	0.05	0.06	0.09	0.05	0.01	0.00	0.00	0.01
Samples:	**PRAD-1752, PRAD-1870 PRAD-2040**												
Microprobe:	Oxford Earth Sciences												
	SiO_2	**TiO_2**	**Al_2O_3**	**FeO**	**MnO**	**MgO**	**CaO**	**Na_2O**	**K_2O**	**P_2O_5**	**SO_2**	**Cl**	**F**
Mean	63.84	0.72	17.92	4.42	0.07	1.97	5.32	4.28	1.33	N/A	N/A	N/A	N/A
S.D.	0.27	0.02	0.49	0.09	0.02	0.03	0.04	0.08	0.02	N/A	N/A	N/A	N/A
Samples:	**PRAD-2375, PRAD-2605**												
Microprobe:	Oxford Earth Sciences												
	SiO_2	**TiO_2**	**Al_2O_3**	**FeO**	**MnO**	**MgO**	**CaO**	**Na_2O**	**K_2O**	**P_2O_5**	**SO_2**	**Cl**	**F**
Mean	63.21	0.70	18.07	4.21	0.07	1.93	5.37	4.42	1.31	N/A	N/A	N/A	N/A
S.D.	0.23	0.03	0.12	0.06	0.02	0.03	0.04	0.38	0.02	N/A	N/A	N/A	N/A
Samples:	**PRAD 2525, PRAD 2812**												
Microprobe:	Oxford Earth Sciences												
	SiO_2	**TiO_2**	**Al_2O_3**	**FeO**	**MnO**	**MgO**	**CaO**	**Na_2O**	**K_2O**	**P_2O_5**	**SO_2**	**Cl**	**F**
Mean	64.03	0.71	17.97	4.21	0.07	1.96	5.32	4.59	1.33	N/A	N/A	N/A	N/A
S.D.	0.21	0.02	0.10	0.07	0.02	0.04	0.03	0.06	0.02	N/A	N/A	N/A	N/A
Samples:	**PRAD-3225, PRAD-3383**												
Microprobe:	Edinburgh												
	SiO_2	**TiO_2**	**Al_2O_3**	**FeO**	**MnO**	**MgO**	**CaO**	**Na_2O**	**K_2O**	**P_2O_5**	**SO_2**	**Cl**	**F**
Mean	63.99	0.72	17.67	4.42	0.08	1.94	5.35	4.50	1.30	0.17	0.00	0.03	0.02
S.D.	0.69	0.01	0.33	0.16	0.01	0.06	0.08	0.94	0.04	0.01	0.00	0.01	0.01

StHs6/80-G

Samples:	PRAD-3336, PRAD-3472, PRAD-3586, PRAD-3666												
Microprobe:	Edinburgh												
	SiO_2	TiO_2	Al_2O_3	FeO	MnO	MgO	CaO	Na_2O	K_2O	P_2O_5	SO_2	Cl	F
Mean	63.73	0.72	17.60	4.43	0.08	1.94	5.35	4.74	1.32	0.16	0.00	0.02	0.03
S.D.	0.40	0.01	0.18	0.13	0.01	0.04	0.06	0.08	0.06	0.01	0.00	0.00	0.02
Samples:	SA03-03-25, SA03-03-85, SA03-03-383, SA03-03-685												
Microprobe:	Edinburgh												
	SiO_2	TiO_2	Al_2O_3	FeO	MnO	MgO	CaO	Na_2O	K_2O	P_2O_5	SO_2	Cl	F
Mean	63.57	0.73	17.73	4.45	0.08	1.96	5.37	4.73	1.35	0.16	0.00	0.03	0.03
S.D.	0.46	0.01	0.22	0.15	0.01	0.05	0.09	0.10	0.06	0.01	0.00	0.01	0.01
Samples:	SA03-03-925, SA03-03-995												
Microprobe:	Edinburgh												
	SiO_2	TiO_2	Al_2O_3	FeO	MnO	MgO	CaO	Na_2O	K_2O	P_2O_5	SO_2	Cl	F
Mean	64.01	0.72	17.65	4.41	0.08	1.94	5.36	4.45	1.31	0.17	0.00	0.02	0.03
S.D.	0.76	0.01	0.35	0.14	0.01	0.06	0.09	1.05	0.04	0.01	0.00	0.00	0.01
Samples:	RF93-77-78, RF93-77-88, RF93-77-372, PRAD-205												
Microprobe:	Edinburgh												
	SiO_2	TiO_2	Al_2O_3	FeO	MnO	MgO	CaO	Na_2O	K_2O	P_2O_5	SO_2	Cl	F
Mean	63.19	0.73	17.58	4.37	0.08	1.96	5.32	4.53	1.30	0.15	0.00	0.02	0.02
S.D.	0.45	0.01	0.25	0.12	0.01	0.04	0.07	0.20	0.05	0.01	0.00	0.00	0.02
Samples:	RF93-77-144												
Microprobe:	Oxford Archaeology												
	SiO_2	TiO_2	Al_2O_3	FeO	MnO	MgO	CaO	Na_2O	K_2O	P_2O_5	SO_2	Cl	F
Mean	63.48	0.73	17.57	4.40	0.06	1.98	5.30	4.63	1.30	N/A	N/A	N/A	N/A
S.D.	0.37	0.04	0.50	0.16	0.04	0.06	0.09	0.12	0.03	N/A	N/A	N/A	N/A
Samples:	RF93-77-267, RF93-77-414, RF93-77-540, RF93-77-604												
Microprobe:	Edinburgh												
	SiO_2	TiO_2	Al_2O_3	FeO	MnO	MgO	CaO	Na_2O	K_2O	P_2O_5	SO_2	Cl	F
Mean	62.85	0.74	17.70	4.38	0.08	1.96	5.39	4.44	1.30	0.14	0.00	0.02	0.03
S.D.	0.75	0.01	0.22	0.18	0.00	0.05	0.09	1.06	0.05	0.01	0.00	0.00	0.01

ATHO-G

Samples:	SA03-03-25, SA03-03-392, SA03-03-399, RF93-77-68, RF93-77-198, RF93-77-438, RF93-77-790												
Microprobe:	Oxford Archaeology												
	SiO_2	TiO_2	Al_2O_3	FeO	MnO	MgO	CaO	Na_2O	K_2O	P_2O_5	SO_2	Cl	F
Mean	75.38	0.26	12.29	3.26	0.13	0.10	1.72	3.97	2.72	N/A	N/A	N/A	N/A
S.D.	0.14	0.03	0.14	0.11	0.05	0.02	0.05	0.13	0.04	N/A	N/A	N/A	N/A

ATHO-G

Samples:	**SA03-03-383, SA03-03-407, SA03-03-413, SA03-03-418, SA03-03-424, SA03-03-427, SA03-03-645**												
Microprobe:	Oxford Archaeology												
	SiO_2	**TiO_2**	**Al_2O_3**	**FeO**	**MnO**	**MgO**	**CaO**	**Na_2O**	**K_2O**	**P_2O_5**	**SO_2**	**Cl**	**F**
Mean	75.94	0.27	12.25	3.18	0.11	0.10	1.73	3.81	2.74	N/A	N/A	N/A	N/A
S.D.	0.30	0.03	0.16	0.14	0.05	0.02	0.03	0.09	0.06	N/A	N/A	N/A	N/A
Samples:	**RF93-77-144**												
Microprobe:	Oxford Archaeology												
	SiO_2	**TiO_2**	**Al_2O_3**	**FeO**	**MnO**	**MgO**	**CaO**	**Na_2O**	**K_2O**	**P_2O_5**	**SO_2**	**Cl**	**F**
Mean	75.73	0.25	12.10	3.33	0.10	0.10	1.73	3.94	2.71	N/A	N/A	N/A	N/A
S.D.	0.32	0.03	0.31	0.16	0.06	0.01	0.04	0.09	0.06	N/A	N/A	N/A	N/A

BHV02g

Samples:	**PRAD-250, PRAD-214, PRAD-223, PRAD-261, PRAD-231**												
Microprobe:	Edinburgh												
	SiO_2	**TiO_2**	**Al_2O_3**	**FeO**	**MnO**	**MgO**	**CaO**	**Na_2O**	**K_2O**	**P_2O_5**	**SO_2**	**Cl**	**F**
Mean	49.32	2.76	13.35	11.06	0.17	7.21	11.24	2.27	0.49	0.24	0.01	0.01	0.05
S.D.	0.45	0.02	0.31	0.26	0.01	0.12	0.12	0.07	0.02	0.02	0.00	0.00	0.01
Samples:	**PRAD-273, PRAD-329, PRAD-336, PRAD-205, PRAD-250, RF93-77-414, PRAD1104, RF93-77-73**												
Microprobe:	Edinburgh												
	SiO_2	**TiO_2**	**Al_2O_3**	**FeO**	**MnO**	**MgO**	**CaO**	**Na_2O**	**K_2O**	**P_2O_5**	**SO_2**	**Cl**	**F**
Mean	49.88	2.79	13.69	10.82	0.17	7.17	11.45	2.29	0.51	0.25	0.01	0.01	0.05
S.D.	0.48	0.02	0.26	0.32	0.01	0.12	0.17	0.10	0.02	0.01	0.00	0.00	0.01
Samples:	**PRAD-336, PRAD-273, PRAD-329, PRAD-323, PRAD-267, PRAD-1104**												
Microprobe:	Edinburgh												
	SiO_2	**TiO_2**	**Al_2O_3**	**FeO**	**MnO**	**MgO**	**CaO**	**Na_2O**	**K_2O**	**P_2O_5**	**SO_2**	**Cl**	**F**
Mean	49.75	2.77	13.48	10.85	0.17	7.16	11.27	2.27	0.51	0.25	0.01	0.01	0.05
S.D.	0.38	0.01	0.18	0.20	0.01	0.08	0.09	0.08	0.04	0.01	0.00	0.00	0.01
Samples:	**PRAD-789, PRAD-844, PRAD-1130, PRAD-868, PRAD-839, PRAD-873**												
Microprobe:	Edinburgh												
	SiO_2	**TiO_2**	**Al_2O_3**	**FeO**	**MnO**	**MgO**	**CaO**	**Na_2O**	**K_2O**	**P_2O_5**	**SO_2**	**Cl**	**F**
Mean	50.24	2.83	13.63	11.04	0.17	7.04	11.58	2.27	0.50	0.23	0.01	0.01	0.04
S.D.	0.37	0.01	0.20	0.33	0.01	0.05	0.11	0.11	0.03	0.01	0.01	0.00	0.01
Samples:	**PRAD841, PRAD-1474, PRAD-784, PRAD-837, PRAD-2375, RF93-77-73**												
Microprobe:	Edinburgh												
	SiO_2	**TiO_2**	**Al_2O_3**	**FeO**	**MnO**	**MgO**	**CaO**	**Na_2O**	**K_2O**	**P_2O_5**	**SO_2**	**Cl**	**F**
Mean	49.78	2.83	13.65	10.85	0.17	7.13	11.43	2.32	0.53	0.22	0.00	0.01	0.04
S.D.	0.54	0.01	0.15	0.28	0.01	0.10	0.14	0.07	0.02	0.01	0.01	0.00	0.01

BHV02g

Samples:	**RF93-77-78, RF93-77-88, RF93-77-372, PRAD-205**												
Microprobe:	Edinburgh												
	SiO_2	**TiO_2**	**Al_2O_3**	**FeO**	**MnO**	**MgO**	**CaO**	**Na_2O**	**K_2O**	**P_2O_5**	**SO_2**	**Cl**	**F**
Mean	49.36	2.77	13.23	10.94	0.17	7.16	11.32	2.30	0.50	0.25	0.00	0.01	0.05
S.D.	0.56	0.03	0.35	0.16	0.01	0.12	0.13	0.07	0.03	0.01	0.00	0.00	0.01
Samples:	**RF93-77-267, RF93-77-414, RF93-77-486, RF93-77-540, RF93-77-604**												
Microprobe:	Edinburgh												
	SiO_2	**TiO_2**	**Al_2O_3**	**FeO**	**MnO**	**MgO**	**CaO**	**Na_2O**	**K_2O**	**P_2O_5**	**SO_2**	**Cl**	**F**
Mean	49.44	2.79	13.64	10.83	0.17	7.12	11.46	2.29	0.53	0.25	0.00	0.01	0.04
S.D.	0.20	0.01	0.08	0.20	0.00	0.02	0.10	0.01	0.06	0.01	0.00	0.00	0.03

Appendix C

PRAD 1-2 Major Element data generated in this study. The sample name, microprobe the analyses were carried out on and sampling resolution are all indicated. Microprobe: OE = Oxford Earth Sciences, OA = Oxford Archaeology and E – Edinburgh.

Name	Microprobe	Resolution	SiO_2	TiO_2	Al_2O_3	FeO	MnO	MgO	CaO	Na_2O	K_2O	P_2O_5	S	Cl	F	Total
PRAD-055	OE	5 cm	59.47	0.49	18.56	3.52	0.13	0.71	2.51	4.23	8.86	N/A	N/A	N/A	N/A	98.47
PRAD-055	OE	5 cm	60.01	0.50	18.65	3.28	0.08	0.72	2.45	4.08	8.70	N/A	N/A	N/A	N/A	98.47
PRAD-055	OE	5 cm	59.45	0.47	18.94	3.49	0.12	0.75	2.42	4.28	8.49	N/A	N/A	N/A	N/A	98.40
PRAD-055	OE	5 cm	59.19	0.45	18.69	3.43	0.12	0.75	2.65	4.26	8.71	N/A	N/A	N/A	N/A	98.25
PRAD-055	OE	5 cm	59.90	0.51	18.44	3.17	0.14	0.72	2.45	4.43	8.46	N/A	N/A	N/A	N/A	98.21
PRAD-055	OE	5 cm	59.40	0.39	18.57	3.26	0.14	0.70	2.53	4.22	8.81	N/A	N/A	N/A	N/A	98.02
PRAD-055	OE	5 cm	59.42	0.47	18.43	3.42	0.08	0.74	2.42	4.24	8.68	N/A	N/A	N/A	N/A	97.89
PRAD-055	OE	5 cm	59.78	0.48	18.59	3.17	0.10	0.57	2.12	4.86	8.14	N/A	N/A	N/A	N/A	97.81
PRAD-055	OE	5 cm	59.56	0.53	18.51	3.20	0.11	0.73	2.36	4.42	8.34	N/A	N/A	N/A	N/A	97.76
PRAD-055	OE	5 cm	58.81	0.45	18.42	3.65	0.13	0.81	2.51	4.21	8.50	N/A	N/A	N/A	N/A	97.50
PRAD-055	OE	5 cm	58.40	0.46	18.52	3.45	0.13	0.77	2.53	4.26	8.89	N/A	N/A	N/A	N/A	97.41
PRAD-055	OE	5 cm	59.24	0.44	18.45	3.35	0.15	0.72	2.36	4.11	8.52	N/A	N/A	N/A	N/A	97.33
PRAD-055	OE	5 cm	59.15	0.47	18.57	3.41	0.10	0.75	2.29	4.94	7.60	N/A	N/A	N/A	N/A	97.26
PRAD-055	OE	5 cm	59.35	0.46	18.85	3.20	0.09	0.60	2.08	4.66	7.84	N/A	N/A	N/A	N/A	97.12
PRAD-055	OE	5 cm	59.34	0.42	18.29	3.26	0.13	0.69	2.34	4.13	8.45	N/A	N/A	N/A	N/A	97.05
PRAD-055	OE	5 cm	59.18	0.43	18.13	3.27	0.11	0.78	2.58	3.81	8.74	N/A	N/A	N/A	N/A	97.03
PRAD-055	OE	5 cm	58.53	0.53	18.23	3.53	0.09	0.92	2.71	4.03	8.41	N/A	N/A	N/A	N/A	96.96
PRAD-055	OE	5 cm	58.97	0.44	18.40	3.13	0.16	0.71	2.33	4.26	8.39	N/A	N/A	N/A	N/A	96.79
PRAD-055	OE	5 cm	58.73	0.43	18.59	3.15	0.15	0.69	2.78	4.03	8.25	N/A	N/A	N/A	N/A	96.79
PRAD-055	OE	5 cm	59.12	0.42	18.35	3.26	0.15	0.71	2.30	4.23	8.26	N/A	N/A	N/A	N/A	96.79
PRAD-055	OE	5 cm	58.83	0.41	18.37	3.34	0.15	0.68	2.29	4.38	8.22	N/A	N/A	N/A	N/A	96.66
PRAD-055	OE	5 cm	57.30	0.50	18.16	3.50	0.15	0.74	2.57	4.32	9.13	N/A	N/A	N/A	N/A	96.37
PRAD-055	OE	5 cm	58.75	0.43	18.82	2.88	0.11	0.50	2.30	3.59	8.95	N/A	N/A	N/A	N/A	96.33
PRAD-055	OE	5 cm	58.37	0.49	18.25	3.42	0.11	0.73	2.41	3.97	8.45	N/A	N/A	N/A	N/A	96.20
PRAD-055	OE	5 cm	58.82	0.52	18.35	3.09	0.03	0.62	2.32	4.57	7.74	N/A	N/A	N/A	N/A	96.06
PRAD-055	OE	5 cm	58.29	0.45	18.21	3.43	0.11	0.74	2.32	3.96	8.47	N/A	N/A	N/A	N/A	95.97
PRAD-055	OE	5 cm	57.62	0.44	18.28	3.58	0.15	0.76	2.46	4.55	8.11	N/A	N/A	N/A	N/A	95.95
PRAD-055	OE	5 cm	57.16	0.43	18.26	3.48	0.08	0.72	2.42	4.01	8.77	N/A	N/A	N/A	N/A	95.34
PRAD-055	OE	5 cm	56.69	0.47	18.57	3.31	0.10	0.70	2.53	4.05	8.87	N/A	N/A	N/A	N/A	95.27
PRAD-120	OE	5 cm	59.45	0.44	18.68	3.25	0.07	0.67	2.42	4.02	9.22	N/A	N/A	N/A	N/A	98.22
PRAD-120	OE	5 cm	59.03	0.43	18.64	3.52	0.12	0.76	2.65	4.18	8.76	N/A	N/A	N/A	N/A	98.10
PRAD-120	OE	5 cm	58.88	0.45	18.44	3.51	0.08	0.72	2.57	4.31	9.11	N/A	N/A	N/A	N/A	98.06
PRAD-120	OE	5 cm	58.93	0.48	18.28	3.60	0.14	0.74	2.65	4.10	8.74	N/A	N/A	N/A	N/A	97.65
PRAD-120	OE	5 cm	59.29	0.47	18.44	3.18	0.07	0.63	2.37	3.94	9.23	N/A	N/A	N/A	N/A	97.63
PRAD-120	OE	5 cm	59.10	0.43	18.24	3.40	0.16	0.73	2.55	4.12	8.79	N/A	N/A	N/A	N/A	97.52
PRAD-120	OE	5 cm	60.04	0.46	18.27	2.73	0.14	0.45	2.15	4.44	8.74	N/A	N/A	N/A	N/A	97.41
PRAD-120	OE	5 cm	58.63	0.50	18.49	3.40	0.09	0.75	2.60	4.14	8.75	N/A	N/A	N/A	N/A	97.34
PRAD-120	OE	5 cm	58.45	0.48	18.43	3.56	0.11	0.75	2.65	4.23	8.66	N/A	N/A	N/A	N/A	97.31
PRAD-120	OE	5 cm	60.48	0.40	18.13	2.75	0.15	0.43	2.14	4.44	8.31	N/A	N/A	N/A	N/A	97.23
PRAD-120	OE	5 cm	58.31	0.45	18.35	3.54	0.12	0.74	2.60	4.18	8.82	N/A	N/A	N/A	N/A	97.09
PRAD-120	OE	5 cm	58.54	0.35	18.81	2.79	0.10	0.47	2.37	4.32	9.34	N/A	N/A	N/A	N/A	97.07
PRAD-120	OE	5 cm	58.23	0.50	18.24	3.52	0.10	0.75	2.74	4.15	8.82	N/A	N/A	N/A	N/A	97.04
PRAD-120	OE	5 cm	58.34	0.42	18.46	3.35	0.02	0.72	2.60	4.14	8.78	N/A	N/A	N/A	N/A	96.83
PRAD-120	OE	5 cm	57.70	0.45	18.01	3.30	0.09	0.76	2.61	4.39	8.69	N/A	N/A	N/A	N/A	96.00
PRAD-120	OE	5 cm	60.36	0.46	18.67	3.43	0.12	0.80	2.62	4.18	8.58	N/A	N/A	N/A	N/A	99.20
PRAD-120	OE	5 cm	60.98	0.48	18.71	3.49	0.14	0.75	2.62	4.24	8.63	N/A	N/A	N/A	N/A	100.04
PRAD-120	OE	5 cm	59.27	0.48	19.17	3.45	0.12	0.71	2.47	4.35	8.50	N/A	N/A	N/A	N/A	98.51

Name	Microprobe	Resolution	SiO_2	TiO_2	Al_2O_3	FeO	MnO	MgO	CaO	Na_2O	K_2O	P_2O_5	S	Cl	F	Total
PRAD-120	OE	5 cm	63.65	0.38	18.97	3.07	0.14	0.59	2.27	4.60	8.50	N/A	N/A	N/A	N/A	102.17
PRAD-120	OE	5 cm	63.25	0.46	19.19	3.17	0.16	0.57	2.18	5.17	8.11	N/A	N/A	N/A	N/A	102.26
PRAD-120	OE	5 cm	62.52	0.47	19.00	3.55	0.12	0.77	2.51	4.32	8.70	N/A	N/A	N/A	N/A	101.96
PRAD-120	OE	5 cm	63.36	0.42	18.67	3.11	0.15	0.55	2.30	3.60	8.61	N/A	N/A	N/A	N/A	100.77
PRAD-120	OE	5 cm	62.02	0.49	18.86	3.52	0.10	0.77	2.53	3.30	8.75	N/A	N/A	N/A	N/A	100.35
PRAD-120	OE	5 cm	61.03	0.46	19.27	3.52	0.11	0.83	2.56	4.37	8.26	N/A	N/A	N/A	N/A	100.41
PRAD-120	OE	5 cm	61.86	0.46	18.93	3.36	0.12	0.78	2.57	4.40	8.55	N/A	N/A	N/A	N/A	101.00
PRAD-205	OE	1 cm	57.94	0.52	18.69	4.20	0.14	1.05	3.56	3.84	8.21	N/A	N/A	N/A	N/A	98.14
PRAD-205	OE	1 cm	57.16	0.60	18.44	4.22	0.08	1.12	3.79	3.76	8.39	N/A	N/A	N/A	N/A	97.56
PRAD-205	OE	1 cm	56.83	0.58	18.50	4.41	0.13	1.33	4.00	3.78	8.30	N/A	N/A	N/A	N/A	97.85
PRAD-205	OE	1 cm	56.54	0.60	18.42	4.49	0.10	1.33	4.11	3.74	8.24	N/A	N/A	N/A	N/A	97.57
PRAD-205	OE	1 cm	56.93	0.58	18.68	4.49	0.15	1.29	3.97	3.67	8.13	N/A	N/A	N/A	N/A	97.89
PRAD-205	OE	1 cm	55.36	0.54	18.18	4.59	0.10	1.39	4.29	3.44	8.38	N/A	N/A	N/A	N/A	96.28
PRAD-205	OE	1 cm	55.98	0.53	18.25	4.73	0.15	1.40	4.41	3.40	8.52	N/A	N/A	N/A	N/A	97.37
PRAD-205	OE	1 cm	57.08	0.59	18.61	4.74	0.10	1.39	4.19	3.86	7.89	N/A	N/A	N/A	N/A	98.45
PRAD-205	OE	1 cm	55.96	0.55	18.26	4.74	0.09	1.38	4.28	3.42	8.46	N/A	N/A	N/A	N/A	97.14
PRAD-205	OE	1 cm	56.46	0.56	18.10	4.81	0.12	1.55	4.45	3.34	8.09	N/A	N/A	N/A	N/A	97.49
PRAD-205	OE	1 cm	55.87	0.56	18.64	4.83	0.10	1.49	4.46	3.09	8.35	N/A	N/A	N/A	N/A	97.39
PRAD-205	OE	1 cm	55.50	0.55	18.19	4.93	0.18	1.43	4.34	3.49	8.29	N/A	N/A	N/A	N/A	96.90
PRAD-205	OE	1 cm	55.56	0.59	18.42	5.02	0.11	1.57	4.55	3.21	7.96	N/A	N/A	N/A	N/A	96.99
PRAD-205	OE	1 cm	55.11	0.65	18.22	5.15	0.12	1.59	4.74	3.32	8.11	N/A	N/A	N/A	N/A	97.02
PRAD-205	OE	1 cm	54.57	0.66	18.16	5.15	0.14	1.66	4.84	3.36	8.24	N/A	N/A	N/A	N/A	96.77
PRAD-205	OE	1 cm	54.74	0.59	18.18	5.16	0.11	1.79	5.09	3.19	7.78	N/A	N/A	N/A	N/A	96.64
PRAD-205	OE	1 cm	54.79	0.57	18.29	5.19	0.12	1.69	4.85	3.42	8.09	N/A	N/A	N/A	N/A	96.99
PRAD-205	OE	1 cm	54.66	0.65	18.16	5.23	0.11	1.84	5.00	3.23	7.73	N/A	N/A	N/A	N/A	96.60
PRAD-205	OE	1 cm	54.88	0.66	18.24	5.40	0.07	1.90	5.08	3.22	7.94	N/A	N/A	N/A	N/A	97.39
PRAD-205	OE	1 cm	61.32	0.36	18.71	2.35	0.10	0.37	2.01	4.15	8.95	N/A	N/A	N/A	N/A	98.31
PRAD-205	OE	1 cm	61.15	0.41	18.60	2.53	0.16	0.41	2.10	4.50	8.51	N/A	N/A	N/A	N/A	98.37
PRAD-205	OE	1 cm	59.82	0.37	18.06	2.56	0.12	0.42	2.11	4.23	8.15	N/A	N/A	N/A	N/A	95.84
PRAD-205	OE	1 cm	58.28	0.40	17.95	2.59	0.09	0.45	2.11	4.40	9.05	N/A	N/A	N/A	N/A	95.31
PRAD-205	OE	1 cm	59.70	0.35	17.64	2.60	0.13	0.44	2.12	4.16	8.52	N/A	N/A	N/A	N/A	95.65
PRAD-205	OE	1 cm	59.85	0.42	18.20	2.65	0.10	0.45	2.13	4.61	8.60	N/A	N/A	N/A	N/A	97.00
PRAD-205	OE	1 cm	60.25	0.44	18.27	2.65	0.16	0.43	2.08	4.66	8.69	N/A	N/A	N/A	N/A	97.62
PRAD-205	OE	1 cm	60.02	0.41	18.23	2.67	0.13	0.43	2.18	4.29	8.50	N/A	N/A	N/A	N/A	96.87
PRAD-205	OE	1 cm	60.89	0.44	18.43	2.68	0.09	0.43	2.12	4.70	8.68	N/A	N/A	N/A	N/A	98.45
PRAD-205	OE	1 cm	60.45	0.45	18.38	2.75	0.08	0.43	2.23	4.68	8.55	N/A	N/A	N/A	N/A	98.00
PRAD-205	OE	1 cm	60.23	0.40	18.41	2.82	0.15	0.42	2.15	4.44	8.45	N/A	N/A	N/A	N/A	97.47
PRAD-205	OE	1 cm	60.29	0.44	18.47	2.83	0.16	0.48	2.18	4.39	8.67	N/A	N/A	N/A	N/A	97.93
PRAD-205	OE	1 cm	59.56	0.43	18.59	2.85	0.13	0.57	2.47	4.43	8.72	N/A	N/A	N/A	N/A	97.75
PRAD-205	OE	1 cm	59.30	0.38	17.75	2.99	0.12	0.61	2.40	3.63	8.56	N/A	N/A	N/A	N/A	95.73
PRAD-205	OE	1 cm	59.76	0.45	18.44	3.02	0.08	0.58	2.34	4.36	9.13	N/A	N/A	N/A	N/A	98.15
PRAD-205	OE	1 cm	59.79	0.41	18.16	3.11	0.15	0.60	2.57	3.87	8.78	N/A	N/A	N/A	N/A	97.43
PRAD-205	OE	1 cm	59.72	0.43	18.36	3.11	0.12	0.65	2.54	3.53	9.29	N/A	N/A	N/A	N/A	97.75
PRAD-205	OE	1 cm	59.62	0.41	18.63	3.15	0.15	0.63	2.47	3.76	9.34	N/A	N/A	N/A	N/A	98.16
PRAD-205	OE	1 cm	58.22	0.43	18.38	3.22	0.07	0.77	2.81	3.71	9.26	N/A	N/A	N/A	N/A	96.86
PRAD-205	OE	1 cm	58.76	0.47	18.46	3.65	0.10	0.92	3.01	4.14	8.30	N/A	N/A	N/A	N/A	97.80
PRAD-205	OE	1 cm	58.50	0.44	17.84	3.65	0.12	0.87	3.15	3.43	8.25	N/A	N/A	N/A	N/A	96.25
PRAD-205	OE	1 cm	57.53	0.43	17.88	3.83	0.08	0.86	3.11	3.70	8.62	N/A	N/A	N/A	N/A	96.04
PRAD-205	OE	1 cm	57.42	0.45	18.41	3.87	0.15	1.05	3.41	3.39	9.22	N/A	N/A	N/A	N/A	97.36
PRAD-205	E	1 cm	57.53	0.60	18.02	4.59	0.15	1.40	4.27	3.64	8.27	0.28	0.07	0.47	0.22	99.52
PRAD-205	E	1 cm	58.26	0.54	17.96	4.39	0.11	1.11	3.67	3.50	8.42	0.20	0.02	0.52	0.21	98.89
PRAD-205	E	1 cm	62.62	0.41	17.22	2.28	0.22	0.20	1.40	6.23	6.37	0.02	0.00	0.79	0.58	98.35
PRAD-205	E	1 cm	58.16	0.49	17.74	4.14	0.12	0.84	3.15	3.68	8.58	0.16	0.09	0.63	0.20	97.97

Name	Microprobe	Resolution	SiO_2	TiO_2	Al_2O_3	FeO	MnO	MgO	CaO	Na_2O	K_2O	P_2O_5	S	Cl	F	Total
PRAD-205	E	1 cm	55.32	0.57	18.17	4.83	0.12	1.57	4.50	3.39	8.27	0.29	0.22	0.46	0.20	97.93
PRAD-205	E	1 cm	56.04	0.60	17.65	5.22	0.13	1.52	4.45	3.03	8.09	0.35	0.14	0.41	0.19	97.82
PRAD-205	E	1 cm	56.76	0.49	17.83	4.10	0.12	1.09	3.57	3.04	9.06	0.21	0.21	0.45	0.20	97.13
PRAD-205	E	1 cm	59.89	0.48	17.62	2.73	0.15	0.45	2.09	4.26	8.45	0.06	0.02	0.64	0.26	97.12
PRAD-205	E	1 cm	54.83	0.58	17.87	4.97	0.13	1.46	4.43	3.35	8.21	0.29	0.24	0.48	0.24	97.08
PRAD-205	E	1 cm	54.88	0.58	17.89	4.85	0.14	1.50	4.37	3.31	8.24	0.30	0.20	0.47	0.23	96.95
PRAD-205	E	1 cm	59.32	0.47	17.56	2.71	0.14	0.46	2.19	4.55	8.46	0.07	0.03	0.64	0.29	96.89
PRAD-205	E	1 cm	55.32	0.57	18.03	4.58	0.13	1.42	4.33	3.06	8.22	0.29	0.23	0.47	0.23	96.87
PRAD-205	E	1 cm	53.86	0.62	18.00	5.25	0.14	1.72	4.93	3.25	7.65	0.34	0.23	0.49	0.20	96.68
PRAD-205	E	1 cm	54.85	0.58	17.88	4.79	0.14	1.41	4.28	3.29	8.29	0.28	0.21	0.48	0.20	96.67
PRAD-205	E	1 cm	53.01	0.71	17.47	5.36	0.11	1.99	5.11	2.87	7.41	0.47	0.14	0.37	0.25	95.28
PRAD-205	E	1 cm	53.53	0.59	17.39	5.00	0.13	1.58	4.58	3.15	7.90	0.32	0.27	0.48	0.20	95.11
PRAD-214	E	1 cm	61.96	0.50	18.13	2.61	0.18	0.28	1.97	5.57	7.74	0.03	0.03	0.80	0.35	100.13
PRAD-214	E	1 cm	60.88	0.58	17.02	4.14	0.21	0.57	2.41	4.99	7.69	0.08	0.00	0.90	0.42	99.90
PRAD-214	E	1 cm	61.05	0.48	18.08	2.80	0.16	0.48	2.28	4.57	8.87	0.07	0.09	0.68	0.26	99.86
PRAD-214	E	1 cm	57.60	0.60	18.10	4.70	0.14	1.32	4.09	3.93	7.92	0.29	0.08	0.46	0.22	99.45
PRAD-214	E	1 cm	61.37	0.50	18.01	2.60	0.19	0.27	1.83	5.50	7.64	0.03	0.04	0.81	0.34	99.13
PRAD-214	E	1 cm	57.53	0.49	18.32	4.35	0.15	1.13	3.64	3.77	8.50	0.22	0.23	0.47	0.19	98.98
PRAD-214	E	1 cm	59.21	0.47	18.05	3.42	0.13	0.78	2.85	3.85	8.88	0.14	0.11	0.54	0.21	98.63
PRAD-214	E	1 cm	57.95	0.50	17.88	3.84	0.14	0.85	3.21	3.88	8.83	0.19	0.20	0.52	0.22	98.20
PRAD-214	E	1 cm	55.02	0.62	18.18	5.08	0.15	1.55	4.77	3.34	8.16	0.31	0.25	0.50	0.20	98.10
PRAD-214	E	1 cm	58.30	0.45	18.13	3.43	0.12	0.77	2.85	4.16	8.72	0.14	0.17	0.48	0.20	97.93
PRAD-214	E	1 cm	59.60	0.49	17.93	2.70	0.16	0.49	2.28	4.59	8.57	0.09	0.04	0.65	0.28	97.88
PRAD-214	E	1 cm	59.45	0.48	18.05	2.72	0.15	0.48	2.25	4.67	8.52	0.06	0.09	0.68	0.27	97.86
PRAD-214	E	1 cm	55.85	0.61	17.74	5.01	0.15	1.38	4.16	3.73	8.05	0.29	0.09	0.52	0.23	97.80
PRAD-214	E	1 cm	59.95	0.39	17.92	2.85	0.14	0.47	2.10	4.09	8.74	0.05	0.06	0.64	0.19	97.58
PRAD-214	E	1 cm	59.14	0.45	17.71	2.86	0.14	0.50	2.16	4.68	8.65	0.07	0.11	0.65	0.23	97.36
PRAD-214	E	1 cm	58.12	0.47	17.93	2.87	0.15	0.48	2.19	4.27	8.80	0.06	0.10	0.66	0.25	96.35
PRAD-214	E	1 cm	58.75	0.39	17.22	2.96	0.14	0.42	2.15	3.98	8.52	0.08	0.04	0.61	0.23	95.49
PRAD-214	E	1 cm	58.45	0.46	17.37	2.69	0.17	0.43	2.12	4.43	8.25	0.06	0.10	0.70	0.26	95.47
PRAD-214	E	1 cm	60.87	0.38	16.14	2.29	0.20	0.22	1.40	5.85	6.22	0.02	0.00	0.79	0.65	95.02
PRAD-223	E	1 cm	58.30	0.58	18.08	4.43	0.15	1.09	3.73	3.94	8.22	0.23	0.06	0.55	0.23	99.59
PRAD-223	E	1 cm	60.70	0.48	18.14	2.79	0.15	0.45	2.17	4.64	8.69	0.05	0.10	0.69	0.26	99.32
PRAD-223	E	1 cm	57.62	0.55	18.19	4.69	0.12	1.17	3.90	3.43	8.18	0.21	0.02	0.51	0.22	98.81
PRAD-223	E	1 cm	55.36	0.64	17.96	5.18	0.15	1.90	4.96	3.35	8.05	0.34	0.24	0.50	0.20	98.81
PRAD-223	E	1 cm	58.44	0.48	18.24	3.54	0.13	0.81	2.90	3.84	9.34	0.13	0.12	0.49	0.18	98.66
PRAD-223	E	1 cm	57.30	0.55	18.22	4.36	0.15	1.04	3.58	3.82	8.45	0.22	0.09	0.53	0.22	98.54
PRAD-223	E	1 cm	56.52	0.56	18.36	4.43	0.14	1.28	4.06	3.64	8.29	0.22	0.24	0.51	0.20	98.44
PRAD-223	E	1 cm	56.47	0.60	18.55	4.81	0.14	1.21	3.98	3.57	7.99	0.25	0.10	0.52	0.22	98.39
PRAD-223	E	1 cm	59.57	0.41	17.91	3.21	0.11	0.76	2.39	3.06	9.86	0.14	0.06	0.36	0.17	98.02
PRAD-223	E	1 cm	56.74	0.58	17.85	4.58	0.14	1.08	3.70	3.91	8.00	0.22	0.09	0.56	0.23	97.68
PRAD-223	E	1 cm	59.52	0.48	17.94	2.72	0.15	0.44	2.18	4.56	8.61	0.06	0.01	0.58	0.28	97.53
PRAD-223	E	1 cm	59.19	0.48	18.04	2.70	0.14	0.49	2.18	4.25	8.80	0.06	0.08	0.66	0.27	97.33
PRAD-223	E	1 cm	56.65	0.52	17.85	4.12	0.14	1.06	3.46	3.41	8.82	0.20	0.18	0.53	0.21	97.15
PRAD-223	E	1 cm	59.83	0.37	16.67	2.74	0.14	0.39	2.05	4.64	7.76	0.04	0.05	0.70	0.26	95.66
PRAD-223	E	1 cm	59.14	0.40	17.19	2.66	0.15	0.39	2.10	4.41	7.90	0.07	0.04	0.75	0.28	95.47
PRAD-223	E	1 cm	58.37	0.47	17.42	2.73	0.14	0.42	2.21	4.46	8.22	0.07	0.05	0.67	0.24	95.46
PRAD-223	OE	1 cm	57.31	0.55	18.13	4.36	0.09	1.19	3.95	3.45	8.35	N/A	N/A	N/A	N/A	97.38

Name	Microprobe	Resolution	SiO_2	TiO_2	Al_2O_3	FeO	MnO	MgO	CaO	Na_2O	K_2O	P_2O_5	S	Cl	F	Total
PRAD-223	OE	1 cm	56.33	0.51	17.92	4.39	0.10	1.13	3.90	3.37	8.03	N/A	N/A	N/A	N/A	95.67
PRAD-223	OE	1 cm	55.72	0.59	18.11	4.41	0.11	1.22	3.93	3.52	8.10	N/A	N/A	N/A	N/A	95.70
PRAD-223	OE	1 cm	56.44	0.59	18.48	4.53	0.12	1.27	4.13	3.62	8.39	N/A	N/A	N/A	N/A	97.57
PRAD-223	OE	1 cm	56.11	0.61	18.45	4.70	0.15	1.30	4.04	3.60	8.22	N/A	N/A	N/A	N/A	97.17
PRAD-223	OE	1 cm	59.52	0.40	18.21	2.48	0.10	0.44	2.23	4.47	8.60	N/A	N/A	N/A	N/A	96.44
PRAD-223	OE	1 cm	59.15	0.44	18.08	2.50	0.19	0.44	2.19	4.43	8.42	N/A	N/A	N/A	N/A	95.82
PRAD-223	OE	1 cm	60.04	0.34	17.92	2.58	0.10	0.46	2.33	4.41	8.46	N/A	N/A	N/A	N/A	96.64
PRAD-223	OE	1 cm	58.72	0.49	17.99	2.62	0.13	0.42	2.05	4.46	8.13	N/A	N/A	N/A	N/A	95.02
PRAD-223	OE	1 cm	59.74	0.42	18.19	2.63	0.21	0.45	2.20	4.67	8.89	N/A	N/A	N/A	N/A	97.39
PRAD-223	OE	1 cm	59.51	0.41	18.28	2.66	0.11	0.42	2.22	4.64	8.65	N/A	N/A	N/A	N/A	96.89
PRAD-223	OE	1 cm	59.67	0.46	18.16	2.72	0.08	0.45	2.20	4.42	8.65	N/A	N/A	N/A	N/A	96.80
PRAD-223	OE	1 cm	58.62	0.45	17.90	2.72	0.17	0.43	2.12	4.35	8.41	N/A	N/A	N/A	N/A	95.16
PRAD-223	OE	1 cm	58.95	0.40	18.17	2.73	0.18	0.47	2.29	4.72	8.70	N/A	N/A	N/A	N/A	96.60
PRAD-223	OE	1 cm	59.16	0.41	18.53	2.79	0.17	0.43	2.18	4.49	9.09	N/A	N/A	N/A	N/A	97.26
PRAD-223	OE	1 cm	59.46	0.37	18.42	2.79	0.17	0.47	2.29	4.47	8.59	N/A	N/A	N/A	N/A	97.04
PRAD-223	OE	1 cm	58.39	0.40	17.90	2.81	0.13	0.51	2.48	4.02	8.72	N/A	N/A	N/A	N/A	95.35
PRAD-223	OE	1 cm	59.02	0.43	18.19	2.83	0.16	0.44	2.16	4.64	8.77	N/A	N/A	N/A	N/A	96.64
PRAD-223	OE	1 cm	59.93	0.43	18.24	2.85	0.08	0.47	2.24	4.50	8.57	N/A	N/A	N/A	N/A	97.32
PRAD-223	OE	1 cm	59.60	0.46	18.07	2.89	0.09	0.55	2.52	4.24	8.81	N/A	N/A	N/A	N/A	97.22
PRAD-223	OE	1 cm	59.34	0.42	18.14	2.89	0.10	0.53	2.48	4.18	8.85	N/A	N/A	N/A	N/A	96.93
PRAD-223	OE	1 cm	58.10	0.49	18.07	2.92	0.12	0.62	2.52	4.24	8.51	N/A	N/A	N/A	N/A	95.58
PRAD-223	OE	1 cm	59.38	0.43	18.28	3.01	0.12	0.46	2.30	4.57	8.61	N/A	N/A	N/A	N/A	97.15
PRAD-223	OE	1 cm	58.45	0.45	18.39	3.22	0.16	0.72	2.78	3.64	9.40	N/A	N/A	N/A	N/A	97.20
PRAD-223	OE	1 cm	57.99	0.46	18.42	3.40	0.13	0.81	2.98	3.58	9.47	N/A	N/A	N/A	N/A	97.22
PRAD-223	OE	1 cm	59.51	0.44	18.11	3.47	0.11	0.66	2.72	3.74	8.84	N/A	N/A	N/A	N/A	97.61
PRAD-231	E	1 cm	61.23	0.49	18.41	3.04	0.14	0.50	2.32	4.70	8.60	0.07	0.03	0.64	0.24	100.40
PRAD-231	E	1 cm	57.08	0.58	18.94	4.63	0.14	1.31	4.12	3.78	8.17	0.26	0.08	0.45	0.26	99.80
PRAD-231	E	1 cm	58.16	0.57	18.21	4.32	0.16	1.10	3.56	4.28	7.86	0.24	0.06	0.57	0.28	99.38
PRAD-231	E	1 cm	60.76	0.49	17.90	2.84	0.15	0.44	2.18	4.88	8.52	0.06	0.09	0.70	0.26	99.28
PRAD-231	E	1 cm	60.17	0.49	18.17	2.89	0.15	0.46	2.22	4.71	8.61	0.07	0.03	0.67	0.26	98.92
PRAD-231	E	1 cm	60.34	0.47	18.41	2.52	0.14	0.43	2.19	4.08	9.30	0.06	0.09	0.65	0.21	98.91
PRAD-231	E	1 cm	60.07	0.42	17.94	3.38	0.13	0.65	2.59	3.57	8.90	0.11	0.07	0.52	0.20	98.54
PRAD-231	E	1 cm	57.90	0.46	18.37	3.67	0.12	0.90	3.10	3.61	9.25	0.15	0.20	0.46	0.17	98.35
PRAD-231	E	1 cm	55.36	0.61	18.07	5.09	0.13	1.63	4.58	3.34	8.10	0.31	0.23	0.49	0.25	98.19
PRAD-231	E	1 cm	56.46	0.61	18.11	4.64	0.12	1.33	4.11	3.46	8.04	0.27	0.11	0.52	0.23	98.00
PRAD-231	E	1 cm	58.78	0.47	18.03	3.29	0.14	0.68	2.66	3.79	9.16	0.11	0.15	0.52	0.20	97.98
PRAD-231	E	1 cm	56.49	0.59	18.39	4.44	0.15	1.26	3.84	3.68	7.96	0.25	0.06	0.53	0.26	97.89
PRAD-231	E	1 cm	59.37	0.47	17.58	2.79	0.16	0.41	2.16	4.64	8.58	0.06	0.10	0.65	0.26	97.23
PRAD-231	E	1 cm	58.96	0.46	17.52	2.80	0.15	0.40	2.14	4.45	8.47	0.06	0.05	0.68	0.27	96.39
PRAD-231	E	1 cm	58.49	0.47	17.64	2.59	0.14	0.41	2.23	4.27	8.34	0.07	0.10	0.66	0.26	95.64
PRAD-231	E	1 cm	58.27	0.45	17.41	2.88	0.15	0.47	2.09	4.40	7.92	0.08	0.10	0.66	0.24	95.13
PRAD-250	E	1 cm	59.84	0.44	17.79	3.73	0.12	0.70	2.94	3.77	8.60	0.13	0.03	0.59	0.21	98.89
PRAD-250	E	1 cm	61.39	0.41	17.79	2.95	0.13	0.50	2.27	4.03	8.47	0.07	0.05	0.60	0.23	98.88
PRAD-250	E	1 cm	60.36	0.46	18.04	2.77	0.16	0.47	2.23	4.68	8.47	0.06	0.08	0.70	0.28	98.76
PRAD-250	E	1 cm	57.74	0.48	18.05	4.14	0.12	1.08	3.44	3.49	9.12	0.20	0.19	0.44	0.18	98.68
PRAD-250	E	1 cm	59.74	0.49	18.27	2.76	0.16	0.46	2.26	4.83	8.58	0.08	0.10	0.69	0.25	98.67
PRAD-250	E	1 cm	60.02	0.47	17.89	2.92	0.15	0.48	2.22	4.30	9.08	0.08	0.10	0.60	0.22	98.52
PRAD-250	E	1 cm	54.89	0.73	17.82	5.86	0.14	1.87	4.96	3.34	7.66	0.40	0.04	0.56	0.25	98.52
PRAD-250	E	1 cm	59.72	0.49	18.58	2.95	0.15	0.45	2.32	4.51	8.32	0.08	0.03	0.67	0.24	98.51
PRAD-250	E	1 cm	56.68	0.52	18.63	3.91	0.15	0.78	3.39	3.65	9.29	0.13	0.02	0.68	0.26	98.09
PRAD-250	E	1 cm	59.61	0.47	18.08	2.68	0.15	0.50	2.35	4.57	8.59	0.08	0.04	0.64	0.23	98.00
PRAD-250	E	1 cm	60.81	0.37	17.97	2.25	0.13	0.37	1.89	4.43	8.81	0.06	0.07	0.56	0.22	97.95
PRAD-250	E	1 cm	58.48	0.47	17.85	3.67	0.12	0.93	3.06	3.45	8.84	0.21	0.04	0.43	0.18	97.71

Name	Microprobe	Resolution	SiO_2	TiO_2	Al_2O_3	FeO	MnO	MgO	CaO	Na_2O	K_2O	P_2O_5	S	Cl	F	Total
PRAD-250	E	1 cm	59.40	0.40	17.43	3.05	0.13	0.50	2.26	4.39	7.77	0.08	0.02	0.52	0.13	96.08
PRAD-261	E	1 cm	60.67	0.49	17.82	3.16	0.16	0.44	2.22	4.66	8.59	0.07	0.02	0.65	0.26	99.21
PRAD-261	E	1 cm	56.65	0.61	18.22	4.42	0.13	1.32	4.15	3.82	8.09	0.29	0.06	0.50	0.24	98.50
PRAD-261	E	1 cm	60.37	0.46	17.99	2.71	0.15	0.36	2.06	4.68	8.59	0.06	0.11	0.63	0.23	98.39
PRAD-261	E	1 cm	60.21	0.50	17.89	2.62	0.18	0.28	1.84	5.38	7.74	0.03	0.03	0.79	0.35	97.85
PRAD-261	E	1 cm	54.87	0.62	17.87	5.06	0.13	1.61	4.81	3.36	7.74	0.30	0.26	0.48	0.24	97.35
PRAD-261	E	1 cm	54.14	0.64	17.86	5.53	0.14	1.81	5.12	3.22	7.59	0.34	0.22	0.50	0.23	97.33
PRAD-261	E	1 cm	56.28	0.58	17.81	4.32	0.14	1.07	3.58	3.80	8.35	0.24	0.07	0.54	0.25	97.04
PRAD-261	E	1 cm	54.11	0.64	17.55	5.32	0.12	1.80	4.91	3.19	7.68	0.36	0.23	0.46	0.22	96.58
PRAD-261	E	1 cm	54.05	0.69	17.61	5.19	0.11	1.92	4.79	2.91	7.77	0.40	0.11	0.39	0.22	96.16
PRAD-261	E	1 cm	58.66	0.40	17.58	3.10	0.13	0.66	2.43	3.83	8.34	0.09	0.07	0.55	0.23	96.07
PRAD-261	E	1 cm	57.83	0.41	17.16	3.56	0.12	0.78	2.74	3.98	8.12	0.13	0.09	0.45	0.18	95.54
PRAD-261	E	1 cm	58.58	0.45	17.51	2.52	0.15	0.39	2.08	4.19	8.42	0.06	0.04	0.64	0.26	95.29
PRAD-267	E	1 cm	61.30	0.48	18.46	2.92	0.15	0.48	2.17	4.74	8.59	0.06	0.00	0.65	0.26	100.27
PRAD-267	E	1 cm	57.67	0.58	18.25	4.76	0.13	1.32	4.07	3.53	8.11	0.24	0.04	0.54	0.24	99.46
PRAD-267	E	1 cm	58.77	0.49	18.35	4.04	0.12	0.97	3.28	3.69	8.79	0.18	0.05	0.47	0.18	99.38
PRAD-267	E	1 cm	60.86	0.48	18.07	2.84	0.16	0.41	2.13	4.80	8.62	0.06	0.02	0.63	0.26	99.33
PRAD-267	E	1 cm	60.14	0.49	18.28	2.72	0.14	0.54	2.27	4.10	9.13	0.08	0.10	0.63	0.26	98.87
PRAD-267	E	1 cm	61.24	0.45	17.60	2.68	0.14	0.46	2.13	4.69	8.35	0.07	0.11	0.62	0.24	98.78
PRAD-267	E	1 cm	56.94	0.57	18.40	4.40	0.14	1.29	3.97	3.81	8.13	0.24	0.06	0.54	0.23	98.71
PRAD-267	E	1 cm	58.11	0.54	17.95	4.10	0.12	1.08	3.57	3.55	8.23	0.19	0.02	0.53	0.22	98.19
PRAD-267	E	1 cm	60.26	0.47	17.86	2.88	0.15	0.39	2.12	4.43	8.46	0.07	0.09	0.67	0.29	98.14
PRAD-267	E	1 cm	59.70	0.47	18.10	2.81	0.14	0.47	2.10	4.64	8.47	0.06	0.10	0.68	0.27	98.00
PRAD-267	E	1 cm	57.69	0.49	17.93	3.84	0.13	1.06	3.35	3.24	9.06	0.19	0.20	0.48	0.18	97.84
PRAD-267	E	1 cm	59.77	0.47	17.80	2.74	0.14	0.46	2.26	4.36	8.68	0.07	0.08	0.62	0.23	97.68
PRAD-267	E	1 cm	59.79	0.26	18.85	2.16	0.07	0.40	2.37	3.42	9.69	0.09	0.03	0.35	0.09	97.55
PRAD-267	E	1 cm	53.72	0.65	18.24	5.34	0.13	1.87	5.19	3.19	7.83	0.34	0.25	0.49	0.23	97.47
PRAD-267	E	1 cm	59.34	0.47	17.91	2.65	0.15	0.43	2.17	4.32	8.36	0.06	0.10	0.64	0.25	96.86
PRAD-267	E	1 cm	58.35	0.41	17.57	2.83	0.12	0.48	2.32	4.19	8.07	0.08	0.03	0.59	0.24	95.27
PRAD-268	OE	5 cm	55.39	0.63	18.12	5.44	0.15	1.63	5.08	3.27	8.13	N/A	N/A	N/A	N/A	97.85
PRAD-268	OE	5 cm	54.67	0.62	18.17	5.40	0.13	1.86	5.15	3.26	7.98	N/A	N/A	N/A	N/A	97.23
PRAD-268	OE	5 cm	54.87	0.64	18.03	5.28	0.14	1.80	5.09	3.32	7.95	N/A	N/A	N/A	N/A	97.12
PRAD-268	OE	5 cm	55.20	0.56	18.10	4.95	0.16	1.71	4.90	3.42	8.15	N/A	N/A	N/A	N/A	97.15
PRAD-268	OE	5 cm	55.11	0.62	18.10	4.86	0.13	1.52	4.56	3.33	8.20	N/A	N/A	N/A	N/A	96.41
PRAD-268	OE	5 cm	56.19	0.53	18.14	4.71	0.15	1.37	4.23	3.51	8.76	N/A	N/A	N/A	N/A	97.61
PRAD-268	OE	5 cm	55.65	0.59	18.04	4.51	0.08	1.32	4.34	3.32	8.61	N/A	N/A	N/A	N/A	96.47
PRAD-268	OE	5 cm	55.97	0.58	18.19	4.49	0.12	1.39	4.43	3.65	8.10	N/A	N/A	N/A	N/A	96.91
PRAD-268	OE	5 cm	55.45	0.57	17.84	4.20	0.11	1.12	3.66	3.69	8.37	N/A	N/A	N/A	N/A	95.00
PRAD-268	OE	5 cm	57.27	0.52	18.31	4.08	0.15	1.15	3.82	3.21	9.13	N/A	N/A	N/A	N/A	97.64
PRAD-268	OE	5 cm	56.48	0.41	18.13	4.02	0.05	1.03	3.47	3.21	9.07	N/A	N/A	N/A	N/A	95.86
PRAD-268	OE	5 cm	57.02	0.42	17.69	3.39	0.11	0.75	2.85	3.31	9.53	N/A	N/A	N/A	N/A	95.07
PRAD-268	OE	5 cm	58.83	0.45	18.24	3.21	0.14	0.61	2.62	3.94	9.43	N/A	N/A	N/A	N/A	97.47
PRAD-268	OE	5 cm	58.82	0.48	18.06	3.13	0.15	0.66	2.65	3.98	8.81	N/A	N/A	N/A	N/A	96.75
PRAD-268	OE	5 cm	58.92	0.42	18.35	2.95	0.13	0.68	2.54	3.80	9.54	N/A	N/A	N/A	N/A	97.33
PRAD-268	OE	5 cm	58.36	0.43	17.95	2.83	0.14	0.48	2.24	4.35	8.45	N/A	N/A	N/A	N/A	95.23
PRAD-268	OE	5 cm	59.19	0.47	18.09	2.80	0.12	0.51	2.26	4.25	8.71	N/A	N/A	N/A	N/A	96.39
PRAD-268	OE	5 cm	59.71	0.42	17.97	2.73	0.10	0.46	2.16	4.55	8.67	N/A	N/A	N/A	N/A	96.78
PRAD-268	OE	5 cm	59.43	0.45	18.17	2.73	0.11	0.43	2.23	4.48	8.72	N/A	N/A	N/A	N/A	96.74
PRAD-268	OE	5 cm	60.01	0.41	18.28	2.72	0.23	0.44	2.19	4.52	8.65	N/A	N/A	N/A	N/A	97.43
PRAD-268	OE	5 cm	58.72	0.45	17.60	2.70	0.10	0.46	2.15	4.08	9.06	N/A	N/A	N/A	N/A	95.31
PRAD-273	E	1 cm	60.25	0.48	18.58	2.98	0.15	0.45	2.22	4.53	8.71	0.07	0.06	0.64	0.26	98.36
PRAD-273	E	1 cm	60.24	0.47	17.93	2.92	0.15	0.42	2.26	4.72	8.84	0.06	0.08	0.66	0.29	97.96
PRAD-273	E	1 cm	59.50	0.47	18.24	3.13	0.12	0.64	2.64	3.89	9.32	0.10	0.15	0.53	0.22	97.95

Name	Microprobe	Resolution	SiO_2	TiO_2	Al_2O_3	FeO	MnO	MgO	CaO	Na_2O	K_2O	P_2O_5	S	Cl	F	Total
PRAD-273	E	1 cm	56.98	0.59	18.51	4.31	0.14	1.20	3.93	3.82	8.35	0.21	0.06	0.57	0.25	97.83
PRAD-273	E	1 cm	55.17	0.63	18.20	5.40	0.14	1.71	4.84	3.38	8.09	0.30	0.25	0.45	0.24	97.56
PRAD-273	E	1 cm	60.50	0.48	17.83	2.81	0.15	0.46	2.24	4.56	8.67	0.06	0.06	0.66	0.26	97.69
PRAD-273	E	1 cm	59.85	0.48	17.78	2.88	0.15	0.40	2.14	4.74	8.64	0.06	0.10	0.70	0.25	97.06
PRAD-273	E	1 cm	58.16	0.47	17.99	3.56	0.13	0.84	3.17	3.49	9.30	0.15	0.19	0.50	0.20	97.11
PRAD-273	E	1 cm	56.29	0.50	17.92	4.29	0.12	1.21	3.78	3.24	9.13	0.22	0.21	0.45	0.19	96.48
PRAD-273	E	1 cm	54.99	0.59	17.99	4.61	0.13	1.42	4.32	3.39	8.20	0.26	0.19	0.48	0.22	95.64
PRAD-273	E	1 cm	59.33	0.48	17.23	2.59	0.16	0.47	2.14	4.33	8.49	0.05	0.08	0.69	0.28	95.22
PRAD-273	E	1 cm	58.50	0.40	17.13	3.34	0.12	0.68	2.26	3.33	8.94	0.12	0.07	0.42	0.18	94.68
PRAD-273	E	1 cm	60.93	0.40	16.23	2.26	0.18	0.20	1.51	5.32	6.73	0.02	0.00	0.79	0.48	93.77
PRAD-273	E	1 cm	57.74	0.39	17.36	3.16	0.11	0.73	2.44	3.11	9.31	0.12	0.06	0.35	0.18	94.35
PRAD-323	E	1 cm	60.70	0.49	18.58	2.83	0.16	0.48	2.17	4.93	8.59	0.07	0.07	0.65	0.29	98.93
PRAD-323	E	1 cm	58.67	0.51	18.88	3.95	0.15	0.90	3.10	4.47	8.02	0.15	0.18	0.56	0.21	98.66
PRAD-323	E	1 cm	60.67	0.49	17.98	2.75	0.15	0.46	2.25	4.41	9.02	0.06	0.10	0.71	0.26	98.17
PRAD-323	E	1 cm	60.71	0.48	18.01	2.69	0.15	0.45	2.23	4.82	8.71	0.07	0.08	0.65	0.23	98.25
PRAD-323	E	1 cm	56.90	0.61	18.11	4.60	0.14	1.37	4.05	3.63	7.93	0.26	0.07	0.52	0.23	97.33
PRAD-323	E	1 cm	56.20	0.58	18.18	4.61	0.13	1.49	4.42	3.21	8.40	0.29	0.21	0.45	0.22	97.23
PRAD-323	E	1 cm	59.81	0.46	17.72	2.81	0.15	0.45	2.15	4.60	8.23	0.07	0.02	0.65	0.33	96.39
PRAD-323	E	1 cm	59.29	0.48	17.45	2.84	0.15	0.44	2.16	4.39	8.40	0.06	0.08	0.69	0.26	95.60
PRAD-323	E	1 cm	57.80	0.41	17.57	3.23	0.15	0.58	2.12	4.09	8.64	0.11	0.03	0.50	0.28	94.58
PRAD-324	OE	5 cm	54.57	0.62	18.32	5.16	0.15	1.73	4.99	3.29	8.09	N/A	N/A	N/A	N/A	96.92
PRAD-324	OE	5 cm	56.72	0.55	18.64	4.91	0.11	1.37	4.10	3.78	8.43	N/A	N/A	N/A	N/A	98.61
PRAD-324	OE	5 cm	56.79	0.59	18.89	4.86	0.10	1.50	4.44	3.35	8.19	N/A	N/A	N/A	N/A	98.71
PRAD-324	OE	5 cm	57.46	0.59	18.84	4.60	0.13	1.37	4.11	3.27	8.50	N/A	N/A	N/A	N/A	98.87
PRAD-324	OE	5 cm	56.59	0.56	18.37	4.41	0.11	1.26	4.03	3.71	8.24	N/A	N/A	N/A	N/A	97.28
PRAD-324	OE	5 cm	57.57	0.59	18.77	4.41	0.14	1.31	4.01	3.66	8.26	N/A	N/A	N/A	N/A	98.72
PRAD-324	OE	5 cm	56.45	0.56	19.80	4.35	0.14	1.20	3.99	3.72	8.21	N/A	N/A	N/A	N/A	98.42
PRAD-324	OE	5 cm	59.12	0.54	19.32	4.34	0.12	1.16	3.83	3.89	8.31	N/A	N/A	N/A	N/A	100.63
PRAD-324	OE	5 cm	55.86	0.56	18.28	4.30	0.11	1.21	3.91	3.72	8.21	N/A	N/A	N/A	N/A	96.16
PRAD-324	OE	5 cm	57.52	0.50	18.59	4.11	0.10	1.13	3.71	3.73	8.42	N/A	N/A	N/A	N/A	97.81
PRAD-324	OE	5 cm	58.80	0.49	18.78	3.95	0.15	1.01	3.31	3.62	8.82	N/A	N/A	N/A	N/A	98.92
PRAD-324	OE	5 cm	59.02	0.50	18.74	3.94	0.13	0.91	3.23	3.99	8.46	N/A	N/A	N/A	N/A	98.93
PRAD-324	OE	5 cm	60.75	0.46	18.88	3.91	0.17	0.88	3.01	3.78	8.66	N/A	N/A	N/A	N/A	100.50
PRAD-324	OE	5 cm	59.99	0.44	18.42	3.60	0.05	0.89	2.89	3.48	8.84	N/A	N/A	N/A	N/A	98.59
PRAD-324	OE	5 cm	58.32	0.47	18.45	3.53	0.11	0.99	3.22	4.16	8.27	N/A	N/A	N/A	N/A	97.52
PRAD-324	OE	5 cm	58.63	0.42	18.57	3.43	0.05	0.76	2.74	3.52	9.42	N/A	N/A	N/A	N/A	97.54
PRAD-324	OE	5 cm	57.96	0.45	18.38	3.42	0.17	0.83	2.96	3.50	8.29	N/A	N/A	N/A	N/A	95.95
PRAD-324	OE	5 cm	58.26	0.49	18.34	3.32	0.11	0.72	2.91	3.65	9.00	N/A	N/A	N/A	N/A	96.79
PRAD-324	OE	5 cm	58.67	0.34	18.23	3.27	0.11	0.79	2.53	2.85	9.53	N/A	N/A	N/A	N/A	96.33
PRAD-324	OE	5 cm	60.31	0.49	18.80	3.19	0.13	0.71	2.69	4.19	8.57	N/A	N/A	N/A	N/A	99.07
PRAD-324	OE	5 cm	57.81	0.44	18.17	2.98	0.07	0.60	2.52	3.88	8.95	N/A	N/A	N/A	N/A	95.40
PRAD-324	OE	5 cm	61.52	0.45	18.55	2.87	0.10	0.45	2.20	4.43	8.60	N/A	N/A	N/A	N/A	99.16
PRAD-324	OE	5 cm	60.15	0.35	17.89	2.83	0.10	0.50	2.13	3.60	8.35	N/A	N/A	N/A	N/A	95.89
PRAD-324	OE	5 cm	60.07	0.45	18.44	2.79	0.16	0.41	2.25	4.47	8.70	N/A	N/A	N/A	N/A	97.73
PRAD-324	OE	5 cm	60.56	0.34	17.98	2.78	0.11	0.47	2.14	3.75	8.53	N/A	N/A	N/A	N/A	96.66
PRAD-324	OE	5 cm	61.37	0.43	18.66	2.78	0.15	0.44	2.16	4.47	8.53	N/A	N/A	N/A	N/A	99.00
PRAD-324	OE	5 cm	61.31	0.41	18.64	2.78	0.15	0.49	2.18	4.39	8.71	N/A	N/A	N/A	N/A	99.05
PRAD-324	OE	5 cm	60.16	0.40	18.50	2.77	0.11	0.47	2.13	3.02	8.31	N/A	N/A	N/A	N/A	95.86
PRAD-324	OE	5 cm	60.17	0.37	18.31	2.76	0.16	0.43	2.14	4.37	8.44	N/A	N/A	N/A	N/A	97.14
PRAD-324	OE	5 cm	62.11	0.44	18.81	2.75	0.15	0.43	2.14	4.57	8.58	N/A	N/A	N/A	N/A	99.97
PRAD-324	OE	5 cm	58.88	0.43	18.08	2.75	0.13	0.46	2.18	4.39	8.77	N/A	N/A	N/A	N/A	96.05
PRAD-324	OE	5 cm	60.25	0.41	18.26	2.73	0.08	0.46	2.27	4.69	8.68	N/A	N/A	N/A	N/A	97.81
PRAD-324	OE	5 cm	62.03	0.46	18.82	2.73	0.15	0.42	2.17	4.53	8.70	N/A	N/A	N/A	N/A	100.01

Name	Microprobe	Resolution	SiO_2	TiO_2	Al_2O_3	FeO	MnO	MgO	CaO	Na_2O	K_2O	P_2O_5	S	Cl	F	Total
PRAD-324	OE	5 cm	57.91	0.43	18.18	2.71	0.16	0.48	2.25	4.47	8.60	N/A	N/A	N/A	N/A	95.18
PRAD-324	OE	5 cm	59.16	0.45	18.23	2.70	0.12	0.45	2.18	4.37	8.89	N/A	N/A	N/A	N/A	96.54
PRAD-324	OE	5 cm	59.58	0.34	17.76	2.68	0.12	0.48	2.18	3.79	8.34	N/A	N/A	N/A	N/A	95.25
PRAD-324	OE	5 cm	59.66	0.40	18.07	2.66	0.11	0.44	2.09	4.44	8.57	N/A	N/A	N/A	N/A	96.44
PRAD-324	OE	5 cm	59.19	0.37	18.30	2.65	0.14	0.48	2.11	3.90	8.52	N/A	N/A	N/A	N/A	95.66
PRAD-324	OE	5 cm	58.69	0.41	18.07	2.62	0.13	0.42	2.13	4.36	8.66	N/A	N/A	N/A	N/A	95.49
PRAD-324	OE	5 cm	58.80	0.38	17.94	2.62	0.12	0.40	2.08	4.46	8.34	N/A	N/A	N/A	N/A	95.13
PRAD-324	OE	5 cm	59.03	0.41	18.22	2.60	0.13	0.45	2.05	3.83	8.41	N/A	N/A	N/A	N/A	95.13
PRAD-324	OE	5 cm	60.72	0.35	17.83	2.51	0.17	0.36	1.88	4.07	7.78	N/A	N/A	N/A	N/A	95.67
PRAD-324	OE	5 cm	60.21	0.40	18.43	2.50	0.11	0.41	2.04	4.28	8.53	N/A	N/A	N/A	N/A	96.92
PRAD-324	OE	5 cm	62.50	0.41	18.70	2.47	0.14	0.35	1.99	4.78	8.43	N/A	N/A	N/A	N/A	99.76
PRAD-324	OE	5 cm	60.32	0.41	18.00	2.39	0.18	0.28	1.79	5.04	7.45	N/A	N/A	N/A	N/A	95.86
PRAD-324	OE	5 cm	61.67	0.38	17.72	2.38	0.18	0.22	1.41	5.10	6.46	N/A	N/A	N/A	N/A	95.52
PRAD-324	OE	5 cm	60.06	0.25	19.15	1.86	0.07	0.31	2.74	3.24	9.24	N/A	N/A	N/A	N/A	96.92
PRAD-329	E	1 cm	59.39	0.47	18.78	3.27	0.13	0.72	2.85	3.64	9.05	0.10	0.10	0.48	0.20	99.18
PRAD-329	E	1 cm	60.58	0.48	18.25	2.80	0.15	0.44	2.13	4.43	8.77	0.06	0.03	0.65	0.25	99.02
PRAD-329	E	1 cm	60.56	0.49	17.96	2.82	0.15	0.47	2.23	4.51	8.49	0.06	0.07	0.65	0.28	98.73
PRAD-329	E	1 cm	59.99	0.48	18.11	2.73	0.15	0.44	2.11	4.32	8.88	0.07	0.10	0.70	0.25	98.32
PRAD-329	E	1 cm	60.66	0.45	17.92	2.72	0.15	0.38	1.99	4.71	8.35	0.04	0.02	0.61	0.25	98.25
PRAD-329	E	1 cm	57.47	0.47	18.63	3.63	0.12	0.92	3.32	3.32	9.16	0.17	0.20	0.47	0.23	98.10
PRAD-329	E	1 cm	60.91	0.41	17.38	2.63	0.15	0.34	1.96	4.20	8.70	0.04	0.03	0.77	0.23	97.74
PRAD-329	E	1 cm	62.81	0.39	16.88	2.26	0.17	0.19	1.47	5.56	6.59	0.02	0.00	0.77	0.41	97.52
PRAD-329	E	1 cm	60.34	0.44	17.89	2.54	0.14	0.42	1.98	4.29	8.50	0.06	0.04	0.61	0.24	97.48
PRAD-329	E	1 cm	57.85	0.54	17.99	3.42	0.15	0.83	3.03	4.56	7.11	0.16	0.02	0.59	0.27	96.52
PRAD-329	E	1 cm	59.47	0.44	17.43	2.52	0.15	0.36	1.94	4.37	8.20	0.06	0.07	0.61	0.25	95.87
PRAD-329	E	1 cm	56.85	0.48	17.71	3.86	0.13	0.83	3.11	3.36	8.37	0.14	0.02	0.57	0.22	95.65
PRAD-329	E	1 cm	61.50	0.39	16.43	2.37	0.17	0.16	1.51	4.98	6.74	0.02	0.00	0.79	0.41	95.47
PRAD-336	E	1 cm	57.42	0.60	18.83	4.44	0.14	1.17	3.84	3.75	8.28	0.23	0.10	0.55	0.24	99.57
PRAD-336	E	1 cm	60.36	0.48	18.77	2.88	0.14	0.47	2.22	4.26	8.75	0.06	0.09	0.66	0.25	99.39
PRAD-336	E	1 cm	60.31	0.49	18.32	2.91	0.15	0.45	2.16	4.65	8.74	0.07	0.07	0.70	0.24	99.25
PRAD-336	E	1 cm	59.15	0.52	18.08	3.69	0.14	0.79	2.97	4.14	8.49	0.15	0.09	0.58	0.26	99.06
PRAD-336	E	1 cm	59.71	0.50	18.10	3.06	0.15	0.50	2.37	4.47	8.64	0.09	0.08	0.67	0.27	98.61
PRAD-336	E	1 cm	56.28	0.59	18.46	4.61	0.14	1.28	3.98	3.57	8.36	0.26	0.10	0.52	0.25	98.41
PRAD-336	E	1 cm	58.65	0.47	18.18	3.46	0.15	0.71	2.81	3.83	9.01	0.10	0.15	0.59	0.22	98.33
PRAD-336	E	1 cm	59.70	0.48	18.03	2.76	0.16	0.47	2.20	4.65	8.32	0.06	0.10	0.67	0.27	97.87
PRAD-336	E	1 cm	54.11	0.61	18.28	5.46	0.13	1.56	4.63	3.18	8.18	0.27	0.28	0.47	0.21	97.39
PRAD-336	E	1 cm	59.18	0.48	17.54	2.74	0.15	0.42	2.23	4.36	8.56	0.06	0.10	0.67	0.26	96.74
PRAD-336	E	1 cm	57.93	0.42	17.89	3.48	0.12	0.74	2.57	3.30	9.15	0.16	0.03	0.40	0.22	96.40
PRAD-336	E	1 cm	58.97	0.46	17.59	2.66	0.16	0.42	2.09	4.44	8.47	0.06	0.01	0.66	0.26	96.25
PRAD-336	E	1 cm	58.20	0.46	17.50	2.80	0.15	0.46	2.14	4.04	8.84	0.08	0.09	0.64	0.23	95.63
PRAD-336	E	1 cm	59.10	0.47	17.07	2.52	0.16	0.38	2.19	4.18	8.13	0.05	0.09	0.69	0.29	95.30
PRAD-404	OE	5 cm	58.42	0.46	18.39	3.18	0.15	0.68	2.63	3.48	9.52	N/A	N/A	N/A	N/A	96.91
PRAD-404	OE	5 cm	60.81	0.38	18.53	3.12	0.08	0.66	2.50	3.46	9.29	N/A	N/A	N/A	N/A	98.82
PRAD-404	OE	5 cm	58.16	0.37	17.96	3.07	0.12	0.74	2.40	2.84	9.35	N/A	N/A	N/A	N/A	95.01
PRAD-404	OE	5 cm	58.11	0.43	18.45	3.06	0.14	0.70	2.53	3.56	9.78	N/A	N/A	N/A	N/A	96.76
PRAD-404	OE	5 cm	59.83	0.40	18.60	2.93	0.12	0.59	2.45	3.85	9.32	N/A	N/A	N/A	N/A	98.08
PRAD-404	OE	5 cm	58.56	0.39	17.68	2.93	0.12	0.54	2.35	4.42	8.09	N/A	N/A	N/A	N/A	95.07
PRAD-404	OE	5 cm	60.80	0.45	18.54	2.82	0.13	0.50	2.29	4.29	8.74	N/A	N/A	N/A	N/A	98.56
PRAD-404	OE	5 cm	62.56	0.41	18.86	2.78	0.16	0.48	2.33	4.38	8.68	N/A	N/A	N/A	N/A	100.64
PRAD-404	OE	5 cm	58.73	0.42	18.10	2.77	0.12	0.48	2.12	4.06	8.92	N/A	N/A	N/A	N/A	95.70
PRAD-404	OE	5 cm	61.31	0.42	18.80	2.76	0.16	0.43	2.10	4.57	8.68	N/A	N/A	N/A	N/A	99.23
PRAD-404	OE	5 cm	61.82	0.39	18.67	2.75	0.13	0.45	2.11	4.55	8.72	N/A	N/A	N/A	N/A	99.60
PRAD-404	OE	5 cm	60.45	0.41	18.42	2.74	0.10	0.45	2.24	4.43	9.00	N/A	N/A	N/A	N/A	98.23

Name	Microprobe	Resolution	SiO_2	TiO_2	Al_2O_3	FeO	MnO	MgO	CaO	Na_2O	K_2O	P_2O_5	S	Cl	F	Total
PRAD-404	OE	5 cm	61.03	0.45	18.69	2.71	0.11	0.45	2.14	4.50	8.66	N/A	N/A	N/A	N/A	98.72
PRAD-404	OE	5 cm	60.10	0.42	18.36	2.69	0.14	0.48	2.16	4.20	8.62	N/A	N/A	N/A	N/A	97.17
PRAD-404	OE	5 cm	59.97	0.34	17.71	2.69	0.15	0.39	1.99	3.86	7.93	N/A	N/A	N/A	N/A	95.02
PRAD-404	OE	5 cm	60.73	0.42	18.68	2.66	0.14	0.43	2.17	4.40	8.59	N/A	N/A	N/A	N/A	98.22
PRAD-404	OE	5 cm	58.35	0.41	18.46	2.66	0.15	0.41	1.92	4.43	8.79	N/A	N/A	N/A	N/A	95.59
PRAD-404	OE	5 cm	59.72	0.34	17.68	2.64	0.14	0.39	1.91	4.17	8.71	N/A	N/A	N/A	N/A	95.68
PRAD-404	OE	5 cm	60.72	0.39	18.51	2.61	0.13	0.44	2.02	4.28	8.57	N/A	N/A	N/A	N/A	97.66
PRAD-404	OE	5 cm	60.27	0.43	18.45	2.57	0.15	0.43	2.06	4.24	8.41	N/A	N/A	N/A	N/A	97.00
PRAD-404	OE	5 cm	61.57	0.40	18.71	2.49	0.14	0.42	2.14	4.61	8.55	N/A	N/A	N/A	N/A	99.02
PRAD-404	OE	5 cm	60.92	0.42	18.37	2.47	0.16	0.28	1.90	5.22	7.86	N/A	N/A	N/A	N/A	97.61
PRAD-404	OE	5 cm	61.09	0.35	18.57	2.36	0.04	0.38	2.25	3.45	9.02	N/A	N/A	N/A	N/A	97.49
PRAD-404	OE	5 cm	59.81	0.36	17.89	2.25	0.13	0.29	1.84	4.93	7.91	N/A	N/A	N/A	N/A	95.38
PRAD-480	OE	5 cm	57.22	0.61	18.75	4.69	0.15	1.38	4.15	3.87	8.08	N/A	N/A	N/A	N/A	98.90
PRAD-480	OE	5 cm	57.41	0.58	18.95	4.50	0.15	1.27	4.01	3.72	8.16	N/A	N/A	N/A	N/A	98.75
PRAD-480	OE	5 cm	57.90	0.56	18.92	4.49	0.14	1.29	3.95	3.62	8.38	N/A	N/A	N/A	N/A	99.24
PRAD-480	OE	5 cm	56.27	0.47	18.37	4.32	0.18	1.21	3.78	3.70	8.30	N/A	N/A	N/A	N/A	96.60
PRAD-480	OE	5 cm	60.54	0.39	18.58	3.44	0.13	0.64	2.66	3.88	8.89	N/A	N/A	N/A	N/A	99.15
PRAD-480	OE	5 cm	58.94	0.40	17.91	3.40	0.13	0.70	2.51	3.08	8.98	N/A	N/A	N/A	N/A	96.05
PRAD-480	OE	5 cm	60.50	0.36	18.70	3.38	0.05	0.77	2.58	3.21	9.84	N/A	N/A	N/A	N/A	99.39
PRAD-480	OE	5 cm	59.41	0.40	18.53	3.37	0.14	0.72	2.49	3.36	9.76	N/A	N/A	N/A	N/A	98.18
PRAD-480	OE	5 cm	60.19	0.43	18.96	3.36	0.10	0.70	2.68	3.95	9.09	N/A	N/A	N/A	N/A	99.47
PRAD-480	OE	5 cm	60.52	0.40	18.78	3.29	0.11	0.73	2.58	3.25	9.99	N/A	N/A	N/A	N/A	99.65
PRAD-480	OE	5 cm	58.79	0.38	18.29	3.24	0.11	0.74	2.57	3.26	9.89	N/A	N/A	N/A	N/A	97.25
PRAD-480	OE	5 cm	58.90	0.48	18.40	3.21	0.16	0.69	2.75	3.87	8.50	N/A	N/A	N/A	N/A	96.94
PRAD-480	OE	5 cm	59.53	0.42	18.55	3.16	0.11	0.65	2.47	3.75	9.23	N/A	N/A	N/A	N/A	97.87
PRAD-480	OE	5 cm	59.19	0.45	18.27	3.11	0.05	0.55	2.47	3.58	9.80	N/A	N/A	N/A	N/A	97.45
PRAD-480	OE	5 cm	59.37	0.37	17.87	3.07	0.10	0.64	2.40	3.47	8.61	N/A	N/A	N/A	N/A	95.89
PRAD-480	OE	5 cm	59.48	0.38	17.87	3.04	0.12	0.63	2.37	3.37	8.95	N/A	N/A	N/A	N/A	96.22
PRAD-480	OE	5 cm	59.61	0.41	18.40	3.03	0.10	0.52	2.54	3.57	9.92	N/A	N/A	N/A	N/A	98.08
PRAD-480	OE	5 cm	60.46	0.41	18.95	3.08	0.10	0.64	2.46	3.95	9.28	N/A	N/A	N/A	N/A	99.32
PRAD-480	OE	5 cm	59.19	0.40	18.32	3.07	0.15	0.62	2.57	4.16	8.97	N/A	N/A	N/A	N/A	97.44
PRAD-480	OE	5 cm	58.83	0.39	18.45	3.02	0.15	0.61	2.57	3.94	9.58	N/A	N/A	N/A	N/A	97.54
PRAD-480	OE	5 cm	59.14	0.36	17.93	2.92	0.20	0.46	2.25	4.10	8.42	N/A	N/A	N/A	N/A	95.78
PRAD-480	OE	5 cm	61.79	0.44	18.89	2.88	0.13	0.48	2.27	4.42	8.79	N/A	N/A	N/A	N/A	100.10
PRAD-480	OE	5 cm	59.12	0.40	18.01	2.87	0.10	0.55	2.40	3.94	8.54	N/A	N/A	N/A	N/A	95.92
PRAD-480	OE	5 cm	58.99	0.40	18.01	2.83	0.11	0.43	2.10	4.45	8.38	N/A	N/A	N/A	N/A	95.69
PRAD-480	OE	5 cm	61.12	0.42	18.72	2.82	0.12	0.44	2.15	4.46	8.59	N/A	N/A	N/A	N/A	98.84
PRAD-480	OE	5 cm	61.52	0.43	18.72	2.81	0.16	0.43	2.11	4.39	8.78	N/A	N/A	N/A	N/A	99.34
PRAD-480	OE	5 cm	60.70	0.40	18.57	2.80	0.16	0.45	2.16	4.43	8.66	N/A	N/A	N/A	N/A	98.34
PRAD-480	OE	5 cm	60.41	0.39	18.26	2.79	0.13	0.42	2.06	4.35	8.50	N/A	N/A	N/A	N/A	97.30
PRAD-480	OE	5 cm	59.48	0.35	17.96	2.76	0.09	0.47	2.19	3.79	8.51	N/A	N/A	N/A	N/A	95.60
PRAD-480	OE	5 cm	59.09	0.45	18.20	2.73	0.18	0.45	2.22	4.22	8.64	N/A	N/A	N/A	N/A	96.17
PRAD-480	OE	5 cm	60.63	0.46	18.49	2.73	0.12	0.40	2.05	4.50	8.66	N/A	N/A	N/A	N/A	98.05
PRAD-480	OE	5 cm	59.24	0.38	18.07	2.73	0.15	0.47	2.17	3.90	8.37	N/A	N/A	N/A	N/A	95.47
PRAD-480	OE	5 cm	60.10	0.39	18.15	2.71	0.11	0.46	2.04	4.28	8.23	N/A	N/A	N/A	N/A	96.47
PRAD-480	OE	5 cm	60.16	0.40	18.36	2.70	0.14	0.44	2.11	4.39	8.48	N/A	N/A	N/A	N/A	97.16
PRAD-480	OE	5 cm	59.19	0.40	18.15	2.68	0.15	0.41	2.14	4.50	8.79	N/A	N/A	N/A	N/A	96.40
PRAD-480	OE	5 cm	60.08	0.31	17.71	2.67	0.08	0.43	1.94	3.84	8.30	N/A	N/A	N/A	N/A	95.37
PRAD-480	OE	5 cm	59.90	0.42	18.25	2.66	0.14	0.43	2.11	4.40	8.65	N/A	N/A	N/A	N/A	96.96
PRAD-480	OE	5 cm	59.25	0.38	18.12	2.65	0.11	0.46	2.20	4.23	8.62	N/A	N/A	N/A	N/A	96.02
PRAD-480	OE	5 cm	59.54	0.42	18.32	2.65	0.09	0.42	2.13	4.22	8.43	N/A	N/A	N/A	N/A	96.21
PRAD-480	OE	5 cm	59.67	0.41	18.21	2.64	0.15	0.43	2.20	4.45	8.70	N/A	N/A	N/A	N/A	96.85
PRAD-480	OE	5 cm	60.23	0.42	18.54	2.43	0.14	0.42	2.29	4.84	8.59	N/A	N/A	N/A	N/A	97.89

Name	Microprobe	Resolution	SiO_2	TiO_2	Al_2O_3	FeO	MnO	MgO	CaO	Na_2O	K_2O	P_2O_5	S	Cl	F	Total
PRAD-480	OE	5 cm	60.37	0.43	18.27	2.42	0.19	0.32	1.79	4.82	7.58	N/A	N/A	N/A	N/A	96.18
PRAD-480	OE	5 cm	59.25	0.36	17.91	2.39	0.14	0.38	1.96	4.38	8.31	N/A	N/A	N/A	N/A	95.08
PRAD-650	OE	5 cm	58.84	0.44	17.97	2.81	0.30	0.29	1.60	6.05	6.52	N/A	N/A	N/A	N/A	94.81
PRAD-650	OE	5 cm	58.76	0.43	18.34	2.96	0.26	0.31	1.54	7.18	6.69	N/A	N/A	N/A	N/A	96.48
PRAD-650	OE	5 cm	59.87	0.43	18.98	2.99	0.27	0.27	1.68	6.87	6.81	N/A	N/A	N/A	N/A	98.16
PRAD-650	OE	5 cm	58.63	0.42	18.43	3.46	0.15	0.69	2.42	5.08	7.81	N/A	N/A	N/A	N/A	97.09
PRAD-650	OE	5 cm	57.53	0.41	18.41	3.53	0.15	0.87	2.78	4.34	8.29	N/A	N/A	N/A	N/A	96.32
PRAD-650	OE	5 cm	58.35	0.39	18.67	3.60	0.16	0.81	2.77	4.84	8.49	N/A	N/A	N/A	N/A	98.08
PRAD-650	OE	5 cm	56.34	0.56	18.26	3.65	0.15	0.95	3.24	4.32	7.40	N/A	N/A	N/A	N/A	94.87
PRAD-650	OE	5 cm	57.42	0.42	18.27	3.66	0.12	0.80	2.82	4.29	8.10	N/A	N/A	N/A	N/A	95.90
PRAD-650	OE	5 cm	57.80	0.58	18.39	3.71	0.15	0.86	3.19	4.39	7.73	N/A	N/A	N/A	N/A	96.79
PRAD-650	OE	5 cm	58.81	0.42	18.93	3.72	0.12	0.87	3.01	4.54	8.31	N/A	N/A	N/A	N/A	98.74
PRAD-650	OE	5 cm	56.83	0.56	18.31	3.74	0.13	0.92	3.26	4.43	7.74	N/A	N/A	N/A	N/A	95.90
PRAD-650	OE	5 cm	58.20	0.50	18.72	3.76	0.10	0.88	3.14	4.67	7.95	N/A	N/A	N/A	N/A	97.92
PRAD-650	OE	5 cm	56.68	0.57	18.03	3.80	0.12	0.95	3.36	4.24	7.55	N/A	N/A	N/A	N/A	95.30
PRAD-650	OE	5 cm	57.45	0.55	18.46	3.83	0.16	0.96	3.40	4.35	7.75	N/A	N/A	N/A	N/A	96.90
PRAD-650	OE	5 cm	56.18	0.60	18.24	3.90	0.15	1.02	3.58	4.15	7.55	N/A	N/A	N/A	N/A	95.36
PRAD-650	OE	5 cm	57.57	0.61	18.69	4.03	0.09	1.06	3.64	4.31	7.79	N/A	N/A	N/A	N/A	97.78
PRAD-650	OE	5 cm	57.19	0.64	18.46	4.03	0.16	0.99	3.63	4.37	7.54	N/A	N/A	N/A	N/A	97.00
PRAD-650	OE	5 cm	57.87	0.59	18.67	4.03	0.12	1.03	3.53	4.35	7.72	N/A	N/A	N/A	N/A	97.92
PRAD-650	OE	5 cm	56.55	0.40	18.09	4.11	0.16	0.96	2.88	4.40	7.76	N/A	N/A	N/A	N/A	95.28
PRAD-650	OE	5 cm	57.55	0.63	18.73	4.15	0.11	1.02	3.50	4.41	7.73	N/A	N/A	N/A	N/A	97.83
PRAD-784	OE	5 cm	58.94	0.45	18.43	2.76	0.25	0.30	1.57	6.28	6.71	N/A	N/A	N/A	N/A	95.69
PRAD-784	OE	5 cm	58.44	0.46	19.22	2.97	0.21	0.30	1.63	6.53	6.80	N/A	N/A	N/A	N/A	96.55
PRAD-784	OE	5 cm	59.11	0.41	19.30	3.03	0.26	0.27	1.72	6.99	6.72	N/A	N/A	N/A	N/A	97.81
PRAD-784	OE	5 cm	58.13	0.41	18.62	2.79	0.14	0.35	1.81	4.89	8.55	N/A	N/A	N/A	N/A	95.69
PRAD-784	OE	5 cm	57.80	0.39	18.87	3.42	0.18	0.77	2.75	4.29	8.59	N/A	N/A	N/A	N/A	97.06
PRAD-784	OE	5 cm	58.39	0.46	19.09	3.53	0.15	0.83	2.94	4.69	8.53	N/A	N/A	N/A	N/A	98.60
PRAD-784	OE	5 cm	56.35	0.41	18.28	3.57	0.15	0.98	3.26	4.20	7.76	N/A	N/A	N/A	N/A	94.95
PRAD-784	OE	5 cm	57.76	0.43	18.91	3.58	0.14	0.81	2.97	4.50	8.69	N/A	N/A	N/A	N/A	97.78
PRAD-784	OE	5 cm	58.17	0.45	18.80	3.60	0.12	0.80	2.85	4.38	8.47	N/A	N/A	N/A	N/A	97.65
PRAD-784	OE	5 cm	57.92	0.40	18.95	3.60	0.13	0.83	3.07	4.38	8.77	N/A	N/A	N/A	N/A	98.05
PRAD-784	OE	5 cm	55.69	0.40	18.44	3.60	0.12	0.80	2.84	4.32	8.17	N/A	N/A	N/A	N/A	94.38
PRAD-784	OE	5 cm	57.67	0.43	19.04	3.62	0.13	0.81	2.88	4.45	8.55	N/A	N/A	N/A	N/A	97.57
PRAD-784	OE	5 cm	57.91	0.42	18.97	3.63	0.14	0.85	2.87	4.58	8.47	N/A	N/A	N/A	N/A	97.82
PRAD-784	OE	5 cm	58.82	0.40	19.26	3.64	0.14	0.81	2.89	4.56	8.51	N/A	N/A	N/A	N/A	99.02
PRAD-784	OE	5 cm	57.83	0.40	18.98	3.68	0.15	0.98	3.28	4.51	8.13	N/A	N/A	N/A	N/A	97.92
PRAD-784	OE	5 cm	58.33	0.42	18.90	3.71	0.12	0.85	2.91	4.55	8.59	N/A	N/A	N/A	N/A	98.38
PRAD-784	OE	5 cm	58.38	0.44	19.11	3.89	0.13	0.98	3.21	4.65	8.13	N/A	N/A	N/A	N/A	98.92
PRAD-784	OE	5 cm	58.08	0.45	18.97	3.93	0.13	1.05	3.44	4.63	8.11	N/A	N/A	N/A	N/A	98.79
PRAD-784	E	1 cm	57.37	0.45	19.19	3.23	0.16	0.87	2.98	4.85	8.73	0.14	0.09	0.67	0.23	98.96
PRAD-784	E	1 cm	57.58	0.45	18.29	3.63	0.15	0.92	2.92	4.45	8.24	0.16	0.06	0.66	0.21	97.72
PRAD-784	E	1 cm	56.94	0.43	18.22	3.78	0.15	0.78	3.01	4.69	8.04	0.13	0.05	0.67	0.19	97.08
PRAD-784	E	1 cm	56.81	0.47	17.74	3.99	0.16	1.03	3.29	4.59	7.70	0.14	0.05	0.63	0.21	96.82
PRAD-784	E	1 cm	55.98	0.44	18.36	3.88	0.16	0.77	3.05	4.36	8.40	0.13	0.05	0.66	0.19	96.44
PRAD-784	E	1 cm	56.20	0.43	18.46	3.72	0.15	0.83	2.91	4.27	8.14	0.12	0.05	0.65	0.22	96.15
PRAD-784	E	1 cm	56.05	0.44	18.63	3.71	0.14	0.74	2.86	4.52	8.00	0.13	0.04	0.63	0.20	96.08
PRAD-784	E	1 cm	56.03	0.61	18.10	3.87	0.15	0.91	3.26	4.33	7.63	0.17	0.07	0.48	0.21	95.81
PRAD-784	E	1 cm	61.11	0.47	16.99	2.27	0.13	0.37	1.96	4.15	7.42	0.05	0.10	0.50	0.15	95.65
PRAD-784	E	1 cm	55.36	0.55	18.73	2.48	0.16	0.38	2.32	4.91	8.67	0.06	0.13	0.56	0.26	94.57
PRAD-784	E	1 cm	54.84	0.45	17.92	3.70	0.15	0.91	2.96	4.59	7.92	0.14	0.06	0.67	0.22	94.53
PRAD-784	E	1 cm	55.32	0.58	17.80	3.66	0.13	0.89	3.26	4.31	7.32	0.16	0.06	0.49	0.19	94.17
PRAD-789	E	1 cm	59.99	0.41	18.13	3.08	0.12	0.78	2.82	3.72	8.70	0.13	0.06	0.45	0.17	98.57

Name	Microprobe	Resolution	SiO_2	TiO_2	Al_2O_3	FeO	MnO	MgO	CaO	Na_2O	K_2O	P_2O_5	S	Cl	F	Total
PRAD-789	E	1 cm	59.55	0.45	18.21	3.73	0.10	0.88	3.14	3.65	8.66	0.14	0.06	0.46	0.16	99.19
PRAD-789	E	1 cm	58.75	0.45	17.11	2.60	0.14	0.50	2.15	4.23	8.61	0.06	0.11	0.70	0.27	95.68
PRAD-789	E	1 cm	57.22	0.45	18.37	3.85	0.14	0.77	2.95	4.32	7.91	0.13	0.04	0.65	0.19	97.00
PRAD-837	E	1 cm	59.60	0.49	18.81	2.81	0.29	0.27	1.70	7.25	6.85	0.03	0.01	1.00	0.64	99.75
PRAD-837	E	1 cm	57.40	0.48	18.79	3.79	0.16	1.04	3.51	4.43	8.58	0.15	0.05	0.65	0.21	99.24
PRAD-837	E	1 cm	57.24	0.49	18.69	3.75	0.16	0.91	3.18	4.77	8.35	0.14	0.08	0.69	0.24	98.68
PRAD-837	E	1 cm	57.66	0.44	18.95	3.47	0.16	0.82	2.90	4.57	8.40	0.13	0.06	0.66	0.19	98.41
PRAD-837	E	1 cm	56.69	0.66	18.89	4.03	0.16	1.10	3.86	4.34	7.61	0.19	0.06	0.44	0.22	98.25
PRAD-837	E	1 cm	56.54	0.47	18.86	3.77	0.17	0.93	3.11	4.68	8.56	0.13	0.07	0.68	0.19	98.15
PRAD-837	E	1 cm	57.53	0.45	18.53	3.65	0.15	0.88	2.91	4.62	8.16	0.14	0.05	0.65	0.20	97.92
PRAD-837	E	1 cm	56.77	0.46	19.11	3.69	0.15	0.84	3.07	4.38	8.25	0.14	0.07	0.67	0.19	97.78
PRAD-837	E	1 cm	57.53	0.61	18.26	3.54	0.16	0.93	3.77	4.20	7.70	0.17	0.08	0.47	0.22	97.63
PRAD-837	E	1 cm	56.68	0.45	18.91	3.61	0.15	0.76	2.91	4.34	8.62	0.14	0.04	0.70	0.26	97.57
PRAD-837	E	1 cm	56.43	0.44	18.53	3.50	0.15	0.86	2.87	4.53	8.67	0.14	0.06	0.68	0.25	97.12
PRAD-837	E	1 cm	58.25	0.51	17.71	3.12	0.36	0.33	1.69	6.81	6.14	0.03	0.03	1.05	0.67	96.71
PRAD-837	E	1 cm	56.77	0.44	17.93	3.57	0.17	0.89	3.00	4.44	8.03	0.13	0.06	0.63	0.19	96.26
PRAD-837	E	1 cm	54.93	0.64	18.28	3.83	0.15	0.98	3.52	4.37	7.77	0.18	0.05	0.47	0.23	95.41
PRAD-837	E	1 cm	56.17	0.43	17.84	3.33	0.17	0.81	2.96	4.31	8.28	0.14	0.02	0.68	0.23	95.36
PRAD-837	E	1 cm	55.20	0.44	18.59	3.55	0.16	0.75	2.90	4.26	8.28	0.14	0.04	0.69	0.20	95.22
PRAD-837	E	1 cm	55.11	0.60	18.14	3.72	0.15	0.88	3.21	4.42	7.23	0.17	0.10	0.48	0.22	94.43
PRAD-837	E	1 cm	55.55	0.57	17.98	3.44	0.13	0.85	3.16	4.59	7.23	0.14	0.10	0.49	0.19	94.41
PRAD-839	E	1 cm	58.35	0.44	18.71	3.77	0.15	0.79	2.69	4.28	8.92	0.14	0.04	0.67	0.20	99.14
PRAD-839	E	1 cm	57.05	0.48	18.56	4.01	0.15	1.19	3.72	4.31	8.40	0.15	0.06	0.64	0.19	98.91
PRAD-839	E	1 cm	57.62	0.47	18.47	3.84	0.16	0.88	3.06	4.41	8.88	0.14	0.05	0.66	0.22	98.84
PRAD-839	E	1 cm	58.03	0.47	18.63	3.44	0.15	0.90	2.99	4.53	8.48	0.15	0.05	0.65	0.22	98.69
PRAD-839	E	1 cm	57.19	0.46	18.69	3.86	0.16	0.84	3.00	4.45	8.77	0.14	0.06	0.65	0.20	98.47
PRAD-839	E	1 cm	57.57	0.46	18.42	3.70	0.15	1.01	2.99	4.65	8.30	0.14	0.05	0.67	0.22	98.34
PRAD-839	E	1 cm	50.44	1.05	15.15	10.04	0.19	3.61	8.32	3.01	5.42	0.20	0.05	0.33	0.15	97.98
PRAD-839	E	1 cm	57.31	0.43	18.52	3.41	0.15	0.83	2.87	4.40	8.21	0.13	0.05	0.65	0.19	97.13
PRAD-839	E	1 cm	59.63	0.47	18.02	2.78	0.22	0.35	1.78	5.71	6.87	0.05	0.05	0.75	0.36	97.03
PRAD-839	E	1 cm	59.38	0.47	17.91	2.99	0.21	0.44	1.83	5.10	7.55	0.08	0.07	0.64	0.27	96.93
PRAD-839	E	1 cm	61.24	0.65	17.09	2.24	0.28	0.33	0.93	6.71	6.22	0.03	0.03	0.65	0.51	96.92
PRAD-839	E	1 cm	59.90	0.48	17.49	2.78	0.24	0.38	1.71	5.97	6.61	0.06	0.05	0.77	0.32	96.77
PRAD-839	E	1 cm	56.79	0.43	18.30	3.61	0.14	0.74	2.72	4.53	7.93	0.13	0.05	0.68	0.17	96.23
PRAD-839	E	1 cm	56.28	0.43	18.11	3.61	0.15	0.78	2.87	4.33	8.15	0.14	0.07	0.63	0.21	95.75
PRAD-839	E	1 cm	60.68	0.67	16.76	2.58	0.28	0.26	0.96	6.78	5.54	0.03	0.03	0.66	0.46	95.71
PRAD-839	E	1 cm	56.22	0.41	18.03	3.53	0.15	0.85	2.93	4.38	7.96	0.14	0.06	0.72	0.15	95.54
PRAD-839	E	1 cm	58.36	0.49	17.49	2.58	0.24	0.42	1.80	5.76	6.74	0.04	0.07	0.81	0.29	95.08
PRAD-841	E	1 cm	57.56	0.46	19.05	3.66	0.16	0.80	3.05	4.90	8.25	0.15	0.05	0.65	0.18	98.90
PRAD-841	E	1 cm	58.20	0.45	18.90	3.35	0.16	0.81	2.88	4.41	8.60	0.15	0.04	0.60	0.24	98.80
PRAD-841	E	1 cm	58.28	0.43	18.90	3.56	0.14	0.68	2.52	5.03	8.20	0.12	0.01	0.63	0.27	98.78
PRAD-841	E	1 cm	56.34	0.61	18.72	4.39	0.14	1.12	3.51	4.48	7.77	0.19	0.06	0.44	0.19	97.96
PRAD-841	E	1 cm	57.66	0.48	17.88	3.93	0.12	0.91	3.17	3.59	8.56	0.15	0.04	0.61	0.27	97.37
PRAD-841	E	1 cm	59.24	0.48	18.03	2.68	0.22	0.36	1.77	5.95	7.24	0.06	0.04	0.75	0.39	97.23
PRAD-841	E	1 cm	58.36	0.64	19.54	4.07	0.15	1.08	3.68	2.17	5.80	0.18	0.06	0.47	0.25	96.43
PRAD-841	E	1 cm	58.60	0.51	17.88	2.56	0.29	0.33	1.58	6.49	6.62	0.04	0.04	0.89	0.51	96.33
PRAD-841	E	1 cm	56.19	0.44	18.37	3.86	0.14	0.82	2.92	4.31	8.15	0.13	0.04	0.64	0.21	96.23
PRAD-841	E	1 cm	56.19	0.43	18.32	3.60	0.16	0.84	2.84	4.28	7.98	0.15	0.07	0.72	0.21	95.78
PRAD-841	E	1 cm	55.61	0.42	18.20	3.81	0.16	0.74	2.88	4.16	8.11	0.13	0.07	0.66	0.19	95.13
PRAD-841	E	1 cm	55.47	0.44	18.04	3.49	0.14	0.88	2.89	4.39	8.11	0.15	0.04	0.66	0.25	94.95
PRAD-841	E	1 cm	55.54	0.43	17.90	3.49	0.16	0.83	2.95	4.06	7.94	0.13	0.06	0.66	0.20	94.36
PRAD-844	E	1 cm	59.95	0.49	18.71	2.91	0.29	0.28	1.65	6.92	6.95	0.02	0.01	1.01	0.63	99.83
PRAD-844	E	1 cm	57.93	0.47	18.71	3.85	0.15	1.09	3.22	4.47	8.38	0.14	0.06	0.62	0.25	99.36

Name	Microprobe	Resolution	SiO_2	TiO_2	Al_2O_3	FeO	MnO	MgO	CaO	Na_2O	K_2O	P_2O_5	S	Cl	F	Total
PRAD-844	E	1 cm	58.14	0.47	18.75	3.60	0.14	0.86	2.88	4.65	8.36	0.14	0.08	0.66	0.26	99.00
PRAD-844	E	1 cm	59.16	0.48	18.28	2.88	0.27	0.29	1.61	6.95	6.77	0.04	0.01	1.00	0.64	98.39
PRAD-844	E	1 cm	56.99	0.61	18.49	4.37	0.14	0.99	3.53	4.47	7.49	0.16	0.08	0.45	0.22	97.99
PRAD-844	E	1 cm	57.79	0.46	18.61	3.44	0.14	0.89	3.02	4.52	8.12	0.13	0.07	0.46	0.20	97.85
PRAD-844	E	1 cm	57.53	0.43	18.16	3.69	0.15	0.72	2.67	4.86	7.92	0.13	0.03	0.62	0.26	97.17
PRAD-844	E	1 cm	57.36	0.45	18.42	3.43	0.14	0.78	2.77	4.40	7.97	0.15	0.05	0.67	0.26	96.85
PRAD-844	E	1 cm	56.16	0.45	17.99	3.57	0.16	0.77	3.17	4.42	8.30	0.15	0.05	0.67	0.20	96.06
PRAD-844	E	1 cm	55.97	0.43	18.10	3.63	0.16	0.83	2.83	4.52	7.91	0.15	0.05	0.65	0.15	95.38
PRAD-844	E	1 cm	56.18	0.44	17.64	3.58	0.15	0.85	2.79	4.40	8.21	0.13	0.06	0.66	0.20	95.29
PRAD-845	OE	5 cm	61.93	0.45	18.06	2.64	0.33	0.19	0.99	7.22	5.75	N/A	N/A	N/A	N/A	97.56
PRAD-845	OE	5 cm	59.16	0.47	19.30	3.05	0.26	0.28	1.63	6.77	6.81	N/A	N/A	N/A	N/A	97.73
PRAD-845	OE	5 cm	59.57	0.44	18.35	2.82	0.25	0.27	1.59	6.65	6.52	N/A	N/A	N/A	N/A	96.48
PRAD-845	OE	5 cm	58.02	0.40	18.86	3.57	0.14	0.93	2.99	4.76	8.13	N/A	N/A	N/A	N/A	97.79
PRAD-845	OE	5 cm	58.40	0.54	19.04	3.69	0.13	0.88	3.34	4.68	7.78	N/A	N/A	N/A	N/A	98.47
PRAD-845	OE	5 cm	58.29	0.42	18.96	3.51	0.14	0.76	2.87	4.64	8.52	N/A	N/A	N/A	N/A	98.10
PRAD-845	OE	5 cm	58.36	0.45	19.07	3.73	0.13	0.98	3.14	4.63	8.27	N/A	N/A	N/A	N/A	98.77
PRAD-845	OE	5 cm	57.12	0.42	18.78	3.43	0.12	0.79	2.91	4.54	8.21	N/A	N/A	N/A	N/A	96.32
PRAD-845	OE	5 cm	58.42	0.45	19.13	3.77	0.13	0.95	3.30	4.43	8.45	N/A	N/A	N/A	N/A	99.01
PRAD-845	OE	5 cm	56.74	0.40	18.57	3.47	0.09	0.77	2.90	4.42	8.23	N/A	N/A	N/A	N/A	95.60
PRAD-845	OE	5 cm	58.18	0.42	18.95	3.48	0.12	0.76	2.90	4.42	8.58	N/A	N/A	N/A	N/A	97.79
PRAD-845	OE	5 cm	58.10	0.41	19.02	3.57	0.14	0.85	3.05	4.38	8.27	N/A	N/A	N/A	N/A	97.79
PRAD-845	OE	5 cm	56.77	0.43	18.68	3.52	0.14	0.88	2.90	4.16	8.28	N/A	N/A	N/A	N/A	95.75
PRAD-868	E	1 cm	58.21	0.51	18.18	2.86	0.14	0.73	2.75	4.02	8.43	0.14	0.03	0.61	0.25	96.88
PRAD-868	E	1 cm	57.59	0.51	17.79	3.15	0.14	0.65	2.78	4.18	8.48	0.14	0.02	0.61	0.28	96.33
PRAD-868	E	1 cm	55.52	0.59	18.27	4.07	0.13	1.00	3.54	4.17	7.15	0.17	0.07	0.53	0.22	95.43
PRAD-873	E	1 cm	61.04	0.46	18.65	2.64	0.25	0.34	1.69	6.55	7.22	0.03	0.00	0.83	0.52	100.23
PRAD-873	E	1 cm	57.51	0.62	18.87	3.93	0.16	1.06	3.65	4.35	8.00	0.17	0.06	0.45	0.19	99.02
PRAD-873	E	1 cm	56.78	0.61	18.50	3.86	0.13	1.03	3.46	4.61	7.77	0.73	0.06	0.45	0.32	98.33
PRAD-873	E	1 cm	57.37	0.59	18.87	3.88	0.14	0.76	3.20	4.45	8.18	0.15	0.06	0.48	0.19	98.32
PRAD-873	E	1 cm	57.86	0.43	18.73	3.31	0.15	0.73	2.87	4.47	7.91	0.14	0.06	0.65	0.17	97.46
PRAD-873	E	1 cm	56.95	0.47	18.41	3.91	0.15	0.95	3.21	4.57	7.77	0.16	0.04	0.63	0.19	97.41
PRAD-873	E	1 cm	56.81	0.60	18.60	3.54	0.14	0.94	3.40	4.62	7.70	0.16	0.06	0.47	0.20	97.24
PRAD-873	E	1 cm	56.71	0.61	18.55	3.80	0.14	0.92	3.25	4.65	7.70	0.18	0.04	0.46	0.22	97.21
PRAD-873	E	1 cm	57.44	0.59	18.18	3.79	0.15	0.90	3.39	4.43	7.44	0.17	0.04	0.46	0.19	97.17
PRAD-873	E	1 cm	56.81	0.45	18.22	3.97	0.16	0.89	3.06	4.25	8.08	0.14	0.04	0.65	0.20	96.92
PRAD-873	E	1 cm	56.59	0.64	18.25	3.83	0.16	0.98	3.39	4.35	7.54	0.18	0.05	0.48	0.24	96.68
PRAD-873	E	1 cm	56.35	0.60	18.31	3.76	0.15	0.92	3.47	4.42	7.59	0.17	0.06	0.46	0.20	96.46
PRAD-873	E	1 cm	56.48	0.43	17.68	3.47	0.13	0.99	3.18	4.23	7.98	0.12	0.07	0.74	0.17	95.67
PRAD-875	OE	5 cm	62.97	0.42	17.88	2.76	0.30	0.25	0.97	7.35	5.65	N/A	N/A	N/A	N/A	98.55
PRAD-875	OE	5 cm	63.29	0.38	17.98	2.44	0.23	0.21	0.97	7.23	5.65	N/A	N/A	N/A	N/A	98.37
PRAD-875	OE	5 cm	60.24	0.45	17.99	2.91	0.28	0.31	1.61	6.48	6.28	N/A	N/A	N/A	N/A	96.54
PRAD-875	OE	5 cm	63.10	0.41	18.09	2.39	0.27	0.16	1.00	6.45	5.68	N/A	N/A	N/A	N/A	97.55
PRAD-875	OE	5 cm	58.21	0.51	18.40	3.64	0.13	0.82	3.16	4.54	7.62	N/A	N/A	N/A	N/A	97.02
PRAD-875	OE	5 cm	58.49	0.58	18.48	3.93	0.11	0.96	3.33	4.53	7.57	N/A	N/A	N/A	N/A	97.99
PRAD-875	OE	5 cm	58.76	0.60	18.52	4.01	0.15	1.07	3.65	4.50	7.54	N/A	N/A	N/A	N/A	98.79
PRAD-875	OE	5 cm	58.63	0.57	18.49	4.01	0.14	1.11	3.66	4.42	7.59	N/A	N/A	N/A	N/A	98.61
PRAD-875	OE	5 cm	58.16	0.56	18.40	3.75	0.12	0.93	3.36	3.67	7.49	N/A	N/A	N/A	N/A	96.44
PRAD-875	OE	5 cm	57.91	0.59	18.85	3.79	0.12	0.96	3.41	2.56	7.34	N/A	N/A	N/A	N/A	95.52
PRAD-1100	OE	5 cm	63.29	0.42	17.67	2.73	0.38	0.24	0.96	7.47	5.89	N/A	N/A	N/A	N/A	99.04
PRAD-1100	OE	5 cm	63.05	0.42	17.88	2.64	0.32	0.23	0.93	7.41	5.82	N/A	N/A	N/A	N/A	98.69
PRAD-1100	OE	5 cm	63.05	0.42	17.57	2.69	0.30	0.23	0.98	7.36	5.84	N/A	N/A	N/A	N/A	98.44
PRAD-1100	OE	5 cm	62.74	0.42	17.62	2.66	0.29	0.22	0.94	7.63	5.80	N/A	N/A	N/A	N/A	98.33
PRAD-1100	OE	5 cm	62.87	0.43	17.74	2.74	0.26	0.20	0.93	7.22	5.87	N/A	N/A	N/A	N/A	98.26

Name	Microprobe	Resolution	SiO_2	TiO_2	Al_2O_3	FeO	MnO	MgO	CaO	Na_2O	K_2O	P_2O_5	S	Cl	F	Total
PRAD-1100	OE	5 cm	62.44	0.46	17.70	2.83	0.33	0.22	0.95	7.48	5.76	N/A	N/A	N/A	N/A	98.16
PRAD-1100	OE	5 cm	62.51	0.43	17.68	2.70	0.32	0.21	0.96	7.49	5.83	N/A	N/A	N/A	N/A	98.14
PRAD-1100	OE	5 cm	62.59	0.45	17.61	2.76	0.32	0.21	0.96	7.29	5.90	N/A	N/A	N/A	N/A	98.08
PRAD-1100	OE	5 cm	62.69	0.44	17.67	2.78	0.28	0.20	0.98	7.25	5.71	N/A	N/A	N/A	N/A	98.00
PRAD-1100	OE	5 cm	62.67	0.43	17.60	2.65	0.30	0.20	0.94	7.38	5.79	N/A	N/A	N/A	N/A	97.96
PRAD-1100	OE	5 cm	62.77	0.45	17.58	2.66	0.32	0.23	0.96	7.18	5.73	N/A	N/A	N/A	N/A	97.88
PRAD-1100	OE	5 cm	62.60	0.44	17.67	2.70	0.35	0.22	0.95	7.21	5.71	N/A	N/A	N/A	N/A	97.86
PRAD-1100	OE	5 cm	62.62	0.44	17.59	2.66	0.30	0.24	0.93	7.29	5.76	N/A	N/A	N/A	N/A	97.82
PRAD-1100	OE	5 cm	62.60	0.43	17.56	2.67	0.34	0.21	0.95	7.19	5.86	N/A	N/A	N/A	N/A	97.82
PRAD-1100	OE	5 cm	62.59	0.43	17.78	2.60	0.27	0.21	0.97	7.22	5.72	N/A	N/A	N/A	N/A	97.79
PRAD-1100	OE	5 cm	62.50	0.42	17.68	2.73	0.31	0.24	0.95	7.27	5.66	N/A	N/A	N/A	N/A	97.75
PRAD-1100	OE	5 cm	62.56	0.44	17.77	2.65	0.33	0.21	0.95	7.01	5.79	N/A	N/A	N/A	N/A	97.70
PRAD-1100	OE	5 cm	62.67	0.44	17.59	2.68	0.31	0.22	0.93	7.12	5.73	N/A	N/A	N/A	N/A	97.68
PRAD-1100	OE	5 cm	62.33	0.44	17.76	2.65	0.29	0.22	0.97	7.27	5.74	N/A	N/A	N/A	N/A	97.67
PRAD-1100	OE	5 cm	62.22	0.41	17.48	2.69	0.29	0.21	0.88	7.66	5.83	N/A	N/A	N/A	N/A	97.67
PRAD-1100	OE	5 cm	62.03	0.44	17.42	3.00	0.32	0.22	0.90	7.52	5.80	N/A	N/A	N/A	N/A	97.65
PRAD-1100	OE	5 cm	62.28	0.48	17.58	2.67	0.33	0.22	0.91	7.32	5.77	N/A	N/A	N/A	N/A	97.58
PRAD-1100	OE	5 cm	62.36	0.45	17.62	2.64	0.35	0.21	0.98	7.16	5.73	N/A	N/A	N/A	N/A	97.50
PRAD-1100	OE	5 cm	62.53	0.42	17.57	2.58	0.31	0.21	0.96	7.13	5.76	N/A	N/A	N/A	N/A	97.46
PRAD-1100	OE	5 cm	62.12	0.43	17.71	2.58	0.30	0.22	0.95	7.24	5.66	N/A	N/A	N/A	N/A	97.18
PRAD-1100	OE	5 cm	62.40	0.43	17.49	2.58	0.33	0.19	0.94	6.97	5.80	N/A	N/A	N/A	N/A	97.13
PRAD-1100	OE	5 cm	61.57	0.42	17.50	2.66	0.31	0.22	0.94	7.10	5.59	N/A	N/A	N/A	N/A	96.30
PRAD-1100	OE	5 cm	61.15	0.44	17.27	2.67	0.31	0.21	0.96	6.85	5.82	N/A	N/A	N/A	N/A	95.68
PRAD-1100	OE	5 cm	61.13	0.42	17.17	2.72	0.31	0.21	0.95	6.94	5.72	N/A	N/A	N/A	N/A	95.58
PRAD-1104	E	1 cm	63.52	0.49	17.66	2.84	0.35	0.27	1.09	7.81	5.80	0.01	0.01	0.85	0.90	101.58
PRAD-1104	E	1 cm	63.48	0.50	17.81	2.59	0.34	0.18	1.03	8.09	5.71	0.02	0.01	0.78	0.75	101.28
PRAD-1104	E	1 cm	62.55	0.49	17.72	2.81	0.35	0.23	1.02	8.41	5.84	0.02	0.00	0.88	0.89	101.21
PRAD-1104	E	1 cm	63.09	0.49	17.59	2.74	0.35	0.20	1.01	8.16	5.84	0.02	0.01	0.84	0.87	101.19
PRAD-1104	E	1 cm	62.14	0.49	17.15	2.72	0.41	0.28	0.78	8.60	5.74	0.02	0.01	1.00	1.40	100.74
PRAD-1104	E	1 cm	62.77	0.49	17.48	2.67	0.34	0.23	1.00	8.17	5.72	0.02	0.01	0.86	0.85	100.62
PRAD-1104	E	1 cm	62.66	0.49	17.17	2.82	0.34	0.23	0.94	8.33	5.71	0.02	0.01	0.85	1.04	100.60
PRAD-1104	E	1 cm	62.65	0.50	17.52	2.59	0.36	0.24	0.98	8.03	5.78	0.02	0.01	0.84	0.96	100.47
PRAD-1104	E	1 cm	62.62	0.49	17.61	2.70	0.36	0.23	0.93	7.75	5.89	0.01	0.00	0.84	0.84	100.27
PRAD-1104	E	1 cm	62.06	0.48	17.33	2.82	0.35	0.23	0.95	7.90	6.01	0.02	0.00	0.84	0.90	99.88
PRAD-1104	E	1 cm	61.93	0.49	17.39	2.74	0.35	0.24	0.97	7.93	5.84	0.02	0.01	0.89	0.89	99.70
PRAD-1104	E	1 cm	62.33	0.48	17.24	2.70	0.35	0.23	0.97	7.69	5.63	0.02	0.01	0.88	0.90	99.43
PRAD-1104	E	1 cm	62.08	0.47	17.05	2.51	0.33	0.25	0.84	7.91	5.76	0.03	0.01	0.84	0.85	98.94
PRAD-1125	OE	5 cm	62.40	0.47	18.21	2.55	0.29	0.21	0.91	7.60	5.83	N/A	N/A	N/A	N/A	98.46
PRAD-1125	OE	5 cm	62.23	0.41	18.20	2.64	0.36	0.22	0.93	7.22	5.83	N/A	N/A	N/A	N/A	98.03
PRAD-1125	OE	5 cm	57.36	0.58	18.65	4.03	0.15	1.00	3.52	4.56	7.62	N/A	N/A	N/A	N/A	97.45
PRAD-1125	OE	5 cm	57.12	0.58	18.87	4.00	0.16	0.95	3.46	4.52	7.75	N/A	N/A	N/A	N/A	97.40
PRAD-1125	OE	5 cm	56.96	0.57	18.67	3.84	0.11	0.93	3.88	4.40	7.93	N/A	N/A	N/A	N/A	97.28
PRAD-1125	OE	5 cm	57.36	0.57	18.39	3.81	0.14	0.96	3.46	4.44	7.78	N/A	N/A	N/A	N/A	96.89
PRAD-1125	OE	5 cm	56.70	0.60	18.86	3.94	0.12	1.04	3.56	4.51	7.55	N/A	N/A	N/A	N/A	96.87
PRAD-1125	OE	5 cm	57.63	0.58	18.60	3.75	0.13	0.94	3.99	3.12	7.81	N/A	N/A	N/A	N/A	96.53
PRAD-1125	OE	5 cm	58.75	0.58	19.01	3.95	0.16	1.00	3.54	4.55	7.85	N/A	N/A	N/A	N/A	99.40
PRAD-1125	OE	5 cm	58.64	0.58	18.88	3.95	0.13	1.04	3.53	4.51	7.95	N/A	N/A	N/A	N/A	99.22
PRAD-1127	E	1 cm	60.27	0.40	19.13	3.64	0.11	1.14	2.24	5.11	7.54	0.20	0.45	0.06	0.07	100.35
PRAD-1127	E	1 cm	61.87	0.50	18.11	2.62	0.22	0.38	1.68	6.36	7.30	0.04	0.36	0.02	0.84	100.30
PRAD-1127	E	1 cm	61.33	0.50	18.49	2.58	0.24	0.36	1.71	6.40	7.34	0.03	0.38	0.01	0.85	100.23
PRAD-1127	E	1 cm	61.14	0.41	17.91	1.70	0.06	0.27	4.21	4.02	9.21	0.02	0.37	0.15	0.09	99.56
PRAD-1127	E	1 cm	57.55	0.65	18.72	4.23	0.17	1.09	3.84	4.38	7.70	0.20	0.23	0.07	0.47	99.30
PRAD-1127	E	1 cm	57.59	0.65	18.57	4.06	0.15	1.09	3.65	4.45	7.71	0.45	0.27	0.07	0.47	99.18

Name	Microprobe	Resolution	SiO_2	TiO_2	Al_2O_3	FeO	MnO	MgO	CaO	Na_2O	K_2O	P_2O_5	S	Cl	F	Total
PRAD-1127	E	1 cm	59.06	0.69	18.56	3.66	0.09	1.55	3.49	3.64	7.73	0.17	0.39	0.02	0.10	99.14
PRAD-1127	E	1 cm	66.71	0.61	13.93	4.31	0.24	0.29	0.73	6.32	4.96	0.06	0.10	0.04	0.43	98.72
PRAD-1127	E	1 cm	60.40	0.48	17.66	2.82	0.21	0.32	1.70	6.20	7.48	0.04	0.46	0.01	0.84	98.60
PRAD-1127	E	1 cm	61.42	0.72	17.07	2.73	0.26	0.33	1.01	6.79	6.17	0.04	0.47	0.05	0.58	97.64
PRAD-1127	E	1 cm	60.14	0.48	17.77	2.64	0.22	0.31	1.60	5.82	7.05	0.05	0.39	0.02	0.84	97.32
PRAD-1127	E	1 cm	57.03	0.44	17.98	3.77	0.14	0.80	2.99	4.58	8.19	0.13	0.20	0.05	0.66	96.97
PRAD-1130	E	1 cm	59.46	0.44	18.74	3.56	0.15	0.73	2.80	4.66	8.71	0.13	0.21	0.03	0.67	100.29
PRAD-1130	E	1 cm	64.48	0.27	18.60	1.47	0.13	0.12	1.09	7.34	6.04	0.01	0.23	0.00	0.37	100.15
PRAD-1130	E	1 cm	57.29	0.45	18.91	3.83	0.16	0.82	3.02	4.47	8.22	0.13	0.19	0.05	0.65	98.18
PRAD-1130	E	1 cm	56.70	0.44	18.87	3.63	0.16	0.85	2.79	4.22	8.53	0.14	0.21	0.04	0.64	97.24
PRAD-1130	E	1 cm	56.77	0.43	18.31	3.77	0.15	0.81	2.76	4.37	8.30	0.12	0.25	0.04	0.68	96.77
PRAD-1130	E	1 cm	56.74	0.43	18.03	3.74	0.16	0.82	3.03	4.20	7.85	0.13	0.16	0.07	0.66	96.02
PRAD-1130	E	1 cm	57.20	0.43	17.66	3.35	0.17	0.81	2.95	4.32	7.84	0.14	0.22	0.04	0.64	95.76
PRAD-1130	E	1 cm	72.48	0.07	12.78	0.85	0.06	0.07	0.70	3.77	4.31	0.01	0.05	0.00	0.16	95.32
PRAD-1130	E	1 cm	55.95	0.43	17.68	3.42	0.15	0.87	3.07	4.15	8.00	0.13	0.17	0.07	0.66	94.74
PRAD-1332	OE	5 cm	57.05	0.61	18.07	5.24	0.16	1.54	4.15	3.39	7.97	N/A	N/A	N/A	N/A	98.17
PRAD-1332	OE	5 cm	56.97	0.66	17.92	5.16	0.13	1.48	4.11	3.32	7.93	N/A	N/A	N/A	N/A	97.67
PRAD-1332	OE	5 cm	57.03	0.66	18.13	5.15	0.13	1.54	4.18	3.42	7.97	N/A	N/A	N/A	N/A	98.22
PRAD-1332	OE	5 cm	56.88	0.63	17.85	5.13	0.15	1.57	4.25	3.38	7.80	N/A	N/A	N/A	N/A	97.64
PRAD-1332	OE	5 cm	56.96	0.62	17.93	5.13	0.12	1.44	4.10	3.35	7.99	N/A	N/A	N/A	N/A	97.64
PRAD-1332	OE	5 cm	56.60	0.64	17.70	5.09	0.12	1.46	4.15	3.24	8.01	N/A	N/A	N/A	N/A	96.99
PRAD-1332	OE	5 cm	56.73	0.63	17.84	5.08	0.14	1.48	4.03	3.39	7.96	N/A	N/A	N/A	N/A	97.29
PRAD-1332	OE	5 cm	56.79	0.60	18.20	5.07	0.12	1.51	4.18	3.48	7.95	N/A	N/A	N/A	N/A	97.89
PRAD-1332	OE	5 cm	57.62	0.55	17.96	4.81	0.17	1.33	3.70	3.49	8.18	N/A	N/A	N/A	N/A	97.80
PRAD-1332	OE	5 cm	57.41	0.58	17.96	4.81	0.13	1.34	3.85	3.50	8.22	N/A	N/A	N/A	N/A	97.79
PRAD-1332	OE	5 cm	57.56	0.56	17.91	4.67	0.15	1.26	3.68	3.50	8.35	N/A	N/A	N/A	N/A	97.63
PRAD-1332	OE	5 cm	57.26	0.59	18.07	4.59	0.11	1.32	3.62	3.54	7.99	N/A	N/A	N/A	N/A	97.08
PRAD-1332	OE	5 cm	59.25	0.46	18.16	3.94	0.11	0.90	3.06	3.72	8.51	N/A	N/A	N/A	N/A	98.10
PRAD-1332	OE	5 cm	59.41	0.46	18.06	3.92	0.15	0.88	3.21	3.64	8.32	N/A	N/A	N/A	N/A	98.04
PRAD-1332	OE	5 cm	59.26	0.44	18.15	3.90	0.10	0.91	3.19	3.65	8.30	N/A	N/A	N/A	N/A	97.89
PRAD-1332	OE	5 cm	60.37	0.41	17.93	3.65	0.10	0.69	2.80	3.63	8.50	N/A	N/A	N/A	N/A	98.08
PRAD-1332	OE	5 cm	58.12	0.42	17.51	3.64	0.11	0.86	3.10	3.45	8.07	N/A	N/A	N/A	N/A	95.28
PRAD-1332	OE	5 cm	58.74	0.43	17.57	3.54	0.10	0.72	2.80	3.71	8.00	N/A	N/A	N/A	N/A	95.59
PRAD-1332	OE	5 cm	58.83	0.41	17.41	3.49	0.11	0.72	2.79	3.41	8.45	N/A	N/A	N/A	N/A	95.61
PRAD-1332	OE	5 cm	59.83	0.40	17.79	3.49	0.10	0.72	2.82	3.72	8.61	N/A	N/A	N/A	N/A	97.47
PRAD-1332	OE	5 cm	58.22	0.40	17.47	3.49	0.08	0.82	2.82	3.43	8.39	N/A	N/A	N/A	N/A	95.10
PRAD-1332	OE	5 cm	58.15	0.40	17.45	3.46	0.09	0.74	2.79	3.32	8.42	N/A	N/A	N/A	N/A	94.81
PRAD-1332	OE	5 cm	60.47	0.41	18.01	3.45	0.13	0.75	2.81	3.68	8.63	N/A	N/A	N/A	N/A	98.35
PRAD-1474	E	5 cm	59.23	0.48	18.20	2.87	0.26	0.32	1.81	7.01	7.23	0.03	0.03	0.92	0.45	98.84
PRAD-1474	E	5 cm	57.83	0.33	19.12	2.36	0.19	0.19	3.15	5.02	8.45	0.01	0.09	0.80	0.58	98.12
PRAD-1474	E	5 cm	59.35	0.40	18.72	3.08	0.11	0.68	1.48	5.33	7.86	0.11	0.05	0.33	0.46	97.96
PRAD-1474	E	5 cm	59.36	0.65	18.14	2.70	0.29	0.27	0.97	7.32	6.74	0.03	0.06	0.82	0.32	97.67
PRAD-1474	E	5 cm	60.05	0.42	17.87	2.90	0.11	0.57	0.89	5.12	8.00	0.05	0.06	0.31	0.49	96.84
PRAD-1474	E	5 cm	57.24	0.41	17.72	3.26	0.14	0.77	2.63	3.78	8.61	0.13	0.09	0.41	0.19	95.38
PRAD-1474	E	5 cm	58.63	0.55	18.24	2.12	0.23	0.28	1.00	7.18	5.87	0.02	0.03	0.56	0.48	95.20
PRAD-1474	E	5 cm	57.31	0.50	16.46	3.74	0.15	0.42	3.21	3.73	7.68	0.08	0.04	0.86	0.43	94.60
PRAD-1474	E	5 cm	57.20	0.38	17.54	3.14	0.15	0.50	2.31	4.19	8.18	0.09	0.10	0.58	0.22	94.57
PRAD-1474	E	5 cm	58.03	0.41	17.28	2.58	0.17	0.32	1.97	4.49	8.24	0.03	0.03	0.66	0.28	94.49
PRAD-1494	OE	5 cm	60.07	0.62	18.32	2.60	0.33	0.30	0.91	6.79	5.79	N/A	N/A	N/A	N/A	95.72
PRAD-1494	OE	5 cm	59.67	0.57	18.24	2.32	0.24	0.32	0.94	6.73	6.26	N/A	N/A	N/A	N/A	95.29
PRAD-1494	OE	5 cm	61.27	0.47	18.47	2.79	0.27	0.29	1.51	6.32	6.50	N/A	N/A	N/A	N/A	97.88
PRAD-1494	OE	5 cm	61.84	0.57	18.44	2.46	0.21	0.39	1.06	5.64	6.49	N/A	N/A	N/A	N/A	97.09
PRAD-1494	OE	5 cm	61.49	0.43	18.81	2.24	0.10	0.35	1.43	5.55	9.18	N/A	N/A	N/A	N/A	99.58

Name	Microprobe	Resolution	SiO_2	TiO_2	Al_2O_3	FeO	MnO	MgO	CaO	Na_2O	K_2O	P_2O_5	S	Cl	F	Total
PRAD-1494	OE	5 cm	59.40	0.47	18.17	2.87	0.23	0.41	1.73	5.26	7.64	N/A	N/A	N/A	N/A	96.17
PRAD-1494	OE	5 cm	59.97	0.42	19.46	3.02	0.18	0.53	2.11	5.14	8.14	N/A	N/A	N/A	N/A	98.96
PRAD-1494	OE	5 cm	60.96	0.41	18.45	2.51	0.22	0.40	1.59	5.10	6.86	N/A	N/A	N/A	N/A	96.50
PRAD-1494	OE	5 cm	59.21	0.43	18.67	2.93	0.11	0.38	1.00	5.03	8.11	N/A	N/A	N/A	N/A	95.86
PRAD-1494	OE	5 cm	58.10	0.48	18.93	2.85	0.13	0.39	3.00	4.92	8.71	N/A	N/A	N/A	N/A	97.49
PRAD-1494	OE	5 cm	59.37	0.39	19.03	2.75	0.19	0.32	1.61	4.89	8.31	N/A	N/A	N/A	N/A	96.86
PRAD-1494	OE	5 cm	59.25	0.43	18.30	2.93	0.14	0.57	1.92	4.66	7.38	N/A	N/A	N/A	N/A	95.58
PRAD-1494	OE	5 cm	56.50	0.30	19.89	2.41	0.16	0.18	3.03	4.65	8.24	N/A	N/A	N/A	N/A	95.36
PRAD-1494	OE	5 cm	58.86	0.29	19.50	2.44	0.17	0.21	2.96	4.65	6.98	N/A	N/A	N/A	N/A	96.06
PRAD-1494	OE	5 cm	56.19	0.71	18.09	3.62	0.18	1.81	4.30	4.35	6.23	N/A	N/A	N/A	N/A	95.46
PRAD-1494	OE	5 cm	63.85	0.43	17.77	2.40	0.09	0.31	2.30	4.20	7.44	N/A	N/A	N/A	N/A	98.79
PRAD-1494	OE	5 cm	59.32	0.37	18.54	3.07	0.16	0.55	2.16	4.15	8.38	N/A	N/A	N/A	N/A	96.69
PRAD-1494	OE	5 cm	58.43	0.34	18.43	2.74	0.15	0.51	2.04	4.00	8.45	N/A	N/A	N/A	N/A	95.09
PRAD-1494	OE	5 cm	58.68	0.37	18.20	2.76	0.08	0.57	2.46	3.99	8.21	N/A	N/A	N/A	N/A	95.30
PRAD-1494	OE	5 cm	57.92	0.67	18.79	5.27	0.12	1.48	3.76	3.99	7.80	N/A	N/A	N/A	N/A	99.79
PRAD-1494	OE	5 cm	58.47	0.50	19.28	3.41	0.12	0.48	3.74	3.96	9.08	N/A	N/A	N/A	N/A	99.04
PRAD-1494	OE	5 cm	65.60	0.16	17.34	1.67	0.14	0.13	2.04	3.89	7.63	N/A	N/A	N/A	N/A	98.59
PRAD-1494	OE	5 cm	58.23	0.37	18.22	2.70	0.14	0.54	2.30	3.83	8.78	N/A	N/A	N/A	N/A	95.09
PRAD-1494	OE	5 cm	58.86	0.43	18.14	3.36	0.11	0.80	2.78	3.82	8.06	N/A	N/A	N/A	N/A	96.35
PRAD-1494	OE	5 cm	59.26	0.35	18.43	2.95	0.12	0.62	2.29	3.76	8.63	N/A	N/A	N/A	N/A	96.41
PRAD-1494	OE	5 cm	58.81	0.38	18.08	2.90	0.11	0.55	2.09	3.69	9.32	N/A	N/A	N/A	N/A	95.92
PRAD-1494	OE	5 cm	55.44	0.47	19.03	3.17	0.11	0.46	3.63	3.59	9.22	N/A	N/A	N/A	N/A	95.10
PRAD-1494	OE	5 cm	61.35	0.33	17.79	2.50	0.11	0.37	2.98	3.57	7.27	N/A	N/A	N/A	N/A	96.28
PRAD-1494	OE	5 cm	56.63	0.49	19.24	3.32	0.15	0.49	3.97	3.47	9.73	N/A	N/A	N/A	N/A	97.48
PRAD-1494	OE	5 cm	54.95	0.53	18.75	3.79	0.14	0.63	4.44	3.45	8.99	N/A	N/A	N/A	N/A	95.68
PRAD-1494	OE	5 cm	61.89	0.31	17.39	2.75	0.16	0.62	3.73	3.38	7.83	N/A	N/A	N/A	N/A	98.06
PRAD-1494	OE	5 cm	59.50	0.38	18.02	3.20	0.15	0.71	2.42	3.33	8.48	N/A	N/A	N/A	N/A	96.19
PRAD-1494	OE	5 cm	57.16	0.47	19.19	3.24	0.09	0.46	4.08	3.13	8.82	N/A	N/A	N/A	N/A	96.65
PRAD-1494	OE	5 cm	57.88	0.47	19.52	2.81	0.07	0.38	4.19	2.51	9.49	N/A	N/A	N/A	N/A	97.30
PRAD-1653	OE	5 cm	59.50	0.45	19.13	2.98	0.30	0.27	1.67	6.88	6.90	N/A	N/A	N/A	N/A	98.09
PRAD-1653	OE	5 cm	59.99	0.35	19.04	2.25	0.16	0.20	1.66	6.42	6.72	N/A	N/A	N/A	N/A	96.79
PRAD-1653	OE	5 cm	58.83	0.45	19.11	2.91	0.21	0.28	1.50	6.57	6.72	N/A	N/A	N/A	N/A	96.57
PRAD-1653	OE	5 cm	60.09	0.35	19.29	2.10	0.17	0.18	1.78	6.00	6.60	N/A	N/A	N/A	N/A	96.55
PRAD-1653	OE	5 cm	58.41	0.44	18.94	2.93	0.24	0.30	1.61	6.45	6.69	N/A	N/A	N/A	N/A	96.01
PRAD-1653	OE	5 cm	58.32	0.41	18.94	2.84	0.21	0.28	1.62	6.52	6.78	N/A	N/A	N/A	N/A	95.92
PRAD-1653	OE	5 cm	58.38	0.42	18.76	3.02	0.28	0.26	1.53	6.62	6.63	N/A	N/A	N/A	N/A	95.91
PRAD-1653	OE	5 cm	58.48	0.45	18.90	2.95	0.24	0.28	1.55	6.34	6.71	N/A	N/A	N/A	N/A	95.89
PRAD-1653	OE	5 cm	57.93	0.39	18.79	2.88	0.24	0.28	1.66	6.43	6.93	N/A	N/A	N/A	N/A	95.53
PRAD-1653	OE	5 cm	57.51	0.40	18.77	2.94	0.28	0.27	1.62	6.66	6.90	N/A	N/A	N/A	N/A	95.34
PRAD-1653	OE	5 cm	57.93	0.44	18.83	3.02	0.19	0.28	1.58	6.49	6.54	N/A	N/A	N/A	N/A	95.30
PRAD-1653	OE	5 cm	57.97	0.36	18.68	2.91	0.26	0.28	1.61	6.38	6.74	N/A	N/A	N/A	N/A	95.17
PRAD-1653	OE	5 cm	57.78	0.40	18.78	2.81	0.21	0.27	1.61	6.19	6.69	N/A	N/A	N/A	N/A	94.72
PRAD-1653	OE	5 cm	57.82	0.44	18.65	2.82	0.29	0.28	1.53	6.30	6.58	N/A	N/A	N/A	N/A	94.71
PRAD-1752	OE	5 cm	59.98	0.44	18.92	3.00	0.27	0.29	1.73	6.77	6.86	N/A	N/A	N/A	N/A	98.26
PRAD-1752	OE	5 cm	60.22	0.42	18.82	3.19	0.26	0.27	1.71	6.57	6.82	N/A	N/A	N/A	N/A	98.26
PRAD-1752	OE	5 cm	59.88	0.44	18.64	3.24	0.30	0.29	1.73	6.40	6.84	N/A	N/A	N/A	N/A	97.74
PRAD-1752	OE	5 cm	58.17	0.40	18.69	3.08	0.21	0.29	1.66	6.39	6.59	N/A	N/A	N/A	N/A	95.48
PRAD-1752	OE	5 cm	59.50	0.42	18.29	3.22	0.23	0.31	1.68	6.37	6.86	N/A	N/A	N/A	N/A	96.88
PRAD-1752	OE	5 cm	60.10	0.42	18.76	3.10	0.24	0.28	1.71	6.34	6.86	N/A	N/A	N/A	N/A	97.81
PRAD-1752	OE	5 cm	60.59	0.46	18.88	3.15	0.27	0.30	1.73	6.34	6.88	N/A	N/A	N/A	N/A	98.60
PRAD-1752	OE	5 cm	60.21	0.43	18.28	3.16	0.24	0.28	1.68	6.33	6.94	N/A	N/A	N/A	N/A	97.55
PRAD-1752	OE	5 cm	59.36	0.44	18.35	3.16	0.23	0.33	1.87	6.32	7.18	N/A	N/A	N/A	N/A	97.23
PRAD-1752	OE	5 cm	60.06	0.42	17.94	3.12	0.28	0.28	1.64	6.27	6.66	N/A	N/A	N/A	N/A	96.66

Name	Microprobe	Resolution	SiO_2	TiO_2	Al_2O_3	FeO	MnO	MgO	CaO	Na_2O	K_2O	P_2O_5	S	Cl	F	Total
PRAD-1752	OE	5 cm	59.22	0.43	18.19	3.11	0.21	0.30	1.68	6.25	6.80	N/A	N/A	N/A	N/A	96.17
PRAD-1752	OE	5 cm	59.84	0.40	18.37	3.18	0.25	0.25	1.69	6.21	6.94	N/A	N/A	N/A	N/A	97.12
PRAD-1752	OE	5 cm	58.04	0.40	18.73	3.26	0.20	0.26	1.63	6.20	6.76	N/A	N/A	N/A	N/A	95.48
PRAD-1752	OE	5 cm	59.04	0.41	18.04	3.23	0.25	0.30	1.68	6.19	6.74	N/A	N/A	N/A	N/A	95.89
PRAD-1752	OE	5 cm	59.94	0.44	18.34	3.20	0.23	0.29	1.64	6.16	6.79	N/A	N/A	N/A	N/A	97.02
PRAD-1752	OE	5 cm	58.53	0.43	18.15	3.12	0.28	0.30	1.67	6.12	6.69	N/A	N/A	N/A	N/A	95.30
PRAD-1752	OE	5 cm	58.10	0.41	17.43	3.04	0.23	0.29	1.63	6.12	6.56	N/A	N/A	N/A	N/A	93.81
PRAD-1752	OE	5 cm	60.48	0.44	18.00	3.14	0.29	0.28	1.68	6.07	6.88	N/A	N/A	N/A	N/A	97.25
PRAD-1752	OE	5 cm	59.28	0.40	18.80	3.02	0.25	0.29	1.64	6.06	6.76	N/A	N/A	N/A	N/A	96.49
PRAD-1752	OE	5 cm	58.95	0.40	17.78	3.19	0.22	0.35	1.94	5.99	7.14	N/A	N/A	N/A	N/A	95.94
PRAD-1752	OE	5 cm	60.17	0.46	18.30	3.01	0.22	0.29	1.70	5.94	6.79	N/A	N/A	N/A	N/A	96.88
PRAD-1752	OE	5 cm	58.58	0.41	18.16	3.15	0.26	0.30	1.73	5.91	6.80	N/A	N/A	N/A	N/A	95.30
PRAD-1752	OE	5 cm	59.86	0.40	17.70	3.06	0.22	0.34	1.70	5.81	7.13	N/A	N/A	N/A	N/A	96.21
PRAD-1752	OE	5 cm	59.19	0.42	18.70	3.17	0.20	0.28	1.69	5.80	7.05	N/A	N/A	N/A	N/A	96.50
PRAD-1752	OE	5 cm	58.91	0.43	17.84	3.10	0.22	0.31	1.66	5.71	6.80	N/A	N/A	N/A	N/A	94.97
PRAD-1752	OE	5 cm	58.93	0.42	18.38	3.11	0.30	0.26	1.61	5.67	6.76	N/A	N/A	N/A	N/A	95.44
PRAD-1870	OE	5 cm	62.93	0.63	19.02	2.72	0.26	0.31	1.09	7.50	6.00	N/A	N/A	N/A	N/A	100.46
PRAD-1870	OE	5 cm	63.58	0.58	18.96	2.44	0.18	0.35	1.18	6.63	6.44	N/A	N/A	N/A	N/A	100.33
PRAD-1870	OE	5 cm	62.84	0.57	18.89	2.67	0.32	0.29	1.03	7.38	6.14	N/A	N/A	N/A	N/A	100.13
PRAD-1870	OE	5 cm	63.14	0.67	18.52	2.57	0.22	0.33	1.17	6.56	6.43	N/A	N/A	N/A	N/A	99.59
PRAD-1870	OE	5 cm	62.32	0.57	19.15	2.64	0.26	0.30	1.06	7.11	6.12	N/A	N/A	N/A	N/A	99.52
PRAD-1870	OE	5 cm	62.99	0.60	18.28	2.61	0.23	0.34	1.06	7.22	6.07	N/A	N/A	N/A	N/A	99.40
PRAD-1870	OE	5 cm	61.90	0.62	19.01	2.58	0.26	0.30	1.09	7.11	6.28	N/A	N/A	N/A	N/A	99.14
PRAD-1870	OE	5 cm	62.34	0.55	18.12	2.61	0.32	0.29	0.94	7.41	5.98	N/A	N/A	N/A	N/A	98.55
PRAD-1870	OE	5 cm	62.52	0.59	18.15	2.61	0.20	0.33	1.12	6.70	6.26	N/A	N/A	N/A	N/A	98.49
PRAD-1870	OE	5 cm	61.06	0.60	18.83	2.57	0.26	0.30	1.06	7.41	6.14	N/A	N/A	N/A	N/A	98.22
PRAD-1870	OE	5 cm	62.26	0.55	17.80	2.68	0.24	0.31	1.03	7.06	6.19	N/A	N/A	N/A	N/A	98.11
PRAD-1870	OE	5 cm	61.97	0.54	18.21	2.58	0.28	0.28	0.99	7.22	5.95	N/A	N/A	N/A	N/A	98.02
PRAD-1870	OE	5 cm	58.02	0.44	18.70	3.94	0.28	0.35	2.10	6.13	7.64	N/A	N/A	N/A	N/A	97.59
PRAD-1870	OE	5 cm	61.22	0.54	18.77	2.64	0.27	0.29	1.00	7.00	5.83	N/A	N/A	N/A	N/A	97.55
PRAD-1870	OE	5 cm	61.94	0.52	17.78	2.62	0.23	0.35	1.24	6.27	6.59	N/A	N/A	N/A	N/A	97.54
PRAD-1870	OE	5 cm	61.47	0.57	18.12	2.56	0.21	0.33	1.09	6.94	6.12	N/A	N/A	N/A	N/A	97.39
PRAD-1870	OE	5 cm	62.20	0.52	17.81	2.52	0.17	0.37	1.18	6.06	6.52	N/A	N/A	N/A	N/A	97.35
PRAD-1870	OE	5 cm	62.39	0.52	17.38	2.52	0.16	0.43	1.24	6.00	6.65	N/A	N/A	N/A	N/A	97.29
PRAD-1870	OE	5 cm	61.07	0.56	18.22	2.79	0.25	0.30	0.97	6.95	5.95	N/A	N/A	N/A	N/A	97.06
PRAD-1870	OE	5 cm	61.85	0.54	17.63	2.48	0.19	0.37	1.18	6.61	6.04	N/A	N/A	N/A	N/A	96.90
PRAD-1870	OE	5 cm	62.08	0.53	17.48	2.45	0.20	0.36	1.22	6.17	6.13	N/A	N/A	N/A	N/A	96.61
PRAD-1870	OE	5 cm	61.50	0.44	17.48	2.48	0.19	0.37	1.30	6.02	6.62	N/A	N/A	N/A	N/A	96.41
PRAD-1870	OE	5 cm	60.70	0.60	18.00	2.52	0.22	0.34	1.09	6.63	6.25	N/A	N/A	N/A	N/A	96.34
PRAD-1870	OE	5 cm	61.44	0.60	17.79	2.32	0.19	0.37	1.17	6.09	6.35	N/A	N/A	N/A	N/A	96.32
PRAD-1870	OE	5 cm	58.79	0.42	18.13	3.26	0.19	0.43	1.94	5.29	7.68	N/A	N/A	N/A	N/A	96.13
PRAD-1870	OE	5 cm	60.59	0.59	17.88	2.50	0.25	0.30	1.02	6.75	5.98	N/A	N/A	N/A	N/A	95.86
PRAD-1870	OE	5 cm	60.32	0.57	18.05	2.51	0.24	0.35	1.04	6.46	6.10	N/A	N/A	N/A	N/A	95.64
PRAD-1870	OE	5 cm	61.08	0.53	17.58	2.36	0.11	0.37	1.18	6.09	6.30	N/A	N/A	N/A	N/A	95.60
PRAD-1870	OE	5 cm	60.48	0.53	17.34	2.45	0.20	0.37	1.12	6.17	6.41	N/A	N/A	N/A	N/A	95.08
PRAD-1870	OE	5 cm	60.87	0.49	17.83	2.37	0.16	0.37	1.08	5.75	6.13	N/A	N/A	N/A	N/A	95.04
PRAD-2040	OE	5 cm	60.93	0.42	19.75	3.17	0.23	0.41	2.00	5.70	8.01	N/A	N/A	N/A	N/A	100.60
PRAD-2040	OE	5 cm	61.89	0.39	18.94	3.00	0.21	0.42	1.96	5.80	7.93	N/A	N/A	N/A	N/A	100.53
PRAD-2040	OE	5 cm	61.28	0.43	19.23	3.01	0.25	0.40	1.90	5.93	7.87	N/A	N/A	N/A	N/A	100.30
PRAD-2040	OE	5 cm	60.46	0.39	19.22	3.22	0.19	0.41	1.99	5.90	7.92	N/A	N/A	N/A	N/A	99.69
PRAD-2040	OE	5 cm	60.49	0.37	19.26	3.15	0.21	0.37	1.99	5.74	8.00	N/A	N/A	N/A	N/A	99.59
PRAD-2040	OE	5 cm	60.45	0.41	19.14	3.20	0.24	0.40	1.99	5.75	7.96	N/A	N/A	N/A	N/A	99.54
PRAD-2040	OE	5 cm	60.40	0.41	18.97	3.16	0.17	0.38	2.01	5.77	8.07	N/A	N/A	N/A	N/A	99.35

Name	Microprobe	Resolution	SiO_2	TiO_2	Al_2O_3	FeO	MnO	MgO	CaO	Na_2O	K_2O	P_2O_5	S	Cl	F	Total
PRAD-2040	OE	5 cm	60.41	0.40	19.28	3.05	0.23	0.40	1.98	5.60	7.98	N/A	N/A	N/A	N/A	99.33
PRAD-2040	OE	5 cm	60.48	0.38	18.98	3.16	0.16	0.40	1.94	5.84	7.94	N/A	N/A	N/A	N/A	99.27
PRAD-2040	OE	5 cm	60.63	0.38	18.88	3.17	0.20	0.40	2.00	5.69	7.91	N/A	N/A	N/A	N/A	99.27
PRAD-2040	OE	5 cm	60.31	0.41	19.09	3.13	0.18	0.36	1.97	5.69	8.00	N/A	N/A	N/A	N/A	99.14
PRAD-2040	OE	5 cm	60.48	0.44	18.61	3.24	0.20	0.38	2.06	5.73	7.98	N/A	N/A	N/A	N/A	99.12
PRAD-2040	OE	5 cm	60.23	0.42	19.33	3.12	0.21	0.40	1.95	5.59	7.85	N/A	N/A	N/A	N/A	99.08
PRAD-2040	OE	5 cm	60.37	0.38	18.82	3.09	0.20	0.37	2.00	5.68	7.96	N/A	N/A	N/A	N/A	98.87
PRAD-2040	OE	5 cm	59.94	0.41	19.14	3.21	0.21	0.40	1.99	5.43	7.75	N/A	N/A	N/A	N/A	98.47
PRAD-2040	OE	5 cm	60.04	0.40	18.34	3.09	0.19	0.35	1.99	5.96	7.97	N/A	N/A	N/A	N/A	98.32
PRAD-2040	OE	5 cm	59.83	0.42	18.55	3.05	0.25	0.40	1.95	5.71	8.04	N/A	N/A	N/A	N/A	98.18
PRAD-2040	OE	5 cm	60.08	0.39	18.21	3.21	0.22	0.40	1.98	5.70	7.91	N/A	N/A	N/A	N/A	98.08
PRAD-2040	OE	5 cm	60.34	0.38	17.98	3.09	0.20	0.38	1.96	5.66	7.91	N/A	N/A	N/A	N/A	97.89
PRAD-2040	OE	5 cm	59.67	0.41	18.63	3.10	0.17	0.40	1.91	5.39	7.86	N/A	N/A	N/A	N/A	97.54
PRAD-2040	OE	5 cm	59.50	0.37	18.22	3.07	0.22	0.41	1.95	5.66	7.87	N/A	N/A	N/A	N/A	97.28
PRAD-2040	OE	5 cm	59.49	0.39	19.25	2.95	0.18	0.35	2.02	4.28	7.85	N/A	N/A	N/A	N/A	96.76
PRAD-2040	OE	5 cm	58.33	0.40	18.15	2.99	0.17	0.36	1.92	5.68	7.64	N/A	N/A	N/A	N/A	95.64
PRAD-2375	OE	5 cm	64.56	1.00	15.30	5.86	0.24	0.64	1.34	5.02	4.03	N/A	N/A	N/A	N/A	97.99
PRAD-2375	OE	5 cm	63.97	0.52	14.40	4.40	0.21	0.30	0.71	5.74	4.53	N/A	N/A	N/A	N/A	94.78
PRAD-2375	OE	5 cm	58.31	0.51	22.02	2.67	0.07	0.68	5.94	3.81	5.84	N/A	N/A	N/A	N/A	99.85
PRAD-2375	OE	5 cm	58.25	0.38	18.06	2.94	0.10	0.61	2.33	3.55	8.70	N/A	N/A	N/A	N/A	94.91
PRAD-2375	OE	5 cm	55.73	0.42	19.26	2.57	0.11	0.37	2.71	4.19	9.50	N/A	N/A	N/A	N/A	94.86
PRAD-2375	OE	5 cm	59.87	0.46	18.35	2.75	0.17	0.36	1.67	5.84	7.11	N/A	N/A	N/A	N/A	96.56
PRAD-2375	OE	5 cm	61.12	0.42	18.33	2.53	0.18	0.32	1.60	5.63	7.32	N/A	N/A	N/A	N/A	97.46
PRAD-2375	OE	5 cm	60.20	0.42	18.13	2.52	0.12	0.35	1.60	5.30	7.28	N/A	N/A	N/A	N/A	95.92
PRAD-2375	E	5 cm	56.00	0.03	26.89	0.71	0.00	0.06	8.94	4.38	2.58	0.03	0.01	0.01	-0.01	99.63
PRAD-2375	E	5 cm	64.47	0.98	16.56	2.00	0.15	0.58	1.69	4.01	8.41	0.04	0.14	0.04	0.38	99.43
PRAD-2375	E	5 cm	60.72	0.51	18.11	2.65	0.22	0.39	1.69	6.25	7.54	0.04	0.01	0.82	0.39	99.33
PRAD-2375	E	5 cm	63.54	0.02	19.61	0.26	0.01	0.01	0.81	3.03	11.81	0.01	0.00	0.01	-0.01	99.11
PRAD-2375	E	5 cm	54.51	0.04	27.70	0.71	0.00	0.02	10.29	5.31	0.42	0.02	0.00	0.02	0.02	99.05
PRAD-2375	E	5 cm	67.82	0.10	16.65	0.56	0.04	0.01	0.43	3.73	9.47	0.01	0.00	0.13	0.09	99.04
PRAD-2375	E	5 cm	67.45	0.03	17.14	0.38	0.05	0.01	0.30	4.43	8.63	0.00	0.01	0.15	0.31	98.89
PRAD-2375	E	5 cm	65.09	0.70	14.20	4.82	0.25	0.39	0.95	6.76	4.77	0.10	0.05	0.34	0.08	98.48
PRAD-2375	E	5 cm	60.60	0.49	18.08	2.54	0.23	0.36	1.60	6.30	6.89	0.05	0.01	0.82	0.38	98.34
PRAD-2375	E	5 cm	60.55	0.49	17.81	2.66	0.22	0.36	1.59	5.96	7.27	0.04	0.01	0.84	0.39	98.17
PRAD-2375	E	5 cm	64.80	0.71	14.14	4.73	0.23	0.40	0.99	6.50	4.71	0.10	0.04	0.35	0.11	97.78
PRAD-2375	E	5 cm	64.16	0.83	14.20	5.07	0.28	0.47	1.06	6.57	4.40	0.14	0.04	0.22	0.09	97.53
PRAD-2375	E	5 cm	56.00	0.51	19.61	2.77	0.14	0.36	2.68	4.49	9.67	0.05	0.14	0.14	0.68	97.23
PRAD-2375	E	5 cm	59.28	0.44	17.85	2.42	0.22	0.35	1.80	5.89	7.34	0.04	0.02	0.85	0.41	96.91
PRAD-2375	E	5 cm	64.51	0.00	19.23	0.08	0.01	0.03	0.22	12.32	0.17	0.00	0.02	0.06	0.01	96.67
PRAD-2375	E	5 cm	67.12	0.53	11.86	4.75	0.25	0.23	0.41	5.66	4.38	0.03	0.04	0.71	0.19	96.16
PRAD-2375	E	5 cm	56.00	0.50	18.14	2.88	0.14	0.44	2.73	4.03	9.45	0.05	0.15	0.14	0.65	95.32
PRAD-2375	E	5 cm	56.60	1.46	17.28	4.16	0.04	1.03	2.87	2.75	8.20	0.60	0.07	0.04	0.23	95.32
PRAD-2375	E	5 cm	56.35	0.40	18.39	2.34	0.13	0.37	2.27	3.70	9.87	0.05	0.19	0.21	0.36	94.63
PRAD-2525	OE	5 cm	59.09	0.47	19.43	3.80	0.14	0.84	2.94	4.91	8.39	N/A	N/A	N/A	N/A	100.02
PRAD-2525	OE	5 cm	59.14	0.47	18.80	3.76	0.13	0.91	3.02	4.24	8.55	N/A	N/A	N/A	N/A	99.01
PRAD-2525	OE	5 cm	59.27	0.41	18.77	3.50	0.13	0.73	2.32	5.48	8.32	N/A	N/A	N/A	N/A	98.94
PRAD-2525	OE	5 cm	58.90	0.43	18.81	3.78	0.10	0.96	3.18	4.41	8.35	N/A	N/A	N/A	N/A	98.92
PRAD-2525	OE	5 cm	58.93	0.44	18.81	3.75	0.12	0.83	2.84	4.60	8.56	N/A	N/A	N/A	N/A	98.88
PRAD-2525	OE	5 cm	59.66	0.40	18.96	3.60	0.13	0.91	2.90	3.76	8.46	N/A	N/A	N/A	N/A	98.79
PRAD-2525	OE	5 cm	58.99	0.41	18.74	3.75	0.12	0.84	2.97	4.47	8.44	N/A	N/A	N/A	N/A	98.72
PRAD-2525	OE	5 cm	58.67	0.41	18.68	3.72	0.16	0.78	2.83	4.56	8.53	N/A	N/A	N/A	N/A	98.34
PRAD-2525	OE	5 cm	58.37	0.46	18.80	3.69	0.13	0.90	2.92	4.66	8.27	N/A	N/A	N/A	N/A	98.21
PRAD-2525	OE	5 cm	58.54	0.40	18.60	3.56	0.13	0.82	2.86	4.38	8.89	N/A	N/A	N/A	N/A	98.17

Name	Microprobe	Resolution	SiO_2	TiO_2	Al_2O_3	FeO	MnO	MgO	CaO	Na_2O	K_2O	P_2O_5	S	Cl	F	Total
PRAD-2525	OE	5 cm	58.70	0.41	18.70	3.38	0.13	0.71	2.62	4.85	8.42	N/A	N/A	N/A	N/A	97.93
PRAD-2525	OE	5 cm	58.51	0.37	18.58	3.60	0.14	0.83	2.81	4.59	8.46	N/A	N/A	N/A	N/A	97.88
PRAD-2525	OE	5 cm	58.31	0.42	18.44	3.57	0.10	0.82	2.82	4.32	8.72	N/A	N/A	N/A	N/A	97.52
PRAD-2525	OE	5 cm	58.27	0.47	18.57	3.66	0.11	0.95	3.04	4.29	8.14	N/A	N/A	N/A	N/A	97.50
PRAD-2525	OE	5 cm	58.55	0.43	18.51	3.54	0.15	0.72	2.60	4.73	8.15	N/A	N/A	N/A	N/A	97.38
PRAD-2525	OE	5 cm	58.37	0.43	18.54	3.43	0.09	0.76	2.50	5.02	8.20	N/A	N/A	N/A	N/A	97.34
PRAD-2525	OE	5 cm	58.04	0.43	18.58	3.75	0.10	0.88	2.94	4.65	7.96	N/A	N/A	N/A	N/A	97.31
PRAD-2525	OE	5 cm	57.84	0.41	18.50	3.56	0.09	0.86	2.88	4.31	8.37	N/A	N/A	N/A	N/A	96.82
PRAD-2525	OE	5 cm	58.55	0.42	18.41	3.69	0.10	0.94	3.04	2.96	8.08	N/A	N/A	N/A	N/A	96.19
PRAD-2525	OE	5 cm	57.32	0.42	18.44	3.39	0.11	0.77	2.87	4.31	8.23	N/A	N/A	N/A	N/A	95.86
PRAD-2525	OE	5 cm	56.83	0.44	17.99	3.68	0.16	0.80	3.02	4.28	8.32	N/A	N/A	N/A	N/A	95.52
PRAD-2525	OE	5 cm	56.43	0.42	18.17	3.59	0.14	0.87	3.10	4.00	7.93	N/A	N/A	N/A	N/A	94.63
PRAD-2525	OE	5 cm	59.25	0.41	18.87	3.66	0.11	0.98	3.21	4.81	8.43	N/A	N/A	N/A	N/A	99.73
PRAD-2525	OE	5 cm	59.39	0.43	18.99	3.82	0.14	1.00	3.13	4.52	8.25	N/A	N/A	N/A	N/A	99.66
PRAD-2525	OE	5 cm	60.18	0.38	19.31	3.12	0.16	0.63	2.54	4.72	8.53	N/A	N/A	N/A	N/A	99.57
PRAD-2525	OE	5 cm	59.50	0.44	19.02	3.62	0.15	0.83	2.86	4.70	8.44	N/A	N/A	N/A	N/A	99.55
PRAD-2525	OE	5 cm	59.81	0.41	18.91	3.56	0.14	0.73	2.67	4.74	8.58	N/A	N/A	N/A	N/A	99.54
PRAD-2525	OE	5 cm	59.58	0.41	19.09	3.55	0.15	0.74	2.58	4.91	8.36	N/A	N/A	N/A	N/A	99.36
PRAD-2525	OE	5 cm	59.26	0.44	18.79	3.73	0.13	0.93	3.06	4.47	8.52	N/A	N/A	N/A	N/A	99.33
PRAD-2525	OE	5 cm	59.05	0.41	18.86	3.72	0.13	0.95	3.14	4.55	8.26	N/A	N/A	N/A	N/A	99.07
PRAD-2525	OE	5 cm	59.41	0.42	18.83	3.60	0.13	0.90	2.89	4.67	8.11	N/A	N/A	N/A	N/A	98.95
PRAD-2525	OE	5 cm	58.73	0.43	18.73	3.83	0.13	1.09	3.31	4.44	8.23	N/A	N/A	N/A	N/A	98.93
PRAD-2525	OE	5 cm	59.75	0.38	18.86	3.38	0.14	0.71	2.65	4.82	8.25	N/A	N/A	N/A	N/A	98.93
PRAD-2525	OE	5 cm	59.48	0.41	18.92	3.49	0.12	0.76	2.64	4.80	8.21	N/A	N/A	N/A	N/A	98.83
PRAD-2525	OE	5 cm	58.86	0.46	18.68	3.60	0.15	0.80	2.86	4.56	8.66	N/A	N/A	N/A	N/A	98.63
PRAD-2525	OE	5 cm	58.64	0.43	18.46	3.82	0.16	1.09	3.32	4.27	8.28	N/A	N/A	N/A	N/A	98.47
PRAD-2525	OE	5 cm	58.85	0.42	19.00	3.42	0.16	0.74	2.44	5.41	7.97	N/A	N/A	N/A	N/A	98.41
PRAD-2525	OE	5 cm	59.08	0.38	18.87	3.49	0.12	0.74	2.62	4.94	8.16	N/A	N/A	N/A	N/A	98.41
PRAD-2525	OE	5 cm	58.94	0.42	18.68	3.58	0.14	0.76	2.75	4.55	8.48	N/A	N/A	N/A	N/A	98.30
PRAD-2525	OE	5 cm	58.69	0.42	18.64	3.74	0.12	0.86	3.05	4.51	8.12	N/A	N/A	N/A	N/A	98.14
PRAD-2525	OE	5 cm	58.47	0.43	18.73	3.69	0.12	0.84	2.88	4.32	8.60	N/A	N/A	N/A	N/A	98.07
PRAD-2525	OE	5 cm	58.41	0.43	18.74	3.62	0.09	0.79	2.90	4.61	8.36	N/A	N/A	N/A	N/A	97.94
PRAD-2525	OE	5 cm	58.20	0.43	18.43	3.73	0.14	0.85	2.99	4.47	8.46	N/A	N/A	N/A	N/A	97.69
PRAD-2525	OE	5 cm	58.61	0.41	18.51	3.49	0.13	0.74	2.69	4.60	8.17	N/A	N/A	N/A	N/A	97.34
PRAD-2525	OE	5 cm	57.43	0.44	18.36	3.92	0.13	1.06	3.43	4.24	7.85	N/A	N/A	N/A	N/A	96.85
PRAD-2525	OE	5 cm	58.28	0.38	18.30	3.40	0.14	0.71	2.66	4.42	8.47	N/A	N/A	N/A	N/A	96.77
PRAD-2525	OE	5 cm	58.00	0.38	18.30	3.56	0.14	0.89	2.93	4.47	7.97	N/A	N/A	N/A	N/A	96.62
PRAD-2525	OE	5 cm	57.94	0.41	18.39	3.42	0.12	0.82	2.88	4.33	8.27	N/A	N/A	N/A	N/A	96.60
PRAD-2525	OE	5 cm	57.69	0.42	18.38	3.48	0.16	0.82	2.99	4.22	8.26	N/A	N/A	N/A	N/A	96.43
PRAD-2525	OE	5 cm	57.01	0.39	18.04	3.54	0.16	0.79	2.81	4.28	7.90	N/A	N/A	N/A	N/A	94.91
PRAD-2525	OE	5 cm	59.07	0.42	19.03	3.76	0.09	0.91	3.15	4.51	8.32	N/A	N/A	N/A	N/A	99.25
PRAD-2525	OE	5 cm	59.38	0.40	18.97	3.60	0.15	0.76	2.70	4.73	8.51	N/A	N/A	N/A	N/A	99.19
PRAD-2525	OE	5 cm	58.32	0.43	19.04	3.59	0.14	0.77	2.82	4.66	8.55	N/A	N/A	N/A	N/A	98.32
PRAD-2525	OE	5 cm	57.84	0.45	18.76	3.70	0.10	0.96	3.09	4.65	8.24	N/A	N/A	N/A	N/A	97.77
PRAD-2525	OE	5 cm	58.45	0.42	18.71	3.47	0.12	0.73	2.76	4.78	8.14	N/A	N/A	N/A	N/A	97.59
PRAD-2525	OE	5 cm	58.46	0.39	18.77	3.37	0.15	0.71	2.60	4.75	8.29	N/A	N/A	N/A	N/A	97.48
PRAD-2525	OE	5 cm	57.91	0.40	18.70	3.52	0.11	0.80	3.00	4.51	8.50	N/A	N/A	N/A	N/A	97.45
PRAD-2525	OE	5 cm	57.07	0.44	18.93	3.76	0.12	0.98	3.22	4.51	8.17	N/A	N/A	N/A	N/A	97.20
PRAD-2525	OE	5 cm	57.77	0.40	18.58	3.50	0.11	0.82	2.87	4.36	8.58	N/A	N/A	N/A	N/A	96.99
PRAD-2525	OE	5 cm	58.18	0.40	18.72	3.40	0.12	0.68	2.56	4.72	8.14	N/A	N/A	N/A	N/A	96.93
PRAD-2525	OE	5 cm	57.68	0.38	19.29	2.96	0.09	0.64	2.50	4.44	8.64	N/A	N/A	N/A	N/A	96.62
PRAD-2525	OE	5 cm	57.90	0.39	18.67	3.44	0.11	0.71	2.64	4.73	8.02	N/A	N/A	N/A	N/A	96.59
PRAD-2525	OE	5 cm	57.30	0.44	18.39	3.63	0.14	0.98	3.22	4.51	7.91	N/A	N/A	N/A	N/A	96.51

Name	Microprobe	Resolution	SiO_2	TiO_2	Al_2O_3	FeO	MnO	MgO	CaO	Na_2O	K_2O	P_2O_5	S	Cl	F	Total
PRAD-2525	OE	5 cm	57.57	0.41	18.45	3.47	0.12	0.81	2.81	4.16	8.36	N/A	N/A	N/A	N/A	96.17
PRAD-2525	OE	5 cm	57.40	0.41	18.48	3.39	0.11	0.83	2.88	4.18	8.00	N/A	N/A	N/A	N/A	95.66
PRAD-2525	OE	5 cm	57.13	0.40	18.22	3.44	0.14	0.72	2.59	4.59	8.09	N/A	N/A	N/A	N/A	95.33
PRAD-2525	OE	5 cm	55.96	0.44	18.37	3.40	0.14	0.79	2.84	4.22	8.19	N/A	N/A	N/A	N/A	94.34
PRAD-2525	OE	5 cm	59.58	0.42	19.15	3.74	0.13	0.84	2.88	4.53	8.54	N/A	N/A	N/A	N/A	99.81
PRAD-2525	OE	5 cm	59.54	0.43	19.06	3.67	0.12	0.86	2.93	4.49	8.43	N/A	N/A	N/A	N/A	99.53
PRAD-2525	OE	5 cm	59.65	0.39	19.24	3.41	0.12	0.75	2.66	4.79	8.22	N/A	N/A	N/A	N/A	99.22
PRAD-2525	OE	5 cm	59.22	0.42	18.96	3.66	0.15	0.82	2.78	4.58	8.40	N/A	N/A	N/A	N/A	98.99
PRAD-2525	OE	5 cm	58.99	0.45	18.73	3.63	0.08	0.88	2.95	4.53	8.39	N/A	N/A	N/A	N/A	98.62
PRAD-2525	OE	5 cm	59.00	0.40	18.97	3.65	0.14	0.75	2.75	4.78	8.16	N/A	N/A	N/A	N/A	98.60
PRAD-2525	OE	5 cm	58.60	0.39	19.07	3.50	0.12	0.72	2.58	4.62	8.57	N/A	N/A	N/A	N/A	98.17
PRAD-2525	OE	5 cm	58.96	0.40	18.78	3.55	0.13	0.72	2.69	4.69	8.25	N/A	N/A	N/A	N/A	98.16
PRAD-2525	OE	5 cm	58.90	0.37	18.79	3.41	0.14	0.70	2.64	4.61	8.27	N/A	N/A	N/A	N/A	97.84
PRAD-2525	OE	5 cm	58.62	0.42	18.73	3.50	0.14	0.71	2.54	4.86	8.29	N/A	N/A	N/A	N/A	97.80
PRAD-2525	OE	5 cm	58.36	0.43	18.69	3.65	0.15	0.87	2.94	4.45	8.17	N/A	N/A	N/A	N/A	97.71
PRAD-2525	OE	5 cm	57.83	0.42	18.51	3.75	0.13	1.01	3.23	4.34	8.32	N/A	N/A	N/A	N/A	97.53
PRAD-2525	OE	5 cm	57.87	0.46	18.52	3.69	0.13	1.01	3.28	4.52	7.99	N/A	N/A	N/A	N/A	97.45
PRAD-2525	OE	5 cm	58.52	0.41	18.60	3.51	0.12	0.79	2.75	4.25	8.42	N/A	N/A	N/A	N/A	97.37
PRAD-2525	OE	5 cm	58.77	0.41	18.34	3.42	0.08	0.70	2.71	4.45	8.24	N/A	N/A	N/A	N/A	97.12
PRAD-2525	OE	5 cm	58.07	0.37	18.59	3.55	0.16	0.89	2.83	4.54	7.97	N/A	N/A	N/A	N/A	96.98
PRAD-2525	OE	5 cm	57.45	0.42	18.61	3.55	0.13	0.85	2.89	4.30	8.27	N/A	N/A	N/A	N/A	96.47
PRAD-2525	OE	5 cm	57.95	0.40	18.44	3.31	0.14	0.69	2.47	4.68	7.87	N/A	N/A	N/A	N/A	95.93
PRAD-2525	OE	5 cm	57.17	0.41	18.32	3.44	0.11	0.73	2.82	4.37	8.41	N/A	N/A	N/A	N/A	95.78
PRAD-2525	OE	5 cm	57.31	0.45	18.21	3.50	0.12	0.87	2.96	4.13	8.18	N/A	N/A	N/A	N/A	95.72
PRAD-2525	OE	5 cm	57.45	0.41	18.42	3.37	0.15	0.69	2.55	4.33	8.21	N/A	N/A	N/A	N/A	95.59
PRAD-2525	OE	5 cm	57.36	0.43	18.30	3.57	0.09	0.77	2.74	4.19	7.90	N/A	N/A	N/A	N/A	95.34
PRAD-2525	OE	5 cm	56.66	0.44	18.08	3.48	0.11	0.84	2.80	4.07	8.15	N/A	N/A	N/A	N/A	94.63
PRAD-2525	OE	5 cm	57.71	0.39	17.74	3.22	0.14	0.65	2.53	4.13	7.78	N/A	N/A	N/A	N/A	94.28
PRAD-2525	OE	5 cm	56.62	0.43	18.01	3.35	0.13	0.81	2.68	4.14	8.07	N/A	N/A	N/A	N/A	94.24
PRAD-2605	OE	5 cm	59.08	0.44	19.16	3.69	0.16	0.86	2.90	4.61	8.44	N/A	N/A	N/A	N/A	99.34
PRAD-2605	OE	5 cm	59.34	0.41	19.09	3.55	0.12	0.68	2.51	4.88	8.34	N/A	N/A	N/A	N/A	98.93
PRAD-2605	OE	5 cm	59.35	0.41	19.05	3.50	0.17	0.67	2.71	4.44	8.55	N/A	N/A	N/A	N/A	98.85
PRAD-2605	OE	5 cm	58.62	0.43	18.94	3.75	0.12	0.85	3.09	4.45	8.28	N/A	N/A	N/A	N/A	98.53
PRAD-2605	OE	5 cm	58.78	0.44	18.84	3.50	0.16	0.82	2.88	4.56	8.57	N/A	N/A	N/A	N/A	98.52
PRAD-2605	OE	5 cm	58.71	0.41	18.80	3.58	0.10	0.83	2.87	4.48	8.68	N/A	N/A	N/A	N/A	98.45
PRAD-2605	OE	5 cm	58.44	0.44	18.78	3.81	0.17	0.91	3.05	4.34	8.44	N/A	N/A	N/A	N/A	98.37
PRAD-2605	OE	5 cm	58.17	0.44	18.71	3.82	0.20	1.01	3.24	4.45	8.16	N/A	N/A	N/A	N/A	98.19
PRAD-2605	OE	5 cm	58.68	0.38	18.97	3.34	0.14	0.67	2.58	4.93	8.50	N/A	N/A	N/A	N/A	98.18
PRAD-2605	OE	5 cm	58.36	0.40	18.85	3.66	0.12	0.79	2.83	4.60	8.53	N/A	N/A	N/A	N/A	98.14
PRAD-2605	OE	5 cm	58.45	0.40	18.75	3.54	0.13	0.80	2.90	4.45	8.50	N/A	N/A	N/A	N/A	97.91
PRAD-2605	OE	5 cm	57.75	0.46	18.65	3.93	0.15	1.02	3.25	4.45	8.21	N/A	N/A	N/A	N/A	97.87
PRAD-2605	OE	5 cm	58.36	0.43	18.70	3.71	0.14	0.77	2.81	4.47	8.43	N/A	N/A	N/A	N/A	97.82
PRAD-2605	OE	5 cm	58.43	0.38	18.83	3.54	0.15	0.76	2.57	4.66	8.29	N/A	N/A	N/A	N/A	97.61
PRAD-2605	OE	5 cm	57.72	0.47	18.75	3.75	0.11	0.91	3.10	4.43	8.33	N/A	N/A	N/A	N/A	97.58
PRAD-2605	OE	5 cm	57.79	0.40	18.73	3.75	0.13	0.78	2.91	4.33	8.69	N/A	N/A	N/A	N/A	97.50
PRAD-2605	OE	5 cm	58.07	0.40	18.73	3.42	0.15	0.67	2.64	4.47	8.83	N/A	N/A	N/A	N/A	97.39
PRAD-2605	OE	5 cm	57.63	0.45	18.77	3.65	0.14	0.77	2.85	4.46	8.50	N/A	N/A	N/A	N/A	97.23
PRAD-2605	OE	5 cm	57.51	0.43	18.60	3.77	0.18	0.92	2.92	4.49	8.10	N/A	N/A	N/A	N/A	96.92
PRAD-2605	OE	5 cm	57.18	0.44	18.79	3.68	0.13	0.92	2.97	4.45	8.32	N/A	N/A	N/A	N/A	96.87
PRAD-2605	OE	5 cm	57.40	0.39	18.53	3.41	0.17	0.67	2.62	4.62	8.43	N/A	N/A	N/A	N/A	96.24
PRAD-2605	OE	5 cm	57.11	0.40	18.47	3.64	0.12	0.88	2.89	4.43	8.22	N/A	N/A	N/A	N/A	96.15
PRAD-2605	OE	5 cm	56.90	0.46	18.25	3.75	0.12	0.87	3.20	4.19	8.10	N/A	N/A	N/A	N/A	95.84
PRAD-2605	OE	5 cm	56.95	0.42	18.41	3.69	0.11	0.87	2.95	4.25	8.06	N/A	N/A	N/A	N/A	95.70

Name	Microprobe	Resolution	SiO_2	TiO_2	Al_2O_3	FeO	MnO	MgO	CaO	Na_2O	K_2O	P_2O_5	S	Cl	F	Total
PRAD-2605	OE	5 cm	56.80	0.40	18.32	3.64	0.10	0.90	2.95	4.35	8.23	N/A	N/A	N/A	N/A	95.69
PRAD-2605	OE	5 cm	57.17	0.42	18.29	3.47	0.12	0.74	2.73	4.33	8.25	N/A	N/A	N/A	N/A	95.53
PRAD-2605	OE	5 cm	56.42	0.42	17.98	3.71	0.11	0.86	2.91	4.35	8.21	N/A	N/A	N/A	N/A	94.98
PRAD-2605	OE	5 cm	56.74	0.37	18.43	3.28	0.19	0.68	2.57	4.55	7.83	N/A	N/A	N/A	N/A	94.64
PRAD-2812	OE	5 cm	60.54	0.50	18.66	3.07	0.32	0.25	1.66	7.06	6.22	N/A	N/A	N/A	N/A	98.28
PRAD-2812	OE	5 cm	60.33	0.43	18.33	2.81	0.18	0.46	1.81	5.39	7.90	N/A	N/A	N/A	N/A	97.63
PRAD-2812	OE	5 cm	60.44	0.37	18.25	2.89	0.12	0.46	1.80	5.55	7.52	N/A	N/A	N/A	N/A	97.40
PRAD-2812	OE	5 cm	60.00	0.48	18.24	2.99	0.36	0.25	1.54	6.79	6.32	N/A	N/A	N/A	N/A	96.98
PRAD-2812	OE	5 cm	60.10	0.46	18.10	2.80	0.18	0.45	1.81	5.33	7.70	N/A	N/A	N/A	N/A	96.94
PRAD-2812	OE	5 cm	60.09	0.44	18.15	2.79	0.17	0.44	1.67	5.72	7.37	N/A	N/A	N/A	N/A	96.82
PRAD-2812	OE	5 cm	59.65	0.49	18.35	2.94	0.33	0.31	1.64	6.65	6.35	N/A	N/A	N/A	N/A	96.71
PRAD-2812	OE	5 cm	59.58	0.48	18.38	2.85	0.30	0.30	1.62	6.44	6.75	N/A	N/A	N/A	N/A	96.69
PRAD-2812	OE	5 cm	59.69	0.45	18.21	2.86	0.29	0.31	1.63	6.36	6.75	N/A	N/A	N/A	N/A	96.53
PRAD-2812	OE	5 cm	59.35	0.48	18.26	3.01	0.32	0.30	1.63	6.62	6.35	N/A	N/A	N/A	N/A	96.32
PRAD-2812	OE	5 cm	60.08	0.42	18.02	2.64	0.17	0.40	1.71	5.68	7.13	N/A	N/A	N/A	N/A	96.25
PRAD-2812	OE	5 cm	59.61	0.44	18.01	2.73	0.22	0.39	1.75	5.40	7.48	N/A	N/A	N/A	N/A	96.04
PRAD-2812	OE	5 cm	59.73	0.39	17.96	2.72	0.19	0.38	1.68	5.79	7.07	N/A	N/A	N/A	N/A	95.91
PRAD-2812	OE	5 cm	59.55	0.45	18.12	2.90	0.27	0.32	1.59	6.38	6.31	N/A	N/A	N/A	N/A	95.89
PRAD-2812	OE	5 cm	59.43	0.44	18.15	2.72	0.21	0.47	1.77	5.09	7.58	N/A	N/A	N/A	N/A	95.85
PRAD-2812	OE	5 cm	59.54	0.42	17.92	2.79	0.20	0.42	1.69	5.45	7.33	N/A	N/A	N/A	N/A	95.73
PRAD-2812	OE	5 cm	59.32	0.44	18.06	2.79	0.23	0.40	1.65	5.55	7.14	N/A	N/A	N/A	N/A	95.58
PRAD-2812	OE	5 cm	59.60	0.40	18.05	2.63	0.21	0.37	1.61	5.30	7.26	N/A	N/A	N/A	N/A	95.45
PRAD-2812	OE	5 cm	58.93	0.49	18.00	2.96	0.32	0.27	1.63	6.53	6.33	N/A	N/A	N/A	N/A	95.43
PRAD-2812	OE	5 cm	59.31	0.43	18.01	2.65	0.20	0.43	1.73	5.38	7.17	N/A	N/A	N/A	N/A	95.30
PRAD-2812	OE	5 cm	58.92	0.48	17.92	2.84	0.28	0.31	1.55	6.44	6.46	N/A	N/A	N/A	N/A	95.19
PRAD-2812	OE	5 cm	59.08	0.39	17.90	2.73	0.21	0.46	1.73	5.20	7.38	N/A	N/A	N/A	N/A	95.07
PRAD-2812	OE	5 cm	59.04	0.44	17.89	2.76	0.14	0.45	1.73	4.98	7.51	N/A	N/A	N/A	N/A	94.95
PRAD-2812	OE	5 cm	59.14	0.47	17.90	2.65	0.18	0.42	1.70	5.35	7.09	N/A	N/A	N/A	N/A	94.89
PRAD-2812	OE	5 cm	54.26	0.68	18.49	4.33	0.12	1.16	3.91	4.15	7.76	N/A	N/A	N/A	N/A	94.85
PRAD-2812	OE	5 cm	58.76	0.38	17.77	2.64	0.21	0.39	1.69	5.25	7.25	N/A	N/A	N/A	N/A	94.35
PRAD-2812	OE	5 cm	58.89	0.40	17.65	2.65	0.19	0.42	1.73	4.85	7.37	N/A	N/A	N/A	N/A	94.16
PRAD-3225	E	5 cm	60.96	0.47	16.17	2.17	0.13	0.31	1.72	4.18	7.33	0.03	N/A	0.52	0.18	94.18
PRAD-3225	E	5 cm	57.67	0.56	18.75	3.00	0.19	0.49	2.90	5.15	8.72	0.10	N/A	0.51	0.19	98.21
PRAD-3225	E	5 cm	56.33	0.65	18.30	3.69	0.18	0.80	3.52	4.74	8.16	0.18	N/A	0.47	0.25	97.26
PRAD-3225	E	5 cm	57.22	0.67	19.14	4.31	0.19	0.90	4.21	5.03	7.87	0.23	N/A	0.49	0.20	100.45
PRAD-3225	E	5 cm	57.66	0.53	18.41	2.88	0.18	0.39	2.55	4.92	8.87	0.07	N/A	0.51	0.24	97.21
PRAD-3225	E	5 cm	57.18	0.54	18.31	2.55	0.18	0.36	2.28	5.21	8.28	0.05	N/A	0.53	0.24	95.72
PRAD-3225	E	5 cm	58.74	0.54	19.04	3.03	0.18	0.45	2.58	5.23	8.59	0.06	N/A	0.50	0.23	99.19
PRAD-3225	E	5 cm	57.95	0.54	18.45	2.59	0.18	0.40	2.37	5.21	8.28	0.06	N/A	0.50	0.21	96.73
PRAD-3225	E	5 cm	51.44	0.92	17.87	6.71	0.17	2.49	7.32	3.79	6.04	0.59	N/A	0.37	0.27	97.97
PRAD-3225	E	5 cm	54.84	0.79	18.81	4.99	0.18	1.48	5.00	4.38	7.24	0.38	N/A	0.43	0.22	98.75
PRAD-3225	E	5 cm	56.91	0.53	18.72	2.76	0.17	0.42	2.44	5.03	8.36	0.05	N/A	0.52	0.25	96.15
PRAD-3225	E	5 cm	51.15	1.02	18.02	7.85	0.19	3.01	8.16	3.48	5.65	0.70	N/A	0.30	0.24	99.77
PRAD-3225	E	5 cm	58.23	0.55	18.92	2.64	0.17	0.40	2.35	5.16	8.56	0.06	N/A	0.50	0.27	97.80
PRAD-3336	E	5 cm	56.57	0.70	19.45	4.02	0.15	1.03	3.51	5.19	7.81	0.20	0.04	0.46	0.18	99.33
PRAD-3336	E	5 cm	55.38	0.72	18.53	4.59	0.15	1.14	3.69	5.69	6.83	0.27	0.03	0.42	0.26	97.71
PRAD-3336	E	5 cm	57.28	0.61	20.01	2.63	0.16	0.40	2.23	5.90	9.13	0.08	0.03	0.59	0.24	99.30
PRAD-3336	E	5 cm	57.24	0.60	19.10	2.69	0.15	0.39	3.59	5.79	8.42	1.00	0.03	0.62	0.37	100.02
PRAD-3336	E	5 cm	56.08	0.58	18.67	2.77	0.15	0.45	2.38	5.75	8.21	0.08	0.05	0.62	0.23	96.00
PRAD-3336	E	5 cm	58.12	0.61	19.74	2.78	0.16	0.42	2.10	5.84	8.85	0.07	0.05	0.61	0.21	99.56
PRAD-3336	E	5 cm	59.33	0.57	19.50	2.70	0.15	0.40	2.37	5.89	8.25	0.05	0.12	0.61	0.18	100.13
PRAD-3336	E	5 cm	57.16	0.59	19.17	2.68	0.15	0.38	2.29	5.33	8.45	0.07	0.05	0.61	0.21	97.15
PRAD-3336	E	5 cm	57.37	0.59	19.31	2.91	0.17	0.39	2.29	5.58	8.57	0.09	0.03	0.62	0.23	98.15

Name	Microprobe	Resolution	SiO_2	TiO_2	Al_2O_3	FeO	MnO	MgO	CaO	Na_2O	K_2O	P_2O_5	S	Cl	F	Total
PRAD-3336	E	5 cm	56.84	0.59	18.76	2.88	0.15	0.39	2.24	5.57	8.34	0.07	0.02	0.63	0.24	96.72
PRAD-3383	E	5 cm	58.52	0.60	18.87	3.92	0.15	0.97	3.58	4.65	7.78	0.19	0.05	0.43	0.17	99.88
PRAD-3383	E	5 cm	56.32	0.62	18.47	4.29	0.15	1.02	3.51	4.29	7.48	0.23	0.05	0.42	0.19	97.04
PRAD-3383	E	5 cm	57.16	0.65	18.84	4.12	0.15	1.05	3.47	4.50	8.07	0.24	0.03	0.43	0.18	98.89
PRAD-3383	E	5 cm	56.98	0.62	18.81	4.39	0.15	1.06	3.66	4.36	7.80	0.23	0.10	0.49	0.16	98.80
PRAD-3383	E	5 cm	57.66	0.59	18.73	3.98	0.15	0.89	3.46	4.62	7.99	0.18	0.09	0.43	0.19	98.98
PRAD-3383	E	5 cm	57.21	0.63	18.33	4.20	0.15	1.04	3.66	4.21	7.67	0.23	0.11	0.46	0.16	98.05
PRAD-3383	E	5 cm	57.16	0.64	18.54	4.26	0.15	1.09	3.84	4.37	7.49	0.36	0.09	0.44	0.18	98.62
PRAD-3383	E	5 cm	57.18	0.57	18.12	3.47	0.14	0.90	3.17	4.26	7.88	0.19	0.06	0.44	0.18	96.55
PRAD-3383	E	5 cm	52.09	0.58	16.62	4.01	0.12	0.92	3.32	4.06	6.69	0.20	0.10	0.48	0.17	89.35
PRAD-3383	E	5 cm	56.74	0.64	18.39	4.35	0.14	1.11	3.80	4.15	7.79	0.24	0.10	0.44	0.20	98.11
PRAD-3383	E	5 cm	57.32	0.64	18.08	4.25	0.14	1.15	3.76	4.40	7.84	0.23	0.08	0.44	0.21	98.53
PRAD-3472	E	5 cm	61.17	0.55	17.82	3.36	0.13	0.86	3.10	4.34	7.48	0.14	0.20	0.39	0.15	99.69
PRAD-3472	E	5 cm	61.70	0.46	16.42	2.06	0.14	0.40	1.87	4.56	7.66	0.05	0.11	0.47	0.15	96.05
PRAD-3472	E	5 cm	60.50	0.46	17.02	2.30	0.14	0.38	1.96	4.45	7.39	0.07	0.12	0.45	0.14	95.38
PRAD-3472	E	5 cm	61.86	0.51	17.18	2.39	0.18	0.29	1.61	6.00	6.56	0.04	0.02	0.69	0.29	97.63
PRAD-3472	E	5 cm	61.10	0.47	17.13	2.53	0.12	0.48	2.02	4.26	7.51	0.08	0.12	0.41	0.16	96.39
PRAD-3472	E	5 cm	60.77	0.46	16.18	2.03	0.14	0.28	1.64	4.53	7.16	0.05	0.10	0.53	0.16	94.01
PRAD-3472	E	5 cm	61.55	0.46	17.09	2.26	0.14	0.34	1.74	4.62	7.46	0.05	0.11	0.51	0.15	96.48
PRAD-3472	E	5 cm	60.31	0.52	17.26	2.58	0.14	0.45	1.94	4.46	7.59	0.10	0.02	0.46	0.21	96.03
PRAD-3472	E	5 cm	60.69	0.62	18.17	3.49	0.12	0.90	3.04	4.37	7.53	0.19	0.22	0.36	0.15	99.86
PRAD-3472	E	5 cm	62.17	0.49	16.51	2.54	0.13	0.53	2.07	4.33	7.61	0.08	0.05	0.46	0.16	97.15
PRAD-3472	E	5 cm	61.46	0.52	17.75	3.33	0.12	0.71	2.81	4.40	7.90	0.14	0.16	0.40	0.16	99.86
PRAD-3586	E	5 cm	57.81	0.55	18.71	2.97	0.15	0.53	3.06	3.75	9.77	0.09	0.20	0.06	0.34	97.99
PRAD-3586	E	5 cm	55.55	0.61	18.80	4.84	0.15	1.19	5.19	2.72	9.19	0.22	0.27	0.06	0.30	99.08
PRAD-3586	E	5 cm	58.11	0.55	18.96	2.23	0.14	0.32	2.56	4.31	9.61	0.03	0.20	0.09	0.43	97.52
PRAD-3586	E	5 cm	57.20	0.53	18.61	2.20	0.16	0.29	2.24	3.66	9.75	0.03	0.13	0.09	0.45	95.35
PRAD-3586	E	5 cm	58.21	0.55	18.62	2.29	0.16	0.27	2.44	3.97	10.10	0.04	0.20	0.08	0.42	97.34
PRAD-3586	E	5 cm	57.33	0.54	17.96	2.26	0.16	0.31	2.37	3.82	9.88	0.03	0.13	0.09	0.44	95.34
PRAD-3586	E	5 cm	58.55	0.56	19.76	2.54	0.16	0.31	2.48	4.21	10.17	0.04	0.20	0.08	0.45	99.51
PRAD-3586	E	5 cm	55.98	0.58	18.57	3.85	0.15	0.96	4.30	3.23	9.87	0.17	0.27	0.06	0.25	98.24
PRAD-3586	E	5 cm	56.51	0.54	17.95	3.08	0.15	0.58	3.14	3.19	9.77	0.10	0.25	0.06	0.33	95.64
PRAD-3586	E	5 cm	57.00	0.54	17.99	2.87	0.16	0.49	2.90	3.57	9.50	0.06	0.21	0.08	0.30	95.67
PRAD-3666	E	5 cm	56.94	0.56	19.16	3.73	0.15	0.70	3.50	4.18	9.49	0.11	0.27	0.16	0.60	99.55
PRAD-3666	E	5 cm	57.37	0.56	18.29	3.59	0.15	0.74	3.52	4.35	9.02	0.10	0.20	0.16	0.57	98.61
PRAD-3666	E	5 cm	56.59	0.55	19.18	3.36	0.15	0.61	3.20	4.31	9.16	0.09	0.18	0.19	0.64	98.23
PRAD-3666	E	5 cm	59.11	0.57	19.46	3.73	0.14	0.73	3.41	4.22	8.99	0.09	0.11	0.16	0.60	101.33
PRAD-3666	E	5 cm	56.63	0.55	18.81	3.53	0.13	0.67	3.45	4.31	9.07	0.09	0.23	0.17	0.60	98.24
PRAD-3666	E	5 cm	57.25	0.56	19.27	3.59	0.15	0.60	3.45	4.35	9.23	0.09	0.22	0.17	0.61	99.55
PRAD-3666	E	5 cm	56.35	0.56	18.61	3.73	0.15	0.73	3.38	4.22	8.74	0.10	0.20	0.18	0.57	97.50
PRAD-3666	E	5 cm	57.87	0.58	19.07	3.72	0.14	0.69	3.48	4.16	9.53	0.11	0.21	0.15	0.54	100.27
PRAD-3666	E	5 cm	58.10	0.56	19.06	3.50	0.14	0.66	3.16	4.08	9.32	0.10	0.19	0.14	0.58	99.57
PRAD-3666	E	5 cm	57.02	0.55	18.79	3.62	0.14	0.67	3.30	4.15	9.20	0.09	0.18	0.17	0.53	98.41

SA03-03 Major Element data generated in this study. The sample name, microprobe the analyses were carried out on and sampling resolution are all indicated. Microprobe: OE = Oxford Earth Sciences, OA = Oxford Archaeology and E – Edinburgh.

Name	Microprobe	Resolution	SiO_2	TiO_2	Al_2O_3	FeO	MnO	MgO	CaO	Na_2O	K_2O	P_2O_5	S	Cl	F	Total
SA03-03-25	E	5 cm	58.02	0.37	18.47	3.63	0.18	0.27	3.06	4.49	8.68	0.06	0.02	0.81	0.28	98.33
SA03-03-25	E	5 cm	58.64	0.37	18.28	3.72	0.18	0.30	3.15	4.45	8.57	0.06	0.02	0.83	0.24	98.82
SA03-03-25	E	5 cm	58.67	0.38	18.69	3.47	0.18	0.28	2.85	4.73	8.81	0.05	0.02	0.81	0.37	99.31
SA03-03-25	E	5 cm	58.03	0.45	18.57	4.17	0.17	0.48	3.75	4.35	8.44	0.05	0.01	0.76	0.28	99.51
SA03-03-25	E	5 cm	57.71	0.37	18.13	3.54	0.16	0.26	3.16	4.38	8.59	0.06	0.01	0.80	0.20	97.38
SA03-03-25	E	5 cm	58.00	0.37	18.24	3.47	0.17	0.27	3.18	4.49	8.31	0.05	0.02	0.79	0.27	97.63
SA03-03-25	E	5 cm	58.77	0.39	18.44	3.58	0.17	0.34	2.98	4.52	9.34	0.07	0.02	0.80	0.23	99.64
SA03-03-25	E	5 cm	59.04	0.38	18.22	3.77	0.18	0.33	3.29	4.34	8.59	0.06	0.02	0.83	0.24	99.29
SA03-03-25	E	5 cm	57.40	0.35	18.26	3.67	0.16	0.26	3.29	4.47	7.95	0.05	0.01	0.83	0.28	97.00
SA03-03-25	E	5 cm	57.89	0.35	18.23	3.54	0.15	0.24	2.69	5.20	9.42	0.05	0.01	0.83	0.10	98.68
SA03-03-80	E	5 cm	61.26	0.35	18.13	3.08	0.16	0.34	2.82	4.11	8.01	0.05	0.01	0.68	0.24	99.22
SA03-03-80	E	5 cm	59.84	0.37	17.67	2.99	0.17	0.32	2.75	4.45	8.06	0.06	0.01	0.70	0.25	97.63
SA03-03-80	E	5 cm	61.81	0.34	18.36	2.63	0.16	0.24	2.58	4.30	8.61	0.04	0.02	0.71	0.26	100.04
SA03-03-80	E	5 cm	60.74	0.35	17.68	2.71	0.17	0.30	2.72	4.27	8.14	0.06	0.01	0.71	0.27	98.14
SA03-03-80	E	5 cm	60.73	0.34	17.70	2.67	0.16	0.27	2.61	4.41	8.12	0.04	0.00	0.73	0.27	98.06
SA03-03-80	E	5 cm	60.61	0.36	18.16	2.95	0.18	0.30	2.64	4.56	8.05	0.05	0.01	0.73	0.25	98.85
SA03-03-80	E	5 cm	59.95	0.35	17.67	2.85	0.16	0.35	2.75	4.34	7.91	0.05	0.01	0.73	0.24	97.35
SA03-03-80	E	5 cm	61.72	0.35	18.13	3.06	0.17	0.34	2.76	4.29	8.22	0.06	0.02	0.68	0.23	100.01
SA03-03-80	E	5 cm	61.36	0.36	17.91	2.76	0.17	0.34	2.68	4.43	8.10	0.04	0.01	0.71	0.25	99.12
SA03-03-80	E	5 cm	60.92	0.35	17.86	3.43	0.15	0.34	2.92	3.61	8.54	0.07	0.02	0.71	0.17	99.08
SA03-03 383	OA	1 cm	59.34	0.37	17.49	3.57	0.03	0.78	2.92	3.79	9.10	N/A	N/A	N/A	N/A	97.38
SA03-03 383	OA	1 cm	54.80	0.66	17.85	5.08	0.22	1.07	4.77	4.55	6.97	N/A	N/A	N/A	N/A	95.97
SA03-03 383	OA	1 cm	57.54	0.54	16.90	4.23	0.24	1.13	3.50	3.57	8.23	N/A	N/A	N/A	N/A	95.88
SA03-03 383	OA	1 cm	65.06	0.15	14.73	2.01	0.18	0.10	2.11	4.39	6.96	N/A	N/A	N/A	N/A	95.67
SA03-03 383	OA	1 cm	58.38	0.45	17.26	3.26	0.14	0.50	2.20	5.01	8.38	N/A	N/A	N/A	N/A	95.58
SA03-03 383	OA	1 cm	59.31	0.40	16.98	3.40	0.11	0.70	2.51	3.51	8.51	N/A	N/A	N/A	N/A	95.43
SA03-03 383	OA	1 cm	64.05	0.12	15.75	1.81	0.11	0.13	2.09	4.31	6.55	N/A	N/A	N/A	N/A	94.92
SA03-03 383	OA	1 cm	63.96	0.17	15.58	1.78	0.15	0.14	1.98	4.22	6.64	N/A	N/A	N/A	N/A	94.61
SA03-03 392	OA	1 cm	60.79	0.56	19.06	2.87	0.43	0.25	0.96	8.06	6.26	N/A	N/A	N/A	N/A	99.24
SA03-03 392	OA	1 cm	61.22	0.36	18.25	3.17	0.10	0.58	1.33	4.72	8.41	N/A	N/A	N/A	N/A	98.13
SA03-03 392	OA	1 cm	61.12	0.51	17.87	2.43	0.19	0.34	1.26	7.25	6.73	N/A	N/A	N/A	N/A	97.71
SA03-03 392	OA	1 cm	60.14	0.47	18.01	2.92	0.24	0.34	1.68	6.95	6.91	N/A	N/A	N/A	N/A	97.64
SA03-03 392	OA	1 cm	60.30	0.43	18.38	2.83	0.21	0.32	1.63	6.09	6.95	N/A	N/A	N/A	N/A	97.15
SA03-03 392	OA	1 cm	61.64	0.34	17.75	3.30	0.12	0.55	1.29	3.44	8.40	N/A	N/A	N/A	N/A	96.82
SA03-03 392	OA	1 cm	61.64	0.53	18.07	2.34	0.12	0.38	1.24	5.63	6.70	N/A	N/A	N/A	N/A	96.65
SA03-03 392	OA	1 cm	59.89	0.39	17.69	2.87	0.27	0.35	1.65	6.30	7.03	N/A	N/A	N/A	N/A	96.46
SA03-03 392	OA	1 cm	63.38	0.16	16.37	1.48	0.20	0.14	1.99	4.24	6.70	N/A	N/A	N/A	N/A	94.65
SA03-03 392	OA	1 cm	63.32	0.19	16.10	1.62	0.15	0.10	1.99	4.33	6.74	N/A	N/A	N/A	N/A	94.55
SA03-03 392	OA	1 cm	63.71	0.07	16.11	1.60	0.08	0.15	1.99	4.18	6.62	N/A	N/A	N/A	N/A	94.51
SA03-03 399	OA	1 cm	62.10	0.38	17.06	2.87	0.16	0.45	2.01	5.70	7.36	N/A	N/A	N/A	N/A	98.09
SA03-03 399	OA	1 cm	59.82	0.41	17.19	2.69	0.25	0.30	1.76	6.48	7.65	N/A	N/A	N/A	N/A	96.56
SA03-03 399	OA	1 cm	59.64	0.37	16.70	3.19	0.13	0.72	2.39	3.87	9.40	N/A	N/A	N/A	N/A	96.41
SA03-03 399	OA	1 cm	61.00	0.45	18.00	2.94	0.24	0.30	1.68	4.37	7.20	N/A	N/A	N/A	N/A	96.19
SA03-03 399	OA	1 cm	60.18	0.43	17.31	2.57	0.23	0.30	1.63	6.37	7.11	N/A	N/A	N/A	N/A	96.12
SA03-03 399	OA	1 cm	59.37	0.41	16.51	2.91	0.24	0.31	1.70	6.71	7.18	N/A	N/A	N/A	N/A	95.34
SA03-03 399	OA	1 cm	63.99	0.14	15.54	1.63	0.12	0.15	1.96	4.17	7.26	N/A	N/A	N/A	N/A	94.96
SA03-03 399	OA	1 cm	59.19	0.43	17.34	2.84	0.21	0.40	1.70	5.80	6.84	N/A	N/A	N/A	N/A	94.73
SA03-03 399	OA	1 cm	58.45	0.49	16.93	3.05	0.20	0.34	1.60	6.62	6.85	N/A	N/A	N/A	N/A	94.52
SA03-03 407	OA	1 cm	60.93	0.47	17.95	2.94	0.18	0.32	1.69	6.72	7.04	N/A	N/A	N/A	N/A	98.24

Name	Microprobe	Resolution	SiO_2	TiO_2	Al_2O_3	FeO	MnO	MgO	CaO	Na_2O	K_2O	P_2O_5	S	Cl	F	Total
SA03-03 407	OA	1 cm	60.30	0.43	18.14	3.05	0.20	0.31	1.87	5.98	7.60	N/A	N/A	N/A	N/A	97.88
SA03-03 407	OA	1 cm	57.45	0.42	19.39	3.80	0.16	0.28	2.13	6.71	7.49	N/A	N/A	N/A	N/A	97.84
SA03-03 407	OA	1 cm	60.51	0.40	18.07	3.04	0.18	0.31	1.71	6.41	6.97	N/A	N/A	N/A	N/A	97.57
SA03-03 407	OA	1 cm	60.42	0.47	17.60	2.85	0.27	0.28	1.74	6.09	7.73	N/A	N/A	N/A	N/A	97.45
SA03-03 407	OA	1 cm	60.16	0.49	17.55	2.99	0.28	0.29	1.65	6.67	6.92	N/A	N/A	N/A	N/A	97.00
SA03-03 407	OA	1 cm	60.53	0.38	17.86	2.78	0.18	0.44	1.99	5.04	7.35	N/A	N/A	N/A	N/A	96.54
SA03-03 407	OA	1 cm	60.04	0.40	17.73	2.87	0.15	0.30	1.84	6.27	6.88	N/A	N/A	N/A	N/A	96.48
SA03-03 407	OA	1 cm	59.44	0.44	17.96	2.92	0.23	0.28	1.61	6.76	6.74	N/A	N/A	N/A	N/A	96.37
SA03-03 407	OA	1 cm	59.81	0.40	17.20	3.21	0.19	0.64	2.38	4.26	8.28	N/A	N/A	N/A	N/A	96.37
SA03-03 407	OA	1 cm	59.40	0.46	17.25	2.94	0.25	0.34	1.81	6.79	6.86	N/A	N/A	N/A	N/A	96.09
SA03-03 407	OA	1 cm	59.06	0.35	17.59	3.35	0.04	0.72	2.41	3.55	9.01	N/A	N/A	N/A	N/A	96.06
SA03-03 407	OA	1 cm	59.20	0.45	17.52	3.00	0.27	0.33	1.73	6.25	7.30	N/A	N/A	N/A	N/A	96.05
SA03-03 407	OA	1 cm	59.51	0.46	17.24	2.87	0.18	0.33	1.72	6.05	7.47	N/A	N/A	N/A	N/A	95.83
SA03-03 407	OA	1 cm	59.07	0.40	17.78	2.81	0.21	0.31	1.71	6.35	6.81	N/A	N/A	N/A	N/A	95.44
SA03-03 407	OA	1 cm	59.12	0.42	17.53	2.90	0.20	0.31	1.69	6.34	6.89	N/A	N/A	N/A	N/A	95.39
SA03-03 407	OA	1 cm	59.31	0.40	17.30	2.69	0.26	0.33	1.63	6.29	6.83	N/A	N/A	N/A	N/A	95.05
SA03-03 407	OA	1 cm	58.76	0.42	17.70	2.52	0.24	0.28	1.68	6.11	6.99	N/A	N/A	N/A	N/A	94.69
SA03-03 407	OA	1 cm	58.57	0.36	16.82	3.21	0.09	0.67	2.41	3.05	9.45	N/A	N/A	N/A	N/A	94.63
SA03-03 413	OA	1 cm	60.20	0.41	17.57	2.90	0.23	0.34	1.76	6.96	7.16	N/A	N/A	N/A	N/A	97.53
SA03-03 413	OA	1 cm	60.67	0.39	17.65	3.01	0.10	0.35	1.73	6.87	7.15	N/A	N/A	N/A	N/A	97.92
SA03-03 413	OA	1 cm	60.23	0.46	17.74	2.79	0.27	0.33	1.70	6.75	6.97	N/A	N/A	N/A	N/A	97.24
SA03-03 413	OA	1 cm	60.69	0.44	17.78	2.93	0.24	0.35	1.81	6.74	7.32	N/A	N/A	N/A	N/A	98.30
SA03-03 413	OA	1 cm	60.69	0.48	17.54	2.97	0.14	0.31	1.84	6.71	7.11	N/A	N/A	N/A	N/A	97.79
SA03-03 413	OA	1 cm	60.48	0.43	17.79	2.90	0.24	0.29	1.79	6.69	7.24	N/A	N/A	N/A	N/A	97.84
SA03-03 413	OA	1 cm	60.62	0.42	17.95	2.99	0.21	0.32	1.78	6.61	7.02	N/A	N/A	N/A	N/A	97.92
SA03-03 413	OA	1 cm	61.10	0.41	17.82	2.92	0.11	0.34	1.71	6.57	7.56	N/A	N/A	N/A	N/A	98.55
SA03-03 413	OA	1 cm	60.84	0.47	18.85	2.97	0.28	0.30	1.76	6.56	7.17	N/A	N/A	N/A	N/A	99.19
SA03-03 413	OA	1 cm	60.84	0.40	17.83	3.02	0.32	0.31	1.64	6.55	7.02	N/A	N/A	N/A	N/A	97.92
SA03-03 413	OA	1 cm	60.26	0.43	17.36	2.92	0.29	0.32	1.69	6.55	6.96	N/A	N/A	N/A	N/A	96.78
SA03-03 413	OA	1 cm	60.95	0.46	17.81	3.08	0.12	0.32	1.49	6.47	7.22	N/A	N/A	N/A	N/A	97.92
SA03-03 413	OA	1 cm	60.22	0.41	17.39	2.83	0.28	0.32	1.71	6.40	7.41	N/A	N/A	N/A	N/A	96.97
SA03-03 413	OA	1 cm	60.76	0.52	17.71	2.91	0.13	0.32	1.81	6.27	7.30	N/A	N/A	N/A	N/A	97.72
SA03-03 413	OA	1 cm	60.41	0.43	17.32	2.96	0.22	0.31	1.76	6.26	7.47	N/A	N/A	N/A	N/A	97.15
SA03-03 413	OA	1 cm	60.41	0.49	17.20	3.21	0.23	0.29	1.71	6.18	7.66	N/A	N/A	N/A	N/A	97.38
SA03-03 413	OA	1 cm	60.72	0.34	17.05	2.60	0.18	0.40	1.79	6.17	7.28	N/A	N/A	N/A	N/A	96.55
SA03-03 413	OA	1 cm	61.48	0.45	16.92	2.88	0.14	0.36	1.76	6.06	7.31	N/A	N/A	N/A	N/A	97.36
SA03-03 413	OA	1 cm	60.47	0.42	17.86	3.08	0.13	0.34	1.74	6.04	7.64	N/A	N/A	N/A	N/A	97.73
SA03-03 413	OA	1 cm	59.42	0.42	16.47	3.01	0.31	0.31	1.64	6.03	7.38	N/A	N/A	N/A	N/A	94.99
SA03-03 413	OA	1 cm	59.28	0.50	17.31	2.82	0.26	0.30	1.63	6.02	7.00	N/A	N/A	N/A	N/A	95.13
SA03-03 413	OA	1 cm	61.29	0.45	17.73	2.67	0.17	0.37	1.75	5.77	7.46	N/A	N/A	N/A	N/A	97.64
SA03-03 413	OA	1 cm	60.92	0.38	16.99	3.01	0.25	0.58	2.34	4.84	8.30	N/A	N/A	N/A	N/A	97.61
SA03-03 413	OA	1 cm	58.77	0.38	16.28	3.02	0.05	0.63	2.41	4.59	7.57	N/A	N/A	N/A	N/A	93.70
SA03-03 413	OA	1 cm	59.98	0.35	16.59	3.37	0.14	0.62	2.26	4.48	8.76	N/A	N/A	N/A	N/A	96.55
SA03-03 413	OA	1 cm	60.38	0.37	16.87	3.16	0.00	0.60	2.40	4.07	9.41	N/A	N/A	N/A	N/A	97.26
SA03-03 413	OA	1 cm	59.50	0.34	16.92	2.97	0.08	0.57	2.26	3.59	9.24	N/A	N/A	N/A	N/A	95.47
SA03-03 413	OA	1 cm	59.27	0.38	17.08	3.38	0.10	0.68	2.52	3.48	9.58	N/A	N/A	N/A	N/A	96.46
SA03-03 413	OA	1 cm	57.93	0.35	17.26	3.53	0.14	0.75	2.63	2.76	9.77	N/A	N/A	N/A	N/A	95.10
SA03-03 418	OA	1 cm	60.24	0.44	17.82	3.05	0.35	0.33	1.82	6.64	7.58	N/A	N/A	N/A	N/A	98.27
SA03-03 418	OA	1 cm	60.61	0.44	17.92	2.81	0.19	0.34	1.82	6.78	7.18	N/A	N/A	N/A	N/A	98.11
SA03-03 418	OA	1 cm	60.71	0.47	17.54	3.20	0.24	0.30	1.75	6.61	7.07	N/A	N/A	N/A	N/A	97.89
SA03-03 418	OA	1 cm	60.44	0.41	17.38	2.96	0.08	0.61	2.41	3.77	9.62	N/A	N/A	N/A	N/A	97.68
SA03-03 418	OA	1 cm	60.77	0.40	17.56	2.91	0.33	0.30	1.70	6.07	7.61	N/A	N/A	N/A	N/A	97.63
SA03-03 418	OA	1 cm	60.76	0.43	17.26	3.09	0.32	0.35	1.68	6.27	7.39	N/A	N/A	N/A	N/A	97.54
SA03-03 418	OA	1 cm	60.56	0.42	17.54	2.84	0.15	0.31	1.71	6.65	7.30	N/A	N/A	N/A	N/A	97.48
SA03-03 418	OA	1 cm	61.04	0.33	17.36	2.88	0.11	0.44	1.85	5.83	7.59	N/A	N/A	N/A	N/A	97.43
SA03-03 418	OA	1 cm	60.26	0.43	17.99	2.69	0.27	0.39	1.85	5.57	7.68	N/A	N/A	N/A	N/A	97.14

Name	Microprobe	Resolution	SiO_2	TiO_2	Al_2O_3	FeO	MnO	MgO	CaO	Na_2O	K_2O	P_2O_5	S	Cl	F	Total
SA03-03 418	OA	1 cm	60.40	0.43	17.78	2.79	0.23	0.30	1.64	6.64	6.79	N/A	N/A	N/A	N/A	96.98
SA03-03 418	OA	1 cm	59.90	0.42	17.41	2.94	0.26	0.33	1.62	6.90	7.07	N/A	N/A	N/A	N/A	96.85
SA03-03 418	OA	1 cm	60.11	0.43	17.43	2.81	0.23	0.31	1.75	6.61	6.98	N/A	N/A	N/A	N/A	96.64
SA03-03 418	OA	1 cm	59.53	0.37	17.47	2.98	0.26	0.32	1.81	6.40	7.10	N/A	N/A	N/A	N/A	96.24
SA03-03 418	OA	1 cm	59.61	0.41	17.79	2.71	0.20	0.25	1.66	6.54	7.05	N/A	N/A	N/A	N/A	96.23
SA03-03 418	OA	1 cm	59.48	0.44	17.51	2.91	0.24	0.33	1.74	6.30	7.05	N/A	N/A	N/A	N/A	96.00
SA03-03 418	OA	1 cm	58.96	0.40	17.19	3.54	0.08	0.69	2.38	3.92	8.76	N/A	N/A	N/A	N/A	95.91
SA03-03 418	OA	1 cm	59.06	0.33	16.91	3.43	0.04	0.85	2.61	2.96	9.69	N/A	N/A	N/A	N/A	95.87
SA03-03 418	OA	1 cm	59.47	0.42	17.49	2.78	0.24	0.34	1.71	6.31	7.09	N/A	N/A	N/A	N/A	95.85
SA03-03 418	OA	1 cm	59.36	0.44	17.29	3.10	0.21	0.31	1.63	6.55	6.86	N/A	N/A	N/A	N/A	95.73
SA03-03 418	OA	1 cm	58.82	0.40	16.80	3.60	0.07	0.77	2.52	3.24	9.52	N/A	N/A	N/A	N/A	95.72
SA03-03 418	OA	1 cm	59.36	0.42	17.49	2.74	0.12	0.30	1.65	6.33	7.23	N/A	N/A	N/A	N/A	95.65
SA03-03 418	OA	1 cm	59.27	0.44	17.44	2.81	0.18	0.31	1.66	6.42	7.02	N/A	N/A	N/A	N/A	95.54
SA03-03 418	OA	1 cm	58.91	0.45	17.38	2.76	0.31	0.32	1.64	6.62	7.05	N/A	N/A	N/A	N/A	95.43
SA03-03 418	OA	1 cm	58.83	0.39	17.23	2.92	0.19	0.30	1.71	6.92	6.91	N/A	N/A	N/A	N/A	95.39
SA03-03 418	OA	1 cm	59.16	0.44	17.23	2.86	0.12	0.33	1.70	6.44	6.86	N/A	N/A	N/A	N/A	95.13
SA03-03 418	OA	1 cm	59.22	0.32	16.42	3.06	0.18	0.64	2.28	3.82	9.15	N/A	N/A	N/A	N/A	95.09
SA03-03 418	OA	1 cm	59.05	0.46	16.88	3.02	0.24	0.30	1.69	6.05	7.10	N/A	N/A	N/A	N/A	94.79
SA03-03 424	OA	1 cm	59.94	0.35	17.87	3.00	0.20	0.34	1.72	6.48	7.55	N/A	N/A	N/A	N/A	97.44
SA03-03 424	OA	1 cm	61.14	0.37	17.42	2.83	0.14	0.35	1.68	5.71	7.66	N/A	N/A	N/A	N/A	97.30
SA03-03 424	OA	1 cm	60.04	0.42	17.40	2.97	0.31	0.33	1.73	6.19	7.65	N/A	N/A	N/A	N/A	97.04
SA03-03 424	OA	1 cm	59.88	0.42	17.59	2.90	0.21	0.31	1.77	6.81	7.15	N/A	N/A	N/A	N/A	97.03
SA03-03 424	OA	1 cm	60.37	0.46	17.32	3.02	0.19	0.30	1.60	6.09	7.41	N/A	N/A	N/A	N/A	96.77
SA03-03 424	OA	1 cm	59.75	0.44	17.24	2.99	0.12	0.32	1.72	6.59	7.59	N/A	N/A	N/A	N/A	96.75
SA03-03 424	OA	1 cm	60.45	0.45	17.28	2.88	0.21	0.34	1.88	5.74	7.45	N/A	N/A	N/A	N/A	96.68
SA03-03 424	OA	1 cm	59.77	0.43	17.18	2.99	0.12	0.33	1.67	6.51	7.60	N/A	N/A	N/A	N/A	96.60
SA03-03 424	OA	1 cm	60.12	0.40	17.15	2.92	0.20	0.34	1.83	5.97	7.55	N/A	N/A	N/A	N/A	96.48
SA03-03 424	OA	1 cm	59.73	0.34	17.06	2.80	0.24	0.36	1.83	5.87	7.28	N/A	N/A	N/A	N/A	95.50
SA03-03 424	OA	1 cm	59.18	0.40	17.22	3.14	0.16	0.30	1.76	6.42	6.90	N/A	N/A	N/A	N/A	95.48
SA03-03 424	OA	1 cm	58.87	0.45	17.38	3.31	0.27	0.32	1.67	6.45	6.73	N/A	N/A	N/A	N/A	95.45
SA03-03 424	OA	1 cm	58.88	0.35	17.54	2.94	0.19	0.29	1.79	6.45	6.96	N/A	N/A	N/A	N/A	95.40
SA03-03 424	OA	1 cm	59.01	0.41	17.00	3.03	0.16	0.33	1.72	6.24	7.48	N/A	N/A	N/A	N/A	95.39
SA03-03 424	OA	1 cm	46.16	0.04	29.40	0.80	0.06	0.14	16.68	1.61	0.47	N/A	N/A	N/A	N/A	95.36
SA03-03 424	OA	1 cm	58.98	0.48	17.22	3.15	0.20	0.27	1.75	6.38	6.91	N/A	N/A	N/A	N/A	95.35
SA03-03 424	OA	1 cm	59.52	0.37	16.39	3.19	0.11	0.59	2.07	5.63	7.47	N/A	N/A	N/A	N/A	95.33
SA03-03 424	OA	1 cm	59.36	0.38	16.91	3.23	0.26	0.36	1.61	6.53	6.63	N/A	N/A	N/A	N/A	95.28
SA03-03 424	OA	1 cm	59.10	0.42	16.96	2.82	0.28	0.32	1.82	6.10	7.23	N/A	N/A	N/A	N/A	95.04
SA03-03 424	OA	1 cm	58.88	0.44	17.38	2.77	0.14	0.29	1.78	5.96	7.01	N/A	N/A	N/A	N/A	94.65
SA03-03 424	OA	1 cm	59.28	0.41	16.02	3.10	0.17	0.44	1.82	5.79	7.58	N/A	N/A	N/A	N/A	94.61
SA03-03 424	OA	1 cm	58.77	0.42	17.06	2.87	0.27	0.32	1.70	6.16	6.98	N/A	N/A	N/A	N/A	94.54
SA03-03 427	OA	1 cm	61.26	0.48	18.34	2.89	0.19	0.35	1.65	6.68	7.30	N/A	N/A	N/A	N/A	99.13
SA03-03 427	OA	1 cm	60.98	0.42	18.76	2.95	0.18	0.33	1.67	6.55	7.10	N/A	N/A	N/A	N/A	98.93
SA03-03 427	OA	1 cm	62.40	0.33	18.18	2.32	0.19	0.34	2.53	5.13	7.20	N/A	N/A	N/A	N/A	98.61
SA03-03 427	OA	1 cm	64.48	0.11	18.29	0.40	0.05	0.00	1.42	4.90	8.96	N/A	N/A	N/A	N/A	98.60
SA03-03 427	OA	1 cm	60.60	0.39	18.08	3.07	0.18	0.33	1.71	6.64	7.30	N/A	N/A	N/A	N/A	98.31
SA03-03 427	OA	1 cm	61.01	0.42	17.81	2.84	0.31	0.30	1.66	6.56	7.24	N/A	N/A	N/A	N/A	98.14
SA03-03 427	OA	1 cm	60.67	0.48	18.08	3.11	0.18	0.35	1.74	6.34	7.21	N/A	N/A	N/A	N/A	98.14
SA03-03 427	OA	1 cm	60.92	0.42	17.74	2.94	0.22	0.29	1.69	6.67	6.98	N/A	N/A	N/A	N/A	97.89
SA03-03 427	OA	1 cm	56.72	0.68	17.11	5.64	0.22	1.44	3.84	4.05	7.94	N/A	N/A	N/A	N/A	97.64
SA03-03 427	OA	1 cm	60.58	0.36	17.32	3.06	0.32	0.32	1.78	6.50	7.17	N/A	N/A	N/A	N/A	97.41
SA03-03 427	OA	1 cm	60.17	0.46	17.73	2.79	0.21	0.34	1.69	7.06	6.93	N/A	N/A	N/A	N/A	97.39
SA03-03 427	OA	1 cm	60.29	0.46	17.70	2.85	0.18	0.30	1.76	6.72	6.98	N/A	N/A	N/A	N/A	97.24
SA03-03 427	OA	1 cm	60.07	0.43	17.70	2.83	0.28	0.32	1.67	6.71	7.17	N/A	N/A	N/A	N/A	97.19
SA03-03 427	OA	1 cm	59.66	0.44	17.64	3.17	0.34	0.32	1.52	7.04	7.05	N/A	N/A	N/A	N/A	97.18
SA03-03 427	OA	1 cm	60.24	0.43	17.97	2.80	0.33	0.27	1.72	6.48	6.86	N/A	N/A	N/A	N/A	97.10
SA03-03 427	OA	1 cm	60.10	0.44	17.64	2.83	0.16	0.30	1.69	6.77	7.09	N/A	N/A	N/A	N/A	97.00

Name	Microprobe	Resolution	SiO_2	TiO_2	Al_2O_3	FeO	MnO	MgO	CaO	Na_2O	K_2O	P_2O_5	S	Cl	F	Total
SA03-03 427	OA	1 cm	60.14	0.47	17.35	2.92	0.17	0.28	1.65	6.73	7.20	N/A	N/A	N/A	N/A	96.91
SA03-03 427	OA	1 cm	59.63	0.38	17.96	3.01	0.20	0.31	1.59	6.66	7.05	N/A	N/A	N/A	N/A	96.79
SA03-03 427	OA	1 cm	60.14	0.42	17.66	2.54	0.09	0.16	0.98	7.23	7.46	N/A	N/A	N/A	N/A	96.70
SA03-03 427	OA	1 cm	58.47	0.43	17.09	3.70	0.39	0.35	0.86	8.17	6.98	N/A	N/A	N/A	N/A	96.44
SA03-03 427	OA	1 cm	59.12	0.42	17.22	3.06	0.21	0.32	1.69	6.87	6.76	N/A	N/A	N/A	N/A	95.67
SA03-03 427	OA	1 cm	58.08	0.46	16.87	3.19	0.29	0.38	1.82	7.11	6.85	N/A	N/A	N/A	N/A	95.04
SA03-03 427	OA	1 cm	58.82	0.48	16.66	3.04	0.34	0.36	1.64	6.52	6.91	N/A	N/A	N/A	N/A	94.77
SA03-03 427	OA	1 cm	57.84	0.44	17.00	2.62	0.18	0.21	0.78	9.04	6.53	N/A	N/A	N/A	N/A	94.64
SA03-03-645	OA	5 cm	60.55	0.61	18.01	2.63	0.18	0.32	1.01	7.15	5.94	N/A	N/A	N/A	N/A	96.41
SA03-03-645	OA	5 cm	59.86	0.61	18.08	2.79	0.32	0.26	1.01	7.56	5.81	N/A	N/A	N/A	N/A	96.29
SA03-03-645	OA	5 cm	59.85	0.64	17.93	2.33	0.27	0.28	1.11	7.37	6.14	N/A	N/A	N/A	N/A	95.93
SA03-03-645	OA	5 cm	59.84	0.59	17.73	2.74	0.24	0.23	1.11	6.68	6.71	N/A	N/A	N/A	N/A	95.87
SA03-03-645	OA	5 cm	60.76	0.57	17.59	2.12	0.19	0.38	1.21	6.52	6.40	N/A	N/A	N/A	N/A	95.75
SA03-03-645	OA	5 cm	60.13	0.61	17.70	2.40	0.24	0.31	1.14	6.89	6.33	N/A	N/A	N/A	N/A	95.74
SA03-03-645	OA	5 cm	60.23	0.52	17.83	2.23	0.18	0.31	1.15	6.62	6.17	N/A	N/A	N/A	N/A	95.23
SA03-03-645	OA	5 cm	59.86	0.48	17.58	2.34	0.25	0.55	1.48	5.59	7.04	N/A	N/A	N/A	N/A	95.16
SA03-03-685	E	5 cm	60.73	0.67	17.66	2.63	0.27	0.32	1.10	7.45	6.20	0.03	0.74	0.38	0.09	98.28
SA03-03-685	E	5 cm	61.44	0.58	17.56	2.48	0.21	0.36	1.19	6.44	6.39	0.06	0.55	0.24	0.11	97.61
SA03-03-685	E	5 cm	60.82	0.57	17.59	2.36	0.21	0.38	1.20	6.56	6.39	0.07	0.56	0.23	0.12	97.03
SA03-03-685	E	5 cm	62.07	0.60	18.16	2.55	0.21	0.36	1.27	6.91	6.71	0.08	0.55	0.22	0.12	99.80
SA03-03-685	E	5 cm	62.64	0.61	18.90	2.65	0.30	0.30	1.01	8.01	6.04	0.04	0.81	0.43	0.05	101.79
SA03-03-685	E	5 cm	60.10	0.63	18.00	2.87	0.25	0.44	1.46	6.87	6.50	0.10	0.64	0.31	0.02	98.19
SA03-03-685	E	5 cm	61.01	0.60	17.63	2.40	0.30	0.27	0.98	7.98	6.04	0.04	0.80	0.48	0.05	98.59
SA03-03-685	E	5 cm	61.70	0.60	18.17	2.67	0.31	0.29	1.03	8.24	5.76	0.03	0.83	0.45	0.04	100.11
SA03-03-685	E	5 cm	61.17	0.60	17.62	2.40	0.21	0.36	1.17	6.56	6.30	0.05	0.55	0.25	0.11	97.36
SA03-03-685	E	5 cm	63.25	0.68	18.80	2.83	0.28	0.27	1.13	8.14	6.27	0.04	0.73	0.32	0.08	102.81
SA03-03-925	E	5 cm	56.86	0.62	18.62	5.46	0.15	2.00	5.18	3.46	7.38	0.30	0.03	0.46	0.22	100.72
SA03-03-925	E	5 cm	60.30	0.38	18.60	3.05	0.14	0.59	2.20	4.06	9.03	0.10	0.09	0.56	0.17	99.27
SA03-03-925	E	5 cm	60.23	0.42	19.10	3.60	0.15	0.80	2.88	4.28	8.70	0.14	0.04	0.63	0.23	101.20
SA03-03-925	E	5 cm	57.50	0.53	18.01	4.31	0.18	1.05	2.70	4.37	8.24	0.21	0.02	0.50	0.20	97.82
SA03-03-925	E	5 cm	58.99	0.36	18.01	2.94	0.14	0.48	2.37	4.16	8.43	0.09	0.12	0.55	0.17	96.81
SA03-03-925	E	5 cm	58.84	0.38	18.02	2.92	0.14	0.53	2.45	4.29	8.63	0.09	0.13	0.56	0.16	97.14
SA03-03-925	E	5 cm	59.37	0.38	18.02	3.11	0.15	0.55	2.39	4.17	8.51	0.11	0.05	0.51	0.15	97.47
SA03-03-925	E	5 cm	58.95	0.38	18.49	2.83	0.15	0.54	2.25	4.16	8.42	0.10	0.11	0.54	0.20	97.13
SA03-03-925	E	5 cm	59.70	0.37	17.77	2.93	0.15	0.56	2.36	4.03	8.54	0.10	0.09	0.54	0.17	97.31
SA03-03-925	E	5 cm	59.86	0.38	18.24	2.97	0.15	0.59	2.35	4.17	8.00	0.08	0.03	0.55	0.22	97.60
SA03-03-925	E	5 cm	59.41	0.51	19.07	4.29	0.14	1.03	3.29	4.69	7.83	0.23	0.01	0.47	0.14	101.11
SA03-03-925	E	5 cm	58.73	0.52	18.28	4.51	0.13	1.25	3.87	3.92	8.17	0.22	0.03	0.47	0.18	100.28
SA03-03-995	E	5 cm	59.74	0.52	17.53	2.87	0.30	0.23	1.50	6.65	6.45	0.04	0.04	0.95	0.52	97.34
SA03-03-995	E	5 cm	58.41	0.37	17.39	3.18	0.15	0.58	2.23	3.82	8.92	0.10	0.09	0.45	0.18	95.87
SA03-03-995	E	5 cm	59.96	0.47	17.62	3.02	0.22	0.45	1.65	5.37	7.63	0.07	0.03	0.62	0.28	97.38
SA03-03-995	E	5 cm	59.63	0.38	18.17	3.06	0.13	0.54	2.23	3.86	8.86	0.09	0.08	0.44	0.19	97.66
SA03-03-995	E	5 cm	58.43	0.37	17.77	2.84	0.13	0.57	2.22	4.00	8.68	0.09	0.09	0.44	0.15	95.79
SA03-03-995	E	5 cm	60.04	0.38	18.15	2.95	0.15	0.44	2.11	4.21	8.83	0.08	0.06	0.53	0.18	98.09
SA03-03-995	E	5 cm	59.39	0.38	17.81	3.12	0.13	0.61	2.17	3.79	8.92	0.10	0.08	0.45	0.17	97.12
SA03-03-995	E	5 cm	58.39	0.38	17.60	2.72	0.15	0.47	2.25	3.75	8.63	0.09	0.01	0.47	0.18	95.09
SA03-03-995	E	5 cm	58.36	0.39	17.75	3.28	0.14	0.55	2.32	3.66	9.04	0.09	0.09	0.42	0.14	96.23
SA03-03-995	E	5 cm	58.14	0.38	17.62	3.17	0.14	0.55	2.37	3.84	8.92	0.10	0.07	0.43	0.20	95.92
SA03-03-995	E	5 cm	59.76	0.40	17.19	2.56	0.18	0.33	2.01	4.82	7.96	0.05	0.03	0.66	0.27	96.22
SA03-03-995	E	5 cm	60.69	0.48	18.08	2.82	0.22	0.48	1.74	5.83	7.32	0.07	0.04	0.67	0.28	98.72
SA03-03-995	E	5 cm	57.75	0.39	17.30	3.05	0.13	0.55	2.36	3.82	8.59	0.12	0.10	0.46	0.17	94.79

RF93-77 Major Element data generated in this study. The sample name, microprobe the analyses were carried out on and sampling resolution are all indicated. Microprobe: OE = Oxford Earth Sciences, OA = Oxford Archaeology and E – Edinburgh.

Name	Microprobe	Resolution	SiO_2	TiO_2	Al_2O_3	FeO	MnO	MgO	CaO	Na_2O	K_2O	P_2O_5	S	Cl	F	Total
RF93-77-68	OA	1 cm	55.54	0.46	19.28	3.86	0.20	0.61	4.04	4.71	8.55	N/A	N/A	N/A	N/A	97.3
RF93-77-68	OA	1 cm	54.31	0.48	18.69	4.50	0.10	0.78	4.51	6.05	7.74	N/A	N/A	N/A	N/A	97.2
RF93-77-68	OA	1 cm	56.28	0.36	19.23	2.81	0.08	0.34	2.88	5.29	9.36	N/A	N/A	N/A	N/A	96.6
RF93-77-68	OA	1 cm	54.91	0.44	18.73	4.20	0.04	0.73	4.27	4.96	8.23	N/A	N/A	N/A	N/A	96.5
RF93-77-68	OA	1 cm	54.77	0.45	18.86	4.02	0.11	0.65	4.11	4.81	8.63	N/A	N/A	N/A	N/A	96.4
RF93-77-68	OA	1 cm	54.99	0.47	18.69	4.03	0.23	0.66	4.02	4.56	8.63	N/A	N/A	N/A	N/A	96.3
RF93-77-68	OA	1 cm	55.37	0.38	18.82	3.85	0.22	0.55	3.78	5.82	7.45	N/A	N/A	N/A	N/A	96.2
RF93-77-68	OA	1 cm	54.81	0.54	18.52	4.09	0.12	0.75	4.26	4.74	8.38	N/A	N/A	N/A	N/A	96.2
RF93-77-68	OA	1 cm	54.65	0.52	18.47	4.15	0.08	0.67	4.16	4.69	8.77	N/A	N/A	N/A	N/A	96.2
RF93-77-68	OA	1 cm	54.62	0.45	18.50	4.22	0.08	0.68	4.27	5.20	8.12	N/A	N/A	N/A	N/A	96.1
RF93-77-68	OA	1 cm	58.81	0.46	16.78	3.62	0.13	0.74	2.59	4.18	8.82	N/A	N/A	N/A	N/A	96.1
RF93-77-68	OA	1 cm	54.59	0.46	18.38	4.05	0.07	0.69	4.14	4.88	8.66	N/A	N/A	N/A	N/A	95.9
RF93-77-68	OA	1 cm	54.27	0.50	18.37	4.35	0.07	0.75	4.33	4.56	8.59	N/A	N/A	N/A	N/A	95.8
RF93-77-68	OA	1 cm	54.52	0.50	18.68	3.85	0.14	0.67	4.10	4.66	8.60	N/A	N/A	N/A	N/A	95.7
RF93-77-68	OA	1 cm	54.58	0.46	18.37	4.08	0.11	0.62	4.02	4.75	8.71	N/A	N/A	N/A	N/A	95.7
RF93-77-68	OA	1 cm	55.02	0.45	18.46	3.64	0.17	0.62	3.87	4.95	8.52	N/A	N/A	N/A	N/A	95.7
RF93-77-68	OA	1 cm	54.54	0.52	18.60	3.88	0.18	0.60	4.00	4.73	8.53	N/A	N/A	N/A	N/A	95.6
RF93-77-68	OA	1 cm	54.43	0.50	18.43	4.25	0.21	0.60	4.00	4.61	8.39	N/A	N/A	N/A	N/A	95.4
RF93-77-68	OA	1 cm	54.51	0.41	18.08	3.96	0.17	0.67	4.10	4.87	8.52	N/A	N/A	N/A	N/A	95.3
RF93-77-68	OA	1 cm	54.55	0.40	17.96	4.00	0.21	0.64	3.78	5.17	8.50	N/A	N/A	N/A	N/A	95.2
RF93-77-68	OA	1 cm	54.03	0.47	18.68	4.09	0.03	0.68	3.99	4.51	8.60	N/A	N/A	N/A	N/A	95.1
RF93-77-68	OA	1 cm	52.21	0.45	17.80	3.68	0.18	0.65	6.84	4.37	8.40	N/A	N/A	N/A	N/A	94.6
RF93-77-73	E	1 cm	59.28	0.53	18.30	3.67	0.14	0.83	2.69	4.16	8.86	0.14	0.04	0.66	0.26	99.5
RF93-77-73	E	1 cm	59.23	0.51	18.68	3.26	0.16	0.62	2.43	4.64	8.63	0.11	0.03	0.79	0.28	99.4
RF93-77-73	E	1 cm	58.60	0.54	18.64	3.77	0.13	0.83	2.91	4.16	8.72	0.13	0.02	0.62	0.23	99.3
RF93-77-73	E	1 cm	59.06	0.51	18.73	3.53	0.13	0.75	2.59	4.07	8.86	0.11	0.04	0.67	0.26	99.3
RF93-77-73	E	1 cm	58.74	0.52	18.52	3.56	0.14	0.71	2.91	4.16	8.88	0.14	0.04	0.66	0.24	99.2
RF93-77-73	E	1 cm	59.16	0.51	18.44	3.66	0.14	0.74	2.65	4.07	8.74	0.12	0.03	0.66	0.24	99.2
RF93-77-73	E	1 cm	59.00	0.52	18.27	3.50	0.14	0.77	2.76	4.33	8.78	0.14	0.03	0.66	0.22	99.1
RF93-77-73	E	1 cm	58.66	0.52	18.68	3.52	0.13	0.76	2.71	4.13	8.81	0.12	0.03	0.67	0.24	99.0
RF93-77-73	E	1 cm	58.81	0.52	18.33	3.36	0.13	0.81	2.63	4.27	8.75	0.15	0.04	0.67	0.24	98.7
RF93-77-73	E	1 cm	58.70	0.52	18.19	3.58	0.13	0.71	2.54	4.23	9.04	0.12	0.03	0.64	0.26	98.7
RF93-77-73	E	1 cm	58.85	0.54	18.27	3.57	0.13	0.74	2.67	4.06	8.78	0.13	0.02	0.66	0.22	98.6
RF93-77-73	E	1 cm	58.68	0.52	18.50	3.29	0.15	0.70	2.60	4.36	8.68	0.14	0.03	0.64	0.23	98.5
RF93-77-73	E	1 cm	58.17	0.52	18.76	3.47	0.14	0.77	2.62	4.75	8.09	0.13	0.02	0.63	0.25	98.3
RF93-77-73	E	1 cm	58.45	0.53	18.25	3.64	0.15	0.77	2.55	4.15	8.77	0.11	0.03	0.66	0.27	98.3
RF93-77-73	E	1 cm	59.06	0.51	18.31	3.41	0.13	0.66	2.40	4.01	8.86	0.12	0.02	0.57	0.24	98.3
RF93-77-73	E	1 cm	57.97	0.52	18.50	3.59	0.13	0.78	2.69	4.18	8.72	0.12	0.02	0.66	0.27	98.1
RF93-77-73	E	1 cm	58.05	0.52	18.46	3.56	0.14	0.72	2.64	4.24	8.76	0.12	0.03	0.64	0.25	98.1
RF93-77-73	E	1 cm	57.94	0.53	18.67	3.59	0.13	0.78	2.74	4.23	8.48	0.13	0.02	0.64	0.20	98.1
RF93-77-73	E	1 cm	57.98	0.52	18.28	3.55	0.13	0.76	2.60	4.43	8.69	0.12	0.02	0.65	0.22	98.0
RF93-77-73	E	1 cm	57.67	0.55	18.49	3.40	0.15	0.77	2.71	4.35	8.64	0.12	0.03	0.72	0.28	97.9
RF93-77-73	E	1 cm	57.73	0.52	18.12	3.67	0.13	0.82	2.61	4.64	8.00	0.14	0.02	0.63	0.28	97.3
RF93-77-73	E	1 cm	57.58	0.51	17.53	3.04	0.15	0.57	2.28	4.24	8.62	0.09	0.00	0.78	0.28	95.7
RF93-77-78	E	1 cm	59.17	0.54	18.44	3.52	0.15	0.62	2.44	4.64	8.77	0.09	0.05	0.77	0.30	99.5
RF93-77-78	E	1 cm	59.31	0.51	18.29	3.69	0.13	0.73	2.68	4.16	8.78	0.15	0.01	0.63	0.27	99.3
RF93-77-78	E	1 cm	59.70	0.51	18.04	3.38	0.14	0.77	2.56	4.16	8.78	0.15	0.03	0.66	0.26	99.1
RF93-77-78	E	1 cm	59.10	0.53	18.82	3.20	0.14	0.56	2.40	4.42	8.79	0.10	0.02	0.76	0.27	99.1
RF93-77-78	E	1 cm	59.38	0.52	18.73	3.39	0.13	0.70	2.49	4.05	8.57	0.14	0.04	0.63	0.23	99.0
RF93-77-78	E	1 cm	59.24	0.53	18.10	3.22	0.14	0.55	2.39	4.78	8.79	0.10	0.03	0.78	0.30	98.9
RF93-77-78	E	1 cm	58.86	0.52	18.44	3.40	0.15	0.61	2.38	4.71	8.70	0.10	0.02	0.76	0.27	98.9

Name	Microprobe	Resolution	SiO_2	TiO_2	Al_2O_3	FeO	MnO	MgO	CaO	Na_2O	K_2O	P_2O_5	S	Cl	F	Total
RF93-77-78	E	1 cm	58.68	0.51	18.67	3.68	0.13	0.76	2.73	4.09	8.54	0.13	0.06	0.65	0.24	98.9
RF93-77-78	E	1 cm	58.98	0.52	18.77	3.25	0.14	0.58	2.42	4.32	8.72	0.09	0.03	0.72	0.31	98.9
RF93-77-78	E	1 cm	59.17	0.51	18.51	3.41	0.13	0.73	2.69	4.09	8.57	0.13	0.03	0.62	0.23	98.8
RF93-77-78	E	1 cm	59.14	0.52	18.59	3.52	0.15	0.69	2.48	3.87	8.70	0.14	0.02	0.63	0.25	98.7
RF93-77-78	E	1 cm	59.24	0.50	17.81	3.57	0.13	0.77	2.53	4.24	8.72	0.13	0.03	0.61	0.25	98.5
RF93-77-78	E	1 cm	58.75	0.50	18.23	3.61	0.14	0.74	2.53	4.22	8.50	0.16	0.02	0.63	0.26	98.3
RF93-77-78	E	1 cm	58.84	0.54	18.09	3.52	0.14	0.77	2.64	3.90	8.65	0.14	0.02	0.65	0.25	98.2
RF93-77-78	E	1 cm	58.99	0.52	17.84	3.45	0.13	0.66	2.59	4.12	8.62	0.13	0.03	0.63	0.21	97.9
RF93-77-78	E	1 cm	58.87	0.51	17.91	3.31	0.14	0.59	2.38	4.47	8.29	0.09	0.04	0.72	0.19	97.5
RF93-77-78	E	1 cm	58.14	0.50	17.93	3.26	0.16	0.54	2.31	4.71	8.47	0.10	0.02	0.75	0.31	97.2
RF93-77-78	E	1 cm	58.06	0.50	18.07	3.28	0.15	0.53	2.32	4.43	8.51	0.10	0.02	0.79	0.30	97.1
RF93-77-78	E	1 cm	58.74	0.53	18.23	3.58	0.15	0.57	2.49	2.53	8.48	0.12	0.01	0.79	0.35	96.6
RF93-77-78	E	1 cm	56.94	0.51	17.73	2.91	0.15	0.60	2.47	4.80	8.55	0.09	0.02	0.79	0.32	95.9
RF93-77-78	E	1 cm	57.77	0.49	17.68	3.17	0.14	0.52	2.19	4.30	8.33	0.10	0.02	0.77	0.30	95.8
RF93-77-78	E	1 cm	56.25	0.49	17.15	3.08	0.13	0.58	2.39	4.61	8.40	0.10	0.05	0.74	0.20	94.2
RF93-77-86	OA	1 cm	59.35	0.45	17.93	3.58	0.14	0.80	2.64	4.25	8.80	N/A	N/A	N/A	N/A	97.9
RF93-77-86	OA	1 cm	59.29	0.45	17.90	3.84	0.16	0.72	2.64	4.33	8.54	N/A	N/A	N/A	N/A	97.9
RF93-77-86	OA	1 cm	59.42	0.48	17.60	3.69	0.20	0.74	2.67	4.38	8.68	N/A	N/A	N/A	N/A	97.9
RF93-77-86	OA	1 cm	58.94	0.59	17.74	3.82	0.13	0.77	2.60	4.27	8.65	N/A	N/A	N/A	N/A	97.5
RF93-77-86	OA	1 cm	59.81	0.46	17.74	3.38	0.12	0.74	2.57	4.15	8.48	N/A	N/A	N/A	N/A	97.5
RF93-77-86	OA	1 cm	59.20	0.49	17.67	3.70	0.08	0.77	2.61	4.18	8.62	N/A	N/A	N/A	N/A	97.3
RF93-77-86	OA	1 cm	59.16	0.46	17.72	3.69	0.04	0.75	2.55	4.63	8.14	N/A	N/A	N/A	N/A	97.1
RF93-77-86	OA	1 cm	59.21	0.52	17.31	3.64	0.11	0.70	2.60	4.23	8.77	N/A	N/A	N/A	N/A	97.1
RF93-77-86	OA	1 cm	59.17	0.51	17.44	3.66	0.17	0.72	2.51	4.05	8.81	N/A	N/A	N/A	N/A	97.0
RF93-77-86	OA	1 cm	59.55	0.40	18.04	2.69	0.21	0.53	2.71	3.63	9.09	N/A	N/A	N/A	N/A	96.9
RF93-77-86	OA	1 cm	59.42	0.48	17.54	3.25	0.18	0.63	2.44	5.06	7.69	N/A	N/A	N/A	N/A	96.7
RF93-77-86	OA	1 cm	58.87	0.55	17.50	3.70	0.12	0.74	2.54	4.07	8.59	N/A	N/A	N/A	N/A	96.7
RF93-77-86	OA	1 cm	58.62	0.48	17.81	3.42	0.09	0.76	2.66	4.07	8.73	N/A	N/A	N/A	N/A	96.6
RF93-77-86	OA	1 cm	59.30	0.52	16.87	3.28	0.18	0.77	2.66	4.35	8.69	N/A	N/A	N/A	N/A	96.6
RF93-77-86	OA	1 cm	59.04	0.46	17.11	3.71	0.12	0.74	2.52	4.36	8.55	N/A	N/A	N/A	N/A	96.6
RF93-77-86	OA	1 cm	58.95	0.44	17.27	3.61	0.09	0.76	2.67	4.30	8.50	N/A	N/A	N/A	N/A	96.6
RF93-77-86	OA	1 cm	58.55	0.49	17.48	3.70	0.05	0.89	2.78	4.13	8.50	N/A	N/A	N/A	N/A	96.6
RF93-77-86	OA	1 cm	58.86	0.46	17.05	3.82	0.14	0.76	2.57	4.07	8.52	N/A	N/A	N/A	N/A	96.3
RF93-77-86	OA	1 cm	58.88	0.47	17.07	3.48	0.18	0.78	2.63	4.10	8.67	N/A	N/A	N/A	N/A	96.3
RF93-77-86	OA	1 cm	58.43	0.41	17.12	3.71	0.13	0.77	2.52	4.43	8.72	N/A	N/A	N/A	N/A	96.2
RF93-77-86	OA	1 cm	58.30	0.51	17.29	3.65	0.11	0.77	2.62	4.36	8.51	N/A	N/A	N/A	N/A	96.1
RF93-77-86	OA	1 cm	58.83	0.47	17.03	3.26	0.14	0.75	2.59	4.06	8.79	N/A	N/A	N/A	N/A	95.9
RF93-77-86	OA	1 cm	58.44	0.45	17.03	3.64	0.08	0.71	2.62	4.20	8.60	N/A	N/A	N/A	N/A	95.8
RF93-77-86	OA	1 cm	57.12	0.56	16.68	4.41	0.15	1.23	3.64	3.70	8.19	N/A	N/A	N/A	N/A	95.7
RF93-77-86	OA	1 cm	58.74	0.48	16.73	3.55	0.06	0.78	2.66	4.16	8.51	N/A	N/A	N/A	N/A	95.7
RF93-77-86	OA	1 cm	58.62	0.43	16.52	3.63	0.19	0.73	2.71	4.30	8.54	N/A	N/A	N/A	N/A	95.7
RF93-77-86	OA	1 cm	58.81	0.52	16.82	3.32	0.16	0.74	2.48	4.03	8.71	N/A	N/A	N/A	N/A	95.6
RF93-77-86	OA	1 cm	58.05	0.42	16.98	3.56	0.15	0.83	2.49	4.39	8.69	N/A	N/A	N/A	N/A	95.6
RF93-77-86	OA	1 cm	58.62	0.49	16.86	3.46	0.08	0.68	2.45	4.65	8.21	N/A	N/A	N/A	N/A	95.5
RF93-77-86	OA	1 cm	58.03	0.50	16.86	3.74	0.10	0.70	2.59	4.19	8.70	N/A	N/A	N/A	N/A	95.4
RF93-77-86	OA	1 cm	58.14	0.49	16.78	3.55	0.22	0.74	2.58	4.23	8.68	N/A	N/A	N/A	N/A	95.4
RF93-77-86	OA	1 cm	57.50	0.48	17.49	3.62	0.04	0.83	2.53	4.34	8.53	N/A	N/A	N/A	N/A	95.4
RF93-77-86	OA	1 cm	58.35	0.47	16.72	3.55	0.05	0.82	2.66	3.97	8.38	N/A	N/A	N/A	N/A	95.0
RF93-77-86	OA	1 cm	58.14	0.48	16.27	3.51	0.12	0.82	2.56	4.23	8.56	N/A	N/A	N/A	N/A	94.7
RF93-77-86	OA	1 cm	58.08	0.47	16.42	3.45	0.07	0.74	2.65	4.26	8.51	N/A	N/A	N/A	N/A	94.6
RF93-77-88	E	1 cm	59.53	0.53	18.07	3.71	0.13	0.77	2.66	4.42	8.81	0.14	0.02	0.64	0.26	99.7
RF93-77-88	E	1 cm	59.27	0.51	18.66	3.69	0.13	0.75	2.65	4.30	8.67	0.12	0.03	0.63	0.26	99.7
RF93-77-88	E	1 cm	59.37	0.52	18.20	3.45	0.14	0.75	2.71	4.21	8.86	0.15	0.04	0.65	0.25	99.3
RF93-77-88	E	1 cm	59.10	0.51	18.10	3.75	0.14	0.78	2.72	4.37	8.63	0.13	0.04	0.63	0.25	99.2
RF93-77-88	E	1 cm	59.26	0.51	18.05	3.61	0.14	0.80	2.64	4.31	8.78	0.12	0.02	0.64	0.23	99.1
RF93-77-88	E	1 cm	58.85	0.55	18.05	3.75	0.15	0.79	2.69	4.39	8.67	0.14	0.02	0.76	0.29	99.1

Name	Microprobe	Resolution	SiO_2	TiO_2	Al_2O_3	FeO	MnO	MgO	CaO	Na_2O	K_2O	P_2O_5	S	Cl	F	Total
RF93-77-88	E	1 cm	59.24	0.52	17.98	3.62	0.14	0.75	2.58	4.22	8.88	0.14	0.05	0.65	0.25	99.1
RF93-77-88	E	1 cm	59.28	0.52	18.12	3.50	0.13	0.82	2.57	4.25	8.77	0.14	0.06	0.64	0.26	99.0
RF93-77-88	E	1 cm	57.04	0.24	22.06	2.38	0.06	0.45	5.69	3.56	6.99	0.07	0.01	0.29	0.12	99.0
RF93-77-88	E	1 cm	58.65	0.53	18.14	3.81	0.13	0.86	2.79	4.24	8.59	0.14	0.03	0.64	0.25	98.8
RF93-77-88	E	1 cm	58.81	0.47	18.36	3.43	0.12	0.71	2.61	4.41	8.74	0.11	0.09	0.62	0.27	98.8
RF93-77-88	E	1 cm	58.70	0.52	18.18	3.50	0.15	0.80	2.62	4.21	8.99	0.13	0.05	0.65	0.24	98.7
RF93-77-88	E	1 cm	58.46	0.52	18.34	3.73	0.13	0.76	2.63	4.31	8.64	0.13	0.07	0.67	0.22	98.6
RF93-77-88	E	1 cm	59.28	0.51	18.10	3.57	0.13	0.75	2.55	4.05	8.56	0.13	0.01	0.59	0.25	98.5
RF93-77-88	E	1 cm	58.45	0.52	18.31	3.40	0.14	0.75	2.60	4.29	8.77	0.14	0.03	0.64	0.24	98.3
RF93-77-88	E	1 cm	58.23	0.53	18.39	3.52	0.14	0.75	2.63	4.34	8.65	0.15	0.03	0.64	0.25	98.3
RF93-77-88	E	1 cm	58.82	0.47	18.39	3.37	0.12	0.73	2.60	4.26	8.57	0.13	0.01	0.58	0.20	98.3
RF93-77-88	E	1 cm	59.97	0.48	18.07	3.00	0.12	0.53	2.45	3.70	8.86	0.12	0.01	0.60	0.22	98.1
RF93-77-88	E	1 cm	56.99	0.49	18.36	3.90	0.14	0.76	3.26	3.85	8.74	0.14	0.05	0.64	0.24	97.6
RF93-77-88	E	1 cm	58.16	0.51	17.87	3.51	0.13	0.76	2.50	4.18	8.44	0.12	0.02	0.58	0.23	97.0
RF93-77-88	E	1 cm	57.61	0.52	17.54	3.61	0.13	0.77	2.57	3.98	8.48	0.13	0.04	0.62	0.22	96.2
RF93-77-144	OA	5 cm	58.50	0.58	18.47	4.40	0.09	1.00	3.36	3.97	8.69	N/A	N/A	N/A	N/A	99.1
RF93-77-144	OA	5 cm	57.97	0.62	18.21	4.42	0.20	1.05	3.47	3.66	8.36	N/A	N/A	N/A	N/A	98.0
RF93-77-144	OA	5 cm	54.89	0.76	17.71	6.41	0.18	2.01	5.11	3.42	7.45	N/A	N/A	N/A	N/A	97.9
RF93-77-144	OA	5 cm	53.91	0.87	17.90	6.77	0.10	2.31	5.76	3.11	6.99	N/A	N/A	N/A	N/A	97.7
RF93-77-144	OA	5 cm	55.22	0.74	17.48	6.45	0.14	1.98	5.21	3.17	7.29	N/A	N/A	N/A	N/A	97.7
RF93-77-144	OA	5 cm	55.57	0.71	18.10	5.72	0.06	1.74	4.66	3.10	7.81	N/A	N/A	N/A	N/A	97.5
RF93-77-144	OA	5 cm	55.04	0.74	17.23	6.15	0.16	1.89	4.94	3.02	8.28	N/A	N/A	N/A	N/A	97.5
RF93-77-144	OA	5 cm	57.94	0.61	17.56	4.46	0.09	1.20	3.41	3.68	8.46	N/A	N/A	N/A	N/A	97.4
RF93-77-144	OA	5 cm	55.29	0.69	17.48	6.20	0.11	1.82	4.86	3.38	7.56	N/A	N/A	N/A	N/A	97.4
RF93-77-144	OA	5 cm	57.47	0.46	18.19	4.52	0.15	1.07	3.45	3.55	8.53	N/A	N/A	N/A	N/A	97.4
RF93-77-144	OA	5 cm	58.05	0.52	18.08	4.19	0.23	0.87	3.03	3.66	8.74	N/A	N/A	N/A	N/A	97.4
RF93-77-144	OA	5 cm	54.89	0.66	17.48	5.99	0.13	1.96	5.03	3.48	7.63	N/A	N/A	N/A	N/A	97.3
RF93-77-144	OA	5 cm	54.59	0.77	17.73	6.42	0.08	1.96	5.04	3.08	7.53	N/A	N/A	N/A	N/A	97.2
RF93-77-144	OA	5 cm	55.80	0.68	17.61	5.55	0.17	1.79	4.60	3.24	7.73	N/A	N/A	N/A	N/A	97.2
RF93-77-144	OA	5 cm	55.22	0.61	17.89	5.44	0.05	1.62	4.88	3.31	8.05	N/A	N/A	N/A	N/A	97.1
RF93-77-144	OA	5 cm	56.40	0.63	17.61	5.08	0.10	1.52	4.09	3.35	8.04	N/A	N/A	N/A	N/A	96.8
RF93-77-144	OA	5 cm	54.66	0.75	17.33	6.09	0.21	1.99	5.04	3.33	7.31	N/A	N/A	N/A	N/A	96.7
RF93-77-144	OA	5 cm	57.02	0.53	17.45	4.38	0.17	1.24	3.51	3.45	8.39	N/A	N/A	N/A	N/A	96.1
RF93-77-144	OA	5 cm	54.09	0.80	17.20	6.03	0.04	2.03	5.25	3.19	7.26	N/A	N/A	N/A	N/A	95.9
RF93-77-144	OA	5 cm	56.85	0.60	16.79	4.58	0.14	1.18	3.52	3.48	8.30	N/A	N/A	N/A	N/A	95.4
RF93-77-144	OA	5 cm	55.38	0.62	16.20	5.31	0.12	1.50	4.12	3.49	8.10	N/A	N/A	N/A	N/A	94.8
RF93-77-198	OA	5 cm	60.64	0.49	17.65	2.84	0.22	0.49	2.27	4.84	8.53	N/A	N/A	N/A	N/A	98.0
RF93-77-198	OA	5 cm	60.95	0.43	17.52	3.03	0.17	0.46	2.17	4.72	8.41	N/A	N/A	N/A	N/A	97.9
RF93-77-198	OA	5 cm	62.89	0.47	17.49	2.29	0.19	0.25	1.60	5.78	6.89	N/A	N/A	N/A	N/A	97.8
RF93-77-198	OA	5 cm	60.62	0.45	17.73	2.78	0.05	0.41	2.18	4.39	8.81	N/A	N/A	N/A	N/A	97.4
RF93-77-198	OA	5 cm	60.46	0.45	17.15	2.85	0.18	0.43	2.19	5.02	8.68	N/A	N/A	N/A	N/A	97.4
RF93-77-198	OA	5 cm	57.09	0.62	17.90	4.67	0.12	1.14	3.70	3.82	8.35	N/A	N/A	N/A	N/A	97.4
RF93-77-198	OA	5 cm	60.29	0.44	17.38	3.03	0.20	0.46	2.40	4.44	8.73	N/A	N/A	N/A	N/A	97.4
RF93-77-198	OA	5 cm	56.28	0.64	17.77	5.00	0.09	1.30	4.00	3.55	8.16	N/A	N/A	N/A	N/A	96.8
RF93-77-198	OA	5 cm	59.81	0.39	16.85	3.63	0.12	0.77	2.89	3.36	8.90	N/A	N/A	N/A	N/A	96.7
RF93-77-198	OA	5 cm	57.88	0.45	17.70	3.85	0.02	0.98	3.00	3.02	9.66	N/A	N/A	N/A	N/A	96.6
RF93-77-198	OA	5 cm	57.22	0.44	17.90	4.11	0.16	1.03	3.32	3.38	8.87	N/A	N/A	N/A	N/A	96.4
RF93-77-198	OA	5 cm	57.56	0.46	17.54	3.77	0.16	1.04	3.11	3.60	9.03	N/A	N/A	N/A	N/A	96.3
RF93-77-198	OA	5 cm	58.29	0.50	17.21	3.56	0.22	0.78	2.93	4.31	8.34	N/A	N/A	N/A	N/A	96.1
RF93-77-198	OA	5 cm	60.05	0.49	16.92	2.73	0.11	0.43	2.18	4.25	8.54	N/A	N/A	N/A	N/A	95.7
RF93-77-198	OA	5 cm	57.64	0.50	17.44	3.95	0.11	1.11	3.36	3.24	8.20	N/A	N/A	N/A	N/A	95.6
RF93-77-198	OA	5 cm	57.35	0.42	17.34	3.81	0.07	0.84	2.96	3.32	9.40	N/A	N/A	N/A	N/A	95.5
RF93-77-198	OA	5 cm	57.34	0.53	17.18	4.15	0.22	1.05	3.47	3.43	7.99	N/A	N/A	N/A	N/A	95.4
RF93-77-198	OA	5 cm	58.07	0.44	16.70	3.51	0.08	0.75	2.76	3.87	8.75	N/A	N/A	N/A	N/A	94.9
RF93-77-198	OA	5 cm	57.89	0.43	16.52	3.54	0.16	0.63	2.75	4.42	8.39	N/A	N/A	N/A	N/A	94.7
RF93-77-198	OA	5 cm	55.98	0.53	16.60	4.48	0.16	1.54	4.32	3.22	7.74	N/A	N/A	N/A	N/A	94.6

Name	Microprobe	Resolution	SiO_2	TiO_2	Al_2O_3	FeO	MnO	MgO	CaO	Na_2O	K_2O	P_2O_5	S	Cl	F	Total
RF93-77-267	E	5 cm	63.69	0.49	17.33	2.68	0.33	0.24	0.91	7.74	5.84	0.01	0.00	0.86	0.84	101.0
RF93-77-267	E	5 cm	63.44	0.49	17.25	2.44	0.35	0.22	1.04	7.88	5.77	0.02	0.00	0.86	0.85	100.6
RF93-77-267	E	5 cm	62.39	0.49	17.93	2.74	0.33	0.20	1.05	7.90	5.83	0.02	0.01	0.85	0.82	100.5
RF93-77-267	E	5 cm	62.94	0.49	17.53	2.58	0.33	0.23	1.00	7.81	5.79	0.01	0.01	0.86	0.93	100.5
RF93-77-267	E	5 cm	63.39	0.48	17.19	2.60	0.35	0.21	0.91	7.74	5.58	0.01	0.01	0.88	0.85	100.2
RF93-77-267	E	5 cm	62.00	0.49	17.96	2.90	0.35	0.25	1.04	7.83	5.62	0.02	0.01	0.89	0.85	100.2
RF93-77-267	E	5 cm	62.30	0.48	17.41	2.77	0.34	0.19	1.00	7.87	5.89	0.02	0.01	0.86	0.86	100.0
RF93-77-267	E	5 cm	62.40	0.49	17.48	2.76	0.34	0.23	1.01	7.85	5.72	0.02	0.00	0.89	0.81	100.0
RF93-77-267	E	5 cm	62.13	0.49	17.32	2.75	0.33	0.26	1.03	7.89	5.83	0.01	0.01	0.86	0.81	99.7
RF93-77-267	E	5 cm	61.99	0.49	17.66	2.69	0.35	0.21	0.92	7.65	5.92	0.02	0.01	0.88	0.89	99.7
RF93-77-267	E	5 cm	62.99	0.48	16.82	2.29	0.35	0.19	1.06	7.68	5.78	0.02	0.03	1.12	0.82	99.6
RF93-77-267	E	5 cm	61.94	0.50	17.33	2.62	0.35	0.23	0.94	7.63	5.74	0.02	0.01	0.91	0.85	99.1
RF93-77-267	E	5 cm	59.68	0.40	18.49	3.20	0.14	0.52	2.27	4.08	8.83	0.10	0.05	0.51	0.21	98.5
RF93-77-267	E	5 cm	60.67	0.66	17.39	2.69	0.32	0.28	0.87	7.59	6.49	0.03	0.01	0.68	0.76	98.4
RF93-77-267	E	5 cm	55.14	0.63	18.27	5.21	0.14	1.59	4.75	3.32	8.01	0.29	0.20	0.51	0.23	98.3
RF93-77-267	E	5 cm	60.72	0.50	17.12	2.63	0.33	0.25	1.02	7.98	5.73	0.03	0.01	0.88	0.85	98.0
RF93-77-267	E	5 cm	60.29	0.67	17.37	2.74	0.34	0.28	0.92	7.58	6.12	0.03	0.02	0.71	0.73	97.8
RF93-77-267	E	5 cm	59.19	0.40	17.89	3.14	0.13	0.56	2.25	4.07	8.68	0.09	0.04	0.44	0.22	97.1
RF93-77-267	E	5 cm	58.02	0.45	18.05	2.84	0.15	0.47	2.21	4.40	8.60	0.07	0.11	0.70	0.28	96.3
RF93-77-372	E	5 cm	60.98	0.46	19.32	2.91	0.24	0.32	1.72	6.49	7.09	0.04	0.02	0.81	0.46	100.9
RF93-77-372	E	5 cm	62.33	0.41	18.58	2.90	0.16	0.49	1.85	4.89	8.37	0.07	0.07	0.50	0.21	100.9
RF93-77-372	E	5 cm	61.25	0.48	18.85	2.76	0.24	0.38	1.66	6.41	7.20	0.04	0.02	0.79	0.48	100.6
RF93-77-372	E	5 cm	60.30	0.47	18.84	3.02	0.24	0.34	1.74	6.64	7.38	0.04	0.01	0.82	0.46	100.3
RF93-77-372	E	5 cm	59.31	0.47	18.91	3.52	0.24	0.38	2.36	6.17	7.44	0.05	0.01	0.90	0.40	100.2
RF93-77-372	E	5 cm	60.76	0.48	18.42	3.13	0.24	0.30	1.64	6.56	7.23	0.04	0.01	0.80	0.47	100.1
RF93-77-372	E	5 cm	60.26	0.48	18.44	3.05	0.26	0.35	1.81	6.71	7.32	0.04	0.02	0.86	0.49	100.1
RF93-77-372	E	5 cm	61.43	0.39	19.12	2.24	0.19	0.25	1.84	6.26	7.31	0.03	0.01	0.62	0.36	100.1
RF93-77-372	E	5 cm	62.48	0.55	17.95	2.35	0.24	0.28	1.16	7.29	6.31	0.04	0.01	0.71	0.41	99.8
RF93-77-372	E	5 cm	60.50	0.48	18.23	3.10	0.25	0.32	1.76	6.58	7.16	0.04	0.00	0.80	0.46	99.7
RF93-77-372	E	5 cm	60.44	0.49	18.53	2.96	0.26	0.34	2.00	6.40	6.99	0.04	0.01	0.80	0.42	99.7
RF93-77-372	E	5 cm	61.80	0.53	18.21	2.41	0.22	0.22	1.19	7.27	6.52	0.02	0.02	0.73	0.39	99.5
RF93-77-372	E	5 cm	60.18	0.47	18.59	2.98	0.25	0.30	1.54	6.66	7.20	0.04	0.01	0.80	0.50	99.5
RF93-77-372	E	5 cm	60.55	0.48	18.28	2.94	0.26	0.36	1.74	6.30	7.16	0.04	0.01	0.82	0.47	99.4
RF93-77-372	E	5 cm	60.15	0.48	17.89	3.03	0.25	0.38	1.72	6.85	7.22	0.04	0.04	0.88	0.47	99.4
RF93-77-372	E	5 cm	60.07	0.48	18.07	3.11	0.25	0.33	1.62	6.62	7.23	0.04	0.01	0.83	0.49	99.2
RF93-77-372	E	5 cm	60.16	0.48	18.16	3.07	0.22	0.49	1.99	6.07	7.26	0.07	0.01	0.70	0.43	99.1
RF93-77-372	E	5 cm	59.90	0.47	18.32	3.00	0.25	0.31	1.66	6.46	7.21	0.04	0.01	0.79	0.47	98.9
RF93-77-372	E	5 cm	59.91	0.46	18.06	2.97	0.24	0.34	1.59	6.74	7.12	0.05	0.01	0.83	0.46	98.8
RF93-77-372	E	5 cm	59.41	0.41	18.21	3.19	0.12	0.72	2.65	3.44	9.68	0.13	0.09	0.36	0.13	98.5
RF93-77-372	E	5 cm	59.62	0.48	18.13	2.82	0.24	0.32	1.63	6.65	6.98	0.03	0.03	0.87	0.49	98.3
RF93-77-372	E	5 cm	58.78	0.40	17.99	3.23	0.14	0.54	2.33	4.28	8.68	0.10	0.09	0.45	0.18	97.2
RF93-77-372	E	5 cm	60.68	0.49	17.40	2.13	0.21	0.25	1.15	6.76	6.16	0.03	0.01	0.74	0.40	96.4
RF93-77-372	E	5 cm	96.05	0.00	0.08	0.09	0.00	-0.01	0.00	0.00	0.03	0.01	0.01	0.00	0.01	96.3
RF93-77-414	E	5 cm	61.21	0.49	18.61	3.14	0.17	0.40	2.23	4.74	8.62	0.07	0.04	0.71	0.26	100.7
RF93-77-414	E	5 cm	60.74	0.49	18.69	2.77	0.15	0.46	2.16	4.42	9.00	0.07	0.04	0.69	0.25	100.0
RF93-77-414	E	5 cm	60.44	0.49	18.57	2.79	0.14	0.46	2.22	4.55	8.48	0.06	0.09	0.71	0.25	99.3
RF93-77-414	E	5 cm	60.11	0.49	18.34	2.88	0.15	0.46	2.21	4.64	8.62	0.07	0.08	0.72	0.29	99.1
RF93-77-414	E	5 cm	59.09	0.46	18.65	3.35	0.14	0.65	2.46	4.00	9.08	0.11	0.15	0.56	0.16	98.9
RF93-77-414	E	5 cm	54.11	0.49	20.03	3.67	0.16	0.63	4.06	5.05	8.75	0.10	0.07	0.66	0.36	98.1
RF93-77-414	E	5 cm	58.57	0.49	18.11	3.03	0.16	0.55	2.47	4.52	8.62	0.06	0.11	0.70	0.29	97.7
RF93-77-414	E	5 cm	59.83	0.47	17.94	2.59	0.16	0.42	2.03	4.51	8.54	0.07	0.03	0.69	0.28	97.6
RF93-77-414	E	5 cm	59.23	0.48	18.06	2.82	0.15	0.41	2.19	4.44	8.49	0.05	0.09	0.69	0.27	97.4
RF93-77-414	E	5 cm	58.82	0.49	18.22	2.82	0.15	0.45	2.11	4.56	8.58	0.06	0.08	0.67	0.25	97.3
RF93-77-414	E	5 cm	59.34	0.47	17.98	2.60	0.15	0.43	2.12	4.39	8.64	0.06	0.08	0.70	0.28	97.2
RF93-77-414	E	5 cm	57.76	0.48	18.20	2.95	0.14	0.70	2.61	3.80	9.22	0.11	0.15	0.55	0.22	96.9
RF93-77-414	E	5 cm	58.63	0.47	17.89	2.67	0.16	0.43	2.13	4.67	8.24	0.07	0.10	0.72	0.29	96.5

Name	Microprobe	Resolution	SiO_2	TiO_2	Al_2O_3	FeO	MnO	MgO	CaO	Na_2O	K_2O	P_2O_5	S	Cl	F	Total
RF93-77-414	E	5 cm	57.51	0.48	18.55	2.54	0.13	0.47	2.39	4.40	8.85	0.07	0.07	0.68	0.27	96.4
RF93-77-414	E	5 cm	53.73	0.05	22.18	0.24	0.02	0.01	0.04	1.01	18.79	0.01	0.01	0.04	0.03	96.2
RF93-77-414	E	5 cm	59.64	0.44	17.72	2.15	0.14	0.41	2.13	4.36	8.26	0.06	0.02	0.61	0.21	96.2
RF93-77-414	E	5 cm	58.15	0.47	18.00	2.59	0.14	0.46	2.31	4.26	8.58	0.08	0.10	0.64	0.29	96.1
RF93-77-414	E	5 cm	58.68	0.45	17.24	2.66	0.15	0.41	2.00	4.25	8.52	0.06	0.01	0.60	0.26	95.3
RF93-77-414	E	5 cm	56.11	0.43	17.57	3.33	0.14	0.73	3.02	3.25	9.11	0.14	0.15	0.57	0.19	94.7
RF93-77-414	E	5 cm	58.68	0.39	16.95	2.47	0.15	0.39	2.02	4.04	8.25	0.06	0.04	0.67	0.22	94.3
RF93-77-414	OA	5 cm	61.13	0.46	18.34	2.79	0.25	0.31	1.68	6.31	7.11	N/A	N/A	N/A	N/A	98.4
RF93-77-414	OA	5 cm	56.19	0.68	14.87	4.82	0.07	3.77	8.15	3.30	6.42	N/A	N/A	N/A	N/A	98.3
RF93-77-414	OA	5 cm	58.65	0.49	18.15	3.82	0.12	0.97	3.39	4.14	8.44	N/A	N/A	N/A	N/A	98.2
RF93-77-414	OA	5 cm	60.24	0.44	17.89	2.83	0.12	0.45	2.25	4.10	9.17	N/A	N/A	N/A	N/A	97.5
RF93-77-414	OA	5 cm	59.23	0.47	17.84	3.39	0.12	0.78	2.53	4.30	8.65	N/A	N/A	N/A	N/A	97.3
RF93-77-414	OA	5 cm	58.72	0.50	17.39	3.46	0.16	0.83	2.89	3.51	9.12	N/A	N/A	N/A	N/A	96.6
RF93-77-414	OA	5 cm	55.17	0.68	17.85	5.22	0.08	1.89	5.10	2.99	7.59	N/A	N/A	N/A	N/A	96.6
RF93-77-414	OA	5 cm	73.05	0.16	12.98	0.65	0.03	0.19	0.80	4.66	3.91	N/A	N/A	N/A	N/A	96.4
RF93-77-414	OA	5 cm	59.96	0.43	17.41	2.90	0.09	0.44	2.14	4.57	8.44	N/A	N/A	N/A	N/A	96.4
RF93-77-414	OA	5 cm	55.35	0.67	17.04	5.61	0.15	1.75	4.70	3.17	7.90	N/A	N/A	N/A	N/A	96.4
RF93-77-414	OA	5 cm	57.10	0.60	16.99	4.53	0.12	1.17	3.78	3.75	8.29	N/A	N/A	N/A	N/A	96.3
RF93-77-414	OA	5 cm	59.23	0.42	17.24	3.09	0.09	0.60	2.51	4.18	8.75	N/A	N/A	N/A	N/A	96.1
RF93-77-414	OA	5 cm	58.37	0.41	17.56	3.36	0.16	0.77	2.82	3.52	9.13	N/A	N/A	N/A	N/A	96.1
RF93-77-414	OA	5 cm	55.07	0.67	17.08	5.17	0.13	1.74	4.95	3.36	7.91	N/A	N/A	N/A	N/A	96.1
RF93-77-414	OA	5 cm	57.97	0.46	17.76	3.77	0.13	0.78	3.02	4.08	8.09	N/A	N/A	N/A	N/A	96.1
RF93-77-414	OA	5 cm	58.44	0.49	17.37	3.54	0.15	0.72	2.77	3.41	9.13	N/A	N/A	N/A	N/A	96.0
RF93-77-414	OA	5 cm	56.12	0.52	17.10	4.64	0.28	1.45	4.42	3.30	8.09	N/A	N/A	N/A	N/A	95.9
RF93-77-414	OA	5 cm	59.64	0.36	17.05	2.66	0.10	0.48	2.13	3.84	8.75	N/A	N/A	N/A	N/A	95.0
RF93-77-414	OA	5 cm	59.11	0.40	17.27	2.76	0.09	0.42	2.13	4.31	8.39	N/A	N/A	N/A	N/A	94.9
RF93-77 450	OA	5 cm	62.50	0.60	18.65	2.71	0.15	0.39	1.20	7.08	6.51	N/A	N/A	N/A	N/A	99.8
RF93-77 450	OA	5 cm	61.08	0.65	19.00	2.85	0.22	0.37	1.10	8.03	6.18	N/A	N/A	N/A	N/A	99.5
RF93-77 450	OA	5 cm	62.59	0.51	18.23	2.56	0.04	0.46	1.25	6.98	6.74	N/A	N/A	N/A	N/A	99.4
RF93-77 450	OA	5 cm	62.15	0.55	18.67	2.49	0.21	0.36	1.11	7.22	6.61	N/A	N/A	N/A	N/A	99.4
RF93-77 450	OA	5 cm	61.47	0.58	18.61	2.56	0.26	0.29	1.08	8.30	5.97	N/A	N/A	N/A	N/A	99.1
RF93-77 450	OA	5 cm	62.20	0.52	18.67	2.55	0.15	0.35	1.20	7.09	6.33	N/A	N/A	N/A	N/A	99.1
RF93-77 450	OA	5 cm	62.04	0.59	18.46	2.72	0.19	0.35	1.16	7.03	6.43	N/A	N/A	N/A	N/A	99.0
RF93-77 450	OA	5 cm	62.60	0.58	17.82	2.54	0.25	0.39	1.28	6.99	6.44	N/A	N/A	N/A	N/A	98.9
RF93-77 450	OA	5 cm	61.75	0.60	18.67	2.33	0.24	0.37	1.17	6.81	6.62	N/A	N/A	N/A	N/A	98.6
RF93-77 450	OA	5 cm	61.21	0.66	18.80	2.76	0.26	0.30	1.07	7.36	6.03	N/A	N/A	N/A	N/A	98.4
RF93-77 450	OA	5 cm	61.59	0.48	18.45	2.53	0.13	0.41	1.29	6.85	6.54	N/A	N/A	N/A	N/A	98.3
RF93-77 450	OA	5 cm	60.48	0.55	18.89	2.83	0.18	0.29	0.99	8.08	5.85	N/A	N/A	N/A	N/A	98.1
RF93-77 450	OA	5 cm	60.38	0.52	18.53	2.71	0.15	0.28	0.99	8.52	5.96	N/A	N/A	N/A	N/A	98.0
RF93-77 450	OA	5 cm	60.84	0.57	18.79	2.43	0.24	0.28	1.10	7.63	5.95	N/A	N/A	N/A	N/A	97.9
RF93-77 450	OA	5 cm	60.76	0.60	18.30	2.62	0.25	0.26	1.07	7.98	5.99	N/A	N/A	N/A	N/A	97.8
RF93-77 450	OA	5 cm	60.13	0.49	18.18	3.05	0.18	0.44	2.25	4.67	8.31	N/A	N/A	N/A	N/A	97.7
RF93-77 450	OA	5 cm	60.62	0.55	18.78	2.72	0.21	0.35	1.18	6.84	6.41	N/A	N/A	N/A	N/A	97.7
RF93-77 450	OA	5 cm	62.04	0.58	17.41	2.39	0.27	0.35	1.27	6.84	6.45	N/A	N/A	N/A	N/A	97.6
RF93-77 450	OA	5 cm	60.26	0.54	18.63	2.52	0.16	0.22	1.00	8.10	6.05	N/A	N/A	N/A	N/A	97.5
RF93-77 450	OA	5 cm	61.26	0.52	18.01	2.56	0.15	0.39	1.23	6.64	6.62	N/A	N/A	N/A	N/A	97.4
RF93-77 450	OA	5 cm	60.40	0.61	18.40	2.57	0.26	0.30	1.18	7.13	6.42	N/A	N/A	N/A	N/A	97.3
RF93-77 450	OA	5 cm	60.43	0.64	18.35	2.49	0.20	0.31	1.16	7.27	6.41	N/A	N/A	N/A	N/A	97.3
RF93-77 450	OA	5 cm	61.04	0.50	18.27	2.46	0.21	0.35	1.21	6.76	6.43	N/A	N/A	N/A	N/A	97.2
RF93-77 450	OA	5 cm	60.86	0.55	18.37	2.36	0.20	0.38	1.14	6.79	6.29	N/A	N/A	N/A	N/A	96.9
RF93-77 450	OA	5 cm	60.27	0.53	18.78	2.59	0.19	0.37	1.23	6.83	6.14	N/A	N/A	N/A	N/A	96.9
RF93-77 450	OA	5 cm	60.34	0.56	18.30	2.43	0.25	0.41	1.19	6.82	6.32	N/A	N/A	N/A	N/A	96.6
RF93-77 450	OA	5 cm	60.76	0.56	18.26	2.47	0.18	0.37	1.25	6.31	6.45	N/A	N/A	N/A	N/A	96.6
RF93-77 450	OA	5 cm	59.57	0.53	18.31	2.55	0.20	0.28	1.03	7.06	5.93	N/A	N/A	N/A	N/A	95.5
RF93-77 450	OA	5 cm	58.93	0.54	17.90	2.43	0.26	0.38	1.18	7.22	6.45	N/A	N/A	N/A	N/A	95.3
RF93-77 540	E	5 cm	60.78	0.48	18.37	2.69	0.26	0.35	1.71	6.57	7.10	0.04	0.02	0.87	0.51	99.8

Name	Microprobe	Resolution	SiO_2	TiO_2	Al_2O_3	FeO	MnO	MgO	CaO	Na_2O	K_2O	P_2O_5	S	Cl	F	Total
RF93-77 540	E	5 cm	60.75	0.38	18.63	2.55	0.11	0.41	2.57	4.08	8.81	0.06	0.02	0.54	0.20	99.1
RF93-77 540	E	5 cm	57.06	0.59	18.40	4.26	0.14	1.12	3.82	4.00	8.22	0.21	0.05	0.55	0.25	98.7
RF93-77 540	E	5 cm	58.95	0.48	18.40	2.92	0.15	0.56	2.53	3.78	9.69	0.07	0.12	0.65	0.25	98.6
RF93-77 540	E	5 cm	57.85	0.52	18.73	3.61	0.12	0.75	2.75	4.28	8.78	0.12	0.05	0.68	0.24	98.5
RF93-77 540	E	5 cm	60.97	0.49	17.46	2.59	0.35	0.22	0.98	7.68	5.73	0.01	0.01	0.88	0.84	98.2
RF93-77 540	E	5 cm	56.68	0.58	18.57	4.01	0.15	1.05	3.60	4.03	8.01	0.21	0.14	0.59	0.23	97.8
RF93-77 540	E	5 cm	58.20	0.50	18.59	2.92	0.15	0.44	2.48	4.50	9.00	0.06	0.04	0.68	0.27	97.8
RF93-77 540	E	5 cm	60.42	0.49	17.26	2.56	0.33	0.21	1.00	7.65	5.81	0.02	0.00	0.88	0.82	97.4
RF93-77 540	E	5 cm	58.68	0.50	18.08	2.87	0.15	0.43	2.32	4.65	8.43	0.06	0.04	0.70	0.30	97.2
RF93-77 540	E	5 cm	60.37	0.70	17.54	2.25	0.25	0.36	1.05	7.17	6.25	0.04	0.07	0.68	0.37	97.1
RF93-77 540	E	5 cm	58.95	0.47	17.96	2.85	0.24	0.26	1.65	6.46	6.78	0.03	0.01	0.84	0.52	97.0
RF93-77 540	E	5 cm	60.62	0.44	17.79	2.30	0.15	0.41	1.33	6.06	6.98	0.06	0.09	0.37	0.18	96.8
RF93-77 540	E	5 cm	56.72	0.48	18.09	3.45	0.13	0.80	3.11	3.22	9.69	0.14	0.18	0.51	0.22	96.8
RF93-77 540	E	5 cm	61.03	0.42	16.37	2.22	0.22	0.20	1.45	6.07	6.63	0.02	0.00	0.90	0.64	96.2
RF93-77 540	E	5 cm	60.78	0.43	16.76	2.07	0.21	0.21	1.44	6.32	6.30	0.02	0.00	0.87	0.60	96.0
RF93-77 540	E	5 cm	58.10	0.45	17.43	2.47	0.14	0.41	2.12	4.34	8.13	0.06	0.03	0.71	0.30	94.7
RF93-77 540	E	5 cm	57.69	0.49	17.50	2.38	0.14	0.41	2.07	4.22	8.39	0.06	0.09	0.69	0.27	94.4
RF93-77 604	E	5 cm	61.78	0.68	18.23	2.63	0.27	0.31	1.19	7.96	6.36	0.05	0.08	0.76	0.43	100.7
RF93-77 604	E	5 cm	61.81	0.67	18.51	2.62	0.28	0.40	1.15	7.70	6.08	0.04	0.06	0.77	0.43	100.5
RF93-77 604	E	5 cm	61.34	0.67	18.03	2.46	0.27	0.29	1.07	7.80	6.63	0.03	0.06	0.74	0.41	99.8
RF93-77 604	E	5 cm	62.27	0.62	17.87	2.35	0.22	0.38	1.11	7.28	6.50	0.05	0.10	0.57	0.30	99.6
RF93-77 604	E	5 cm	60.19	0.47	18.66	2.81	0.24	0.32	1.66	6.50	7.17	0.04	0.01	0.86	0.51	99.4
RF93-77 604	E	5 cm	60.04	0.49	18.75	2.65	0.25	0.34	1.71	6.51	7.28	0.05	0.01	0.88	0.49	99.4
RF93-77 604	E	5 cm	99.39	0.00	-0.01	0.02	0.01	0.00	-0.03	0.01	0.01	0.00	0.00	0.01	-0.01	99.4
RF93-77 604	E	5 cm	61.26	0.68	18.01	2.32	0.27	0.31	1.03	7.80	6.33	0.05	0.09	0.73	0.38	99.3
RF93-77 604	E	5 cm	60.45	0.67	17.60	2.67	0.27	0.31	1.12	7.75	6.35	0.04	0.06	0.76	0.41	98.5
RF93-77 604	E	5 cm	58.22	0.41	18.61	3.54	0.11	0.83	2.92	4.17	8.48	0.14	0.20	0.45	0.21	98.3
RF93-77 604	E	5 cm	61.02	0.67	17.74	2.42	0.25	0.29	1.08	7.67	5.88	0.04	0.08	0.73	0.37	98.2
RF93-77 604	E	5 cm	59.58	0.69	17.88	2.53	0.25	0.33	1.11	7.26	6.32	0.05	0.09	0.69	0.32	97.1
RF93-77 604	E	5 cm	60.22	0.60	17.81	2.48	0.20	0.39	1.19	6.84	6.36	0.05	0.11	0.57	0.28	97.1
RF93-77 604	E	5 cm	59.90	0.59	17.48	2.49	0.26	0.26	1.12	6.83	6.81	0.03	0.06	0.76	0.36	96.9
RF93-77 604	E	5 cm	58.86	0.46	17.93	2.75	0.14	0.38	2.25	4.40	8.54	0.06	0.03	0.69	0.27	96.8
RF93-77 604	E	5 cm	59.49	0.59	17.92	2.28	0.20	0.37	1.23	6.70	6.55	0.05	0.11	0.57	0.27	96.3
RF93-77 604	E	5 cm	59.85	0.59	17.52	2.47	0.21	0.34	1.13	6.66	6.29	0.06	0.10	0.55	0.27	96.0
RF93-77 604	E	5 cm	57.97	0.47	17.52	2.60	0.15	0.39	2.23	4.55	8.41	0.06	0.10	0.72	0.24	95.4
RF93-77 790	OA	5 cm	58.27	0.47	19.17	3.76	0.21	0.73	2.38	4.97	8.60	N/A	N/A	N/A	N/A	98.6
RF93-77 790	OA	5 cm	57.81	0.43	19.16	4.00	0.15	0.81	2.96	4.76	8.44	N/A	N/A	N/A	N/A	98.5
RF93-77 790	OA	5 cm	58.41	0.45	19.08	3.73	0.06	0.76	2.64	4.76	8.59	N/A	N/A	N/A	N/A	98.5
RF93-77 790	OA	5 cm	58.09	0.50	18.55	3.91	0.20	0.86	3.15	4.55	8.32	N/A	N/A	N/A	N/A	98.1
RF93-77 790	OA	5 cm	57.42	0.40	18.80	4.14	0.22	0.82	2.86	4.74	8.57	N/A	N/A	N/A	N/A	98.0
RF93-77 790	OA	5 cm	58.65	0.37	18.82	3.23	0.07	0.64	2.70	4.46	8.70	N/A	N/A	N/A	N/A	97.6
RF93-77 790	OA	5 cm	57.74	0.44	19.12	3.80	0.11	0.71	2.65	4.74	8.31	N/A	N/A	N/A	N/A	97.6
RF93-77 790	OA	5 cm	57.64	0.35	19.24	3.69	0.10	0.77	2.88	4.55	8.31	N/A	N/A	N/A	N/A	97.5
RF93-77 790	OA	5 cm	57.68	0.45	18.79	3.81	0.17	0.75	2.71	4.86	8.19	N/A	N/A	N/A	N/A	97.4
RF93-77 790	OA	5 cm	58.22	0.35	18.68	3.63	0.04	0.70	2.81	4.10	8.86	N/A	N/A	N/A	N/A	97.4
RF93-77 790	OA	5 cm	57.83	0.42	18.86	3.57	0.15	0.71	2.58	4.64	8.37	N/A	N/A	N/A	N/A	97.2
RF93-77 790	OA	5 cm	57.63	0.44	18.80	3.78	0.15	0.77	2.70	4.42	8.38	N/A	N/A	N/A	N/A	97.1
RF93-77 790	OA	5 cm	56.65	0.45	18.27	4.26	0.13	1.08	3.15	4.98	8.04	N/A	N/A	N/A	N/A	97.0
RF93-77 790	OA	5 cm	57.22	0.43	18.62	3.78	0.23	0.85	2.95	4.35	8.38	N/A	N/A	N/A	N/A	96.8
RF93-77 790	OA	5 cm	56.74	0.41	18.41	4.00	0.14	1.09	3.22	4.49	8.11	N/A	N/A	N/A	N/A	96.6
RF93-77 790	OA	5 cm	57.61	0.44	18.55	3.74	0.08	0.84	2.99	4.23	8.07	N/A	N/A	N/A	N/A	96.6
RF93-77 790	OA	5 cm	57.78	0.43	18.63	3.71	0.20	0.70	2.30	4.51	8.27	N/A	N/A	N/A	N/A	96.5
RF93-77 790	OA	5 cm	56.65	0.42	18.50	3.74	0.22	0.78	3.01	4.53	8.53	N/A	N/A	N/A	N/A	96.4
RF93-77 790	OA	5 cm	56.49	0.40	18.63	3.89	0.26	0.81	2.81	4.58	8.23	N/A	N/A	N/A	N/A	96.1
RF93-77 790	OA	5 cm	57.19	0.41	18.83	3.26	0.21	0.69	2.30	4.94	8.16	N/A	N/A	N/A	N/A	96.0
RF93-77 790	OA	5 cm	57.26	0.38	18.43	3.41	0.12	0.68	2.51	4.94	7.99	N/A	N/A	N/A	N/A	95.7

Name	Microprobe	Resolution	SiO_2	TiO_2	Al_2O_3	FeO	MnO	MgO	CaO	Na_2O	K_2O	P_2O_5	S	Cl	F	Total
RF93-77 790	OA	5 cm	56.56	0.44	18.70	3.65	0.09	0.75	2.68	4.70	8.06	N/A	N/A	N/A	N/A	95.6
RF93-77 790	OA	5 cm	56.82	0.38	18.41	3.74	0.12	0.71	2.74	4.68	8.00	N/A	N/A	N/A	N/A	95.6
RF93-77 790	OA	5 cm	56.41	0.44	18.42	3.71	0.23	0.88	2.71	4.77	7.85	N/A	N/A	N/A	N/A	95.4
RF93-77 790	OA	5 cm	55.93	0.38	18.74	3.66	0.14	0.64	1.61	5.95	8.28	N/A	N/A	N/A	N/A	95.3
RF93-77 790	OA	5 cm	56.20	0.39	18.76	3.53	0.06	0.71	2.56	4.97	8.12	N/A	N/A	N/A	N/A	95.3
RF93-77 790	OA	5 cm	55.24	0.41	18.82	3.72	0.10	0.83	3.01	4.86	8.04	N/A	N/A	N/A	N/A	95.0
RF93-77 790	OA	5 cm	55.79	0.41	18.49	3.68	0.21	0.80	2.79	4.51	7.94	N/A	N/A	N/A	N/A	94.6
RF93-77 790	OA	5 cm	58.27	0.47	19.17	3.76	0.21	0.73	2.38	4.97	8.60	N/A	N/A	N/A	N/A	98.6
RF93-77 790	OA	5 cm	57.81	0.43	19.16	4.00	0.15	0.81	2.96	4.76	8.44	N/A	N/A	N/A	N/A	98.5
RF93-77 790	OA	5 cm	58.41	0.45	19.08	3.73	0.06	0.76	2.64	4.76	8.59	N/A	N/A	N/A	N/A	98.5
RF93-77 790	OA	5 cm	58.09	0.50	18.55	3.91	0.20	0.86	3.15	4.55	8.32	N/A	N/A	N/A	N/A	98.1
RF93-77 790	OA	5 cm	57.42	0.40	18.80	4.14	0.22	0.82	2.86	4.74	8.57	N/A	N/A	N/A	N/A	98.0
RF93-77 790	OA	5 cm	58.65	0.37	18.82	3.23	0.07	0.64	2.70	4.46	8.70	N/A	N/A	N/A	N/A	97.6
RF93-77 790	OA	5 cm	57.74	0.44	19.12	3.80	0.11	0.71	2.65	4.74	8.31	N/A	N/A	N/A	N/A	97.6
RF93-77 790	OA	5 cm	57.64	0.35	19.24	3.69	0.10	0.77	2.88	4.55	8.31	N/A	N/A	N/A	N/A	97.5
RF93-77 790	OA	5 cm	57.68	0.45	18.79	3.81	0.17	0.75	2.71	4.86	8.19	N/A	N/A	N/A	N/A	97.4
RF93-77 790	OA	5 cm	58.22	0.35	18.68	3.63	0.04	0.70	2.81	4.10	8.86	N/A	N/A	N/A	N/A	97.4
RF93-77 790	OA	5 cm	57.83	0.42	18.86	3.57	0.15	0.71	2.58	4.64	8.37	N/A	N/A	N/A	N/A	97.2
RF93-77 790	OA	5 cm	57.63	0.44	18.80	3.78	0.15	0.77	2.70	4.42	8.38	N/A	N/A	N/A	N/A	97.1
RF93-77 790	OA	5 cm	56.65	0.45	18.27	4.26	0.13	1.08	3.15	4.98	8.04	N/A	N/A	N/A	N/A	97.0
RF93-77 790	OA	5 cm	57.22	0.43	18.62	3.78	0.23	0.85	2.95	4.35	8.38	N/A	N/A	N/A	N/A	96.8
RF93-77 790	OA	5 cm	56.74	0.41	18.41	4.00	0.14	1.09	3.22	4.49	8.11	N/A	N/A	N/A	N/A	96.6
RF93-77 790	OA	5 cm	57.61	0.44	18.55	3.74	0.08	0.84	2.99	4.23	8.07	N/A	N/A	N/A	N/A	96.6
RF93-77 790	OA	5 cm	57.78	0.43	18.63	3.71	0.20	0.70	2.30	4.51	8.27	N/A	N/A	N/A	N/A	96.5
RF93-77 790	OA	5 cm	56.65	0.42	18.50	3.74	0.22	0.78	3.01	4.53	8.53	N/A	N/A	N/A	N/A	96.4
RF93-77 790	OA	5 cm	56.49	0.40	18.63	3.89	0.26	0.81	2.81	4.58	8.23	N/A	N/A	N/A	N/A	96.1
RF93-77 790	OA	5 cm	57.19	0.41	18.83	3.26	0.21	0.69	2.30	4.94	8.16	N/A	N/A	N/A	N/A	96.0
RF93-77 790	OA	5 cm	57.26	0.38	18.43	3.41	0.12	0.68	2.51	4.94	7.99	N/A	N/A	N/A	N/A	95.7
RF93-77 790	OA	5 cm	56.56	0.44	18.70	3.65	0.09	0.75	2.68	4.70	8.06	N/A	N/A	N/A	N/A	95.6
RF93-77 790	OA	5 cm	56.82	0.38	18.41	3.74	0.12	0.71	2.74	4.68	8.00	N/A	N/A	N/A	N/A	95.6
RF93-77 790	OA	5 cm	56.41	0.44	18.42	3.71	0.23	0.88	2.71	4.77	7.85	N/A	N/A	N/A	N/A	95.4
RF93-77 790	OA	5 cm	55.93	0.38	18.74	3.66	0.14	0.64	1.61	5.95	8.28	N/A	N/A	N/A	N/A	95.3
RF93-77 790	OA	5 cm	56.20	0.39	18.76	3.53	0.06	0.71	2.56	4.97	8.12	N/A	N/A	N/A	N/A	95.3
RF93-77 790	OA	5 cm	55.24	0.41	18.82	3.72	0.10	0.83	3.01	4.86	8.04	N/A	N/A	N/A	N/A	95.0
RF93-77 790	OA	5 cm	55.79	0.41	18.49	3.68	0.21	0.80	2.79	4.51	7.94	N/A	N/A	N/A	N/A	94.6